Graph-based modelling and hierarchical distributed control design for decentralized high-pressure pumps

Stefan Josef Niederberger

UNIVERSITÉ HAUTE-ALSACE

École doctorale MSII — ED 269

Graph-based modelling and hierarchical distributed control design for decentralized high-pressure pumps

THÈSE

présentée et soutenue publiquement le 19 December 2019

pour l'obtention du

Doctorat de l'Université de Haute-Alsace

(mention automatique)

par

Stefan Josef NIEDERBERGER

Composition du jury

Président :	Pr Didier THEILLIOL	Laboratoire CRAN – Univ. de Lorraine
Rapporteurs :	Dr Luc DUGARD	Laboratoire Gipsa-Lab – Univ. Grenoble Alpes
	Pr Eric BIDEAUX	Laboratoire Ampère – INSA Lyon
Examinateur :	Pr Didier THEILLIOL	Laboratoire CRAN – Univ. de Lorraine
Invités :	Pr Roland ANDEREGG	Institute of Automation – FHNW Windisch
	M. Patrick BAUMANN	Zaugg Maschinenbau AG
	M. Peter REINBOLD	Jet Cut Power GmbH
Directeur de thèse :	Pr Michel BASSET	Institut IRIMAS – Univ. de Haute-Alsace
Co-encadrants :	Mcf Rodolfo ORJUELA	Institut IRIMAS – Univ. de Haute-Alsace
	Pr Pascal SCHLEUNIGER	Institute of Automation – FHNW Windisch

Mis en page avec la classe thesul.

Acknowledgments

The work presented in this manuscript has been established in collaboration with the team MIAM (Modélisation et Identification en Automatique et Mécanique) at the UHA and the IA (Institute of Automation), an institute of the FHNW. It has been employed for industries, namely zmb watercut and Jet Cut Power, and funded by the InnoSuisse.

The three years of research has been an intensive experience. Managing the diverging interests of industry and academics has been quite challenging but offered many opportunities to evolve personal competences. I spent most of the time with the IA, where the test bench has been located. However, the collaboration with the MIAM has always been extraordinary. I had the chance to meet kind and always interested people at the universities, during the formations and at the conferences. The rich exchange helped truly to evolve this research. Eventually, I look back at many interesting discussions and I am very happy for all the support I've received at the very different assignments. I would like to thank all the people who contributed to this work.

I address my thanks to all jury members for evaluating and verifying the rather large manuscript. I am very grateful for the favorable reviews and for the motivating feedbacks from Luc Dugard, concerning the robust control, as well as from Eric Bideaux, regarding the modelling of fluid flow systems. Equally great thanks to Didier Theilliol who took the double-roles as exterminator and president. I have been happy to hear about the great interests for enhancing the work presented. In any case, thanks for their personal participation. It has been a great pleasure to meet these specialists.

I would like to express my sincere reconnaissance to Michel Basset, a great patron, and Rodolfo Orjuela, a great supporter. Their steady care and understanding enabled this manifold manuscript and various other publications. Both relied on my person and promoted my PhD at the UHA. All the unconstrained discussions improved my scientific work. Their theoretical and, even more, their human competences taught me a balanced approach of working. I am also very thankful for all the delightful friendships and enriching encounters with the MIAM. The only thing I regret is not to have spent more time at the UHA during this period.

I am equivalent grateful for the employment at the FHNW. The rich research work, the chance to participate for lecturers and to supervise students allowed me to attain complementary competences. I have especially to thank Roland Anderegg for his constant benevolence during all the years and for supporting the various conferences as well as to Pascal Schleuniger for the many helpful advises, for all organizational efforts and for the detailed revision of my manuscript. I like to thank Sebastian Gaulocher, who initiated the collaboration between UHA and FHNW, for its theoretical advises and Thomas Besselmann for the revision of a paper. Here, I must thank Sandro Born, Martin Hunziker and Markus Birchmeier as steady supporters of the test bench and for supplying all needs at the laboratory.

Thanks to the industries Toni Zaugg, Patrick Baumann and Sascha Niggli from zmb waterjet as well as Peter Reinbold, Mathias Kennel and Daniel Lustenberger from Jet Cut Power for the fruitful cooperation by establishing a test bench and building the high-pressure pump prototypes. This allowed to validate the work as presented in this manuscript. Also, the very best to Pascal Zeugin, Jean-Paul John, Daniel Begert, Jan Gebhardt and all the students involved for deriving measurements at the test bench and realizing experiments.

Finally, my reconnaissance to Mélanie Gaugler and Betty Labigang at the administration of the UHA as well as to Silvia Rüegger and Hanny Gerber at the administration of the FHNW to satisfy all needs for my PhD and the related industrial project. The remarkable benevolent of the MIAM and IA has enabled this transnational collaboration.

Contents

General introduction

Motivation

In the recent years, increasing the energy efficiency has become a major objective for industry. The large energy demand for waterjet machining motivates to investigate novel concepts for high-pressure generation. Conventional high-pressure pumps for waterjet machining are driven by means of hydraulic drives. The latest developments of electrical direct drives with high-torque servo motors allow for replacing these hydraulic drives. This significantly improves the energy efficiency of high-pressure pumps.

In contrast to hydraulically driven pumps, electrically driven pumps can be flexibly combined and spatially distributed, taking the individual demands of entire waterjet facilities into account. This results in scalable high-pressure networks of decentralized pumps and interconnected work stations, which enables industry to improve the overall energy efficiency of waterjet machining.

However, these decentralized pumps require a control and managing strategy, which has to be easily adapted to the various waterjet facilities in compliance with Industry 4.0. This aims at reducing the installation time for high-pressure pumps and simplifying the maintenance of waterjet facilities. The managing enables an optimal allocation of the available pumps with respect to the time-varying demands of waterjet machining. It will reduce wear and degradation, when every pump collaborates within a high-pressure network to run at a desired operating point. The subsequent work addresses these challenges to establish a flexible and sustainable waterjet machining by means of Industry 4.0.

Energy efficient high-pressure pump

In most cases, a conventional high-pressure pump supplies a single work station as shown in the illustration of Figure 1. A high-pressure pipe directly interconnects a hydraulically driven pump and a work station. The pump pressurizes water by means of two pressure intensifiers, where the work station holds a cutting head producing a waterjet. Abrasive added to the waterjet allows for cutting of hard and brittle materials. Introducing an example for waterjet cutting, a typical operating pressure of 400 MPa and its water consumption of about 5 l/min result in an energy demand of about 33.3 kW per work station.

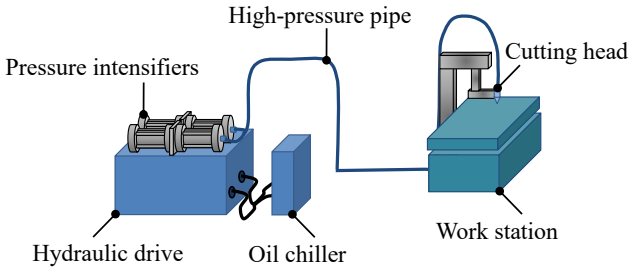

Figure 1 – Common setup for waterjet machining: a hydraulically driven high-pressure pump supplies a single work station.

Insofar as waterjet machining is an energy intensive process, any increase of efficiency attains significant energy savings. The hydraulic drive can be identified as a major source of losses with its energy efficiency of typically below 70%. The above example results in a drive input power of at least 47.6 kW. Thus, replacing the hydraulic drive aims at improving the energy efficiency of high-pressure pumps. Moreover, it will enhance the utilization of waterjet machining and yields new applications in fields, where hydraulics is proscribed to avoid contamination, e.g. food industry and medical treatments.

For these reasons, different manufacturers investigate energy efficient high-pressure pumps. They intent to replace the hydraulic drive system by electric servo drives. The illustration of Figure 2 compares a hydraulically driven pump (a) to an electrically driven pump (b). The novel pump design introduces modular piston pumps. Its pumping units consist of an independent electric drive which displaces a piston by means of a spindle shaft. In this case, combining two pumping units allows for a continuous pressure generation. Using electric servo drives, with its efficiency of above 90%, reduces the energy demand of waterjet machining. With respect to the previous example, this decreases the expected drive input power to 37.0 kW. That corresponds to energy savings of up to 10.6 kW (22.2%), which results in an annual saving of 33.9 MWh for a two-shift pump operation. Moreover, implementing an electric drive further reduces the pump size by 40% and decreases the noise level.

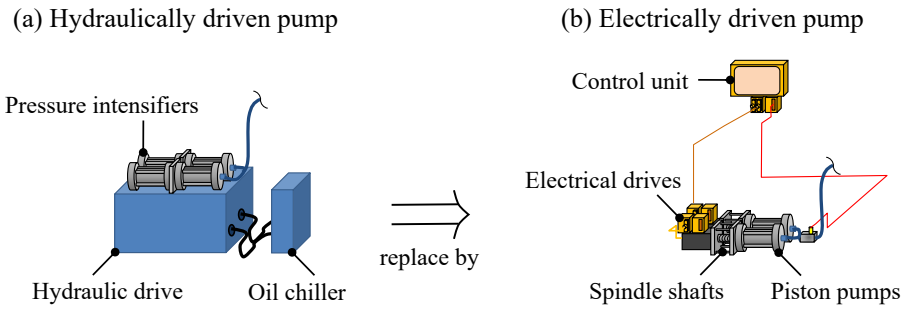

Figure 2 – Energy efficient high-pressure pump: replacing hydraulically driven pressure intensifiers by electrically driven piston pumps.

Apart from efficiency concerns, waterjet machining is subject to ongoing enhancements in cutting quality. Waterjet machining requires to attenuate pressure fluctuations for more than 20 dB by means of the available high-pressure pumps. These fluctuations originate from work stations when switching on and off a cutting head with respect to the cutting process. This switching causes a varying water consumption and consequently induces pressure fluctuations, which propagate across the high-pressure piping. Since the hydraulic drive of a conventional high-pressure pump acts as an attenuator, pressure fluctuations become sufficiently rejected as long as the pump remains at its predefined operating point. Additional high-pressure attenuators, installed to the piping system, reduce pressure fluctuations and improve cutting quality. However, these attenuators are costly and subject to fast degradation.

Energy efficient high-pressure pumps come along with a major drawback. Pressure fluctuations cause a time-varying load cycle acting on the spindle shafts and instantaneously affecting the electric drives. Thus, effective disturbance rejection by means of high-pressure pumps becomes a challenging task for control and involves high performance motion dynamics. In fact, an electric drive has to reproduce the disturbance rejection characteristics of a hydraulically driven pump. Whereas the novel pump design reduces the drive system complexity, its control design must meet enhanced requirements. Overcoming these difficulties allows for an electrically driven pump to run at any pressure range without additional high-pressure attenuators. This thesis provides a low-level control design for energy efficient high-pressure pumps that aims at robust disturbance rejection. It is further expected to deal with the degradation of electrically driven pumps and to reduce the wear due to pressure fluctuations.

Energy efficient waterjet facilities

A hydraulically driven pump is difficult to scale with respect to the increased water consumption of interconnection work stations. Scaling the size of a pressure intensifier will, indeed, allow for a higher pump rate, but equally increase the load acting on the pistons. This will degrade its live cycle and deteriorate the energy efficiency what is limiting the maximal size of a single high-pressure pump. The illustration of Figure 3 presents exemplarily a waterjet facility with several work stations. The pump size, its noise level and heat dissipation require a hydraulically driven pump to be located in a remote machine room. Interconnecting all work stations of a facility results in long high-pressure pipes, which further decreases the overall energy efficiency.

On the other hand, an electrically driven pump is modular. This allows for scaling a waterjet facility with respect to the individual demands. Moreover, the reduced pump size and minimal noise level enable the distribution of high-pressure pumps at different locations in a waterjet facility, as shown in the illustration of Figure 4. Decentralized pumps supply several work stations according to their water consumption. The high-pressure piping interconnects pumps and work stations to realize a scalable high-pressure network. This reduces the overall piping lengths and aims to optimize the energy efficiency of entire waterjet facilities.

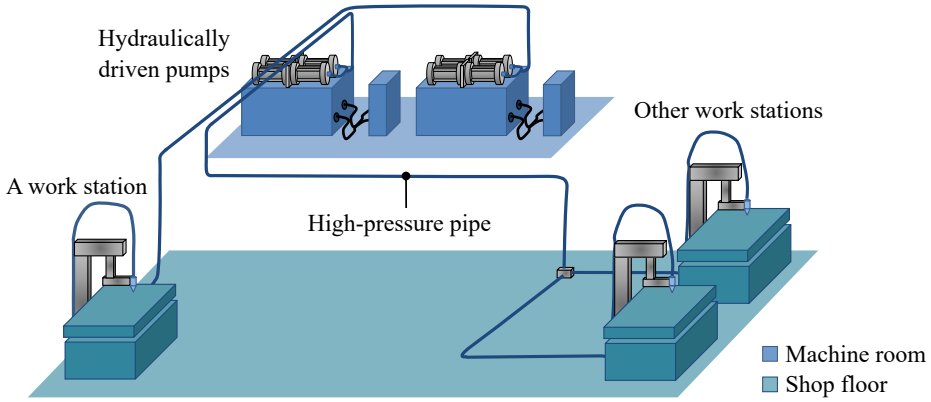

Figure 3 – Conventional waterjet facility: remote hydraulically driven pumps interconnected to work stations, using long high-pressure pipings.

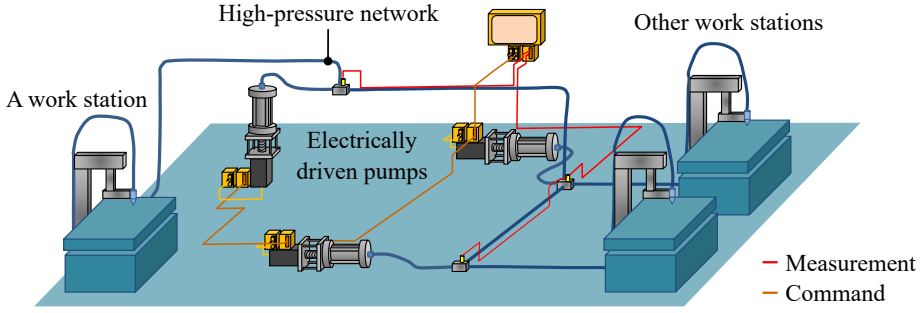

Figure 4 – Future waterjet facility: distributed electrically driven pumps interconnected to work stations, resulting in a high-pressure network.

This new concept of decentralized high-pressure pumps requires a control concept that provides a flexibility and scalability taking the wide variety of high-pressure networks into account to realize future waterjet facilities. Pressure fluctuations will propagate through the high-pressure network, causing time-varying load cycles on the decentralized pumps. This load will vary for every pump. It depends on the network topology, the pump locations and the switching state of each work station. As a consequence, each pump will obtain a different pump rate.

For example, an inferior pump runs close to its lower saturation, while an other superior pump will reach its upper saturation, providing the major fluid flow. Neither of the two pumps will operate on an energy efficient operating point and the superior pump will suffer a decrease of its life cycle. Even worse, this significantly deteriorates the capability to attenuate pressure fluctuations. Every pump, if running close to saturation, has insufficient margins to increase its pump rate when needed. Instead of all interconnected pumps to contribute for disturbance rejection, only the remaining inferior pumps respond as desired. This will reduce the overall available control effort and consequently degrade the control performance for disturbance rejection.

Moreover, it becomes possible that distributed pumps counteract against each others due to their coupling over the high-pressure network, since a pump itself may induce pressure fluctuations. Neighbouring pumps will compensate these additional fluctuations, which however increases the overall energy demands of a waterjet facility. As a consequence, decentralized pumps should cooperate to balance the overall control effort, whereas each pump should provide robust performance and stability for its local region. Hence, this thesis investigates a distributed high-level managing that ensures a flexible and scalable application to unique high-pressure networks of various waterjet facilities.

Objectives

The energy efficient high-pressure pumps are modular due to their electric drives and flexible to deal with the individual water consumption of different facilities. Enabling sustainable waterjet machining requires to deal with complex high-pressure networks of arbitrary topology, for which the number of interconnected pumps and work stations are most likely different and vary for every facility. Independent work stations induce pressure fluctuations when switching their cutting heads with respect to an unknown switching pattern and the coupling of decentralized pumps may degrade the overall energy efficiency if a global managing strategy is missing. However, industry dislikes to establish a centralized pump supervisor. In a typical waterjet facility, each high-pressure pump is locally controlled without any command from supervisory level. Thus, a pump operates autonomously and serves the demand of a work station. This autonomy should remain unchanged when introducing high-pressure networks with interconnected pumps. All of this requires a control design that reduces the engineering effort when setting up future waterjet facilities and that guarantees a reliable and energy efficient pump operation even for high-pressure networks of arbitrary topology and varying water consumption.

In order to deal with the previous objectives, this thesis aims to employ a hierarchical distributed control design that allocates the control task to two layers: a low-level control that has to reject any local pressure fluctuations by means of the available high-pressure pumps and a high-level managing that has to balance the pump rates to converge to a global average value. The hierarchical allocation of disturbance rejection and pump rate balancing should guarantee a reliable and energy efficient pump operation, while the physical distribution among all available pumps ensures its scalability. This requires each decentralized pump to execute exactly the same algorithm, while exchanging information.

Any efficient evaluation and verification of a hierarchical distributed control design requires a modelling methodology that is flexible to describe high-pressure networks of arbitrary topology, while taking a wide range of operation into account. Waterjet machining involves a wide pressure range from 40 to 400 MPa and includes non-linearities, whereas high-pressure pumps as well as work stations are subjects to parameter variations. Besides describing the pressure propagation along a piping, using the governing equations from fluid dynamics, high-pressure network of various topology will be represented by means of graphs. It is further required to identify and classify the expected range of parameter variations. Modelling and control design must then consider the most prevalent varying parameters.

This thesis provides a framework for modelling of high-pressure networks and employs a robust control design for decentralized pumps. The modelling methodology and control design are essential for establishing decentralized pumps and enhancing energy efficient waterjet facilities. A test bench has been built in the laboratory at the FHNW, in order to validate the modelling methodology and to verify the low-level control design. The verified modelling framework has been used to model more complex topologies, which allows for evaluating the high-level managing by means of simulations. The main contribution is given when applying the graph-based modelling methodology to high-pressure networks and evaluating the hierarchical distributed control design for decentralized pumps. This framework contributes to the latest research work and developments in waterjet machining with a specific emphasis to recent industrial perspectives.

Work context

The manufacturer Jet Cut Power GmbH produces conventional hydraulically driven high-pressure pumps, where Zaugg Maschinenbau AG (zmb) engineers automated work stations, e.g. for waterjet machining. The University of Applied Sciences and Arts Northwestern Switzerland (FHNW) developed in collaboration with the above mentioned industrial partners an energy efficient high-pressure pump. This electrically driven pump challenges the major cause of energy loss by replacing the hydraulic drives of conventional high-pressure pumps. It is highly scalable and flexible to equip various waterjet facilities. Consequently, a research cooperation has been established to investigate novel concepts for energy efficient waterjet machining.

The diagram of Figure 5 provides insight into the collaboration between industrial and research partners. This research has been founded by Swiss Innovation Agency (Innosuisse). It aims to develop a hierarchical distributed control design applied on high-pressure networks used for waterjet machining. This design procedure should reduce engineering efforts when setting up future waterjet facilities and guarantee a reliable pump operation even for high-pressure networks of arbitrary topology. The electric drive has been particularly developed in collaboration with other third parties from the industry.

This thesis has originated from an academic collaboration between the Institut de Recherche en Informatique, Mathématiques, Automatique et Signal (IRIMAS) from the Université de Haute-Alsace (UHA) in Mulhouse, France and the Institute of Automation (IA) from the FHNW in Windisch, Switzerland. Both institutes have specific knowledge in modelling and control of dynamic systems. These complementary competences become united to advance the research activities for future waterjet facilities.

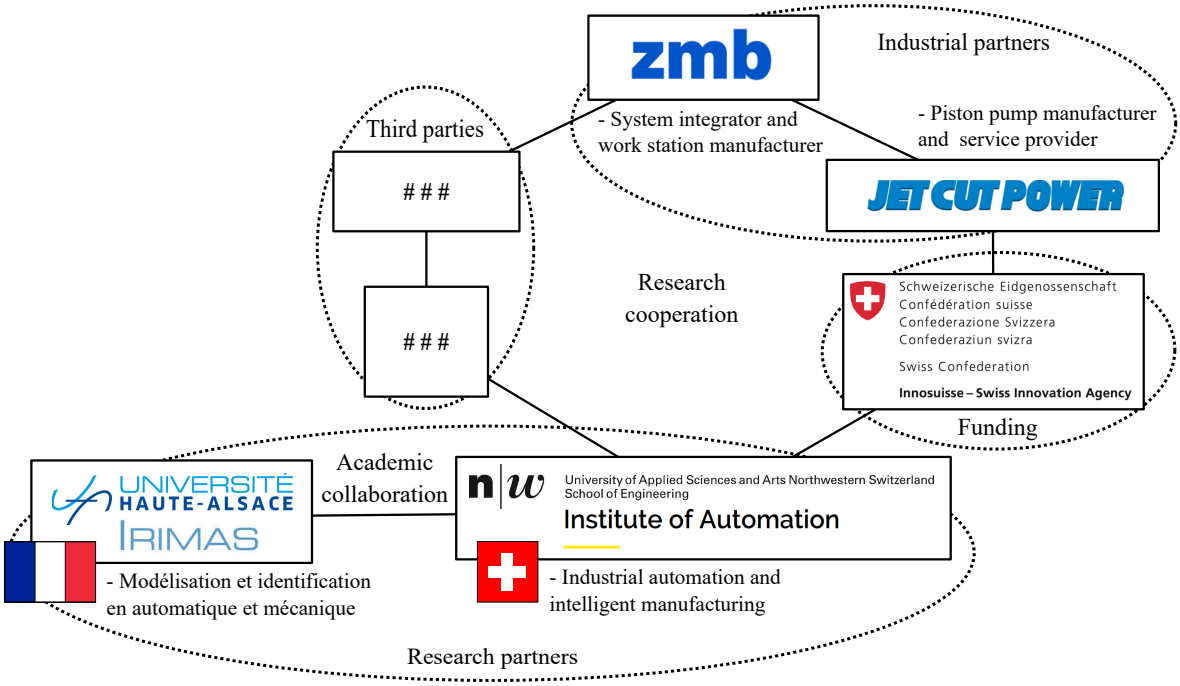

Figure 5 – Research cooperation and academic collaboration: industrial and research partners to investigate novel concepts for energy efficient waterjet machining.

Thesis outline and Contribution

This thesis is organized in three parts. **Part I** is dedicated to the practical application of waterjet machining. It provides information to obtain requirements for modelling and control design. **Part II** introduces a modelling framework employed for future waterjet facilities. The derived models are validated by means of measurements. **Part III** investigates the robust control design for high-pressure pumps and gives a perspective to distributed managing.

Part I: Waterjet machining

The investigations of **Chapter 1** introduce typical waterjet facilities and overview conventional waterjet machining. This allows for classifying waterjet machining with respect to common waterjet applications, manufacturing processes, and work station setups. The basic principle of high-pressure generation is then explained when comparing hydraulically and electrically driven pumps. It classifies the high-pressure pumps with respect to drive system and pumping chamber design. These classifications allow for deriving specifications for future energy efficient and scalable waterjet facilities. The system description of **Chapter 2** specifies use cases and introduces network topologies, while presenting the high-pressure test bench. This test bench has been explicitly built for these subsequent investigations. Selected high-pressure networks will be subject for modelling, where use cases aim at verifying the modelling methodology, validating the low-level control design and evaluating the high-level managing. Apart from that, this section discusses the novel design of an electrically driven pump, as installed on the test bench. It introduces the system components, its control structure and the concept of model-based synchronization by means of camming.

A first contribution in this part provides the state of the art for waterjet machining. This allows to classify the various waterjet applications with respect to the work station setup, cutting head configuration and manufacturing process. That further involves to establish a high-pressure test bench and to introduce the design of a novel electrically driven high-pressure pump [Niederberger and Kurmann, 2017]. Network topologies and use cases are defined, which consider common waterjet applications. Extending these specifications contributes to the design of future energy efficient and scalable waterjet facilities. Another contribution is given when applying the model-based synchronization to the pump prototypes [Niederberger, 2018]. This eventually allows for considering a high-pressure pump as a continuous source of fluid flow that facilitates the low-level control design.

Part II: Modelling framework

The **Chapter 3** is dedicated to derive a graph-based modelling methodology. The governing equations describing fluid dynamics has been approximated by means of finite differences, while considering fluid flow at equilibrium. This yields a lumped parameter model that represents a piping section by means of homogeneous segments. Mapping these segments to a graph allows for a flexible and scalable representation of high-pressure networks with arbitrary topologies. A simulation study verifies the computational efforts and resulting simulation accuracy due to approximations and spacial discretization. In contrast to established modelling approaches, the graph-based modelling methodology employs a pressure-dependent bulk modulus and relates this to a pressure-dependent fluid density. This improves the simulation accuracy for a wide pressure range from 40 to 400 MPa. Pressure-dependent parameters as well as fluid flow characteristics have been identified using the high-pressure test bench. This allows for scaling a high-pressure network model without revising its parametrization. The implementation of the graph-based modelling methodology in *MATLAB Simulink* provides a toolbox that simplifies the modelling of future waterjet facilities and avoids cost intensive experiments at a test bench. **Chapter 4** shows the application of this toolbox to model various networks topologies by means of graphs. These high-pressure network models reduce the time expanses for validating the low-level control design and evaluating the high-level managing. Experimental studies validate the graph-based modelling by means of measurements using a test bench.

In this part, a first contribution is given by proposing a graph-based modelling methodology for high-pressure networks, which includes the most prevalent parameter variations to deal with the wide pressure range of waterjet machining. This graph-based modelling has been published in [Niederberger et al., 2018]. Another contribution is given when introducing a toolbox by implementing the graph-based modelling into *MATLAB Simulink* and providing an experimental parameter identification for specific high-pressure components. This toolbox is valuable for industry and allows for modelling of various waterjet facilities without the need for an individual parametrization. Applying this toolbox to model different high-pressure networks and validating the obtained network models, using the measurement data from a test bench, demonstrate the benefits of a graph-based modelling but also reveal its limitations. Promising results have been presented in [Niederberger et al., 2019c].

Part III: Control design

The **Chapter 5** is dedicated to the robust low-level control design for decentralized high-pressure pumps. It considers the unknown switching of work stations and the interaction between neighbouring pumps as exogenous disturbances to the network subsection, while taking non-linearities

and uncertain parameters into account to obtain robust performance and stability for a wide range of operation. Introducing a linearised perturbed plant model to describe a network subsection for control design allows for a sensitivity analysis of parameter variations by means of simulations and for comparing different complex uncertainty descriptions. The control requirements for a high-pressure pump are specified with respect to the needs for waterjet machining. An electrically driven high-pressure pump is investigated to define the generalized plant for H_∞ controller synthesis. A signal-based approach introduces shaping functions on the input channel and weighting functions on the output channel considering the expected signal dynamics and control requirements. The investigations of **Chapter 6** propose to aggregate shaping functions by merging their singular values with respect to the Euclidean vector norm. That reduces the dimension of the H_∞ optimization problem for controller synthesis and results in a reduced-order state feedback controller. Employing a structured controller synthesis yields a suboptimal robust PI controller, suitable for industrial use. Robustness analysis allows for determining the permissible network subsection size for which a high-pressure pump guarantees desired performance and stability. This leads to an iterative procedure that maximizes the uncertainty range, while synthesizing a quasi-optimal PI controller. The proposed Δ-K iteration preserves the order of a generalized plant. It is therefore suitable when using unstructured uncertainties and employing a structured controller synthesis. Simulations verify the reduced state feedback controller and the quasi-optimal PI controller, using detailed high-pressure network models. A preliminary PI controller has been implemented to the electrically driven pump for experimental validation on the test bench. The robust control of a single high-pressure pump is an important milestone for the industrial implementation. Simulations of decentralized pumps, interconnected by means of a high-pressure network, show that these pumps will run at arbitrary pump rates if any high-level managing is missing. Many approaches become available to manage electrically driven pumps. The investigations of **Chapter 7** present the application of average consensus to balance distributed pumps without explicitly implementing a control law. This causes each pump to converge to the time-varying average pump rate, while considering information from neighbouring pumps. Simulations reveal the ability of the high-level managing to balance interconnected pumps to a common pump rate, which corresponds to the average overall water consumption. That provides a perspective for further developments towards energy efficient waterjet facilities.

The contribution here provides suitable shaping and weighting functions, when considering a signal-based approach to introduce a robust control design for decentralized high-pressure pumps. This requires to verify different system descriptions and to introduce a suitable uncertainty model, considering the varying parameters. A major contribution is given, when merging input channels by means of joint shaping functions [Niederberger et al., 2019b]. This reduces the dimension of the generalized plant, implemented for control design. Another contribution is provided, when applying H_∞ controller synthesis to derive controllers of different structures and comparing these controllers by means of a detailed simulation study. An extended PI controller has been found suitable for implementation on a high-pressure pump with respect to industrial needs. The robust control design reduces the effort for installing a pump in a facility. Another contribution is given when proposing the Δ-K iteration. This gives a practical use and provides a straight forward procedure for a quasi-optimal H_∞ controller synthesis. The concept of distributed balancing by means of average consensus gives eventually a perspective to the managing of interconnected pumps [Niederberger et al., 2019a].

The hierarchical distributed control design for electrically driven high-pressure pumps provides a versatile framework, including modelling of high-pressure networks and control design of decentralized pumps. This aims at the implementation of Industry 4.0 capabilities to enhance the operation of future waterjet facilities.

Publications

International

1. Niederberger, S., Orjuela, R., Schleuniger, P., Anderegg, R., and Basset, M. (2018). A graph-based modelling methodology for high-pressure networks applied on waterjet machining. *Mechatronics*, 55(1):115 – 128.

2. Niederberger, S., Orjuela, R., and Basset, M. (2019b). Robust control design for electrically driven high-pressure pumps using H_∞ approach with joint shaping functions. In *Proceedings of the 18th European Control Conference (ECC)*, pages 459 – 464, Naples, Italy.

3. Niederberger, S., Orjuela, R., Schleuniger, P., Anderegg, R., and Basset, M. (2019c). Extended validation of a graph-based modelling methodology for high-pressure networks. In *Proceedings of the 8th IFAC Symposium on Mechatronic Systems*, pages 488 – 493, Vienna, Austria.

4. Niederberger, S. and Basset, M. (2019). A graph-based modelling methodology for high-pressure networks applied on waterjet machining. In *Proceedings of the 10th International Workshop for Optimization in Logistics and Industrial Applications (IWOLIA)*, pages –, Bordeaux, France.

5. Niederberger, S., Orjuela, R., Schleuniger, P., Anderegg, R., and Basset, M. (2020). Distributed managing of decentralized high-pressure pumps using dynamic average consensus. *Control Engineering Practice*, -(-):(submitted).

National

6. Niederberger, S. and Kurmann, L. (2017). Hochdruckwasserstrahlschneiden mit energieeffizienten Hochdruckpumpen. *Tätigkeitsbericht 2016 Institut für Automation*, pages 18 – 20. University of Applied Sciences and Arts Northwestern Switzerland.

7. Niederberger, S. (2018). Energieeffiziente Hochdruckpumpe für einen flexiblen Einsatz in der Wasserstrahlbearbeitung. *Tätigkeitsbericht 2017 Institut für Automation*, pages 40 – 42. University of Applied Sciences and Arts Northwestern Switzerland.

8. Niederberger, S., Orjuela, R., and Basset, M. (2019a). Modelling and hierarchical control design for decentralized high-pressure pumps. In *Proceedings of the 2019 Journées Nationales en Modélisation, Analyse et Conduite des Systèmes dynamiques GDR MACS*, pages –, Mulhouse, France.

9. Niederberger, S. (2020). Graphen-basierte Modellierung und hierarchisch verteilte Regelung dezentraler Hochdruckpumpen. *Tätigkeitsbericht 2019 Institut für Automation*, pages 8 – 9. University of Applied Sciences and Arts Northwestern Switzerland.

Nomenclature

Distributed pumps interconnected to a high-pressure network are subject for subsequent investigations. Applying modelling and control design requires to introduce a set of different indexes. It is outlined that a high-pressure network interconnects N pumps, denoted by $n \in \{1, ..., N\}$, with M cutting heads, denoted by $m \in \{1, ..., M\}$. Each pump n is assigned to an agent $i \in \{1, ..., N\}$, subject for managing. On the other hand, a high-pressure network $\mathcal{N}_{kj}$ holds nodes $k \in J$ interconnected to other nodes $j \in J \setminus k$ by means of branches. The network topology will be represented by a graph $\mathcal{G} = (\mathcal{V}, \mathcal{E})$ that consists of nodes $v \in \mathcal{V}$ and branches $e \in \mathcal{E}$. It is also useful to distinguish between physical variables used for modelling (see Chapter 3), such as pressures $p(t)$ and fluid flows $Q(t)$, and logical variables used for control (see Chapter 5), e.g. control variable $u(t)$, system state $\mathrm{x}(t)$ and measured variable $y(t)$.

a	Fluid speed of sound	(m/s)
A	System matrix	(-)
c_1, c_2	Friction loss parameters	(-), (-)
d, d_w	Disturbance variable, weighted disturbance variable	(m^3/s), (-)
d_0	Operating point for d	(m^3/s)
D, D_k	Cross section diameter of a piping/segment, node k	(m), (m)
D_H	Cross section diameter of a cutting head nozzle	(m)
e, e_w	Control error, weighted control error	(Pa), (-)
f, f_{kj}	Switching function of a segment, branches kj	(-), (-)
G	Transfer function	(-)
G_a, G_s	Linear actuator, pressure gauge	(-), (-)
G_n, G_p	Nominal plant, perturbed plant	(-), (-)
h	Pressure head of a segment	(m)
H, H_δ	Fluid flow resistance, uncertain fluid flow resistance	(-), (-)
H_H, H_V	Flow resistance of a cutting head, check-valve	(-), (-)
i, j, k	Original agents, target node/agent, original node	(-), (-), (-)
I, J	Set of nodes/agents	
kj	Branch from original node k to target node j	(-)
K, K_k	Fluid bulk modulus, fluid bulk modulus of node k	(Pa), (Pa)
K_0, K_δ	Initial fluid bulk modulus, uncertain fluid bulk modulus	(Pa), (Pa)
K, $\tilde{\mathrm{K}}$, K^*	Feedback controller, extended and optimized design	(-)
K_{PI}, K_{SS}	PI controller, state space controller	(-), (-)
l_0	Initial length of a segment	(m)
L, L_n	Length of a piping, piping section n	(m), (m)
L	Loop transfer function	(-)
m	Fluid mass	(kg)
M_x	First order finite difference matrix in x	(m)
M	Transfer function matrix / augmented system	(-)
n, n_w	Noise channel, weighted noise channel	(Pa), (-)
N	Set of agents in direct neighbourhood	
p, p_k	Pressure state of a segment, node k	(Pa), (Pa)
p_{max}, p_0	Maximal pressure, initial pressure	(Pa), (Pa)
p_x	Pressure at position x	(Pa)
p_C, p_H, p_N	Pressure in a pumping chamber, cutting head, network	(Pa), ...
p_P, p_S	Pressure at a pump outlet, water supply	(Pa), (Pa)
p, $\mathrm{p_w}$	Perturbation channel, weighted perturbation channel	(Pa), (-)
P	Interconnection transfer function matrix	(-)

Q, Q_{kj}	Fluid flow of a segment, branch kj	(m^3/s), (m^3/s)
Q_{ext}, Q_{max}	Exogenous fluid flow, maximal fluid flow	(m^3/s), (m^3/s)
Q_H, Q_V	Fluid flow through a cutting head, check-valve	(m^3/s), (m^3/s)
Q_k, Q_P	Displacement fluid flow of a node k, piston	(m^3/s), (m^3/s)
r, r_w	Reference variable, weighted reference variable	(Pa), (-)
R_n, R_r, R_y	Scaling on n, r, y	(Pa^{-1}), ...
R_u	Scaling on u	(m^3/s)
Re	Reynolds number	(-)
s, s_n	Distance for a segment, piping section n	(m), (m)
s_{max}, s_P, s_0	Maximal stroke, piston position, initial position	(m), (m), (m)
S, S_k	Cross section of a piping/segment, node k	(m^2), (m^2)
S_{kj}	Cross section of branch kj	(m^2)
S_H, S_V, S_P	Cross section of a cutting head, check-valve, piston	(m^2), ...
S_0, S_δ	Initial cross section, uncertain cross section	(m^2), (m^2)
t, t_0	Time coordinate, time initial condition	(s), (s)
T, $\tilde{T}$	Generalized plant and reduced generalized plant	(-), (-)
u, u_w	Control variable, weighted control variable	(m^3/s), (-)
u_d, u_g	Disturbed control input, Scaled control variable	(m^3/s), (-)
u_0	Operating point for u	(m^3/s)
v, v_k	Fluid flow velocity of a segment, node k	(m/s), (m/s)
v_P	Displacement velocity of a piston	(m/s)
V, V_k	Fluid volume of a piping/segment, node k	(m^3), (m^3)
V_C	Fluid volume of a pumping chamber	(m^3)
V_0, V_δ	Initial volume, uncertain fluid volume	(m^3), (m^3)
w	Generalized input channel	(-)
W	Weighting/shaping function	(-)
W_a, W_m	Additive and multiplicative uncertainties	(-), (-)
W_{ia}, W_{im}	Inverse additive and inverse multiplicative uncert.	(-), (-)
x	Position coordinate	(m)
x	State variable	(Pa)
x_0, x_δ	Operating point for x, uncertain operating point	(Pa), (Pa)
y, y_g	Measured variable, scaled measured variable	(Pa), (-)
z	Generalized output channel	(-)
α	Horizontal angle of a piping	(rad)
β	Uncertainty bound for stability	(-)
γ	Peak magnitude value	(-)
Δ	Uncertainty block / set of structured uncertainty	(-)
Δ_a, Δ_m	Additive and multiplicative uncertainty blocks	(-), (-)
Δ_{ia}, Δ_{im}	Inverse additive and inverse uncert. blocks	(-), (-)
Δd	Deviation around operating point d_0	(m^3/s)
Δp, Δp_{kj}	Pressure difference of a segment, between node k and j	(Pa), (Pa)
Δp_v	Pressure friction loss	(Pa)
Δp_V	Pressure difference of a check-valve	(Pa)
Δu,	Deviation around operating point u_0	(m^3)
Δx, Δx_k	Length of a segment, node k	(m), (m)
$\Delta\mathrm{x}$	Deviation around operating point x_0	(Pa)
ΔQ	Fluid flow difference of a segment	(m^3/s)

ΔQ_{kj}	Total fluid flow at node k	(m^3/s)
ΔS_{kj}	Cross section difference from node k to branch kj	(m^2)
ζ, ζ_{kj}	Discharge coefficient of a segment, branch kj	(-)
ζ_H, ζ_V	Discharge coefficient of a cutting head, check-valve	(-), (-)
θ_P	Spindle shaft angular position	(rad)
ϑ, ϑ_{kj}	Interconnection coefficient of a segment, branches kj	($m^3/\sqrt{kg}$), ...
Θ_{kj}	Network interconnection matrix	($m^3/\sqrt{kg}$)
κ_0, κ_1	Fluid bulk modulus parameters	(Pa), (-)
λ	Friction loss coefficient of a piping/segment	(-)
$\lambda(A)$	Eigenvalues of matrix A	(-)
μ	Relative fluid mass	(kg/m^2)
$\bar{\mu}(\cdot)$	Expected value of a signal	($\cdot$)
$\mu_\Delta(\mathrm{M})$	Structured singular value of M with respect to Δ	(-)
ϱ, ϱ_k, ϱ_0	Fluid density of a segment, node k, initial fluid density	(kg/m^3), ...
$\rho(\mathrm{M})$	Spectral radius of system M	(-)
$\bar{\sigma}(\mathrm{M})$	Largest singular values of system M	(-)
Σ	Dynamic system/subsystem	(-)
τ, τ_d	Time constant, time delay	(s), (s)
τ_r, τ_s	Rise time, settling time	(s), (s)
φ	Dependent variable	($\cdot$)
ϕ	Camshaft angular position	(rad)
ξ	Residuals of measurement and simulation	(Pa)
ω_P	Spindle shaft angular velocity	(rad/s)
$\mathcal{C}$	Hydraulic capacity	(m^3/Pa)
$\mathcal{E}$, e	Set of branches and branch (edge)	
$\mathcal{F}$	Camming function	(-)
$\mathcal{G}$	Graph of vertices $\mathcal{V}$ and branches $\mathcal{E}$	
$\mathcal{L}$	Hydraulic inductivity	(kg/m^4)
$\mathcal{N}$, $\mathcal{N}_{kj}$	High-pressure networks, network with branches kj	
$\mathcal{S}_{zw}$	Sensitivity function from w to z	(-)
$\mathcal{T}_{zw}$	Complementary sensitivity function from w to z	(-)
$\mathcal{V}$, v	Set of nodes and node (vertices)	
$\mathbb{G}$	Set of transfer functions	
$\mathbb{N}$	Set of natural numbers	
$\mathbb{R}$	Set of real numbers	

List of Figures

List of Tables

Résumé étendu en français

Motivations

La technologie au jet d'eau sous très haute pression est largement utilisée dans de nombreuses applications industrielles telles que la manufacture et l'usinage (découpe, décapage, nettoyage de surface, etc.). La production conventionnelle des hautes pressions nécessaire à ces applications est réalisée à l'aide de pompes hydrauliques centralisées qui présentent l'inconvénient de n'offrir qu'un faible rendement. L'avènement récent des systèmes électriques à entraînement direct pilotés à l'aide de servomoteurs à grand couple a ouvert la possibilité d'électrifier les pompes à haute pression dans la perspective d'améliorer leur rendement. Cette nouvelle génération de pompes électriques haute pression présente d'autres avantages, à savoir, une interconnexion en réseau plus aisée ainsi qu'une distribution spatiale reconfigurable respectant les demandes individuelles des postes de travail de l'installation. Cette nouvelle technologie, mise à la disposition des industriels, permet d'améliorer le rendement global de l'installation d'usinage grâce à la mise en place de réseaux de distribution haute pression évolutifs interconnectant des pompes électriques décentralisées à des postes de travail. L'interconnexion aisée des pompes électriques offre la possibilité de réduire le temps nécessaire à leur mise en place et simplifie la reconfiguration globale de l'installation.

L'interconnexion décentralisée des pompes requiert cependant une stratégie évoluée de commande couplée à un mécanisme de gestion facilement adaptables aux différentes topologies de l'installation. La stratégie de commande bas niveau vise à réduire les fluctuations de la pression générée par chaque pompe au sein du réseau. Le mécanisme de gestion haut niveau, quant à lui, alloue d'une façon optimale la contribution individuelle de la pression générée par chaque pompe en fonction des demandes des différents postes de travail. L'objectif est de maintenir les performances globales de l'installation grâce à la collaboration des différentes pompes, chaque pompe travaillant dans un point de fonctionnement donné. Le travail présenté dans le cadre de cette thèse vise à relever ces défis en proposant une technologie au jet d'eau reconfigurable et écologiquement durable en accord avec l'industrie 4.0.

Rendement des pompes à haute pression

Dans bon nombre d'applications industrielles, une pompe hydraulique conventionnelle à haute pression alimente un seul poste de travail. L'interconnexion entre la pompe et le poste de travail, tous deux souvent déportés, est réalisée au moyen d'un tuyau résistant aux hautes pressions. La pompe charge en pression l'eau à l'aide de deux intensificateurs de pression et le poste de travail équipé d'une tête de coupe génère le jet d'eau. L'usinage de matériaux durs et cassants est rendu possible grâce à l'abrasif (sable, etc.) ajouté au jet d'eau.

L'usinage à jet d'eau étant un procédé énergivore, un gain en efficacité aussi faible soit-il se traduit directement par un gain d'énergie globale. Le système à entraînement hydraulique représente à lui seul la principale source de perte d'efficacité en raison de son faible rendement généralement inférieur à 70%. Remplacer l'entraînement hydraulique par un entraînement électrique beaucoup plus efficace représente un moyen d'améliorer le rendement. Cette électrification élargit par ailleurs le champ des applications de la technologie au jet d'eau. Elle permet, à titre d'exemple, de l'étendre à l'industrie alimentaire et/ou pharmaceutique où l'utilisation des systèmes à entraînement hydraulique est proscrite en raison des risques de contamination. Ces raisons justifient l'intérêt accru accordé à l'électrification des pompes à haute pression.

Cette nouvelle génération de pompes électriques est constituée de pistons modulables. Chaque piston est déplacé à l'aide d'un système vis-écrou actionné par un système à entraînement électrique. Cet ensemble constitue une unité de pompage. L'idée est de combiner judicieusement deux unités de pompage électriques afin de générer une pression de charge continue. L'utilisation d'actionneurs électriques, dont le rendement est supérieur à 90%, réduit la consommation d'énergie lors de l'usinage par jet d'eau rendant le procédé industriel plus écoresponsable. Leur utilisation permet par ailleurs, de réduire jusqu'à 40% les dimensions de la pompe tout en réduisant le niveau de bruit.

Il convient de remarquer que le procédé d'usinage par jet d'eau requiert une atténuation des fluctuations de la pression, d'au minimum 20 dB, obtenue au moyen des pompes. Ces fluctuations proviennent essentiellement de l'ouverture et/ou la fermeture de la buse de coupe de chaque poste de travail en fonction de la tâche d'usinage. Or, ces cycles de commutation génèrent une consommation variable d'eau qui induit des fluctuations indésirables de la pression, lesquelles se propagent à travers les tuyaux. L'usage des pompes hydrauliques permet de rejeter suffisamment ces fluctuations. Ces pompes agissent en effet comme des atténuateurs de pression à condition toutefois que leur point de fonctionnement prédéfini ne soit pas modifié. L'ajout d'atténuateurs de pression tout au long du tuyau contribue aussi à réduire ces fluctuations et à améliorer la qualité de l'usinage. Ces atténuateurs sont néanmoins coûteux et se dégradent très rapidement au fil du temps.

Les pompes électriques, quant à elles, présentent un inconvénient majeur en matière de rejet des fluctuations de pression. Les fluctuations induisent en effet des cycles de charge variables qui impactent instantanément l'actionneur électrique. Leur atténuation, au moyen de pompes électriques, représente un défi à relever. L'objectif est de reproduire, à l'aide d'une stratégie de commande, les mêmes caractéristiques de rejet que celles offertes par une pompe hydraulique. La nouvelle génération de pompes électriques permet de réduire dès sa conception la complexité du système à entraînement mais nécessite en revanche une stratégie de commande évoluée. Relever ces défis permettra aux pompes électriques de travailler dans un point de fonctionnement quelconque tout en évitant le recours aux atténuateurs additionnels. Cette thèse propose une stratégie de commande bas niveau pour une pompe électrique haute pression qui permet un rejet robuste des perturbations. Cette stratégie serait par ailleurs en mesure de réduire les dégradations de l'entraînement électrique dues aux fluctuations de la pression.

Rendement du procédé d'usinage par jet d'eau

La modification, en fonction de la consommation d'eau des postes de travail, des capacités de charge des pompes classiques à entraînement hydraulique s'avère délicate. Augmenter les dimensions des intensificateurs de pression permet d'augmenter le débit de la pompe mais accroît la sollicitation des pistons. Elle conduit à une dégradation de leur cycle de vie et diminue le rendement énergétique du procédé, limité par les dimensions maximales de chaque pompe. Les dimensions de chaque pompe, le niveau de bruit généré et la dissipation de la chaleur nécessaire au bon fonctionnement de l'installation obligent à déporter la pompe dans une salle des machines. L'interconnexion des postes de travail nécessite alors le recours à de longs tuyaux qui dégradent à leur tour le rendement global de l'installation.

Les pompes électriques présentent l'avantage d'être modulables. Elles facilitent la reconfiguration des installations suivant les demandes de chaque station de travail. La réduction des

dimensions et du niveau de bruit des pompes électriques rend possible leur décentralisation. Les pompes décentralisées fournissent les différents postes de travail en fonction de leurs besoins en eau. Le réseau ainsi mis en place, entre les pompes et les postes de travail, parce qu'il présente l'avantage d'être reconfigurable et de réduire la longueur des tuyaux, améliore le rendement global de l'installation.

Ce nouveau concept d'installation décentralisée des pompes exige toutefois le développement d'une stratégie de commande en mesure de s'adapter à une grande variété de topologies du réseau. Les fluctuations de la pression dans le réseau sont également à l'origine de cycles de charge variables au niveau de chaque pompe décentralisée. La charge appliquée à chaque pompe varie en fonction de la topologie globale du réseau, du positionnement des pompes et des commutations des têtes de coupe de chaque poste de travail. Le débit d'eau fourni par chaque pompe peut par conséquent différer. Par ailleurs, un phénomène d'interférence entre les pompes distribuées peut être occasionné par leur couplage dans le réseau. Les pompes voisines peuvent compenser ces fluctuations additionnelles mais au prix d'une surconsommation d'énergie. Pour contrer ce phénomène d'interférence, la mise en œuvre d'un mécanisme de coopération entre les différentes pompes permet d'équilibrer l'effort global de commande. Chaque pompe doit garantir des performances robustes et la stabilité autour de son voisinage. Cette thèse propose un mécanisme de gestion haut niveau des pompes qui assure leur coopération et permet d'augmenter le degré de flexibilité et d'évolution des réseaux haute pression.

Objectifs généraux

La nouvelle génération de pompes électriques haute pression présente l'avantage d'être modulable, versatile et capable de répondre à la demande individuelle de consommation d'eau de différentes installations. La mise en place d'un usinage à jet d'eau écologiquement durable se heurte au problème posé par l'interconnexion de pompes en réseau de topologie inconnue. En effet, le nombre de pompes décentralisées et de postes de travail peut considérablement varier d'une installation à l'autre.

Les postes de travail, en fonction du motif d'usinage, génèrent des fluctuations de pression provoquées par l'ouverture et la fermeture des buses de coupe. L'atténuation de ces fluctuations passe par la mise en place d'une stratégie de commande bas niveau. D'autre part, le couplage des différentes pompes décentralisées peut dégrader le rendement global si aucun mécanisme de gestion haut niveau n'est utilisé. Toutefois, le recours à un mécanisme centralisé peut s'avérer très compliqué voire impossible. En effet, dans les installations conventionnelles d'usinage à jet d'eau chaque pompe haute pression est localement pilotée sans qu'aucun ordre ne soit envoyé par un mécanisme haut niveau. Chaque pompe opère de façon autonome et répond à la demande d'un poste de travail. Cette notion d'autonomie doit être préservée dans un contexte de mise en réseau de pompes électriques décentralisées.

L'ensemble de ces raisons justifie le développement d'une démarche de synthèse de commande en mesure de réduire l'effort d'ingénierie nécessaire à la mise en place d'une future installation. Cette démarche doit aussi garantir le fonctionnement économe et fiable de chaque pompe quelles que soient la topologie du réseau et la consommation en eau. Ces travaux de recherche proposent une stratégie de commande hiérarchisée et distribuée visant à découper en deux niveaux le problème de commande. La commande bas niveau doit rejeter les fluctuations locales de pression

au moyen des pompes disponibles. La commande haut niveau gère la coopération entre les pompes afin d'équilibrer les taux de charge de chaque pompe vers une valeur moyenne globale. L'allocation hiérarchisée en rejetant les perturbations et en équilibrant les taux de charge des pompes favorise le fonctionnement performant, fiable et économe de chaque pompe. La distribution spatiale des pompes disponibles facilite l'évolution de l'installation. Toute évaluation et vérification d'une stratégie hiérarchisée de commande passe par une phase de modélisation qui permet de décrire un réseau haute pression de topologie quelconque. Dans le contexte d'usinage à jet d'eau, le réseau est soumis à de fortes variations dans un domaine de pression relativement large qui allant de 40 à 400 MPa fait apparaitre des phénomènes non linéaires. D'autre part, les pompes électriques haute pression ainsi que les postes de travail sont soumis à des variations paramétriques. La modélisation et la synthèse des lois de commande doivent prendre en compte les variations les plus pertinentes de ces paramètres.

Contexte de travail

Ces travaux de thèse s'inscrivent dans le cadre d'une coopération entre universitaires et industriels. Ils associent les compétences complémentaires de l'Institut de Recherche en Informatique, Mathématiques, Automatique et Signal (IRIMAS) de l'Université de Haute-Alsace (UHA, France) et de l'Institute of Automation (IA) de l'University of Applied Sciences and Arts Northwestern Switzerland (FHNW, Suisse) pour répondre aux besoins de deux industriels suisses, Jet Cut Power GmbH fabricant de pompes hydrauliques haute pression et Zaugg Maschinenbau AG (zmb) spécialisé dans l'automatisation des postes de travail. Ces travaux de thèse ont été financés par la Swiss Innovation Agency (Innosuisse).

Plan de la thèse

La synthèse des stratégies de commande hiérarchisées et distribuées dédiée aux pompes électriques haute pression est développée dans cette thèse. Cette synthèse passe par une phase de modélisation du réseau haute pression suivie d'une phase de conception des lois de commande. Ces deux tâches, modélisation et conception, sont essentielles à la mise en place des pompes décentralisées en vue d'améliorer le rendement énergétique global de l'installation. Un banc d'essais a été spécifiquement construit dans le laboratoire (Institute of Automation, Suisse) de la FHNW afin de valider la méthodologie de modélisation proposée ainsi que la stratégie de commande bas niveau. Après avoir fait l'objet d'une validation exhaustive, cette démarche de modélisation a été employée afin d'évaluer en simulation le mécanisme de gestion haut niveau proposé.

Ce manuscrit comporte sept chapitres organisés en trois parties. La **Partie I** propose un aperçu global des applications industrielles de l'usinage à jet d'eau. Elle fournit aussi quelques éléments permettant d'établir les exigences à respecter lors de la modélisation et de la conception des stratégies de commande. La **Partie II** présente la démarche de modélisation proposée des réseaux haute pression. Les modèles obtenus sont validés à partir des mesures issues du banc d'essais. La **Partie III** est consacrée à la synthèse des lois de commande robustes bas niveau et expose quelques résultats préliminaires sur la conception du mécanisme de gestion haut niveau.

Chapitre 1 – Introduction à l'usinage à jet d'eau

L'objectif principal de ce chapitre est d'offrir un aperçu global des cas d'utilisation d'usinage à jet d'eau les plus rencontrés dans les applications industrielles. Une classification est proposée suivant le type d'application, les procédés industriels et les configurations des postes de travail. Le principe de génération de hautes pressions est également exposé à partir d'une comparaison entre le fonctionnement conventionnel d'une pompe hydraulique et celui d'une pompe électrique. Ces pompes sont classées en fonction du système d'entraînement (hydraulique ou électrique) et de la conception de la chambre de pompage. De cette classification découlent les exigences des futures installations évolutives ayant un haut niveau de rendement énergétique. La conception de ces nouvelles installations passe d'une part par la définition de cas d'utilisation lors de la modélisation et d'autre part par la spécification des exigences de la stratégie de commande.

Le chapitre comporte trois sections. La **Section 1.1** présente un court état de l'art des installations industrielles d'usinage à jet d'eau. La **Section 1.2** est dédiée à la présentation des principaux composants impliqués dans l'usinage conventionnel. Après l'exposé des applications d'usinage conventionnel, une classification est établie à partir des configurations des postes de travail et des procédés de fabrication (coupe, décapage, etc.). Les symboles standard employés pour dessiner les diagrammes des installations conventionnelles à jet d'eau sont présentés. Enfin, la **Section 1.3** expose les principes de génération des hautes pressions et dresse une classification des pompes en fonction du type d'entraînement (hydraulique ou électrique).

Contributions

Le classement établi à partir des applications (procédés industriels) et de la configuration des postes de travail (tête de coupe simple, tête de coupe multiple, regroupement des stations, etc.) constitue la première contribution de ce chapitre. Ce dernier introduit également quelques exemples d'applications parmi les plus répandues ainsi que les principes de génération des hautes pressions. Ces principes sont illustrés à travers la présentation d'une nouvelle génération de pompes électriques haute pression et du banc d'essais utilisé.

Les fondements de la génération des pressions sont exposés de façon à présenter les solutions technologiques de génération des hautes pressions au moyen de pompes à pistons. Les principes de fonctionnement des pompes classiques et des nouvelles pompes sont brièvement expliqués. Une dernière contribution porte sur la comparaison entre la conception classique et la nouvelle conception de pompes hautes pressions employées par la suite. Ces travaux comprennent deux conceptions de chambres de pompage associées à deux systèmes d'entraînement.

Conclusions

Une pompe hydraulique haute pression, employée dans la découpe des contours, est présentée afin d'illustrer une application courante de la technologie à jet d'eau haute pression. Différents cas d'utilisations sont définis à partir de la classification des applications de l'usinage à jet d'eau et des postes de travail. Ces cas d'utilisation sont mis à profit lors de la validation de la méthodologie de modélisation et de la vérification des stratégies de commande.

Les postes de travail permettent de définir les configurations des têtes de coupe. L'application industrielle permet quant à elle de spécifier les cycles d'ouverture/fermeture des têtes de coupe. D'autre part, la notation standard utilisée lors de la description des circuits hydrauliques a été

adaptée à la description des réseaux haute pression qui relient des pompes décentralisées aux têtes de coupe des différents postes de travail.

L'étude de la conception des chambres de pompage a permis d'établir une similitude entre les pompes hydrauliques et électriques. Les pompes électriques à pistons couplés ne parviennent pas à atteindre les hautes pressions nécessaires à l'usinage à jet d'eau alors que celles à pistons à simple ou à double effet permettent la génération de pressions allant jusqu'à 400 MPa. Bien qu'adaptées aux applications d'usinage à jet d'eau, ces pompes ont fait l'objet de peu de travaux.

Chapitre 2 – Description du banc d'essais

Le Chapitre 2 s'appuie sur la description du banc d'essais pour introduire les cas d'utilisation, spécifier les topologies des réseaux et définir les séquences de commutation d'ouverture/fermeture de la tête de coupe (patterns). Ce banc d'essais, spécialement construit pour ces recherches, permet la configuration des différentes topologies des réseaux à modéliser. Quant aux cas d'utilisation, ils servent à vérifier la qualité du modèle obtenu, à valider la stratégie de commande bas niveau proposée et à évaluer le mécanisme de gestion haut niveau.

Le concept proposé pour améliorer l'efficacité énergétique des installations à jet d'eau fait intervenir des pompes décentralisées au sein des réseaux haute pression. Les pompes hydrauliques conventionnelles, n'offrant qu'un faible rendement, ne sont pas en mesure d'opérer dans l'intervalle de fonctionnement souhaité. Les pompes électriques utilisées dans cette thèse permettent de contourner ces difficultés en réduisant la complexité du système d'entraînement et en offrant la possibilité d'opérer dans un point de fonctionnement quelconque. Ce chapitre présente donc une nouvelle conception de pompe électrique haute pression comportant deux pistons à effet simple indépendants. Il expose également les composants du système, sa structure de commande et le concept de synchronisation des deux pistons nécessaire au bon fonctionnement de la pompe. La synchronisation est réalisée au moyen d'un modèle de vilebrequin virtuel servant à calculer les trajectoires de référence nécessaires aux déplacements des deux pistons. Ces trajectoires sont obtenues à partir de la modélisation de la pression générée à l'intérieur d'une chambre de pompage.

Ce chapitre comporte trois sections. La **Section 2.1** présente un état de l'art des pompes haute pression. La **Section 2.2** expose la configuration du banc d'essais ainsi que les topologies des réseaux. Puis, elle décrit les cas d'utilisation ainsi que quelques séquences de commutation de têtes de coupe représentatives des applications industrielles. La **Section 2.3** expose en détail la pompe électrique haute pression équipant le banc test, son principe de fonctionnement ainsi que la solution mise en œuvre pour gérer la synchronisation des pistons.

Contributions

Le chapitre débute par la présentation du banc d'essais qui permet d'interconnecter deux pompes électriques à deux postes de travail. Différentes topologies de réseaux haute pression peuvent être alors configurées pour les besoins de la validation expérimentale des modèles mathématiques et des stratégies de commande. Ces topologies de réseaux haute pression et plusieurs cas d'utilisation sont définis sur la base des classifications établies au cours du chapitre précédent. Les configurations envisagées sont représentatives des cas d'utilisation rencontrés dans les applications industrielles. Ces topologies et ces cas d'utilisation serviront de fil conducteur tout au

long du manuscrit afin d'illustrer la méthodologie de modélisation et la démarche de synthèse des lois de commande.

Le banc test est équipé de pompes électriques multi-pistons dont la conception est fondée sur la combinaison de deux unités de pompage. La description du principe de fonctionnement d'une unité de pompage constitue la première contribution de ce chapitre. Cette pompe électrique est modulable mais requiert un mécanisme de synchronisation du déplacement des pistons afin de générer un flux constant. La présentation du mécanisme de synchronisation des pistons à l'aide d'un modèle constitue la deuxième contribution de ce chapitre. L'utilisation de ce mécanisme permet de considérer chaque pompe électrique comme une source continue de flux, dans un large domaine de fonctionnement, à condition que les fluctuations de la pression qu'elle engendre soient minimisées. Pour ce faire, la synthèse d'une loi de commande bas niveau pour chaque pompe et d'un mécanisme de gestion haut niveau de plusieurs pompes est requise.

Conclusions

Un banc test a été construit dans le laboratoire pour réaliser l'identification paramétrique, la validation des modèles mathématiques et la vérification de la stratégie de commande. La description des topologies des réseaux et des configurations des têtes de coupe a fait appel à la notation standard. Les applications industrielles présentées au cours du Chapitre 1 ont servi à définir les topologies des réseaux ainsi que les configurations des têtes de coupe employées lors de la validation. Plusieurs configurations reliant deux pompes haute pression à deux têtes de coupe indépendantes (deux postes de travail) ont été présentées. Ces cas d'utilisations seront employés ultérieurement pour effectuer des mesures sur le banc test et des simulations numériques.

Ce chapitre expose également la pompe électrique à deux pistons ainsi que le mécanisme nécessaire à la synchronisation des déplacements des pistons. Les déplacements précis des pistons passent par une phase de génération de trajectoires comportant un déphasage. Ces trajectoires sont calculées à partir des relations liées à la génération des hautes pressions au moyen de chambres de pompage couplées. La synchronisation apportée par ces trajectoires évite des interférences entre les unités de pompage et permet de produire un flux constant d'eau. Le suivi de ces trajectoires est réalisé à l'aide d'une commande en position des servomoteurs.

Ces trajectoires de mouvement sont ensuite améliorées par l'introduction d'une accélération croissante prenant en compte le jerk maximum admissible. Il est ainsi possible de maximiser le flux de sortie généré par la pompe. Cependant, le calcul des trajectoires faisables constitue un problème d'ordre élevé dont la résolution requiert une procédure d'optimisation. Les trajectoires issues de cette optimisation ont été implantées sur le banc test à l'aide de splines cubiques générant les références de position pour la commande de mouvement.

L'introduction de trajectoires adaptatives minimisant les fluctuations de pression au moment de la commutation entre les unités de pompage ouvre d'intéressantes perspectives. Ces trajectoires peuvent être définies, par exemple, à l'aide de tables de correspondance (*look-up tables*). La trajectoire à suivre, selon le point de fonctionnement de la pression désiré, peut par exemple être générée par le biais d'une interpolation cubique.

Chapitre 3 – Méthodologie de modélisation des réseaux haute pression

Les futures installations à jet d'eau haute pression combinent plusieurs pompes décentralisées afin d'élargir les réseaux haute pression de topologie arbitraire. Une démarche de modélisation flexible et évolutive est indispensable à la conception de ces réseaux et/ou au développement d'une architecture appropriée de commande pour ces pompes. Cette démarche de modélisation doit à la fois prendre en compte les non linéarités intrinsèques au procédé et les variations des paramètres dans un domaine relativement grand (variant de 40 et 400 MPa). Elle doit aussi offrir un certain degré de flexibilité en vue de la modélisation d'un réseau de topologie quelconque connectant un nombre quelconque de pompes et de postes de travail décentralisés.

Des environnements de simulation numérique, tels que *Matlab* et sa boîte à outils *Simscape*, *Modelica* ou *AMESim*, permettent de modéliser des systèmes hydrauliques standard grâce à certains composants hydrauliques de base disponibles dans les librairies. Malheureusement, les composants spécifiques à la modélisation des réseaux haute pression ne sont pas toujours disponibles. La modélisation d'une installation à jet d'eau donnée devient alors complexe et très coûteuse en temps. Le manque de composants validés dans les intervalles d'application envisagés limite par ailleurs la réutilisabilité du modèle obtenu. Afin de pallier les difficultés mentionnées, une démarche de modélisation de futures installations reconfigurables doit offrir divers composants haute pression accompagnés d'une procédure de modélisation des différentes topologies du réseau. Les paramètres variables des composants doivent être décrits au moyen de modèles mathématiques appropriés et expérimentalement identifiés à l'aide du banc d'essais. Le paramétrage de ces composants doit être valable dans un large domaine de fonctionnement.

Le Chapitre 3 est dédié au développement d'une méthodologie de modélisation fondée sur la notion de graphes. Les équations à dérivées partielles gouvernant la dynamique des fluides sont approchées au moyen de différences finies en considérant le flux de fluide à l'équilibre. Cette démarche aboutit à l'obtention d'un modèle à paramètres localisés où chaque section de tuyauterie est représentée par un segment homogène. La connexion de ces segments au moyen d'un graphe offre une représentation flexible et évolutive d'un réseau haute pression de topologie arbitraire. Une analyse en simulation permet d'évaluer le temps de calcul et la précision des prédictions en fonction de la discrétisation spatiale et des approximations effectuées. L'originalité de l'approche proposée, au regard des méthodologies présentes dans la littérature, réside dans l'utilisation d'un module d'élasticité isostatique dépendant de la pression et relié à la densité de fluide elle aussi dépendante de la pression. Ce couplage améliore la précision du modèle dans un large domaine de fonctionnement allant de 40 à 400 MPa.

Ce chapitre comporte quatre sections. La **Section 3.1** propose un état de l'art des approches de modélisation des systèmes haute pression et de la théorie des graphes. La **Section 3.2** expose les principes fondamentaux associés à la dynamique d'un fluide. Le recours à ces principes permet d'obtenir un modèle à paramètres distribués. Les fluctuations de pression dans un tuyau sont étudiées au moyen de simulations numériques réalisées à l'aide de ce modèle. La **Section 3.3** décrit la démarche de modélisation générique des réseaux haute pression réalisée au moyen de graphes. Elle introduit les intervalles des variations paramétriques qui seront pris en considération pour obtenir un modèle à paramètres localisés. Enfin, la **Section 3.4** présente les paramètres dépendant de la pression (associés à certains composants) et leur procédure d'identification expérimentale.

Contributions

Ce chapitre propose une méthodologie de modélisation qui permet de modéliser, à l'aide de graphes, des réseaux haute pression de topologies diverses. Les composants du modèle sont considérés comme des segments homogènes, chaque segment représentant un état local de la pression à partir du principe de conservation du moment et de la continuité du fluide. La méthodologie de modélisation proposée introduit, dans les équations gouvernant la physique du système, une densité de fluide ainsi qu'un module d'élasticité isostatique qui dépendent de la pression. Elle permet ainsi d'améliorer la précision du modèle dans un large domaine de fonctionnement. Les segments sont par la suite interconnectés à l'aide de graphes tout au long du trajet parcouru par le fluide. Chaque nœud du graphe représente un état de la pression et chaque branche alloue un flux de fluide aux interconnexions. Les graphes offrent le degré de flexibilité nécessaire à la modélisation des réseaux de topologies différentes. Cette démarche conduit à l'obtention de modèles à paramètres localisés qui permettent d'approximer le caractère non linéaire des réseaux haute pression.

La principale contribution du chapitre porte sur le développement d'une démarche de modélisation, à l'aide de graphes, de réseaux haute pression. L'originalité de l'approche proposée réside dans la prise en compte dans les équations gouvernant la dynamique du fluide de deux paramètres variant, à savoir, le module de compressibilité et la masse volumique. Les équations ainsi modifiées sont alors associées à un graphe. La flexibilité et la versatilité inhérentes aux graphes rendent possible la modélisation des réseaux à topologie variable. Ce chapitre aborde également l'identification, dans un large domaine de fonctionnement, de paramètres physiques et de caractéristiques du fluide dépendant de la pression. Cette procédure d'identification permet la modélisation de réseaux haute pression dans un large intervalle sans avoir à réitérer l'étape d'identification paramétrique initiale.

D'un point de vue pratique, une boîte à outils de simulation facilitant la description des réseaux haute pression est développée. Ce simulateur prend en compte la dépendance des caractéristiques du fluide (module de compressibilité, masse volumique) à la pression. Tout déplacement de flux de fluide est modélisé comme une excitation externe et les déplacements des pistons sont modélisés comme une modification du volume du fluide.

Conclusions

Le comportement dynamique du fluide, représentant certains phénomènes de propagation dans une section donnée d'un tuyau, est présenté. Puis une méthodologie de modélisation d'un réseau haute pression est développée à partir d'un graphe. L'idée est d'associer des sections de tuyau à des segments homogènes. Ces segments sont alors interconnectés à l'aide d'un graphe de façon à reproduire la topologie du réseau. Chaque segment représente un état local de la pression et ses interconnexions sont caractérisées en considérant un flux de fluide stationnaire.

Cette méthodologie de modélisation est dérivée des équations fondamentales de la dynamique des fluides en approximant un modèle distribué à l'aide de différences finies. Cette démarche de modélisation conduit à un ensemble d'équations différentielles qui représentent le réseau haute pression sous la forme d'un modèle à paramètres localisés. L'erreur introduite par l'approximation proposée est évaluée par le biais de diverses simulations en considérant la même section de tuyau à modéliser. La segmentation du réseau en sections doit satisfaire le compromis classique

précision-complexité du modèle. La proposition d'une procédure optimale de segmentation ouvre d'intéressantes perspectives. Toutefois, les résultats obtenus montrent qu'une précision acceptable pour les applications industrielles est atteinte en considérant des segments d'un mètre de long.

Les paramètres intervenant dans le modèle ont fait l'objet d'une identification, dans un large domaine de fonctionnement allant de 0 à 400 MPa, à l'aide des mesures issues du banc d'essais. Considérer ce domaine de fonctionnement permet d'enrichir les données disponibles dans la littérature jusque-là limitées à 100 MPa. Un outil de modélisation générique, sous la forme d'une boîte à outils, est proposé afin de modéliser des réseaux haute pression de diverses topologies et de complexité croissante. Cet outil épargne le recours à des essais expérimentaux spécifiques pour valider chaque modèle. Les modèles validés servent, par exemple, à tester les stratégies de commande bas niveau proposées par la suite. L'extension de ce travail à l'identification d'autres composants du réseau constitue une perspective à envisager.

Chapitre 4 – Application et validation de l'approche de modélisation

Le développement des futures installations passe par une phase de modélisation du réseau haute pression envisagé. Cette phase de modélisation peut être effectuée à l'aide de la démarche de modélisation développée. Les paramètres dépendant de la pression et les caractéristiques du flux de fluide ont été identifiés à partir des mesures issues du banc d'essais. L'utilisation de cette boîte à outils *Matlab/Simulink* simplifie la modélisation des futures installations et évite les coûts engendrés par des campagnes d'essais spécifiques. Le Chapitre 4 illustre l'utilisation de cette boîte à outils lors de la modélisation des réseaux haute pression de topologies diverses et compte tenu des cas d'utilisation spécifiés. Les modèles obtenus sont soumis à une validation exhaustive à partir des mesures issues du banc test. Cette validation montre que les modèles restent précis dans un large domaine de fonctionnement. Ils peuvent être facilement adaptés afin de prendre en compte les modifications du réseau sans remettre en question l'identification paramétrique. Le temps nécessaire à la mise au point d'un modèle pour les futures installations industrielles est ainsi réduit.

Ce chapitre comporte trois sections. La **Section 4.1** présente les objectifs visés lors de la démarche de modélisation. Au cours de la **Section 4.2**, cette démarche est appliquée à la modélisation de composants souvent rencontrés puis à la modélisation de réseaux complexes. Enfin, les modèles obtenus sont validés expérimentalement au cours de la **Section 4.3**.

Contributions

La démarche de modélisation est illustrée en considérant diverses configurations du banc d'essais. Dans un premier temps, elle est appliquée à une pompe électrique haute pression, composée de deux pistons indépendants interconnectés, reliée à une tête de coupe simple. Dans un deuxième temps, elle est appliquée aux configurations plus complexes des réseaux précédemment définis. D'autre part, un modèle à paramètres localisés prenant en compte les incertitudes paramétriques fait l'objet d'une discussion. Le modèle de premier ordre ainsi obtenu sert de point de départ à des travaux de recherche sur le développement de stratégies de commande robustes bas niveau.

Le nombre important d'expériences conduites pour valider les modèles proposés constitue une contribution importante de ce chapitre. En effet, tous les modèles obtenus sont validés ex-

périmentalement à partir des mesures issues du banc test. Différentes configurations du banc test, combinant deux pompes électriques et deux têtes de coupe, ont été mises en œuvre. Ces configurations correspondant aux cas d'utilisation déjà définis reproduisent certaines applications industrielles.

Les performances des modèles obtenus sont comparées à celles obtenues à partir des approches de modélisation proposées dans la littérature. Ces résultats montrent qu'une compressibilité de fluide variable permet de réduire les erreurs de modélisation et améliore la précision des prédictions. La précision de la simulation est évaluée à partir de divers résultats expérimentaux qui considèrent des points de mesure placés à différents endroits du réseau. Différents cycles de commutation de têtes de coupe, agissant comme des perturbations, sont également utilisés lors de ces validations.

L'approche de modélisation est concrétisée sous la forme d'une boîte à outils qui permet d'élaborer facilement en *Matlab/Simulink* un modèle de réseau. Cette boîte à outils représente un atout pour les industriels du secteur qui cherchent à modéliser de futures infrastructures haute pression en un temps réduit sans avoir besoin d'un paramétrage individuel.

Conclusions

Ce chapitre offre un cadre de modélisation, matérialisé par une boîte à outils, à la description des réseaux haute pression généralisés. La boîte à outils développée permet aux industriels partenaires du projet de concevoir et d'optimiser les futures installations à jet d'eau. Afin d'illustrer les performances de cette boîte à outils, 6 topologies de réseau ont été étudiées. Chaque modèle obtenu a fait l'objet d'une validation expérimentale en considérant 2 pressions de fonctionnement, 2 buses de diamètre diffèrent et 2 séquences de commutation des têtes de coupe.

Dans ce chapitre, les différents modèles sont validés expérimentalement à l'aide des données issues du banc d'essais. Ces résultats montrent qu'une modélisation considérant une densité de fluide constante génère une erreur statique de la pression alors qu'un module d'élasticité isostatique constant est à l'origine d'un mauvais transitoire de la réponse. La prise en compte d'une compressibilité variable de fluide permet d'améliorer la précision du modèle dans un domaine de fonctionnement compris entre 100 MPa et 400 MPa. Les différents cas d'utilisation sélectionnés, représentatifs des configurations industrielles, montrent les aptitudes du modèle à caractériser la propagation de la pression en différents points du réseau. Les résultats de validation en différents points du réseau prouvent l'excellente précision obtenue grâce à la démarche de modélisation proposée. Une augmentation des résidus est cependant constatée quand le banc test opère à un faible taux de pompage. Une prise en compte des pertes occasionnées par les frictions pour de petites vitesses du fluide permettrait d'améliorer le modèle dans ce cas de fonctionnement.

La méthodologie proposée rend possible la modélisation flexible des réseaux de diverses topologies avec un effort raisonnable. Cet avantage est particulièrement utile à la modélisation des réseaux de diverses topologies, à l'optimisation d'une future installation et à l'évaluation des stratégies de commande. Par ailleurs, les modèles proposés de complexité croissante seront par la suite utilisés afin d'évaluer le mécanisme haut niveau dédié à la gestion des pompes décentralisées.

Les perspectives envisagées portent principalement sur la validation des modèles en considérant d'autres topologies, un dysfonctionnement du clapet anti-retour ayant nui à la finalisation

de toutes les expériences de validation initialement prévues. Remarquons que la commutation du clapet anti-retour est très sensible à tout différentiel de la pression. L'introduction d'un modèle de commutation comportant un mécanisme d'hystérésis peut éventuellement réduire les erreurs résiduelles de simulation. Il a également été constaté des pertes de pression et/ou des dépassements quand les trajectoires des pistons de la pompe ne sont pas correctement synchronisées. Les modèles obtenus, en reproduisant ce comportement, peuvent servir à optimiser les trajectoires et à améliorer ainsi la génération de la pression.

Chapitre 5 – Stratégies de commande robustes bas niveau

Le fonctionnement des pompes électriques couplées requiert le développement d'une stratégie de commande bas niveau en mesure de limiter l'impact de certains phénomènes indésirables. En effet, toute fluctuation de la pression impacte directement la qualité de la coupe par jet d'eau. Or, les têtes de coupe introduisent naturellement des fluctuations de la pression lors d'un cycle inconnu de commutation d'ouverture/fermeture nécessaire à la tâche d'usinage. Les fluctuations engendrées par une consommation variable d'eau doivent par conséquent être compensées à l'aide des pompes haute pression disponibles. Chaque pompe, placée à un endroit quelconque du réseau, doit rejeter les fluctuations locales de pression sans pour autant déstabiliser l'ensemble du réseau. Bien évidemment, la compensation des fluctuations de pression doit être réalisée en limitant l'effort de commande. Ces pompes doivent donc opérer dans un large domaine de fonctionnement afin d'atténuer les perturbations exogènes. Cependant, le large domaine de fonctionnement de la pression et les configurations variables des postes de travail induisent des comportements non linéaires, des incertitudes paramétriques importantes ainsi que des variations paramétriques affectant le fonctionnement global de l'installation. Pour toutes ces raisons, l'utilisation des lois de commande robustes bas niveau s'impose et nécessite la proposition d'une description mathématique appropriée à leur synthèse.

Le Chapitre 5 est dédié à la conception d'une stratégie de commande robuste bas niveau pour chaque pompe haute pression décentralisée. Lors de la conception de cette stratégie de commande, les cycles inconnus de commutation des têtes de coupe et les interactions entre les pompes voisines sont considérés comme des perturbations exogènes agissant dans une sous-section du réseau. Les non linéarités et les incertitudes paramétriques doivent aussi être prises en compte afin de garantir la stabilité et les performances robustes dans un large domaine de fonctionnement. Afin de mener une analyse de sensibilité de la variation des paramètres, un modèle perturbé linéarisé décrivant une sous-section de réseau est proposé. Plusieurs sortes de description des incertitudes sont envisagées puis comparées afin de choisir le modèle de synthèse le plus pertinent. Le modèle sélectionné sert de point de départ à la synthèse d'une loi de commande robuste H_∞. Cette dernière doit satisfaire un cahier des charges formalisé à partir des besoins exprimés par les industriels partenaires du projet. Lors d'une synthèse H_∞ classique, les exigences en termes de rejet de perturbation et d'effort de commande visant à éviter des saturations sont traduites sous la forme de gabarits fréquentiels. D'autres gabarits fréquentiels peuvent aussi être introduits afin de traduire les dynamiques des signaux d'entrée, par exemple, le bruit de mesure et la commutation des perturbations. L'étude proposée dans ce chapitre permet, après avoir défini le modèle de synthèse, de dresser la forme de ces gabarits pour poser le problème H_∞. Une pompe électrique haute pression est utilisée comme cas d'étude pour définir un schéma d'interconnexion standard. Tous les composants du système traité sont alors combinés pour construire ce schéma qui définit le problème d'optimisation H_∞ à résoudre.

Ce chapitre est découpé en quatre sections. La **Section 5.1** établit un état de l'art des techniques de commande robuste et met l'accent sur les approches dites décentralisées, distribuées et en réseau. La **Section 5.2** expose les principes fondamentaux associés à la théorie de la synthèse du régulateur H_∞. La **Section 5.3** présente le système à commander ainsi que son modèle non linéaire. Une étude des variations paramétriques conduit à la proposition d'un modèle linéarisé de complexité réduite. Ce modèle de premier ordre est issu d'une linéarisation, autour d'un point de fonctionnement, d'un modèle de pompe haute pression interconnectée à une sous-section inconnue du réseau. Le point de fonctionnement, autour duquel la linéarisation est effectuée, est considéré comme un paramètre incertain additionnel. La **Section 5.4** illustre comment l'emploi d'une description non structurée des incertitudes permet de modéliser les variations des paramètres présentes dans les installations. Une réécriture du modèle incertain sous une forme standard Δ-M à l'aide d'une transformation fractionnelle linéaire supérieure permet d'obtenir un modèle perturbé. Ce modèle est le point de départ de la synthèse du régulateur H_∞ réalisée au cours du chapitre suivant.

Contributions

Ces travaux visent à effectuer une synthèse de commande robuste H_∞ pour une pompe électrique haute pression. Les réseaux haute pression étant affectés par un grand nombre de perturbations, la stratégie de commande à concevoir doit offrir un degré élevé de robustesse. La commande H_∞ est une technique qui se révèle bien adaptée à la résolution de ce type de problème de commande. La formalisation du problème H_∞ et l'obtention d'une représentation du système généralisée interconnectant une pompe décentralisée à des têtes de coupe figurent parmi les principales contributions de ce chapitre.

Une description du système assortie d'un modèle des incertitudes qui englobe les variations paramétriques est nécessaire à la synthèse d'une commande H_∞ adaptée aux applications à jet d'eau. Dans cette perspective, ce chapitre propose une analyse exhaustive des variations des paramètres et des descriptions possibles des incertitudes. La dernière contribution du chapitre est liée à la définition appropriée des gabarits et des fonctions de pondération nécessaires à la synthèse H_∞. D'un point de vue méthodologique, une fusion des signaux d'entrée au moyen des gabarits joints est développée en vue de réduire la dimension du problème d'optimisation à résoudre lors de la synthèse H_∞.

Conclusions

Une discussion portant sur la synthèse d'une stratégie de commande robuste et décentralisée pour les pompes électriques haute pression est proposée dans ce chapitre. L'objectif est de synthétiser un régulateur bas niveau pour chaque pompe installée dans un réseau de topologie inconnue. Pour ce faire, le réseau est découpé en portions, en sous-sections. La pression dans chaque sous-section est alors régulée par une pompe haute pression associée. En émettant l'hypothèse d'une synchronisation parfaite des pistons de chaque pompe, un modèle de premier ordre est obtenu afin de décrire la génération de la pression dans une sous-section. Ce modèle représente les principales incertitudes paramétriques. Les autres éléments présents dans l'installation ont été modélisés à l'aide de fonctions de transfert établies à partir des valeurs nominales fournies par les constructeurs.

Dans un deuxième temps, la sensibilité paramétrique du modèle a été évaluée. Cette étude montre qu'une tête de coupe avec une buse de section décroissante est à l'origine d'une augmentation du gain entre le signal d'entrée et celui de sortie en basses fréquences. Une buse complètement fermée engendre un phénomène d'intégration pur. L'augmentation de la pression de fonctionnement diminue le gain entre l'entrée et la sortie. D'autre part, l'augmentation de la section de la buse n'affecte pas le gain entre la perturbation et la pression de sortie en basses fréquences. En conclusion, une pompe haute pression est en capacité de réguler la pression dans une sous-section du réseau en rejetant les perturbations induites par le séquencement inconnu d'ouverture/fermeture des têtes de coupe.

Dans cette étude, les incertitudes paramétriques sont initialement modélisées sous la forme d'incertitudes structurées et non structurées. La forme des incertitudes non structurées est finalement retenue à l'issue de l'étude comparative réalisée. L'incertitude inverse additive fournit des résultats satisfaisants dans l'intervalle des incertitudes paramétriques étudié. Elle permet d'introduire un signal associé aux perturbations en utilisant une transformation linéaire fractionnelle. Les paramètres incertains peuvent ainsi être séparés du modèle nominal du système afin de proposer des gabarits appropriés à la synthèse de la loi de commande. Par ailleurs, une incertitude inverse multiplicative de sortie offre des résultats similaires. L'une des pistes envisagées pour améliorer la modélisation des incertitudes consiste à utiliser une description des incertitudes à l'aide des facteurs premiers. Choisir une incertitude complexe non structurée présente des avantages lors de la synthèse du contrôleur. Elle permet de simplifier la procédure visant à maximiser la dimension du sous-réseau, mais introduit un niveau de conservatisme supplémentaire lors de la conception de la loi de commande.

Chapitre 6 – Synthèse des lois de commande robustes bas niveau

Les exigences à respecter par le régulateur dans le domaine temporel ont été étudiées au cours du Chapitre 5. Des fonctions de pondération appropriées dans le domaine fréquentiel ont donc pu être déduites. Le système augmenté obtenu prend en compte les perturbations agissant sur le système, la description des incertitudes paramétriques et les exigences à respecter par le régulateur. Ce système augmenté est le point de départ de la synthèse H_∞ du régulateur. Les travaux présentés au cours de ce chapitre portent principalement sur l'agrégation de fonctions de pondération en fusionnant leurs valeurs singulières à l'aide de la norme euclidienne. Cette fusion permet, en diminuant la dimension du problème d'optimisation H_∞, de réduire le temps de calcul. Cette démarche a été utilisée avec succès lors de la synthèse d'un retour d'état d'ordre réduit. Afin de satisfaire les contraintes industrielles, la même démarche a également été appliquée à la synthèse d'un régulateur de type PI suivant une synthèse H_∞ structurée.

Il convient de remarquer que la longueur de chaque sous-section, dans laquelle la pompe doit atténuer les fluctuations de pression, est inconnue car la topologie de l'installation est a priori inconnue. Il faut par conséquent déterminer la longueur maximale de la sous-section pour laquelle la pompe garantit le niveau d'atténuation souhaité. La longueur admissible de la sous-section est considérée comme un paramètre incertain qui dépend d'une part, de l'effort maximum que la pompe peut fournir et d'autre part, des performances de rejet de perturbation. Ces deux aspects étant nécessaires au maintien d'un niveau de qualité de l'usinage à jet d'eau, une analyse de robustesse est proposée pour établir la dimension de la sous-section dans laquelle la pompe garantit les performances désirées. La structure du régulateur doit être compatible avec les exigences de mise en œuvre formulées par les industriels. Cet aspect est pris en considération grâce

à une synthèse structurée du régulateur. La structure du régulateur retenue, de type PI, permet de répondre aux exigences du cahier des charges en matière de stabilité et de performances dynamiques tout en maximisant la largeur de la sous-section. La synthèse est réalisée en appliquant une procédure itérative qui maximise l'intervalle de l'incertitude et synthétise à chaque itération un régulateur PI quasi-optimal. La procédure Δ-K proposée préserve l'ordre du système généralisé. Elle est alors en adéquation avec une description non structurée des incertitudes et avec une synthèse structurée du régulateur.

La mise en œuvre des futures installations à jet d'eau haute pression nécessite une commande robuste bas niveau pour les pompes haute pression, chaque pompe stabilisant une portion du réseau. Les portions correspondent à des sous-sections qui peuvent être alors interconnectées en vue de former un réseau haute pression de pompes décentralisées. Cependant, le couplage de multiples pompes dans le réseau peut conduire à une augmentation de la consommation d'énergie et limiter la stabilité globale du réseau si les pompes interfèrent les unes avec les autres. La stabilité et les performances robustes des pompes haute pression distribuées doivent être alors validées au moyen de simulations suivies de validations expérimentales. Les modèles des réseaux haute pression proposés ont permis de tester le régulateur par retour d'état réduit ainsi que le régulateur quasi-optimal PI. D'un point de vue expérimental, un régulateur PI a été implanté dans le banc test afin de piloter l'une des pompes disponibles.

Ce chapitre comprend quatre sections. La **Section 6.1** présente les objectifs de la synthèse d'un régulateur robuste. Le système généralisé perturbé et les fonctions de pondération sont combinés au cours de la **Section 6.2** afin d'obtenir un système généralisé. En appliquant une transformation linéaire fractionnaire inférieure, ce système est transformé en forme standard P-K. Un régulateur par retour d'état réduit est alors synthétisé à partir des fonctions de pondération jointes. Ses performances sont ensuite comparées à celles obtenues à l'aide d'un régulateur de type PI synthétisé à partir d'une démarche H_∞ structurée. Une synthèse sous-optimale H_∞ est également étudiée à partir d'une procédure itérative Δ-K qui permet d'ajuster les fonctions de pondération. Cette procédure aboutit à la synthèse d'un régulateur qui vérifie le cahier des charges tout en maximisant l'intervalle des incertitudes liées à la taille inconnue d'une sous-section du réseau. Dans la **Section 6.3**, les performances du régulateur sont évaluées en simulation en considérant différentes topologies modélisées à l'aide de la méthodologie par graphes proposée. Le comportement des régulateurs obtenus, en présence de non linéarités et de variations paramétriques, peut ainsi être évalué. Lors de la phase de validation expérimentale menée dans la **Section 6.4**, un régulateur structuré de type PI est implanté dans le banc test. L'étude expérimentale est aussi reproduite à l'aide de modèles de validation en boucle fermée afin de tester les stratégies de commande. Elle permet de vérifier la bonne implantation du régulateur ainsi que la démarche de modélisation au moyen de la boîte à outils développée. La boîte à outils ainsi validée permet de mener des études poussées en simulation, au-delà des limites physiques du banc test, qui serviront à la conception de futures installations.

Contributions

Une contribution de ce chapitre porte sur la synthèse H_∞ d'une loi de commande robuste pour une pompe haute pression qui tient compte des variations paramétriques et des perturbations exogènes. Lors de la synthèse, des gabarits fréquentiels sont utilisés afin de définir les intervalles de variation des signaux d'entrée. Les performances dynamiques et la pénalisation de l'effort de commande sont quant à elles prises en compte en introduisant des fonctions de transfert.

Cette démarche conduit à la construction d'un modèle généralisé englobant la modélisation non structurée des incertitudes et la description fréquentielle des signaux d'entrée. Afin de diminuer l'ordre de ce modèle, une fusion des signaux d'entrée par le biais de gabarits joints est introduite. Si cette démarche permet de réduire la dimension du problème H_∞ à résoudre, elle peut cependant augmenter le degré de conservatisme de la solution. Enfin, la résolution du problème d'optimisation conduit à un premier régulateur par retour d'état. Ce régulateur sert par la suite de point de comparaison avec les autres régulateurs structurés synthétisés.

La synthèse d'un régulateur structuré constitue une autre contribution du chapitre. L'approche proposée conduit à l'obtention d'un régulateur de type PI aisé à implanter dans les applications industrielles. Ce régulateur doit garantir la stabilité et permettre de réguler la pression dans une sous-section d'une longueur donnée. L'approche H_∞ est également mise à profit pour déterminer la longueur maximale de la sous-section du réseau associée à la pompe. L'analyse des variations paramétriques et le modèle d'incertitudes qui en résulte conduisent à l'obtention de marges robustes de performances dans lesquelles la stabilité et les performances sont garanties. La mise en œuvre d'une procédure itérative de type Δ-K permet d'obtenir un régulateur quasi optimal de type PI tout en maximisant les limites de l'intervalle des incertitudes. Cette procédure se révèle très pratique et fournit un moyen d'effectuer une synthèse quasi optimale d'un régulateur H_∞.

Plusieurs campagnes de simulation sont menées à l'aide de modèles de validation complexes afin d'établir une comparaison entre les performances obtenues avec la stratégie par retour d'état et celles obtenues avec le régulateur structuré de type PI. Une première synthèse du régulateur PI est testée en conditions réelles grâce au banc d'essais. Ce dernier a été configuré pour une seule pompe puis pour l'interconnexion de deux pompes. Toutes les configurations proposées utilisent deux têtes de coupe indépendantes afin de générer des fluctuations de pression. L'approche de synthèse du régulateur bas niveau est validée avec succès. Toutefois, les expériences menées montrent l'apparition de couplages dynamiques entre les pompes interconnectées et révèlent la nécessité de mettre en place un mécanisme de gestion haut niveau afin de coordonner les efforts fournis par les pompes.

Conclusions

Dans ce chapitre, la démarche de synthèse H_∞ d'un régulateur pour une pompe haute pression est validée. Les fonctions de pondération introduites permettent de prendre en compte les performances souhaitées et l'effort de commande. Le système interconnecté est mis en forme à l'aide d'une transformation linéaire fractionnaire de façon à séparer le régulateur des autres composants du système. Un système généralisé nécessaire à la synthèse H_∞ de la loi de commande est ainsi obtenu. L'utilisation des gabarits joints permet de regrouper plusieurs signaux d'entrée du système généralisé réduisant la dimension du problème H_∞ à résoudre et l'effort de calcul. L'application de cette démarche au cas spécifique de la commande d'une pompe haute pression conduit à l'obtention d'un régulateur par retour d'état. Les résultats observés mettent en évidence des similitudes entre les performances du régulateur d'état d'ordre réduit (plus simple à implanter) et celles du régulateur d'état de plein ordre.

Par ailleurs, la procédure d'optimisation formulée conduit également à l'obtention d'un régulateur de type PI. Ce dernier a été modifié en régulateur par retard de phase en introduisant un filtre passe bas. La structure PI de complexité réduite est simple à implanter par les industriels. Les performances des régulateurs par retour d'état et PI sont comparées à partir de simulations

numériques considérant différentes topologies de réseaux. Les modèles mathématiques de validation sont issus de la méthodologie de modélisation proposée. Le régulateur PI n'est cependant pas en mesure de fournir le même niveau de performances que le régulateur par retour d'état. Les performances obtenues sont proches à condition de limiter la longueur de la sous-section du réseau. D'autre part, la structure par retard de phase introduit un pôle additionnel qui judicieusement placé permet d'obtenir des performances similaires à celles fournies par le régulateur par retour d'état. Les propriétés du régulateur par retour d'état sont alors approchées dans une bande de fréquences donnée sans impacter la longueur de la sous-section.

Une contribution importante de ce chapitre porte sur la démarche globale de synthèse d'un régulateur pour une pompe installée dans un réseau haute pression de topologie inconnue. Le réseau doit être découpé en sous-sections dont la pression intérieure est régulée par une pompe. La longueur de la sous-section est alors considérée comme un paramètre incertain lors de la synthèse du régulateur. Une procédure itérative Δ-K est proposée afin de déterminer la longueur maximale de la sous-section pour laquelle les performances souhaitées en boucle fermée sont garanties. Cette procédure permet d'effectuer une synthèse de type H_∞ tout en augmentant itérativement l'intervalle de l'incertitude Δ. Cette démarche aboutit à un régulateur K qui maximise la taille admissible de la sous-section. Comparativement à la synthèse initiale, une augmentation de 61% de la longueur de la sous-section a pu être obtenue.

Enfin, un premier régulateur de type PI a fait l'objet d'une validation expérimentale à l'aide du banc d'essais. Les mesures obtenues ont été comparées aux prédictions fournies par les modèles de simulation. Ces résultats montrent la bonne cohérence entre les simulations et la réalité. En raison d'un dysfonctionnement du banc test, cette phase de validation expérimentale n'a malheureusement pas pu être menée plus loin, par exemple, pour tester le régulateur par retard de phase. Néanmoins, grâce à la bonne qualité des prédictions fournies par le modèle, le régulateur par retard de phase a fait l'objet de plusieurs validations en simulation en considérant diverses topologies couplant deux pompes à deux têtes de coupe. Ces modèles en boucle fermée servent au cours du chapitre suivant à tester et à valider un mécanisme de gestion haut niveau.

Chapitre 7 – Perspectives. Vers la proposition d'un mécanisme de gestion haut niveau

La première partie de ce manuscrit de thèse est consacrée à la proposition d'une méthodologie de modélisation, basée sur des graphes, pour des réseaux haute pression. Elle rend possible la modélisation du comportement des pompes décentralisées interconnectées à des postes de travail spatialement distribués dans une installation. Au cours de la deuxième partie, une stratégie de commande robuste bas niveau pour une pompe haute pression est élaborée à l'aide de cette modélisation. La commande bas niveau permet à une pompe de réguler la pression dans une portion de sous-section du réseau. Toutefois, l'interconnexion entre les pompes dans un réseau requiert un mécanisme haut niveau de gestion. Enfin, le Chapitre 7 expose quelques travaux préliminaires dédiés à la conception de ce mécanisme de gestion haut niveau des pompes décentralisées dans la perspective d'optimiser la consommation d'énergie des installations à jet d'eau.

La mise en œuvre d'une stratégie de commande bas niveau pour une seule pompe électrique haute pression suscite l'intérêt des industriels. La solution proposée est facilement implantable car seules sont nécessaires des informations locales. Toutefois, les simulations réalisées montrent que des pompes décentralisées connectées dans un réseau présentent des taux de fonctionnement

arbitraires si aucun mécanisme de gestion n'intervient. En effet, chaque pompe atteint un taux de pompage différent suivant la topologie du réseau et le cycle d'ouverture/fermeture des têtes de coupe. Ce comportement peut conduire à la détérioration prématurée des pompes et dégrader leurs capacités de rejet des perturbations.

Ce chapitre propose un court état de l'art des approches classiques de commande hiérarchisée et montre les limites de l'utilisation directe de ces approches dans un contexte d'usinage à jet d'eau. Les travaux préliminaires exposés dans ce chapitre initient les travaux de recherche dédiés à la commande de plusieurs pompes interconnectées. Ces travaux ont pour objet la conception d'un mécanisme de gestion en mesure d'équilibrer les taux de fonctionnement des pompes haute pression sans qu'aucune connaissance a priori sur leur position dans le réseau ne soit nécessaire. Ce chapitre présente quelques résultats préliminaires en simulation sur la gestion des pompes distribuées à l'aide d'une approche dite par consensus moyen. Le mécanisme de gestion des pompes combiné à une commande distribuée offre un bon compromis entre la quantité d'informations requise sur les sous-sections voisines et les effets de retard de transmission, de perte de paquets, etc.

Différentes approches peuvent être envisagées pour la gestion des pompes électriques en fonction des informations disponibles sur les pompes voisines. Ce chapitre présente l'utilisation de l'approche par consensus moyen pour équilibrer les taux de fonctionnement des pompes distribuées. L'équilibrage des pompes couplées dans une installation assure la convergence, dans un temps de réaction acceptable, de toutes les pompes vers un taux moyen de pompage variant dans le temps. Dans l'approche proposée, aucun système centralisé de gestion faisant appel à une communication entre les pompes n'est considéré. Par conséquent, les pompes peuvent continuer à opérer, avec un taux de pompage sous-optimal, et à alimenter les postes de travail même si la communication est défaillante. Les simulations montrent les capacités du mécanisme de gestion proposé à équilibrer des pompes interconnectées vers un taux de pompage moyen. Ce taux reflète la consommation moyenne d'énergie de l'ensemble de l'installation.

Le chapitre est composé de quatre sections. La **Section 7.1** propose un état de l'art des méthodes de gestion distribuées, en particulier de la commande prédictive (*Model Predictive Control, MPC*), de l'allocation de commande (*Control Allocation*) et de la commande coopérative (*Cooperative Control*). La formulation du problème proposée dans la **Section 7.2** souligne la nécessité d'introduire un mécanisme de gestion. La méthode de consensus moyen distribué est adoptée afin d'estimer le taux moyen de pompage des agents interconnectés, c'est-à-dire des pompes. Enfin, les objectifs associés à une gestion par consensus moyen et à la spécification du canal de communication à l'aide d'une description par graphes sont introduits. Une approche intégrée, développée au cours de la **Section 7.3**, permet à chaque pompe haute pression de converger vers un taux moyen. Deux algorithmes de gestion haut niveau sont évalués en simulation dans la **Section 7.4**. Cette étude fournit les premières simulations pour équilibrer les charges des pompes distribuées à l'aide d'une approche par consensus moyen dynamique.

Contributions

Dans ce chapitre, la méthode par consensus moyen dynamique est appliquée à la gestion de pompes électriques haute pression. Chaque pompe peut être assimilée à un agent qui fournit une estimation locale du taux moyen de pompage en échangeant l'estimation locale avec les pompes voisines. Chaque pompe disposant d'une commande bas niveau robuste, une description haut

niveau des agents (les pompes) à l'aide de dynamiques discrètes peut être proposée. Dans ce chapitre, les algorithmes sont développés en temps continu en considérant un moyen de communication parfait (les délais de transmission sont par exemple négligés) pour le partage des estimations locales entre les agents voisins. L'approche par consensus moyen dynamique utilisée pour estimer le taux moyen de pompage des pompes distribuées constitue l'une des contributions de ce chapitre. Les pompes haute pression connectées dans un réseau restent « flottantes » si aucune action de rétroaction n'est donnée par un algorithme de gestion. La commande bas niveau proposée maintient les pressions de sortie autour d'une référence globale en présence de perturbations occasionnées par l'ouverture/fermeture des têtes de coupe. Ceci conduit à la génération de différents taux de flux pour chaque pompe en fonction de sa position dans le réseau.

La proposition d'un algorithme d'équilibrage distribué considérant le réseau haute pression comme moyen de communication constitue une autre contribution du chapitre. Il permet d'ajuster directement la référence de la pression pour chaque agent-pompe de façon à garantir la convergence de chaque pompe vers une valeur moyenne. Cette approche fait appel à la stratégie de commande bas niveau déjà synthétisée ainsi qu'au couplage entre les pompes pour équilibrer leurs taux individuels et ce, sans avoir à ajouter de stratégie de commande.

Les résultats de simulation présentés dans ce chapitre combinent tous les résultats des chapitres précédents. La méthodologie de modélisation par graphe permet de représenter des installations à jet d'eau complexes impossibles à reproduire à l'aide du banc d'essais. La stratégie de commande bas niveau, appliquée à chaque pompe, permet de placer chaque pompe (chaque agent) dans une position arbitraire du réseau. Grâce à cette commande robuste, les fluctuations de pression sont atténuées. Enfin, le mécanisme de gestion haut niveau par consensus dynamique moyen ajuste le fonctionnement de chaque pompe de façon à ce qu'elle opère à un taux moyen de pompage variant dans le temps.

Conclusions

Un réseau de pompes haute pression distribuées peut être assimilé à un système sur-actionné. Dans ce chapitre, plusieurs solutions au problème de commande de ce type de systèmes sont d'abord exposées. L'équilibrage du taux de charge au moyen d'une allocation de commande adaptative est une solution possible pour réaliser la synchronisation des pompes. La procédure d'adaptation est nécessaire car la distribution optimale de l'effort de commande peut varier en fonction du cycle d'ouverture/fermeture des têtes de coupe et du nombre de pompes disponibles. Toutefois, la mise en place d'une telle procédure d'optimisation nécessite de connaître les informations sur le fonctionnement de toutes les pompes. Or, en pratique, cette connaissance peut s'avérer très compliquée à obtenir dans les installations industrielles. Une stratégie coopérative MPC (*Model Predictive Control*) permet également d'aborder la gestion des régulateurs distribués. Cette approche est fondée sur l'utilisation de modèles locaux appropriés pour effectuer le suivi des trajectoires de chaque agent. Fournir un modèle pour chaque installation à jet d'eau constitue la première limite de cette approche. La deuxième limite est liée au besoin d'estimer les séquences de commutation des têtes de coupe qui affectent le comportement dynamique du réseau de distribution de pression. Cette discussion met en lumière les limites des approches classiques et justifie le choix d'une approche par consensus moyen dynamique. Cette dernière permet en effet de garantir un effort moyen de commande des pompes distribuées en présence d'une consommation variable d'eau. Une distribution équilibrée au moyen d'un consensus moyen constitue par conséquent une piste intéressante à explorer pour traiter le problème de commande

de futures installations à grande échelle. L'approche par consensus est adaptée à des topologies de communication inconnues et à un nombre variable d'agents. Si la communication entre un agent est rompue, les agents restant ne convergent pas forcément vers une moyenne globale mais l'installation continue toujours à opérer. Bien évidemment, en pratique, d'autres contraintes doivent être considérées afin de garantir le suivi, avec une erreur nulle, d'un signal de dynamique arbitraire. Ces contraintes sont liées par exemple aux limites de la bande passante de la communication, à la synchronisation, à la propagation des retards, aux restrictions de la topologie du réseau, etc. L'introduction d'informations a priori sur la dynamique du signal et sur la topologie du réseau doit permettre d'améliorer l'approche proposée.

Dans ce chapitre, une topologie en anneau est utilisée afin de modéliser le canal de communication entre les agents (les pompes). Cette topologie requiert une communication bidirectionnelle et conduit à l'obtention d'un graphe fortement connecté qui garantit une convergence en temps fini. Bien que rarement implémentée en pratique, cette topologie en anneau constitue un point de départ pour ces travaux. L'algorithme de commande doit être vérifié en considérant des graphes fortement connectés et déséquilibrés. Des études en simulation, à l'aide de la méthodologie de modélisation proposée, permettent de vérifier l'algorithme de gestion haut-niveau développé. Les perspectives envisagées portent principalement sur l'évaluation d'une procédure qui conduit au réglage optimal des paramètres de la stratégie de commande par équilibrage distribué. La convergence des pressions et de l'erreur statique doivent être aussi évaluées en présence de retards, de perte de paquets d'information et de perte d'agents. Enfin, l'algorithme proposé d'équilibrage distribué utilise le réseau de distribution de pression comme un moyen additionnel de communication. Il s'avère donc essentiel de compléter ces travaux par une étude approfondie sur la stabilité globale du réseau en considérant différentes topologies du réseau de distribution.

Part I

Waterjet machining

1

Introduction to waterjet machining

Contents

1.1 Introduction

Objectives

This work motivates the concept of energy-efficient waterjet facilities. To design these future waterjet facilities requires to develop a graph-based modelling for high-pressure networks and a hierarchical distributed control design for high-pressure pumps. That requires to define suitable use cases for modelling and to specify requirements for control design. This requires to investigate conventional waterjet machining and to derive specifications for future facilities with respect to industrial needs.

State of the art

The overview in [Molitoris et al., 2016] allows for understanding the past and continuing developments of waterjet machining. Investigating the inventions given by various patents will enrich this overview. Waterjet machining found early industrial applications in 1930, applying a pressure of about 10 MPa for burring of castings. A system to cut hard materials has been first proposed in [Schwacha, 1961], generating a high-pressure of 690 MPa. This system found application in the aerospace industry to cut steel and later to cut composite materials, which are sensitive to thermal stress. The investigations in [Rice, 1965] about pulsed waterjets at 340 MPa aimed at introducing waterjet machining to other industries.

Progress to improve the durability of waterjet nozzles has been obtained with the research for ceramics [Chadwick et al., 1973], while nozzles with reduced inner diameters (about 0.051 mm) that operates at pressures of 4800 MPa has been proposed in [Franz, 1973]. The experiments in [Hashish, 1984] first introduced abrasive particles to waterjet cutting. This increases the material removal rate and consequently improves the productivity of waterjet machining. These developments, see also [Hashish et al., 1987], marks the breakthrough of conventional waterjet machining in various industrial applications. The cutting head design as known today and commonly used for abrasive waterjet cutting has been introduced in [Chalmers, 1991] and [Xu, 1998]. Since then, the design of hydraulically driven pumps has undertaken great progress. Waterjet cutting with increased high-pressures of about 700 MPa is investigated in [Susuzlu et al., 2004], where an improved efficiency of 30% is reported in [Hashish, 2009], when waterjet machining with a pressure of 600 MPa.

Advancements of multi-axis machining that allows for cutting of complex contours and surfaces by means of waterjets are overviewed in [Folkes, 2009]. The text book [Nee, 2015] reviews recent process technologies used for waterjet machining. Its shows the entire range of common applications, from surface cleaning to the cutting of 2-dimensional contours and complex 3-dimensional shapes, whereas cutting quality and process efficiency are of interest.

Contribution

The main research effort still lies in terms of improving the cutting process of waterjet machining. Most activities aim to increase the material removal rate or enhancing the cutting quality. Despite economizing the waterjet machining in terms of production time, its sustainability is sparsely investigated. The design of electrically driven high-pressure pumps and the concept of decentralized pumps in high-pressure networks arise increased interest from the industry. Enabling these future research activities, this chapter reviews the common applications for waterjet machining and discusses the principles of high-pressure generation.

This chapter is structured as follows: Section 1.2 introduces the high-pressure components used for conventional waterjet machining, discusses common waterjet applications and classifies waterjet machining by distinguishing different work station setups as well as manufacturing processes. It further outlines typical waterjet facilities when introducing the principal symbols to present them. The principles of high-pressure generation is given in Section 1.3 when classifying high-pressure pumps with respect to the drive systems. This will compare the most common hydraulically driven pumps with the recent electrically driven high-pressure pumps.

1.2 Conventional waterjet machining

A waterjet facility consists of high-pressure pumps that supply cutting heads, generating a waterjet. Cutting heads are commonly installed in work stations used for waterjet machining. Where high-pressure pumps represents a fluid flow source, a cutting heads can be considered as a pressure sink.

Conventional high-pressure pumps pressurizes water by means of pistons which are typically displaced with a hydraulic drive. Different pump sizes are available with respect to the desired operating pressure and pump rate. The properties of a typical hydraulically driven pump are given in Table 1.1, which operates in the same power range as the investigated electrically driven pump. Where the electric drive operates on a wide pressure range, the hydraulic drive has to be adjusted for every waterjet facility that the pump runs properly at a desired pressure point. This hydraulically driven pump shows an increased frame size, weight and noise level in contrast to the electrically driven pump, discussed in Table 2.7 of Section 2.3. The image of Figure 1.1 shows exemplarily a high-pressure pump of Type JCP 22 LC with two hydraulically driven pressure intensifiers. Each intensifier pressurizes water with its single acting piston.

Table 1.1 – Properties of a hydraulically driven high-pressure pump (Type JCP 22 LC): with a hydraulic pumping unit driven by a 22 kW asynchronous motor.

Properties	Value	Unit
Maximal pressure	400	(MPa)
Input fluid flow	2.8	(l/min)
Drive power	22	(kW)
Frame size	1.15x1.1x1.05	(m)
Weight	800	(kg)
Noise level	74	(dB)

Figure 1.1 – Example of a conventional high-pressure pump (Type JPC 22 LC): hydraulically driven pressure intensifiers with two single acting pistons.[1]

Each cutting head consists of a nozzle holder and an pneumatic on/off-valve. The holder contains a nozzle with diamond inlet. The diamond inlet has a single cavity that shapes the waterjet, where the on/off-valve will interrupt the high-pressure water supply to the nozzle. This enables a cutting head to control the waterjet generation whenever needed. The nozzle size will determine the fluid flow consumption of a cutting head with respect to the operating pressure. It is common to distinguish those nozzles with respect to the diamond inlet inner diameter. Most

[1] Illustrations courtesy of Jet Cut Power GmbH, Schönenwerd.

common nozzles are listed in Table 1.2. The image of Figure 1.2 shows as example a cutting head, which is typically used for pure water cutting.

Table 1.2 – Properties of cutting head nozzles: nozzles inner diameter and operating pressures determining the output fluid flow (l/min).

		Pressure (MPa)			
		100	200	300	400
Nozzles inner	0.10	0.13	0.19	0.23	0.26
diameters (mm)	0.15	0.30	0.42	0.51	0.59
	0.20	0.53	0.74	0.91	1.05
	0.25	0.82	1.16	1.42	1.64
	0.30	1.18	1.67	2.05	2.37
	0.35	1.61	2.28	2.79	3.22
	0.40	2.10	2.98	3.64	4.21

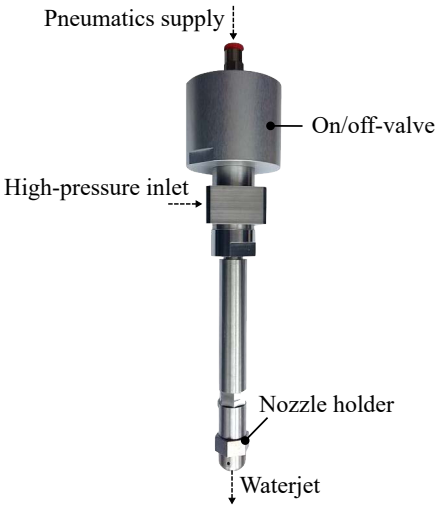

Figure 1.2 – Example of a cutting head used for pure water applications: pneumatically actuated on/off-valve and nozzle holder generating the waterjet.[2]

A work station holds a given amount of cutting heads and guides them over a work piece. The impact of the waterjet will cause a material removal. An operator can program the work station to realize a desired cutting contour using a terminal. A Computer Numerical Control (CNC) will then trigger the cutting heads to turn on its waterjet for cutting and to turn it off while moving to a subsequent cutting position. The image of Figure 1.3 shows exemplarily a work station which is equipped with a single cutting head, used for waterjet cutting. The work piece is positioned on a cutting bed. A 3-axis positioner will guide the cutting head over the work piece to cut a 2D-contour.

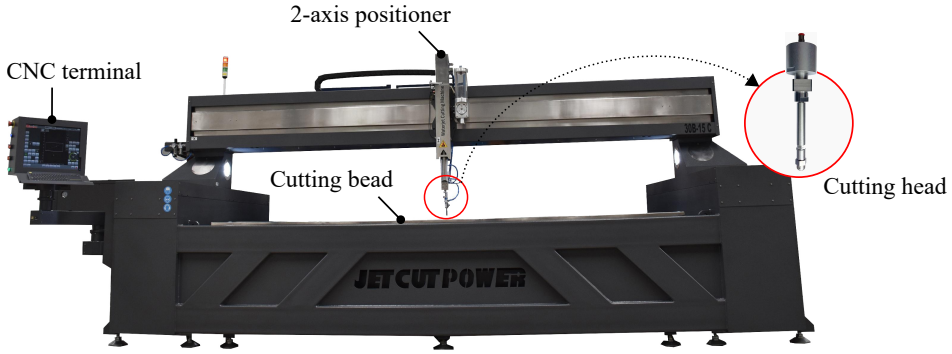

Figure 1.3 – Example of a work station used for waterjet cutting: CNC work station guiding a cutting head over a work peace to cut a desired 2D-contour.[2]

[2]Illustrations courtesy of Jet Cut Power GmbH, Schönenwerd.

1.2.1 Common waterjet applications

Waterjet machining can be found in metal, composite, textile, food and many other industries, see [Folkes, 2009], [Wang and Shanmugam, 2009]. It is of first choice for contour cutting with reduced thermal stress and for surface stripping without the use of chemicals. The manifold applications require operating pressures typically from 100 to 400 MPa. Beside various pure water applications, abrasive waterjet cutting is prevalent to achieve an increased material removal rate when machining hard and brittle materials, see [Molitoris et al., 2016].

The diagram in Figure 1.4 classifies waterjet machining and its typical pressure range. It basically distinguishes between surface cleaning ($<$ 200 MPa pressure) and waterjet cutting ($>$ 200 MPa pressure). Waterjet cutting is further separated with respect to pure water cutting and abrasive cutting. Pure water cutting is typically applied to cut organic material such as leader, food as well as plastics with a pressure up to 300 MPa. Abrasive is added to cut materials such as metal sheets or stone with a pressure up to 400 MPa.

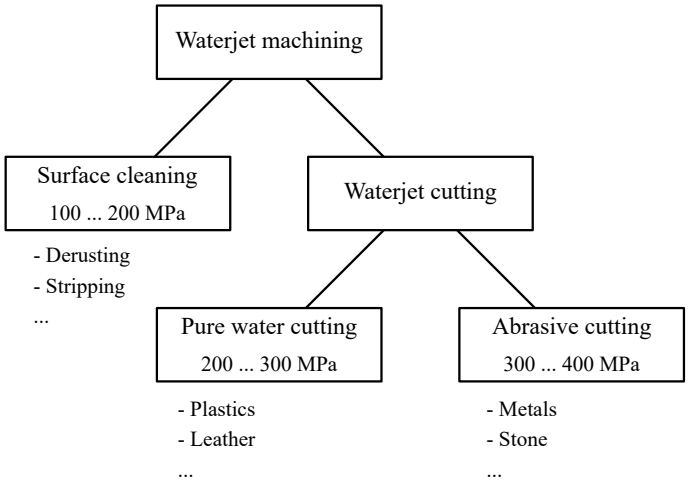

Figure 1.4 – Common waterjet applications: classification of waterjet machining according to its operating pressure.

Waterjet cutting: The image of Figure 1.5 (a) depicts a work station for abrasive cutting. It consists of a 3-axis positioner which is equipped with a cutting head. The work station will move the cutting head along a desired 2D-contour. The abrasive is added within a cutting head, but after passing the diamond nozzle. The waterjet is then cutting a work piece which lies on the cutting bead. The impact of the abrasive particles will increase the material removal rate and therefore improve the effectiveness of waterjet machining.

Surface cleaning: The cleaning machine, as shown in the image of Figure 1.5 (b), provides another typical application. A high-pressure pump supplies a common rail that is located above a holding device. The common rail holds 16 nozzles which are arranged in series to cover a large surface. A cylindrical matrix is then installed on the holding device which brings the matrix into rotation. The series of nozzles will then strip off any paint from the matrix surface.

All of the investigations in this work consider the following general assumption:

Assumption 1.1. *Neither the cleaning nor the cutting process affects the high-pressure generation itself. The pressure generation is rather characterized by the nozzle installed and becomes disturbed when switching the on/off-valve of a cutting head.*

As a consequence of Assumption 1.1, common waterjet applications will be investigated with respect to operating pressure, cutting head configuration and switching pattern.

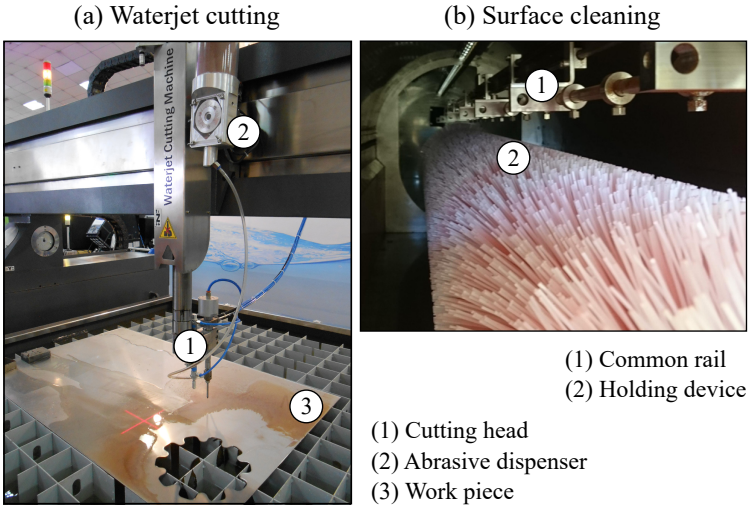

Figure 1.5 – Example of waterjet applications: (a) work station equipped with a single cutting head after cutting a desired 2D-couture in a steel sheet. (b) stripping machine with 16 nozzles on a common rail and holding device for matrices used to strip off paint from its surface.[3]

1.2.2 Classifying waterjet machining

The different work stations hold a given amount of cutting heads that generates the waterjets. A cutting head can be equipped with nozzles of different inner diameters. Every work station will open and close its cutting heads with respect to the individual demands for waterjet machining. This leads to a varying overall fluid flow consumption that has to be compensated by the installed high-pressure pump. The resulting switching pattern of a work station, when switching its cutting heads, is unknown to the high-pressure pump. It is therefore assumed as an exogenous disturbance.

The diagram of Figure 1.6 presents useful characteristics to classify waterjet machining. Requirements for waterjet machining vary with respect to the waterjet application, its work station setup and manufacturing process. The operating pressure is determined by the waterjet application. A cutting head configuration depends on the work station setup, while the manufacturing process defines the switching pattern for each cutting head. The cutting head configuration, its operating pressure and switching pattern determines the overall water consumption, which is limited by the available pump rate.

Typical work station setups found in industry are presented in Table 1.3. When abrasive cutting, the water demand of a single cutting head can already occupy an entire pump. This setup of single work stations with single cutting heads is widely spread in the industry. When pure water cutting, the water demand of a single cutting head is usually smaller. Hence, a high-pressure pump either supplies a single work station with multiple cutting heads or it supplies

[3] Illustrations courtesy of Jet Cut Power GmbH, Schönenwerd.

several interconnected work stations with a single cutting head each. The first case of a single work station with multiple cutting heads is often used to cut identical contours in parallel. This aims to enhance the effectiveness of waterjet machining. These cutting heads switch simultaneously and nozzles with identical inner diameter are installed. The second case of several interconnected work stations with single cutting heads will represent a cluster for cutting individual contours. These cutting heads switch independently and various nozzles might be installed.

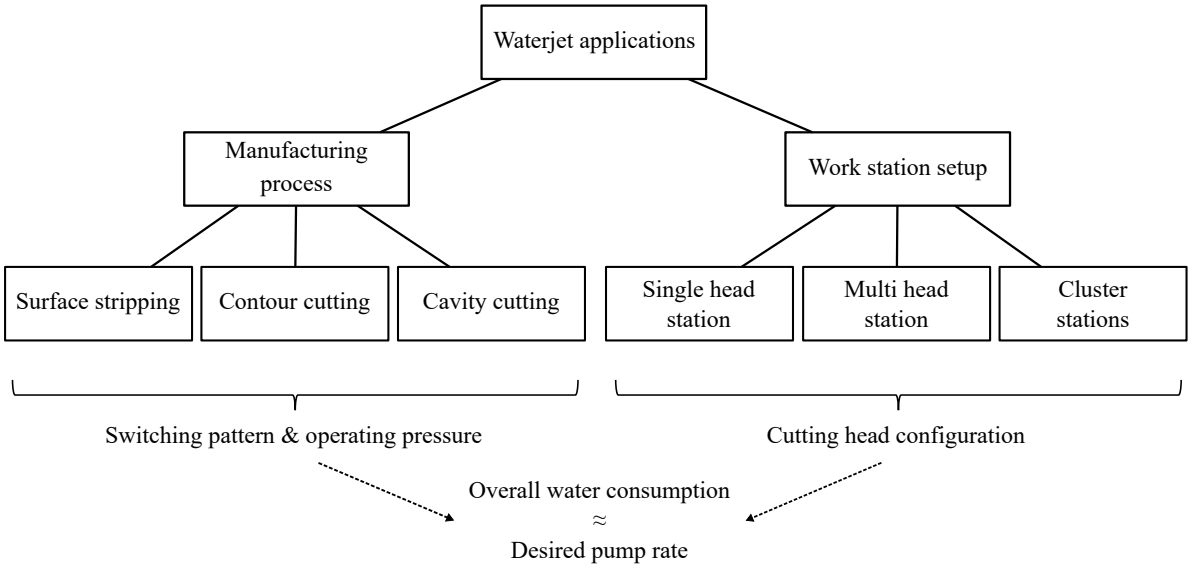

Figure 1.6 – Characteristics for waterjet machining: classification of waterjet machining with respect to waterjet application, manufacturing process and work station setup.

Table 1.3: Work station setups: waterjet machining classified according to typical work station setups found in industry and assigned to waterjet applications.

	Work station	Cutting head	Switching mode	Surface cleaning	Pure water cutting	Abrasive cutting
Single head station	single	single	-			x
Multi head station	single	multi	simultaneous	x	x	
Cluster stations	multi	single	independent		x	

Multiple, simultaneously switching cutting heads can be considered as alike as a single cutting head with a larger nozzle installed, if the switching heads are located in near neighbourhood and if the nozzles are chosen such that an identical water consumption will result. The first case is not given for a cluster of multiple work stations. A single high-pressure pump can supply multiple cutting heads, as long as it serves the overall water consumption. In practice, it is rarely seen to aggregate multiple pumps for increasing the pump rate.

These work station setups include different cutting head configurations, as specified in Table 1.4. A surface cleaning application is chosen that desires a pressure of 200 MPa. The cleaning machine is equipped with a common rail of 16 nozzles. For nozzles of 0.10 mm inner diameter each, an overall water consumption of 2.98 l/min will results. A single 0.40 mm nozzle will require

an equivalent flow rate. On the other hand, a pure water cutting application is presented that desires a pressure of 300 MPa. A single work station is thereby equipped with 4 parallel cutting heads to simultaneously cut 4 identical contours. A nozzle of 0.15 mm inner diameter is installed each, resulting in an overall water consumption of 2.04 l/min. A single 0.30 mm nozzle will result in an equivalent flow rate. Eventually, an abrasive cutting application is chosen that desires a pressure of 400 MPa. A single work station is considered with a single cutting head. The cutting head holds a nozzle of 0.25 mm inner diameter, resulting in a flow rate of 1.55 l/min.

Table 1.4: Cutting head configurations: typical parametrisation for common waterjet applications with respect to possible work station setups.

	Operating pressure (MPa)	Nozzles of diameter (mm)	Equivalent diameter (mm)	Water consumption (l/min)
Surface cleaning	200	16 x 0.10	1 x 0.40	2.98
Pure water cutting	300	4 x 0.15	1 x 0.30	2.04
Abrasive cutting	400	1 x 0.25	1 x 0.25	1.55

Typical manufacturing processes found in industry require different switching patterns as specified in Table 1.5. It relates the common waterjet applications to three corresponding manufacturing processes. Any stripping process uses multiple interconnected cutting heads with a simplified design. They remain open for the entire stripping process. In some cases the on/off-valve is totally removed. Contour and cavity cutting distinguish different switching patterns. Both can be seen as a periodic process, but its cycle time and on/off-ratio can vary in a wide range. Cavity cutting features a short cycle time and a limited on/off-ratio, while contour cutting has a longer cycle time with an increased on/off-ratio. The on-time is defined for an open valve when cutting a contour or cavity. The off-time is given for a closed valve when moving to a subsequent cutting position.

Table 1.5: Manufacturing processes: waterjet machining classified according to typical manufacturing processes found in industry and assigned to waterjet applications.

	Cycle time (s)	On/off-ratio (%)	Surface cleaning	Pure water cutting	Abrasive cutting
Stripping	30 ... 600	100	x		
Contour	3 ... 60	80 ... 90		x	x
Cavity	0.5 ... 2.0	50 ... 70		x	x

The overall water consumption will vary due to the individual switching behaviour of all cutting heads. Cutting head configuration, operating pressure and switching pattern give the overall water consumption, which defines the desired pump rate (see Figure 1.6). The switching patterns for multiple interconnected work stations with independent cutting heads can superimpose, which results in an arbitrarily varying water consumption. Details will be given in Chapter 2.2, when providing specific use cases for waterjet machining.

1.2.3 Typical waterjet facilities

Industrial installations for waterjet machining typically consist of decentralized high-pressure pumps, which are remotely installed to supply single work stations for waterjet machining. A single work station setup can be depicted as a high-pressure pump with a cutting head directly interconnected by a piping, as shown in the diagram of Figure 1.7. This diagram uses the standard symbols according to ISO 1219. However, it adapts them for high-pressure systems to illustrate network topologies and its configurations for different use cases.

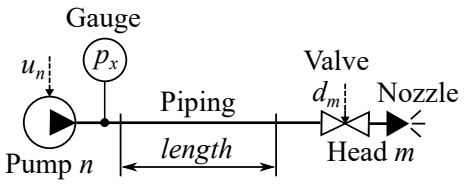

Figure 1.7 – Standard symbols (ISO 1219) used to draw diagrams of high-pressure networks: n pumps are interconnected to m cutting heads by means of piping. A cutting head is composed by an on/off-valve and a nozzle. Operating pressures are measured at positions, denoted by x.

A high-pressure pump is considered as a single fluid flow source for any principle of pressure generation and drive system. Hence, the control signal $u_n(t) = [0, 1]$ allows for adjusting the desired input fluid flow of a pump n within 0% and 100% of its maximal pump rate possible. A cutting head is considered as a single pressure sink. Its symbol consists of an on/off-valve and a nozzle. The on/off-valve is switching with respect to the signal $d_m(t) \in \{0, 1\}$ that controls the fluid flow to pass a cutting head m. The nozzle is interchangeable and defines the resulting water consumption with respect to the operating pressure. The various work stations installed in a waterjet facility are not taken into account in this work, since the material removal itself will not influence the high-pressure pump and its pressure generation, referring to Assumption 1.1. But the cutting head switching pattern is unknown to the high-pressure pump and will directly affect the pressure generation. It is usually given by the work station with respect to the manufacturing process and is therefore considered as a disturbance signal $d(t)$. Pressure gauges can be installed in the high-pressure network. They measure the pressures $p_x(t)$ at positions x, used for control and validation.

The interconnections between pumps and cutting heads are realized by high-pressure piping sections. Hence, the total of interconnected piping of a cutting application is referred to a high-pressure network. These networks will vary for different waterjet facilities. However, the network topology of every application can be assumed as static, since waterjet machining is interrupted to change any piping installation.

Recall the conventional waterjet facility and the future waterjet facility, as shown in Figure 3 and 4 of the General introduction part, and representing these examples by applying the above standard symbols provides the diagrams in Figure 1.8. It can be seen that the first application (a) consist of two independent high-pressure networks, while the second application (b) spans a single network with increased complexity. The conventional waterjet facility is composed of a work station setup with two simultaneously switching cutting heads and a cluster of two work stations with independent cutting heads, where a high-pressure pump supplies the cutting heads for each work station setup. On the other hand, the future waterjet facility represents a cluster of interconnected work stations with independent as well as parallel cutting heads, where several pumps supply the entire network. These interconnected pumps are no longer located in a remote machine room. They are distributed in the waterjet facility, reducing the overall piping length.

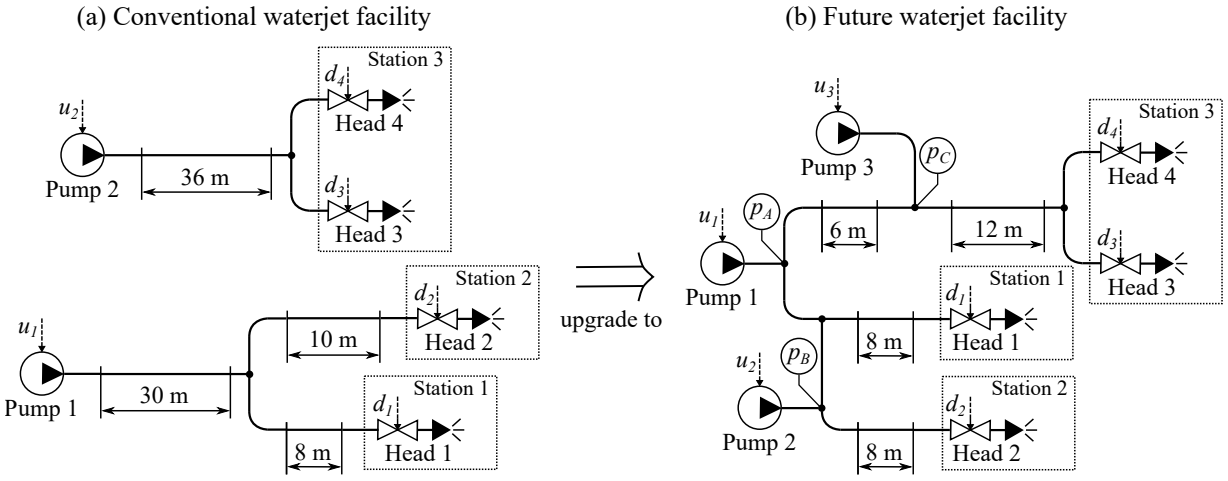

Figure 1.8 – Diagrams of high-pressure networks with different topologies: upgrading conventional waterjet facilities (a) to future energy-efficient facilities (b).

1.3 Principles of high-pressure generation

A pump is an electro-mechanical machine with the task of moving a fluid. It is dedicated to perform a hydraulic work. Referring to the text book [Will and Gebhardt, 2014], the hydraulic work P can be understood as the amount of fluid dV which will be moved within a period dt under load, hence a pump induces a displacement fluid flow $Q = dV/dt$. The fluid flow is referred to the fluid passing through a defined cross section S with a speed v such as $Q = S\ v$. Speaking of a load can relate to the differential pressure Δp between the pump intake and outtake or equivalently to the actual pumping head h. Both are related in terms of $\Delta p = -\varrho\ g\ h$, where ϱ denotes the fluid density and $g \approx 9.81$ m/s^2 is the local acceleration of gravity. The hydraulic work is then defined as $P = Q\ \Delta p$.

Multiple pumps can be set up in parallel to increase the flow rate, while each pump is loaded with the same pressure. On the other hand, multiple pumps can be set up in serial to increase the overall pumping head, while each pump must move the same amount of fluid. Considering future waterjet facilities, high-pressure pumps will be combined in parallel to cover the increase water consumption of several interconnected work stations.

Particularly for waterjet machining, high-pressure is generated when displacing water by means of reciprocating pistons. The water has to meet firm requirements to preserve sensitive high-pressure components, e.g. seals. Table 1.6 gives the requirements provided by the manual of a hydraulically driven high-pressure pump (Type JCP 22 LC).

1.3.1 Classifying high-pressure pumps

Hydraulically driven high-pressure pumps, used for waterjet machining, pressurize water by means of pressure intensifiers. A pressure intensifier increases the pressure, provided from a hydraulic drive, with respect to its piston cross sections. The illustration of Figure 1.9 shows a pressure intensifier (a) and a piston pump (b). The pressure intensifier consists of two chambers separated by a double-acting piston of different cross sections. This piston is floating and can move axially between the chambers.

Table 1.6: Properties of cutting water: mains water is subject to softening and filtering to fulfil requirements for waterjet machining.

Properties	Value	Unit
Electric conductivity	< 20	(mS/cm)
pH value	6.8 - 7.5	
Hardness	< 0.1	(° fH)
Particle quantity	< 100	(mg/l)
Particle size	< 10	(μm)

The low-pressure side has a wide cross section S_1, where the high-pressure side features a significantly smaller cross section S_2. The hydraulic pressure p_1 on the low-pressure side acts on the cross section S_1 of the piston that causes a force $F = S_1\ p_1$. This force induces a water pressure $p_2 = F\ S_2^{-1}$ on the high-pressure side with respect to the cross section S_2. That yields the working principle $S_1\ p_1 = S_2\ p_2$ of a pressure intensifier, as given in [Will and Gebhardt, 2014]. Hence, a hydraulic pressure of about 28 MPa applied on the low-pressure side is intensified with respect to the cross section ratio S_1/S_2. Considering a ratio of 1 : 12.5 induces a water pressure of about 350 MPa into the high-pressure side.

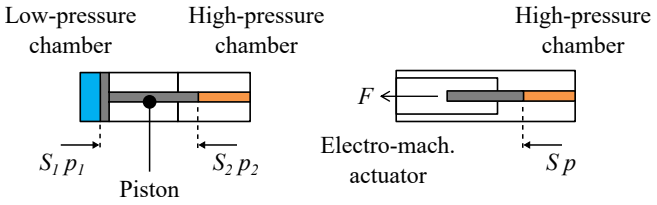

(a) Pressure intensifier (b) Piston pump

Figure 1.9 – High-pressure generation using a pressure intensifier (a) and a piston pump (b): a pressure intensifier pressurizes water (high-pressure chamber) by means of hydraulics (low-pressure chamber), whereas a piston pump is directly driven by an electro-mechanical actuator.

A hydraulically driven high-pressure pump is straight forward to realize with standard hydraulic components. However, its energy efficiency is unsatisfying due to the hydraulic drive. Electrically driven high-pressure pumps replace the hydraulic drive to overcome this downside, while the high-pressure side remains unchanged.

The piston pump holds a chamber that contains a single-acting piston with cross section S, which is directly displaced by a electro-mechanical actuator. A piston displacement pressurizes the fluid within a pumping chamber. Thus, the water pressure p from the high-pressure side causes a force $F = S\ p$ that acts directly on the actuator. For example, inducing a water pressure of 350 MPa with a standard piston of 15 mm diameter requires a force of up to 62 kN.

Drive system and pumping chamber design allow for classifying four types of high-pressure pumps, as shown in diagram of Figure 1.10. With respect to the drive system, hydraulically driven pumps and electrically driven pumps can be distinguished. Each can be further assigned with respect to the principle of pressure generation. It is thereby prevalent to group pressure intensifiers as well as piston pumps, considering double-acting and single-acting operation. On the other hand, electrically driven pumps with single-acting pistons can be further assigned to coupled and independent piston operation.

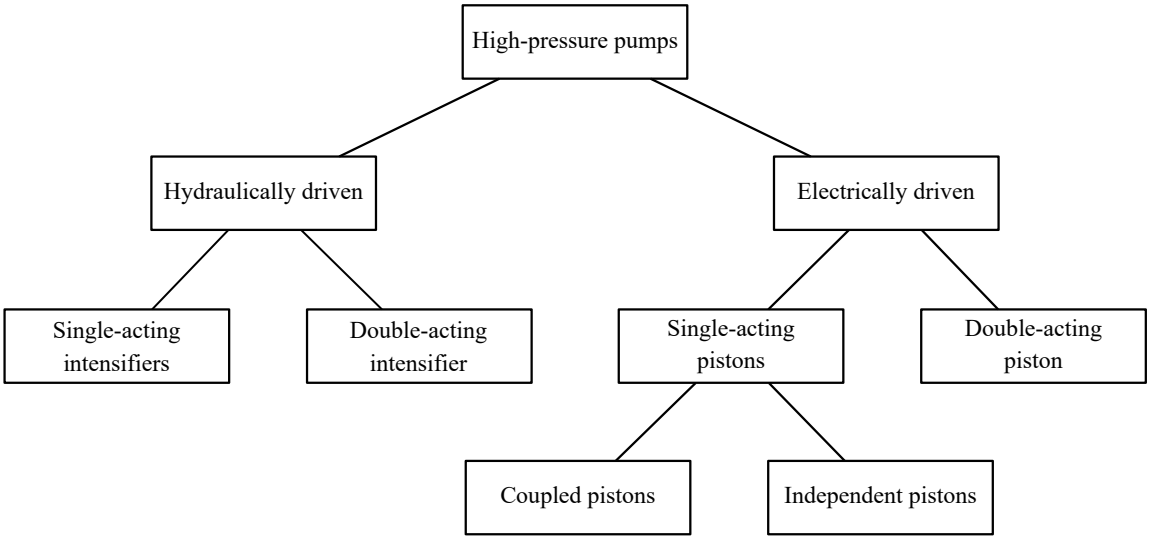

Figure 1.10 – Types of high-pressure pumps: classification of high-pressure pumps with respect to drive system and pumping chamber design.

All of them feature at least two pumping chambers. This enables approximately a continuous pump output fluid flow and consequently realizes a nearly steady pressure generation. However, the principle of pressure generation by reciprocating pistons will induce sinusoidal pressure fluctuations, which will degrade the quality of waterjet machining. The range of pressure fluctuation will vary depending on the pump design. It is common to use multiple pistons and additional high-pressure attenuators to reduce any pressure fluctuations. However, such attenuators are sensitive and cost intensive components. The subsequent sections will provide detailed characteristics of different high-pressure pumps.

1.3.2 Hydraulically driven intensifier pumps

Because of the high load acting at a piston when generating high-pressure, it is evident to utilize hydraulic drives. Hydraulically driven pumps with double-acting intensifiers generate unsteady pressure trends. Due to the coupling of both pumping chambers with a central piston, a half-sinusoidal input fluid flow will result. Consequently, large high-pressure attenuators are installed between pump and high-pressure piping. That guarantees a steady pressure trend, sufficiently for waterjet machining.

An alternative pump design consists of two single-acting intensifiers. Independent pistons pressurize each pumping chamber. The pistons are coupled with the hydraulic drive. These pistons run in a phase-shifted operation to obtain a nearly continuous overall fluid flow. This allows for minimizing pressure fluctuations when switching between the pistons. Optimizing the phase-shifted operation for a specific operating point can further improved the pressure generation such as no high-pressure attenuator will be needed. However, to retract the piston of a single-acting intensifier requires additional pneumatics support.

The schematic of Figure 1.11 shows the hydraulic drive to operate a single-acting intensifier pump (a) and a double-acting intensifier pump (b). Both pump designs are deployed for conventional waterjet machining. They are driven with hydraulic drives of identical configuration. A conventional piston pump supplies a hydraulic circuit, which is regulated to desired pressure. A asynchronous motor powers the pump at constant speed, which runs directly from energy

mains. The hydraulic circuit contains a solenoid valve that applies the pressure to one of both single-acting intensifier or to the double-acting intensifier, respectively. Attenuators are installed at high-pressure side to compensate pressure fluctuations, induced due to the switching of the solenoid valve.

Double-acting intensifier

The hydraulic drive is supplying the double-acting hydraulic cylinder of a single pressure intensifier to realize a reciprocating operation. This enables to displace two coupled high-pressure pistons, which are oriented in opposite directions of motion. The direction of motion will be switched by a solenoid valve, when a piston reaches its maximum stroke. This is detected by proximity sensors. The reciprocating operation induces a sinusoidal input fluid flow due to the coupled high-pressure pistons, see e.g. [Xu et al., 2008].

Single-acting intensifiers

The hydraulic drive is alternately supplying two independent pressure intensifiers. Each intensifier consists of a single-acting hydraulic cylinder that displaces a high-pressure piston. Its control is again straight forward based on a solenoid valve and proximity sensors. The solenoid valve coordinates both pressure intensifiers. The piston of one intensifier will extend to generate an displacement fluid flow, while the other is retracting. A proximity sensor switches the solenoid valve, when a piston reaches its maximum stroke. This results in a phase-shifted reciprocating operation of both pressure intensifiers. The valve design is often optimized for a smooth switching characteristics to minimize pressure fluctuations, see e.g. [Fabien et al., 2010].

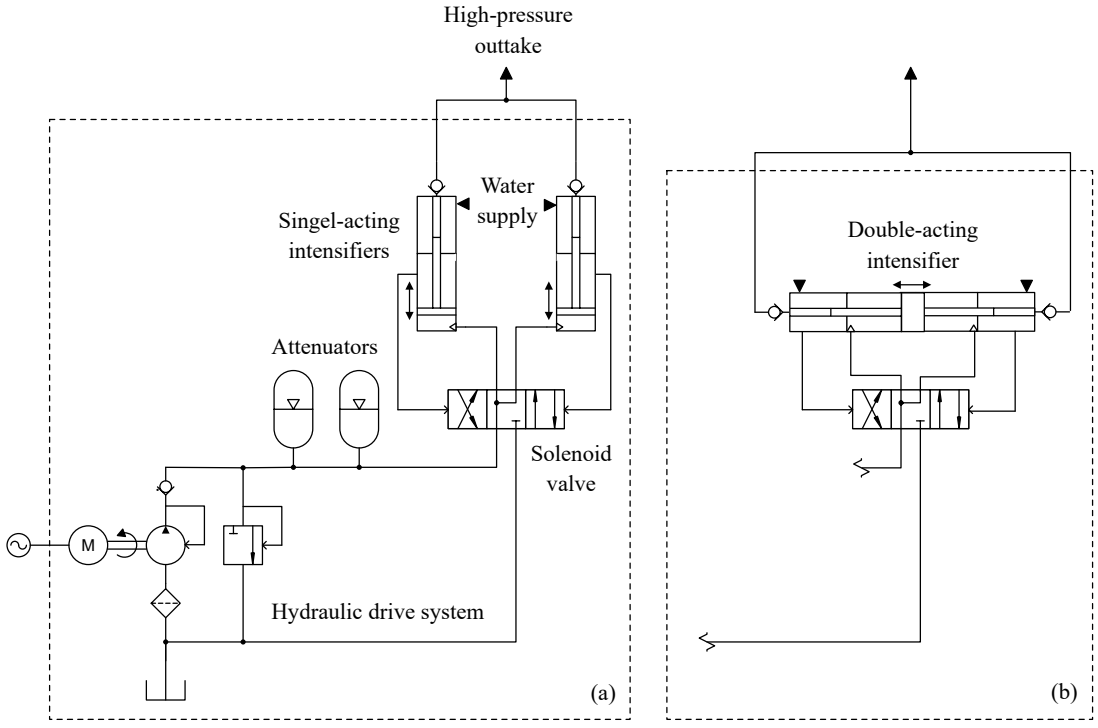

Figure 1.11 – Physical setup of a high-pressure pump with a conventional hydraulic drive: operating two single-acting intensifiers (a) and a double-acting intensifier (b).

1.3.3 Electrically driven piston pumps

Electrically driven pumps with coupled pistons became recently available. A asynchronous motor drives multiple pistons using a mechanical crankshaft. These pumps with coupled pistons, as described in the text book [Michael and Gracey, 2006], are fast evolving in the industry and gradually achieving pressures of up to 200 MPa. This is sufficient for pure water applications. Further advances in the field of electric servo drives enable novel pump designs. In this regard, an electrically driven pump with independent pistons has been proposed in [Niederberger and Kurmann, 2014]. It consists of servo motors, each driving a spindle shaft to displace a piston. The novel pump design allows for pressures of above 400 MPa and can be employed for future waterjet facilities. Its functional principle is introduced in Section 2.3. An alternative pump design with a double-acting piston is proposed in [Borgarelli, 2015]. The high-pressure chambers of both pump designs are identical to the hydraulically driven single-acting intensifier pump. The progression from hydraulically to electrically driven actuators is well illustrated in [Qiao et al., 2017].

Single-acting pistons

The schematic of Figure 1.12 (a) illustrates an electrically driven pump that consists of two independent pistons, which are individually displaced by electric servo motors. The motors are driven by frequency converters. It is possible to synchronize both pistons by means of motion control, that allows for realizing a dynamic phase-shift. This aims at generating a steady pressure trend while compensating any pressure fluctuation for an arbitrary operating point. A high-pressure attenuator is no longer required, see e.g. [Niederberger and Kurmann, 2014].

Double-acting piston

The schematic of Figure 1.12 (b) illustrates an electrically driven pump that consists of two independent pistons, coupled to a spindle shaft which is driven by a common electric servo motor. This provides a constants phase-shift of 180°between each piston and leads to a periodically altering overall fluid flow, following the superposition of two sinusoidal. The constant phase-shift does not allow for compensation of pressure fluctuations. It therefore requires a high-pressure attenuator to compensate pressure fluctuations, see e.g. [Borgarelli, 2015].

1.4 Conclusion

In this chapter, a hydraulically driven high-pressure pump that supplies a work station for contour cutting has been introduced as a typical application of conventional waterjet machining. It is proposed to classify the different waterjet applications with respect to the manufacturing process and the work station setup. This allows for defining suitable use cases, useful when evaluating the modelling methodology, and for verifying the control design of future waterjet facilities. Where the work station setup defines the cutting head configuration, the manufacturing process specifies switching patterns applied on the work stations. On the other hand, standard symbols describing common hydraulic circuits are adapted to describe the configuration of high-pressure networks, interconnecting distributed pumps with cutting heads of various work stations.

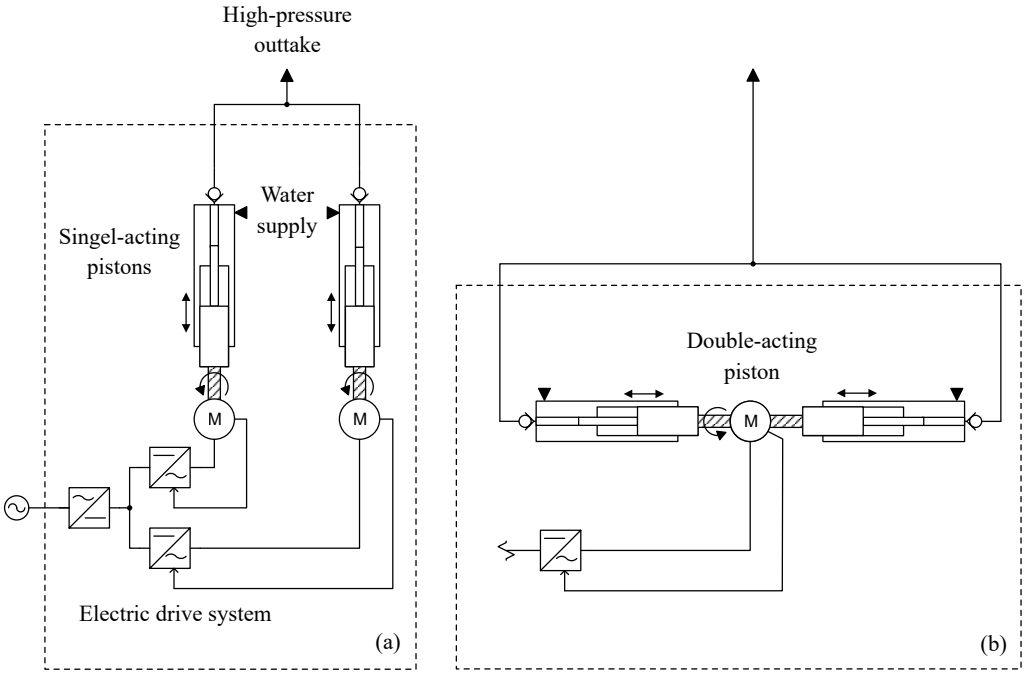

Figure 1.12 – Physical setup of a high-pressure pump with electric drives: two drives units displacing independent pistons (a) and a single drive unit displacing coupled pistons using a crankshaft (b).

The principal of pressure generation has been discussed to explain the common approaches used for high-pressure generation by means of piston pumps. The functional principles of well established and newly emerging concepts are briefly explained. It compares the novel pump design, considered in the subsequent work, with the conventional approaches for pressure generation. This investigation considers two different pumping chamber designs in combination with two drive system concepts.

A close similarity between hydraulically and electrically driven pumps is found, regarding the pumping chamber design. Where electrically driven pumps with coupled pistons barely reach the pressure needed for waterjet machining, experimental pump designs with independent single-acting and double-acting pistons obtain pressures up to 400 MPa. These pumps are suitable for waterjet machining, but related literature is rarely found. The subsequent chapter will present an electrically driven pump with independent single-acting pistons, while introducing a high-pressure test bench. It further defines all use cases, network topologies and switching patterns in detail, which has been employed for this thesis.

2

System description

Contents

2.1 Introduction

Objectives

The concept of energy-efficient waterjet facilities considers decentralized pumps to establish high-pressure networks. These decentralized pumps require a new drive system, since hydraulically driven pumps suffer from a low energy efficiency. Moreover, they fail to run within the required operating range. To overcome these drawbacks, electrically driven high-pressure pumps reduce the drive complexity and provide the ability to operate at any desired operating point. The drive system complexity becomes reduced at the expanses of a demanding control strategy. To evaluate future control strategies and to verify high-pressure network model requires the development of a high-pressure test bench and to define suitable use cases, which represent future waterjet facilities.

State of the art

In most today's applications, waterjet machining includes a remote high-pressure pump that feeds a single work station [Nee, 2015]. A high-pressure intensifier pump is developed in [Olsen, 1974] to enhance the high-pressure generation. This has been a milestone for the industrial availability of waterjet machining. Recent developments relate to this pump design, using hydraulically driven pressure intensifiers. Two double-acting intensifiers have been combined in [Trieb et al., 2007] with a phase shift operation to reduce pressure fluctuations induced by the pump, where a single-acting pump with phased intensifiers is investigated in [Xu et al., 2008]. The modelling and identification of double-acting pump is presented in [Fabien et al., 2010], while machine diagnostics for a multiple phased single-acting pump is shown in [Ferretti et al., 2015] that further reduces pressure fluctuations. The working principle of an electrically driven high-pressure pump with single-acting pistons has been first introduced in [Niederberger and Kurmann, 2014]. Experimental studies revealed energy savings of more than 30% compared to the conventional pump design.

Contribution

This chapter first presents a high-pressure test bench capable to interconnect two electrically driven pumps with two work stations. That allows for configuring the high-pressure piping to represent various high-pressure networks. This aims at validating specific high-pressure network models by means of measurements and evaluating future control strategies, as will be shown in a subsequent chapter. For this purpose, suitable high-pressure network topologies and use cases will be introduced with respect to the investigations of the previous chapter. These topologies and use cases are then referred to in the subsequent chapters when verifying the modelling methodology and control design.

This chapter further investigates the novel pump design of an electrically driven high-pressure pump and presents the working principle of phase-shifted single-acting pistons. An electrically driven pump is modular and manages to synchronize the pistons with an adjustable phase-shift. This synchronization is realized using a virtual crankshaft (camming). It generates the reference trajectories, as required to displace the pistons by means of motion control. These trajectories are generated, taking a model into account that describes the pressure generation within a pumping chamber. It enables the electrically driven high-pressure pump to run on a wide operating range, while any pressure fluctuations, induced by the pump, become minimized.

This section is structured as follows: Section 2.2 presents the considered test bench setups and network topologies. It specifies the use cases for future waterjet facilities, subject for investigation, and introduces switching patterns to reproduce selected manufacturing processes. Section 2.3 presents the energy efficient high-pressure pump, implemented to the test bench. It investigates its working principle, considering the piston synchronization by means of model-based camming.

2.2 Test bench for scalable high-pressure networks

A preliminary test bench combines an early prototype of the electrically driven pump with a standard cutting head to verify the novel pumping technology. This setup is insufficient to represent scalable high-pressure networks. Thus, an extended test bench has been deployed in collaboration with the industry. This requires to design an enhanced electrically driven pump, including its production and the installation in the laboratory, where the extended test bench is assembled. This extended test bench has been established in the laboratory of the FHNW. It is dedicated to experimental studies of the subsequent investigations, e.g. for parameter identification, model validation and controller verification. It consists of two independent high-pressure pumps and two independent cutting heads. This allows for defining high-pressure networks which correspond to common waterjet facilities, but also to realize topologies which represent future waterjet facilities with limited complexity. The test bench can be configured, taking the various cutting head configurations into account given for typical work station setups. Its cutting heads can be switched with respect to varying switching patterns as required from common manufacturing processes. Its high-pressure pumps can be regulated to a desired pump rate such as to obtain the operating pressure in compliance with different waterjet applications.

This section introduces different high-pressure networks subject for modelling and control design. Basic topologies are used to validate the proposed graph-based modelling methodology. The validated modelling methodology is then applied to model more complex topologies which are too time consuming and cost intensive for realizing on a test bench. Use cases are defined with respect to operating pressure, cutting head configuration and switching pattern. They are assigned to experiments for parameter identification and model validation.

2.2.1 Test bench setup

The test bench, as shown in image of Figure 2.1, is configurable to represent different network topologies. The high-pressure network can interconnect two independent electrically driven pumps and two independent cutting heads. The pumps can simultaneously pressurize the high-pressure network at arbitrary positions, while the cutting heads realize the desired switching patterns. A cutting head reproduces the discharge flow of a work station when generating a waterjet. The waterjet is immediately discharged into a containment. This corresponds to a pressure sink, while a high-pressure pumps represents a fluid flow sources.

By taking the various cutting head configurations into account, each cutting head can be equipped with a diamond nozzle of 0.1 to 0.4 mm inner diameter. This enables a cutting head to represent various work station setups, from a single cutting head configuration of up to 0.4 mm nozzle to a single work station with up to 16 synchronously switching cutting heads of 0.1 mm nozzles. Interconnecting a second cutting head allows for realizing a cluster of 2 work stations with independently switching cutting heads. Considering a second pump, allows for a test bench setup which represents complex network topologies of future high-pressure facilities. These networks are realized by interconnecting common high-pressure piping.

The control variable $u_n(t) = [0, 1]$ regulates a high-pressure pump $n \in \{1, 2\}$ to an corresponding pump rate, where the disturbance variable $d_m(t) = \{0, 1\}$ switches the on/off-valve of a cutting head $m \in \{1, 2\}$. This affects the overall water consumption for which the pump rate has to be adjusted, where the control signal is proportional to the desired pump rate. The diagram in Figure 2.2 represents the high-pressure test bench schematically. The pressure $p_x(t)$ can be measured at different network positions x using 4 pressure gauges. The applied network positions will be defined later in this section, when introducing the investigated network topologies. In general, pressure measurements near to a high-pressure pump are denoted as $p_{Pn}(t)$, where n relates to the corresponding pump and measurements near to a cutting head are denoted as $p_{Hm}(t)$, where m relates to the corresponding cutting head. Any other measurement positions within a high-pressure network are denoted as $p_{Ni}(t)$, with i as a consecutive numbering.

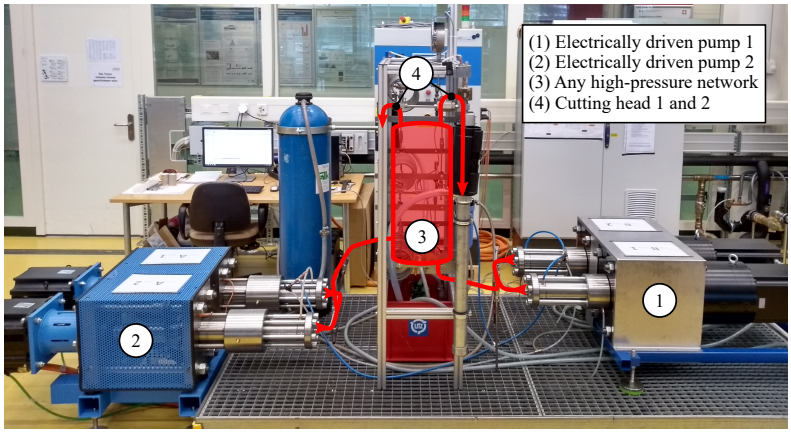

Figure 2.1 – High-pressure test bench: two electrically driven piston pumps supply two cutting heads over a configurable high-pressure network.

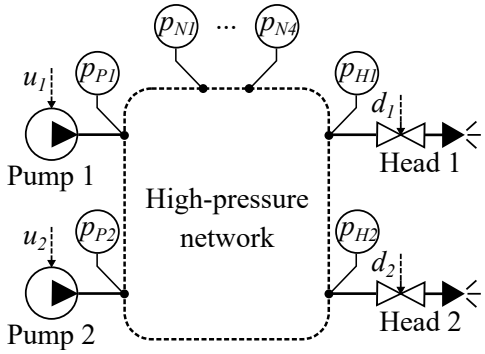

Figure 2.2 – Test bench topology: pumps and cutting heads interconnected with a configurable high-pressure network to represent various waterjet facilities.

The schematic in Figure 2.3 shows the test bench setup used to derive experiments for parameter identification, model validation and controller verification. An offline computer is used to design the desired experiments. This computer employs *MATLAB Simulink* to evaluate the experiments in advance by means of simulations. The design of experiment is then transmitted to an online computer, if the simulations achieved the desired parameters, e.g. bounded control

values considering pump saturations or bounded pressure state with respect to system limits. This computer employs *Studio 5000* to parametrize the test bench with respect to a planned experiment and to execute this experiment. It stores the measurement data locally while executing an experiment. After termination of the experiment, the experimental data are sent to the offline computer, which evaluates the data by means of *MATLAB*. A control unit (PLC) is employed to control the test bench, while executing an experiment. It sets the required pump rates $u_n(t)$ for each high-pressure pump and the switching states for each cutting head, considered as disturbances $d_m(t)$. A digital output module is connected to the PLC that controls the on/off-valve of a cutting heads with respect to specified switching patterns. An analogue input module is connected to the PLC that measures the pressure trends $p_x(t)$ of 4 pressure gauges at a sampling rate of 250 Hz each. The pressure gauges have a wide operating range of 0 to 500 MPa.

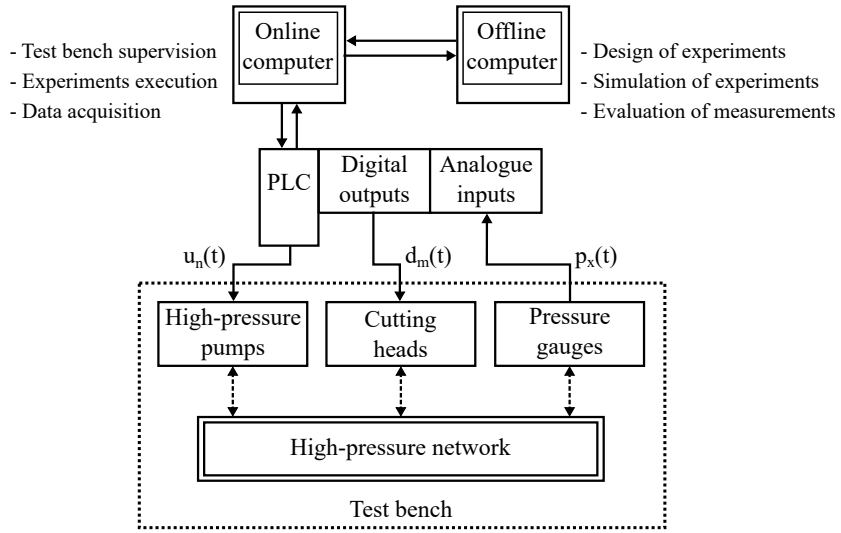

Figure 2.3 – Test bench hardware setup: hardware employed to regulate the test bench and to execute experiments.

The test bench is realized using the hardware listed in Table 2.1. The displacement fluid flow is evaluated for each piston by measuring the piston velocities. Each high-pressure pump provides all data needed to the PLC. More information is given when introducing the electrically driven piston pump used with the test bench. As long as any low-level control is missing, each pump is regulated to produce a steady pump rate. That causes a continuous overall fluid flow. Without considering the cutting head configuration or switching state, any pressure trend could be reached. Hence, simulations are important to estimate the expected pressures for a specific experiment that all process variables remains within permitted limits, given by the test bench and high-pressure pumps.

2.2.2 Investigated network topologies

The test bench can be configured to represent different work station setups, which correspond to common waterjet facilities. Specific setups will be chosen with regards to parameter identification, model validation and controller verification. The selected setups begin with basic topologies interconnecting a single pump to a single cutting head and are gradually extended to more complex networks including two coupled pumps and two independent switching cutting heads. Complementary to experiments on the test bench, all of these high-pressure networks will be

Table 2.1: Test bench hardware configuration: hardware used for data acquisition and to control the switching heads.

Components	Type	Properties
Control unit (PLC)	1x Rockwell, CompactLogix ###	1 ms update time.
Digital output module	1x Rockwell, Compact I/O ###	
Analogue input module	1x Rockwell, Compact I/O ###	0.2% accuracy, 16 bit resolution, $\geq$ 0.7 ms sampling rate.
Pressure gauges	4x Gefran, ###	0.1% accuracy, $<$ 1 ms response time.

modelled in *MATLAB Simulink*, applying the proposed graph-based modelling methodology, given in Chapter 3. This aims at validated high-pressure network models, which are useful to simulate future waterjet facilities.

1 pump - 1 cutting head network topologies

Initial topologies consider a single pump feeding a single cutting head. Pump and cutting head are directly interconnected with a high-pressure piping. This setup involves two topologies as depicted in diagrams of Figure 2.4. Topology (a) establishes a short piping section of about 3 m length between pump and cutting head, while topology (b) represents a long piping of about 19 m. The long piping is expected to increase the fluid flow resistance that yields an increased pressure loss from pump to cutting head.

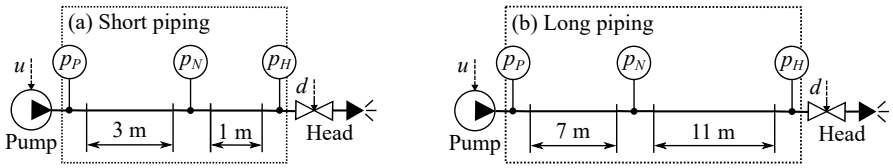

Figure 2.4 – 1 pump - 1 head topologies: single pump setup with an independent cutting head directly interconnected with **(a) Short piping** and **(b) Long piping**.

The pressure is measured at the test bench intake $p_P(t)$, at a piping connector within the high-pressure network $p_N(t)$ and at the test bench outtake $p_H(t)$. The first topology has been used to validate the robust low-level control design by means of simulations, see Chapter 6, while the second topology has been used to validate the graph-based modelling methodology for a wide pressure range with measurements from the test bench, see Chapter 4.

1 pump - 2 cutting heads network topologies

Extended topologies consider a single pump feeding two cutting heads. Pump and cutting heads are connected with a more complex high-pressure network. This setup includes again two topologies as depicted in the diagram of Figure 2.5. Where topology (c) realizes a symmetric network

with 6 m of piping length from the joint to a cutting head each, the topology (d) features an asymmetric network with about 11 m for cutting head 1 and 1 m for cutting head 2. The symmetric topology is expected to generate identical resistances for both fluid flow paths that should result in a symmetric fluid flow distribution, when assuming identical diamond nozzles for every cutting head. Hence, the influence of configuring different cutting heads can be clearly distinguished. The asymmetric topology is expected to cause different resistances for each fluid flow path that should result in an asymmetric fluid flow distribution, even for identical diamond nozzles. The cutting heads will be identically configured to investigate the influence from the network topology.

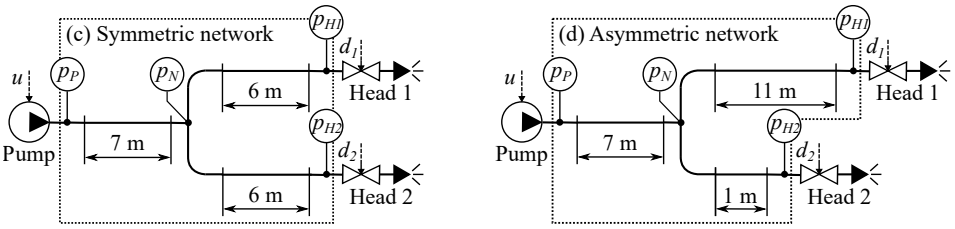

Figure 2.5 – 1 pump - 2 heads topologies: single pump setup with independent cutting heads connected to **(c) Symmetric network** and **(d) Asymmetric network** topologies.

The pressure is measured at the test bench intake $p_P(t)$, at the piping connector $p_N(t)$ that couples the pump to both cutting heads and at both test bench outtake positions $p_{H1}(t)$ and $p_{H2}(t)$. Both topologies are used to identify the model parameters for various high-pressure components (see Section 3.4), to verify the proposed high-pressure network models (Section 4.3) and to validate the derived low-level controllers (Section 6.4), using measurements from the test bench. Different experiments have been derived on the same setup regarding parameter identification and model validation. However, model and controller validation will employ the same measurement data. Where the high-pressure network model is validated in open-loop, the low-level controller is validated in closed-loop control.

2 pumps - 2 cutting heads network topologies

Finally, networked topologies consider two pumps feeding two cutting heads. Pumps and cutting heads are connected with complex high-pressure networks. This setup provides a wide variety to distribute pumps and cutting heads in a network. It considers three topologies as depicted in the diagram of Figure 2.6. The symmetric distributed topology (e) as well as the asymmetric distributed topology (f) consider two centrally interconnected cutting heads with a piping of about 1 m length. Where topology (e) realizes a symmetric network with 6 m of piping length from the joint to a high-pressure pump each, the topology (f) features an asymmetric network with about 11 m for pump 1 and 1 m for pump 2. The decentralized distributed topology (g) features a symmetric high-pressure network, but both pumps and both cutting heads are spatially distributed. The first two setups aim to investigate the behaviour of two interconnected pumps when applying identical disturbances at a single network position. Different disturbances are applied at other network positions, considering the third setup. This can affect both pumps, even for a symmetric network topology.

The pressure is measured at both test bench intake positions $p_{P1}(t)$ and $p_{P2}(t)$, at the piping connector $p_N(t)$ that couples both pumps and at both test bench outtake positions $p_{H1}(t)$ and

$p_{H2}(t)$. These topologies are used to verify robust low-level controllers, distributed to several coupled pumps and before establishing any high-level managing. The model validation is extended with these complex high-pressure networks, again comparing open-loop simulations and measurements. The resulting validated simulation models represent future waterjet facilities. They are then employed to verify the high-level managing by means of simulations, see Section 7.4.

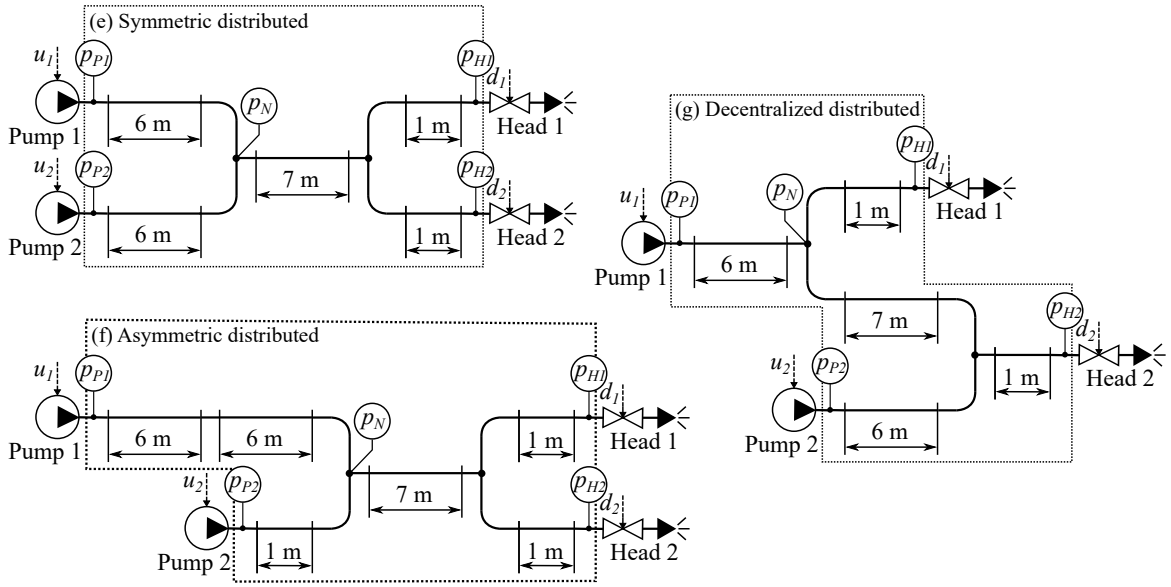

Figure 2.6 – 2 pumps - 2 heads topologies: distributed pumps with independent cutting heads connected to **(e) Symmetric distributed**, **(f) Asymmetric distributed** and **(d) Decentralized distributed** network topologies.

This section described the selected topologies for configuring the test bench. Table 2.2 gives an overview of the introduced network topologies. It relates them to its utilization and assigns them to use cases, which are defined in the subsequent section.

Table 2.2: Test bench network topologies: setups applied to the test bench and modelling subject for simulation.

Topologies	Pumps	Heads	Utilization	Use cases
(a) Short piping (b) Long piping	1	1	Control design and modelling verification	1
(c) Symmetric network (d) Asymmetric network	1	2	Parameter identification, model and controller validation	2
(e) Symmetric distribution (f) Asymmetric distribution (g) Decentralized distribution	2	2	Extended model and extended controller validation, managing verification	3

2.2.3 Use case definition

Here, 3 use cases are taken into account for measurements with the test bench and for simulation in *MATLAB Simulink*. Use case 1 considers a 1 pump - 1 head setup that represents a basic waterjet facility. Use case 2 deals with a 1 pump - 2 heads setup that represents an extended facility, while use case 3 represents a 2 pumps - 2 heads setup of a future waterjet facility. Various experiments have been derived while taking different switching patterns and various nozzle configurations into account, with respect to the identified manufacturing processes and work station setups. According to the waterjet applications, two different operating pressures have been considered for the use cases 1 and 2. Experiments for use case 3 have been limited for a single operating pressure, since more as sufficient combinations become available when combining two high-pressure pumps and two cutting heads.

Use case 1

To verify the low-level control design and the graph-based modelling methodology, the test bench has been configured considering the 1 pump - 1 head topology with a short piping (a) and a long piping (b). Two different experiments have been realized for each topology. A first experiment at 200 MPa operating pressure, where the cutting head holds a 0.35 mm nozzle and a second at 350 MPa pressure, where a 0.25 mm nozzle has been installed. These experiments include the measurements listed in Table 2.3. Different measurements have been realized using the same topology and configuration, but with respect to different switching patterns.

In a first step, the modelling methodology has been verified considering the test bench in open-loop. Therefore, a high-pressure pump cannot compensate any pressure fluctuations induced by switching a cutting head. Hence, a stripping application is chosen, where the cutting head remains open for any time. In a second step, the control design has been verified considering an application for contour cutting and another application for cavity cutting. This requires different switching patterns as introduced in the subsequent section.

Table 2.3: Configuration for use case 1: measurements derived on different test bench setups to verify the robust low-level control design and the graph-based modelling methodology.

Meas.	Topology	Pressure (MPa)	Nozzle ⌀(mm)	Switching pattern	Utilization
R-1	(a) Short	100 . . . 400	0.25	Strip.	Mdl. verif.
B-1		200	0.35	Contour	Ctr. verif.
B-2		350	0.25	Contour	Ctr. verif.
B-3	(b) Long	200	0.35	Contour	Param. ident.
B-4				Contour	Mdl. valid.
B-5				Cavity	Mdl. valid.
B-6		350	0.25	Contour	Param. ident.
B-7					Mdl. valid.

Use case 2

To identify the parameters of high-pressure components and to validate high-pressure network models, derived with the graph-based modelling methodology, as well as to validate the low-level controllers, derived with robust control design, the test bench has been configured considering the 1 pump - 2 heads topology with a symmetric network (c) and an asymmetric network (d). All experiments have been derived at 200 MPa operating pressure as well as at 350 MPa, while different cutting head configurations have been evaluated. These experiments include the measurements listed in Table 2.4. Again, different measurements have been realized using the same topology and configuration, but with respect to different switching patterns. First experiments focus on a symmetric cutting head configuration, where both cutting heads hold a 0.25 mm nozzle. Subsequent experiments investigate an asymmetric configuration, where head 1 holds a 0.3 mm nozzle and head 2 a 0.2 mm nozzle. Here, the symmetric network topology combined with an asymmetric cutting head configuration allows for investigating the effects of different cutting head nozzles. Subsequent experiments focus on the asymmetric cutting head configuration only. Here, the asymmetric network topology combined with a symmetric cutting head configuration allows for investigating the effects of different fluid flow paths in a high-pressure network.

In a first step, measurements considering an application for contour cutting have been assigned for parameter identification. The other measurements have been used for model validation. The identification data have been used to identify the discharge coefficient ζ of cutting head nozzles as well as the friction loss coefficient λ for high-pressure piping sections, as introduced later in this work. In a second step, an initial low-level controller has been validated with measurements considering an application for contour cutting as well as for cavity cutting. Hence, two different switching patterns will disturb the high-pressure pump, which operates now in closed loop control to compensate any pressure fluctuations.

Table 2.4: Configuration for use case 2: measurements derived on different test bench setups to validate high-pressure network models and low-level controllers as well as to identify network parameters.

Meas.	Topology	Pressure (MPa)	Nozzle 1 ⌀(mm)	Nozzle 2 ⌀(mm)	Switching pattern	Utilization
E-1	(c) Sym. net.	200	0.25	0.25	Contour	Param. ident.
E-2		350	0.15	0.15	Contour	Param. ident.
E-3		200	0.3	0.2	Contour	Param. ident.
E-4					Contour	Mdl. & Ctr. valid.
E-5					Cavity	Mdl. valid.
E-6		350	0.2	0.1	Contour	Param. ident.
E-7						Mdl. & Ctr. valid.
E-8	(d) Asym. net.	200	0.25	0.25	Contour	Param. ident.
E-9						Mdl. & Ctr. valid.
E-10		350	0.15	0.15	Contour	Param. ident.
E-11						Mdl. & Ctr. valid.

Use case 3

The test bench has been configured considering the 2 pumps - 2 heads topology with a symmetric distributed network (e), an asymmetric distributed network (f) and a decentralized network (g) to validate high-pressure network models of increased complexity, to validate the low-level controllers with respect to these complex network topologies and to verify the high-level managing design, used to balance both high-pressure pumps to an average pump rate. All experiments have been derived at 200 MPa operating pressure only, while evaluating different cutting head configurations. These experiments include the measurements listed in Table 2.5. Various measurements have been realized with the same topology and configuration, but with respect to other switching patterns only applied at the cutting head 2, while cutting head 1 remains open for any time. This allows for investigating the effects of a single source of disturbance affecting two pumps at different network locations. Two experiments have been realized for each topology. A first experiment investigated a symmetric cutting head configuration, where both cutting heads hold a 0.2 mm nozzle. The subsequent experiment considered an asymmetric configuration, where head 1 holds a 0.1 mm nozzle and head 2 a 0.3 mm nozzle. All three switching patterns have been applied with respect to each test bench setup, considering an application for surface stripping, contour cutting and cavity cutting. Basically, all of them are of interest when verifying the high-level managing. Measurements considering the stripping application are used for an extended model validation, while measurement considering cavity cutting are used for an extended controller validation. The measurements considering contour cutting are used for model validation as well as for controller validation.

Table 2.5: Configuration for use case 3: measurements derived on different test bench setups to validate high-pressure network models and low-level controllers as well as to verify the high-level managing design.

Meas.	Topology	Pres. (MPa)	Noz. 1 ⌀(mm)	Noz. 2 ⌀(mm)	Switch. pattern	Utilization
D-1	(e) Sym. dis.	200	0.2	0.2	Strip.	Mdl. val.
D-2					Contour	Mdl. & Ctr. val.
D-3					Cavity	Mdl. val.
D-4	(f) Asym. dis.	200	0.2	0.2	Strip.	Mdl. val.
D-5					Contour	Mdl. & Ctr. val.
D-6					Cavity	Mdl. val.
D-7	(g) Dezen. dis.	350	0.1	0.3	Contour	Manag.
D-8					Cavity	Manag.

2.2.4 Investigated switching patterns

Different experiments have been conducted while opening and closing cutting heads with defined switching patterns. These experiments vary with respect to the cutting head configuration, network topology and switching pattern. Particularly, two switching patterns are defined considering the investigated manufacturing processes: an application for contour cutting and an application for cavity cutting. The cycle times and on/off-ratios of Table 2.6 have been exemplary chosen to realize the different switching patterns.

Single cutting head (Use case 1)

The measurements of use case 1 has been derived considering a 1 pump - 1 head setup. To realize the contour cutting application, the single cutting head will open for a cutting period of 60 seconds, followed by a hold period in closed position for another 60 seconds, as depicted in diagram of Figure 2.7 (a). On the other hand, to realize the cavity cutting application, the single cutting head will open for a cutting period of 0.5 seconds, followed by a hold period in closed position for another 0.5 seconds, as depicted in diagram of Figure 2.7 (b). Both switching patterns will be periodically repeated.

Table 2.6: Switching patterns: specification of switching patterns with respect to typical manufacturing processes used for experiments.

	Cycle time (s)	On/off-ratio (%)
Contour	60	50
Cavity	0.5	50

These switching patterns realize 2 different states of the high-pressure test bench, where the resulting water consumption depends on the cutting head configuration and operating pressure. For an operating pressure of 200 MPa and a cutting head configured with a 0.35 mm nozzle, a maximal fluid flow consumption of 2.4 l/min results. For an operating pressure of 350 MPa and a cutting head configured with a 0.25 mm nozzle, a maximal fluid flow consumption of 1.6 l/min results. A closed cutting head wont require any water. However, when a pump continues to operate, the operating pressure will increase without limits.

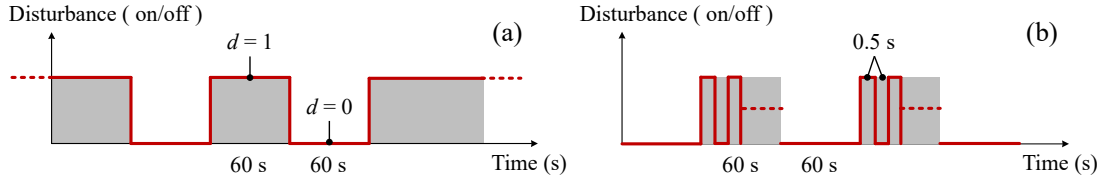

Figure 2.7 – Switching pattern for a single cutting head configuration: cutting head in open position as initial condition for performing contour cutting (a) and cavity cutting in repeated cycles (b).

Two active cutting heads (Use case 2)

The measurements of use case 2 have been derived considering a 1 pump - 2 heads setup. To realize a contour cutting application, both cutting heads will open for a cutting period of 60 seconds, followed by a hold period in closed position for another 60 seconds, as depicted in diagram of Figure 2.8 (a). On the other hand, to realize a cavity cutting application, each cutting head will open for a cutting period of 0.5 seconds, followed by a hold period in closed position for another 0.5 seconds, as depicted in diagram of Figure 2.8 (b). Both switching patterns will be repeated periodically with a 90° phase shift between both cutting heads.

These switching patterns realize 4 different test bench states, where the resulting water consumption depends on each cutting head configuration. If cutting head 1 holds a nozzle of

0.3 mm diameter, while the cutting head 2 is configured with a 0.2 mm nozzle and combining all possible switching states, 4 different fluid flows ($Q(t) \in \{0,\ 0.78,\ 1.61,\ 2.39\}$ l/min) will result, considering a continuous operating pressure of 200 MPa. If cutting head 1 holds a nozzle of 0.2 mm diameter, while the cutting head 2 is configured with a 0.1 mm nozzle and combining all possible switching states, 4 different fluid flows ($Q(t) \in \{0,\ 0.27,\ 1.01,\ 1.28\}$ l/min) will result, considering a continuous operating pressure of 350 MPa. If both cutting heads hold a nozzle of 0.25 mm diameter and combining all possible switching states, again 4 different fluid flows ($Q(t) \in \{0,\ 1.16,\ 1.17,\ 2.33\}$ l/min) will result, considering a continuous operating pressure of 200 MPa. Eventually, if both cutting heads hold a nozzle of 0.15 mm diameter and combining all possible switching states, 4 different fluid flows ($Q(t) \in \{0,\ 0.61,\ 0.71,\ 1.32\}$ l/min) will result, considering a continuous operating pressure of 350 MPa.

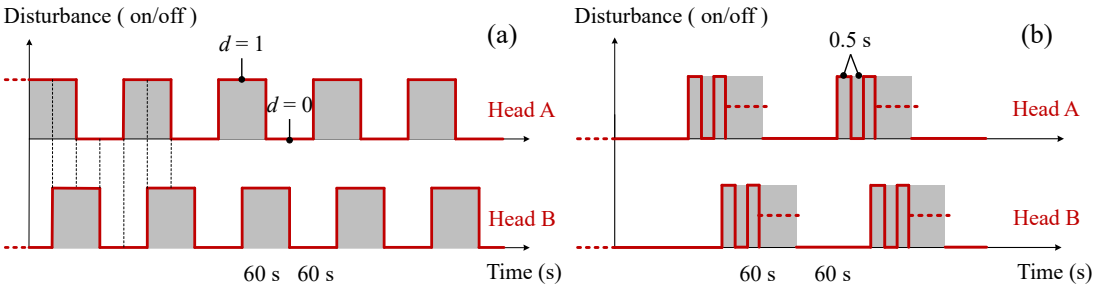

Figure 2.8 – Switching pattern for a two cutting head configuration: cutting head A in open and B in closed position as initial condition for performing contour cutting with 90° phase shift (a) and cavity cutting in repeated cycles of 90° phase shift (b).

Active and passive cutting head (Use case 3)

The measurements of use case 3 have been derived considering a 2 pumps - 2 heads setup. Only cutting head 2 will open for a cutting period of 60 seconds, followed by a hold period in closed position for another 60 seconds to realize a contour cutting application, as depicted in diagram of Figure 2.9 (a). Equivalently, the cutting head 2 will open for a cutting period of 0.5 seconds, followed by a hold period in closed position for another 0.5 seconds to realize the cavity cutting application, as depicted in diagram of Figure 2.9 (b). Both switching patterns will be repeated periodically.

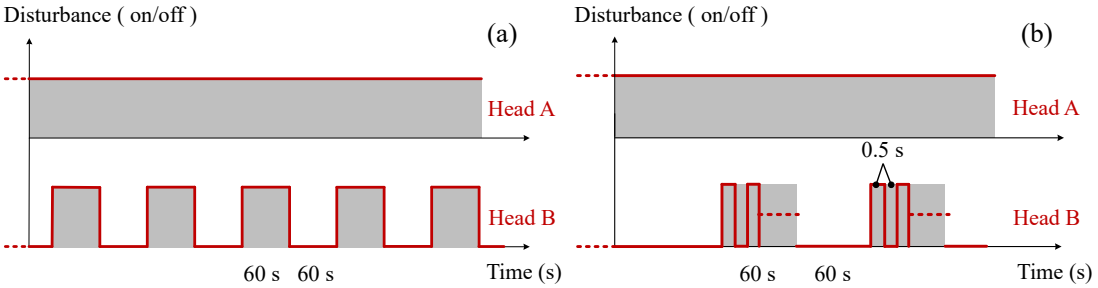

Figure 2.9 – Switching pattern for a two cutting head configuration: cutting head A remains in open position for all time, while cutting head B performs contour cutting (a) and cavity cutting (b) in repeated cycles.

2.3 Novel electrically driven pump with single-acting pistons

This section presents the novel electrically driven high-pressure pump, designed considering the concept mentioned in [Niederberger and Kurmann, 2014], which is installed with the previously introduced high-pressure test bench of Section 2.2. It pressurizes water by means of pistons, which are displaced with electric drives, see the properties listed in Table 2.7. The electric drive allows for operation on a wide pressure range without any adjustments for different waterjet applications. Its size is reduced by 40% and its energy efficiency is enhanced by 30%, compared to a hydraulically driven pump that operates in the same power range. The electrically driven pump provides an enhanced pumping performance due to the improved overall efficiency. This results in an increased maximal pressure in contrast to the hydraulically driven pump, discussed in Table 1.1 of Section 1.2.

The image of Figure 2.10 shows a prototype including two electrically driven pumping units. Its modular pump design is scalable to meet the increased fluid flow demands of future large-scale waterjet facilities by combining a desired amount of pumping units. However, the single-acting pistons require a precise positioning and an accurate synchronization to realize a steady pressure trend. This will be taken into account when introducing the motion control and a model-based camming, both introduced later in this section.

Table 2.7 – Properties of a electrically driven high-pressure pump: high pressure pump prototype.

Properties	Value	Unit
Maximal pressure	480	(MPa)
Input fluid flow	3.2	(l/min)
Drive power	27.5	(kW)
Frame size	1.45x1.0x0.55	(m)
Weight	ca. 600	(kg)
Noise level	ca. 60	(dB)

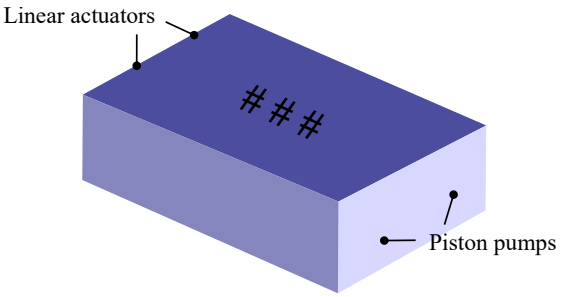

Figure 2.10 – Novel high-pressure pump prototype: two single-acting pistons with independent electric drives.

The pistons of both pumping units operate alternately with a phase shift of 180°, such as to produce a steady output fluid flow. This guarantees a continuous operation with reduced pressure fluctuations. The image of Figure 2.11 gives the physical setup of a pumping unit.

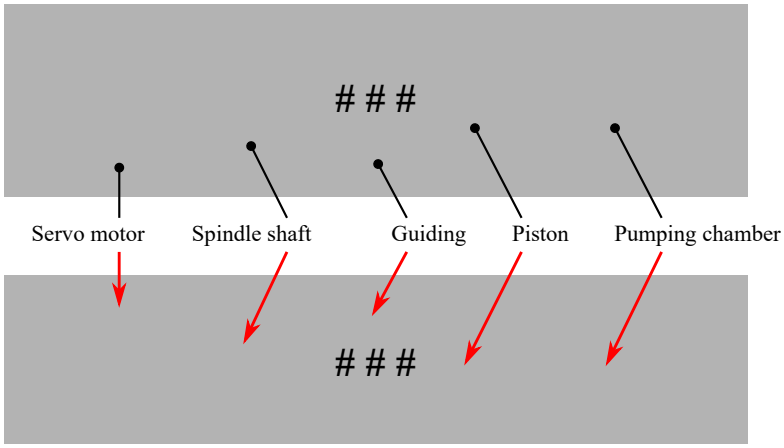

Figure 2.11 – Modular pumping unit: independent synchronous motor positioning a piston by means of a spindle shaft to pressurize water in its pimping chamber.

To position a piston, a spindle shaft transforms the rotative motion of a servo motor to a linear piston displacement. An angular motor velocity ω_P results in a linear piston velocity

$$v_P = \frac{h}{2\pi}\,\omega_P \tag{2.1}$$

where $h = ###$ m denotes the spindle pitch. Any piston displacement then induces a fluid flow $Q_P = S_P\,v_P$ with respect to the piston surface S_P. The pumping chamber limits the maximal available piston stroke $s_{max} = ###$ mm. A pressure p in the chamber acts on the piston surface and caused the force $F = S_P\,p$ that is transformed to a motor torque

$$T = \frac{h}{2\pi}\,F\ . \tag{2.2}$$

An absolute encoder measures the angular position θ_P of the servo motor, which is mounted at the motor rotary shaft. Its angular velocity ω_P is derived from low-pass filtering the time derivative of the position signal according to the first-order filter

$$\frac{d}{dt}\omega_P = a_{LP}\left(\frac{d}{dt}\theta_P - \omega_P\right) \tag{2.3}$$

with filter coefficient a_{LP} chosen to obtain a bandwidth of 27.162 kHz. The angular position θ_P and velocity ω_P are feedback signals, eventually used for motion control.

2.3.1 Pump setup

The overview of Figure 2.12 shows the hardware setup of a electrically driven pump. It is realized by means of two pumping units, using the hardware mentioned in Table 2.8. Each pumping unit requires a frequency converter (FC), that has to realize the motion control task. It drives the synchronous motors to displace the pistons within the available piston stroke, using the feedback signals from absolute encoders. A power supply powers both frequency converters from mains. This setup allows for energy recuperation, considering both pumping units and its phase-shifted operation. That aims further to improve the energy efficiency of high-pressure pumps.

The control architecture of an electrically driven high-pressure pump is given in diagram of Figure 2.13. Cutting heads will switch on and off with respect to the disturbance signal $d(t)$. This results in a varying water consumption and induces pressure fluctuations into the high-pressure network. These fluctuations have to be compensated with the available high-pressure pumps. A pressure control has to regulate the measured pressure $y(t) = p_P(t)$ at the pump outtake to a steady reference pressure r desired for waterjet machining. The high-pressure pump will provide an output fluid flow $u_g(t)$ proportional to the commanded pump rate $u(t)$.

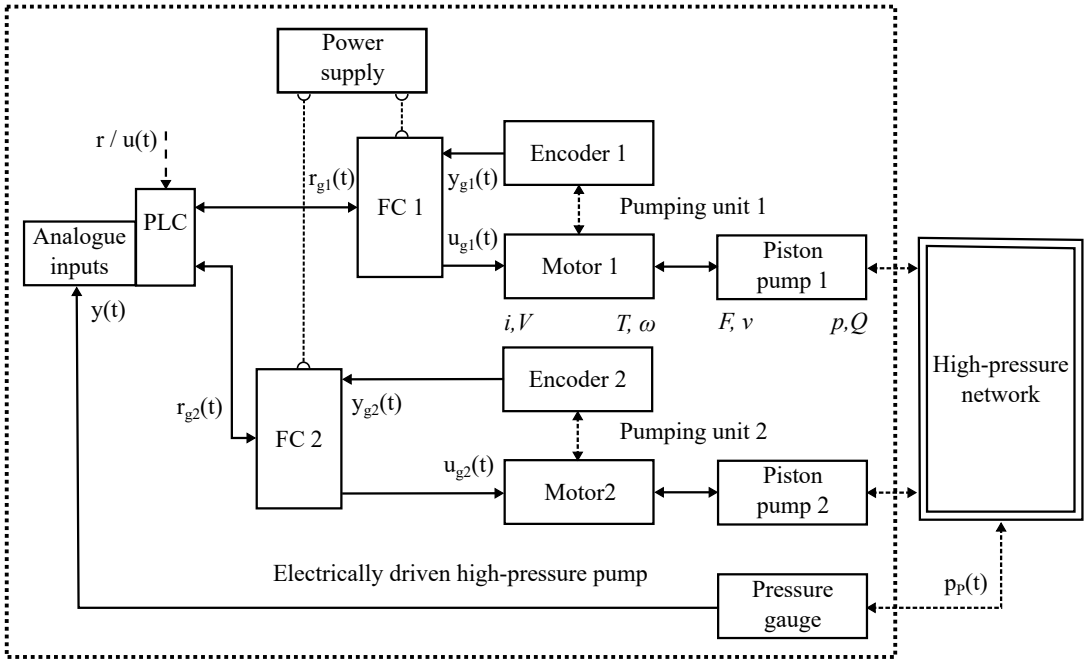

Figure 2.12 – High-pressure pump hardware setup: a PLC generates the position commands to synchronize both piston pumps by means of camming. The piston pumps are driven by independent frequency converters, which realize the motion control loops to displace the pistons, where each synchronous motor provides measurement data from encoders.

The camming follows a reference position trajectory, one for each pumping unit. This trajectory is dynamic and must be adjusted with respect to the reference pressure r. It defines the position command $r_{gn}(t)$ for motion control n with respect to the feedback position $y_{gn}(t) = s_{Pn}(t)$. The motion control consists of three feedback loops in series, regulating the piston position $s_{Pn}(t)$, its velocity $v_{Pn}(t)$ and the motor current $i_n(t)$. The pumping units alternately feed the high-pressure network such as to induce a continuous input fluid flow u_g.

Table 2.8: High-pressure pump hardware configuration: hardware used to built an electrically driven pump that consists of two pumping units.

Components	Type	Properties
Control unit (PLC)	1x Rockwell, CompactLogix ###	1 ms update time.
Power supply	1x Rockwell, Kinetix ###	
Frequency converter	2x Rockwell, Kinetix ###	25 μs cycle time.
Synchronous motor	2x Wittenstein, ###	131.8 Hz dynamic bandwidth.
Absolute encoder	2x Sick, ###	12 bit Resolution, 0.3° s accuracy, 200 kHz output frequency.

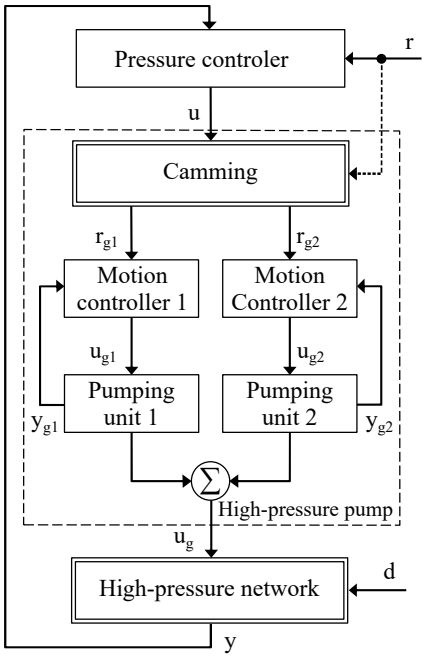

Figure 2.13 – Hierarchical control design for modular high-pressure pumps: each pumping unit is controlled by local motion control. The units are synchronized by means of camming.

2.3.2 High-pressure generation using single-acting pistons

The working principle of a high-pressure pump with two pumping units will be explained, while investigating the single-acting piston as depicted in the illustration of Figure 2.14. A check-valve in the intake duct passively connects the pumping chamber with the water supply. An other check-valve in the outtake duct passively connects the pumping chamber with the high-pressure piping. These check-valves restrict the fluid flow to desired direction, from the water supply to the pumping chamber and from the pumping chamber to the piping.

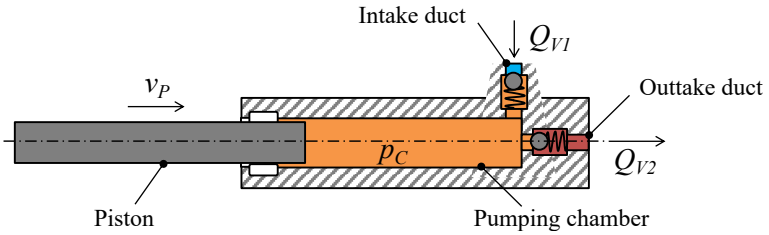

Figure 2.14 – Pumping unit with a single-acting piston: piston displacement pressurize water for high-pressure generation.

These check-valves allow for defining three pumping states for pressure generation: both check-valves will be closed to pressurize the pumping chamber (State 1), where the outtake check-valve will open to feed the high-pressure network (State 2), and the intake check-valve will open to fill the pumping chamber (State 3), while the outtake check-valve is closed.

Introducing the pressure generation by means of a piston pump, the model

$$p_C = \frac{1}{\mathcal{C}} \int \left(Q_{V1} - Q_{V2} + Q_P \right) \, dt \tag{2.4}$$

describes the pressure p_C within a pumping chamber, as derived from [Will and Gebhardt, 2014]. The fluid in a pumping chamber holds a capacity $\mathcal{C}$. The stroke of the piston will change the chamber volume V_C, providing a displacement fluid flow Q_P. The fluid capacity $\mathcal{C}$ therefore defines the pressure change for any change of volume dp/dV. Any piston displacement with velocity v_P induces a displacement fluid flow $Q_P = S_P \, v_P$ with respect to the piston cross section S_P. A check-valve at the intake duct enables an input fluid flow

$$Q_{V1} = \sigma(\Delta p_{V1}) \; H_{V1} \sqrt{|\Delta p_{V1}|} \tag{2.5}$$

to fill the pumping chamber, while an other check-valve at the outtake duct enables an output fluid flow

$$Q_{V2} = \sigma(\Delta p_{V2}) \; H_{V2} \sqrt{|\Delta p_{V2}|} \tag{2.6}$$

to feed the high-pressure piping. Considering the Heaviside-Function

$$\sigma(z) = \begin{cases} 0, & z \leq 0 \\ 1, & z > 0 \end{cases} , \tag{2.7}$$

for $\Delta p_{V1} \to z$ and $\Delta p_{V2} \to z$, respectively, represents the switching behaviour of a check-valve with respect to the pressure difference $\Delta p_{V1} = p_S - p_C$ over the intake duct and the pressure difference $\Delta p_{V2} = p_C - p_P$ over the outtake duct. The switching dynamics itself is neglected.

The intake check-valve will open, if the pressure p_C within the chamber decreases bellow the supply pressure p_S. This is the case, when the piston moves in descending direction. The outtake

check-valve will open, if the pressure within the chamber p_C increases above the pressure of the piping p_P. This is the case, when the piston moves in ascending direction. Therefore, an output flow Q_{V2} results, depending on the pressure difference Δp_{V2} over the outtake check-valve and an input flow Q_{V1} results, depending on the pressure difference Δp_{V1} over the intake check-valve. H_{V1} and H_{V2} denote to the characteristics of the check-valves and correspond to a fluid flow resistance. Considering the model (2.4), pressure equilibrium within a pumping chamber will be obtained for $Q_{V1} + Q_P = Q_{V2}$ and $dp/dt = 0$. A reciprocating piston displacement determines the passive switching of both check-valves, as depicted in Figure 2.15 (a) - (c). The corresponding pumping cycle is therefore assigned to the three pumping states:

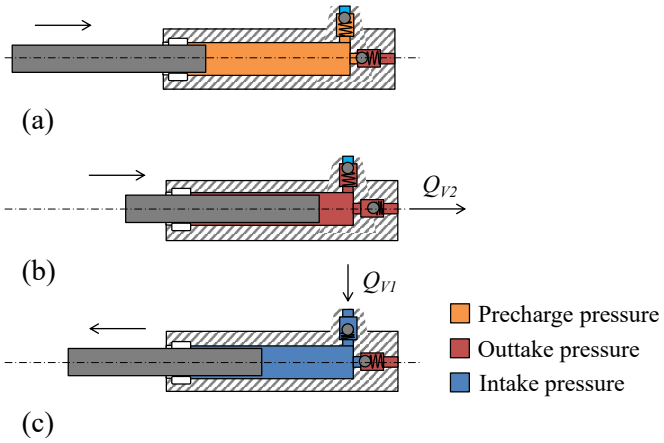

Figure 2.15 – Functional principle of a piston pump illustrated at the three states of a pumping cycle: (a) pressurization of the pumping chamber, (b) hauling the pressurized fluid to the piping and (c) filling the chamber from the water supply.

Pumping state 1 (Pressurization)

The piston is entirely retracted, the pumping chamber is filled with water and its pressure is equal to the water supply. While the piston moves with velocity v_P in ascending direction, the pressure within the chamber begins to increase. Both check-valves stay closed as long as the pressure in the chamber remains below the pressure of the high-pressure piping. This can be expressed with the conditions

$$\sigma(\Delta p_{V2}) = 0, \ \Delta p_{V2} < 0 \tag{2.8a}$$
$$\sigma(\Delta p_{V1}) = 0, \ \Delta p_{V1} < 0 \tag{2.8b}$$

that causes $Q_{V1} = 0$ as well as $Q_{V2} = 0$. The piston position will determine the pressurization within a pumping chamber. This can be seen by applying conditions (2.8a) and (2.8b) for (2.5) and (2.6), while evaluating (2.4) that

$$p_C = \frac{1}{\mathcal{C}} \int (S_P \, v_P) \, dt = \frac{1}{\mathcal{C}} \, S_P \, s_P \, . \tag{2.9}$$

Hence, the piston position s_P directly defines the resulting pumping chamber pressure before opening a check-valve.

Pumping state 2 (Hauling)

The piston continues to move and the pumping chamber is pressurized to the pressure of the high-pressure piping. The outtake check-valve will open since conditions

$$\sigma(\Delta p_{V2}) = 1,\ \Delta p_{V2} \geq 0 \tag{2.10a}$$
$$\sigma(\Delta p_{V1}) = 0,\ \Delta p_{V1} < 0 \tag{2.10b}$$

are met. The pumping chamber then feeds the high-pressure piping until the piston is fully extended. This can be seen by applying conditions (2.10a) and (2.10b) for (2.5) and (2.6), while evaluating (2.4) that

$$p_C = \frac{1}{\mathcal{C}} \left(S_P\ s_P - H_{V2} \int \sqrt{|\Delta p_{V2}|}\ dt \right) . \tag{2.11}$$

A pressure equilibrium will be obtained when the output fluid flow Q_{V2} equals to the induced fluid flow Q_P. Thus, the pump reaches a steady operating pressure, where it provides a continuous output flow, equal to the overall water consumption.

Pumping state 3 (Filling)

The piston is fully extended now and it begins to move in descending direction. The pressure within the pumping chamber rapidly decreases and the outtake check-valve will close. As soon as the pressure within the chamber drops bellow the supply pressure, the intake check-valve opens and the chamber will be refilled with water, according to conditions

$$\sigma(\Delta p_{V2}) = 0,\ \Delta p_{V2} < 0 \tag{2.12a}$$
$$\sigma(\Delta p_{V1}) = 1,\ \Delta p_{V1} \geq 0\ , \tag{2.12b}$$

until the piston is fully retracted. This can be seen by applying conditions (2.12a) and (2.12b) for (2.5) and (2.6), while evaluating (2.4) that

$$p_C = \frac{1}{\mathcal{C}} \left(S_P\ s_P + H_{V1} \int \sqrt{|\Delta p_{V1}|}\ dt \right) . \tag{2.13}$$

Hence, the induced fluid flow Q_P from piston displacement becomes negative. The filling state is not of interest for modelling the high-pressure generation, thus the water supply is neglected. Introducing these 3 pumping states require the following assumptions:

Assumption 2.1. *Realizing a proper pumping operation, it is desired that the pumping chamber is either connected to the water supply or to the high-pressure piping* $\forall\ t > 0$.

Assumption 2.2. *An exception is given for the initial condition when assuming* $p_C(t) = p_S$ *and* $p_P(t) = p_S$. *That causes all check-valves to remain open* $\forall\ t = 0$, *if (2.7) holds.*

Assumption 2.3. *Instead of modelling the filling of a pumping chamber over a intake check-valve, it is here assumed that the pressure* $p_C(t)$ *within a pumping chamber cannot drop below the supply pressure* p_S, *such as* $p_C(t) \geq p_S\ \forall\ t$.

Assumption 2.4. *Further assuming a water supply of infinite capacity allows for considering the supply pressure* p_S *to remain constant, in particular* $p_S \approx 0.4\ MPa$.

2.3.3 Coupling of N pumping units

High-pressure pumps combine several pumping units to produce a continuous output fluid flow. To obtain this, every piston is synchronized with respect to the previously introduced pumping states. A position trajectory will be generated for each piston and realized by means of motion control. This trajectory will determine the pressure generation within a pumping chamber and consequently passively affecting the check-valve switching. Any positioning error of the piston displacement immediately affects the displacement fluid flow, what induces pressure fluctuations.

First considering the camshaft of Figure 2.16 to coupled N pistons of a high-pressure pump. It introduces a constant phase-shift of $2\pi/N$ between each pumping unit. This allows for defining the induced overall fluid flow

$$Q_P(t) = \sum_{n=1}^{N} Q_{Vn}(t) \tag{2.14}$$

of a high-pressure pump as a superposition of the sinusoidal output fluid flows $Q_{Vn}(t)$ of every single pumping unit n, subject for static synchronization.

A displacement fluid flow

$$Q_{Pn}(t) = \frac{d}{dt}\mathcal{F}\left(\phi(t) + \frac{2\pi\ n}{N}\right)\frac{2}{N\ S_P} \tag{2.15}$$

feeds its pumping chamber with respect to the camshaft angular position $\phi(t)$, where the angular speed $\omega(t) = d\phi(t)/dt = f(u(t))$ is manipulated by the control variable $u(t)$ to generate a desired overall fluid flow $Q_P(t)$. The camming function $\mathcal{F}(\cdot)$ defines the phase-shifted trajectories, which map the angular camshaft position ϕ to the individual piston displacements s_{Pn}. A dynamic camming function will be further discussed in the subsequent section, when introducing the model-based synchronization.

The chamber pressure

$$p_{Cn}(t) = \frac{1}{\mathcal{C}}\int \left(Q_{Pn}(t) - Q_{Vn}(t)\right) dt \tag{2.16}$$

is obtained with respect to (2.4) and Assumption 2.3, while considering an output fluid flow

$$Q_{Vn} = \sigma(\Delta p_{Vn})\ H_{Vn}\sqrt{|\Delta p_{Vn}|} \tag{2.17}$$

with respect to (2.6) and Assumption 2.1. This fluid flow depends on the pressure difference $\Delta p_{Vn}(t) = p_{Cn}(t) - p_P(t)$ between chamber pressure $p_{Cn}(t)$ and piping pressure $p_P(t)$. From check-valve switching given by (2.7) follows that $Q_{Vn}(t) \in \mathbb{R}^+\ \forall\ t$.

2.3.4 Model-based synchronization by means of camming

The model-based synchronization will be discussed for a high-pressure pump with two single-acting pistons ($N = 2$), as proposed in [Niederberger and Kurmann, 2014]. The camming generates reference trajectories for each piston with respect to the desired operating pressure. It replaces the static coupling of a camshaft and synchronizes both pumping units to generate a continuous output fluid flow. Similar trajectories are also found in [Ferretti et al., 2015] to predict the piston positions for single-acting intensifier pumps, used for condition monitoring.

Trajectories are chosen with respect to Assumption 2.1 – 2.4, such as only one pumping chamber is coupled to the high-pressure network at a time. The plots in Figure 2.17 present the position (a), velocity (b) and acceleration (c) references for a typical pumping cycle. Such a

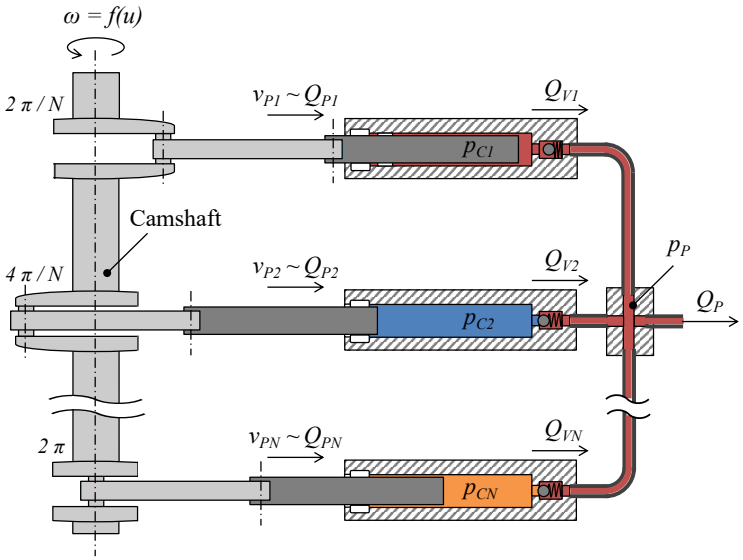

Figure 2.16 – Camshaft to couple N pistons: the camshaft enables a static synchronization of multiple pistons, generating a sinusoidal output fluid flow.

reference trajectory represents the previously defined pumping states: Pressurization takes place in interval t_1, t_2 and t_3, hauling for t_4 and t_5, filling for t_6, t_7 and t_8, while a piston is ascending to its maximal stroke s_{max} and descending to its initial position $s_0 = 0$. The trajectory of a pumping cycle is then defined by the piston positions $s(t_i)$ for an interval t_i of a cycle i.

This periodic pumping cycle can be seen as a master axis which realizes a reciprocating piston displacement with respect to the virtual camshaft angle $\phi = [0 \ldots 2\pi]$. The pistons are considered as slave axis realizing a piston stroke $s_{Pn} = [0, s_{max}]$. To synchronize both pumping units, the slave axes are coupled to a master axis with a phase shifted of π. This concept is known by the industry as camming. It enables a dynamic synchronization of both pistons with respect to the desired operating pressure. That aims at a continuous output fluid flow $Q_P(t) = [0, Q_{max}]$ for a given pump rate $u(t) = [0, 1]$, when steady-state pressure is obtained.

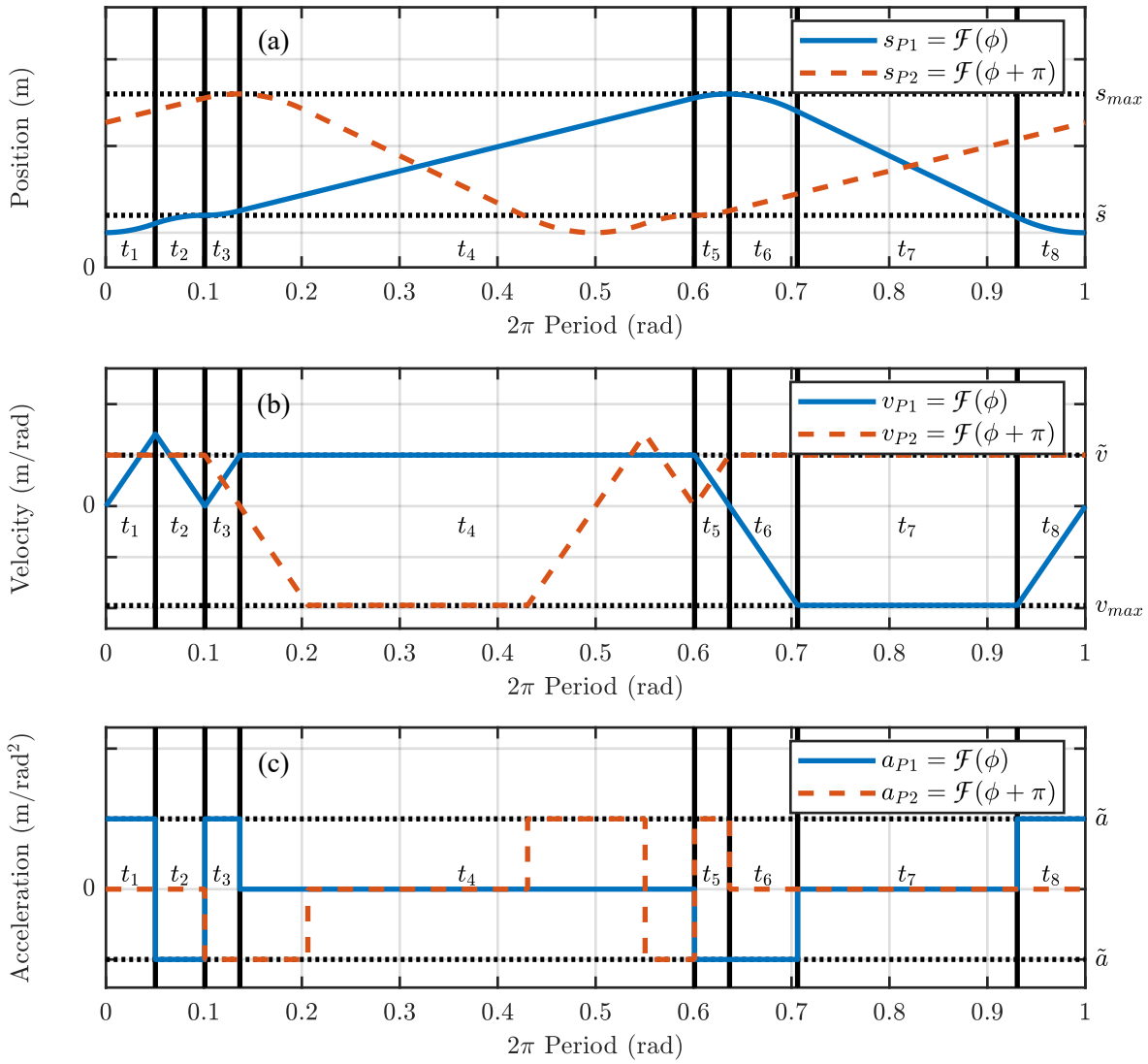

Figure 2.17 – Reference trajectories used for camming: example of a reference trajectory representing the desired piston position (a), velocity (b) and acceleration (c) values for a pumping cycle with a phase-shift of 180° between both pistons.

The position trajectory of a pumping cycle must fulfil the following conditions to avoid piston collision in the pumping chamber and pressure fluctuations in the high-pressure piping due to couplings between pumping units:

1. The piston position s must be in between the available stroke for all time ($0 < s < s_{max}$). The available stroke must be reached by the end of hauling (t_5). And the initial position must be reached by the end of filling (t_8), such as

$$s_1 + s_2 + s_3 + s_4 + s_5 = s_6 + s_7 + s_8 = s_{max} \tag{2.18}$$

2. A specific piston position $\tilde{s} = f_s(p)$ must be reached before deceleration at the end of pressurization (t_2) to obtain the desired operating pressure p, this requires

$$s_1 + s_2 = \tilde{s} \ . \tag{2.19}$$

3. A specific piston velocity $\tilde{v} = f_v(Q)$ must be reached before hauling (t_3) that corresponds to the desired overall fluid flow Q. This velocity must be held constant while hauling

$$v_4 = \tilde{v} \ . \tag{2.20}$$

4. The acceleration at the end of pressurization (t_3) and the deceleration at the end of hauling (t_5) are symmetric and simultaneous (regarding the two phase shifted pistons), so that the overall flow rate will stay constant and

$$t_5 = t_3 \ . \tag{2.21}$$

5. The hauling (t_3, t_4) will last half if the pumping cycle. Therefore always one piston pump is continuously hauling at a time. The filling and pressurization will last for the other half the of cycle, such as

$$t_4 + t_5 = t_1 + t_2 + t_3 + t_6 + t_7 + t_8 = \pi \ . \tag{2.22}$$

It is further the highest available acceleration $\tilde{a}$ applied, to maximize the resulting interval t_4 for hauling and to minimize the desired peak velocity v_7 for filling. Taking the above conditions (2.18 - 2.22) into account, allows for deriving the time intervals in terms of $\tilde{a}$, $\tilde{v}$, $\tilde{s}$ and s_{max}, while considering the 1-dimensional kinematics of piston displacement ($v = \int a \ dt$ and $s = \int v \ dt$), hence the timing for all periods becomes

$$\begin{pmatrix} t_1 \\ t_2 \\ t_3 \\ t_4 \\ t_5 \\ t_6 \\ t_7 \\ t_8 \end{pmatrix} = \frac{1}{2\pi} \begin{pmatrix} \sqrt{\frac{\tilde{s}}{\tilde{a}}} \\ \sqrt{\frac{\tilde{s}}{\tilde{a}}} \\ \tilde{v}/\tilde{a} \\ \frac{(s_{max}-\tilde{s})}{\tilde{v}} - \frac{\tilde{v}}{\tilde{a}} \\ \tilde{v}/\tilde{a} \\ -\tilde{z} - \sqrt{\tilde{z}^2 - \frac{s_{max}}{\tilde{a}}} \\ \frac{s_{max}}{\tilde{a}(-\tilde{z}-\sqrt{\tilde{z}^2-\frac{s_{max}}{\tilde{a}}})} + \tilde{z} + \sqrt{\tilde{z}^2 - \frac{s_{max}}{\tilde{a}}} \\ -\tilde{z} - \sqrt{\tilde{z}^2 - \frac{s_{max}}{\tilde{a}}} \end{pmatrix} , \tag{2.23}$$

as derived in [Niederberger and Kurmann, 2014] by solving a quadratic equation, where

$$\tilde{z} = \sqrt{\frac{\tilde{s}}{\tilde{a}}} - \frac{(s_{max} - \tilde{s})}{2\tilde{v}} + \frac{\tilde{v}}{2\tilde{a}} \ . \tag{2.24}$$

The corresponding velocities $v(t)$ and positions $s(t)$ will be derived by integration of the acceleration $a(t)$ over the intervals t. The trajectory design can be further extended by introducing intermediate time intervals. This allows for optimizing a trajectory for limited jerk, but requires to solve a cubic equation.

A single reference value $u(t)$, the master axis cycle frequency, will command the high-pressure pump. An increasing cycle frequency will cause a faster pumping cycle due to the assignment

$$s_{Pn}(t) = \mathcal{F}\left(\phi(t) + \frac{2\pi \ n}{N}\right) \ , \tag{2.25}$$

$$\phi(t) = \int u(t) \ dt \ mod \ 2\pi \ . \tag{2.26}$$

This adjusts the piston velocity to realize the desired fluid flow rate for hauling. Both pistons attain a stroke within 2π-period of a full camshaft rotation at a phase shift of π. This phase shift guarantees the decoupling of both pumping chambers, assuming a perfect synchronization.

Assumption 2.5. *It is assumed that a π-periodic ramp function*

$$s(\phi) := \begin{cases} 0, & \phi(t) = 0 \text{ or } \phi(t) = \pi \\ \frac{s_{max}}{\pi}\phi(t), & 0 < \phi(t) < \pi \end{cases} \tag{2.27}$$

approximates the reciprocating operation for two pistons, where $\phi(t) \in [0, \pi]$ refers to the angular position of half a camshaft rotation. The resulting piston velocity

$$v(t) = \frac{d}{dt}\phi(t)\ \frac{d}{d\phi}s(\phi) = \omega(t)\ \frac{d}{d\phi}s(\phi) \tag{2.28}$$

of two interconnected pumping chambers is then proportional to the camshaft angular speed $\omega(t)$ and the high-pressure piping is continuously feed, such as $Q_P \sim u(t)$.

Assumption 2.6. *Steady-state around desired operating pressure requires fluid flow equilibrium $Q_{Pn} = Q_{Vn}$. This yields that the piping pressure $p_P(t)$ maintain at operating pressure and that the pressure within a pumping chamber $p_{Cn}(t)$ has reached operating pressure, when the check-valve to the high-pressure piping opens, thus*

$$p_{Cn}(\phi(t) = 0) = p_{Pn}(t)\ . \tag{2.29}$$

A perfect synchronization (Assumption 2.5) allows for evaluating the two pumping units by the overall induced fluid flow $Q_P(t) \sim \tilde{v}$. Each pumping chamber becomes exactly pressurized to the desired operating pressure and a continuous overall fluid flow will occur, if Assumption 2.6 holds. As a consequence, the piston position $\tilde{s} = f_s(p)$ varies for every operating pressure p, resulting in different position trajectories, as shown in plot of Figure 2.18.

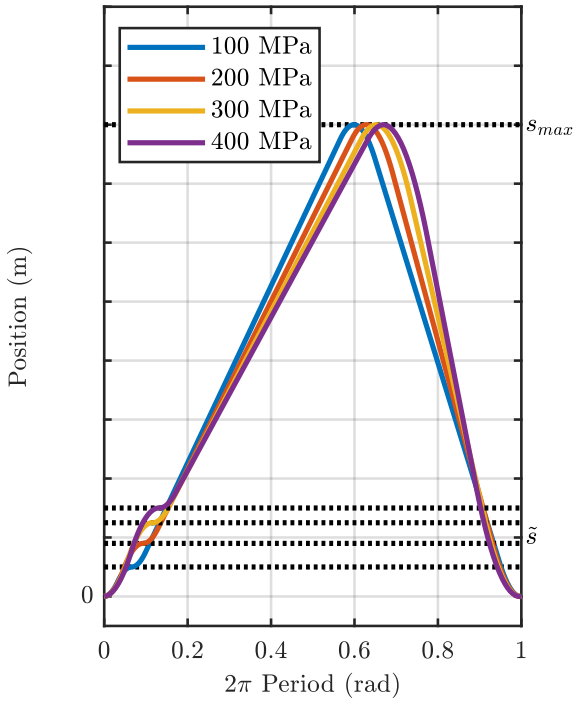

Figure 2.18 – Pressure-dependent position trajectories: desired piston displacement to obtain continuous output fluid flow for different operating pressures.

The relation between chamber pressure p_C and piston position $\tilde{s}$ is given in the plot of Figure 2.19. It corresponds to the function $f_s(p)$ that represents the model used to synchronize the pumping units. This model will be introduced in Section 4.2. On the other hand, the desired piston velocity $\tilde{v}$ to derive a steady-state fluid flow Q_P depends on the number of pumping units N and the piston cross section S_P, such as $f_v(Q) = 2\ N^{-1}\ Q\ S_P^{-1}$.

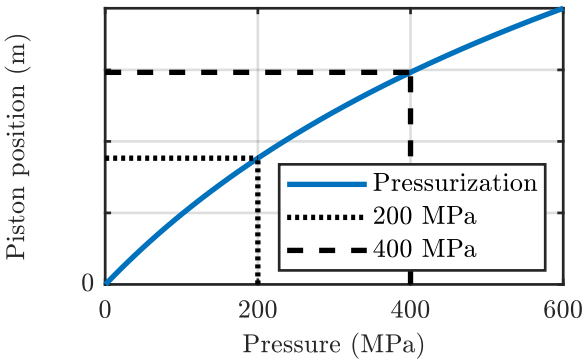

Figure 2.19 – Relation between chamber pressure and piston displacement: expected position position to pressurize a pumping chamber.

The electrically driven high-pressure pump with independent pistons is prevalent to realize a virtual camshaft by means of model-based camming. However, it is important to understand, that it is not possible to excite the high-pressure piping directly by the pistons velocities. A reference trajectory is always desired to synchronize all pumping units and to guarantee a continuous overall fluid flow at the pump outtake. If synchronization fails, the fluid flow will vary even when a constant pump rate is demanded ($du(t)/dt = 0$). This will induce undesired pressure fluctuations.

2.3.5 Motion control

Motion control tracks the reference trajectory from camming with minimal position error. The resulting closed-loop dynamics enables a wide bandwidth of 131.8 Hz. This is required to deploy desired performance for disturbance rejection. Figure 2.20 shows the control structure, which is available with the frequency converter introduced in Section 2.3. It consists of a position control loop, followed by a velocity control loop and a torque control loop.

The position controller provides the reference for the velocity controller and the velocity controller provides the reference for the torque controller. The command value r_{gn} for the position controller is maintained by camming, while the commanded velocity and acceleration, subject to feed forward, are derived by differentiation of the reference position trajectory. The feedforward gains F_v and F_a apply these command values to the corresponding control loops.

Proportional and integral action (PI) is applied for the position and velocity loop, where only proportional action (P) is implemented to the torque loop, while following the controller tuning discussed in [Ramasamy and Sundaramoorthy, 2008]. The position feedback is measured by absolute encoders. The velocity feedback filter F_s is given by Equation (2.3). A load observer estimates the motor torque and velocity for feedback to the control loops. This observer-based control improves the noise sensitivity of the torque and velocity feedback signals, as discussed in [Yang et al., 2011], and enables an increased closed-loop bandwidth. The acceleration output from velocity loop is converted to an equivalent torque with the torque scalar $K_J = J$, while the

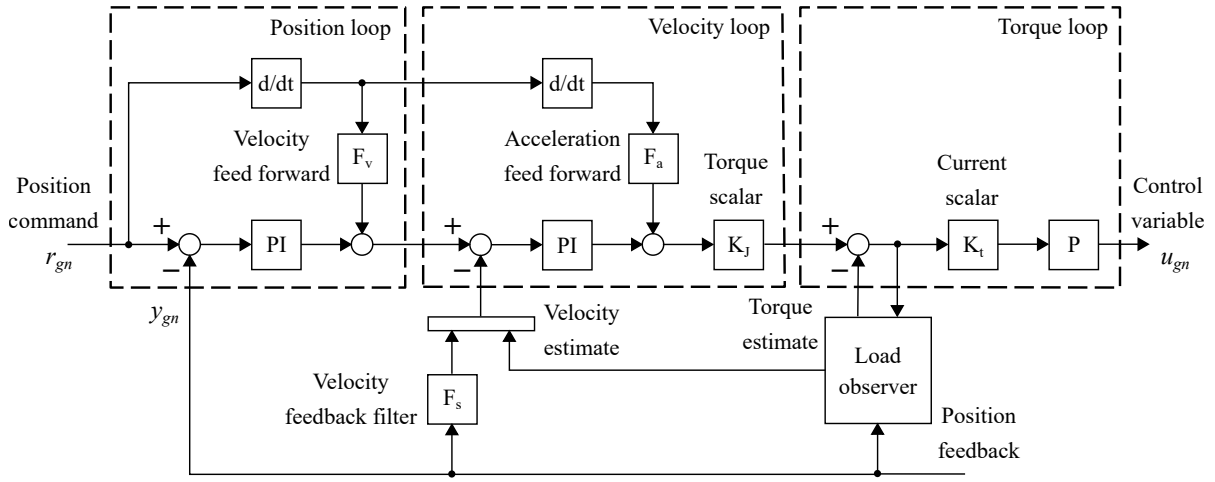

Figure 2.20 – Structure of motion control: implemented position, velocity and current control loop to the frequency converters and its load observer.

torque output is scaled to an equivalent motor current with the current scalar $K_t = 1/(N\ K)$, where J is the motor inertia, K its motor constant and N denotes the pole pair number.

The controller gains are tuned with respect to the reference trajectories by successive tuning, such as a closed-loop bandwidth of 131.8 Hz and an angular position error of $< 0.002°$ has been obtained. This corresponds to a linear position error of $< 6.4\ \mu$m. The obtained parametrisation of the control loops is listed in Table 2.9

Table 2.9: Parametrization of motion control: control loop bandwidth, forward gains, feedback filter and load observer.

Properties	Value	Unit
Position loop bandwidth	###	(Hz)
Velocity loop bandwidth	###	(Hz)
Torque loop bandwidth	###	(Hz)
Velocity feedback filter b/w	###	(Hz)
Load observer bandwidth	###	(Hz)
Velocity feedforward gain	###	(%)
Acceleration feedforward gain	###	(%)

2.3.6 Pressure fluctuations and check-valve hysteresis

The synchronization of two interconnected pumping units by means of model-based camming and its effect on the resulting pressure trend is exemplary shown with two experiments. Both experiments have been conducted with the same position trajectories. These trajectories are optimized for an operating pressure of 350 MPa, which refers to the trajectory reference value. A nozzle of 0.3 mm inner diameter has been installed to the cutting head. Consequently, a displacement fluid flow of 35.5 cm^3/s would be ideal to generate a pressure of 350 MPa. However, the pump rate has been slightly modified so that experiment 1 would clearly show the effects of over excitation, whereas experiment 2 would cause an under excitation. Both experiments are

derived by means of simulations, using a detailed simulation model, and have been verified with measurements from the test bench.

Experiment 1) Over excitation: the displacement fluid flow has been raised to 37.0 cm^3/s to obtain an increased pressure steady-state of about 380 MPa. The insufficient pressurization leads to a periodic pressure loss towards 350 MPa, as can be observed in Figure 2.21 (a). However, the pressure will asymptotically rise towards the desired steady-state value, once the check-valve of the precharged pumping chamber has been pushed open.

Experiment 2) Under excitation: the displacement fluid flow has been reduced to 34.5 cm^3/s. This results in a decreased pressure steady-state of about 320 MPa. The excessive pressurization causes a periodic pressure overshoot towards 350 MPa, of Figure 2.21 (b). Complementary to the first experiment, the pressure will asymptotically fall towards the desired steady-state value, once the check-valve is closed.

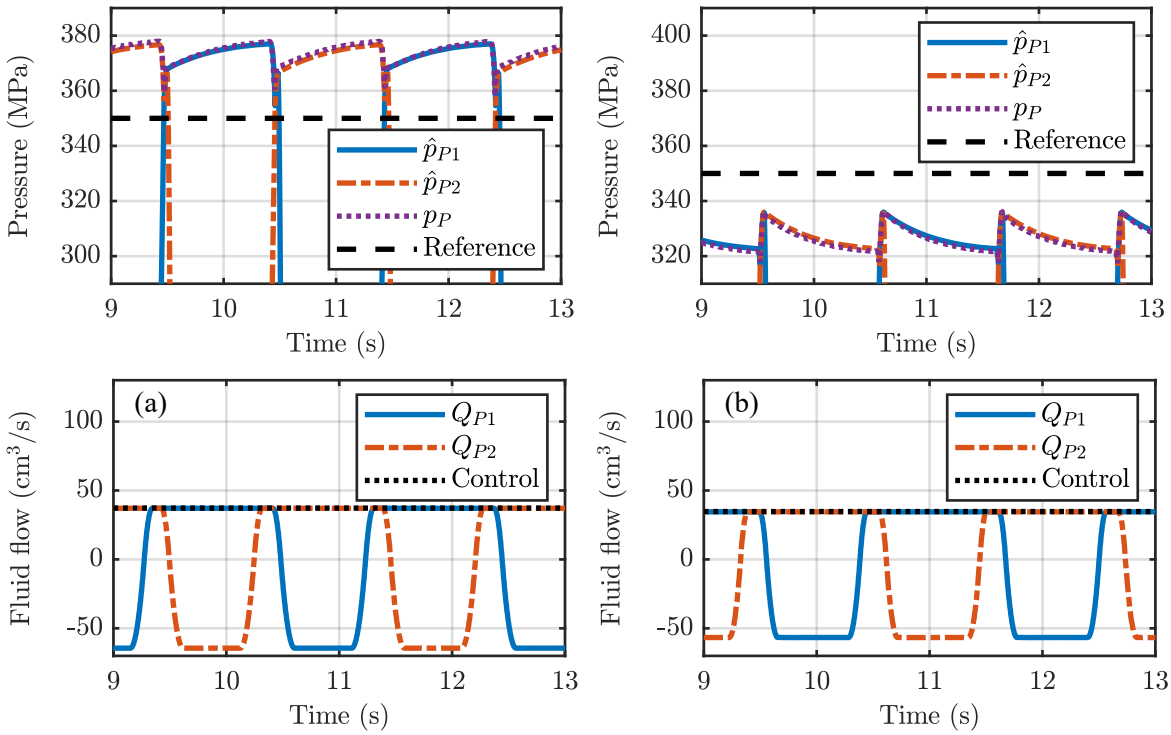

Figure 2.21 – Measured pump output pressure compared to simulated pressure trends and corresponding displacement fluid flows using a 350 MPa trajectory: over excitation (a) causing a periodic pressure loss and under excitation (b) casing a periodic pressure overshoot.

The pressure generation is sensitive to any deviations of the desired displacement flow. The pumping chambers with the pressure states p_{P1} and p_{P2} affect the overall pump output pressure p_P. The pressure differences Δp_{V1} and Δp_{V2} over the corresponding check-valves restrict the induced fluid flows Q_{V1} and Q_{V2} to positive directions. On the other hand, the piston displacement fluid flows Q_{P1} and Q_{P2} follow the three states of a pumping cycle, as previously introduced.

Detailed pressure trends of both experiments are shown in Figures 2.22 (a) and (b). The three pumping states of pressurization, hauling and filling are clearly distinguished. A check-valve becomes passively controlled by any piston displacement that pressurizes the corresponding

pumping chamber. Consequently, a piston displacement indirectly affects the coupling between the pumping chambers and piping. Depending on the amount of pressurization, pressure losses or pressure overshoots can occur, whenever a check-valves opens too early or, respectively too late.

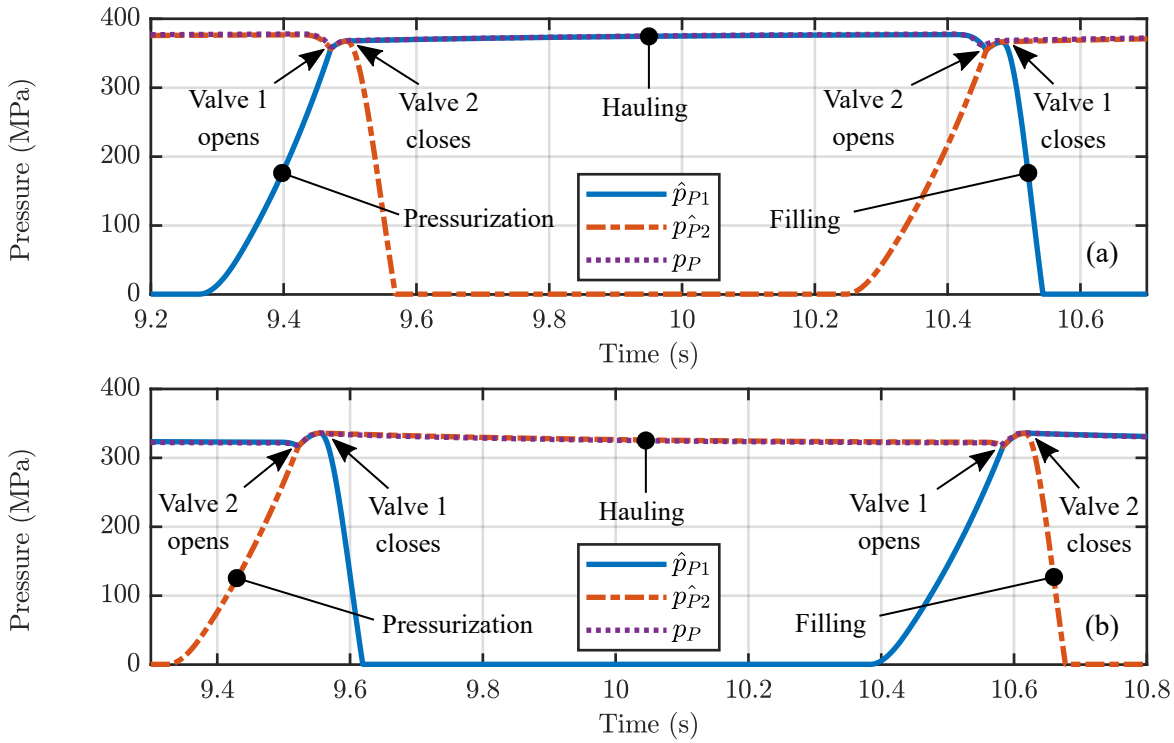

Figure 2.22 – Simulated pumping chamber pressures for a pumping cycle and resulting pump output pressure from measurement due to check-valve switching hysteresis: experiment 1 (a) shows the pressure trend at 380 MPa and experiment 2 (b) shows the pressure trend at 320 MPa.

A similar behaviour is reported in [Trieb et al., 2007] for the pressure generation of intensifier pumps. To avoid any interaction between pumping chambers, a precise synchronization of the pumping units is required. This is realized by means of model-based trajectories (camming) and a precise motion control.

2.4 Conclusion

This chapter presented the test bench established in the laboratory. This test bench exclusively serves for parameter identification, model validation and controller verification, as related to the subsequent research work. The standard symbols, introduced in Section 1.2, have been applied to describe network topologies and cutting head setups, which provide the test bench configurations. The previously presented waterjet applications have been taken into account, when defining use cases suitable to investigate future waterjet facilities. It considers up to two high-pressure pumps interconnected to two independent cutting heads. These use cases will be taken into account for measurements at the test bench as well as for simulations.

The design and implementation of a hierarchical control design for the novel electrically driven high-pressure pump is the major contribution of this chapter. This requires to understand the functional principle of a pumping unit, for which three pumping states have been defined.

The pump design and the underlying motion control has been presented first, which aims at a precise displacement of pistons by means of servo motors. Providing the relation for high-pressure generation with coupled pumping chambers and introducing essential assumptions allow for generating reference trajectories, which avoid interactions between pumping units and realize a continuous output fluid flow. These trajectories are subject for tracking, using motion control.

The introduction of the model-based synchronization is another contribution that allows for considering a high-pressure pump as a continuous fluid flow source. This becomes valuable for low-level control design (Section 5.3) and for high-level managing of multiple interconnected pumps (Section 7.2). The presented phase-shifted trajectories give a understanding for the synchronization of two pumping units. This is required to operate the pump prototypes installed in the test bench. These position trajectories have been further improved, realizing an increased acceleration by introducing a maximal jerk limit. This maximizes the achievable overall fluid flow, generated by a high-pressure pump. However, this leads to a higher-order problem that requires optimization to find a distinct solution of a feasible trajectory. These optimized trajectories have been implemented to the PLC, using cubic splines to generate the position references for motion control. Further, adaptive trajectories are required to minimize any pressure fluctuations when switching between pumping units. This is eventually realized by look-up tables, which provide reference piston positions for cubic interpolation. That generate variable position trajectories, taking the desired operating pressure into account.

Part II

Modelling framework

3

Graph-based modelling methodology

Contents

3.1 Introduction

Objectives

Future waterjet facilities combine several decentralize pumps to span high-pressure networks of arbitrary topology. To configure these high-pressure networks and even more, to develop a suitable control architecture that deals with decentralized pumps, requires a flexible and scalable modelling methodology. This modelling methodology must also consider non-linearities and varying parameters for a wide pressure range of 40 to 400 MPa, as well as various setups for waterjet machining. In addition, it must ensure the flexible modelling of arbitrary network topologies that interconnect any number of decentralized pumps and work stations.

Common engineering tools, such as the *Simscape* toolbox from *MATLAB Simulink*, *Modelica* or *AMESim*, are well established to model and design very specific dynamic systems, as applied in [Lino et al., 2007] and [Ferretti et al., 2015]. However, modelling becomes time consuming, since it requires to derive an individual model for every waterjet facility. These standard libraries include various hydraulic system components, but the specific high-pressure components, used for waterjet machining, are not always available. As a consequence, it misses validation and parametrisation with respect to the non-linearities, as given by a wide pressure range of various waterjet applications.

The main objective is to provide a flexible modelling methodology for scalable waterjet facilities, while taking various high-pressure components into account and providing a procedure for modelling of different high-pressure networks. The parametrization of these high-pressure components should consider a wide pressure range. As a consequence, the varying parameters have to be described with suitable mathematical models and experimentally identified, using the high-pressure test bench of Section 2.2.

State of the art

Modelling high-pressure networks for different waterjet facilities is a time-consuming task. A prevalent approach describes the fluid dynamics with respect to the principle of continuity and momentum conservation, as found in various text books such as [Streeter et al., 1998]. This modelling by means of algebraic differential equations is applied for very specific high-pressure systems, such as for a high-pressure pump supplying a single workstation (see [Momber, 1995], [Tremblay and Ramulu, 1999], [Fabien et al., 2010] and [Ferretti et al., 2015]) or for common rails of a diesel engines (see [Hountalas and Kouremenos, 1998], [Lino et al., 2007], [Wang et al., 2011] and [Wang et al., 2016b]). These approaches offers a limited flexibility to cope with various network topologies, since a mathematical model has been obtained for a selected high-pressure component. However, it is well established that graph-based approaches improve the modelling flexibility for networked systems [Mohammadpour and Grigoriadis, 2010]. Considering distributed parameter systems, the algebraic differential equations will be assigned to graphs to recover the system dynamics, while considering various network topologies, as proposed in [Aalto, 2008] and [Corbet et al., 2018] to describe the fluid flow dynamics in piping networks or in [Koeln et al., 2016] and [Pangborn et al., 2017] to combine thermal and fluid flow systems. Nevertheless, describing high-pressure networks by means of graphs seems less investigated.

High-pressure systems

Dealing with waterjet machining, a model for intensifier pumps with high-pressure attenuators is presented in [Tremblay and Ramulu, 1999]. Experimental studies reveal the effect of bulk

modulus and fluid density for pressure fluctuations at 153.4, 181.0 and 215.5 MPa. Both are fluid characteristic parameters, which vary for a wide pressure range. The fluid density affects the fluid flow characteristics and causes to change the pressure steady-state. The bulk modulus defines the fluid compressibility and determines the transient pressure behaviour. More than a decade later, a lumped parameter model is adopted in [Fabien et al., 2010] for a similar setup, where a pressure-dependent fluid density is taken into account. For this purpose, model parameters have been experimentally identified with measurement data at 153.4 MPa. Other researchers have modelled high-pressure pumps for diagnostics and condition monitoring e.g. using *Modelica* for a multi-domain simulation of a phased intensifier pump (see [Ferretti et al., 2015]). They also investigated the pressure generation in relation to the piston displacement, such as to develop a model-based fault detector. Nevertheless, most authors focus on the modelling of waterjets and the resulting material removal to enhance the efficiency of waterjet machining, while the high-pressure generation remained ignored. For example, a generalized material removal model has been proposed in [Momber, 1995] to study various particle sizes and fluid flow rates for abrasive waterjet cutting.

The study of automotive applications revealed that fuel injection systems for combustion engines have a similar setup as common waterjet facilitites: a high-pressure pump supplies injectors, which are interconnected by means of piping. A direct injection engine with an operating pressure of about 50 MPa is modelled in [Hountalas and Kouremenos, 1998]. Reasonable accuracy has been realized by introducing a pressure-dependent bulk modulus. More recent studies deal with common rail injection systems. Many of them focus on the injection process, e.g. a *MATLAB Simulink* model is utilized in [Wang et al., 2011] to study the injection rate, while others are interested in high-pressure generation and control. A mathematical model for control design and its implementation, using *MATLAB Simulink*, is presented in [Lino et al., 2007]. This modelling considers a variable bulk modulus. It is experimentally validated for a pressure range of 30 to 90 MPa and verified with multi-domain simulations in *AMESim*. For control design, a mathematical model has been also developed in [Wang et al., 2016b] and validated using *AMESim* for a pressure of 150 MPa. However, the validation results reveal some discrepancies regarding the transient behaviour of pressure generation.

An accurate simulation of a high-pressure system requires to introduce pressure-dependent parameters, such as a variable bulk modulus and fluid density. Consequently, the available modelling must be extended to cope with high-pressure networks of arbitrary topologies without increasing the modelling effort. A promising approach is the graph-based modelling.

Graph-based modelling

Graphs are often used to represent vehicular traffic, data packet flow, power lines and many more. Various text book, see for example [Mohammadpour and Grigoriadis, 2010] and [Ford and Fulkerson, 2016], provide an introduction to the general framework and its application. Improving the modelling for a traffic system, it is proposed in [Mercier, 2009] to assign a hyperbolic conservation laws to a graph. The graph represents the traffic network, while considering the dynamics of traffic flow. In particular, the flow of data packets is often represented with graphs. By extending this, it is proposed in [Espitia et al., 2017] to model communication networks by means of fluid dynamics and the use of fluid dynamic models for data networks is validated in [Manzo et al., 2012]. Compartment modelling is suggested in [Mounier and Bastin, 2001] and [Bastin and Guffens, 2006], where partial differential equations has been introduced in [D'Apice et al., 2008] to describe the packet evolution. More recent work deals with stability issues and the control of compartments, see [Briat et al., 2012] and [Bastin and Coron, 2013].

The claim of an universal model, for simulating a piping network of any topology, reaches back to [Kralik et al., 1984], presenting a node-oriented concept of discretization in space and introducing a continuity equation to describe the fluid flow. Partial differential equations are assigned by [Aalto, 2010] to describe the fluid flow along piping sections, which have been interconnected to a network. Whereas in [Corbet et al., 2018], the transient solution for a diffusion equation is mapped to a graph, describing the fluid flow of petroleum infrastructures. Each node corresponds to a storage and a branch defines the fluid flow between storages.

A graph-based approach is presented in [Koeln et al., 2016] and [Pangborn et al., 2018], modelling thermal and fluid flow systems with respect to the conservation of mass and energy. Conservation laws are investigated in [Borsche and Kall, 2014], using graphs to represent spatially distributed physical systems as lumped parameter models. The Riemann problem for networked systems, derived from the above conservation laws, is discussed in [Garavello and Piccoli, 2009]. Numerical methods to efficiently solve the Riemann problem are investigated in [Borsche and Kall, 2016]. Such models are often applied to thermal systems, e.g. [Ramallo-González et al., 2013]. Moreover, the application of conservation laws and balancing equations to graphs is described in [van der Schaft and Maschke, 2009]. A node corresponds to a system state that associates the conservation law, while each branch balances the differences between system states. This aims at a general class of physical network systems, taking mechanics, hydraulics and heat transfer into account. This approach is further generalized to passive physical systems using Hamiltonian formulation, see [van der Schaft, 2017].

On the one hand, there are two approaches for high-pressure generation, taking a wide pressure range into account. Modelling approaches for waterjet facilities consider a variable fluid density, where common rail models assume a variable bulk modulus. However, neither of those approaches have been found to perform sufficient to reproduce pressure fluctuations for a wide pressure range of several 100 MPa. On the other hand, numerous studies assign dynamic equations to graphs. Introducing in this way a flexibility and scalability to model networked systems of various topology. However, a flexible modelling methodology that considers a wide pressure range with reasonable accuracy remains unattained, especially for high-pressure networks.

Contribution

This chapter proposes a graph-based methodology that models high-pressure networks of various topologies. It assigns high-pressure components of common waterjet facilities to homogeneous segments, each representing a local pressure state with respect to the principle of momentum conservation and fluid flow continuity. The proposed methodology introduces to the governing equation a pressure-dependent fluid density as well as a pressure-dependent bulk modulus. This aims to improve the simulation accuracy for a wide pressure range. The segments are subsequently interconnected along the fluid flow path by means of graphs. These graphs are flexible to model different network topologies. Where each node represents a pressure state, every branch allocates a fluid flow to the interconnections. This results in lumped parameter models that approximate the non-linear characteristics of various high-pressure networks.

The major contribution is given when presenting the graph-based modelling methodology for high-pressure networks. This requires to introduce both variable parameters (bulk modulus and fluid density) into the governing equations of fluid dynamics and to assign these modified equations to a graph. In this way, the graph-based modelling offers a flexibility and scalability to cope with different network topologies of various waterjet facilities. This work further identifies pressure-dependent fluid characteristic as well as various parameters, related to the high-pressure components. In this way, various high-pressure networks can be modelled for a wide pressure

range without revising the initial parameter identification.

This chapter is structured as follows: Section 3.2 provides the fundamentals to describe the fluid flow dynamics. These fundamentals are used to derive a distributed parameter model. Using the distributed parameter model allows for investigating pressure fluctuations in a piping by means of numerical simulations. To derive a generalized model for high-pressure networks, Section 3.3 introduces the expected parameter variations which are taken into account to derive a lumped parameter model. On this place, the proposed graph-based modelling methodology is presented. Experiments presented in Section 3.4 introduce the pressure-dependent parameters and identify specific high-pressure components.

3.2 Fluid dynamics and modelling fundamentals

This section is dedicated to the modelling principles describing a 1-dimensional fluid flow. The principles of fluid flow continuity and momentum conservation are shown in [Streeter et al., 1998] to describe the fluid flow dynamics of a piping section. The resulting equations have been simplified when approximating its partial differentials, using finite differences, and assuming a stationary fluid flow. This yields a lumped parameter model, which represents the pressure state of homogeneous segments by means of first order differentials.

Introducing the fundamentals of fluid dynamics, the piping section of Figure 3.1 is considered. A fluid segment of initial length s_1 moves with a velocity v_1 along a piping section at height h_1 and of cross section S_1. The pipe will ascent to a higher position h_2 and widen to a cross section S_2. This causes the fluid to decelerate to a velocity v_2 and a segment of reduced length s_2. Common literature, e.g. [Böswirth and Bschorer, 2012] and [Spurk, 2013], describe this situation by assuming an incompressible fluid flow that implies a constant fluid density ϱ.

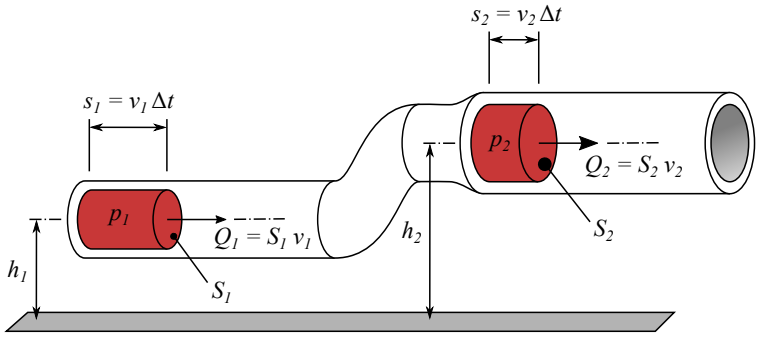

Figure 3.1 – A simple piping section to introduce the Bernoulli equation: an initial fluid segment is moved to a subsequent position while conserving its momentum.

A first principle, the **conservation of momentum**, is given by the Bernoulli equation [Spurk, 2013]

$$\underbrace{p_1}_{static} + \underbrace{\frac{\varrho}{2} v_1^2}_{dynamic} + \underbrace{\varrho \int_{s_1}^{s_2} \frac{\partial}{\partial t} v_1 \, ds}_{transient} + \underbrace{\varrho \, g \, h_1}_{head} = p_2 + \frac{\varrho}{2} v_2^2 + \varrho \int_{s_1}^{s_2} \frac{\partial}{\partial t} v_2 \, ds + \varrho \, g \, h_2 + \underbrace{\Delta p_v}_{loss} \, . \quad (3.1)$$

Considering the left-hand side, the first term corresponds to the static pressure p_1 of an initial fluid segment, the second term describes its dynamic pressure with respect to the fluid flow velocity v_1 and the third term is dedicated to its transient $\partial v_1 / \partial t$, where the last term includes

the pressure head h_1. The right-hand side of (3.1) includes an additional pressure loss term Δp_v due to the fluid flow resistance along the piping section. The applications for waterjet machining (see Section 1.2) allow for a fundamental assumption:

Assumption 3.1. *The induced static pressure is assumed much greater than any pressure head, hence the pressure head*

$$\varrho \; g \; h_i \approx 0 \tag{3.2}$$

can be neglected, thus the transient term

$$\varrho \int_{s_1}^{s_2} \frac{\partial}{\partial t} v_i \; ds \approx 0 \tag{3.3}$$

becomes small and a stationary fluid flow results.

By considering Assumption 3.1, the Bernoulli equation (3.1) is then reduced to

$$p_1 + \frac{\varrho}{2} \; v_1^2 = p_2 + \frac{\varrho}{2} \; v_2^2 + \Delta p_v \; , \tag{3.4}$$

which represents the characteristics of a stationary fluid flow along a horizontal piping.

A second principle, the **fluid flow continuity**, implies that the sum of all fluid flows Q_i passing a piping section remains unchanged such as

$$\sum_i Q_i = 0 \; . \tag{3.5}$$

Hence, the input fluid flow $Q_1 = S_1 \; v_1$ entering to a piping section equals to the output fluid flow $Q_2 = S_2 \; v_2$ leaving the pipe, where S_i denotes the piping cross section at position $i \in \{1, 2\}$. With respect to the fluid flow continuity (3.5), any expansion of cross section S causes a decrease of the fluid flow velocity v, while the fluid flow Q remains unchanged. Thus, introducing $Q_1 = Q_2$ into the conservation of momentum (3.4) yields that any change of the dynamic pressure causes a change of the static pressure.

3.2.1 Distributed parameter modelling

Investigating the fluid dynamics along a piping section of length L and constant cross section S requires another fundamental assumption.

Assumption 3.2. *The cross section inner diameter $D(x)$ remains significantly smaller than the piping length L, such as $D(x) \ll L \; \forall \; x = [0, L]$, whereas the cross section remains unchanged along a piping section, such as $\partial D(x)/\partial x \approx 0$.*

The illustration of Figure 3.2 considers a fluid segment ∂x that holds a finite volume $\partial V = S \; \partial x$. This piping determines a 1-dimensional fluid flow path and defines the direction of positive fluid flow along the position coordinate x, hence the transient behaviour of a fluid segment is described by a system of two partial differential equations [Streeter et al., 1998]: The first equation is known as **equation of continuity**

$$\frac{\partial}{\partial t} \; p(x,t) + v(x,t) \frac{\partial}{\partial x} \; p(x,t) - a^2 \varrho \frac{\partial}{\partial x} \; v(x,t) = 0 \; , \tag{3.6}$$

taking the potential energy into account and the second equation is known as **equation of motion**

$$\frac{\partial}{\partial t} \; v(x,t) + v(x,t) \frac{\partial}{\partial x} \; v(x,t) - \frac{1}{\varrho} \frac{\partial}{\partial x} \; p(x,t) + \frac{\lambda}{2D} \; v(x,t) \; |v(x,t)| - g \; \sin\alpha = 0 \; , \tag{3.7}$$

describing the kinetic energy. Both partial differential equations depend on the position coordinate x and time t. The coefficient a is the characteristic speed of sound of the fluid, λ denotes the friction loss coefficient and D the cross section inner diameter. The squared fluid flow velocity $v(x,t)$ induces a fluid flow resistance and α denotes the horizontal angle of a piping section that takes into account the effect of any pressure head. The speed of sound a and density ϱ are fluid characteristic constants, while the diameter D, coefficient λ and angle α are parameters of specific high-pressure components, such as a piping. It is further noted that the resulting fluid flow resistance is proportional to the squared velocity, with respect to the fluid flow direction [Streeter et al., 1998].

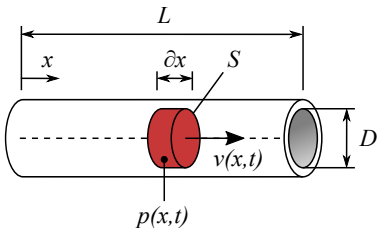

Figure 3.2 – A piping section of constant cross section S: considering a fluid segment ∂x of pressure state $p(x,t)$ and fluid flow velocity $v(x,t)$ with respect to the position coordinate x and time t.

Two assumptions have been obtained to facilitate its practical application.

Assumption 3.3. *The first order partial derivative of the pressure $p(x,t)$ with respect to the position variable x is small compared to the corresponding time derivative, this yields*

$$\frac{\partial}{\partial x}\, p(x,t) \ll \frac{\partial}{\partial t}\, p(x,t)\ . \tag{3.8}$$

Assumption 3.4. *The first order partial derivative of velocity $v(x,t)$ with respect to the position variable x is small compared to the time derivative, that yields*

$$\frac{\partial}{\partial x}\, v(x,t) \ll \frac{\partial}{\partial t}\, v(x,t)\ . \tag{3.9}$$

By Assumption 3.3, it is very common to eliminate the cross term of (3.6). Likewise, the cross term of (3.7) will be eliminated with respect to Assumption 3.4. On the other hand, from Assumption 3.1 follows a horizontal piping, such as $\alpha \approx 0$. These assumptions reduce (3.6) and (3.7) to obtain the governing system of partial differential equations

$$\frac{\partial}{\partial t} p(x,t) - a^2 \varrho \frac{\partial}{\partial x} v(x,t) = 0 \tag{3.10a}$$

$$\frac{\partial}{\partial t} v(x,t) - \frac{1}{\varrho}\frac{\partial}{\partial x} p(x,t) + \frac{\lambda}{2D} v(x,t)\,|v(x,t)| = 0\ , \tag{3.10b}$$

that describes the dynamics of a fluid segment. The dependent variables $p(x,t)$ and $v(x,t)$ refer to the pressure state and to the fluid flow velocity, respectively. Both partial differential equations are coupled since any difference of fluid flow velocity induces a pressure change and any pressure difference causes a fluid flow. This modelling approach has been found in different studies related to high-pressure systems, e.g. [Tremblay and Ramulu, 1999], [Hountalas and Kouremenos, 1998], [Lino et al., 2007] and [Gupta et al., 2011]. It presents the transient characteristics of fluid flow along a horizontal piping.

Investigations with finite element methods (FEM) often model an ideal fluid flow without any friction losses, thus assuming $\lambda \approx 0$. This reduces (3.10a) and (3.10b) to

$$\frac{\partial}{\partial t}\, p(x,t) = a^2 \varrho \frac{\partial}{\partial x}\, v(x,t) \tag{3.11a}$$

$$\frac{\partial}{\partial t}\, v(x,t) = \frac{1}{\varrho}\frac{\partial}{\partial x}\, p(x,t)\ , \tag{3.11b}$$

a system of coupled partial differential equations without any dissipative term. The principle of fluid flow continuity (3.11a) indicates that a velocity gradient along the position coordinate $\partial v(x,t)/\partial x$ causes a pressure variation in time $\partial p(x,t)/\partial t$. The momentum conservation (3.11b) shows that a pressure gradient along the position coordinate $\partial p(x,t)/\partial x$ will induce a velocity variation in time $\partial v(x,t)/\partial t$, which means that a fluid becomes either accelerated or decelerated.

Discretization in space and implementation

The system of partial differential equations (3.11a) and (3.11b) is investigated with numerical simulations using *MATLAB*. This requires the discretization of a piping section with length L into n homogeneous fluid segments of length Δx, such as $L = n\ \Delta x$. For that, the partial differentials in space $\partial f(x)/\partial x$ become approximated with finite differences. This requires that the length Δx of a fluid segment is significantly smaller as the piping inner diameter D, such as $\Delta x \ll D$.

The finite differences are obtained by **Taylor expansion**

$$f(x \pm \Delta x) = f(x) \pm \frac{\partial}{\partial x} f(x)\Delta x + \frac{\partial^2}{\partial x^2} f(x)\frac{\Delta x^2}{2!} \pm \dots\ , \tag{3.12}$$

which can be evaluated for its backward differences $f(x - \Delta x)$ when considering a preceding segment as well as for its forward differences $f(x + \Delta x)$ when considering a subsequent segment. Subtracting the forward differences and the backward differences, obtained from (3.12), yields

$$f(x + \Delta x) - f(x - \Delta x) = f(x) + \frac{\partial}{\partial x} f(x)\Delta x - f(x) + \frac{\partial}{\partial x} f(x)\Delta x\ , \tag{3.13}$$

while higher order terms have been assumed to be small. Rearranging (3.13) yields the central differences

$$\frac{\partial}{\partial x} f(x) \approx \frac{f(x + \Delta x) - f(x - \Delta x)}{2\ \Delta x}\ , \tag{3.14}$$

which is the symmetric approximation of a partial differential [Langtangen and Linge, 2017]. Substituting the partial differentials in (3.11a) and (3.11b) yields

$$\frac{d}{dt}\, p(x,t) = a^2 \varrho\ \frac{v(x + \Delta x, t) - v(x - \Delta x, t)}{2\ \Delta x} \tag{3.15a}$$

$$\frac{d}{dt}\, v(x,t) = \frac{1}{\varrho}\ \frac{p(x + \Delta x, t) - p(x - \Delta x, t)}{2\ \Delta x}\ . \tag{3.15b}$$

The notation $f(x + n\Delta x) := f(n)$, allows for defining a **finite difference scheme**

$$\frac{\partial}{\partial x}\begin{pmatrix} f(1) \\ \vdots \\ f(N) \end{pmatrix} \approx \underbrace{\frac{1}{2\ \Delta x}\begin{pmatrix} 3 & -4 & 1 & 0 & \cdots & 0 \\ 1 & 0 & -1 & 0 & & \\ 0 & \ddots & \ddots & \ddots & & \vdots \\ \vdots & & \ddots & \ddots & \ddots & 0 \\ & & 0 & 1 & 0 & -1 \\ 0 & \cdots & 0 & -1 & 4 & -3 \end{pmatrix}}_{M_x} \cdot \begin{pmatrix} f(1) \\ \vdots \\ f(N) \end{pmatrix} , \tag{3.16}$$

which evaluates each fluid segment $n = \{2\ \ldots\ N-1\}$ of a piping with respect to the central differences (3.14). The boundary segments $n = 1$ and $n = N$ requires the forward and backward differences, respectively. The resulting finite difference matrix M_x is useful for numerical implementation using for example *MATLAB*. Applying (3.16) in (3.15a) and (3.15b) results in a system of equations

$$\frac{d}{dt}\begin{pmatrix} p \\ v \end{pmatrix} \approx \begin{pmatrix} 0 & a^2\varrho\ M_x \\ 1/\varrho\ M_x & 0 \end{pmatrix} \cdot \begin{pmatrix} p \\ v \end{pmatrix} \tag{3.17}$$

that is employed for simulations, where $p = (p(1) \ldots p(N))^{-1}$ and $v = (v(1) \ldots v(N))^{-1}$. It is possible to further improve simulation accuracy when defining a finite difference scheme of higher orders, though, this will require increased calculation efforts.

Numerical simulations

Simulations have been derived for a piping section of $L = 4$ m length and an inner diameter of $D = 2.4$ mm. This corresponds to the topology **(a) Short piping** and connects a single high-pressure pump with a cutting head, see Section 2.2. The piping is filled with water at any time. Subsequent simulations consider the physical properties given in Table 3.1. A piping is divided, with respect to Assumption 3.2, into $N = 16'667$ homogeneous segments of $\Delta x \leq 0.24$ mm length, such as $\Delta x < 0.1\ D$. Applying (3.17) yields a system of equations with a finite difference matrix M_x of dimension N. This system is numerically solved using *MATLAB R2017b* and applying the solver *ode45* with variable step size. The solver has been configured for a relative tolerance of 10^{-4}. It has been running on a Windows 10 machine with an Intel Core i7-7600U 2.80 GHz processor and 16.0 GB RAM.

The fluid flow velocity and pressure states of every segment n have been set to the initial conditions $v_n(t < 0) = v_0$ and $p_n(t < 0) = p_0$, respectively. The boundary condition on the first segment $n = 1$ at the piping intake will be a function in time that describes an exogenous input fluid flow. The input fluid flow velocity $v_1(t < 0) = v_0$ will be increased at $t = 0$ to $v_1(t > \tau) = 1.1\ v_0$ with respect to

$$v_1(t) = \left(1 - 0.1\ \cos\left(\pi\frac{t}{\tau}\right)\right) v_0, \quad 0 \leq t \leq \tau\ , \tag{3.18}$$

taking the maximal dynamic range of a high-pressure pump into account with $\tau = 7.6$ ms. This boundary condition (3.18) is applied for system excitation and consequently induces a pressure fluctuation that propagates along the piping.

Table 3.1: Physical properties of pure water: characteristics of water (H_2O) at 25°C and 0.1 MPa (1 bar) [Schmidt and Grigull, 1981].

Properties	Symbol	Value	Unit
Fluid density	ϱ	997	(kg/m^3)
Characteristic speed of sound	a	1484	(m/s)
Bulk modulus	K	2.1739	$\times\ 10^9$ (Pa)

Two different cases will be studied with respect to the boundary condition on the last segment $n = N$ at the piping outtake. For both cases, the output fluid flow velocity $v_N(t < 0) = v_0$ will vary as function of the corresponding pressure state $p_N(t) \geq 0\ \forall\ t$:

(A) Open piping end: The cutting head is opened, though any nozzle has been removed. This case investigates the fluid dynamics for a piping section without the characteristics of a nozzle. That applies the boundary condition

$$v_N(t) = \sqrt{\frac{2}{\varrho}}\ \zeta\ \sqrt{p_N(t)}, \quad t \geq 0\ , \tag{3.19}$$

referring to the discharge equation [Böswirth and Bschorer, 2012]. For which a discharge coefficient $\zeta = \#\#\#$ has been derived, while estimating the friction loss for turbulent flow characteristics [Blasius, 1913], see (3.32) and (3.33).

(B) Nozzle contraction: A high-pressure pump cannot provide the fluid flow required, if a nozzle is missing. Consequently, this case considers a nozzle of $D_H = 0.35$ mm inner diameter with a discharge coefficient of $\zeta = \#\#\#$. It adopts the discharge equation (3.19) to

$$v_N(t) = \frac{S_H}{S}\ \sqrt{\frac{2}{\varrho}}\ \zeta\ \sqrt{p_N(t)}, \quad t \geq 0\ , \tag{3.20}$$

where $S_H = D_H^2\pi/4$ denotes the nozzle cross section.

These boundary conditions enable all segments to reach a bounded steady-state pressure, such as $\lim_{t\to\infty} p_n(t) < \infty$. The simulations of Figures 3.3 - 3.6 has been obtained with respect to boundary condition (A), initializing each segment to v_0 for $p_0 = \{20, 50, 100, 200\}$ MPa and considering (3.19), as summarized in Table 3.2. Any increasing input fluid flow at the piping intake induces a pressure fluctuation. This fluctuation propagates through the piping and reaches the piping outtake with a time delay $\tau_d(t)$, where it will be reflected until an equilibrium is obtained. According to [Liptak, 2018], this time delay is expected to change with respect to the piping length L and fluid flow velocity $v(t)$, such as $\tau_d(t) = L/v(t)$. It is seen that the pressure steady-state will change for different fluid flow velocities. For example, a velocity change of 10% from $v_0 = 419$ to $\lim_{t\to\infty} v_n(t) \approx 461$ m/s, causes a pressure change of 50% from $p_0 = 20$ to $\lim_{t\to\infty} p_n(t) \approx 30$ MPa. It is further observed for any increased operating pressure, that the sensitivity as well as the damping ratio will decrease. However, the resulting fluid flow velocity $v(t)$ approaches the characteristics speed of sound a. This is critical for the underlying modelling principle (3.1) that considers an incompressible fluid flow. It is only valid for $v(t) \ll a$ [Spurk, 2013].

Table 3.2: Configurations for numerical simulations with boundary conditions A and B: initial conditions, resulting equilibrium points and relative delays per piping length.

Sim.	Velocity $v(t)$			Pressure $p(t)$			Rel. delay	
	$t = 0$ (m/s)	$\lim_{t\to\infty}$ (m/s)	Rel. ratio (%)	$t = 0$ (MPa)	$\lim_{t\to\infty}$ (MPa)	Rel. ratio (%)	$t = 0$ (ms/m)	$\lim_{t\to\infty}$ (ms/m)
A-1	419	461	10	20	30	50	2.4	2.2
A-2	663	729	10	50	74	48	1.5	1.4
A-3	937	1031	10	100	145	45	1.1	1.0
A-4	1325	1458	10	200	288	44	0.8	0.7
B-1	2.76	3.04	10	20	29	44	362.3	328.9
B-2	4.36	4.80	10	50	72	44	229.4	208.3
B-3	6.17	6.79	10	100	144	44	162.1	147.3
B-4	8.72	9.60	10	200	288	44	114.7	104.2

The simulations of Figures 3.7 - 3.10 has been obtained with respect to the adapted boundary condition (B). An increased fluid flow velocity at the piping intake propagates towards the piping outtake, where a nozzle is located. The pressure state of every segment will raise continuously and obtain steady-state for the entire piping. It is seen that the nozzle influences the dynamic behaviour with respect to (3.20). The induced pressure trend features an increased raise time without any oscillations. The rise time for the fluid flow velocity $v_n(t)$ increases, while the time delay along a piping becomes small in contrast to the transient pressure trend $p_n(t)$. The resulting fluid flow velocities are far bellow any critical values for to the underlying modelling principle, such as $v(t) \ll a \; \forall \; t$ holds.

As a consequence, the subsequent section will introduce a lumped parameter model. It approximates the piping dynamics described by (3.10a) and (3.10b) for future high-pressure networks by considering fluid flow equilibrium.

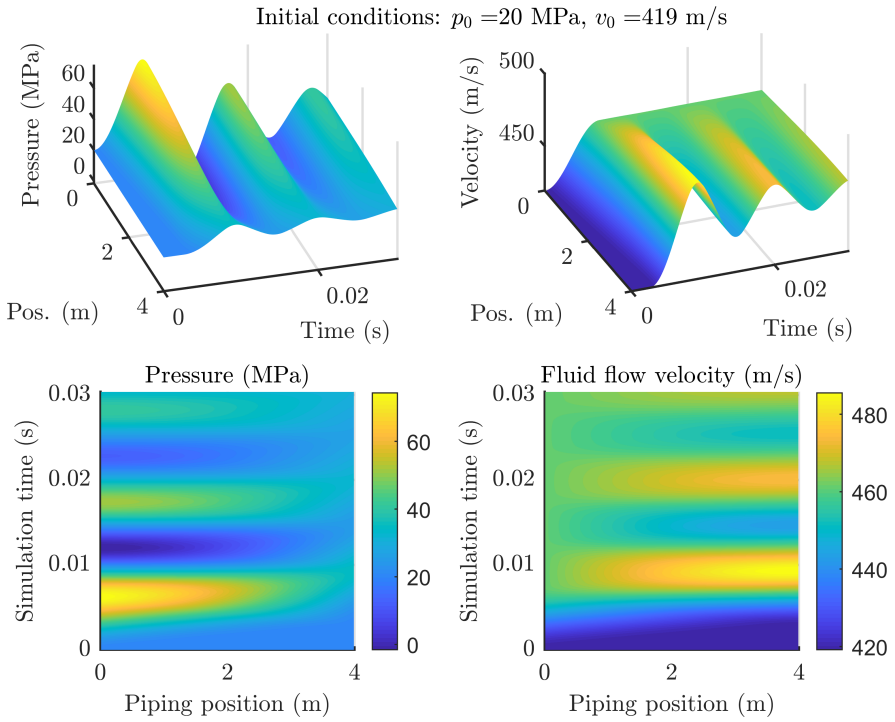

Figure 3.3 – Simulated pressure trend and fluid flow velocity for boundary conditions (A-1): piping without any nozzle installed when increasing the fluid flow velocity to $v_\infty = 461$ m/s.

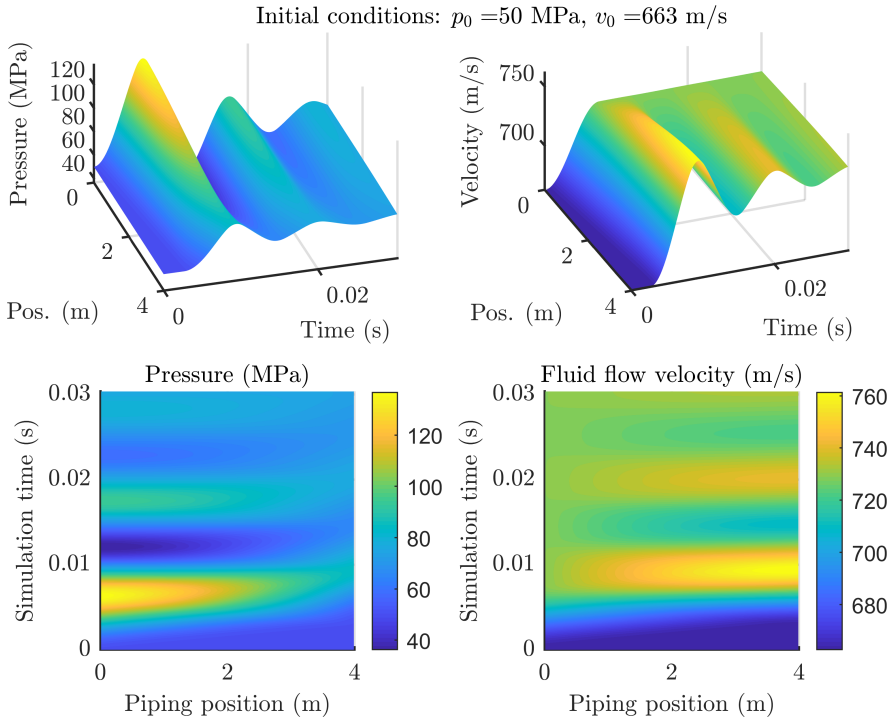

Figure 3.4 – Simulated pressure trend and fluid flow velocity for boundary condition (A-2): piping without any nozzle installed when increasing the fluid flow velocity to $v_\infty = 729$ m/s.

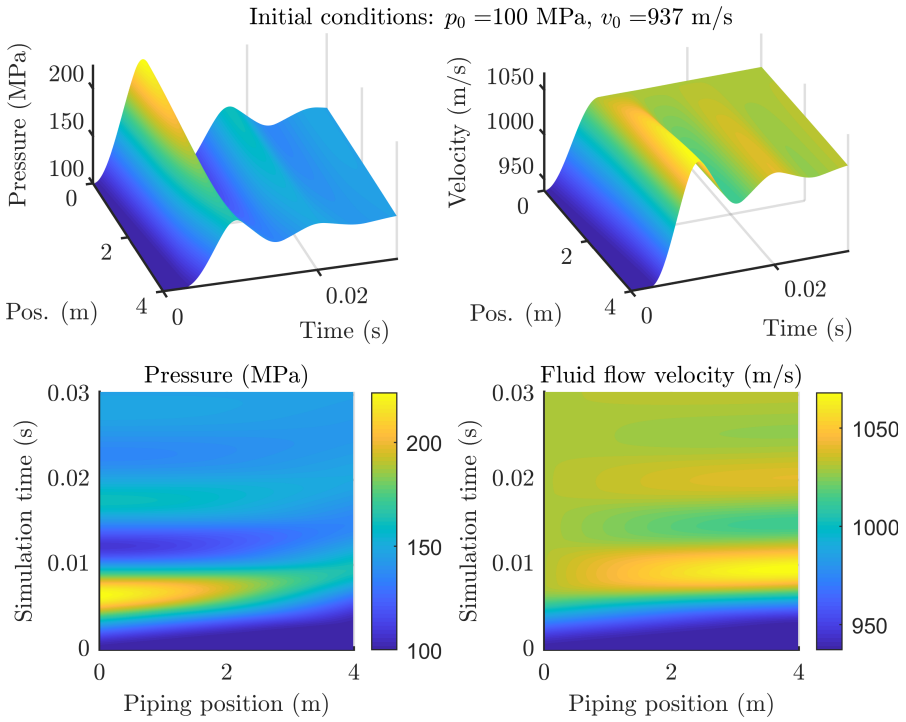

Figure 3.5 – Simulated pressure trend and fluid flow velocity for boundary condition (A-3): piping without any nozzle installed when increasing the fluid flow velocity to $v_\infty = 1031$ m/s.

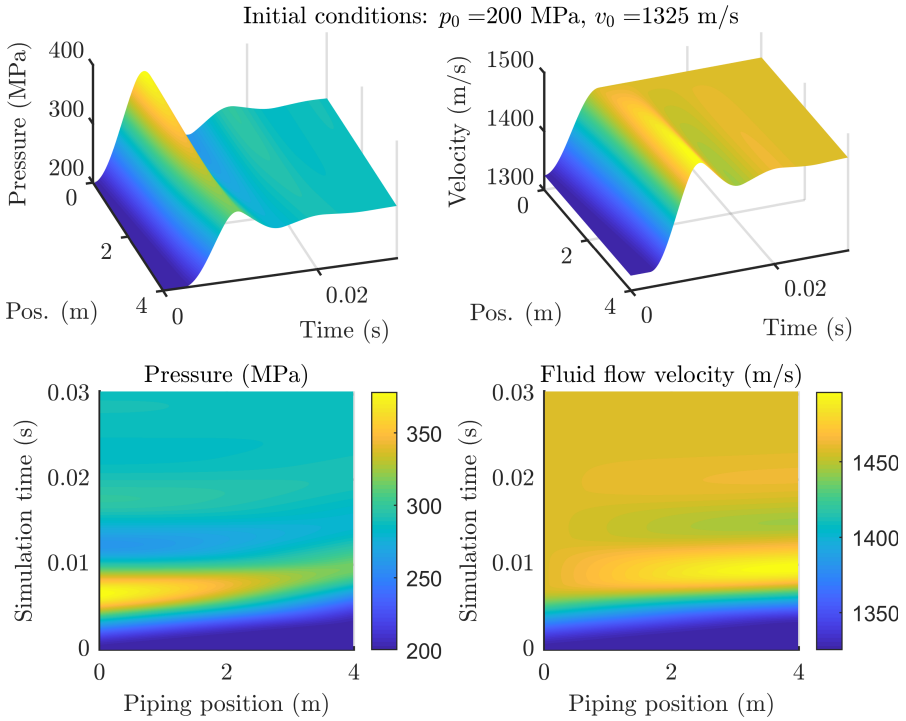

Figure 3.6 – Simulated pressure trend and fluid flow velocity for boundary condition (A-4): piping without any nozzle installed when increasing the fluid flow velocity to $v_\infty = 1458$ m/s.

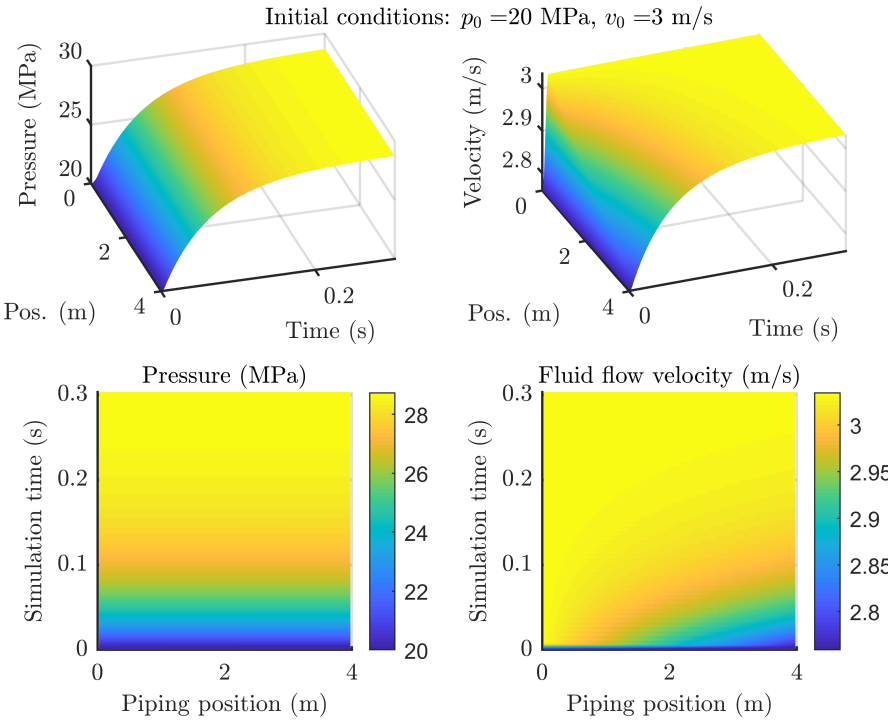

Figure 3.7 – Simulated pressure trend and fluid flow velocity for boundary condition (B-1): piping with nozzle when increasing the fluid flow velocity to $v_\infty = 3$ m/s.

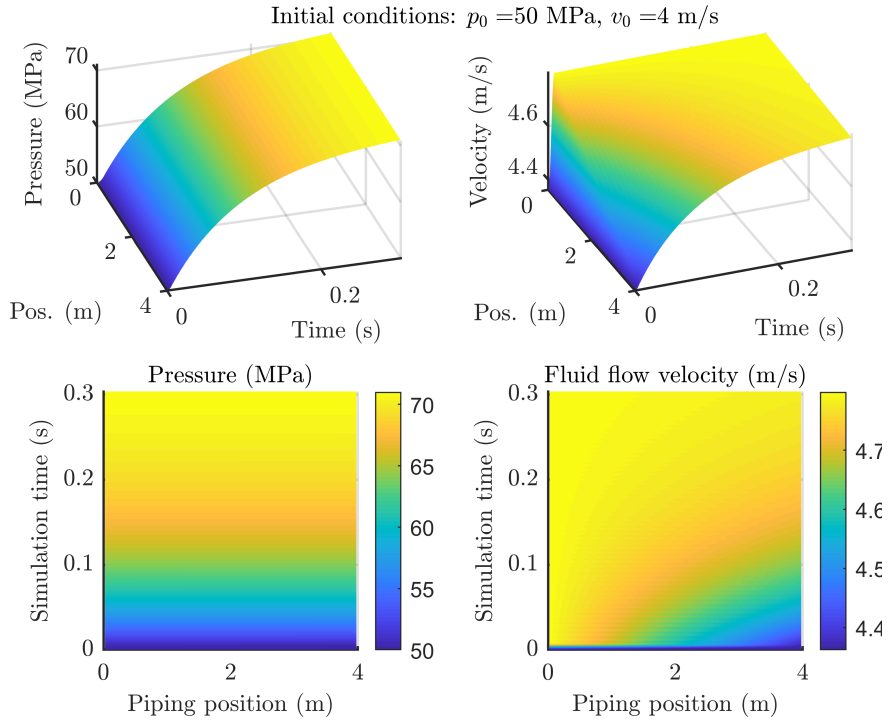

Figure 3.8 – Simulated pressure trend and fluid flow velocity for boundary condition (B-2): piping with nozzle when increasing the fluid flow velocity to $v_\infty = 4.8$ m/s.

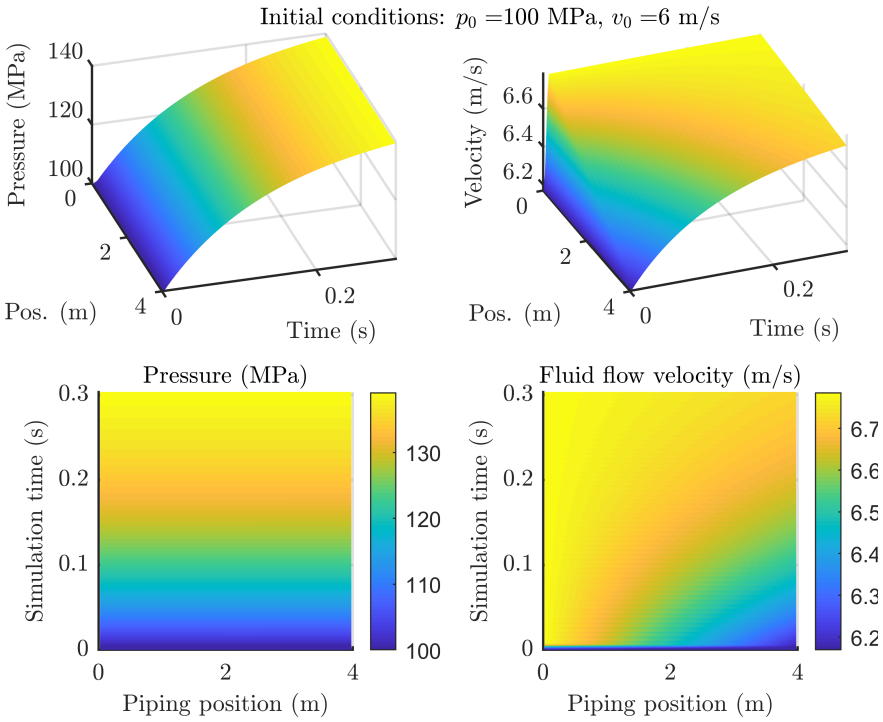

Figure 3.9 – Simulated pressure trend and fluid flow velocity for boundary condition (B-3): piping with nozzle when increasing the fluid flow velocity to $v_\infty = 6.8$ m/s.

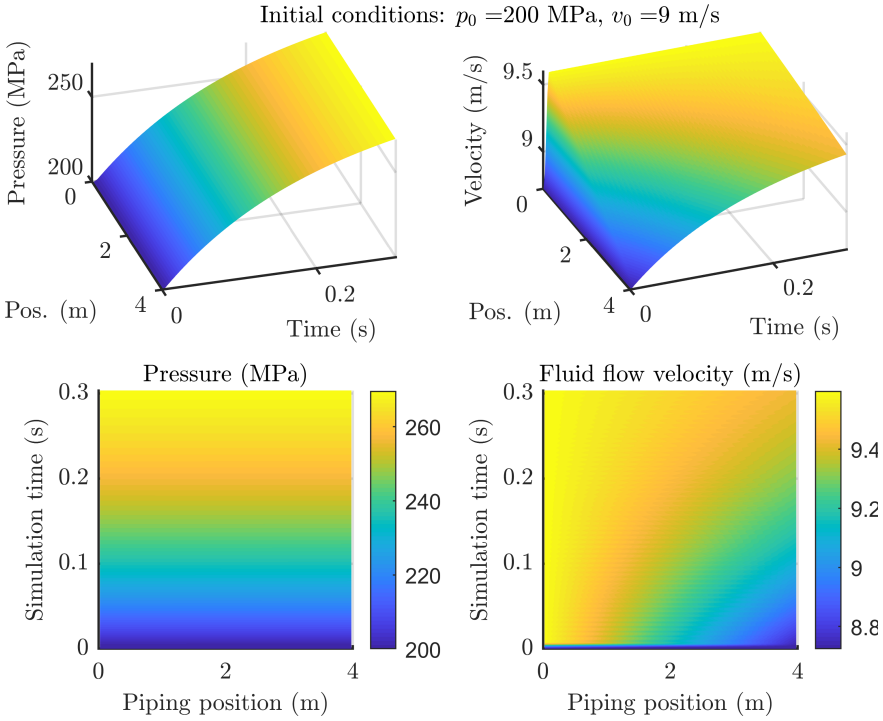

Figure 3.10 – Simulated pressure trend and fluid flow velocity for boundary condition (B-4): piping with nozzle when increasing the fluid flow velocity to $v_\infty = 9.6$ m/s.

3.2.2 Lumped parameter modelling

Approximating the governing equations (3.10a) and (3.10b), which describe the fluid dynamics, with finite differences assigns a specific fluid volume $V = S\ \Delta x$ to homogeneous segments, as shown in the illustration of Figure 3.11. This results in a lumped parameter model that represents a system of algebraic differential equations and lumps the distributed parameters to discrete pressure states, assuming a stationary fluid flow [Ford and Fulkerson, 2016].

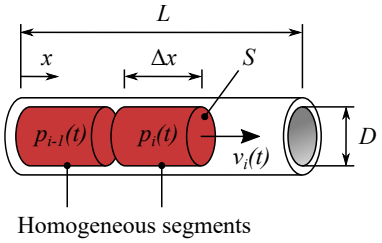

Figure 3.11 – A piping section of constant cross section S: homogeneous segments of length Δx along the position coordinate x with pressure state $p(t)$ and fluid flow velocity $v(t)$.

To obtain ordinary differential equations, the Taylor series expansion (3.12) is again used, approximating the first order partial derivatives in x. The **backward differential**

$$\frac{\partial}{\partial x} v(x,t) \approx \frac{v(x,t) - v(x - \Delta x, t)}{\Delta x} \tag{3.21}$$

substitutes the fluid flow velocity gradient in (3.10a), where the **forward differential**

$$\frac{\partial}{\partial x} p(x,t) \approx \frac{p(x + \Delta x, t) - p(x,t)}{\Delta x} \tag{3.22}$$

gives the pressure gradient for (3.10b), in which Δx denotes the length of a homogeneous segment. The fluid flow velocity is then substituted by the fluid flow according to $v(t) = Q(t)\ S^{-1}$, while the notations

$$\Delta Q_i^-(t) := Q_{i-1}(t) - Q_i(t) \tag{3.23}$$

and

$$\Delta p_i^+(t) := p_i(t) - p_{i+1}(\Delta x, t) \tag{3.24}$$

are introduced. This assigns a fluid segment i at location $x = 0$ for $f(x \pm n\Delta x) = f_{i \pm n}$. The backward differential (3.21) refers to a fluid flow relative to a previous segment, denoted by superscript «+» and the forward differential (3.22) consequently indicates a pressure difference relative to a subsequent segment, denoted with a superscript «−». Applying the differential (3.21) for (3.10a) and the differential (3.22) for (3.10b) yields, with respect to the notations (3.23) and (3.24), the system of ordinary differential equations

$$\frac{d}{dt} p_i(t) \approx \frac{a^2 \varrho}{S\ \Delta x} \Delta Q_i^-(t) \tag{3.25a}$$

$$\frac{d}{dt} Q_i(t) \approx \frac{S}{\varrho \Delta x} \Delta p_i^+(t) - \frac{\lambda}{2D\ S} Q_i(t) |Q_i(t)| \ , \tag{3.25b}$$

describing the dynamics of a homogeneous segment. As an increased fluid flow difference $\Delta Q^-(t)$ induces a pressure $p(t)$, an increased pressure difference $\Delta p^+(t)$ yields a fluid flow $Q(t)$. The squared of the resulting fluid flow causes the fluid flow difference to decrease until a pressure equilibrium has been obtained. For simplicity, the subscript i is omitted for the subsequent sections.

Fluid dynamic parameters

The hydraulic capacity $\mathcal{C}$ (see [Will and Gebhardt, 2014]) determines an increase of pressure $dp(t)/dt$ with respect to the fluid flow difference. It is defined as

$$\mathcal{C} = \frac{S\ \Delta x}{a^2 \varrho} = \frac{V}{K} \tag{3.26}$$

where $V = S\ \Delta x$ is the fluid volume and $K = a^2 \varrho$ corresponds to the bulk modulus. Here, the **bulk modulus**

$$K = -\frac{dp}{dV/V} \tag{3.27}$$

is expressed in [Streeter et al., 1998] as a measure of the relative change in volume dV/V to a change in pressure dp. Substituting this in (3.26) yields $\mathcal{C} = dV/dp$.

In the same manner, the hydraulic inductivity $\mathcal{L}$ (see [Will and Gebhardt, 2014]) determines an increase of fluid flow $dQ(t)/dt$ with respect to the pressure difference. It is given by

$$\mathcal{L} = \frac{\Delta x\ \varrho}{S} = \frac{m}{S^2} = \frac{\mu}{S}\ , \tag{3.28}$$

where $m = \varrho\ V$ denotes the fluid mass within a volume section and $\mu = m\ S^{-1}$ corresponds to a mass relative to its cross section.

Assuming a typical high-pressure pipe of $\Delta x = 1$ m length and $S = 4.5239$ mm^2 cross section results in a hydraulic capacity of $\mathcal{C} \approx 2 \times 10^{-15}$ m^3/Pa and in a hydraulic inductivity of $\mathcal{L} \approx 2 \times 10^8$ kg/m^4. The physical properties for these computations are given in the above Table 3.1. The small capacity in contrast to the inductivity, leads to a far slower dynamics of (3.25a) compared with (3.25b), what is evidence of a stiff behaviour. This can cause difficulties for solving efficiently the system of differential equations (3.25a - 3.25b) with numerical methods. Cross section S and fluid density ϱ affect the dynamics for both differential equations, but none of them can be chosen freely.

Solving for fluid flow equilibrium

Assuming a stationary fluid flow allows for solving the differential equation (3.25b) for its equilibrium ($dQ(t)/dt = 0$). This provides an algebraic differential equation that simplifies the approximated equation of continuity and results in a **lumped parameter model**

$$\frac{d}{dt}p(t) \approx \frac{K}{V}\Delta Q^-(t) \tag{3.29a}$$

$$Q(t) \approx S\ \sqrt{\frac{2}{\varrho}}\ \zeta\ \sqrt{|\Delta p^+(t)|}\ sign\left(\Delta p^+(t)\right) \tag{3.29b}$$

that approximates the local pressure state of a homogeneous segment, which becomes determined by the **fluid flow resistance**

$$H = S\ \sqrt{\frac{2}{\varrho}}\ \zeta \tag{3.30}$$

with respect to the non-linear interconnection to the neighbouring segments. The Signum function

$$sign(x) = \begin{cases} -1, & x < 0 \\ 0, & x = 0 \\ 1, & x > 0 \end{cases} \tag{3.31}$$

is required to recover the fluid flow direction along a fluid flow path. The flow resistance H requires to determine the **discharge coefficient**

$$\zeta = \sqrt{\frac{D}{\Delta x \, \lambda}} \, , \tag{3.32}$$

for every homogeneous segment, with respect to the cross section inner diameter D and length Δx. This discharge coefficient needs further approximation by estimating the friction loss coefficient

$$\lambda < \frac{c_1}{\mathrm{Re}^{c_2}} \approx 0.0456 \, , \tag{3.33}$$

with $c_1 = 0.3164$ and $c_2 = 0.25$ for turbulent flow characteristics [Blasius, 1913], as a Reynolds number $\mathrm{Re} > 2320$ is assumed.

The resulting algebraic equation (3.29b) is also known as discharge equation, see [Böswirth and Bschorer, 2012] or [Spurk, 2013]. It is found in many studies, e.g. [Lino et al., 2007], [Liu et al., 2013] and [Wang et al., 2016b], to describe the fluid flow through components, such as valves and nozzles. For example, the evaluation of (3.32) for a piping section of $\Delta x = 1$ m and $D = 2.4$ mm, while considering the above approximation (3.33), yields a discharge coefficient with $\zeta > 0.2$. On the other hand, [Susuzlu et al., 2004] reports an enlarged discharge coefficient of $\zeta = [0.6, 0.7]$ for cutting heads, due to the small nozzle inner diameters. The friction loss coefficients of specific high-pressure components, used for modelling, will be experimentally obtained in the Section 3.4.

The resulting system of algebraic differential equations (3.29a) and (3.29b) is less demanding for solving with a numerical solver, since the fast dynamics from (3.25b) has been resolved for fluid flow equilibrium. As a consequence, it becomes possible that fast changing pressure fluctuations will be reproduced with reduced accuracy. Since the modelling for high-pressure networks is eventually applied to verify the control design, at least the induced fluctuations due to the switching of cutting heads has to be taken into account. Hence, the subsequent section will investigate the simplified formulation by means of simulations.

Numerical simulations

Pressure fluctuations in a short piping section will be investigated for different piping lengths ($L = \{0.5, 1, 2, 5, 10\}$ m), while deriving simulations with the distributed parameter model as well as with the lumped parameter model. The distributed parameter model will introduce a discretization with finite differences implementing $N = L/\Delta x$ homogeneous segments of length $\Delta x = 0.24$ mm. On the other hand, the lumped parameter model considers all of the piping as a single segment $N = 1$, resulting in a first order model. Both models are numerically simulated using *MATLAB R2017b* and applying the solver *ode45*, where the solver has been configured for a relative error of 10^{-4}.

From the previous simulations in this section, it has been observed that the pressure sensitivity and oscillation amplitudes increase for small operating pressure. The subsequent simulations consider an initial pressure of $p_0 = 100$ MPa. This corresponds to the smallest expected operating pressure for waterjet machining, where the largest sensitivity is expected. A sinusoidal input fluid flow of amplitude v_0 will be applied at the piping intake. The initial fluid flow velocity $v_n(t < 0) = v_0$ has been derived with respect to (3.20). That results in the input boundary condition

$$v_1(t) = \left(1 - \cos\left(\pi \frac{t}{\tau} - 0.5 \, \pi\right)\right) v_0, \quad t \geq 0 \, , \tag{3.34}$$

taking the maximal dynamic range of a high-pressure pump into account with $\tau = 7.6$ ms. The output fluid flow velocity $v_N(t < 0) = v_0$ will vary in function to the corresponding pressure

state $p_N(t) \geq 0 \; \forall \; t$, considering the output boundary condition **(B) Nozzle contraction**. This investigation aims to determine the minimal length of a homogeneous segment and guarantees an useful simulation accuracy, when applying the lumped parameter model.

The plots of Figure 3.12 - 3.16 show the simulation results for the distributed parameter model, when reaching oscillation around an operating point. For a piping of $L > 5$ m length, the sinusoidal excitation hits resonance of the piping. This results in a phase shift of about 180° between the input pressure $p_1(t)$ and output pressure $p_N(t)$, see Figure 3.16.

The plots of Figure 3.17 - 3.21 evaluate the simulation errors, while comparing the estimated fluid flow velocities and pressure states at the piping outtake for the distributed parameter model and the lumped parameter model. The 180° phase shift is observed using either of the models, but the output pressure amplitude decreases only for the lumped parameter model. This is observed for a piping of $L > 2$ m length and results in increased simulation errors. To aggregate the distributed parameter model to homogeneous segments of length $\Delta x < 1$ m seems to be acceptable for practical use. Simulation effort will be reduced, while the relative error per segment remains below 0.5%.

However, the error propagation has to be considered when connecting several homogeneous segments in series. Table 3.3 compares the simulation error for a piping of $L = 20$ m length that is modelled with $n = \{4, 10, 20, 40, 100\}$ segments. Where a distributed parameter model requires an enhanced computational effort for simulating a large piping section, the lumped parameter model reduces the simulation complexity with acceptable error and provides a flexible modelling for high-pressure networks of arbitrary topologies. The investigated topologies will be approximated, considering homogeneous segments of length $\Delta x \approx 1$ m.

Table 3.3: Simulation error comparing distributed and lumped parameter model: modelling a piping of 20 m length with different numbers of homogeneous segments.

Segments n	length Δx (m)	rmse (MPa)	Max. rel. error (%)	Dist. param Rel. sim. time (s/s)	Lump. param. Rel. sim. time (s/s)
4	5	5.24	10.1	0.0381	0.0388
10	2	2.87	7.8	0.0826	0.0291
20	1	0.24	0.9	0.187	0.0309
40	0.5	0.19	0.7	0.522	0.0351
100	0.2	0.09	0.4	3.74	0.0589

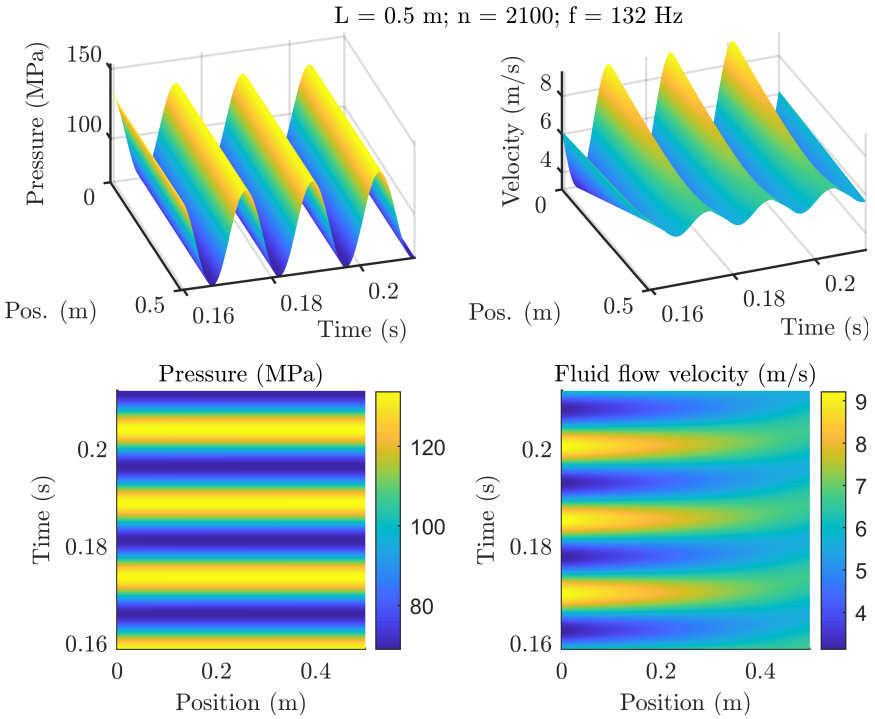

Figure 3.12 – Simulated pressure trend and fluid flow velocity for a piping segment of 0.5 m: simulation using finite differences with 2100 elements.

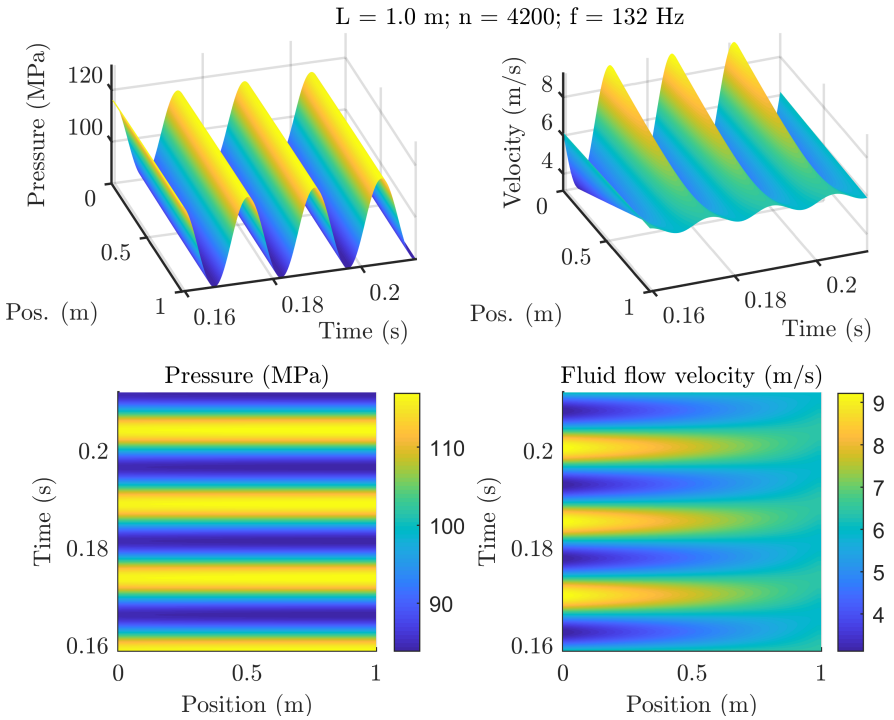

Figure 3.13 – Simulated pressure trend and fluid flow velocity for a piping segment of 1 m: simulation using finite differences with 4200 elements.

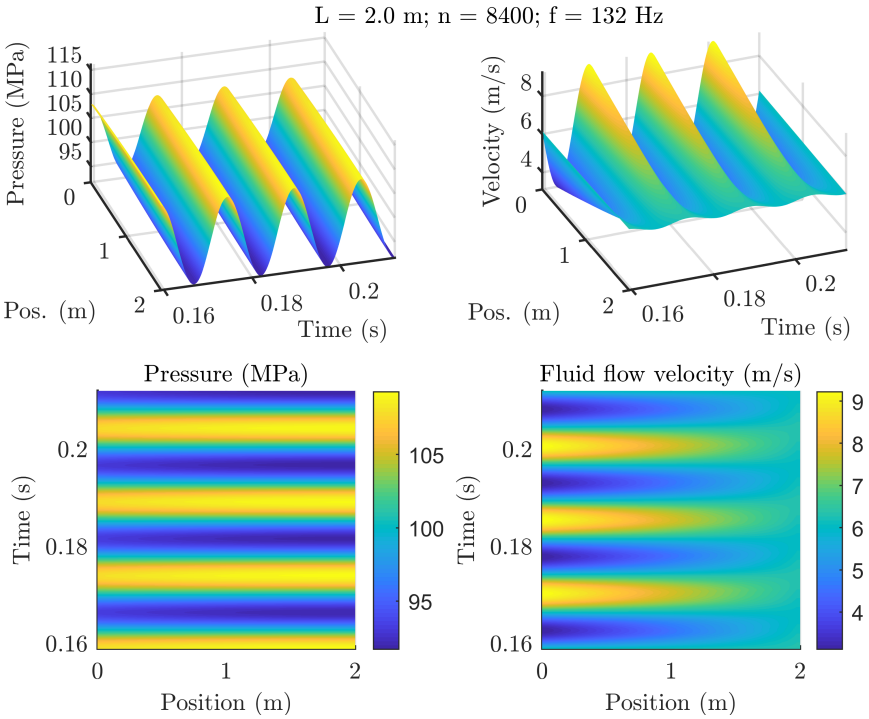

Figure 3.14 – Simulated pressure trend and fluid flow velocity for a piping segment of 2 m: simulation using finite differences with 8400 elements.

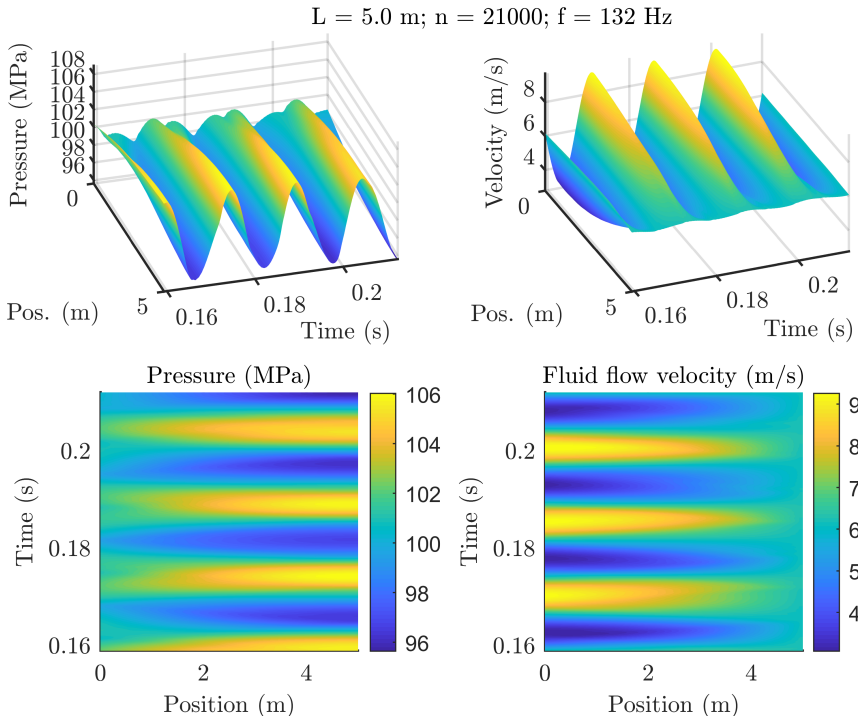

Figure 3.15 – Simulated pressure trend and fluid flow velocity for a piping segment of 5 m: simulation using finite differences with 21000 elements.

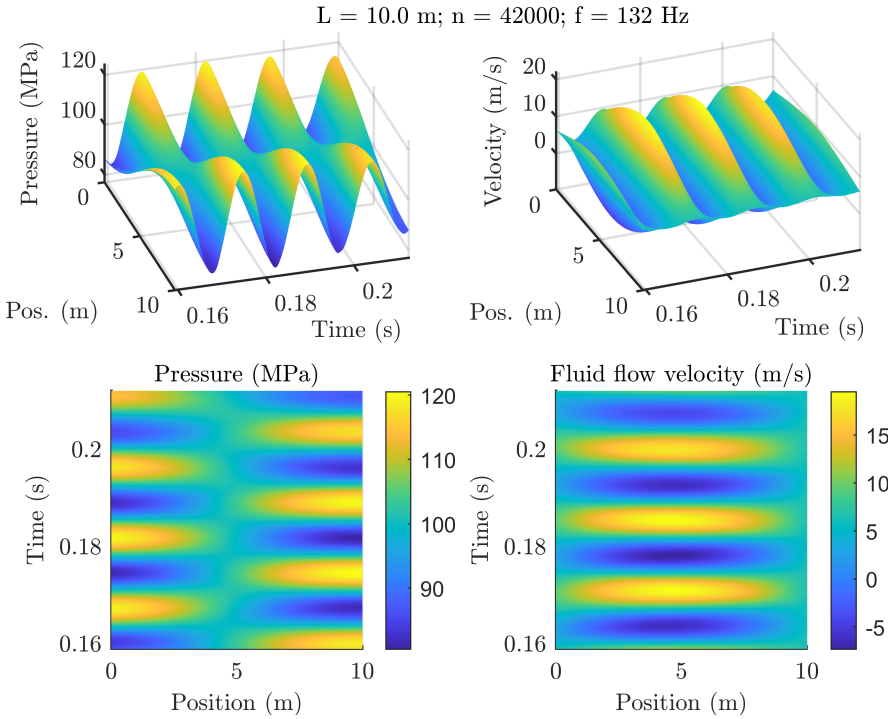

Figure 3.16 – Simulated pressure trend and fluid flow velocity for a piping segment of 10 m: simulation using finite differences with 42000 elements.

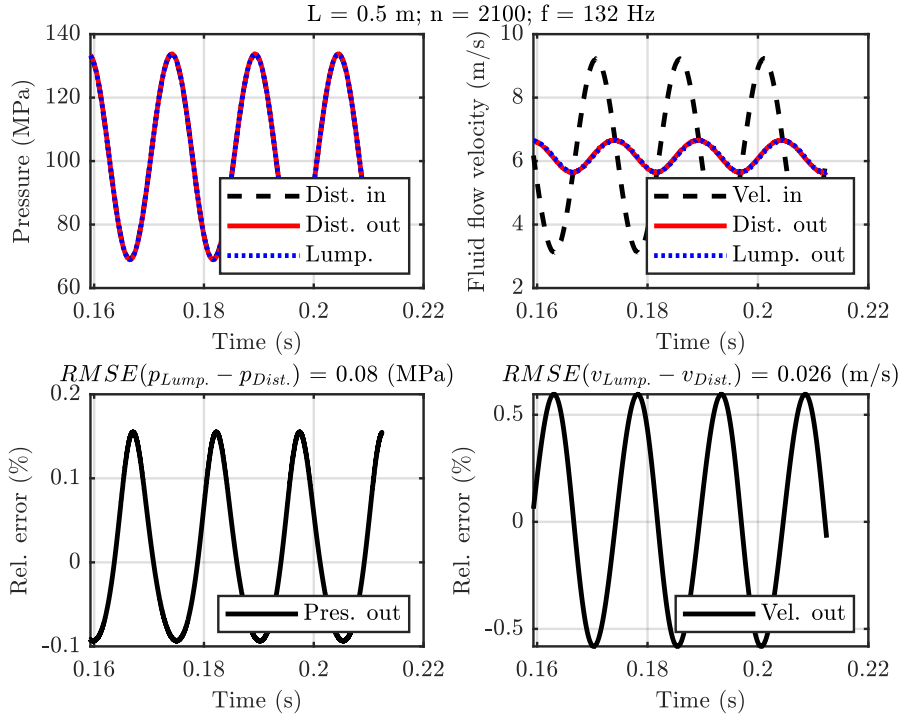

Figure 3.17 – Error between distributed and lumped parameter model for a piping segment of 0.5 m: simulation using finite differences with 2100 elements.

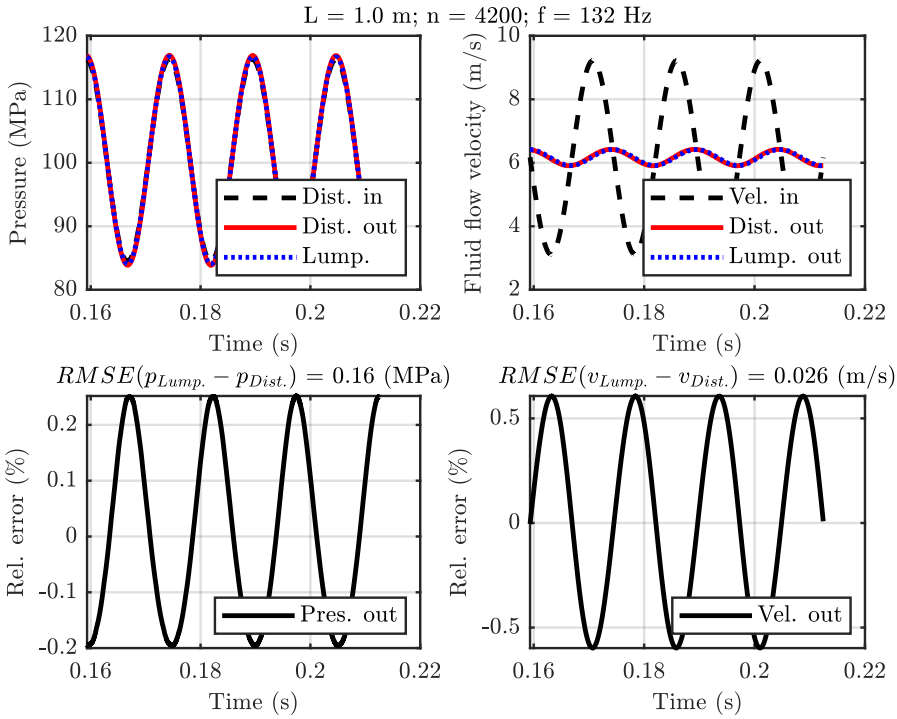

Figure 3.18 – Error between distributed and lumped parameter model for a piping segment of 1 m: simulation using finite differences with 4200 elements.

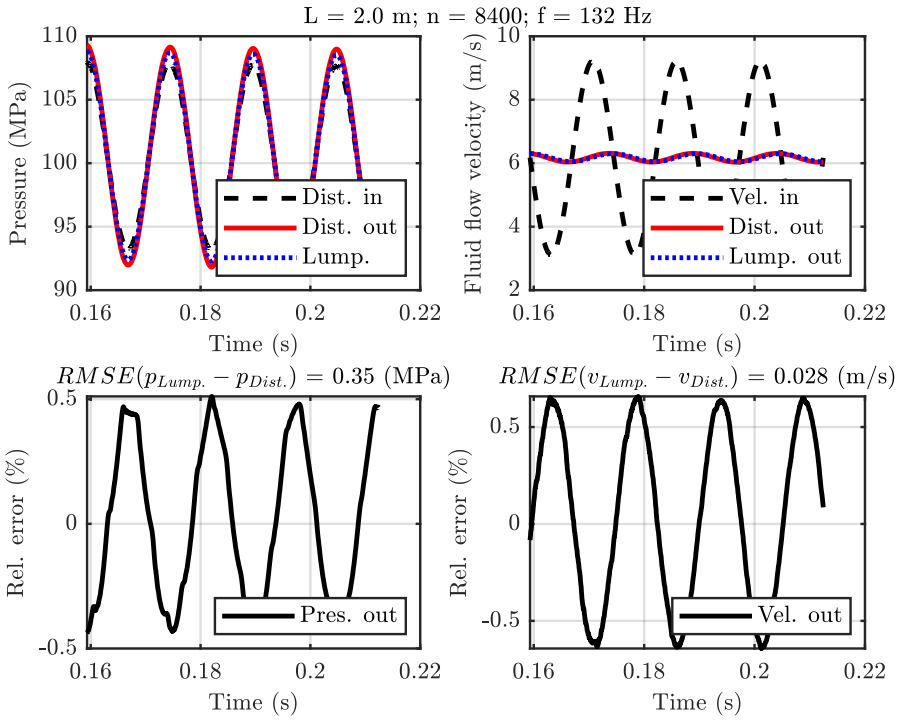

Figure 3.19 – Error between distributed and lumped parameter model for a piping segment of 2 m: simulation using finite differences with 8400 elements.

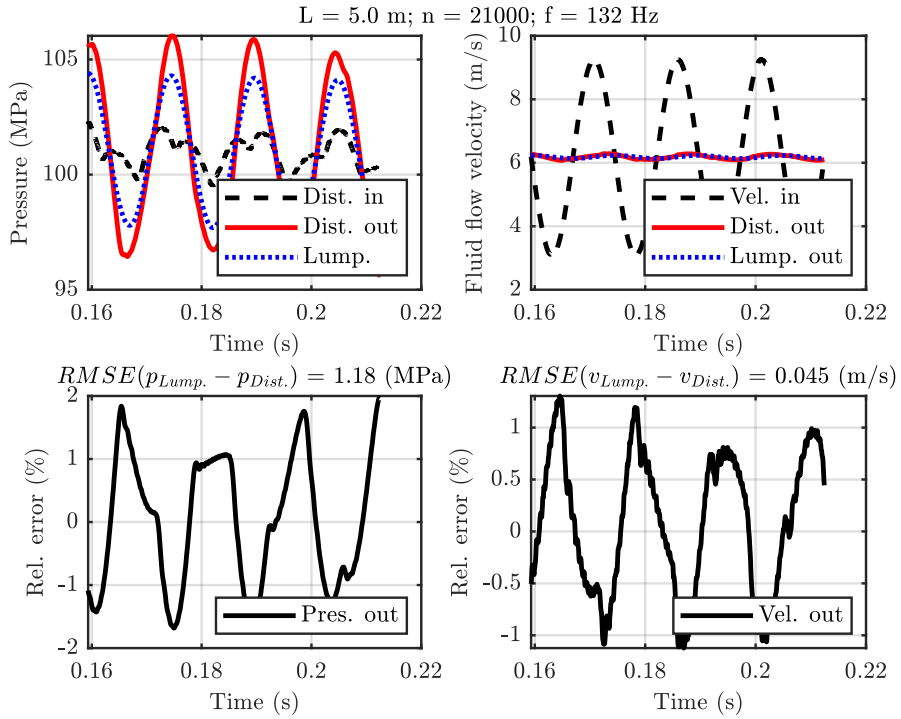

Figure 3.20 – Error between distributed and lumped parameter model for a piping segment of 5 m: simulation using finite differences with 21000 elements.

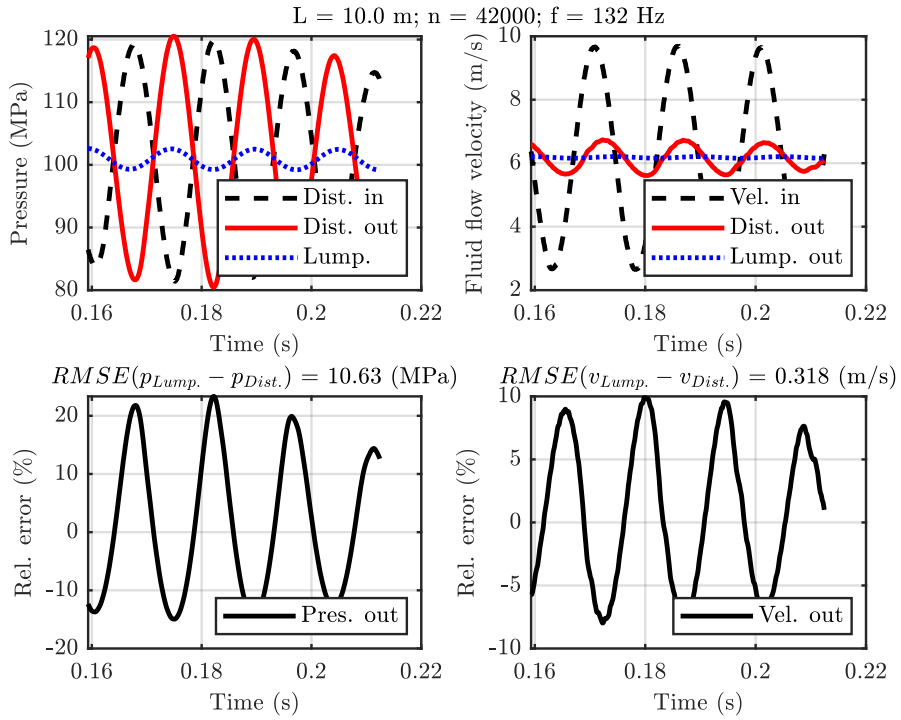

Figure 3.21 – Error between distributed and lumped parameter model for a piping segment of 10 m: simulation using finite differences with 42000 elements.

3.3 Framework for generalized high-pressure networks

The concept of lumped parameter modelling aims at an approximative numerical simulation of the 1-dimensional fluid flow along a piping with reduced computational effort. It describes a piping section by means of homogeneous segments, representing a pressure state around its operating point, while assuming a stationary fluid flow. However, the wide pressure range for waterjet machining requires to introduce varying parameters and to consider exogenous inputs for excitation. This section introduces these varying parameters and presents a graph-based modelling to obtain a generalized framework, as published in [Niederberger et al., 2018]. In contrast to other approaches, using graphs allows for representing entire waterjet facilities with reduced modelling effort and considering parameter variations improves simulation accuracy for a wide pressure range. The resulting high-pressure network models consist of a system of first order differential equations, representing homogeneous segments and recovering the fluid flow paths of arbitrary network topologies.

3.3.1 Varying parameters and exogenous inputs

Measurements show that the wide pressure range for waterjet machining affects the fluid density and bulk modulus, see [Tremblay and Ramulu, 1999]. Due to a variable fluid density and bulk modulus, the introduced Bernoulli equation (3.1) becomes insufficient for describing a high-pressure network. Consequently, it is useful to introduce the most prevalent parameter variations to address the wide pressure range of different waterjet applications and to subsequently provide a generalized description for high-pressure networks.

High-pressure networks involve parameter variations, which are either related to the fluid characteristics or to specific high-pressure components. The fluid compressibility includes a pressure dependent bulk modulus $K(p)$ as well as a pressure dependent fluid density $\varrho(p)$. High-pressure components define the fluid volume $V(t)$ and the flow path, given by the Heaviside function $\sigma(x, \Delta p)$, cross section $S(x)$ and discharge coefficient $\zeta(x)$. These parameter variations can be classified as dependent variables:

Parametric variables: these uncertainties are subject to change with respect to any other time-varying variable, such as $c = f(\varphi(t))$. The dependent variable $\varphi(t)$ is a priori unknown. This applies for a variable bulk modulus $K = f(p(t))$ as well as for a variable fluid density $\varrho = f(p(t))$, which are variable with respect to the pressure state $p(t)$.

Time dependent variables: these uncertainties are directly dependent on time t, such as $c = f(t)$. The function $f(t)\ \forall\ t \geq 0$ is a priori known and defined. Consequently, the parameter variation itself will be a priori known. This applies for very specific segments where its volume $V = f(t)$ varies in time. For example when a piston is displaced within a pumping chamber.

Local variables: These uncertainties can vary dependent on the position coordinate x, such as $c = f(x)$. The function $f(x)\ \forall\ x = [0, L]$ is a priori known for the entire high-pressure network. This applies on the cross section $S = f(x)$ and the discharge coefficient $\zeta = f(x)$ which can vary for different segments.

Local parametric variables: another uncertainty considers a change with respect to a varying variable as well as its position coordinate x, such as $c = f(x, \varphi(t))$. The function $f(x, \varphi(t))\ \forall\ x = [0, L]$ is a priori known and defined with respect to the parameter x. However, the dependent variable $\varphi(t)$ is unknown. A switching parameter is considered when

introducing the Heaviside function $\sigma = f(x, \Delta p(t))$, which allows for controlling the fluid flow between specific homogeneous segments of a network with respect to the differential pressure $\Delta p(t)$ between segments, if needed.

Where (3.29a) describes the pressure dynamics of a homogeneous segment, (3.29b) defines the fluid flow between interconnected segments. Considering the parameter variations for the lumped parameter model (3.29a) - (3.29b) yields

$$\frac{d}{dt}p(t) \approx \frac{K(p)}{V(t)}\left(\Delta Q^{-}(t) + Q_{ext}(t)\right) \tag{3.35a}$$

$$Q(t) \approx \sigma(x, \Delta p)\; S(x)\; \sqrt{\frac{2}{\varrho(p)}}\; \zeta(x)\; \sqrt{|\Delta p^{+}(t)|}\; sign\left(\Delta p^{+}(t)\right)\;, \tag{3.35b}$$

where the exogenous excitation $Q_{ext}(t) = [0, Q_{max}]$ is introduced. This excitation is considered as a possible external input fluid flow at a network position, where a pumping unit is located. A fluid flow difference $\Delta Q^{-}(t)$ induces a change of pressure $dp(t)/dt$ with respect to the bulk modulus $K(p)$ and the segment volume $V(t)$. On the other hand, any pressure difference $\Delta p^{+}(t)$ causes a fluid flow $Q(t)$ with respect to the fluid density $\varrho(p)$, the cross section $S(x)$ along the fluid flow path and its discharge coefficient $\zeta(x)$. The cross section can vary between different interconnected segments. Thus, a change of cross section ΔS affects the discharge coefficient.

Fluid compressibility

The transient behaviour of pressure generation depends on the bulk modulus K, hence the Newton-Laplace formula [Streeter et al., 1998]

$$K = a^2 \varrho \tag{3.36}$$

assigns the fluid density ϱ to the bulk modulus K with respect to the speed of sound a. Since $\varrho(p)$ is expected to vary with respect to the pressure p, $K(p)$ will vary as well. Consequently, a linear parametric model of form

$$K(p) = \kappa_0 + \kappa_1\; p \tag{3.37}$$

is frequently proposed, see [Hountalas and Kouremenos, 1998] and [Lino et al., 2007], to describe a pressure-dependent bulk modulus. On the other hand, [Streeter et al., 1998], [Spurk, 2013] and others relates the bulk modulus directly to a change of fluid density with the formula

$$K = \frac{dp}{d\varrho/\varrho}\;, \tag{3.38}$$

dual to (3.27). Combining (3.37) with (3.38) while separating the variables and integrating yields

$$\int \frac{1}{\kappa_0 + \kappa_1\; p}\; dp = \int \frac{1}{\varrho}\; d\varrho\;. \tag{3.39}$$

Referring to [Susuzlu et al., 2004] and [Fabien et al., 2010], an explicit solution is derived and rearranged to represent a pressure-dependent fluid density

$$\varrho(p) = \varrho_0 \left(1 + \frac{\kappa_1\; p}{\kappa_0}\right)^{1/\kappa_1} \tag{3.40}$$

whereby ϱ_0 denotes the initial density. In this respect, the variable compressibility affects the transient behaviour of (3.35a) as well as the steady-state given by the discharge equation (3.35b). Its coefficients κ_0 and κ_1 will be experimentally identified for a pressure range up to 400 MPa.

Fluid volume

The transient behaviour of pressure generation also depends on the fluid volume

$$V(t) = S\ \Delta x(t)\ . \tag{3.41}$$

This volume can vary with respect to the length $\Delta x(t)$ of specific high-pressure components. For example, a piston displacement changes the volume of a pumping chamber. This variable fluid volume is then expressed as

$$V(t) = S\ l_0 - \int Q_{ext}(t)\ dt\ , \tag{3.42}$$

considering the initial length l_0 and the displacement fluid flow

$$Q_{ext}(t) = S_P\ v_P(t)\ , \tag{3.43}$$

when a piston of cross section S_P becomes displaced with the velocity $v_P(t)$. The volume variation (3.42) and the displacement fluid flow (3.43), respectively, are a priori known periodic functions and therefore considered as an external input fluid flow that excites the high-pressure network. However, most components feature a constant displacement fluid flow, such as $Q_{ext}(t) = 0\ \forall\ t > 0$.

Flow path

Eventually, a switching law determines the existence of a fluid flow along a flow path. It is associated to a dependent variable, which restricts the flow direction. Modelling a check-valve, it is proposed to introduce the Heaviside function

$$\sigma(x, \Delta p) := \begin{cases} 1, & \Delta p(t)\ >\ 0 \\ 0, & \Delta p(t)\ \leq\ 0 \end{cases}\ , \tag{3.44}$$

where the switching behaviour depends on the pressure difference $\Delta p(t)$. In addition, the cross section $S(x)$ can change along the fluid flow path. This causes a change of the discharge coefficient

$$\zeta(x) = \sqrt{\frac{1}{1 + \Delta x/D\ \lambda - (1 - \Delta S/S)^2}}\ , \tag{3.45}$$

where ΔS denotes to the change of cross section along the fluid flow path and $S = D^2\pi/4$.

The varying parameters (3.37) and (3.42) are introduced to the differential equation (3.35a), where the varying parameter (3.40) and the discharge coefficient (3.45) are considered for the algebraic equation (3.35b). This results in the **generalized description**

$$\frac{d}{dt}p(t) \approx \frac{\kappa_0 + \kappa_1\ p(t)}{S\ l_0 - \int Q_{ext}(t)\ dt} \left(\Delta Q^-(t) + Q_{ext}(t)\right) \tag{3.46a}$$

$$Q(t) \approx \sigma(t)\ S \sqrt{\frac{2}{\varrho_0} \left(1 + \frac{\kappa_1\ p(t)}{\kappa_0}\right)^{-1/\kappa_1}}\ \zeta\ \sqrt{|\Delta p^+(t)|}\ sign\left(\Delta p^+(t)\right) \tag{3.46b}$$

for homogeneous segments. Whereby each segment represents a local pressure state $p(t)$, the dependent variable x is not noted for simplicity. A pressure-dependent fluid density $\varrho(p)$ as well as a pressure-dependent bulk modulus $K(p)$ enable a wide pressure range. This is subject to improve the simulation precision, as a subsequent model validation will reveal.

3.3.2 Graph-based modelling

The modelling of different waterjet facilities requires a flexible approach that interconnects homogeneous segments to reproduce arbitrary network topologies. Using graphs, as described in [Ford and Fulkerson, 2016], seems prevalent to map homogeneous segments and recovering the fluid flow path for various high-pressure networks. A graph $\mathcal{G} = (\mathcal{V}, \mathcal{E})$ consists of branches or edges $\mathcal{E}$ that interconnects nodes or vertices $\mathcal{V}$. The pressure state

$$p(t) \rightarrow p_k(t) \tag{3.47}$$

of a segment k is assigned to a network node and the fluid flow rate

$$Q(t) \rightarrow Q_{kj}(t) \tag{3.48}$$

between segments k and j is assigned to a network branch. The differential scheme (3.24) becomes

$$\Delta p^{+}(t) \rightarrow \Delta p_{kj}(t) := p_k(t) - p_j(t) \tag{3.49}$$

that couples interconnected nodes and (3.23) becomes

$$\Delta Q^{-}(t) \rightarrow \Delta Q_{kj}(t) := \sum_{j=1}^{N} Q_{kj}(t) \ , \tag{3.50}$$

with respect to the fluid flow continuity (3.5), determining N simultaneous interconnections of a node k to any other node $j = \{1, \ldots, N\}$. A possible displacement fluid flow is assigned to each node $Q_{ext}(t) \rightarrow Q_k(t)$, while the sum in (3.50) conserves the fluid flow at every node

$$Q_{jk}(t) = -Q_{kj}(t) \ , \tag{3.51}$$

with respect to the fluid flow direction. Therefore, the output flow rate $Q_{kj}(t)$ from a previous segment yields an input flow rate $Q_{jk}(t)$ to a subsequent segment.

This results in a network description $\mathcal{N} = (\mathcal{G}, dp/dt, Q)$ of homogeneous segments to represent specific high-pressure networks using lumped parameters. Different network sections will be consequently assigned to $J \rightarrow \mathbb{N}$ homogeneous segments. The illustration in Figure 3.22 maps each segment, depicted in (a), to a node$k \in J$, as shown in (b). Every node k can be interconnected to other nodes $j \in J \setminus k$.

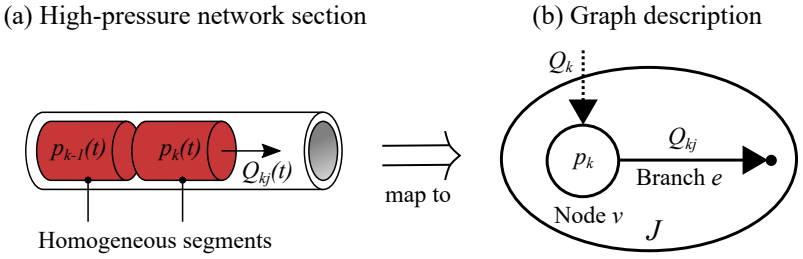

Figure 3.22 – Modelling framework for high-pressure networks: assigning a network section to $k \in J$ segments (a) and representing the segments by means of graph (b).

Consequently, a node $v \in \mathcal{V}$ represents a pressure state $p_k(t)$, such as

$$\frac{d}{dt} p_k(t) : \mathcal{V} \rightarrow \mathbb{R} \ , \tag{3.52}$$

whereas a branch $e \in \mathcal{E}$ establishes a fluid flow $Q_{kj}(t)$, such as

$$Q_{kj}(t) : \mathcal{E} \to \mathbb{R} \ , \tag{3.53}$$

with positive flow direction from segment k to j. With the above introduced assignments (3.47 - 3.50), the **network description**

$$\mathcal{N}_{kj} : \begin{cases} \dfrac{d}{dt} p_k(t) & = \dfrac{K_k(p)}{V_k(t)} \left(\Delta Q_{kj}(t) + Q_k(t) \right) \\ \\ Q_{kj}(t) & = \vartheta_{kj}(t) \sqrt{\dfrac{2}{\varrho_k(p)} \ |\Delta p_{kj}(t)|} \ sign\left(\Delta p_{kj}(t) \right) \end{cases} \tag{3.54}$$

is obtained, which represents a high-pressure network using lumped parameters. It yields a system of algebraic differential equations. These equations approximate the local pressure states of homogeneous segments, including non-linearities due to interconnections to neighbouring segments.

Each node k holds a fluid volume $V_k(t)$. The fluid volume and the bulk modulus $K_k(p)$ determine the transient behaviour of a node k, whereas the parameter $\vartheta_{kj}(t) = \sigma_{kj}(t) \ S_{kj} \ \zeta_{kj}$ and the fluid density $\varrho_k(p)$ determine the fluid flow along a branch kj. The fluid characteristic parameters $K_k(p)$ and $\varrho_k(p)$ are expected to vary according to the corresponding pressure states $p_k(t)$. Consequently, the variable fluid volume (3.42) becomes

$$V_k(t) = S_k \ \Delta x_k - \int Q_k(t) \ dt \tag{3.55}$$

and the linear parametric model (3.37) yields

$$K_k(p) = \kappa_0 + \kappa_1 \ p_k(t) \tag{3.56}$$

and its explicit solution (3.40) becomes

$$\varrho_k(p) = \varrho_0 \left(1 + \frac{\kappa_1 \ p_k(t)}{\kappa_0} \right)^{1/\kappa_1} \ , \tag{3.57}$$

whereby ϱ_0 denotes the initial fluid density. The parameter $\vartheta_{kj}(t)$ holds the interconnection cross section S_{kj}, its discharge coefficient ζ_{kj} and the Heaviside function σ_{kj}. The discharge coefficient represents the flow resistance along the fluid flow path, while the Heaviside function indicates the existence of a fluid flow path between node k and j. If the cross section changes along the fluid flow path, its discharge coefficient ζ_{kj} needs to be adjusted and (3.45) becomes

$$\zeta_{kj} = \sqrt{\frac{1}{1 + \Delta x_k / D_k \ \lambda_{kj} - (1 - \Delta S_{kj} / S_{kj})^2}} \ , \tag{3.58}$$

where $\Delta S_{kj} = S_k - S_{kj}$ denotes the cross section difference.

Describing network topologies

The symbols of Figure 3.23 are employed to derive a graph-based network description that recovers a desired network topology when interconnecting nodes by means of branches. An exogenous fluid flow Q_k can be applied on every node, where a node represents a pressure state p_k that simulates the network pressure $\hat{p}_x$ at position x, see (b) and (c). The fluid flow Q_{kj} along a branch can be restricted, see (f) and (g).

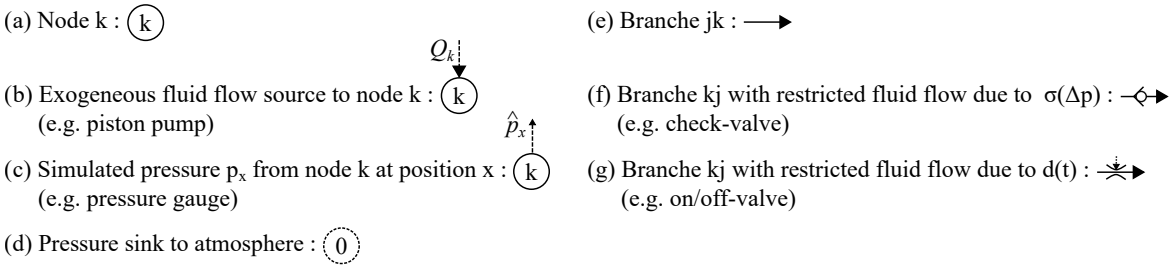

Figure 3.23 – Principal symbols to illustrate waterjet facilities by means of graphs: branches interconnect nodes to recover the fluid flow path of a high-pressure network.

These symbols allow for representing different high-pressure components by means of graphs as illustrated in Figure 3.24. The high-pressure pump, as shown in (a), consist of two pumping chambers (piston pumps). Each chamber is represented by a node, which includes an exogenous input fluid flow. Both chambers are interconnected by means of branches. These branches restrict the fluid flow to positive direction with respect to the pressure differences. Modelling a high-pressure piping, see (b), an initial piping section can be subdivided, if needed, to represent the pressure propagation with desired accuracy. On the other hand, a connector is a single node that couples any amount of input and output branches, as shown in (c), and a cutting head couples a node that discharges a waterjet to atmosphere, see (d).

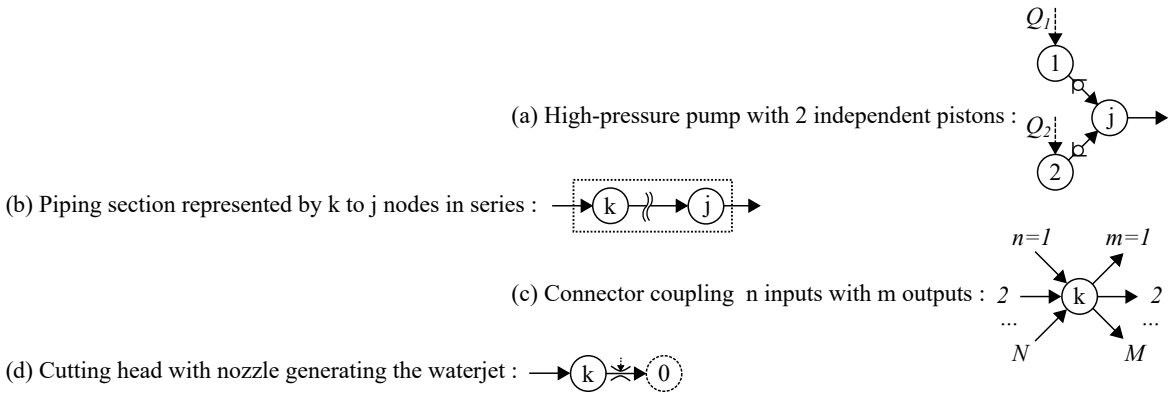

Figure 3.24 – Combination of symbols to illustrate typical high-pressure components by means of graphs: branches provide various functionalities to determine and to manipulate the fluid flow.

The proposed graph-based modelling methodology is expected to model various network topologies with reduced complexity, when considering typical high-pressure components. It recovers the fluid flow path of a waterjet facility, with respect to the principle of continuity and momentum conservation. A high-pressure network couples any number of high-pressure pumps and cutting heads, where the fluid flow from a pumping chamber to a cutting head is usually denoted to a positive fluid flow direction.

3.4 Parameter identification for waterjet machining

This chapter is dedicated to identify the parameters required by the above introduced graph-based modelling methodology. It aims at a parametrization of specific high-pressure components, independent of any network topology. This results in a parametrized simulation toolbox, capable to model different high-pressure networks without revising parameter identification.

The two model coefficients κ_0 and κ_1 of the parametric model (3.37) are first identified, which also define the pressure-dependent fluid density of equation (3.38). For this, the pressure generation within a high-pressure pump has been investigated. Different measurements have been obtained, while pressurizing water in a pumping chamber by means of piston displacement. This experiment has been derived independent of the test bench configuration. The parametric model of Section 3.3 describes a pressure-dependent bulk modulus. This is a fluid characteristic parameter, that is unaffected by any high-pressure component or network topology.

On the other hand, cutting head discharge coefficient and piping friction loss coefficient have been derived from different experiments at the test bench, while taking the use cases of Table 3.4 into account. The 2 basic measurements (**B-3,6**) have been selected for parameter identification. The other measurements from use case 1 have been used to verify the modelling methodology and control design. The 6 extended measurements (**E-1,3,5,8,10,12**) have been selected for parameter identification. The other measurements from use case 2 have been used for the model and controller validation. The setups for use case 1 include a single high-pressure pump interconnected to a single cutting head, where the setups for use case 2 include a high-pressure pump that supplies 2 cutting heads. Using 2 cutting heads results in 4 possible switching states when applying the switching pattern for contour cutting. E.g. installing 6 different nozzles would allow for investigating 12 switching states.

Table 3.4: Excerpt of experiments for use case 1 and 2: measurements derived on different test bench setups to identify different network parameters.

Meas.	Topology	Pressure (MPa)	Nozzle 1 ⌀(mm)	Nozzle 2 ⌀(mm)	Switching pattern
B-3	(b) Long	200	0.35	-	Contour
B-6		350	0.25	-	
E-1	(c) Sym. net.	200	0.25	0.25	Contour
E-2		350	0.15	0.15	
E-3		200	0.3	0.2	
E-6		350	0.2	0.1	
E-8	(d) Asym. net.	200	0.25	0.25	Contour
E-10		350	0.15	0.15	

In combination with the use cases, 4 different topologies have been assumed and 2 different operating pressures have been applied. Pressure gauges have been installed after the pump, before both cutting heads and in the centre connector that couples the cutting heads to the pump. This allows for identifying 10 piping sections of different lengths. Consequently, 24 different parametrizations for waterjet machining have been taken into account, when identifying the cutting head discharge coefficient ζ for nozzles of various inner diameter and to identify the piping friction loss coefficient λ for piping sections of various lengths. These identified parameters are needed to fully define and parametrize the above derived high-pressure network models. The induced overall fluid flow will be estimated by evaluating the piston displacements. The pressure will be measured on different network locations x using pressure gauges. Hence, the fluid flow estimation $\hat{Q}(t)$ and the different pressure measurements $p_x(t)$, depicted in diagram of Figure 3.25, have been taken into account to identify the required model parameters.

It has to be mentioned, that the pump requires closed-loop control to obtain the desired operating pressure. It is desired to track the operating pressure, while attenuating switching

disturbances. Otherwise, the pressure will exceed given bounds of the test bench, when switching a cutting head. For this reason, the high-pressure pump holds by default a PI controller (6.46), as provided in Section 6.4.

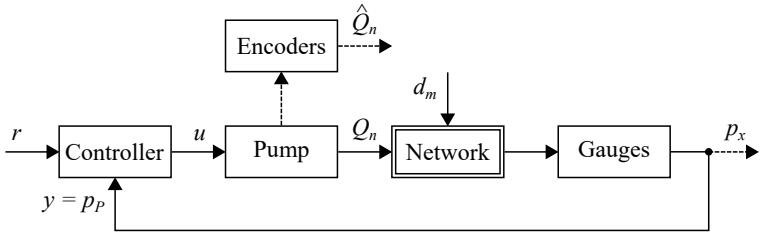

Figure 3.25 – Experimental setup for parameter identification: pressure gauges measure the pressure $p_x(t)$ at different positions when applying an input fluid flows $Q_n(t)$ and switching the cutting heads $d_m(t)$.

3.4.1 Identification of bulk modulus and fluid density

The bulk modulus of water is often regarded as a constant $K_0 = 2.08$ GPa. This is true for a relatively small changes of pressure $< \pm 10$ MPa. The bulk modulus increases to 2.68 GPa for water pressurized to 100 MPa. Detailed studies have analysed fluid density as well as bulk modulus [Chen and Millero, 1986] and tabular data have been collected for a pressure range of 0.1 to 100 MPa [Schmidt and Grigull, 1981]. This tabular data contain information to estimate a pressure-dependent bulk modulus, but further experimental data are necessary to validate the parametric model (3.37), introduced in Chapter 3, for a pressure range up to 400 MPa. This is realized with respect to the method proposed in [B.Titurus et al., 2010], for the identification of hydraulic characteristics from steady piston displacement.

Design of experiment

As discussed in Section 3.3, the bulk modulus

$$K = -\frac{dp}{dV/V} \tag{3.59}$$

defines, that any variation in fluid volume $V(t)$ induces a change in pressure $p(t)$. This relationship will be applied to experimentally determine the bulk modulus $K(p)$ of water at high-pressure. If a pumping chamber is entirely shot, the measured piston position $s_P(t)$ defines the volume variation

$$V(t) = V_0 - S_P \; s_P(t) \; , \tag{3.60}$$

where V_0 corresponds to the initial chamber volume and S_P is the piston cross section. As a consequence, any positive piston displacement pressurizes the water within a pumping chamber.

The pressure increase is captured by a high-pressure gauge at the pumping chamber outtake. An external check-valve replaces the outtake check-valve, that is positioned right after the pressure gauge. One pumping unit is pressurizing the high-pressure piping to the maximal pressure allowed (400 MPa). That causes the external check-valve at the other pumping unit to be closed. This allows for pressurizing the pumping chamber without any interaction with the piping, as long as its pressure remains below maximal pressure.

Data acquisition is performed at a sampling rate of 10 Hz. This is sufficient, since the piston will move with a slow velocity to avoid any dynamic effects to the pressure generation. The measured pressure $\tilde{p}(t)$ requires adjustments, such as to retrieve the absolute pressure

$$p(t) = \tilde{p}(t) - p_g - p_s \ , \tag{3.61}$$

where $p_g = \varrho \ g \ h$ is the pressure head given by the height h between piping and pressure gauge and p_s is the pressure given by the water supply.

Table 3.5 discusses the design of experiment. The initial pumping chamber volume has been varied for each run by choosing a different initial piston position, which affects the sensitivity of pressure generation. When performing these experiments, the piston has been slowly displaced so that a nearly isothermal process of pressure generation is expected, while the fluid temperature remains constant. The various runs have been assigned to two different pumping chambers, to evaluate volume uncertainties. In addition, all runs have been repeated for two different velocities, evaluating adiabatic effects.

Table 3.5: Design of experiment for parameter identification to determine the pressure-dependant bulk modulus.

Experiments	Pumping chamber	Initial position (###)	Piston velocity (mm/s)
1...8	1	$\{0, 40, 80, 120\}$	$\{1, 2\}$
9...16	2	$\{20, 60, 100, 140\}$	$\{1, 2\}$

The plots in Figure 3.26 and 3.27 present the measured and adjusted pressures (3.61) in (a) as well as the derived pumping chamber volume (3.60) in (b) for a piston velocity of $v_P = 1$ mm/s and $v_P = 2$ mm/s, respectively. While some initial piston positions have been dedicated to the pumping chamber 1, others correspond to the chamber 2.

The experimental data shown below is processed to evaluate the bulk modulus for each data sample i. For that, a numerical approximation of (3.59) using central differences yields

$$K(p_i) = -\frac{p_{i+1} - p_{i-1}}{V_{i+1} - V_{i-1}} \ V_i \ . \tag{3.62}$$

Equations (3.59) and (3.61) are then used to derive the parameters κ_0 and κ_1. For this, the parametric model

$$K(p) = \kappa_0 + \kappa_1 \ p \tag{3.63}$$

is evaluated by means of linear regression and further applied to estimate the fluid density

$$\varrho(p) = \varrho_0 \left(1 + \frac{\kappa_1 \ p}{\kappa_0}\right)^{1/\kappa_1} \tag{3.64}$$

for different operating pressures.

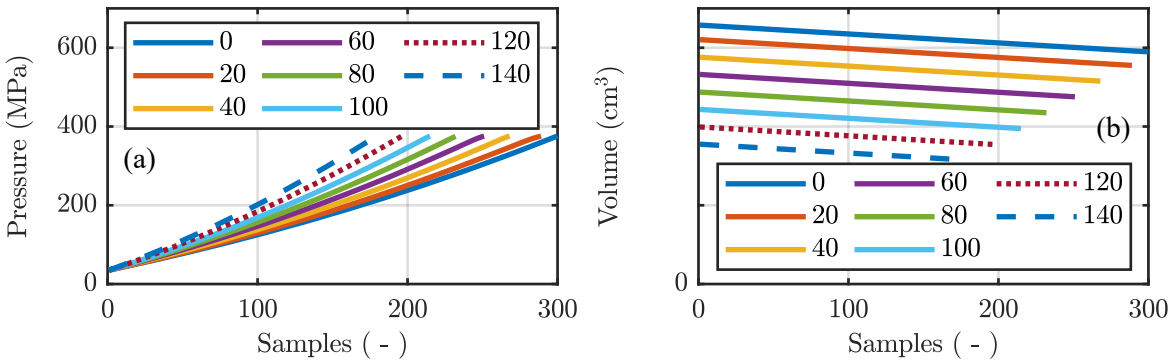

Figure 3.26 – Experiments with $v_P = 1$ mm/s: measured pressure trends and pumping chamber volumes, while displacing the pistons from different initial positions s_0.

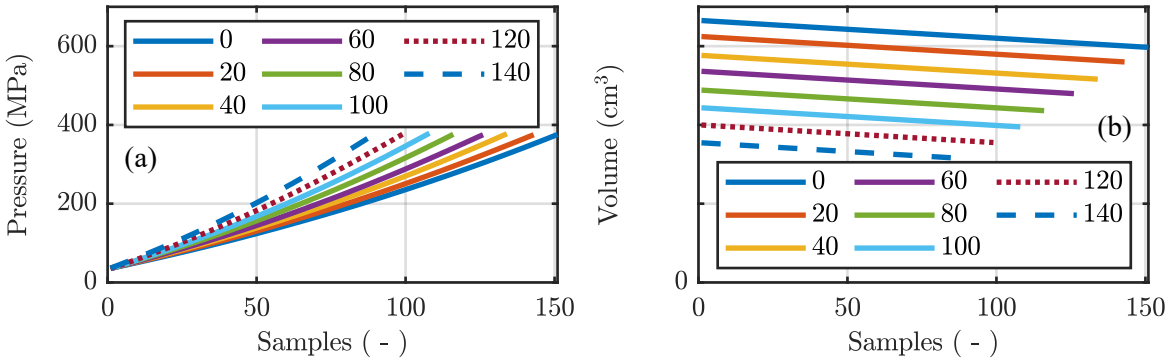

Figure 3.27 – Experiments with $v_P = 2$ mm/s: measured pressure trends and pumping chamber volumes, while displacing the pistons from different initial positions s_0.

Results

A robust least-square method is applied to fit the parametric model (3.63). Therefore, the least absolute residual method of [Thanoon, 2015] has been examined to generate a linear regression model with tight confidence intervals. Table 3.6 presents the identified model coefficients. The resulting fit achieves a determination coefficient of $r^2 = 0.9959$. The prediction errors are reasonable with a sum of square error of $sse = 4.0759$ and a root mean square error of $rmse = 0.0382$.

Table 3.6: Identified coefficients of the parametric model and its confidence intervals describing the pressure-dependent bulk modulus.

Coefficient	Fitted value	95% confidence bounds	Unit
κ_0	###	[###, ###]	(GPa)
κ_1	###	[###, ###]	(-)

The regression analysis of Figure 3.28 shows the estimated bulk modulus with respect to its pressure state (a), the residuals of the measurement data (b), its probability (c) and density distribution (d). The experimental data are compared to tabular data [Schmidt and Grigull, 1981], which estimate the bulk modulus for pressures below 100 MPa. An increased scattering

is observed for higher pressures, indicating an enlarged sensitivity and a drift is found in the measured data of higher and lower pressures, due to acceleration and deceleration of the piston.

Considering relation (3.64) yields the variation of fluid density with respect to the operating pressure, as shown in Figure 3.29. It follows almost a linear relationship, with an average slope of about 0.5 kg/m^3/MPa. Thus, the proposed modelling methodology could be further simplified. Increasing the pressure from 0.1 to 400 MPa causes to increase the bulk modulus by 86.8% and the fluid density by 20.2%. While a variable bulk modulus will affect the transient behaviour of pressure generation, the variable fluid density cause a shift of the resulting steady-state, see also the experimental studies of Section 4.3 for more details.

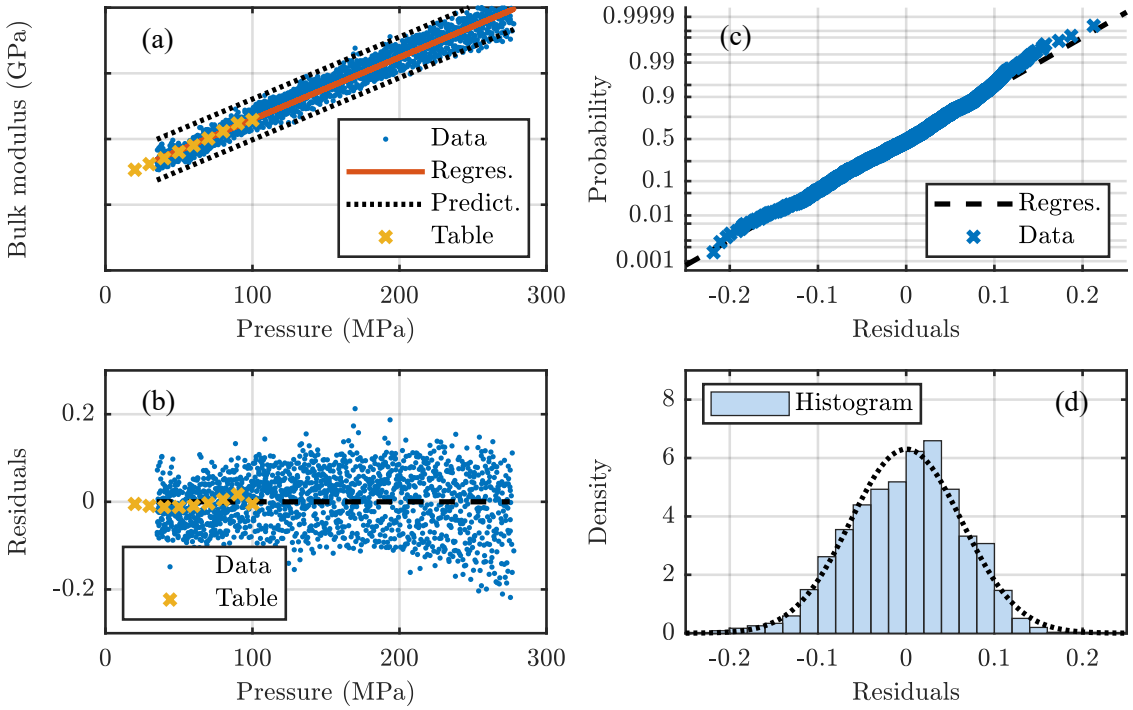

Figure 3.28 – Measurement data derived by experiment to identify bulk modulus and fluid density: data samples with fitted model and prediction interval (a), resulting residuals (b), corresponding regression analysis (c) and distribution of data samples (d).

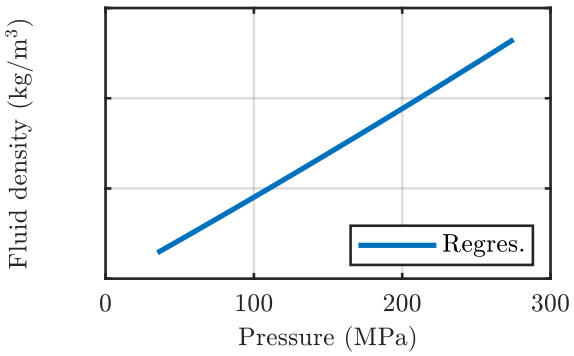

Figure 3.29 – Relation between chamber pressure and fluid density: expected fluid density, when pressurizing a pumping chamber.

3.4.2 Identification of cutting head discharge coefficient

Measurements derived from the test bench considering topology **(c) Symmetric network** and **(d) Asymmetric network** have been used, to identify the discharge coefficient ζ for nozzles of various cross sections, while taking cutting head configurations for nozzles of $D = \{0.1, 0.15, 0.2, 0.25, 0.3\}$ mm inner diameter into account. These measurements are advantageous, as they provide a wide variation of fluid flow velocities and operating pressures. Parameter identification has been performed, again considering the method in [B.Titurus et al., 2010].

Design of experiment

The discharge equation

$$Q(t) = \zeta \underbrace{S \sqrt{\frac{2}{\varrho(p)} p(t)}}_{x_{Subs.}} \tag{3.65}$$

obtained from Section 3.2, allows for defining a model for identifying the discharge coefficient ζ. The fluid density $\varrho(p)$ has been adjusted according to (3.64), taking the above identified pressure-dependent bulk modulus into account. Introducing the substitution variable $x_{Subs.}$ allows for fitting a linear regression

$$Q_i = \zeta \, x_i \tag{3.66}$$

that describes the relationship between fluid flow and the substitution variable, with respect to the discharge coefficient. The substitution variable combines the measured pressure $p(t)$ from the pressure gauge, located right before a cutting head, with the nozzle cross section S, given by the cutting head configuration. The plots in Figure 3.30 show the experimental data used to identify the discharge coefficient. Each data point corresponds to a steady-state operating point, derived from the experiments. For that, measurement data at steady-state pressure $p(t)$ have been evaluated with respect to each cutting head switching state, when a steady input fluid flow $Q(t)$ has been obtained. The fluid flow and nozzle cross section reveal a prevalent correlation, where fluid flow and cross section seems unaffected by the operating pressure.

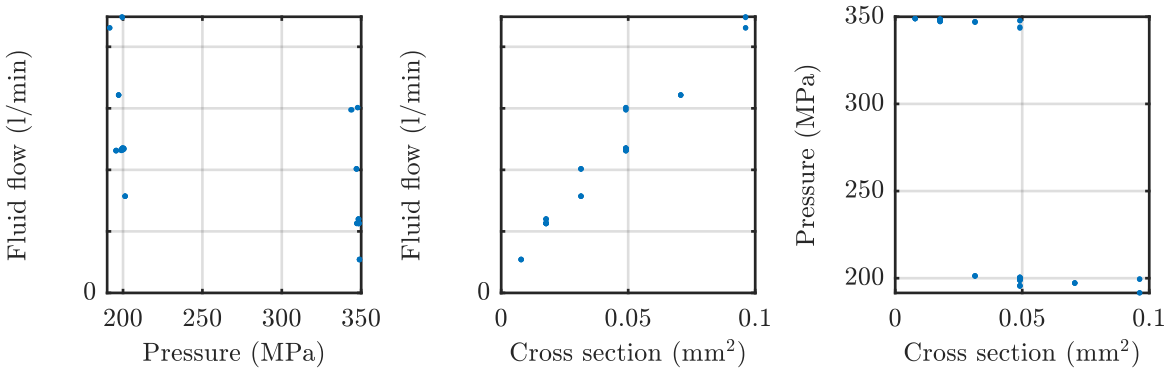

Figure 3.30 – Comparison of experimental data used to identify the friction loss coefficient: considering the estimated fluid flows, the absolute pressures from measurements and the nozzle cross sections, given from the test bench setup.

Results

Again, the robust least-square method (see [Thanoon, 2015]) is applied to fit (3.66). Table 3.7 presents the identified discharge coefficient. The resulting fit achieves a determination coefficient of $r^2 = 0.9986$. The prediction errors are reasonable with a sum of square error of $sse = 0.0193$ and a root mean square error of $rmse = 0.0182$.

Table 3.7: Identified discharge coefficient with linear regression and its confidence interval.

Coefficient	Fitted value	95% confidence bounds	Unit
ζ	###	[###,###]	(-)

The regression analysis of Figure 3.31 shows the estimated discharge coefficient with respect to the substitution variable $x_{Subs.}$ (a), the residuals of the measurement data (b), its probability (c) and density distribution (d). The resulting probability is light-tailed for the negative part of the residuals, hence a small variance is expected. Its density becomes asymmetric in contrast to the theoretical distribution. Thus, more measurement data with enhanced variance would improve the linear regression. Nevertheless, a sufficient significance is derived regarding the different operating points. However, an exact model for the nozzle friction loss coefficient and a reliable prediction of its parameter remains difficult. A disturbing factor is any nozzle wear, which influences the inner cross section S that is assumed as constant.

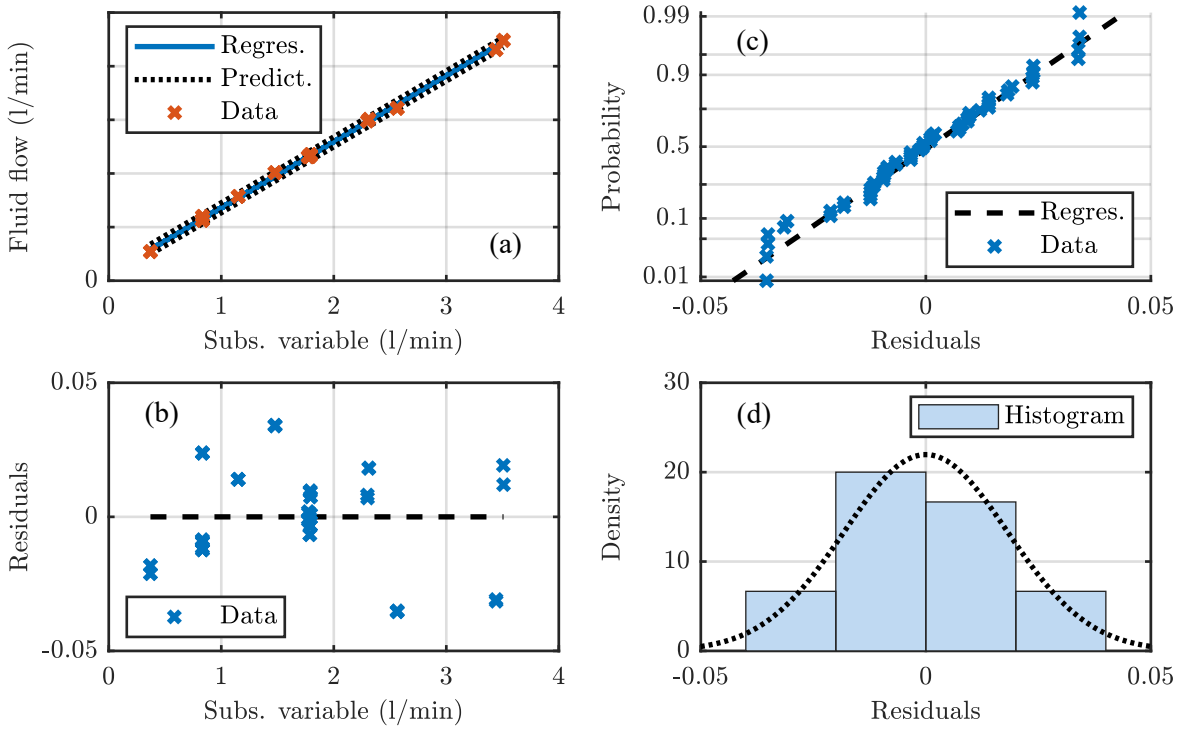

Figure 3.31 – Measurement data derived by experiment to identify the cutting head discharge coefficient: data samples wit fitted model and prediction interval (a), resulting residuals (b), corresponding regression analysis (c) and distribution of data samples (d).

3.4.3 Identification of piping friction loss coefficient

Measurements derived from the test bench considering topology **(c) Symmetric distributed** and **(d) Asymmetric distributed** are also subject to identify the friction loss coefficient λ for piping sections of various lengths $L = \{0.91, 3.80, 5.94,\ 6.31, 7.17, 8.08, 11.34, 11.90, 13.06, 13.11, 18.09, 18.17\}$ m. The friction loss coefficient λ has been identified for a high-pressure piping of $D = 2.4$ mm inner diameter, considering the method in [B.Titurus et al., 2010].

Design of experiment

Substituting the definition

$$\zeta = \sqrt{\frac{D}{\Delta x\ \lambda}} \tag{3.67}$$

also introduced in Section 3.2, into the discharge equation (3.65) yields

$$\Delta p(t) = \lambda\ \underbrace{\frac{\varrho(p)\ L}{2\ D\ S^2}\ Q^2(t)}_{x_{Subs.}}\ . \tag{3.68}$$

This allows for defining a model to identify the friction loss coefficient λ. The fluid density $\varrho(p)$ has been adjusted according to (3.64), taking the above identified pressure-dependent bulk modulus into account. Introducing the substitution variable $x_{Subs.}$ allows for fitting a linear regression

$$Q_i = \lambda\ x_i \tag{3.69}$$

that describes the relationship between fluid flow and the substitution variable, with respect to the friction loss coefficient. The substitution variable combines the estimated fluid flow from a high-pressure pump with a piping section of length L, given by the distances between different pressure gauges. These define the pressure differences $\Delta p(t) = p_x(t) - p_{x-1}(t)$ with fluid flow path of positive direction from a preceding position at $x - 1$ to position x. The plots in Figure 3.32 show the experimental data used to identify the discharge coefficient. Each data point corresponds to a steady-state operating point derived from the experiments. For that, steady-state pressure $p(t)$ has been evaluated from measurement data, when obtaining steady input fluid flow $Q(t)$ with respect to each cutting head switching state. The parameters of the experiment reveal a significant variation within the desired pressure range. A correlation between fluid flow and pressure difference can be expected.

Results

The robust least-square method (see [Thanoon, 2015]) is applied to fit (3.69). Table 3.8 presents the identified discharge coefficient. The resulting fit achieves a determination coefficient of $r^2 = 0.967$. The prediction errors are reasonable with a sum of square error of $sse = 8.326$ and a root mean square error of $rmse = 0.303$.

Table 3.8: Identified friction loss coefficient with linear regression and its confidence intervals.

Coefficient	Fitted value	95% confidence bounds	Unit
λ	###	[###, ###]	(m)

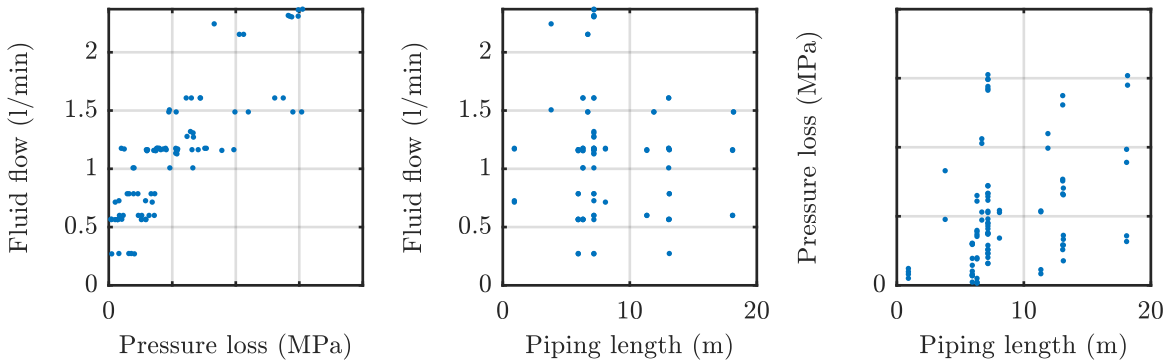

Figure 3.32 – Comparison of experimental data used to identify the friction loss coefficient: considering the estimated fluid flows, the calculated pressure differences from measurements and the piping lengths, given from the test bench setup.

The regression analysis of Figure 3.33 shows the estimated coefficient λ with respect to the substitution variable $x_{Subs.}$ (a), the residuals of the measurement data (b), its probability (c) and density distribution (d). The resulting probability is acceptable, hence measurement data with sufficient variance has been available for linear regression. It has to be mentioned that straight pipings have been considered only. The effect of curved pipings, junctions and connectors are subject for further investigations, which aim at improving the simulation toolbox and providing additional validated high-pressure components. For this work, any change of friction loss due to curves and diameter variations remain subject of estimation.

3.5 Conclusion

In this chapter, the fluid dynamic to represent the pressure propagation along a piping section has been discussed. The main contribution has been given, when introducing a graph-based modelling methodology to describe high-pressure networks. It assigns piping sections to homogeneous segments. These segments are then interconnected by means of graphs to recover the initial network topology. Each segment is represented as a local pressure state and its interconnections are characterized, considering a stationary fluid flow. This methodology has been derived from the fundamentals of fluid dynamics, by approximating a distributed parameter model using finite differences. This results in algebraic differential equations, which represent a high-pressure network as a lumped parameter model. The error due to approximation has been investigated by means of simulations, while considering a defined piping section. At least a discretization of 1 m is required to achieve the desired simulation accuracy.

Further, a framework to describe generalized high-pressure networks has been described. It takes into account a variable fluid compressibility, that relates to a variable fluid volume and a pressure-dependent bulk modulus. Any displacement fluid flow has been considered as an external excitation, where a piston displacement has been modelled as a change in the fluid volume. The bulk modulus, however, has been represented by a parametric model, which has been further used to derive a pressure-dependent fluid density. Its coefficients have been experimentally identified.

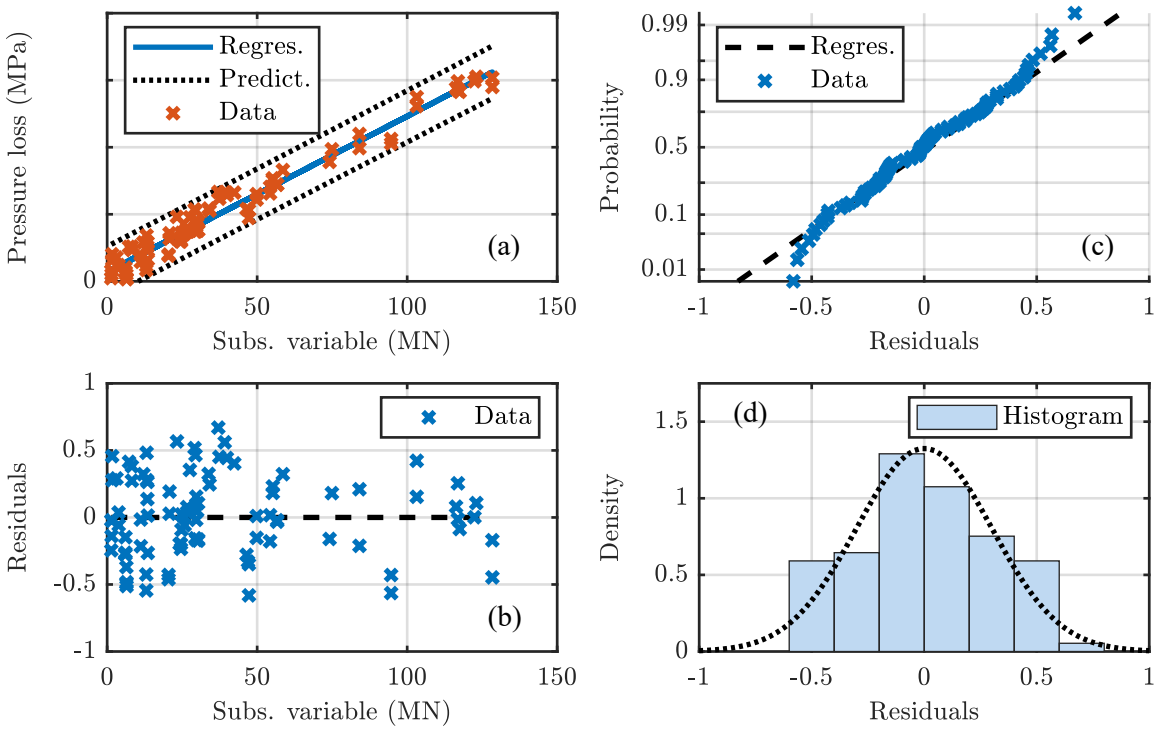

Figure 3.33 – Measurement data derived by experiment to identify piping friction loss coefficient: data samples with fitted model and prediction interval (a), resulting residuals (b), corresponding regression analysis (c) and distribution of data samples (d).

Model parameters have been identified by means of measurements. In particular, a pressure dependent bulk modulus has been investigated for a wide pressure range from 0 to 400 MPa. This extends the known tabular data from literature, which have been limited to 100 MPa. The parametrized simulation toolbox enables a flexible modelling of various waterjet facilities with network topologies of increased complexity, but without necessarily validating each high-pressure network model with work intensive measurements. Nevertheless, validated network models will be used in Chapter 6 to verify the low-level control design. Further work should continue to identify the model parameters for other high-pressure components. On the other hand, as the segmentation of network sections constitutes a trade-off between simulation accuracy and model complexity, it would be valuable to evaluate an optimal segmentation procedure.

4

Application and model validation

Contents

4.1 Introduction

Objectives

The development of future waterjet facilities requires the application of the graph-based modelling methodology, which provides high-pressure network models. These models represent the coupling of decentralized pumps, needed for evaluating the low-level control design and for investigating the distributed high-level managing by means of simulations. On the other hand, the subsequent low-level control design requires a simplified model and a suitable description of the uncertainties, as taken into account for controller synthesis.

The derived high-pressure network models have to be validated by means of measurements, considering different network topologies and taking the previously defined use cases into account (see Section 2.2). These models should remain accurate for a wide pressure range and scalable to various network topologies, without having to revise parameter identification and model validation. This should reduce the time expanses for modelling of future waterjet facilities.

Contribution

The application of the graph-based modelling methodology is exemplary presented for a test bench setup, considering an electrically driven high-pressure pump with independent pistons interconnected to a single cutting head. This modelling procedure is then extended for the introduced network topologies of Chapter 2 to obtain high-pressure network models, which represent future waterjet facilities. On the other hand, a lumped parameter model is discussed, which takes parameter uncertainties into account. This first-order model of a high-pressure pump seems suitable for further investigations related to robust control.

Extensive experimental studies constitute a main contribution to this chapter. The obtained high-pressure network models have been validated by measurements, derived from the test bench. It considers setups with two coupled high-pressure pumps supplying two independent cutting heads, while applying defined use cases, which correspond to typical waterjet applications. First results compare the resulting simulation accuracy to existing modelling approaches. It is shown that a variable fluid compressibility improves simulation accuracy and modelling errors can be reduced. Detailed results investigate the simulation accuracy of the graph-based modelling methodology for measurements at different network position, while applying various switching disturbances.

This chapter is structured as follows: Section 4.2 applies the graph-based modelling methodology first to describe common high-pressure components and second to model the introduced high-pressure networks. The derived network models will be validated in Section 4.3 by means of measurements.

4.2 Applying the modelling methodology

In this section, the topology **(a) Short piping** is exemplarily modelled to provide a lumped parameter model and second, to derive a graph-based modelling. The illustration of Figure 4.1 shows the analysed high-pressure network and its configuration in detail. It includes an electrically driven high-pressure pump and a cutting head. The high-pressure pump has two pistons, each represents a fluid flow source. The pistons are displaced with velocities v_1 and v_2 to generate the displacement fluid flow Q_1 and Q_2. The displacement fluid flow of each piston is proportional to its velocity. These induce the pumping chamber pressures p_1 and p_2. The outtake ducts of each

pumping chamber contains internal check-valves, which ensure the unidirectional output fluid flow $Q_{13} \geq 0$ and $Q_{23} \geq 0$ from the pumping chambers to the connector. These outtake ducts reduce the fluid flow cross sections for a first time, before it passes the check-valves. A coupling connects the pumping chambers to the high-pressure piping, where the cross section is further reduced, while the output flows of both cylinders are merged to the overall fluid flow Q_{34}. At this position, a pressure gauge has been installed to measure the pump pressure p_3. High-pressure piping sections directly interconnect the high-pressure pump with a cutting head, where a second pressure gauge measures the cutting head pressure p_8. The cutting head includes an on/off-valve and a nozzle. It is independently controlled by a work station. An electromagnetic actuator switches the on/off-valve. If the on/off-valve is open, the nozzle will generate a waterjet. This results in the discharge fluid flow Q_{80}, which represents a pressure sink to the atmosphere. This nozzle reduces the fluid flow cross section one last time. Such a cutting head can be equipped with nozzles of different inner diameter, to reproduce the discharge flow of various work stations. The fluid flow from a piston pump to a cutting head is dedicated to a positive flow direction.

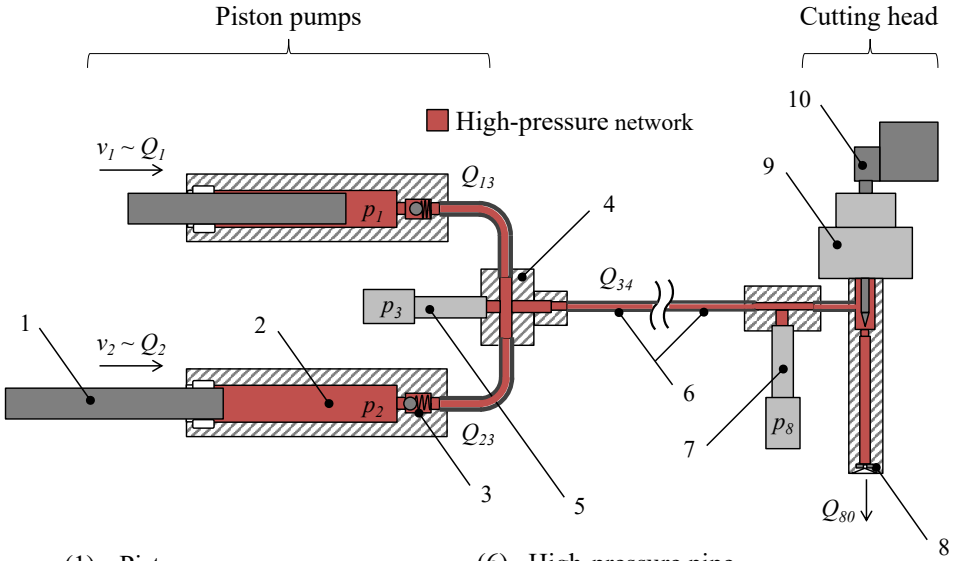

Figure 4.1 – Illustration of the investigated high-pressure network: two pistons of a high-pressure pump induce its displacement fluid flows to supply a cutting head, that generates a discharge fluid flow.

Applying the lumped parameter modelling as well as applying the graph-based modelling is restricted to different constraints and assumptions. The following requirements must be met for implementation:

1. A high-pressure network is divided into segments $k \in J$ of constant cross section S_k.
2. The use cases are restricted to high-pressure pumps with parallel pistons. Therefore, each pumping chamber is filled from the same water supply and each high-pressure pump is considered as an independent continuous system, which generates a steady output fluid flow.

3. All high-pressure components are considered to be ideal, e.g. the pressure stress will not cause any recognizable expansion and leakage is negligible.
4. Degradation of components, such as nozzle wear, is not modelled.
5. The water supply is not part of the high-pressure network. Instead, the supply pressure p_S defines the lower bounds for all pressure states $p_k(t)$, such as $p_k(t) \geq p_S \ \forall t$.
6. Water supply and environment are assumed to represent an infinitely large pressure potential, such as p_S and p_0 are invariant and $\nabla p(x,t) = 0$. This is fulfilled by high-pressure applications, when a steady water supply is guaranteed and since the cutting head discharges the water against the atmosphere.
7. The initial condition $p_k(t=0) = p_S$ requires the entire high-pressure network to be filled with water.
8. Any piston displacement influences the chamber volume $V_k(t)$ and, thereby, the dynamics of pressure generation. The piston position is determined by a trajectory, hence the volume variation is a priori known.
9. As the pressure difference between each segment $\Delta p_{kj}(t)$ almost disappears for a steady-state, the modelling error from discharge coefficient estimation becomes small.
10. The use cases are restricted to switching non-linearities. These allow only discrete states such as closed or open, which can be well defined with a Heaviside function. The available steady-states of a specific high-pressure network can therefore be characterized by combining all possible switching states.
11. When introducing the Heaviside function $\sigma_{kj}(t)$, no switching dynamics are modelled.

4.2.1 Lumped parameter model

Applying the results from the previous section allows for describing different high-pressure components by means of lumped parameters. The above example distinguish between, pumping chambers, check-valves, piping sections and cutting heads. Each component represents either a local pressure state, with respect to (3.46a), or defines the fluid flow path, considering (3.46b). Pumping chambers and piping sections correspond to the first, while check-valves and cutting heads relate to the second one. The lumped parameter models of individual components can be interconnected to represents a waterjet facility.

Pumping chamber

The pumping chamber is modelled as a volume $V_C(t) = V_0 - S_P \ s_P(t)$, in which an input fluid flow $Q_P = S_P \ v_P$ is generated by piston displacement and an output fluid flow Q_V will result for an open check-valve. Any difference between input and output flow rate will cause a change in pressure

$$\frac{d}{dt} p_C(t) \approx \frac{\kappa_0 + \kappa_1 \ p_C(t)}{V_0 - S_P \ s_P(t)} \left(S_P \ s_P(t) - Q_V(t) \right) \tag{4.1}$$

within the pumping chamber, see (2.16). The dynamic of pressure generation will be affected by the chamber volume V_C and the bulk modulus $K(t) = \kappa_0 + \kappa_1 \ p_C(t)$. The chamber volume changes with respect to the piston position $s_P(t) = \int v_P(t) \ dt$, where V_0 is the initial chamber volume for a fully retracted piston.

Check-valve

The check-valve will open, when the pressure within the chamber increases above the pressure of the piping. Depending on the differential pressure $\Delta p_V(t) = p_N(t) - p_C(t)$ at the check-valve, a fluid flow

$$Q_V(t) \approx \sigma(\Delta p_V)\ S_V\ \sqrt{\frac{2}{\varrho_0}\ \left(1 + \frac{\kappa_1\ p_C(t)}{\kappa_0}\right)^{-1/\kappa_1}}\ \zeta_V\ \sqrt{|\Delta p_V(t)|}\ sign\left(\Delta p_V(t)\right) \tag{4.2}$$

results, see (2.17), with respect to its cross section S_V and the discharge coefficient

$$\zeta_V = \sqrt{\frac{1}{1 + L/D\ \lambda - (1 - \Delta S_V/S_V)^2}}\ , \tag{4.3}$$

that is determined by the friction loss λ along the subsequent piping of length L and the change of cross section $\Delta S_V = S - S_V$. Only a positive flow can occur ($Q_V(t) \in \mathbb{R}^+$), for that, $\sigma(\Delta p_V)$ is assigned to the Heaviside-function (3.44). It represents the switching of the check-valve dependent on the pressure difference $\Delta p_V(t)$. The switching dynamics itself is neglected.

High-pressure piping

The piping is assigned to its volume $V_0 = S\ L$ that remains unchanged during pump operation. It couples the input and output fluid flows of all high-pressure components. Any deviation from the fluid flow equilibrium will cause a change in pressure

$$\frac{d}{dt} p_N(t) \approx \frac{\kappa_0 + \kappa_1\ p_N(t)}{V_0}\ \left(Q_P - Q_H\right)\ , \tag{4.4}$$

with respect to its compressibility. The input fluid flows from both pumping chambers, Q_{V1} and Q_{V2}, generate the overall pump rate of a high-pressure pump Q_P, see (2.14). The generated pump rate has to correspond to the fluid flow consumption of a cutting head, such as $Q_H = Q_{V1} + Q_{V2}$, to reach steady-state pressure. Any friction loss, from the fluid flow along a pipe, and possible time delays are not considered, when describing the high-pressure piping as a lumped parameter. However, a piping section can be further assigned to multiple segments of different length and inner diameter and individually combined, e.g. to couple multiple cutting heads.

Cutting head

The piping pressure p_N, applied on the cutting head, causes the output fluid flow

$$Q_H(t) \approx S_H\ \sqrt{\frac{2}{\varrho_0}\ \left(1 + \frac{\kappa_1\ p_N(t)}{\kappa_0}\right)^{-1/\kappa_1}}\ \zeta_H\ \sqrt{p_N(t)}\ d(t) \tag{4.5}$$

with respect to the cross section $S_H \in \{0.1, 0.15, 0.2, 0.25, 0.3, 0.35, 0.4\}$ of the nozzle installed. Only a positive fluid flow can result ($Q_V(t) \in \mathbb{R}^+$), since the nozzle generates a waterjet and releases pressure. While ζ_H denotes to the resistance of the nozzle, its coupling with the piping will be enabled or disabled by a on/off-valve. This is defined as a switching disturbance $d(t) \in \{0, 1\}$, manipulating the output fluid flow, that is associated to the water consumption of a cutting head. It is controlled independently by the waterjet application.

Summarizing the above results allows for stating a simplified description for waterjet facilities by means of lumped parameters, which represent the coupling of n piston pumps with m cutting heads at a common interconnection point. This yields the **lumped parameter model**

$$\frac{d}{dt}p_N(t) = \frac{K(p_N)}{V_C(t)+V_0}\left(\sum_n \sigma_n(t)\ Q_n(t) - \sum_m H_m\sqrt{p_N(t)}\ d_m(t)\right) \tag{4.6a}$$

$$\frac{d}{dt}V_C(t) = \sum_n (Q_n(t) - V_{0,n}) \tag{4.6b}$$

of a waterjet facility.

Assuming perfectly synchronized pumping units allows further for implementing a simplified model (4.6a - 4.6b) for low-level control design, see Section 5.3. This lumped parameter model is sufficient to represent a high-pressure network subsection with limited piping length. It is further employed for model-based synchronization by means of camming, as shown bellow. In contrast to that, a graph-based modelling enables to describe complex topologies of various high-pressure networks, representing future waterjet facilities. Its application is given in the subsequent section.

Model-based synchronization

The pumping chamber model (4.1) is useful to design the trajectories for synchronizing the pistons of a high-pressure pump. If the check-valve is entirely closed, the pressure within a pumping chamber will increase relative to the piston displacement

$$\frac{dp_C}{ds_P} \approx \frac{\kappa_0 + \kappa_1\ p_C}{V_0/S_P - s_P}\ , \tag{4.7}$$

for which (4.1) becomes independent of parameter t and $Q_V(t) = 0$. Separating the variables of (4.7) and integrating both side results in

$$\int \frac{1}{\kappa_0 + \kappa_1\ p_C}\ dp_C \approx \int \frac{1}{V_0/S_P - s_P}\ ds_P\ , \tag{4.8}$$

where solving the integrals (4.8) and rearranging yields

$$p_C \approx \frac{e^{-\kappa_1(log(V_0/S_P - s_P)+c)} - \kappa_0}{\kappa_1}\ , \tag{4.9}$$

which describes the pumping chamber pressure with respect to the piston position, taking a variable bulk modulus into account. Evaluating (4.9) for the integration constant yields

$$c = -\left(\frac{log(\kappa_0 + \kappa_1\ p_S)}{\kappa_1} + log\left(\frac{V_0}{S_P}\right)\right)\ , \tag{4.10}$$

while expecting the pumping chamber pressurized to $p_C(s_P = 0) = p_S$, as initial condition, and considering a fully retracted piston. The analytic solution (4.9) provides the desired piston position $\tilde{s} = s_P$ of Equation (2.19) for trajectory generation in Section 2.3. That requires to synchronize the pistons with respect to the pressurization position

$$s_P \approx \frac{V_0}{S_P} - e^{-log(\kappa_0+\kappa_1 p_C)/\kappa_1 - c}\ . \tag{4.11}$$

The plot in Figure 4.2 shows the relative change of volume by means of piston displacement to pressurize a pumping chamber according to (4.11). The pistons need to operate alternately providing a steady input fluid flow. Assuming that a steady-state fluid flow equilibrium is reached, the fluid flow consumption of a cutting head corresponds then to the desired piston velocity $\tilde{v} = Q_H(t)/S_P$, further required in (2.20) for trajectory generation.

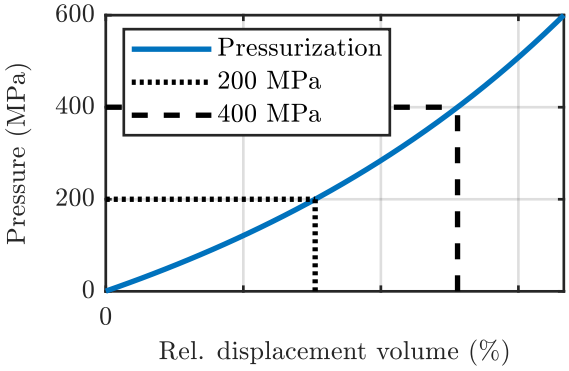

Figure 4.2 – Piston pressurization position: estimated position to pressurize pumping chamber by means of piston displacement.

4.2.2 Graph-based network model

The use of graphs assigns homogeneous segments to the initial fluid flow path of a high-pressure network. This results in a system of equations considering the network description (3.54). This system of equations models the pressure propagation for various waterjet facilities, considering distributed high-pressure pumps interconnected to work stations. The segmentation of high-pressure components is realized according to the following procedure [Niederberger et al., 2018]:

1. Identify the high-pressure components which are dedicated to change the cross section along its fluid flow path.

2. Divide the high-pressure network along the identified components into sections n of lengths L_n, wherever a cross section changes, such as $S_n \neq S_{n+1}$.

3. Chose a propagation time τ, that adequately represents the expected dynamics of pressure generation, as induced by any exogenous fluid flow Q_{ext}. This can be done by analysing the dynamic range of pumps and cutting heads.

4. If $L_n > a\,\tau$, subdivide the initial segments with respect to the fluid's speed of sound a, into homogeneous segments k of length $\Delta x_k < a\,\tau$ for $k = \lfloor L_n/\Delta x_k \rfloor$. Otherwise, $\Delta x_k = L_n$ and $k = n$.

5. Simulate the derived network model with the exogenous dynamics on Q_{ext} to investigate whether the desired dynamic range of pressure generation has been met.

6. Repeat steps 3 to 5 with varying propagation times to provide a reasonable trade-off between model complexity and accuracy.

As a result, a constant cross section is preserved for each segment. These segments are subdivided, if needed, to satisfy the underlying principles of fluid flow continuity and momentum conservation. However, it has to be mentioned that not every initial segment needs further partitioning into equally spaced homogeneous segments to accomplish the desired dynamic range for simulation.

Applying this procedure on the high-pressure network topology **(a) Short piping**, presented at the beginning of this section, the high-pressure components are equally divided along the fluid flow path, wherever a cross section changes. Consequently, the two check-valves, the connector and the nozzle separate the high-pressure network into two pumping chambers, a coupling, a high-pressure piping and a cutting head. Table 4.1 assigns the components of the investigated high-pressure network to $N = 8$ nodes.

Table 4.1: List of nodes and branches for topology (a): assignment of the different high-pressure components to nodes k and branches kj.

k	Nodes:	kj	Branches:
1	Pumping chamber 1	[13]	Check-valve 1
2	Pumping chamber 2	[23]	Check-valve 2
3	Coupling	[34]	Connector
4 ... 7	High-pressure piping	[45] ... [78]	High-pressure piping
8	Cutting head	[80]	Nozzle

All nodes are therefore interconnected as schematically shown in Figure 4.3. The high-pressure piping of length $L = 4.8$ m is subdivided into $n = 4$ segments of length $l = 1.2$ m to obtain a propagation time τ of less than 1 ms, taking a cutting head switching dynamics with a rise time of 10 ms into account. This results in a graph network $\mathcal{N}_{kj}^{(\mathrm{a})}$ that consists of

$$kj \ \in \ \{[13], [23], [34], [45], [56], [67], [78], [80]\} \tag{4.12}$$

branches and

$$k \ \in \ \{1, 2, 3, 4, 5, 6, 7, 8\} \tag{4.13}$$

nodes of homogeneous segments, which describes a spatially distributed waterjet facility. Each segment corresponds to a node. The number of segments N defines the model order. This yields a model of order 8. As the final 6 segments are serially interconnected $kj = \{[34] \dots [80]\}$, the pumping chambers follow independent flow paths $kj = \{[13], [23]\}$ that are coupled at segment $k = 3$.

By applying (3.54) to the assignments (4.12) and (4.13), the fluid flow path is recovered with respect to the network description

$$\mathcal{N}_{kj}: \quad \frac{d}{dt} p_k = \frac{K_k}{V_k} \sqrt{\frac{2}{\varrho_k}} \ \vartheta_{kj} \ \sqrt{|\Delta p_{kj}|} \ sign\left(\Delta p_{kj}\right) + \frac{K_k}{V_k} \ Q_k \ , \tag{4.14}$$

where $p_k \in \mathbb{R}^k$, $Q_k \in \mathbb{R}^k$ and $\Delta p_{kj} \in \mathbb{R}^N$. The corresponding matrix representation

$$\frac{d}{dt}\begin{pmatrix} p_1 \\ \vdots \\ p_8 \end{pmatrix} = \begin{pmatrix} \frac{K_1}{V_1}\sqrt{\frac{2}{\varrho_1}} & & 0 \\ & \ddots & \\ 0 & & \frac{K_8}{V_8}\sqrt{\frac{2}{\varrho_8}} \end{pmatrix} \cdot \underbrace{\begin{pmatrix} -\vartheta_{13} & 0 & & & & \cdots & 0 \\ 0 & -\vartheta_{23} & 0 & & & & \vdots \\ \vartheta_{13} & \vartheta_{12} & -\vartheta_{34} & 0 & & & \\ 0 & 0 & \vartheta_{34} & -\vartheta_{45} & 0 & & \\ & & \ddots & \ddots & \ddots & \ddots & \\ \vdots & & & 0 & \vartheta_{67} & -\vartheta_{78} & 0 \\ 0 & \cdots & & & 0 & \vartheta_{78} & -\vartheta_{80} \end{pmatrix}}_{\Theta_{kj}} \begin{pmatrix} \sqrt{|\Delta p_{13}|}\ sign\,(\Delta p_{13}) \\ \vdots \\ \sqrt{|\Delta p_{80}|}\ sign\,(\Delta p_{80}) \end{pmatrix} + \begin{pmatrix} \frac{K_1}{V_1} & & 0 \\ & \ddots & \\ 0 & & \frac{K_8}{V_8} \end{pmatrix} \begin{pmatrix} Q_1 \\ \vdots \\ Q_8 \end{pmatrix} \tag{4.15}$$

includes the interconnection matrix $\Theta_{kj} \in \mathbb{R}^{k \times N}$, that maintains the fluid flow continuity at each node k. It is composed by $\vartheta_{kj} = \zeta_{kj} S_{kj} \sigma_{kj}$, which represents the possible fluid flows along the branches from a node k to an other node j, and eventually defines a network topology with N interconnections.

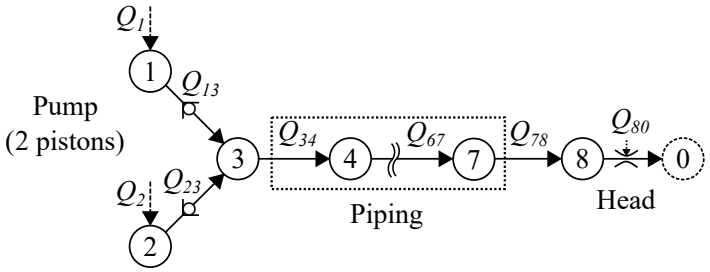

Figure 4.3 – Network diagram corresponding to topology (a): scheme to assign the investigated high-pressure network to homogeneous segments of nodes and branches.

The proposed modelling methodology directly allocates the parameters of the involved high-pressure components to the corresponding segments. Regarding the above network description, Table 4.2 shows the parameters of each segment. The Heaviside functions $\sigma(\Delta p_{13})$ and $\sigma(\Delta p_{23})$ restrict the fluid flow of the check-valves to its positive direction, as each piston induces the displacement flow rates Q_1 and Q_2. The derived high-pressure network $\mathcal{N}_{kj}$ from (4.12) and (4.13) has been numerically simulated in *MATLAB Simulink* and validated with measurements, see the subsequent chapter. In fact, a simulation toolbox has been established that reduces the expenditure of time, when modelling different network topologies subject to represent various waterjet facilities.

Applying the same procedure to all high-pressure networks from Section 2.2, generates a network model for each topology **(a) - (g)**. These models are defined by means of graphs and

therefore straight forward to implement in *MATLAB Simulink* for numerical simulations. From definition (4.14) results different network models, which are equivalent to the matrix representation (4.15). The parameters for the pumping chambers, its coupling and all cutting heads are the same as introduced above. Only the piping sections and its interconnections vary to represent the different high-pressure networks. Hence, the subsequent modelling discusses the segmentation of the piping sections into homogeneous segments, while considering the different network topologies.

Table 4.2: Model parameters for topology (a): parameters of each segment, corresponding to (4.12), (4.13) and grouped in nodes and branches.

k	S_k (mm^2)	Δx_k (mm)	Q_k (cm^3/s)	kj	S_{kj} (mm^2)	ζ_{kj} $(-)$	σ_{kj} $(-)$	d_{kj} $(-)$
1	###	###	$Q_{ext}(t)$	[13]	1.77	###	$f(\Delta p_{13})$	1
2	###	###	$Q_{ext}(t)$	[23]	1.77	###	$f(\Delta p_{23})$	1
3	8.04	790	0	[34]	4.52	###	1	1
4 ... 7	4.52	1200	0	[45] ... [78]	4.52	###	1	1
8	18.09	180	0	[80]	D_H	###	1	$D_H(t)$

Modelling 1 pump - 1 cutting head setups

Equivalent to the above discussed topology **(a) Short piping**, the topology **(b) Long piping** is represented as a graph, considering homogeneous segments of about 1 m length. Table 4.3 assigns the high-pressure components to $N = 22$ nodes. All nodes are interconnected as schematically illustrated in Figure 4.4 (b). The piping section 1 of length $L = 11.3$ m is therefore subdivided into $n = 11$ segments of length $l = 1.026$ m, whereas the piping section 2 of length $L = 7.2$ m is subdivided into $n = 7$ segments of length $l = 1.031$ m.

Table 4.3: List of nodes and branches for topology (b): assignment of the different high-pressure components to nodes k and branches j, k.

k	Nodes:	kj	Branches:
1	Pumping chamber 1	[1,3]	Check-valve 1
2	Pumping chamber 2	[2,3]	Check-valve 2
3	Coupling	[3,4]	Connector
4 ... 21	High-pressure piping	[4,5] ... [21,22]	High-pressure piping
22	Cutting head	[22,0]	Nozzle

The discretization is again chosen to guarantee a desired propagation time with respect to the high-pressure components. This results in a graph network $\mathcal{N}_{kj}^{(b)}$ that consists of

$$kj \in \{[1,3],[2,3],[3,4],\ldots,[14,15],\ldots,[21,22],[22,0]\} \tag{4.16}$$

branches and

$$k \in \{1,\ldots,22\} \tag{4.17}$$

nodes of homogeneous segments. This yields a lumped parameter model of order 22. The simulated pressure states are evaluated at the segments 4, 14 and 21 for model validation. These are

assigned to the pressures $p_P(t)$, $p_N(t)$ and $p_H(t)$. Table 4.4 summarize the assignments of piping sections to homogeneous segments for topology (a) and (b).

Table 4.4: Piping segmentation for topologies (a) and (b): parameters used to simulate the piping sections, considering the short and long network topology, respectively.

Short network model

Section	Section length L	Number of segments n	Segment length Δx	Discharge coefficient ζ
1	4.8 m	4	1.2 m	###

Long network model

Section	Section length L	Number of segments n	Segment length Δx	Discharge coefficient ζ
1	11.29 m	11	1.0264 m	###
2	7.22 m	7	1.0314 m	###

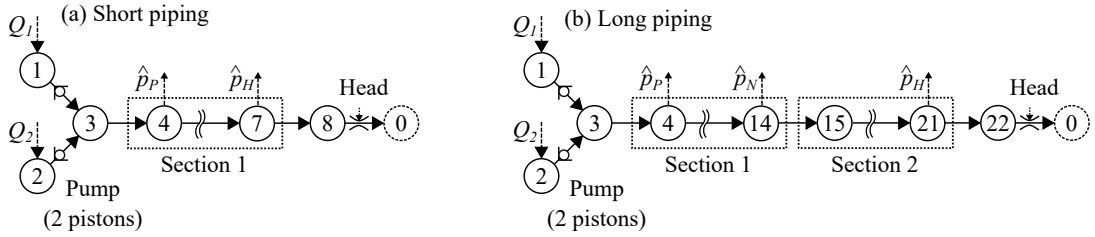

Figure 4.4 – Network assignment for topologies (a) and (b): corresponding graph network for the short and long piping network topologies used for modelling.

Modelling 1 pump - 2 cutting heads setups

Figure 4.5 assigns the high-pressure networks for the topologies **(c) Symmetric network** and **(d) Asymmetric network** to graphs, again considering homogeneous segments of about 1 m length. This segmentation results in a graph network $\mathcal{N}_{kj}^{(c)}$ of

$$kj \in \{[1,3],[2,3],[3,4],\ldots,[10,11],\ldots,[16,17],[17,0],[10,18],\ldots,[23,24],[24,0]\} \tag{4.18}$$

branches for the symmetric network topology and an other graph network $\mathcal{N}_{kj}^{(d)}$ of

$$kj \in \{[1,3],[2,3],[3,4],\ldots,[10,11],[11,12],[12,0],[10,13],\ldots,[23,24],[24,0]\} \tag{4.19}$$

branches for the asymmetric topology. Lumped parameter models of order 24 results for both high-pressure networks, when evaluating (4.14) for (4.18) and (4.19), respectively.

The parameters of Table 4.5 summarizes the piping sections used to simulate the symmetric and asymmetric network topologies. For segmentation, the networks have been divided into three sections of length L. The number of segments n per section clearly distinguishes both network topologies. The symmetric network model features 6 states for both network sections interconnecting a cutting head each. Regarding the asymmetric network model, the section to head 1 features 1 state while head 2 is connected over 11 states.

Table 4.5: Piping segmentation for topologies (c) and (d): parameters used to simulate the piping sections, considering the symmetric and asymmetric network topology, respectively.

Symmetric network model

Section	Section length L	Number of segments n	Segment length Δx	Discharge coefficient ζ
1	7.17 m	7	1.0243 m	###
2	5.94 m	6	0.9900 m	###
3	6.31 m	6	1.0517 m	###

Asymmetric network model

Section	Section length L	Number of segments n	Segment length Δx	Discharge coefficient ζ
1	7.17 m	7	1.0243 m	###
2	0.91 m	1	0.9100 m	###
3	11.34 m	11	1.0309 m	###

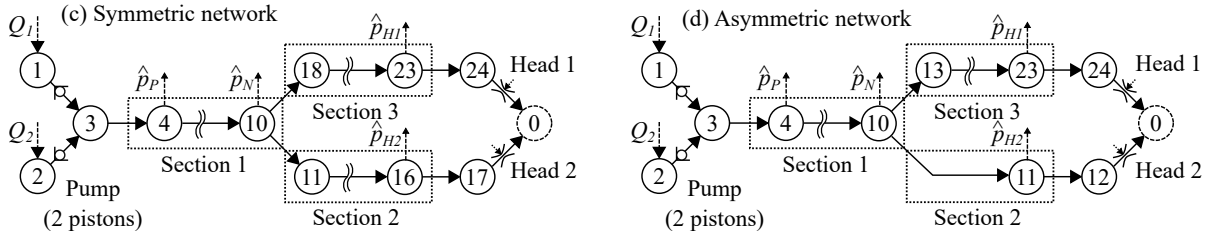

Figure 4.5 – Network assignment for topologies (c) and (d): corresponding graph networks for the symmetric and asymmetric network topologies used for modelling.

Modelling 2 pumps - 2 cutting heads setups

Figure 4.6 assigns the high-pressure networks for topology **(e) Symmetric distributed**, **(f) Asymmetric distributed** and **(g) Decentralized distributed** to graphs, again considering homogeneous segments of about 1 m length. This segmentation results in a network $\mathcal{N}_{kj}^{(\mathrm{e})}$ of

$$\begin{aligned} kj \in \{&[1,3],[2,3],[3,4],\ldots,[9,19],[10,12],[11,12],\\ &[12,13],\ldots,[18,19],[25,26],[26,27],[27,0],[25,28],[28,29],[29,0]\} \end{aligned} \tag{4.20}$$

branches for the symmetric distributed network topology and an other network $\mathcal{N}_{kj}^{(\mathrm{f})}$ of

$$\begin{aligned} kj \in \{&[1,3],[2,3],[3,4],\ldots,[15,20],[16,18],[17,18],\\ &[18,19],[19,20],\ldots,[26,27],[27,28],[28,0],[26,29],[29,30],[30,0]\} \end{aligned} \tag{4.21}$$

branches for the asymmetric distributed topology, as well as a network $\mathcal{N}_{kj}^{(\mathrm{g})}$ with

$$\begin{aligned} kj \in \{&[1,3],[2,3],[3,4],\ldots,[9,19],\ldots,[25,28],[10,12],\\ &[11,12],[12,13],\ldots,[18,28],\ldots,[9,26],[26,27],[27,0],[28,29],[29,0]\} \end{aligned} \tag{4.22}$$

for the decentralized distributed topology. Lumped parameter models of order 29 and 30 results, when evaluating (4.14) for (4.20), (4.21) and (4.22), respectively.

The parameters of Table 4.6 summarizes the piping sections, used to simulate the symmetric distribute, asymmetric distributed and decentralized distributed network topologies. For segmentation, the networks have been divided into five sections of length L. The number of segments n per section clearly distinguishes the network topologies. The symmetric distributed network model features 6 states for both network sections, interconnecting the high-pressure pumps. Regarding the asymmetric distributed network model, the section from pump 1 features 11 states, while pump 2 is connected over 2 states. The symmetric as well as the asymmetric distributed models interconnect two cutting heads over the same connector. On the other hand, the decentralized distributed model connects each pump individually to a cutting head, using a section of 6 states each. The sections, containing a pump and its corresponding cutting head, are coupled over a piping section of 8 states.

Table 4.6: Piping segmentation for topologies (e), (f) and (g): parameters used to simulate the piping sections, considering the symmetric, asymmetric and decentralized distributed network topology, respectively.

Symmetric distributed network model

Section	Section length L	Number of segments n	Segment length Δx	Discharge coefficient ζ
1	6.38 m	6	1.1383 m	###
2	6.48 m	6	1.0808 m	###
3	4.94 m	5	0.9880 m	###
4	0.84 m	1	0.8400 m	###
5	0.94 m	1	0.9400 m	###

Asymmetric distributed network model

Section	Section length L	Number of segments n	Segment length Δx	Discharge coefficient ζ
1	10.82 m	11	0.9832 m	###
2	2.03 m	2	1.0150 m	###
3	5.86 m	6	0.9767 m	###
4	0.63 m	1	0.6300 m	###
5	1.16 m	1	1.1600 m	###

Decentralized distributed network model

Section	Section length L	Number of segments n	Segment length Δx	Discharge coefficient ζ
1	6.08 m	6	1.0125 m	###
2	5.50 m	6	0.9167 m	###
3	7.98 m	8	0.9975 m	###
4	0.41 m	1	0.4100 m	###
5	1.38 m	1	1.3800 m	###

It is further outlined, that the electrically driven pump, installed at the test bench, is considered as two exogenous fluid flow source (Q_1 and Q_2, one for each piston) and that a cutting head is represented by a pressure sink to atmosphere. The pressure states $\hat{p}_{P1}(t)$ and $\hat{p}_{P2}(t)$, $\hat{p}_N(t)$, $\hat{p}_{H1}(t)$ and $\hat{p}_{H2}(t)$ are evaluated for model validation and controller verification, see Chapter 4 and 6.

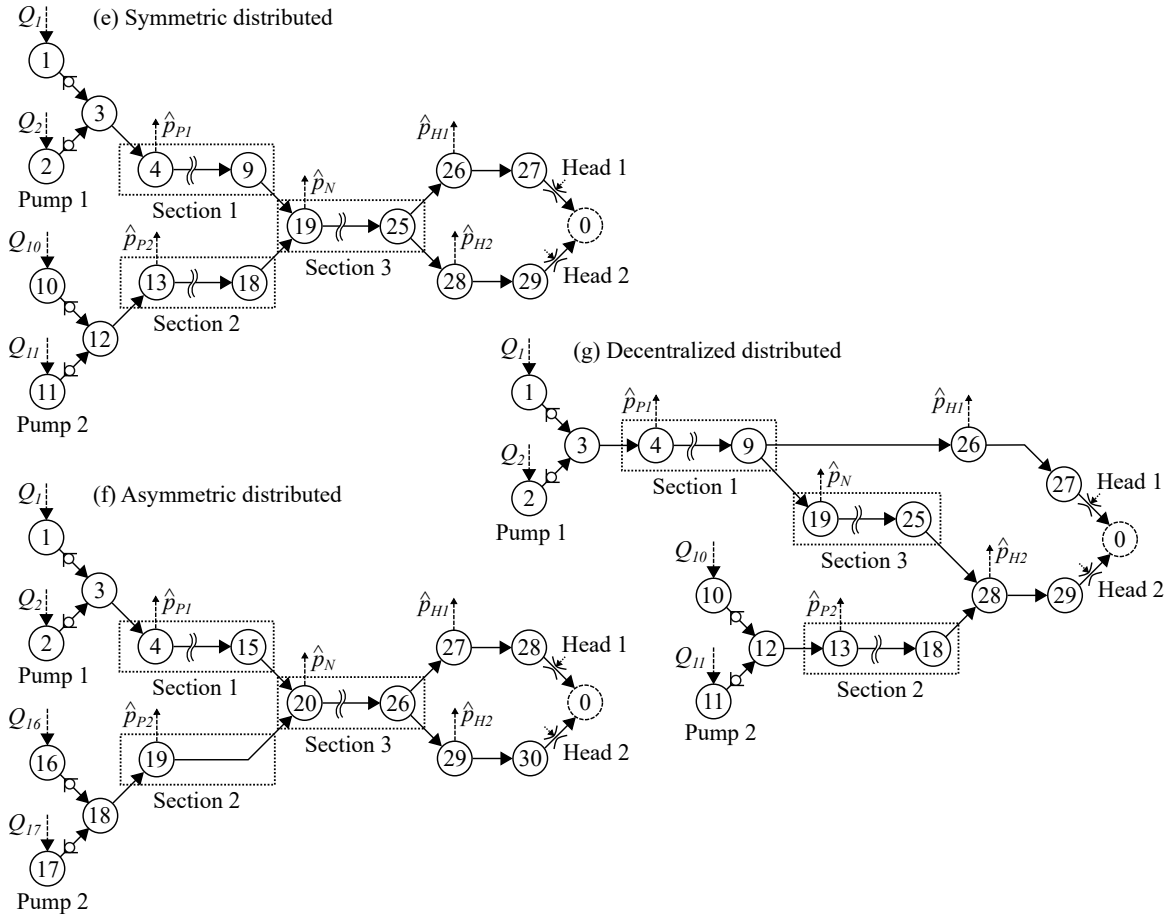

Figure 4.6 – Network assignment for topologies (e), (f) and (g): corresponding graph networks for the symmetric, asymmetric and the decentralized distributed network topologies.

4.3 Experimental studies

The graph-based modelling methodology has been applied in Section 4.2 to obtain high-pressure network models for defined network topologies. This chapter will first verify the graph-based modelling methodology with respect to the variable bulk modulus and variable fluid density, while considering a basic test bench configuration. For that, a high-pressure network has been modelled, which directly interconnects a single high-pressure pump with a cutting head, when using the graph-based modelling methodology as well as applying alternative approaches from literature. These alternative approaches consider a constant bulk modulus or a constant fluid density. The simulated pressure trends, which originate form the different modelling approaches, will be compared to measurement data from the test bench. The experiment have been derived with respect to a wide pressure range from 100 to 400 MPa, while operating the pump in open-loop control. This is only possible, if the cutting head remains open.

This chapter will then validate the different high-pressure network models, using again measurement data from the test bench. For that, the test bench has been configured with respect to different network topologies: considering a single high-pressure pump that supplies a single cutting head, a single pump with two cutting heads and two pumps with two cutting heads. The cutting heads will switch independently, according to given switching patterns, whereas a

constant operating pressure is obtained by means of closed-loop control. This aims to generate a varying water consumption, which results in different fluid flow velocities and pressure losses along the high-pressure piping.

All simulation results have been obtained with *Simulink R2017b* using the *ode23s* solver with variable step size. The solver has been configured for a relative tolerance of 10^{-4} and an absolute tolerance of 10^3. It has been running on a *Windows 10* machine with an *Intel Core i7-7600U* 2.80 GHz processor and 16.0 GB RAM.

4.3.1 Graph-based modelling methodology validation

The proposed graph-based modelling methodology has been verified, considering a basic high-pressure network used for waterjet machining. The topology **(a) Short piping** has been considered, interconnecting a single high-pressure pump with one cutting head. A first model has been derived, using the graph-based modelling methodology (3.54), which takes into account a pressure-dependent fluid density $\varrho = f(p(t))$ as well as a pressure-dependent bulk modulus $\kappa = f(p(t))$. In contrast to that, two alternative models have been derived by using approaches from literature. More precisely, a first approach considers a constant fluid density with a variable bulk modulus, such as [Hountalas and Kouremenos, 1998] and [Lino et al., 2007]. The system pressure p is thereby simulated using the differential equation

$$\frac{dp}{dt} = \frac{K}{V}\left(\frac{dV}{dt} - Q\right) \ , \tag{4.23}$$

where the difference between an output fluid flow Q and the displacement volume dV/dt induces a pressure, with respect to the fluid volume V and the pressure-dependent bulk modulus [Hountalas and Kouremenos, 1998]

$$K = 12\,(1000 + p) \ . \tag{4.24}$$

The output fluid flow is derived by the algebraic equation

$$Q = sign\ (\Delta p)\ \zeta\ S\ \sqrt{\frac{2\ |\Delta p|}{\varrho}} \ , \tag{4.25}$$

which considers the fluid flow resistance ζ along a cross section S, for $d\varrho/dt = 0\ \forall\ t > 0$.

A second approach considers a constant bulk modulus with a variable fluid density, such as [Ferretti et al., 2015]. The output fluid flow (4.25) thereby considers a pressure-dependent fluid density [Fabien et al., 2010]

$$\varrho = \varrho_0 \left(1 + \frac{7.5048\ p}{2209.4}\right)^{1/7.5048} \ , \tag{4.26}$$

assuming $dK/dt = 0\ \forall\ t > 0$. Both approaches will be employed using the assignments (3.52) and (3.53), as defined in Section 3.3 to derive a network description, while considering a constant fluid density and a constant bulk modulus, respectively.

The measurement **R-1** of Table 4.7 has been selected to investigate the pressure generation for a wide pressure range from 100 to 400 MPa. This experiment is subject for a stripping process, hence the cutting head remains open for all time. It has been configured with a nozzle of 0.25 mm inner diameter. The pump rate is manually increased, until the produced overall fluid flow corresponds to the resulting water consumption, such as to obtain the desired operating pressure.

Table 4.7: Excerpt of experiments for use case 1: measurements derived on different test bench setups to verify the graph-based modelling methodology.

Meas.	Topology	Pressure (MPa)	Nozzle ⌀(mm)	Switching pattern
R-1	(a) Short	100 ... 400	0.25	Strip.

The high-pressure pump operates in open-loop control. This enables a pump to attain the desired operating pressure, as long as the switching state of the cutting head remains unchanged. As a result, the coupling of two pumping units to a cutting head and the pressure generation over a wide pressure range enable to investigate the effects of varying parameters for the different modelling approaches: the graph-based modelling (3.54), the model for constant bulk modulus (4.26) and the model for constant fluid density (4.24).

The block diagram of Figure 4.7 illustrates the experimental setup, as used for model verification. For each experiment, reference position trajectories have been loaded to the test bench. These trajectories enable a periodical piston displacement, where the pump rate $u(t)$ defines the cycle time of piston displacement and provides the desired fluid flow rate Q. Encoders measure the actual piston positions and its velocities, while pressure gauges measure the pressure trends $p_x(t)$ at different network positions x. The PLC acquires the data with a sampling rate of 200 Hz. The measured piston positions and velocities has been evaluated to estimate the induced fluid flow $\hat{Q}$ of each pumping unit. These fluid flows are then used as model inputs for numerical simulations, where the simulated pressure trends $\hat{p}_x(t)$ have been compared to measurements $p_x(t)$ to provide the residuals $\xi(t)$. The simulations are repeated for the different modelling approaches.

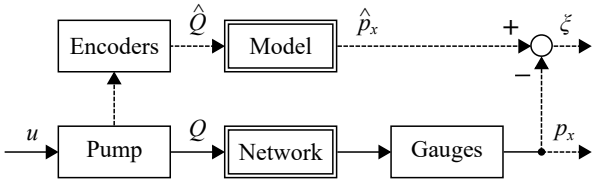

Figure 4.7 – Experimental setup to verify the modelling methodology: pressure gauges measure the pressures $p_x(t)$ at positions x, when applying an input fluid flows $Q(t)$. The estimated fluid flows $\hat{Q}(t)$ are used as model inputs and the simulated pressure trends $\hat{p}_x(t)$ have been compared to measurements.

Varying operating pressures (Stairs from 0 to 400 MPa)

The measurement data shown in plots of Figure 4.8 overview the experiment, used to compare the graph-based modelling methodology with the other approaches from literature (e.g [Ferretti et al., 2015] and [Lino et al., 2007]). The reference trajectories implemented to the high-pressure pump have been optimized for a pressure of 200 MPa. Operating points below this pressure cause pressure overshoots and operating points above this pressure result in pressure losses. This phenomena has been already explained in Section 2.3, when introducing the model-based synchronization. For experiment **R-1**, the cutting head has been configured with a nozzle of 0.25 mm inner diameter. Thus, an induced overall fluid flow of $Q_{200} = 1.14$ l/min is required to obtain a steady-state pressure of 200 MPa. However, the overall fluid flow $Q(t) = \{0.6, 0.8, 1.0, 1.2, 1.4, 1.2, 1.0, 0.8, 0.6\} \cdot Q_{200}$ has been varied to follow a stair.

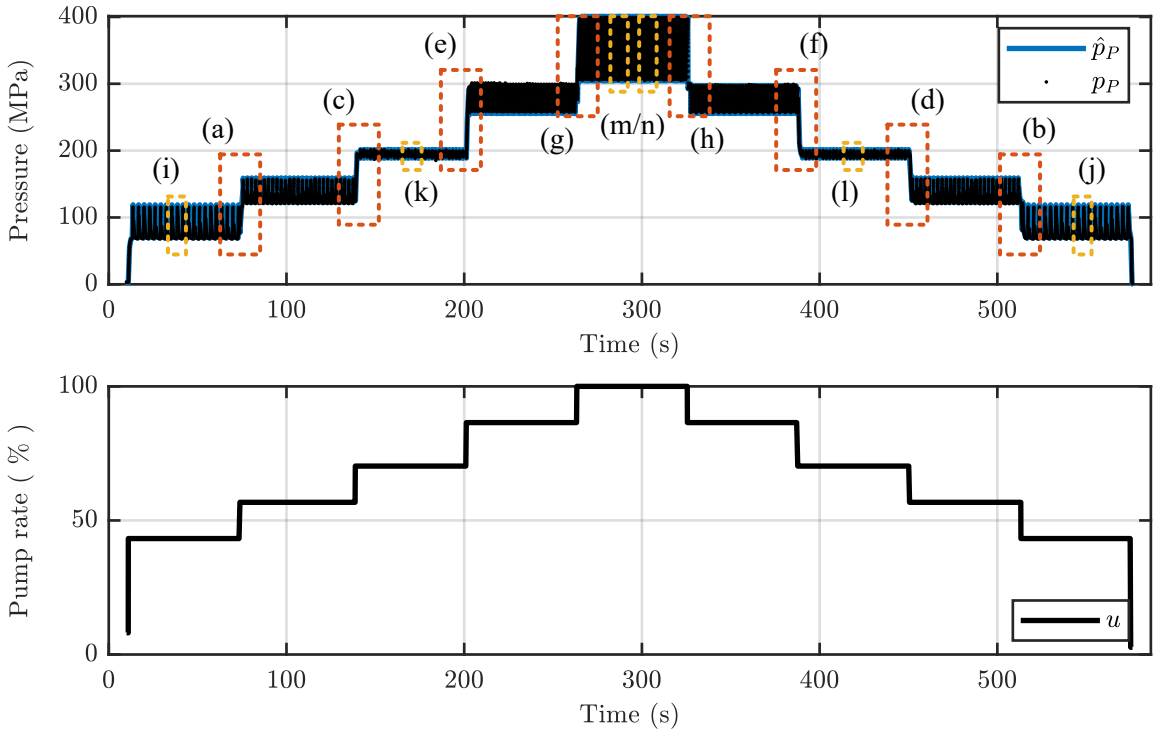

Figure 4.8 – Overview of measurement R-1: measured pump output pressure and corresponding reference displacement flow rate, for a cutting head configured with a 0.25 mm nozzle and position trajectories optimized for 200 MPa.

The zoomed-in plots of Figures 4.9 - 4.12 present the measured and simulated pressure trends for steps, applied to increase and decrease the displacement flow rate, around an operating pressure of 100, 200, 300 and 400 MPa, respectively. The simulation data of three different modelling approaches have been compared, using varying parameters (3.54), constant bulk modulus (4.26) and constant fluid density (4.24). Where the first plot of each step has been obtained by the graph-based modelling methodology (1a-h), which considers a pressure-dependent bulk modulus as well as a pressure-dependent fluid density, the second and third plots consider a model for constant bulk modulus with $K_{140} = 2.7374$ GPa (2a-h) and a model for constant fluid density with $\varrho_{270} = 1104.6$ kg/m^3 (3a-h). For each simulation, transient behaviour as well as the expected steady-states is improved, when considering variable parameters.

The zoomed-in plots of Figure 4.13 - 4.15 compare the measured with the simulated pressure trends, for operating points at 100, 200 and 400 MPa, and show the resulting residuals. The pressure has been obtained from the pump outtake position (1i-n) and from the cutting head intake position (2i-n). Additional to the graph-based modelling methodology, the model for constant bulk modulus and the model for constant fluid density has been considered. The parametrization of the alternative models has been individually obtained, to minimize the root mean square error (*rmse*) between the simulated pump output pressure and the experimental data. The constant bulk modulus of minimal *rmse* has been found for a pressure of 140 MPa and the constant fluid density of minimal *rmse* has been found for a pressure of 270 MPa. In contrast to that, the introduced variable parameter model has been applied, without initial parameter tuning.

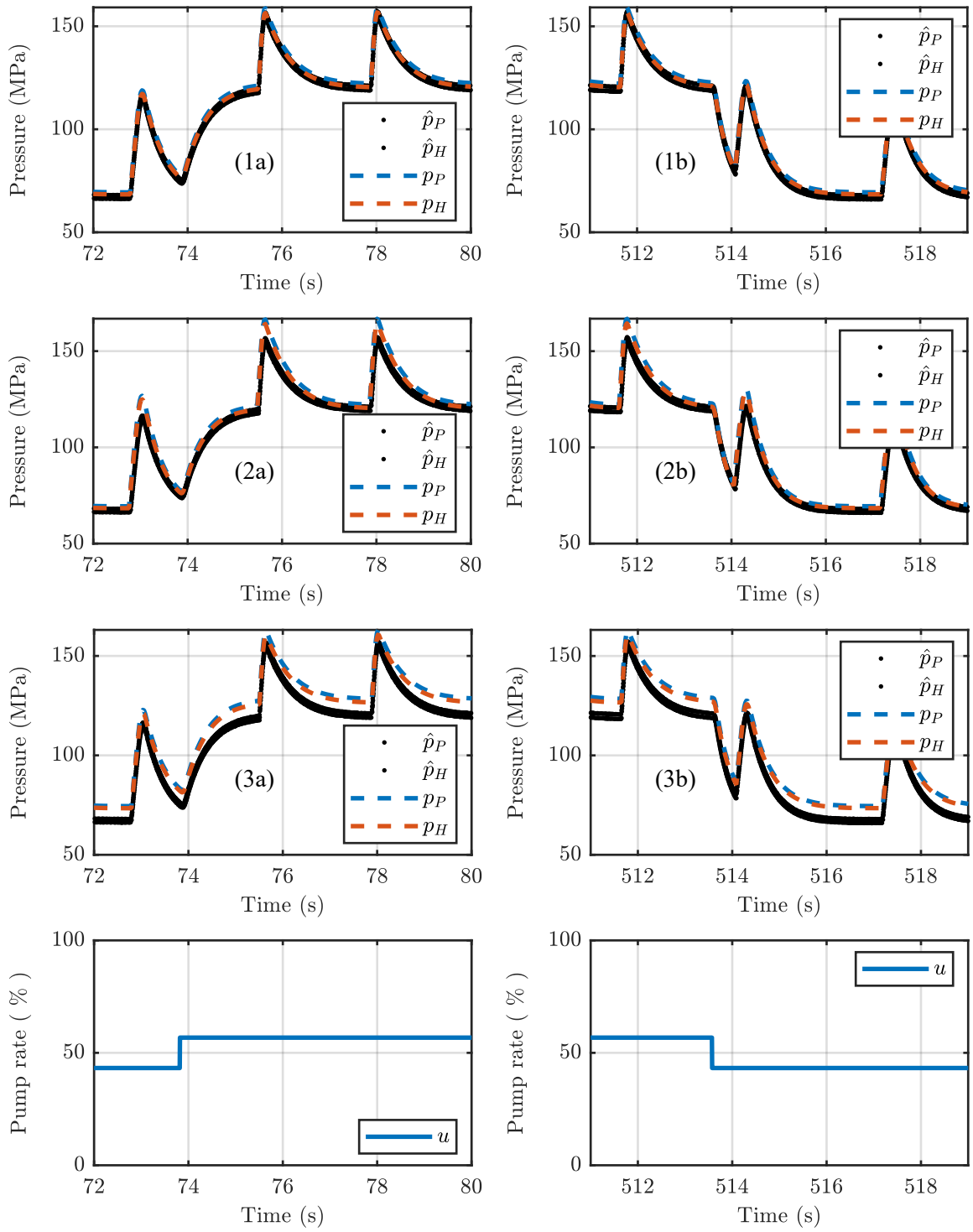

Figure 4.9 – Step response for operating pressure around 100 MPa, considering varying parameters (1a/b), constant bulk modulus (2a/b) and constant fluid density (3a/b): zoom-in of measured and simulated pressure at pump outtake and cutting head intake for a reference step on the induced overall fluid flow.

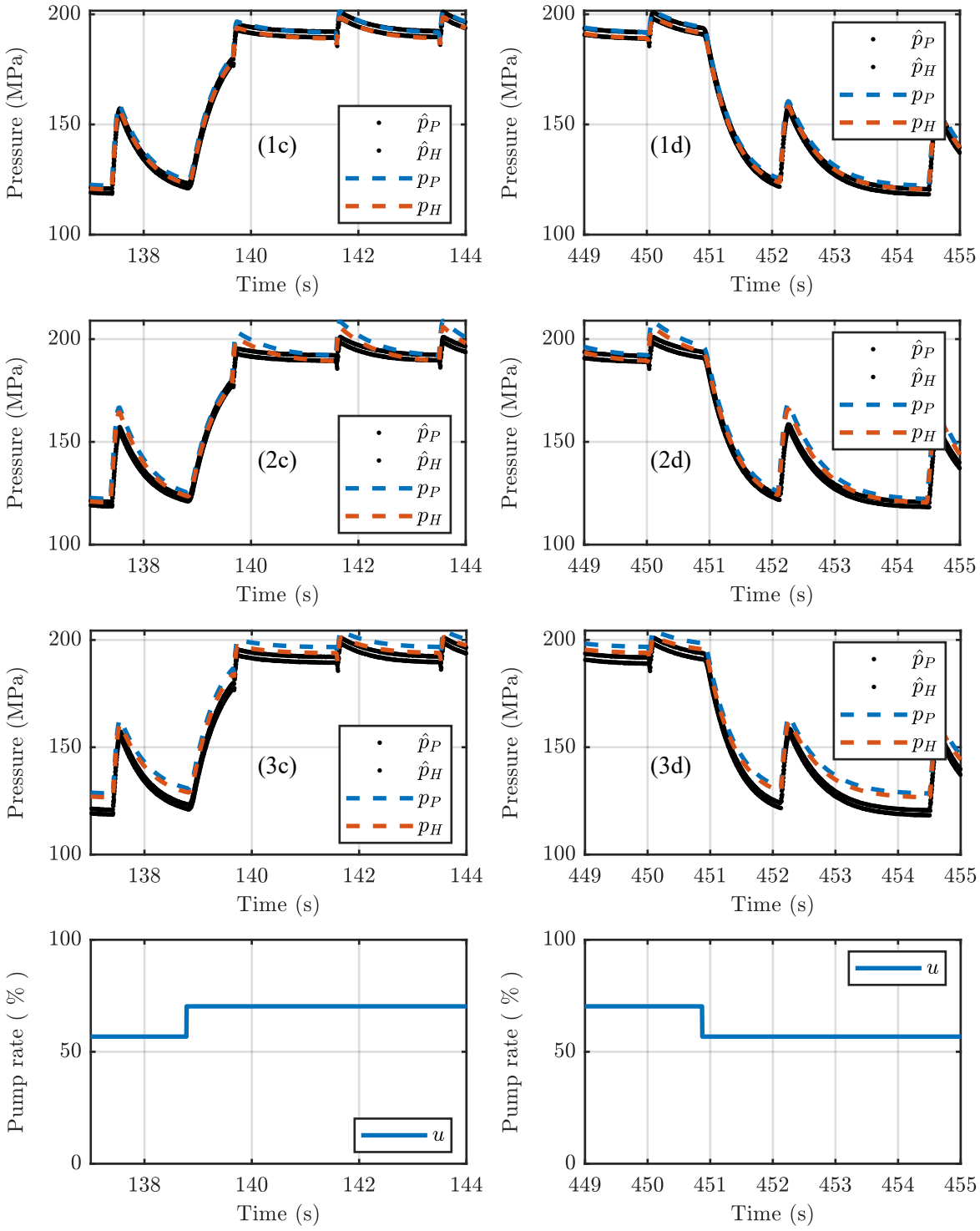

Figure 4.10 – Step response for operating pressure around 200 MPa, considering varying parameters (1c/d), constant bulk modulus (2c/d) and constant fluid density (3c/d): zoom-in of measured and simulated pressure at pump outtake and cutting head intake for a reference step on the induced overall fluid flow.

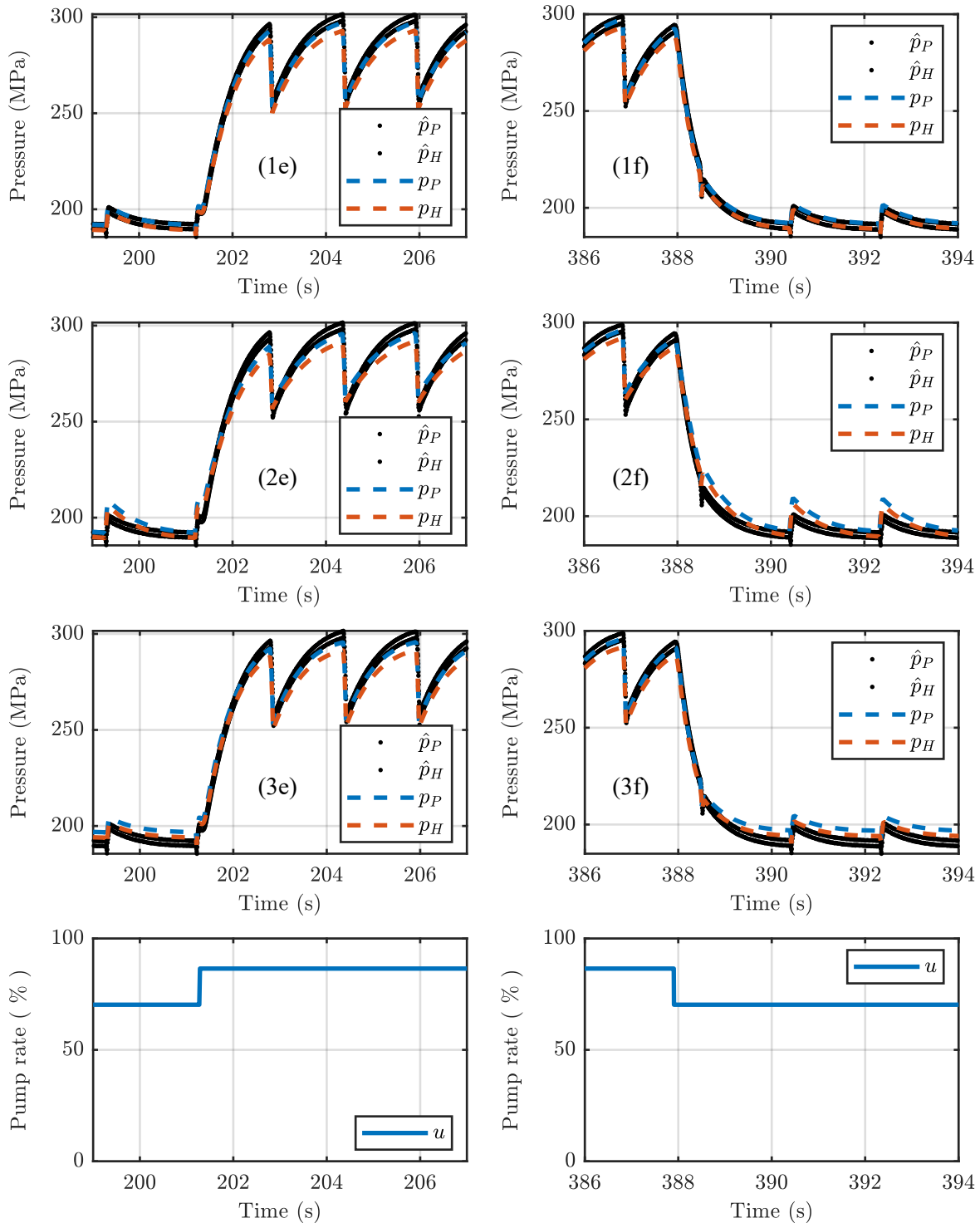

Figure 4.11 – Step response for operating pressure around 300 MPa, considering varying parameters (1e/f), constant bulk modulus (2e/f) and constant fluid density (3e/f): zoom-in of measured and simulated pressure at pump outtake and cutting head intake for a reference step on the induced overall fluid flow.

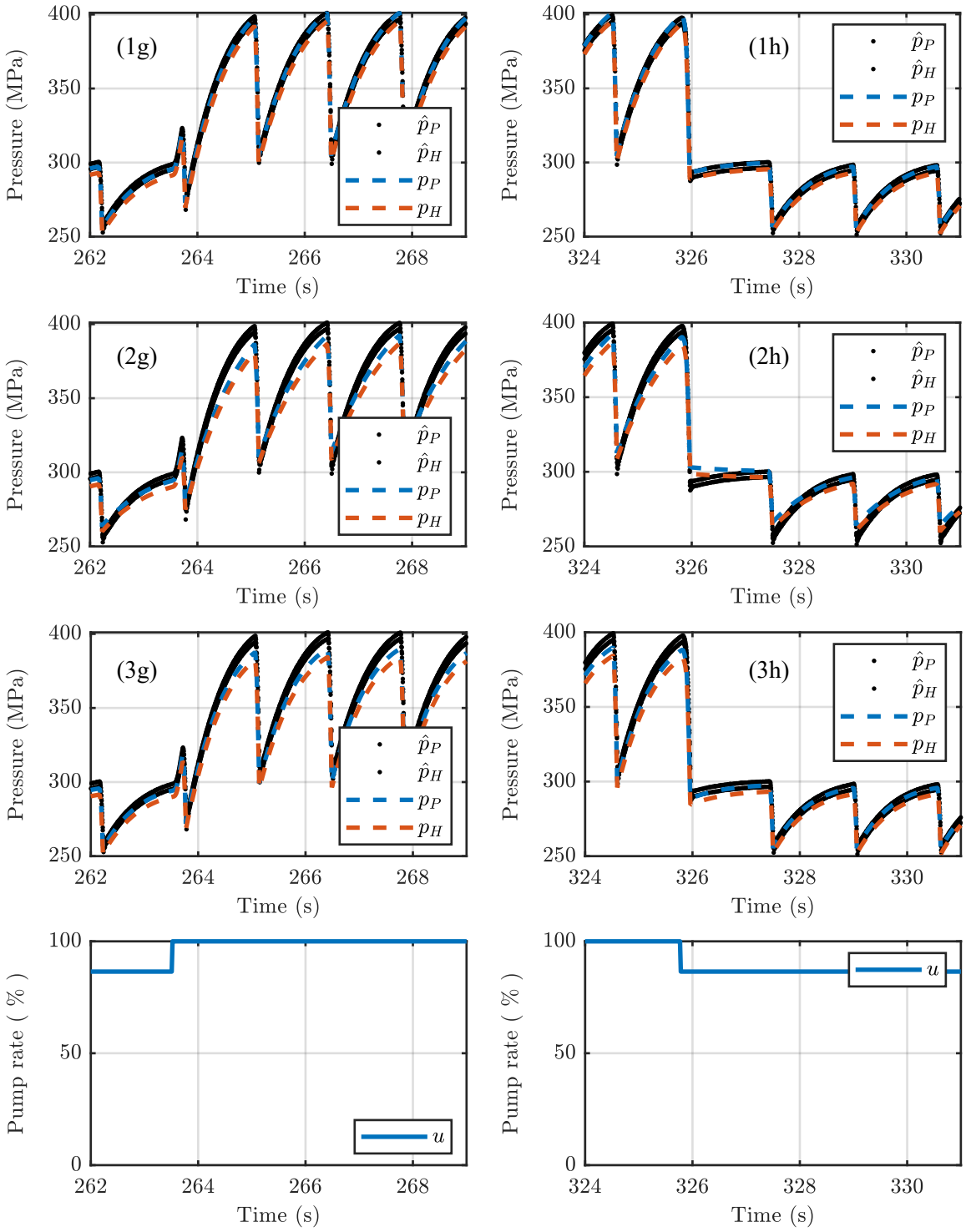

Figure 4.12 – Step response for operating pressure around 400 MPa, considering varying parameters (1g/h), constant bulk modulus (2g/h) and constant fluid density (3g/h): zoom-in of measured and simulated pressure at pump outtake and cutting head intake for a reference step on the induced overall fluid flow.

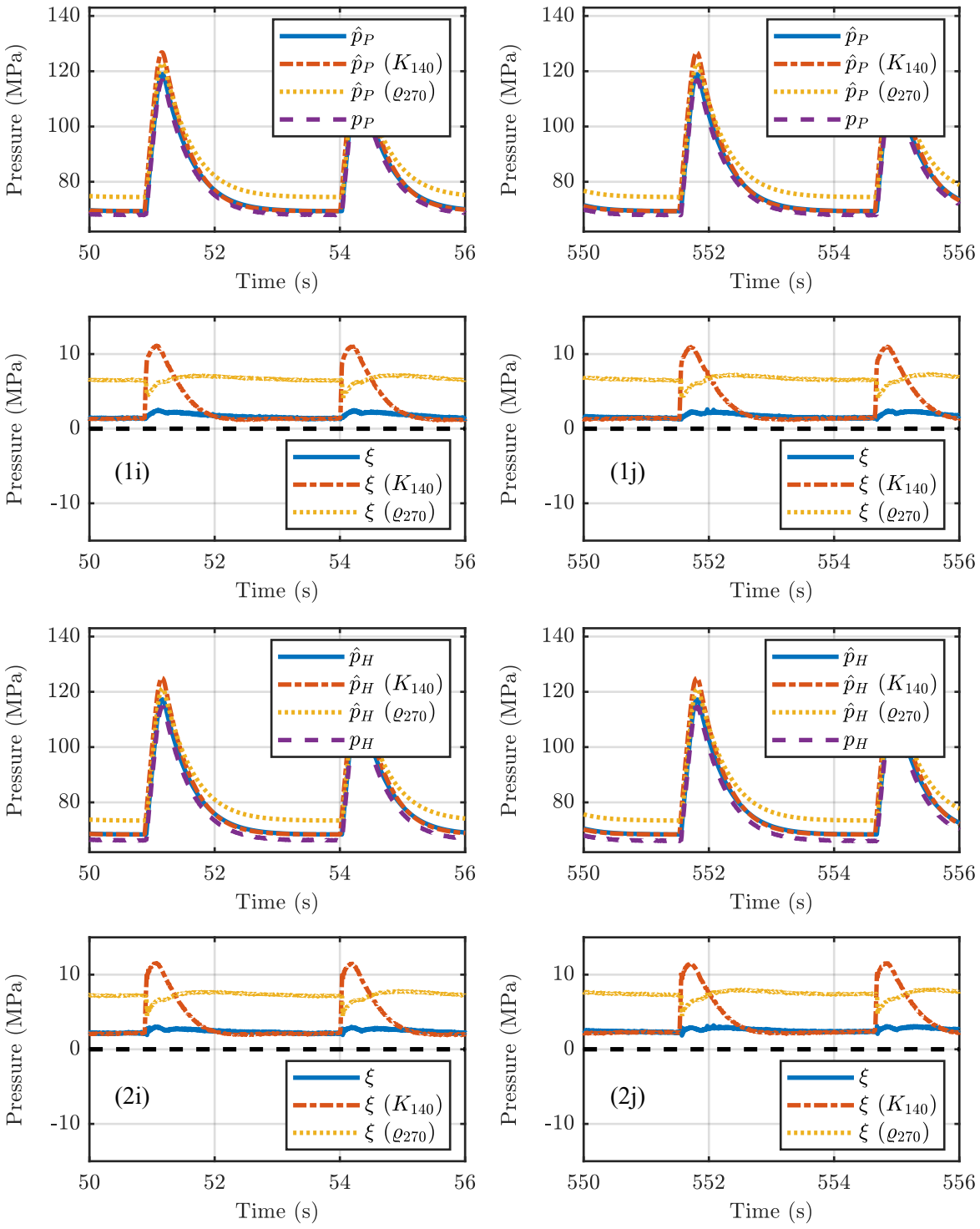

Figure 4.13 – Steady-state of measured and simulated pump output pressure (1i/j) and cutting head input pressure (2i/j) around 100 MPa: the proposed modelling methodology is thereby compared to simulations with constant bulk modulus and constant fluid density.

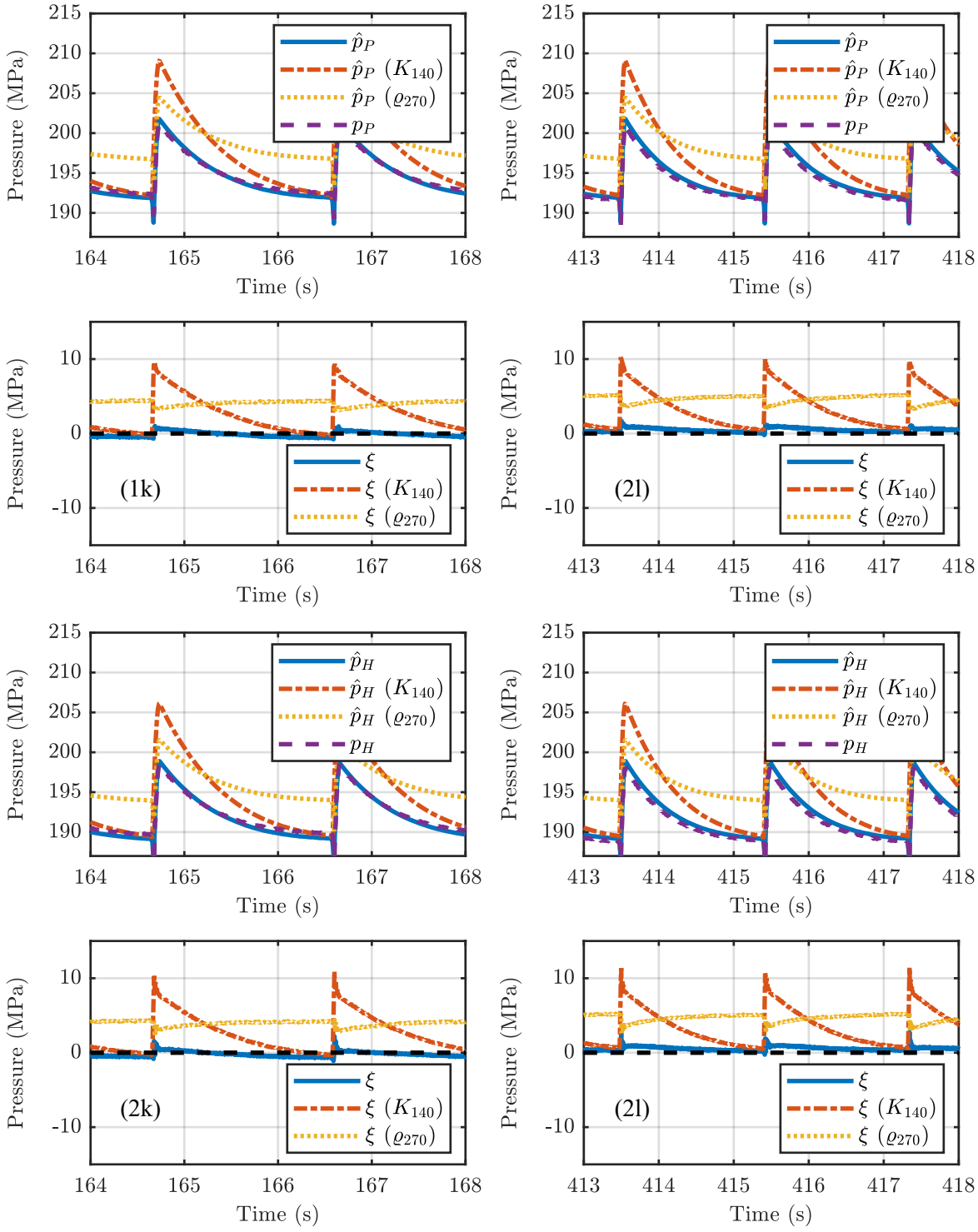

Figure 4.14 – Steady-state of measured and simulated pump output pressure (1k/l) and cutting head input pressure (2k/l) around 200 MPa: the proposed modelling methodology is thereby compared to simulations with constant bulk modulus and constant fluid density.

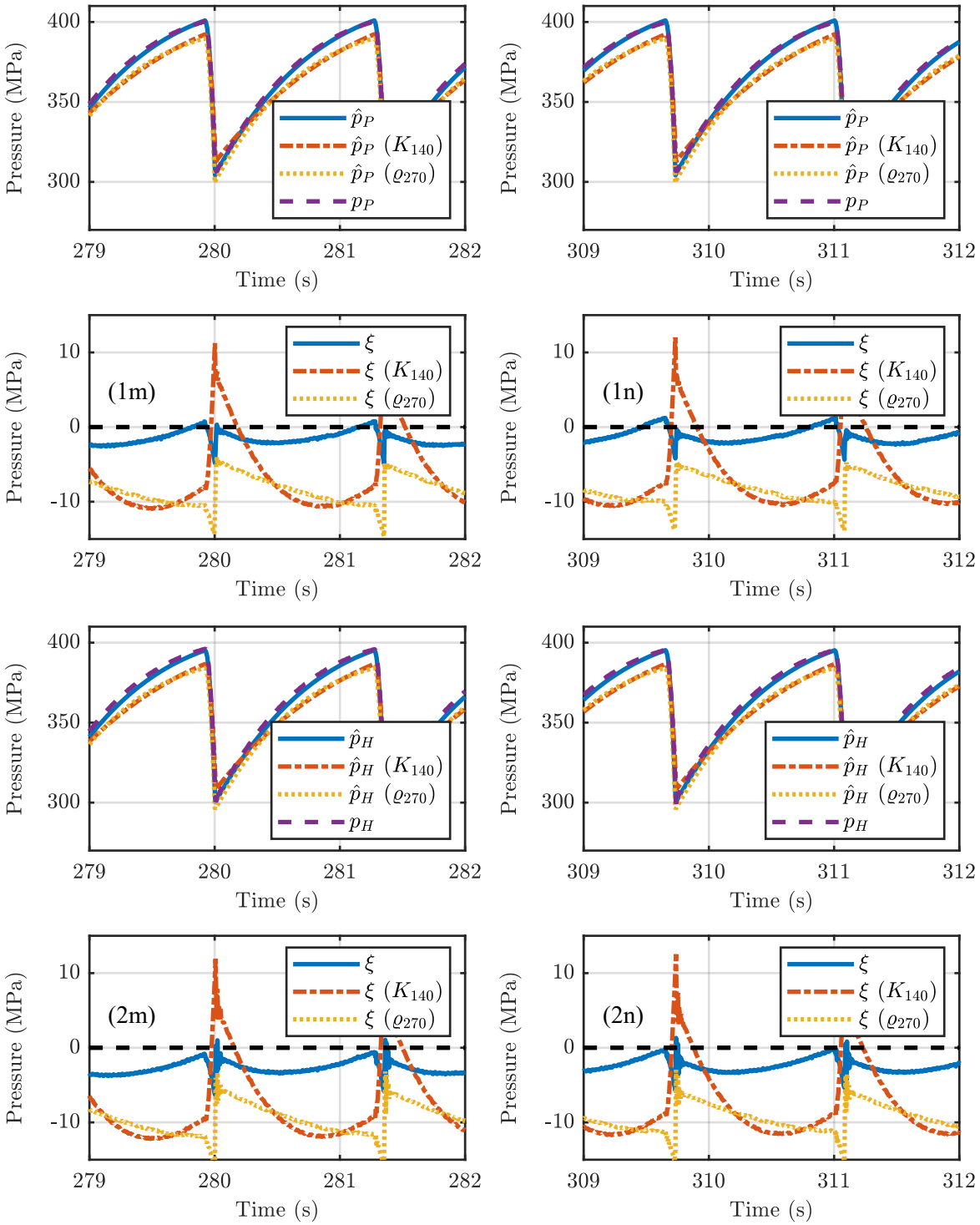

Figure 4.15 – Steady-state of measured and simulated pump output pressure (1m/n) and cutting head input pressure (2m/n) around 400 MPa: the proposed modelling methodology is thereby compared to simulations with constant bulk modulus and constant fluid density.

Summary

It has been shown that a pressure-dependent bulk modulus is essential to track the transient behaviour within a desired pressure range. Hence, applying a constant bulk modulus results in an incorrect transient behaviour, that converges towards the desired steady-state. On the other hand, a constant fluid density causes a transient behaviour similar to the measurement, but with an incorrect steady-state. Therefore, a pressure-dependent fluid density is desired to meet the steady-state over a wide pressure range. Table 4.8 lists the correlation coefficient R and $rmse$ for all the discussed models. This evaluation is based on the experimental and simulation data over a time interval of 30 seconds at a constant operating point.

Table 4.8: Correlation coefficients R and $rmse$ to compare the model's accuracy for different operating pressures.

Modelling methodology	Pos.	100 MPa		200 MPa		400 MPa		overall
		R	$rmse$	R	$rmse$	R	$rmse$	$rmse$
Varying parameters	p_P	0.9999	2.42	0.9980	1.63	0.9996	1.52	2.12
($K = f(p)$, $\varrho = f(p)$)	p_H	0.9999	2.83	0.9966	2.31	0.9995	2.12	2.62
Constant bulk modulus	p_P	0.9957	5.10	0.9687	4.22	0.9946	3.92	6.03
($K = K_{140}$, $\varrho = f(p)$)	p_H	0.9955	5.39	0.9663	4.65	0.9943	5.03	5.40
Constant fluid density	p_P	0.9994	7.33	0.9978	6.53	0.9991	6.44	7.25
($K = f(p)$, $\varrho = \varrho_{270}$)	p_H	0.9994	7.76	0.9975	7.16	0.9989	6.25	6.74

All models achieve a correlation coefficient of $R > 0.9687$. As the graph-based modelling methodology obtains a $rmse < 2.42$ for all observed operating points, an increase to $rmse > 5.10$ has been observed for both models, using constant parameter. Modelling approaches that either consider a variable fluid density (e.g. [Fabien et al., 2010], [Ferretti et al., 2015]) or a variable bulk modulus (e.g. [Hountalas and Kouremenos, 1998], [Lino et al., 2007]) are sufficient for simulations around a specific operating point. However, the proposed methodology improves the simulation accuracy, when a wide pressure range is desired.

4.3.2 High-pressure network model validation (1 pump configuration)

This section investigates the simulation accuracy for high-pressure networks, when applying the graph-based modelling methodology for configurations with two cutting heads. For that, the pressure generation in a high-pressure network becomes disturbed, when switching the different cutting heads in open and close position. Two cutting heads are distributed in the network, while a single high-pressure pump operates at a defined position. This pump is in closed-loop control, aiming at a constant reference pressures of 200 and 350 MPa, respectively. For this reason, the pump holds by default a PI controller (6.46), as specified in Section 6.4. It will adjust its induced overall fluid flow, such as to compensate any switching disturbances. Thus, a wide variety of fluid flow rates from 0 to 2.45 l/min will be obtained, depending on the switching state of each cutting head. Here, the graph-based modelling methodology has been applied to model different network topologies, which interconnect a high-pressure pump with two cutting heads.

This model validation considers three specific network topologies, for which measurement data have been derived from the high-pressure test bench. The topology **(b) Long piping** interconnects the high-pressure pump to a single cutting head, while the topologies **(c) Symmetric network** and **(d) Asymmetric network** consider two cutting heads. Different measurements have been obtained for simulation and experimental validation, as listed in Table 4.9. This section provides an overview, plots extending these results are given in Appendix A.1. The basic measurements (**B-4,5,7**) consider a high-pressure pump, that directly interconnects a single cutting head. The first 3 extended measurements (**E-4,5,7**) consider the symmetric network topology, including two cutting heads, while both cutting heads have been asymmetrically configured with nozzles of different inner diameter. The last 2 extended measurements (**E-9,11**) consider the asymmetric network topology, while both cutting heads have been symmetrically configured with identical nozzles. This allows for investigating and distinguishing the effects due to an asymmetric work station configuration and an asymmetric waterjet facility, respectively. Considering the symmetric network model, each cutting head holds nozzles of different inner diameters. Thus, a different fluid distribution results for both cutting heads, due to the nozzles installed, and different pressure losses occur for each network section. Considering the asymmetric network model, both cutting heads are equipped with identical nozzles. Thus, the asymmetric setup causes different pressure losses along each network section. This will slightly affect the fluid distribution between the cutting heads.

Table 4.9: Excerpt of experiments for use case 1 and 2: measurements derived with different test bench setups and used for model validation.

Meas.	Topology	Pressure (MPa)	Nozzle 1 ⌀(mm)	Nozzle 2 ⌀(mm)	Switching pattern	
B-4 B-5	(b) Long	200	0.35	-	Contour Cavity	(Appendix A.1)
B-7		350	0.25	-	Contour	(Appendix A.1)
E-4 E-5	(c) Sym. net.	200	0.3	0.2	Contour Cavity	(Appendix A.1)
E-7		350	0.2	0.1	Contour	(Appendix A.1)
E-9	(d) Asym. net.	200	0.25	0.25	Contour	
E-11		350	0.15	0.15	Contour	(Appendix A.1)

All experiments are derived for two operating points, each taking different switching patterns and different nozzle configurations into account. Contour cutting is investigated for each basic and extended measurement. A cutting head will exemplarily open for a cutting period of 60 seconds, followed by a hold period in closed position for another 60 seconds. Regarding the extended measurements, this switching pattern will be repeated periodically for both cutting heads with a phase shift of 90°. The measurements B-5 and E-5 investigate cavity cutting, where the switching pattern is modified to realize an on/off period of 0.5 seconds. Consequently, a large variety of measurement data for different operating points, switching patterns, cutting head configurations and network topologies has been obtained to validate the high-pressure network models, as derived by the graph-based modelling methodology.

The diagram of Figure 4.16 illustrates the experimental setup, as implemented for model validation. The cutting heads open and close with respect to the predefined switching patterns, given by the disturbance signals $d_m(t) = [d_1(t), d_2(t)]$. The low-level control will then adjust the pump rate, using the control signal $u(t)$, to obtain the desired reference pressure $p_s(t)$. The model-based synchronization ($Q_1(t) = f_1(u(t))$, $Q_2(t) = f_2(u(t))$) displaces both pistons such as $Q_1(t) + Q_2(t) = [0 : 2.45]$ l/min ($0 \leq u(t) \leq 1$), see Equations (2.15) and (2.26) in Section 2.3. Different locations have been defined at the test bench, to measure the pressure states. Variable $p_P(t)$ denotes the input pressure at the pump outtake, $p_N(t)$ gives the pressure at the network junction and $p_{Hm}(t)$ gives the pressure at the cutting heads, where $m \in \{1, 2\}$ refers to the first and second cutting head, respectively. The induced fluid flows $Q(t) = [Q_1(t), Q_2(t)]$ of both pistons are estimated by measuring the piston displacements. All measured and estimated input signals ($\hat{Q}$ and d_m) are fed into the high-pressure network models for simulation. The measured data $p_x(t) = [p_P(t), p_N(t), p_{H1}(t), p_{H2}(t)]$ are then compared to the simulated pressure states $\hat{p}_x(t) = [\hat{p}_P(t), \hat{p}_N(t), \hat{p}_{H1}(t), \hat{p}_{H2}(t)]$ to validate the simulations for different measurement positions. The measurement data have been captured with a sampling rate of 500 Hz.

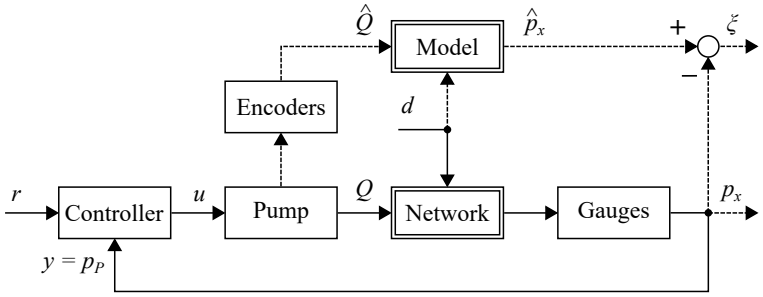

Figure 4.16 – Experimental setup for model validation: pressure gauges measure the pressures $p_x(t)$ at different positions, while applying an input fluid flows $Q(t)$. The estimated input fluid flows $\hat{Q}(t)$ are used as model inputs and the simulated pressure trends $\hat{p}_x(t)$ have been compared to the measurements.

The derived high-pressure network models from Section 4.2 have been numerically simulated in *MATLAB Simulink*, using the developed toolbox to realize a straight forward implementation of the graph-based modelling methodology. The solver ode23s for variable step-size has been configured for a relative tolerance of 10^{-5} and an absolute tolerance of 10^3. This enables a simulation precision of 10^{-2} MPa.

Contour cutting: asymmetric cutting heads

A continuous operating point of 200 MPa pressure is chosen. Two cutting heads will open and close alternately with a phase shift of 90°. Considering the measurement E-4, cutting head 1 holds a nozzle of 0.3 mm inner diameter, while the cutting head 2 is configured with a 0.2 mm nozzle. As a consequence when combining all possible switching states, four different fluid flows will result: $Q(t) \in \{0,\ 0.78,\ 1.61,\ 2.39\}$ l/min. A similar experiment for a 350 MPa setup (measurement E-7) is given in the Appendix A.1. The plots of Figure 4.17 show input pressure trend, induced overall fluid flow and cutting head switching pattern for simulation and measurement for an entire switching cycle.

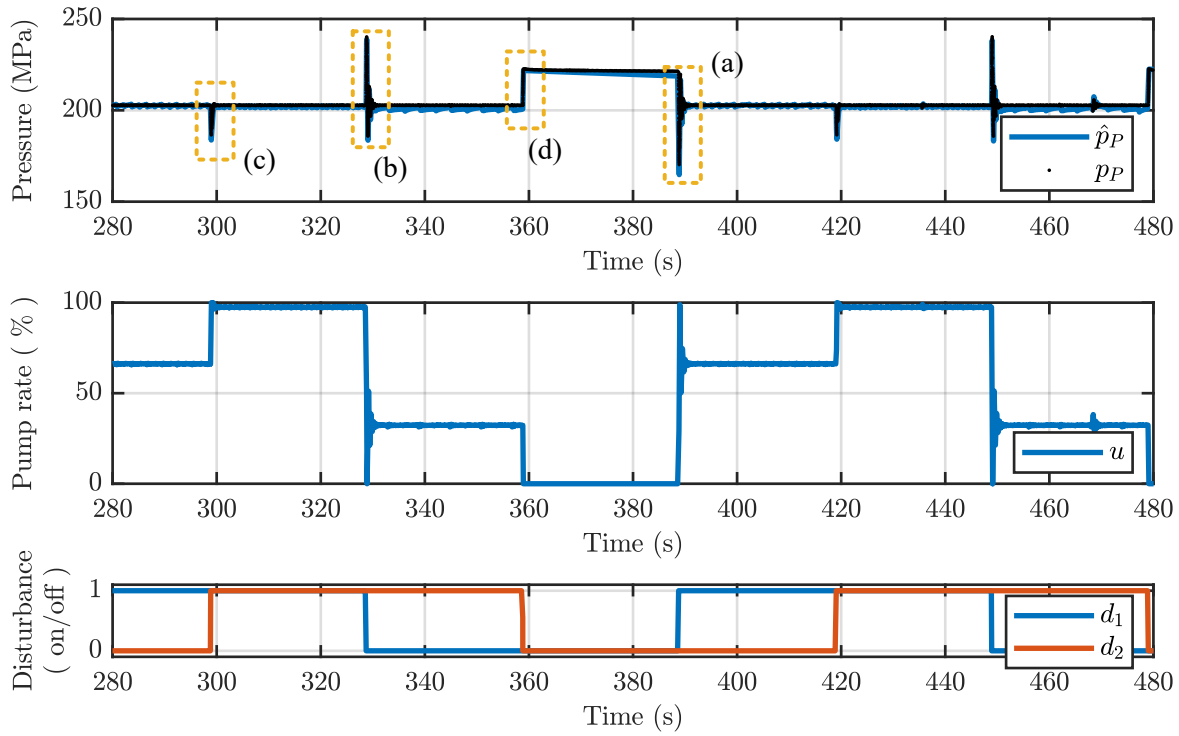

Figure 4.17 – Overview of experiment E-4, considering a 1 pump - 2 cutting head setup at 200 MPa with different nozzle sizes: pressure trend $p_P(t)$ and pump rate $u(t)$ due to switching pattern $d(t)$ for selected switching cycles.

Zoomed-in plots for every measurement position are presented in the subsequent plots, when first opening cutting head 1, followed by the opening of cutting head 2 and then closing head 1, followed by the closing of head 2. The plots of Figure 4.18 show the zoom-in for opening and closing of cutting head 1 (a/b), as well as for opening and closing of cutting head 2 (c/d). The input and system pressures are given in the first plot, both output pressures in the second plot and the corresponding switching pattern in the third plot.

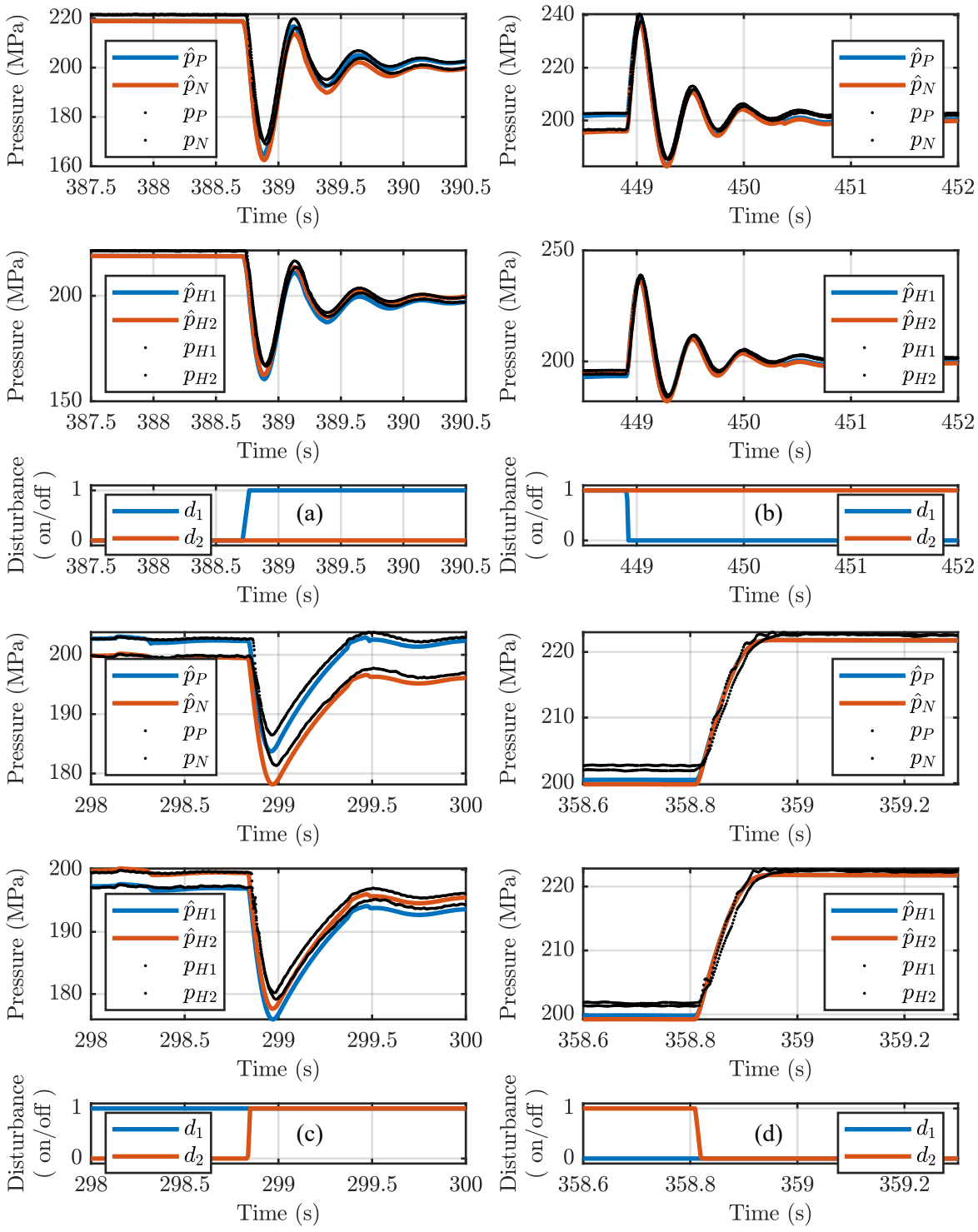

Figure 4.18 – Zoom-in pressure trends of the 1 pump - 2 cutting head setup at 200 MPa: opening of cutting head 1 (a) and closing of cutting head 1 (b), as well as opening of cutting head 2 (c) and closing of cutting head 2 (d).

Contour cutting: symmetric cutting heads

A continuous operating point of 200 MPa pressure is chosen. Two cutting heads will open and close alternately with a phase shift of 90°. Considering the measurement E-9, both cutting heads hold a nozzle of 0.25 mm inner diameter. When combining all possible switching states, four different fluid flows will result: $Q(t) \in \{0,\ 1.16,\ 1.17,\ 2.33\}$ l/min. A similar experiment for a 350 MPa setup (measurement E-11) is given in the Appendix A.1. The fluid flow differs slightly between each nozzle, due to the asymmetric network configuration, which causes different pressure losses along each piping section. The plots in Figure 4.19 show input pressure trend, induced overall fluid flow and cutting head switching pattern for simulation and measurement of an entire switching cycle.

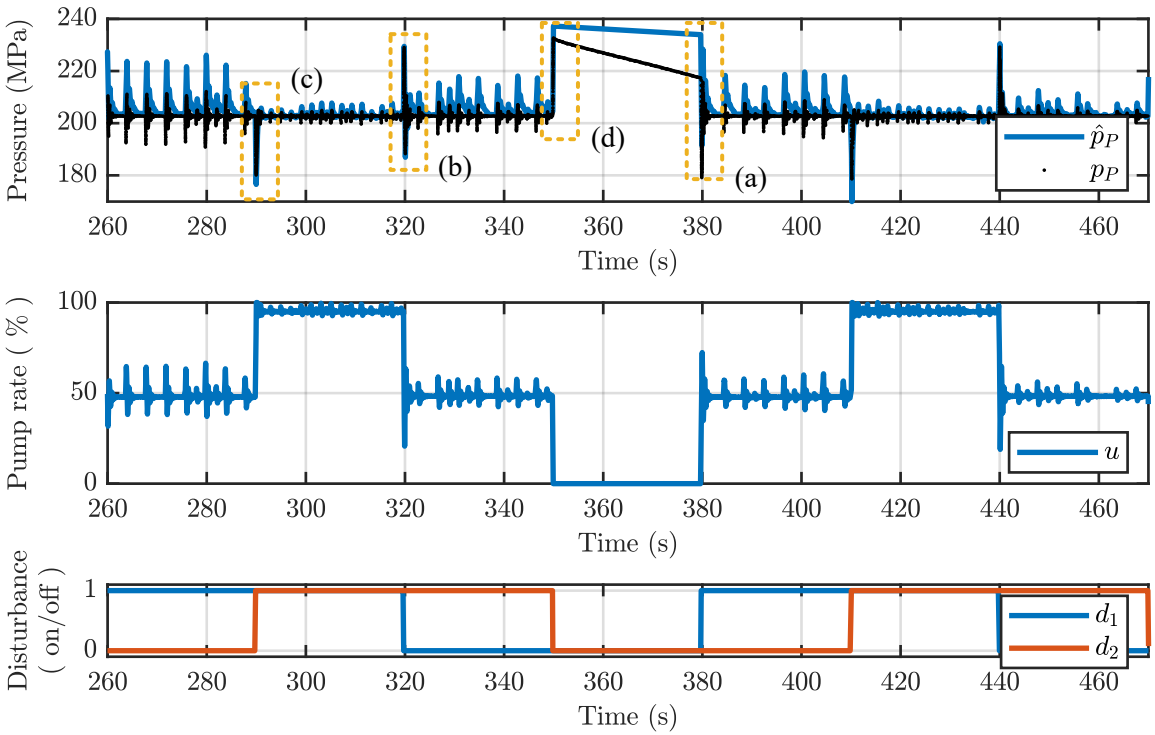

Figure 4.19 – Overview of experiment E-9, considering a 1 pump - 2 cutting head setup at 200 MPa with nozzles of the same size: pressure trend $p_P(t)$ and pump rate $u(t)$ due to switching pattern $d(t)$ for selected switching cycles.

Zoomed-in plots for every measurement position are given in the subsequent plots, when first opening cutting head 1, followed by the opening of cutting head 2 and the closing of head 1, followed by the closing of head 2. The plots of Figure 4.20 show the zoom-in for opening and closing cutting head 1 (a/b), as well as for opening and closing cutting head 2 (c/d). The input and system pressures are given in the first plot, both output pressures in the second plot and the corresponding switching pattern in the third plot.

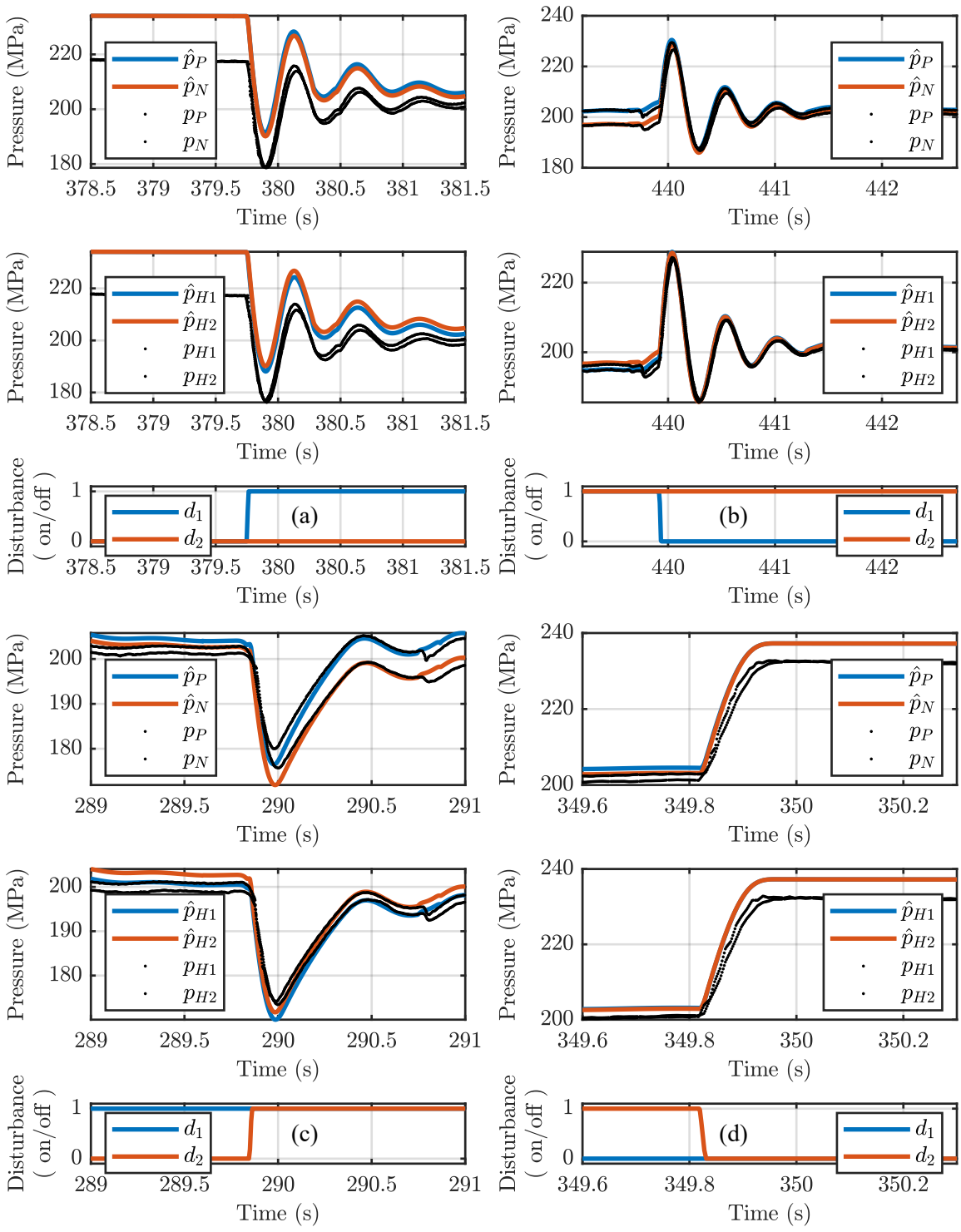

Figure 4.20 – Zoom-in pressure trends of the 1 pump - 2 cutting head setup trend at 200 MPa: opening of cutting head 1 (a) and closing of cutting head 1 (b), as well as opening of cutting head 2 (c) and closing of cutting head 2 (d).

Summary for 1 pump configurations

Contour cutting: the above section investigates the contour cutting at 200 MPa operating point, applied on the topologies (c) Symmetric network and (d) Asymmetric network. It considers extended topologies, including the switching of two cutting heads. The topology (b) Long piping has been initially introduced, see Appendix A.1. This basic topology can be considered as a reference, when switching a single cutting head. Table 4.10 compares the *rmse* for the residuals between measured and simulated data for the experiments with a single cutting head. Table 4.11 provides the *rmse*, considering the experiments with two cutting heads. The residuals have been evaluated for a period of 2 seconds, when switching a cutting head. Thus, each column corresponds to a zoomed-in plot, where each row provides a measurement position. Supplementary measurements and simulations have been obtained at an operating point of 350 MPa pressure. Also these results are summarized in the Tables 4.10 - 4.11 and discussed in the Appendix A.1.

Table 4.10: *rmse* (MPa) to compare the different experiments, derived for contour cutting with a single cutting head.

Measurement	Pos.	Fig. (a) $d \to 0$	Fig. (b) $d \to 1$	
B-4	p_P	2.5477	1.1286	
((b) Long piping)	p_N	2.4082	1.9424	(Appendix A.1)
(200 MPa)	p_H	2.4117	1.9281	
B-7	p_P	15.8584	6.0390	
((b) Long piping)	p_N	17.5059	6.1853	(Appendix A.1)
(350 MPa)	p_H	16.6050	6.2981	

In general, the simulated pressure trends follow the measured dynamics, for the switching of different cutting heads at various network position, with reasonable accuracy. The amplitude of disturbance varies with respect to the cutting head configuration, causing the pump to run on its entire operating range. Whenever all cutting heads shut close, the system reaches a pure integral behaviour and becomes very sensitive of any change of input fluid flow. Complementary, it is recognized that the cutting head is not able to entirely shot close. Thus, in real application, a small output flow remains that causes a steady pressure loss (see Figure 4.20 (a/d)). The simulations remain about their static pressure as the idealized cutting head model does not consider any effects of leakages. This results in an increased *rmse*. Referring to the basic topologies (Table 4.10), a relative error of about 1% is observed, when opening a cutting head ($d \to 1$) at 200 MPa. The error increases to 2%, for the 350 MPa operating point, and it becomes further increased to above 4%, when closing a cutting head ($d \to 0$). The relative error for the extended topologies (Table 4.11) range between 0.3 - 0.7%, insofar as these unfavourable cases for closed cutting heads are not evaluated. In addition, the cutting head will close with a time delay of nominal 144 ms and open with 45 ms delay. These delays can vary within a standard deviation of about 8 and 2.5 ms, respectively, as investigated in the system description (see Chapter 2). This deviation can cause varying residuals, when a cutting head is switching far off the nominal delay time.

Table 4.11: *rmse* (MPa) to compare the different experiments, derived for contour cutting with asymmetric and symmetric cutting heads.

Measurement	Pos.	Fig. (a) $d_1 \to 1$ $d_2 = 0$	Fig. (b) $d_1 \to 0$ $d_2 = 1$	Fig. (c) $d_1 = 1$ $d_2 \to 1$	Fig. (d) $d_1 = 0$ $d_2 \to 0$	
E-4	p_P	2.3083	2.2394	1.2013	0.7246	
((c) Sym. network)	p_N	2.9671	2.5961	1.4402	0.6662	
(200 MPa)	p_{H1}	2.8849	2.5689	1.4331	0.5950	
	p_{H2}	2.2483	2.2453	1.2345	0.5925	
E-7	p_P	2.8172	2.2289	4.1477	1.0991	
((c) Sym. network)	p_N	1.4212	2.5854	2.2301	0.3928	(Appendix A.1)
(350 MPa)	p_{H1}	2.1638	2.3143	3.0765	0.6746	
	p_{H2}	1.5375	2.3619	2.3801	0.5502	
E-9	p_P	6.0825	0.4364	1.2065	5.0967	
((d) Asym. network)	p_N	6.7886	1.1651	1.3519	5.3109	
(200 MPa)	p_{H1}	6.7740	1.2433	1.3076	5.4195	
	p_{H2}	7.1273	0.7716	1.2476	5.2175	
E-11	p_P	2.6541	1.0427	1.6741	10.4430	
((d) Asym. network)	p_N	2.6247	1.5006	1.7329	11.2671	(Appendix A.1)
(350 MPa)	p_{H1}	2.7952	1.6923	1.8193	10.9516	
	p_{H2}	2.3882	1.3909	1.6246	10.9348	

On the other hand, the high-pressure network becomes frequently disturbed by the switching behaviour of check-valves. This causes the pressure to decrease or increase rapidly, since the produced overall fluid flow of the pump is no longer in balance with the consumed fluid flow of the cutting head, see periodic spikes in Figure 4.19. The pump will adjust its fluid flow, as fast as possible, to compensate this disturbance, induced by a pumping chamber itself. Simulations will not reproduce this check-valve hysteresis, as the idealized pumping chamber model considers a simple switching function (see Chapter 3). The hysteresis appears to occur by incidence, for yet unknown fluid flow conditions. The check-valves seem less sensitive for experiments using large nozzles, as it is the case for measurements at 200 MPa operating pressure. However, it becomes very sensitive and the simulations perform inaccurate, when considering the 350 MPa experiments (see Appendix A.1). The check-valve hysteresis will be discussed later in this section.

A wide pressure range can be investigated for ramping up and down a pump to its operating pressure (0 MPa $\to$ 200 MPa and 0 MPa $\to$ 350 MPa), as shown in Appendix A.1. An offset between simulations and measurements is observed, for pressures below 100 MPa, which decreases for higher pressures. As long as a pump operates apart from the configured operating pressure, its pumping units are inadequately synchronized. This induce additional pressure fluctuations as a consequence of the phase-shifted pump operation. In this case, the check-valve switching behaviour is well reproduced by means of simulations.

The fluid flow resistance characterizes the pressure loss for a piping section, using a single parameter model. This seems insufficient for a wide pressure range, especially the residuals increase for high fluid flow rates. This effect scales for an increased network size, hence the simulation accuracy for a long piping becomes worse. Comparing the experiments (Table 4.10),

derived from basic topologies, with the results (Table 4.11), considering extended topologies, shows an increased *rmse*. As a consequence, the modelling could be improved by introducing a more complex description of the fluid flow resistance. It is further expected, that any wear of the nozzles inner diameter will cause a deviation of the resulting steady-state pressure. Since the model is parametrized for the nominal nozzle diameter, the residuals between measurement and simulation will increase with respect to the operating hours.

Cavity cutting: the Appendix A.1 shows, complementary to the contour cutting application, results for cavity cutting at 200 MPa operating point. These are equally applied on the topologies (b) Long piping and (c) Symmetric network. This basic topology is again considered as a reference, when switching a single cutting head. The Table 4.12 compares the *rmse* for the residuals between measured and simulated data of the experiments with a single cutting head. The Table 4.13 provide the *rmse* considering the experiments with two cutting heads. The residuals have been evaluated for a period of 3 switching cycles. A column corresponds to a zoomed-in plot, where a row provides a measurement position.

Table 4.12: *rmse* (MPa) to compare the different experiments, derived for cavity cutting with a single cutting head.

Measurement	Pos.	Fig. (a) $d = \{0,1\}$	Fig. (b) $d = \{0,1\}$	
B-5	p_P	2.5403	2.0139	
((b) Long piping)	p_N	4.1987	4.1190	(Appendix A.1)
(200 MPa)	p_H	4.1991	4.1420	

Table 4.13: *rmse* (MPa) to compare the different experiments, derived for cavity cutting with asymmetric and symmetric cutting heads.

Measurement	Pos.	Fig. (a) $d_1 = \{0,1\}$ $d_2 = 0$	Fig. (b) $d_1 = \{0,1\}$ $d_2 = \{0,1\}$	Fig. (c) $d_1 = 0$ $d_2 = \{0,1\}$	
E-5	p_P	2.9488	4.8987	4.7719	
((c) Sym. network)	p_N	3.7786	5.7320	5.1903	(Appendix A.1)
(200 MPa)	p_{H1}	3.8152	5.6843	5.0483	
	p_{H2}	3.2608	4.4720	4.6131	

It is remarkable how precisely the simulated pressure trends follow the measured trends for every measurement position, even for pressure fluctuations of about 100 MPa in amplitude. Considering the basic topology, a relative error of about 1% has been found, for a measurement position at the pump outtake, where the error reaches about 2%, at the network and cutting head positions (see Table 4.12). The errors are slightly increased for the extended topologies and reach from 1.5 - 3% (see Table 4.13).

The disturbing check-valve hysteresis does not occur for transient pressure trends, but seems sensitive for steady-state operation around desired operating point. However, the closing of all cutting heads again induce pressure overshoots, followed by a continuous pressure loss. The first effect is sensitive for any mismatch of the input fluid flow that may cause a decreased simulation accuracy, while the second effect is not taken into account for modelling.

Check-valve hysteresis

All simulation models are configured for an optimal phase-shifted pump operation. Thus, any pressure fluctuation due to switching check-valves will disappear in simulation, when reaching the operating pressure. In reality, some hysteresis can be observed for the switching of the check-valves, causing pressure fluctuations. Taking this hysteresis into account can improve the simulation accuracy. Nevertheless, the occurrence of this effect remains unpredictable.

Observing the pressure trends of measurements E-9 and E-11, as well as comparing these with simulations, derived from nominal model, show the effect of check-vale hysteresis. In the plots of Figure 4.21 (a), it is seen that the model follows the excitation given by the phase-shifted pump operation, but possible pressure losses are missing. Hence, the simulated pressure trend lies above the measurement for the time samples between 436 and 438 seconds. Alternatively, the plots of Figure 4.21 (b) show the pressure trends, when taking a possible check-valve hysteresis into account. The simulation model applies thereby possible pressure losses, but that results in a deterioration, whenever no hysteresis occurs, see time samples between 438 and 440 seconds. The same behaviour has been observed at 350 MPa pressure, using the same model, see the plots of Figure 4.22 (a) for nominal model and (b) considering check-valve hysteresis.

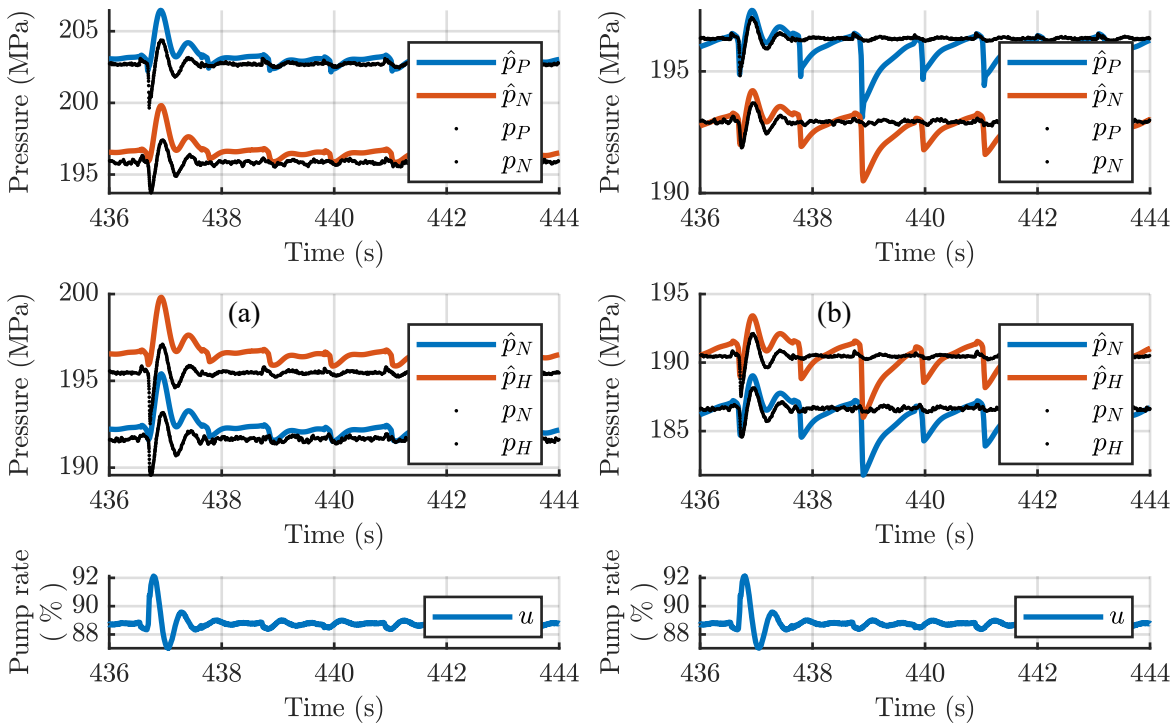

Figure 4.21 – Check-valve hysteresis at 200 MPa operating pressure of the 1 pump - 1 cutting head setup: considering optimal phase-shift (a) and simulated hysteresis (b).

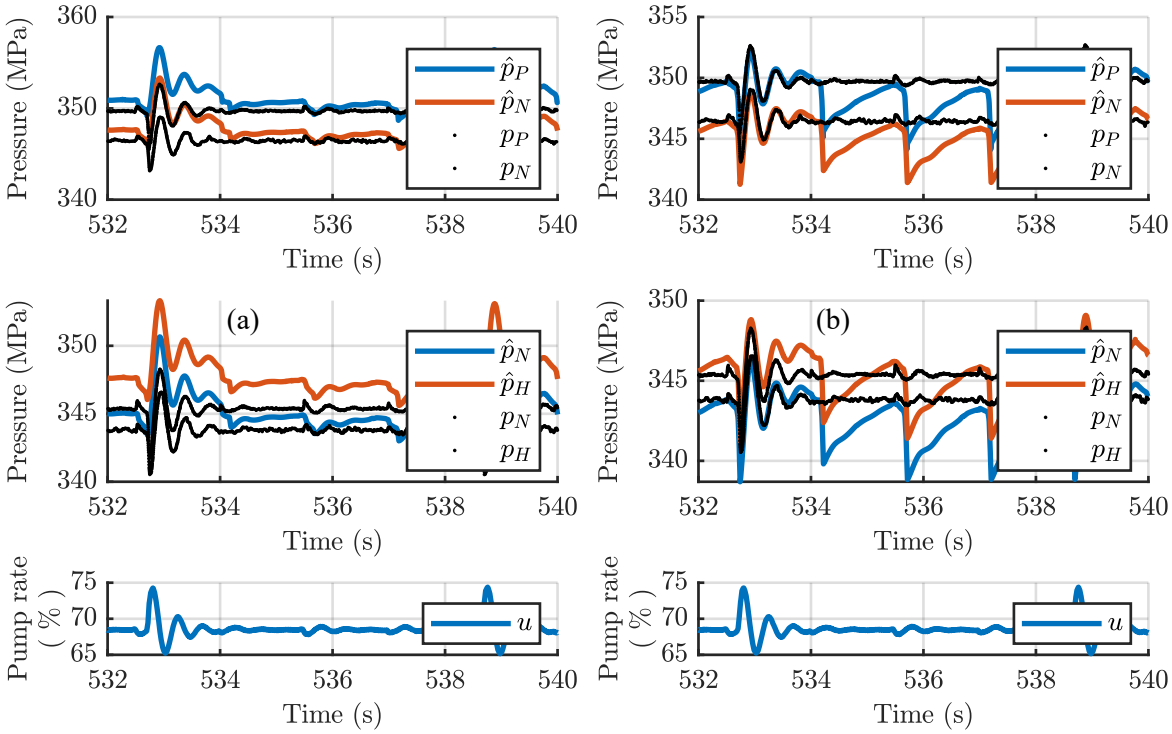

Figure 4.22 – Check-valve hysteresis at 350 MPa operating pressure of the 1 pump - 1 cutting head setup: considering optimal phase-shift (a) and simulated hysteresis (b).

4.3.3 High-pressure network model validation (2 pump configuration)

This section investigates the simulation accuracy for more complex high-pressure networks, when applying the graph-based modelling methodology for configurations with two high-pressure pumps. The pressure generation in a high-pressure network becomes again disturbed, when switching different cutting heads in open and close position. Both cutting heads remain locally coupled, where two decentralized high-pressure pumps are taken into account. Both pumps are in closed-loop control, aiming at a constant reference pressure of 200 MPa. For this reason, pump 1 holds the PI controller (6.47), whereas pump 2 has by default the PI controller (6.48), see Section 6.4. The high-pressure pumps will then adjust its induced overall fluid flow, such as to compensate any disturbances. Thus, a wide variety of fluid flow rates from 0 to 2.45 l/min per pump will be obtained, depending on the switching state of the cutting heads. Here, the graph-based modelling methodology has been applied to model network topologies, which interconnect two high-pressure pumps with two cutting heads.

This model validation considers two specific network topologies, for which measurement data have been derived from the high-pressure test bench. Both, the topologies **(e) Symmetric distributed** and **(f) Asymmetric distributed**, interconnect two cutting heads at a local position. Different measurements have been obtained for simulation and experimental validation, as listed in Table 4.14. The first 3 distributed measurements (**D-1,2,3**), considering the symmetric distributed network topology, include two pumps and two cutting heads, where the piping from each pump to the cutting heads have the same length. The last 3 distributed measurements (**D-4,5,6**) consider the asymmetric distributed network topology, where the piping from a pump to the cutting heads have different lengths. For all measurements, both cutting heads have been symmetrically configured, with identical nozzles of 0.2 mm inner diameter. This allows for distin-

guishing the effects due to the network topology and for investigating the effects from coupling of two pumps.

Table 4.14: Excerpt of experiments for use case 3: measurements derived with different test bench setups and used for model validation.

Meas.	Topology	Pressure (MPa)	Nozzzle 1 ⌀(mm)	Nozzzle 2 ⌀(mm)	Switching pattern
D-1	(e) Sym. dis.	200	0.2	0.2	Strip.
D-2					Contour
D-3					Cavity
D-4	(f) Asym. dis.	200	0.2	0.2	Strip.
D-5					Contour
D-6					Cavity

All experiments take different switching patterns into account. The measurements D-1 and D-4 investigate the stripping process, where all cutting heads remain open. The measurements D-2 and D-5 investigate contour cutting. Here, a cutting head will exemplarily open, for a cutting period of 60 seconds, followed by a hold period in closed position, for another 60 seconds. Regarding the distributed measurements, the other cutting head will remain in open position for all time. The measurements D-3 and D-6 investigate cavity cutting, where the switching pattern is modified to realize an on/off period of 0.5 seconds. Consequently, a large variety of measurement data have been obtained to validate the high-pressure network models, derived by the graph-based modelling methodology.

The experimental setup implemented for model validation remains the same as already illustrated in the diagram of Figure 4.16. The cutting heads open and close with respect to the predefined switching pattern, as given by the disturbance signals $d_m(t) = [d_1(t), d_2(t)]$. A decentralized low-level control will then adjust the pump rates of each high-pressure pump, using the control signal $u_n(t) = [u_1(t), u_2(t)]$, to obtain the desired reference pressure $p_s(t)$. Again, different locations have been defined to measure the pressure states at the test bench. $p_{Pn}(t)$ denotes the input pressures at a pump outtake, where $n \in \{1, 2\}$ refers to the first and second high-pressure pump, respectively. $p_N(t)$ gives the pressure at the network junction and $p_H(t)$ gives the pressure between the two locally coupled cutting heads. The induced fluid flows $Q_n(t) = [Q_{n1}(t), Q_{n2}(t)]$, of each piston, are again estimated by measuring the piston displacements. Measured data $p_x(t) = [p_{P1}(t), p_{P2}, p_N(t), p_H(t)]$ are then compared to the simulated pressure states $\hat{p}_x(t) = [\hat{p}_{P1}(t), \hat{p}_{P2}(t), \hat{p}_N(t), \hat{p}_H(t)]$ to validate the simulations for different measurement positions. Data acquisition and simulations are identically configured, as introduced in the previous section.

Contour cutting: symmetric and asymmetric distributed pumps

A continuous operating point of 200 MPa is chosen. The second cutting head will open and close, while the first cutting head remains open. Both cutting heads hold a nozzle of 0.2 mm inner diameter. For this configuration, two different fluid flows will result: $Q(t) \in \{0.78,\ 1.56\}$ l/min. The plots of Figure 4.23 and Figure 4.24 show the input pressure trends, induced overall fluid flows and cutting head switching pattern, considering an entire switching cycle for the symmetric and asymmetric topology of measurements D-2 and D-5, respectively.

Zoomed-in plots for the switching of cutting head 2 is given in the subsequent plots, when first closing then opening cutting head 2. The plots of Figure 4.25 and Figure 4.26 show the zoom-in for closing (a) and opening (b) cutting head 2 for the symmetric and asymmetric topology. The input pressures are given in the first plot, the network and output pressure is shown in the second plot.

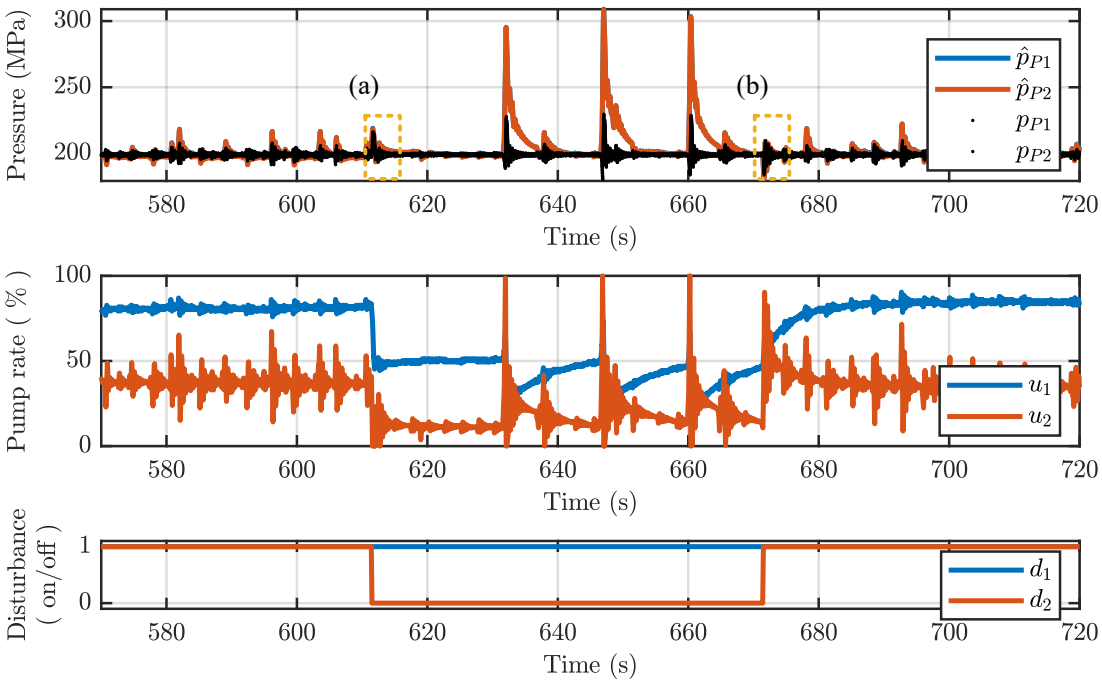

Figure 4.23 – Overview of experiment D-2 for a 2 pump - 2 cutting head setup with symmetric topology: pressure trend $p_P(t)$ and pump rate $u(t)$, due to switching pattern $d(t)$ for selected switching cycles.

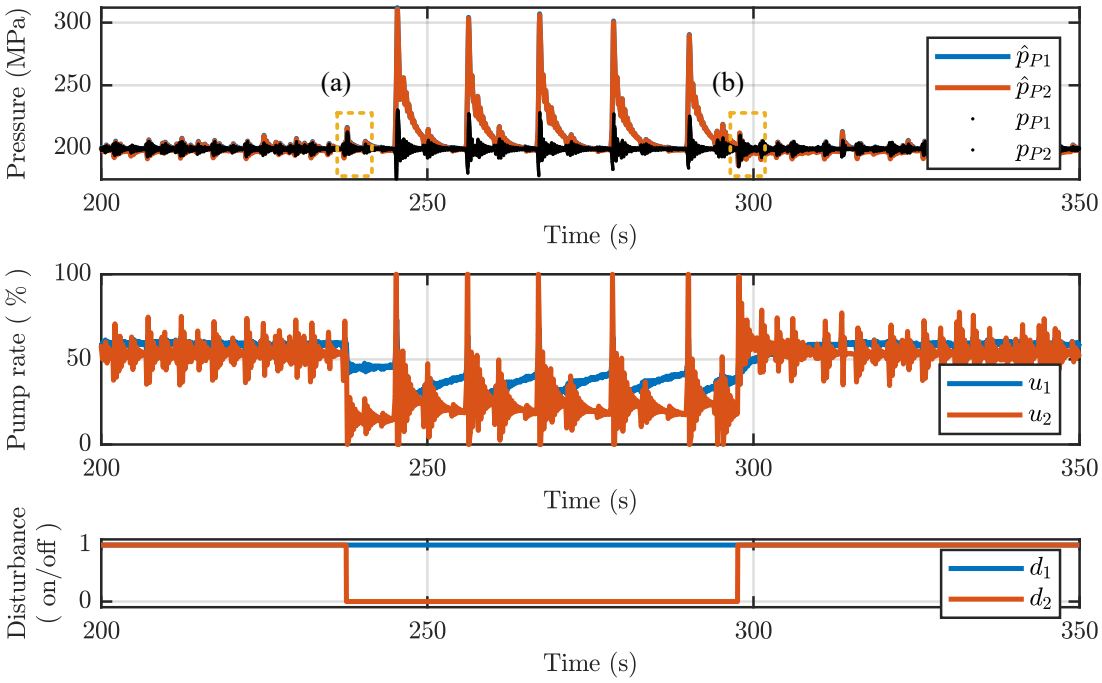

Figure 4.24 – Overview of experiment D-5 for a 2 pump - 2 cutting head setup with asymmetric topology: pressure trend $p_P(t)$ and pump rate $u(t)$, due to switching pattern $d(t)$ for selected switching cycles.

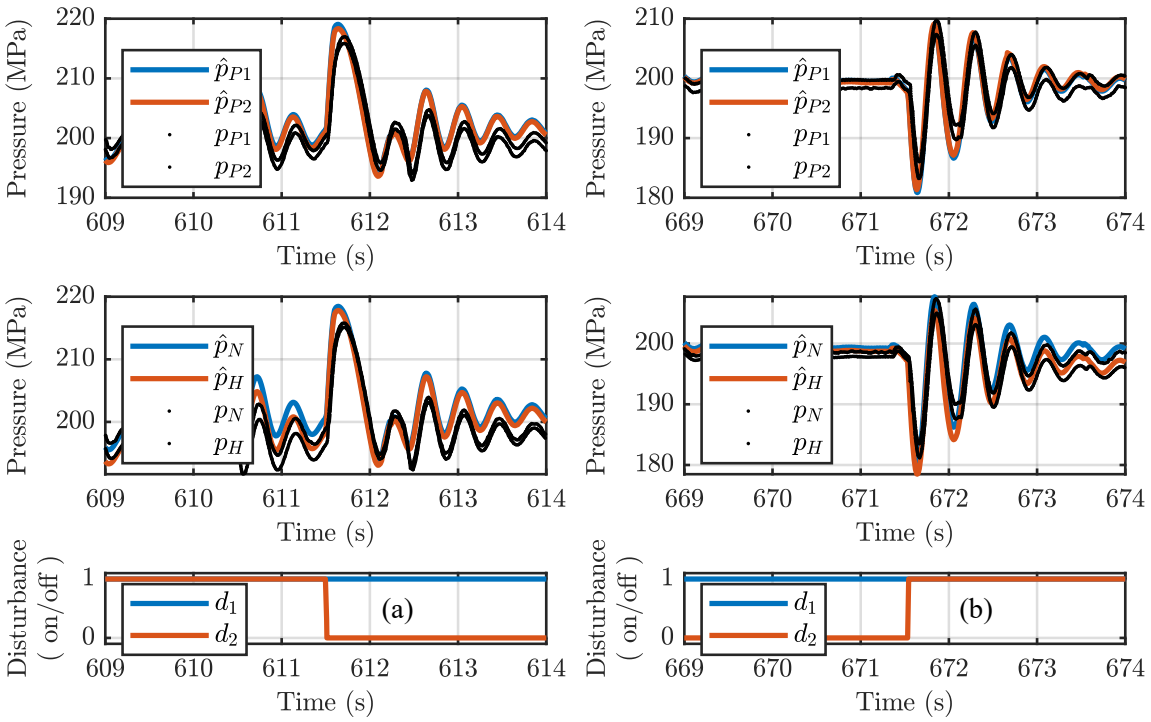

Figure 4.25 – Zoom-in pressure trends of a 2 pump - 2 cutting head setup with symmetric topology: opening of cutting head 1 (a) and closing of cutting head 1 (b).

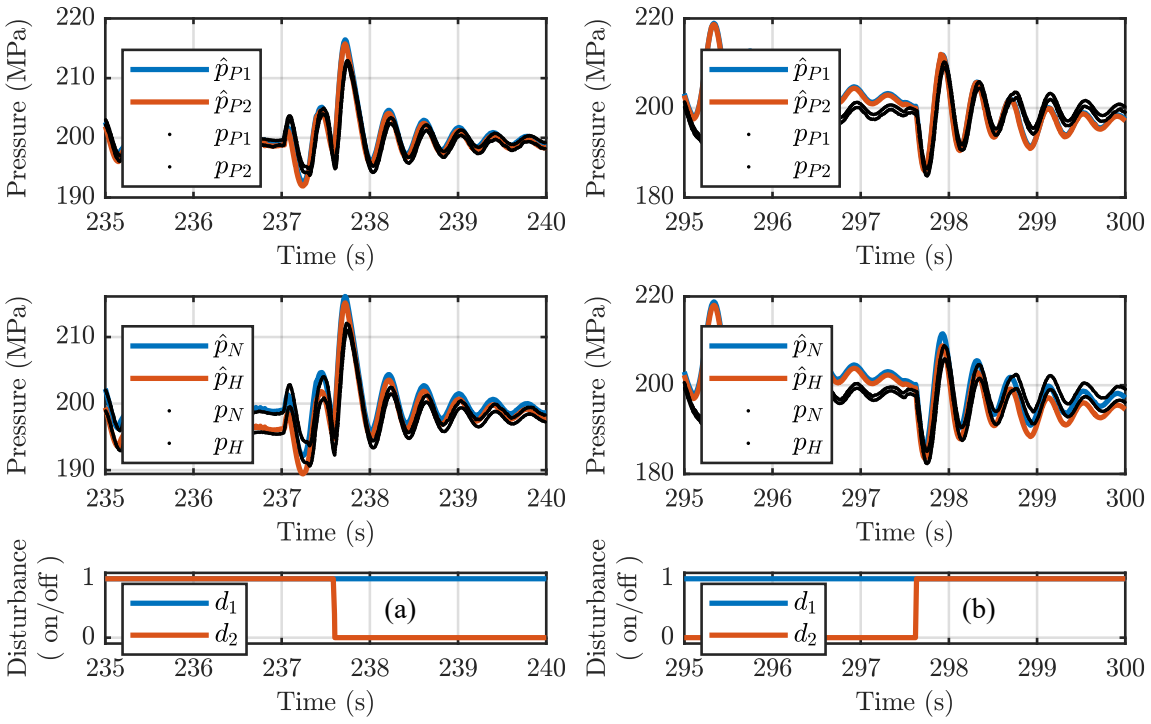

Figure 4.26 – Zoom-in pressure trends of a 2 pump - 2 cutting head setup with asymmetric topology: opening of cutting head 1 (a) and closing of cutting head 1 (b).

Summary for 2 pump configurations

Contour cutting: this section investigated the contour cutting at 200 MPa operating point, applied on the topology (e) Symmetric distributed and (f) Asymmetric distributed. Table 4.15 compares the *rmse* for the residuals between measured and simulated data. The residuals have been evaluated for a period of 2 seconds, when switching a cutting head. A column corresponds to a zoomed-in plot, where a row provides a measurement position.

Table 4.15: *rmse* (MPa) to compare the different experiments, derived for contour cutting with asymmetric and symmetric pumps.

Measurement	Pos.	Fig. (a) $d_1 = 1$ $d_2 \to 0$	Fig. (b) $d_1 = 1$ $d_2 \to 1$
D-2	p_{P1}	3.4457	2.1907
((e) Sym. distributed)	p_{P2}	2.6469	2.5147
(200 MPa)	p_N	3.0621	2.0327
	p_H	3.3019	2.2074
D-5	p_{P1}	2.1502	2.3855
((f) Asym. distributed)	p_{P2}	1.5301	3.1949
(200 MPa)	p_N	1.9381	2.4712
	p_H	2.1375	2.5016

The simulated pressure trend follows the measurement with reasonable accuracy, while reproducing the varying water consumption due to the switching of cutting heads. However, the model fails for disturbances that originate from the pumping chambers. It is observed, that the check-valve malfunction becomes tremendous for small fluid flow rates. The pump rate equilibrium becomes entirely disturbed. The low-level control increases the induced fluid flow to compensate any resulting pressure losses. Since, the simulation model is not capable to predict any check-valve malfunction, the increased fluid flow cause the model to predict non-existing pressure overshoots, see Figure 4.23 and 4.24. Nonetheless, the simulations aim to reproduce those pressure fluctuations in a high-pressure network, which are induced by the switching of cutting heads. These fluctuations are well reproduced, see Figures 4.25 and 4.26. The resulting *rmse* are close to the values, as previously reported for a single pump configuration (see Table 4.11). This results in a relative error from about 1 - 2%. But again, the deviation for an expected pressure loss will increase for long piping sections. The pressure loss will be further discussed below.

Cavity cutting: the Appendix A.2 shows, complementary to the contour cutting application, results for cavity cutting at 200 MPa operating point, again applied on the topologies (e) Symmetric distributed and (f) Asymmetric distributed. Table 4.16 provides the *rmse*, considering the experiments with two cutting heads. The residuals have been evaluated for a period of 3 switching cycles. A column corresponds to a zoomed-in plot, where a row provides a measurement position.

The simulated pressure trend reproduces the measured transient behaviour with desired accuracy, considering large pressure fluctuations. But an offset is observed between the switching periods, which disappears whenever a switching occurs. This offset concerns the simulated pressure trends for every measurement position, with respect to the asymmetric distributed network, and causes the relative error to reach almost 5%.

Table 4.16: *rmse* (MPa) to compare the different experiments derived, for cavity cutting with asymmetric and symmetric pumps.

Measurement	Pos.	Fig. (a) $d_1 = 1$ $d_2 = \{0, 1\}$	
D-3	p_{P1}	3.0554	(Appendix A.2)
((e) Sym. distributed)	p_{P2}	3.3177	
(200 MPa)	p_N	2.9057	
	p_H	3.1889	
D-6	p_{P1}	9.0982	(Appendix A.2)
((f) Asym. distributed)	p_{P2}	7.6913	
(200 MPa)	p_N	8.8256	
	p_H	9.0329	

Starting up procedure

A single high-pressure pump is not capable to reach the desired operating pressure for an increased water consumption of the defined cutting head configuration. The pump will run at its upper limit. When starting the second pump, both pumps will obtain an individual pump rate equilibrium to attain the desired operating pressure. The simulations allow for evaluating the pressure generation in a pumping chamber of each pumping unit. The plots of Figure 4.27 and Figure 4.28 show the estimated pressures for every pumping chamber considering the symmetric and asymmetric topology of measurements D-1 and D-4, respectively. It is shown that pressure fluctuations, measured at the pump outtake, correspond to the switching between pumping units. The low-level control of each high-pressure pump is compensating these fluctuations, resulting in a varying pump rate.

As soon as desired operating pressure is obtained, pressure fluctuations, due to the switching between pumping units, should become small. However, the check-valves from the second pump have malfunctions, which require a large control effort $u_2(t)$. The locally induced fluctuations become partially compensated by means of control. Nevertheless, remaining fluctuations propagate along the high-pressure network and can be observed at the first pump, which responds with control effort $u_1(t)$.

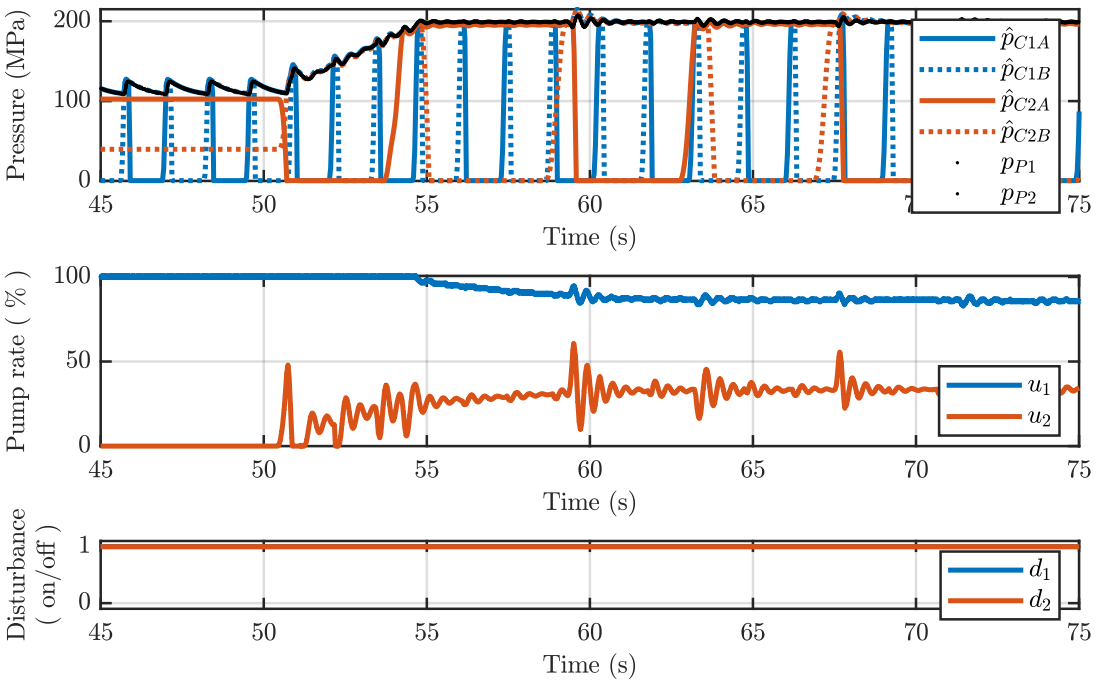

Figure 4.27 – Start up of experiment D-1, considering a 2 pump - 2 cutting head setup at 200b MPa: simulated pressure trends for each pumping chamber, compared to measured pressure at pump outtake, and resulting pump rates for the symmetric distributed network.

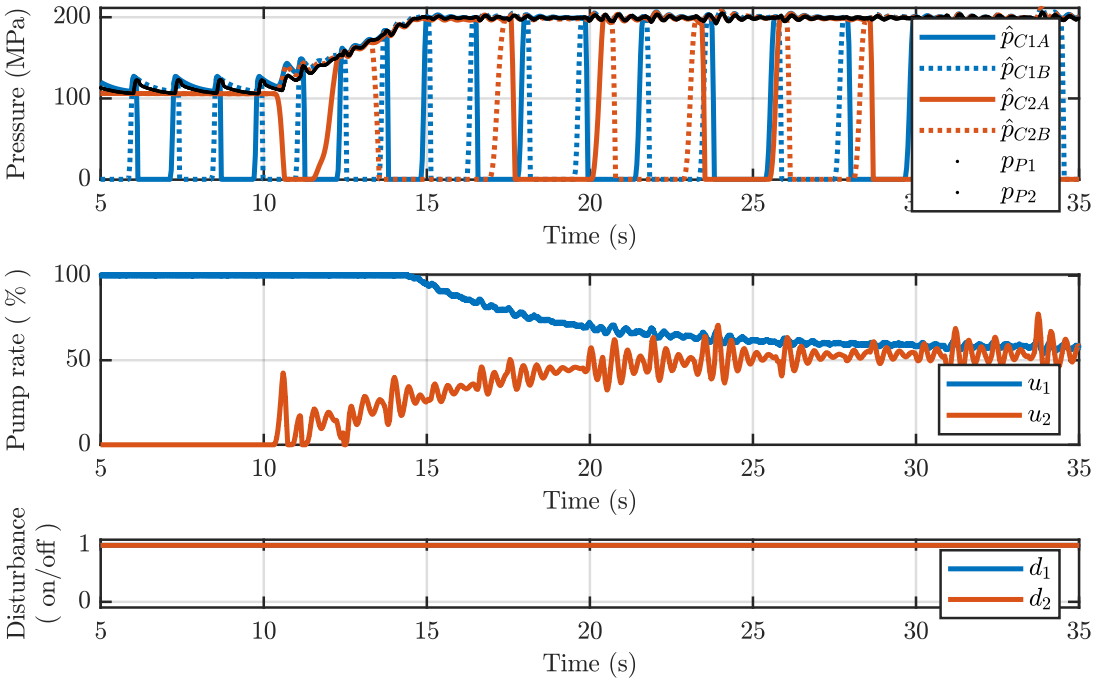

Figure 4.28 – Start up of experiment D-4, considering a 2 pump - 2 cutting head setup at 200 MPa: simulated pressure trends for each pumping chamber, compared to measured pressure at pump outtake, and resulting pump rates for the asymmetric distributed network.

4.4 Conclusion

This chapter implemented a framework in *MATLAB Simulink* to describe generalized high-pressure networks. The obtained simulation toolbox can be used by the industrial partners to design and optimize future waterjet facilities. This toolbox has been applied to the different network topologies, as introduced in Section 2.2. This results in high-pressure network models, which are useful for numerical simulations. So far, 6 network topologies have been investigated, using the graph-based modelling methodology. Each network model has been then experimentally validated for 2 nozzle configurations and 2 switching patterns, using measurements at 2 operating pressures.

Another contribution of this chapter validates the different network models with experimental data, using the high-pressure test bench. It has been found that modelling a constant fluid density cause a steady-state pressure error and a constant bulk modulus is responsible for a divergent transient behaviour. Therefore, an improved model accuracy has been achieved for a desired pressure range of 100 to 400 MPa, when a variable fluid compressibility is considered.

Representative use cases have been selected, showing the abilities to simulate the pressure propagation for different network positions. The presented validation obtained excellent results with desired accuracy, considering different measurement positions. Nonetheless, increasing residuals have been reported, when operating the test bench on low pump rates. To improve this circumstance, the friction losses for small fluid flow velocities should be further investigated.

It has been further recognized that the check-valve switching is very sensitive to any pressure mismatches. An accurate switching hysteresis, therefore, will reduce the resulting simulation residuals. Pressure losses or overshoots have been observed, if any trajectory imperfectly synchronizes the pistons. The derived model reproduces this behaviour and can be used to improve the pressure generation by means of optimized position trajectories. The check-valve malfunction complicates to accomplish all experiments and interferes the model validation process.

Using the proposed modelling methodology, it is possible to flexibly model various network topologies with reasonable effort. This becomes advantageous when modelling various network topologies, to optimize entire waterjet facilities, and when evaluating novel control strategies for energy efficient waterjet machining. High-pressure network models of increased complexity have been introduced in Chapter 7, which allow for evaluation of distributed high-level managing. Further work should continue to validate the simulation toolbox, taking more complex high-pressure networks into account.

Part III

Control design

5

Robust decentralized low-level control

Contents

5.1 Introduction

Objectives

Electrically driven high-pressure pumps need a sophisticated control strategy. In fact, a precise control of coupled pumps is mandatory to avoid undesired interactions and a wide dynamic range is required to attenuate exogenous disturbances. Cutting heads induce pressure fluctuations, when switching on and off a waterjet with respect to an a priori unknown switching pattern. Any pressure fluctuation will degrade the cutting quality. Thus, a varying water consumption has to be compensated by means of the available high-pressure pumps. The control objective is further to guarantee a continuous steady-state pressure for a given pressure reference. Also pressure fluctuations, due to exogenous disturbances, has to be eliminated within limited control effort. Each pump, located at a different network subsection, requires to reject local pressure fluctuations with out destabilizing the overall high-pressure network. In addition, different types of parameter variations will affect a waterjet facility. It includes a wide pressure range and a varying workstation configuration, which consequently introduces non-linear dynamics. A waterjet facility involves significant uncertainties. This necessitates a suitable description for robust control design.

State of the art

Recent research work in the field of waterjet machining intends to improve cutting quality [Ahmed et al., 2018], and process efficiency [Averin, 2017]. Literature is found in related fields to deal with pressure generation and its control. Several papers in the automotive industry are investigating common rail injection systems: including high-pressure pump, common rail and injectors. This configuration is comparable to high-pressure systems for waterjet machining. In [Lino et al., 2007], a non-linear system model is used to derive a sliding mode controller, whereby pressure fluctuations are compensated with an additional solenoid valve. The design of a regulation mechanism to attenuate pressure pulsation more efficiently and its control with a time-varying model-based compensator is presented in [Gupta et al., 2011]. However, a high-pressure pump for waterjet machining has to attenuate pressure fluctuations without additional components, such as valves. A promising pressure disturbance rejection control is recently discussed in [Wang et al., 2016b]. It suggests an extended state observer-based controller and compares it with a PID control design. On the other hand, an extended state estimator, based on a non-linear pressure control algorithm, has been applied in [Kemmetmüller et al., 2010] to deal with unknown loads at axial piston pumps. Even though a hydraulic unit is used to control a piston pump, the experimental setup is similar to the high-pressure setup for waterjet machining. An even more exotic application for pressure generation is the so called free piston engine. For that, a mathematical model has been derived and the concept of trajectory-based non-linear feedforward control has been introduced in [Li et al., 2015]. However, the robust control of electrically driven high-pressure pumps seems poorly investigated.

Regarding a future waterjet facility as a high-pressure network that interconnects distributed high-pressure pumps with work stations, while considering an unknown network topology, motivates to investigate decentralized and robust control. The state of the art with respect to decentralized (a), distributed (b) and networked controls (c), as compared in the diagrams of Figure 5.1, distinguishes between large-scale and networked systems. A large-scale system includes numerous coupled system components, which are spread over a large spacial domain, e.g. power, water and traffic systems. A networked system involves collaborating or interacting participants, which are interconnected by means of a communication channel, e.g. vehicle platoons

and flight formations. Decentralized control aims to reduce the complexity of controller synthesis for large-scale systems. In contrast to centralized control design, a system is decomposed into subsystems (see [Bakule, 2014]). A decentralized controller K is then synthesized for each subsystem Σ. The most relevant classes of decomposed systems are the so called disjoint subsystems, overlapping subsystems and symmetric composite systems, see [Bakule, 2008] for details.

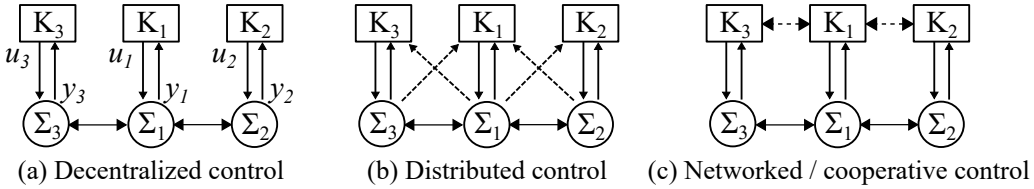

Figure 5.1 – Diagram for decentralized, distributed and networked control: a system is separated in subsystems to reduce the complexity of control design. Whereas decentralized control considers an independent controller per subsection, distributed control takes into account the state of neighbouring subsections and networked control enables a data exchange between controllers.

As a result of decomposition, the whole system is controlled by several independent controllers, whereby couplings between subsystems may degrade the control performance and affect stability. This drawback is addressed, when introducing robust control to large-scale systems. Thus, the concept of robust decentralized control for networked subsections as well as the concepts of distributed and networked control are prevalent starting points for further investigations.

Decentralized robust control: decentralized robust control of networked systems is discussed in [Iftar, 2013]. Subsystem models are used for local control design and a robustness bound is introduced, taking any coupling between interconnected subsystems into account. Robust decentralized control for large-scale systems is applied in [Benlatreche et al., 2008], considering overlapping subsystems. The degradation of performance in contrast to centralized control is investigated. Both approaches obtain stability regarding the overall system.

The design of decentralized robust PI controllers is presented in [Marquez et al., 2008]. Its extension to gain-scheduling is interesting to improve the robust control design for high-pressure pumps, meeting advanced performance requirements. A design framework for overlapping controllers is given in [Swarnakar et al., 2009]. It improves performance in contrast to simple PI control. Overall stability is obtained for non-linear systems under load variation. On the other hand, a synthesis for distributed control of networked systems is proposed in [Viccione et al., 2009], when describing time-varying uncertainties by means of a linear parameter-varying (LPV) system.

Distributed and networked controls: whereas some distributed control schemes allow for feedback values of neighbouring subsystems to be used for control, others consider communication links between decentralized controllers. These approaches aim at an improved performance in the case of strongly coupled subsystems. A distributed robust control for electrical power systems is discussed in [Dekker et al., 2010] and compared with model predictive control. Each controller exchange its subsystem state with neighbouring controllers. Interpreting the subsystems as uncertainties and improving the control performance, by employing an exchange of information, is presented in [Demir and Lunze, 2011]. A distributed control approach, generating a hierarchical architecture, is proposed in [Tang and Daoutidis, 2017]. This architecture represents the interconnection of subsystems, as employed for control.

Networked control considers communication channels between controllers or between controllers and subsystems, respectively. In both cases, control design concerns reliability and determinism, due to transport delays and packet loss. This allows for dealing with serious stability concerns. Many papers can be found to challenge these concerns, e.g. [Annaswamy et al., 2012], [Yu and Antsaklis, 2013], [Ma et al., 2014] and [Shu and Lin, 2014], while others consider event-based communication to improve network efficiency, e.g. [Stöcker and Lunze, 2013], [Zhang et al., 2014], [Sigurani et al., 2015] and [Abara and Hirche, 2017]. Networked control is excluded of the subsequent research work. Despite promising results in distributed control, it is in some instances conceivable for large-scale systems to manage the decentralized controllers with respect to global objectives and system constraints, e.g. optimizing the energy efficiency by reducing the overall control effort, balancing the load of actuators to avoid local actuator saturation etc.

Contribution

Since high-pressure networks include large plant perturbations, decentralized control requires to implement robustness for disturbances from neighbouring network sections. Taking the robust decentralized approach presented in [Marquez et al., 2008] and [Iftar, 2013] into account, H_∞ synthesis seems favourable to deal with these perturbations and disturbances. This work aims to employ H_∞ controller synthesis to obtain a robust control design for electrically driven high-pressure pumps. A contribution here is given, when introducing the detailed problem formulation and obtaining the interconnection system that represents a network subsection, interconnecting a decentralized high-pressure pump to cutting heads. This involves to derive a perturbed plant model, suitable for robust control design. The challenge is to handle the non-linear characteristics of high-pressure generation and to deal with the parameter uncertainties for different waterjet applications. Another contribution is given, when analysing the expected parameter variations and evaluating different uncertainty descriptions. The investigated parametric uncertainties will be lumped to unstructured uncertainties. This is expected to enhance the controller synthesis.

This chapter is structured as follows: Section 5.2 introduces the fundamental principles from the theory of H_∞ controller design. Section 5.3 presents the investigated high-pressure system and its non-linear plant model. A linearised model with reduced complexity is derived with respect to the varying parameters. For that, the high-pressure pump, interconnected to an unknown network subsection, will be described as a first order model and linearised on its operating point. The operating point is then considered as an additional uncertain parameter. Wide parameter variations cause a high complexity. Employing an unstructured uncertainty description lumps the parameter variations for various waterjet facilities, as shown in Section 5.4. Transforming the uncertainty model into standard $\Delta-$M form, by using upper linear fractional transformation, describes a perturbed plant model. This model will be implemented in the subsequent chapter for H_∞ controller synthesis. Further, weighting functions are defined to specify requirements on performance for disturbance rejection and to penalize the control effort with respect to actuator saturations. Shaping functions are defined to consider the dynamic range of exogenous input signals, such as measurement noise and switching disturbance.

5.2 H_∞ control design fundamentals

This section introduces notations and concepts valuable for robust control design and established in literature, such as [Skogestad and Postlethwaite, 2005] and [Gu et al., 2013]. All subsequent investigations refer to linear, time-invariant dynamic systems Σ, described by the continuous-time

state space description

$$\Sigma := \begin{cases} \dot{\mathrm{x}}(t) = A\mathrm{x}(t) + Bu(t) \\ y(t) = C\mathrm{x}(t) + Du(t) \ , \end{cases} \tag{5.1}$$

where $\mathrm{x}(t) \in \mathbb{R}^n$ is the state vector, $u(t) \in \mathbb{R}^m$ corresponds to the input vector and $y(t) \in \mathbb{R}^p$ denotes the output vector. Hence, the outputs $y(t)$ are measured to control the states $\mathrm{x}(t)$ to desired values, using the available inputs $u(t)$.

The transfer function representation

$$G(s) = C\left(s\mathrm{I} - A\right)^{-1} B + D \tag{5.2}$$

is derived, when applying Laplace transform to (5.1). This requires for the initial conditions $\mathrm{x}(t = 0) = 0$ and introduces the Laplace operator $s = j\omega$. The H_∞ controller synthesis is a frequency domain approach, thus, notation of the formalism will be given in terms of transfer functions.

5.2.1 Linear fractional transformation (LFT)

The linear fractional transformation (LFT) is a valuable concept for robust control design. It allows for transforming a perturbed plant into the $\Delta-$M configuration and transforms a feedback control system into P$-$K configuration. The first configuration is useful for robustness analysis, where the second configuration will be introduced for H_∞ controller synthesis.

$\Delta-$M configuration

The dynamic system (5.1) can be rearranged in a standard $\Delta-$M configuration [Skogestad and Postlethwaite, 2005], including the interconnection system M and the uncertainty block Δ. The block diagram of Figure 5.2 shows the interconnection system M and the uncertainty block Δ. The interconnection system holds the exogenous input $w(t) \in \mathbb{R}^m$ and the exogenous output $z(t) \in \mathbb{R}^n$, where the uncertainty block is interconnected by $d(t) \in \mathbb{R}^q$ and $e(t) \in \mathbb{R}^p$.

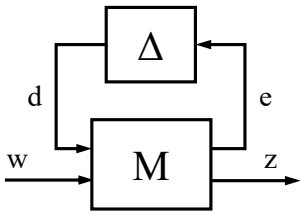

Figure 5.2 – Block diagram of standard $\Delta-$M configuration: interconnection system M and uncertainty block Δ, containing the parametric uncertainties.

The interconnection transfer function matrix M is then partitioned as

$$\begin{bmatrix} e \\ z \end{bmatrix} = \mathrm{M} \begin{bmatrix} d \\ w \end{bmatrix} = \begin{bmatrix} \mathrm{M}_{11} & \mathrm{M}_{12} \\ \mathrm{M}_{21} & \mathrm{M}_{22} \end{bmatrix} \begin{bmatrix} d \\ w \end{bmatrix}, \quad d = \Delta \ e \ , \tag{5.3}$$

with respect to the input and output channels, such as $\mathrm{M}_{11} \in \mathbb{G}^{p\times q}$, $\mathrm{M}_{12} \in \mathbb{G}^{p\times m}$, $\mathrm{M}_{21} \in \mathbb{G}^{n\times q}$ and $\mathrm{M}_{22} \in \mathbb{G}^{n\times m}$. The matrix M_{11} holds transfer functions to assign the uncertainty block Δ from $d(t)$ to $e(t)$, providing an upper feedback loop. Evaluating (5.3) from $w(t)$ to $z(t)$ gives the transfer function for the nominal plant $G_n(s) = \mathrm{M}_{22}$.

Upper linear fractional transformation (ULFT)

Matrix manipulations with respect to the augmented interconnection system (5.3) allows for verifying the upper linear fractional transformation (ULFT) [Safonov, 1981]

$$F_u(\mathrm{M}, \Delta) = \mathrm{M}_{22} + \mathrm{M}_{21}\Delta(\mathrm{I} - \mathrm{M}_{11}\Delta)^{-1}\mathrm{M}_{12} = G_\mathrm{p}(s) \tag{5.4}$$

of M and Δ, which describes the perturbed plant $G_\mathrm{p}(s) = F_u(\mathrm{M}, \Delta)$ that provides the closed-loop system $z = G_\mathrm{p}(s)\ w$, taking the plant perturbations into account.

P−K configuration

A closed-loop control system can be rearranged in a standard P−K configuration [Skogestad and Postlethwaite, 2005]. It will separate the controller block K and establishes the interconnection system P, as depicted in the block diagram of Figure 5.3. This new interconnection system holds the exogenous input channel $w(t) \in \mathbb{R}^m$ and the exogenous output channel $z(t) \in \mathbb{R}^n$, where the controller block is interconnected by the control variable $u(t) \in \mathbb{R}^q$ and measurement variable $y(t) \in \mathbb{R}^p$.

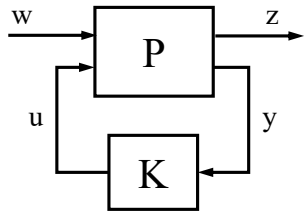

Figure 5.3 – Block diagram of standard P−K configuration: interconnection matrix P and controller K of desired structure.

The interconnection transfer function matrix P is then partitioned as

$$\begin{bmatrix} z \\ y \end{bmatrix} = \mathrm{P} \begin{bmatrix} w \\ u \end{bmatrix} = \begin{bmatrix} \mathrm{P}_{11} & \mathrm{P}_{12} \\ \mathrm{P}_{21} & \mathrm{P}_{22} \end{bmatrix} \begin{bmatrix} w \\ u \end{bmatrix}, \quad u = K\ y\ , \tag{5.5}$$

with respect to the input and output channels, such as $\mathrm{P}_{11} \in \mathbb{G}^{n\times m}$, $\mathrm{P}_{12} \in \mathbb{G}^{n\times q}$, $\mathrm{P}_{21} \in \mathbb{G}^{p\times m}$ and $\mathrm{P}_{22} \in \mathbb{G}^{p\times q}$. The matrix P_{22} holds transfer functions to assign the controller block K from $y(t)$ to $u(t)$, providing a lower feedback loop. Evaluating (5.5) from $w(t)$ to $z(t)$ gives the nominal plant $G_n(s) = \mathrm{P}_{11}$.

Lower linear fractional transformation (LLFT)

Matrix manipulations with respect to the augmented interconnection system (5.5) allow for verifying the lower liner fractional transformation (LLFT) [Safonov, 1981]

$$F_\ell(\mathrm{P}, \mathrm{K}) = \mathrm{P}_{11} + \mathrm{P}_{12}\mathrm{K}(\mathrm{I} - \mathrm{P}_{22}\mathrm{K})^{-1}\mathrm{P}_{21} \tag{5.6}$$

of P and K, which describes the generalized plant $T(s) = F_\ell(\mathrm{P}, \mathrm{K})$ that provides the closed-loop system $z = T(s)\ w$, as desired for control design.

5.2.2 Norms and properties

The L_2 signal norm and the H_∞ system norm is briefly recapitulated as they will find excessive use in the subsequent sections. Discussing the small gain theorem is essential to understand requirements on stability and performance for the loop transfer functions of an interconnected systems. Especially, its formulation by means of H_∞ allows for evaluating the control design in terms of frequency domain specifications.

L_2-norm

The Euclidean norm (L_2-norm) applied on a vector signal $z(t)$ is defined by [Gu et al., 2013]

$$\|z(t)\|_2 = \left(\int_{-\infty}^{\infty} |z(t)|^2 dt \right)^{1/2} , \tag{5.7}$$

where the squared of the L_2-norm is referred to the signal energy $\|z(t)\|_2^2$. This norm will be used to define the H_∞ system norm and for controller synthesis in stacked notation, it is particularly referred to the control design with joint shaping functions, as presented in Section 6.2.

H_∞-norm

Considering a linear and stable system $G(s)$, with input channel $d(t)$ and output channel $e(t)$, that describes the transfer function $d(t) \rightarrow e(t)$ by means of $e = G(s)\, d$. The H_∞-norm of $G(s)$ is obtained by the maximum L_2-norm of the input and output signals [Skogestad and Postlethwaite, 2005], such as

$$\|G\|_\infty = \max_{d \neq 0} \frac{\|e\|_2}{\|d\|_2} . \tag{5.8}$$

Thus, the H_∞-norm is also called induced L_2-norm. It can be interpreted as the maximal largest singular value

$$\|G\|_\infty = \max_{\omega} \bar{\sigma} \left(G(j\omega) \right) , \tag{5.9}$$

while evaluating the system for all frequencies ω. Since H_∞ corresponds to the linear space of all stable linear systems, this is a crucial measure for robust stabilization.

In other terms, the H_∞-norm of a stable transfer function $G(s)$ is the maximal peak value of the corresponding magnitude

$$\|G(s)\|_\infty = \sup_{\omega} |G(j\omega)| . \tag{5.10}$$

Small gain theorem

Considering the stable loop transfer function $\mathrm{L}(s)$ The small gain theorem is often defined in terms of the spectral radius [Skogestad and Postlethwaite, 2005]

$$\rho \left(\mathrm{L}(j\omega) \right) = \max_i |\lambda_i \left(\mathrm{L}(j\omega) \right)| \tag{5.11}$$

that is the maximum eigenvalue magnitude. The closed-loop system is then stable if

$$\rho \left(\mathrm{L}(j\omega) \right) < 1 \; \forall \; \omega \tag{5.12}$$

and since $\rho(\mathrm{L}) \leq \|\mathrm{L}\|$, the small gain theorem states that the closed loop system is stable, if

$$\|\mathrm{L}(j\omega)\| < 1 \; \forall \; \omega , \tag{5.13}$$

where $\|\mathrm{L}\|$ has to satisfy the triangle inequality [Desoer and Vidyasagar, 1975]. This is true for any induced norms, such as the H_∞-norm, and thus for the largest singular value $\bar{\sigma}(\mathrm{L})$.

Internal stability is not necessary guaranteed, when interconnecting stable systems. Applying the small gain theorem (5.13), a feedback configuration, interconnecting the time-invariant, linear and stable systems G_1 and G_2 in closed-loop path with G_1 in the forward path and G_2 in the backward path, is internally stable, if and only if $\|G_1G_2\|_\infty < 1$ and $\|G_2G_1\|_\infty < 1$ [Desoer and Vidyasagar, 1975]. With respect to the multiplicative property

$$\|G_1G_2\| \;\leq\; \|G_1\| \cdot \|G_2\| \tag{5.14}$$

of the triangle inequality and considering the H_∞-norm, yields $\|G_1\|_\infty \cdot \|G_2\|_\infty < 1$ as a sufficient condition of stability for an interconnected system.

The small gain theorem is essential for H_∞ controller synthesis. It is more conservative than the spectral radius, but very useful to evaluate the control requirements for stability and performance in terms of largest singular values $\bar{\sigma}$.

5.2.3 Robust stability and performance analysis

Structured singular values are a general concept for analysing stability and performance of dynamic systems [Gu et al., 2013]. Even though introducing unstructured uncertainties to simplify the robust control design for high-pressure pumps (see Section 5.4), its properties for stability and performance will be derived, using the definitions obtained from structured singular values. Further, the condition for internal stability is briefly introduced.

Structured singular values

For a perturbed plant $G_\mathrm{p} = F_u(\mathrm{M}, \Delta)$ robust stabilization can be obtained, referring to [Skogestad and Postlethwaite, 2005], if

$$\det\left(\mathrm{I} - \mathrm{M}(j\omega)\Delta(j\omega)\right) \neq 0 \;\forall\; \omega \;. \tag{5.15}$$

The nominal feedback system M is internally stable for

$$\Delta : \overline{\sigma}(\Delta) < 1 \tag{5.16}$$

where Δ is the nominal set of structured uncertainty.

To allow a closed-loop system to be robustly stable, all the uncertainties in Δ must be small, that $\mathrm{I} - \mathrm{M}\Delta$ wont become singular for any frequency ω. This eventually defines the structured singular value $\mu_\Delta(\mathrm{M})$ of an interconnection system M with respect to the uncertainty Δ.

The robust stabilization criterion (5.15) and internal stability (5.16) give the inverse structured singular value [Doyle, 1987]

$$\mu_\Delta^{-1}(\mathrm{M}) = \underset{\Delta}{\text{minimize}} \;\; \left(\overline{\sigma}(\Delta) : \det\left(\mathrm{I} - \mathrm{M}(j\omega)\Delta(j\omega)\right) = 0\right) \;. \tag{5.17}$$

This corresponds to the smallest magnitude for $\overline{\sigma}(\Delta)$ to make $\mathrm{I} - \mathrm{M}\Delta$ singular and is subject for evaluation to obtain the structured singular value [Packard and Doyle, 1993]

$$\mu_\Delta(\mathrm{M}) = \sup_\omega \mu_\Delta\left(\mathrm{M}(j\omega)\right) \;, \tag{5.18}$$

which corresponds to a frequency dependent stability margin.

It follows that a nominal feedback system M is robustly stable, with respect to the uncertainty Δ, if and only if [Skogestad and Postlethwaite, 2005]

$$\mu_{\Delta}(\mathrm{M}) \leq \frac{1}{\beta} \,, \tag{5.19}$$

whereby β denotes an uncertainty bound for guaranteed stability.

For the general case of structured uncertainties holds [Gu et al., 2013]

$$\begin{aligned} \text{Nominal stability} &\Leftrightarrow \text{M internally stable} \,, && (5.20a)\\ \text{Nominal performance} &\Leftrightarrow \|\mathrm{M}_{22}\|_{\infty} < 1 \,, && (5.20b)\\ \text{Robust stability} &\Leftrightarrow \mu_{\Delta}\left(\mathrm{M}_{11}(s)\right) < 1 \,, && (5.20c)\\ \text{Robust perfomance} &\Leftrightarrow \mu_{\Delta}\left(\mathrm{M}(s)\right) < 1 \,. && (5.20d) \end{aligned}$$

Due to difficulties for calculating the structured singular value μ_{Δ}, it is estimated by lower and upper bounds, such as

$$\rho(\mathrm{M}) \leq \mu_{\Delta}(\mathrm{M}) \leq \overline{\sigma}(\mathrm{M}) \,. \tag{5.21}$$

The lower bound can be obtained by the spectral radius ρ and the upper bound can be given by the largest singular value $\overline{\sigma}$.

Considering a complex unstructured uncertainty and if Δ is a full matrix yields $\rho(\mathrm{M}) = \mu_{\Delta}(\mathrm{M}) = \bar{\sigma}(\mathrm{M})$. For this case, the above conditions for robustness are simplified

$$\begin{aligned} \text{Robust stability} &\Leftrightarrow \|\mathrm{M}_{11}\|_{\infty} < 1 \,, && (5.22a)\\ \text{Robust perfomance} &\Leftrightarrow \mu_{\Delta}\left(\mathrm{M}_{11}(s)\right) < 1 \,. && (5.22b) \end{aligned}$$

An uncertain system is then guaranteed stable for all normalized structured uncertainties Δ, such as $\|\Delta(s)\|_{\infty} \leq 1$.

Internal stability

A system Σ is internally stable, if it contains no hidden unstable poles and when applying a bounded exogenous signal to any system input results in a bounded response at every system output (BIBO stability, see [Gu et al., 2013]). Hence, internal stability is given, if and only if all poles p_i lie in the left hand plane (LHP), such as $\mathrm{Re}\left\{\lambda_i(A)\right\} < 0 \;\forall\; i$, where $\lambda_i(A)$ denotes the eigenvalues of a system in state space description. The poles are obtained by the roots of the characteristic equation: $\det\left(s\mathrm{I} - A\right) = 0$.

5.3 Problem formulation

The initial control design problem considers the decentralized and robust control of decoupled high-pressure pumps, following the approach in [Marquez et al., 2008] and [Iftar, 2013]. A robust low-level controller is thereby designed, attenuating the impact from the switching of cutting heads to a network subsection. This aims to reduce the coupling between neighbouring subsections by means of local disturbance rejection, using the available high-pressure pumps. Further investigations can expand this approach by considering the dynamics of overlapping network sections. This is promising to enhance the resulting closed-loop system performance, as suggested in [Benlatreche et al., 2008] and [Swarnakar et al., 2009]. However, a distributed control approach that exchanges information between controllers, see for example [Demir and Lunze,

2011], is undesirable for high-pressure pumps, since availability and reliability of communication is not guaranteed for any waterjet facility. Nevertheless, the energy efficiency of coupled and robustly controlled pumps can be improved by implementing a high-level managing, which copes with restricted means of communication. A perspective on that approach is given in Chapter 7.

The illustration of Figure 5.4 shows exemplarily the separation of a high-pressure network in network subsections, with respect to the locations of the high-pressure pumps. The cutting heads within a network subsection become concatenated, see head 3 and 4. The size of each subsection remains an unknown parameter for the low-level control design. To guarantee robust performance and stability requires to specify the upper and lower bounds of this parameter.

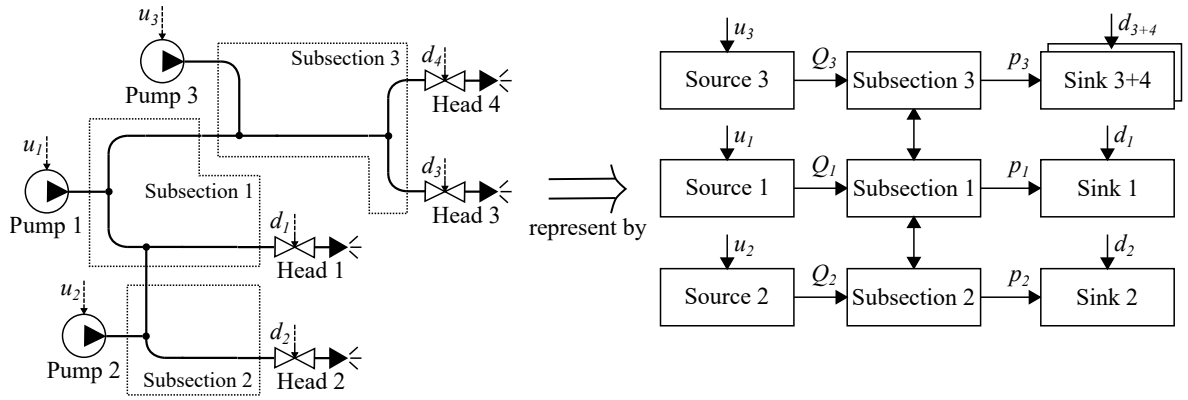

Figure 5.4 – Separation of a high-pressure network into network subsections for control design: high-pressure pumps and concatenated cutting heads to introduce fluid flow sources and pressure sinks, respectively.

Recall the derived lumped parameter model of Section 4.2 that describes the pressure generation in a pumping chamber, interconnected to a network subsection with respect to (4.6a - 4.6b). Extending this model with a possible interconnection to neighbouring subsections yields the **network subsection model**

$$\frac{d}{dt}p_N^i(t) = \frac{K(p_N^i)}{V_C^i(t) + V_0^i}\left(Q_P^i(t) - H_i^*\sqrt{p_N^i(t)}\; d_i^*(t) - \sum_j H_{ij}\sqrt{|p_N^i - p_N^j|}\; sign\left(p_N^i - p_N^j\right)\right) \tag{5.23}$$

with input fluid flows $Q_P^i(t) = \sum_n Q_{Vn}^i(t)$ from the high-pressure pump of section i given by two pumping chambers $n = \{1, 2\}$ and the varying chamber volumes

$$\frac{d}{dt}V_C^i(t) = \sum_n \left(Q_{Pn}^i(t) - V_{0,n}^i\right) \ . \tag{5.24}$$

Whereas H_i^* and $d_i^*(t)$ concatenates all cutting heads of a network subsection to describe an overall output fluid flow, the interconnection matrix H_{ij} weights the couplings to neighbouring subsections j that assigns an intermediary fluid flow.

This network subsection model (5.23 - 5.24) is useful to represent entire waterjet facilites, subject for low-level control design. It allows for modelling the coupled network subsections (see Figure 5.4), representing a complex high-pressure network. The resulting model can be implemented for decentralized and distributed control design, see control schemes of Figure 5.1 (a) and

(b). A first robust design approach will consider the interconnection to neighbouring subsections as exogenous disturbances (see also [Marquez et al., 2008] and [Iftar, 2013]). This will result in isolated network subsections and is based on the following assumption:

Assumption 5.1. *It is assumed that an electrically driven high-pressure pump manages to attenuate any pressure fluctuations at its corresponding network subsection i by means of robust low-level control, such that the pressure difference to a neighbouring subsection j remains smaller than a desired percentage overshoot M_P, such as* $100 \ \times \ |p_N^i - p_N^j| \ / \ r < M_P$.

From Assumption 5.1 follows that $p_N^i \gg |p_N^i - p_N^j|$, for which the coupling term to neighbouring subsection in (5.23) is neglected ($H_{ij} = 0 \ \forall \ j$) and results in the isolated subsection description

$$\frac{d}{dt} p_N(t) = \frac{K(p_N)}{V_C(t) + V_0} \left(Q_P(t) - H^* \sqrt{p_N(t)} \ d^*(t) \right) \tag{5.25}$$

with

$$\frac{d}{dt} V_C(t) = \sum_n \left(Q_{Pn}(t) - V_{0,n} \right) \ , \tag{5.26}$$

where the amplitude and dynamic range of pressure fluctuations by means of switching cutting heads, as well as induced fluctuations from neighbouring subsections are included in a possible exogenous input and output fluid flow, this occurs from $|d(t)| < 1$.

The isolated network subsection considers a single high-pressure pump and a cutting head, which become interconnected with a piping of bounded size, as illustrated by the diagram of Figure 5.5. A high-pressure pump defines the maximal fluid flow for a network subsection, taking the actuator dynamics and saturation into account. This gives the maximally allowed water consumption in a network subsection. The high-pressure pump consists of two pistons, driven by independent linear actuators, see Section 1.3. The pistons alternately supply the high-pressure piping, such as to induce a continuous fluid flow. This is realized by synchronization with phase-shifted reference trajectories, given by means of camming, and a precise motion control, as introduced in Section 2.3. Thus, the high-pressure pump represents a fluid flow source, dedicated to a network subsection. A cutting head represents the overall water consumption of a network subsection, with respect to the expected switching dynamics. The cutting head can be equipped with nozzles of different size. The fluid flow consumption will vary, with respect to the installed nozzle and the operating pressure. In addition, an on/off-valve will interrupt this fluid flow, according to an unknown switching pattern that is given by the waterjet application.

The subsequent robust low-level control design deals with the pressure control, which has to track a reference pressure $r(t)$ for the measurement signal $y(t)$ that corresponds to a subsection pressure state $\mathrm{x}(t)$. Usually, a constant operating point is required for waterjet machining, where the on/off-valve switching is considered as a disturbance $d(t)$. This affects the water consumption, with respect to an unknown switching pattern, for which the pump rate has to be adjusted, by means of control, to attenuate any pressure fluctuation. The control signal $u(t)$ defines the output fluid flow $u_g(t)$ of a high-pressure pump, for which $u(t) \approx u_g(t)$.

Consequently, each isolated network subsection, with its corresponding fluid flow source and pressure sink, corresponds to a decentralized control loop, as depicted in Figure 5.6. This control loop is subject for robust control design.

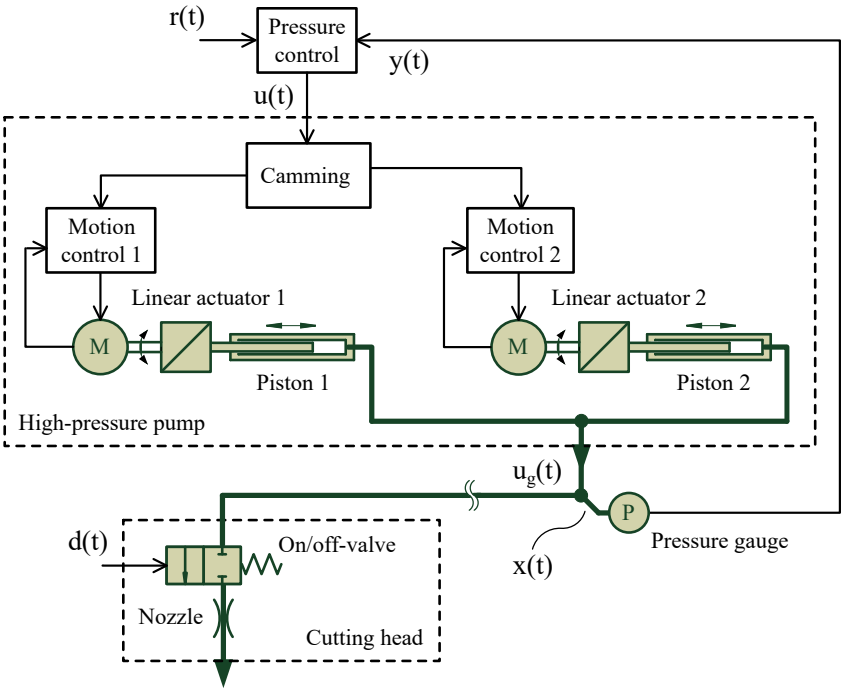

Figure 5.5 – Schematic diagram of the high-pressure system: a single high-pressure pump and a cutting head interconnected to a network subsection. The high-pressure pump consist of two linear actuators. Each linear actuator is controlled by motion control, whereby both plungers are synchronized by means of camming.

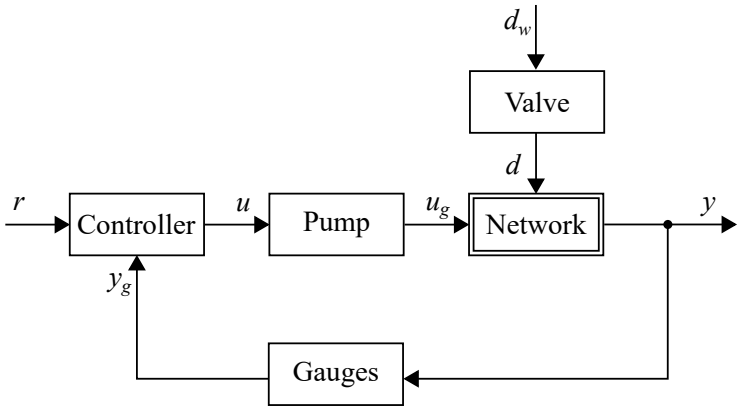

Figure 5.6 – Overview of all system components relevant for control design: isolated network subsection represented as a decentralized control loop.

5.3.1 Low-level control objectives

The control objective is first specified with respect to the acceptable steady-state error and by means of time domain constraints, considering the closed-loop system. These constraints will then be used to derive specifications in frequency domain for an open-loop system. The industry defines constraints on pressure fluctuations, with respect to the waterjet application, such as to guarantee a desired cutting quality. Measurements with hydraulically driven high-pressure pumps reveal that waterjet machining with reasonable cutting quality, requires pressure fluctuations of

less than 10% when switching a cutting head, see also [Tremblay and Ramulu, 1999] and [Trieb et al., 2007]. This further implies a settling time of $\tau_s < 0.5$ s and a damping ratio of $\varsigma > 0.5$ to limit high frequencies acting on the pump actuators, see [Xu et al., 2008] and [Niederberger and Kurmann, 2014]. The control signal must be limited, such that the actuator remains within saturation bounds, i.e. $u_g = [0,\ 5.447\ \ell/\text{min}]$ considering the pump prototype installed at the test bench.

The hard constraints are dedicated to disturbance rejection. It requires to obtain a desired reference pressure $r(t) = [40, 400]$ MPa $\rightarrow$ x(t) with minimal pressure fluctuations $|e(t)| < 0.1\ r(t)$ when applying a disturbance step $d(t) \in \{-1, 1\}$, even for large plant perturbations. Pressure fluctuations refer to the error, $e(t) = r(t) - y(t)$, between desired and measured pressure state x$(t) \rightarrow y(t)$. The soft constraints are dedicated to reference value tracking. It asks for any steady-state error $\lim_{t\to\infty} e(t) = 0$ to disappear and no overshoot for a reference value step, considering the undisturbed plant.

Time domain

Although, the high-pressure pump frequency response for $u(t) \rightarrow y(t)$, as well as the switching valve response for $d(t) \rightarrow y(t)$ will be represented using second order models and the high-pressure network will be approximated with a first order model, the time domain specifications for closed-loop performance is typically defined in terms of a unit step response, applied on a second order system [Skogestad and Postlethwaite, 2005]

$$G(s) = \frac{\omega_n^2}{s^2 + 2\ \varsigma\ \omega_n\ s + \omega_n^2}\ . \tag{5.27}$$

The poles of this model are found at $s = -\sigma \pm j\omega$. Its natural frequency $\omega_n = \sqrt{\sigma^2 + \omega^2}$ and damping ratio $\varsigma = \sigma/\omega_n$ follow from the real part σ and imaginary part ω.

The imaginary part further defines the rise time

$$\tau_r = \pi/(2\ \omega) \tag{5.28}$$

for $y(t)$ to first cross the steady-state value, if $\varsigma < 1$. The real part gives the settling time

$$\tau_s = -\ln\ \varepsilon/\sigma\ , \tag{5.29}$$

where $\varepsilon = 100 \times (r(t) - y(t))/r(t)$ is the percentage steady-state error to the desired reference value. The percentage overshoot

$$M_P \approx -e^{\sigma\pi/\omega} = -e^{\varsigma\pi/\sqrt{1-\varsigma^2}} \tag{5.30}$$

depends on the real and imaginary part. It can be expressed in terms of the damping ratio.

This allows for obtaining the damping ratio

$$\varsigma \approx \frac{\ln\ M_P}{\sqrt{\pi^2 + (\ln\ M_P)^2}}\ , \tag{5.31}$$

with respect to a specified overshoot, when rearranging (5.30). Combining the real part $\sigma = -\ln\ \varepsilon/\tau_s$ and imaginary part $\omega = \pi/(2\ \tau_r)$ defines the natural frequency

$$\omega_n = \sqrt{\left(-\frac{\ln\ \varepsilon}{\tau_s}\right)^2 + \left(\frac{\pi}{2\ \tau_r}\right)^2} \tag{5.32}$$

by terms of steady-state error, settling time and rise time, where (5.31) gives an approximation

$$\omega_n \approx \frac{\sqrt{\pi^2 + (\ln M_P)^2}\, \ln \varepsilon}{\tau_s \ln M_P} \,, \tag{5.33}$$

considering steady-state error, overshoot and settling time. Hence, (5.31) and (5.32) define constraints on the dominant closed-loop poles for $r(t) \to y(t)$ and $d(t) \to y(t)$, using time domain specifications and assuming a second order model.

Therefore, unit steps on the scaled reference input $r(t)$ and on the scaled disturbance input $d(t)$ are considered to specify time domain control objectives for the investigated high-pressure system. The hard constraints for disturbance rejection give objectives at the scaled plant output $y(t)$ with respect to an input step on disturbance $d(t)$, as listed in Table 5.1. This yields a settling time of ≤ 0.5 seconds, enables an overshoot of $\pm 10\%$ and requires all steady-state error to disappear. Rise time does not need specification.

Table 5.1: Time domain control objectives for disturbance rejection: hard constraints for unit step $d(t) \to y(t)$.

Requirements	Objectives	Conditions
Settling time (2% $e(t)$):	$0.98 \leq y(t) \leq 1.02$	$t \geq 0.5$ seconds
Overshoot:	$0.9 \leq y(t) \leq 1.1$	$t \geq 0$ seconds
Steady-state error:	$e(t) = 0$	$t \to \infty$

On the other hand, the soft constraints for reference value tracking provide objectives to the scaled plant output $y(t)$ with respect to an input step on $r(t)$, as shown in Table 5.2. This yields a rise time of ≤ 10 seconds, no overshoot and no steady-state error. The settling time does not need any specification.

Table 5.2: Time domain control objectives for reference tracking: soft constraints for unit step $r(t) \to y(t)$.

Requirements	Objectives	Conditions
Rise time (90% $r(t)$):	$\lvert y(t) \rvert \geq 0.9$	$t \geq 10$ seconds
Overshoot:	$\lvert y(t) \rvert \leq 1.0$	$t \geq 0$ seconds
Steady-state error:	$e(t) = 0$	$t \to \infty$

For both cases, no steady-state error is desired, thus $\lim_{t\to\infty} e(t) = 0$. To obtain this constraint for a plant, without a pole at $s = 0$, the closed-loop system requires integral action by means of control. The objectives on disturbance rejection and reference tracking requires step responses as approximated with the two following second order models

$$G_{Hard}(s) = \frac{53.7053}{s^2 + 8.6651s + 53.7053} \tag{5.34}$$

and

$$G_{Soft}(s) = \frac{1.9465}{s^2 + 2.7904s + 1.9465} \,, \tag{5.35}$$

when applying (5.31) and (5.32) to the specifications of Table 5.1 and 5.2. The plot in Figure 5.7 shows the corresponding step responses of the systems (5.34) and (5.35). Since reference tracking

and disturbance rejection are complementary control design requirements, it is not possible to satisfy all objectives given by the hard constraints and soft constraints, using a controller with one degree of freedom. Nevertheless, introducing an additional degree of freedom to the reference input $r(t)$, may rectify this limitation.

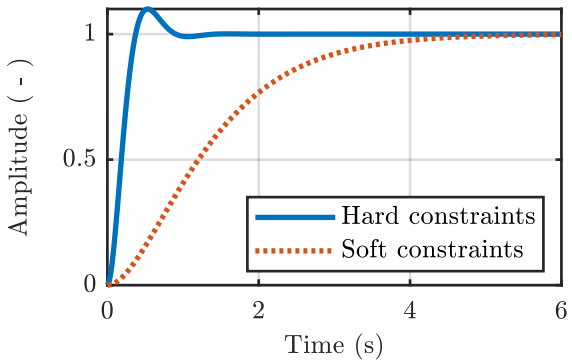

Figure 5.7 – Step responses for the hard and soft constraints: considering a second order model to represent the control objectives for $d(t) \rightarrow y(t)$ and $r(t) \rightarrow y(t)$.

Frequency domain

The time domain specifications become more comprehensive, when considering its representation in frequency domain. These frequency domain specifications are useful to define objectives with respect to specific frequencies. It further allow for introducing constraints to noise attenuation in addition to reference tracking and disturbance rejection, see [Skogestad and Postlethwaite, 2005]. Reference tracking and disturbance rejection typically concerns performance at the low frequencies, where noise requires attenuation at high frequencies, where $\mathcal{T}(j\omega) + \mathcal{S}(j\omega) = 1$ has to hold for every frequency, with sensitivity function $\mathcal{S}(s)$ (5.61) and complementary sensitivity function$\mathcal{T}(s)$ (5.62). Both functions will be discussed in the subsequent section, when introducing the interconnection system for control design. Here, reference tracking and disturbance rejection require the open-loop gain $|\mathrm{L}(j\omega)|$ to be large for low frequencies. Introducing therefore the weighting function $W_1(s)$ for condition $|\mathcal{S}(j\omega)|\ |W_1(j\omega)| < 1$ yields

$$|1 + \mathrm{L}(j\omega)| > |W_1(j\omega)| \ . \tag{5.36}$$

On the other hand, noise rejection requires the open-loop gain $|\mathrm{L}(j\omega)|$ to be small for high frequencies, hence $|\mathcal{T}(j\omega)| \approx |\mathrm{L}(j\omega)|$. This is written as condition $|\mathcal{T}(j\omega)|\ |W_2(j\omega)| < 1$, considering a weighting function $W_2(s)$ gives

$$|\mathrm{L}(j\omega)| < |W_2(j\omega)|^{-1} \ . \tag{5.37}$$

Consequently, $|\mathcal{S}(j\omega)| \ll 1$ and $|\mathcal{T}(j\omega)| \approx 1$ for low frequencies and $|\mathcal{T}(j\omega)| \ll 1$ and $|\mathcal{S}(j\omega)| \approx 1$ for high frequencies. To derive these weighting functions by terms of time domain specifications, the second order models (5.34) and (5.35), considering the hard and soft constraints, have been substituted in (5.36) and (5.37) with respect to $\mathrm{L}(s) = G(s)/(G(s) - 1)$. This defines a lower bound $|W_1(s)|$ to guarantee performance and an upper bound $|W_2(s)|$ for possible noise attenuation, as depicted in the plot of Figure 5.8. When the resulting open-loop system remains within these bounds, the specified control constraints will be met.

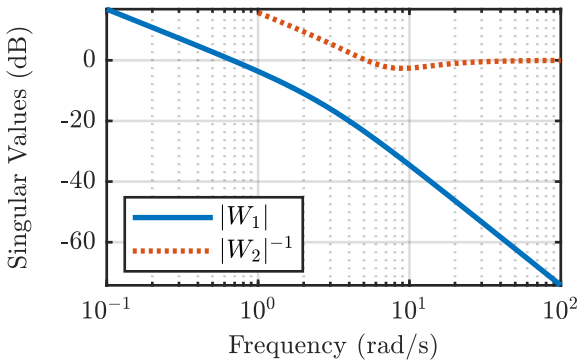

Figure 5.8 – Singular values of weighting function W_1 and inverse weighting function W_2^{-1}: derived from the hard and soft constraints to specify minimal and minimal bounds for desired performance.

However, these control constraints will not guarantee closed-loop stability and performance for large plant perturbations. Referring to the next section, robust stability and performance require to introduce a representative uncertainty description. The following list summarizes the requirements for robust control design:

- The controller K($j\omega$) must stabilize the perturbed plant $G_\mathrm{p}(j\omega)$.
- A hard constraint is to retrieve sufficient rejection for input disturbances. Thus, the singular values of the sensitivity function and perturbed plant $\sigma(G_\mathrm{p}(j\omega)\,\mathcal{S}(j\omega))$ should become small for low frequencies.
- A first soft constraint is to guarantee a satisfying reference tracking with zero steady-state error. This indicates that $\overline{\sigma}(\mathcal{T}(j\omega)) \approx \underline{\sigma}(\mathcal{S}(j\omega)) \approx 1$.
- A second soft constraint is employed to obtain a reasonable noise attenuation, for measurement noise on plant output. The singular values of the complementary sensitivity function $\sigma(\mathcal{T}(j\omega))$ should become small for high frequencies.
- In addition, the control effort, needed for an effective disturbance rejection, should be minimal. This requires the sensitivity function, perturbed plant and controller $\sigma(K(j\omega)\,G_\mathrm{p}(j\omega)\,\mathcal{S}(j\omega))$ to be small with a roll-off for high frequencies.
- Finally, robust stability should be enabled for any destabilizing uncertainty. Assuming an inverse additive uncertainty model, the largest singular value of the sensitivity function and the nominal plant should be smaller than the largest singular value of the uncertainty $\overline{\sigma}(\Delta_{ia}(j\omega)) = \overline{\sigma}(G_n(j\omega)\,\mathcal{S}(j\omega))^{-1}$.

5.3.2 First order plant model

The high-pressure system of Figure 5.5 can be described in a simplified meaner by means of a non-linear model. This model of first order becomes affected by various varying parameters. Section 5.4 will discuss and classify these parameters to define the uncertainty range and to analyse its sensitivity with respect to the input and output channels. This section investigates the linearisation of the first order model around an operating point, with respect to different approximations and simplifications to provide a model for control design.

The diagram of Figure 5.9 presents this model evaluation process. The non-linear model provides the starting point of investigation. An approximated model has been obtained, when linearising it with respect to independent parameters. These parameters are then substituted after linearisation by the dependent variables. On the other hand, an extended model results, when first introducing the dependent variables and then linearising around operating point. It is further simplified by its evaluation on equilibrium.

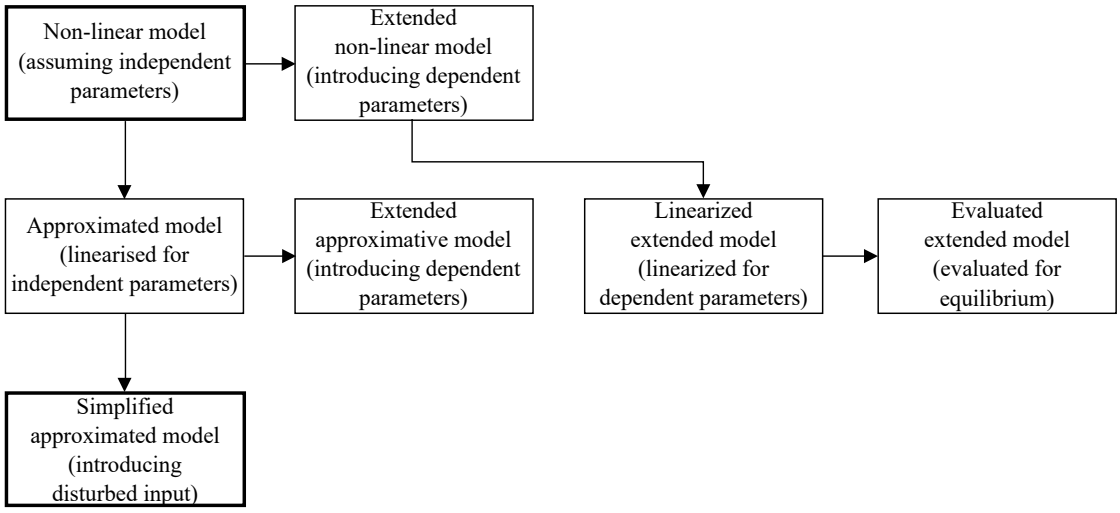

Figure 5.9 – Overview of the plant model evaluation process: different linearised and approximated models to represent the high-pressure system subject to control design.

These different linear models has been compared with respect to various time and parameter-dependent variables. The simplified approximated model has been finally identified to provide best approximation of the non-linear model. It is further simplified by assuming a disturbed input channel. This allows for separating the uncertainties and provides the perturbed plant for control design.

Non-linear plant

To model the high-pressure system of Figure 5.5 for control design, assumes a perfect synchronization of both pumping units without any interactions. This is obtained by means of motion trajectories, as described in Section 2.3, causing one of the pumping units to the pumping state of hauling, while the other is retracting and pressurizing. This enables a high-pressure pump to generate a steady overall fluid flow. As a consequence, only one pumping chamber at a time is interconnected to the corresponding network subsection. Thus, the normalized control variable $u(t)$ of the pressure controller refers to the desired piston velocity $v_P(t)$, while hauling. This piston displacement generates a steady fluid flow $Q_P(t) = S_P \; v_P(t)$ that corresponds to the effective control value $u_g(t) \rightarrow Q_P(t)$ of a high-pressure pump. Referring to the derived lumped parameter model (5.25 - 5.26) allows for introducing the **non-linear plant model**

$$\boxed{\frac{d}{dt}\mathrm{x}(t) = \frac{K_\delta}{V_\delta}\left(u_g(t) - H_\delta\sqrt{\mathrm{x}(t)}\; d(t)\right)} \tag{5.38}$$

that describes a common pressure state $\mathrm{x}(t) \rightarrow p_N(t)$ of a network subsection and represents all time-varying and parameter-varying variables in terms of parametric uncertainties.

This non-linear plant model represents the pressure, established in a high-pressure network subsection, and its interconnected pumping chamber, where the network subsection couples a high-pressure pump to a corresponding cutting head. A high-pressure pump induces an input fluid flow $u_g(t)$, where the nozzle of a cutting head causes an output fluid flow, with respect to the pressure state. This output fluid flow is affected by the on/off-valve. This valve has an unknown switching behaviour of discrete states $d(t) \in \{0, 1\}$. Where the bulk modulus K_δ and fluid volume V_δ affect the input gain as well as the system dynamics, any variation of the flow resistance H_δ will change the feedback gain. The disturbance input can be considered as an variable gain, in particular, applied on the system feedback path. This first order model is non-linear in $\mathrm{x}(t)$ and describes a bilinear relation between $\mathrm{x}(t)$ and $d(t)$, as depicted in the block diagram of Figure 5.10.

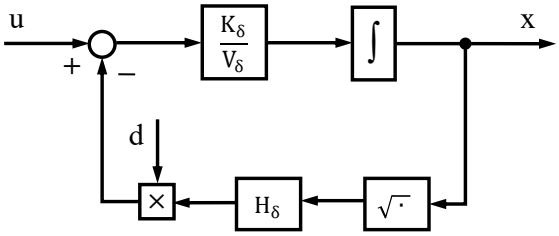

Figure 5.10 – Non-linear plant model: block diagram of the bilinear first order model with varying parameters.

Notice that this model is subject to different parameter variations, as listed in Table 5.3. These uncertainties deal with parameter variations, given by the high-pressure network configuration and the pump prototype (see Section 2.2 and 2.3, respectively). The subscript δ labels the uncertain characteristics of the corresponding parameters. $H_\delta \in [H_{min},\ H_{max}]$ is the varying fluid flow resistance of a cutting head nozzle, defining the output fluid flow. $K_\delta \in [K_{min},\ K_{max}]$ denotes a varying fluid bulk modulus and $V_\delta \in [V_{min},\ V_{max}]$ represents a varying fluid volume, both defining the dynamics of pressure generation.

Table 5.3: Uncertainty range of varying parameters obtained from test bench setup and high-pressure pump design.

			Nominal value	Min value	Max value	Relative range
Flow resistance	H_δ	$\times 10^{-9}$	###	0	###	100%
Fluid volume	V_δ	(cm^3)	###	###	###	37%
Bulk modulus	K_δ	(GPa)	###	###	###	28%
Operating point	x_δ	(MPa)	220	40	400	82%
Nozzle section	S_δ	(mm^2)	0.0653	0.0050	0.1260	92%

The installed nozzle strongly affects the fluid flow resistance

$$H(t) = S_\delta\ \zeta\ \sqrt{\frac{2}{\varrho(t)}} \longmapsto H_\delta\ , \tag{5.39}$$

where $S_\delta = [S_{min},\ S_{max}]$ denotes an uncertain nozzle cross section, ζ represents its fluid flow coefficient and $\varrho(t)$ is the fluid density.

It has been shown in Section 3.3, that it is useful to describe the variable bulk modulus

$$K(t) = \kappa_0 + \kappa_1 \mathrm{x}(t) \longmapsto K_\delta \tag{5.40}$$

by means of the pressure state $\mathrm{x}(t)$, where κ_0 and κ_1 denote the identified coefficients of a linear model. Also the variable fluid density

$$\varrho(t) = \varrho_0 \left(1 + \frac{\kappa_1 \mathrm{x}(t)}{\kappa_0}\right)^{1/\kappa_1} \tag{5.41}$$

can be modelled with respect to the pressure state and the same parameters κ_0 and κ_1, as given in Section 3.4.

Introducing (5.39) and (5.40) into (5.38) results in an extended plant model

$$\frac{d}{dt}\mathrm{x}(t) = \frac{\kappa_0 + \kappa_1 \mathrm{x}(t)}{V_\delta} \left(u_g(t) - S_\delta \, \zeta \sqrt{\frac{2}{\varrho_0} \left(1 + \frac{\kappa_1 \mathrm{x}(t)}{\kappa_0}\right)^{-1/\kappa_1}} \sqrt{\mathrm{x}(t)} \; d(t) \right) \; , \tag{5.42}$$

which introduces dependent variables on $\mathrm{x}(t)$, improving in this way the accuracy over a wide pressure range. The remaining parametric uncertainties correspond to the unknown cutting head configuration, specified by the nozzle cross section S_δ, and the unknown high-pressure network topology, given by the fluid volume V_δ.

Linearised plant

Both first order models, the non-linear plant model (5.38) and the extended plant model (5.42) can be linearised around their operating points (x_0, u_0, d_0) by the first order Taylor expansion

$$\begin{aligned} \frac{d}{dt}\mathrm{x}(t) = {} & f(\mathrm{x}_0, u_0, d_0) + \frac{\partial}{\partial x} f(\mathrm{x}_0, u_0, d_0) \Delta \mathrm{x}(t) \\ & + \frac{\partial}{\partial u} f(\mathrm{x}_0, u_0, d_0) \Delta u(t) + \frac{\partial}{\partial d} f(\mathrm{x}_0, u_0, d_0) \Delta d(t) \; , \end{aligned} \tag{5.43}$$

where $\Delta \mathrm{x}(t)$, $\Delta u(t)$ and $\Delta d(t)$ refer to the corresponding deviations around the operating points with respect to

$$\mathrm{x}(t) = \mathrm{x}_0 + \Delta \mathrm{x}(t) \; , \tag{5.44a}$$

$$u(t) = u_0 + \Delta u(t) \; , \tag{5.44b}$$

$$d(t) = d_0 + \Delta d(t) \; . \tag{5.44c}$$

The expansion (5.43) holds for small deviation around the operating points. It gives the state space description

$$\begin{aligned} \Delta \dot{\mathrm{x}}(t) &= A \; \Delta \mathrm{x}(t) + B_1 \; \Delta u(t) + B_2 \; \Delta d(t) \\ \Delta y(t) &= C \; \Delta \mathrm{x}(t) + D_1 \; \Delta u(t) + D_2 \; \Delta d(t) \end{aligned} \; , \tag{5.45}$$

with separated control input $u(t)$ and disturbance input $d(t)$, whereby

$$\begin{aligned} A = \frac{\partial}{\partial \mathrm{x}} g(\mathrm{x}_0, u_0, d_0); \;\; B_1 = \frac{\partial}{\partial u} g(\mathrm{x}_0, u_0, d_0); \;\; B_2 = \frac{\partial}{\partial d} g(\mathrm{x}_0, u_0, d_0) \; , \\ C = \frac{\partial}{\partial \mathrm{x}} h(\mathrm{x}_0) = 1; \;\; D_1 = \frac{\partial}{\partial u} h(\mathrm{x}_0) = 0; \;\; D_2 = \frac{\partial}{\partial d} h(\mathrm{x}_0) = 0 \; . \end{aligned} \tag{5.46}$$

The linearisation of the non-linear plant model (5.38) according to (5.45) yields the following **approximated model**

$$\boxed{\Delta\dot{\mathrm{x}}(t) = -\frac{K_\delta H_\delta d_0}{2V_\delta\sqrt{\mathrm{x}_0}}\,\Delta\mathrm{x}(t) + \frac{K_\delta}{V_\delta}\,\Delta u(t) - \frac{K_\delta H_\delta\sqrt{\mathrm{x}_0}}{V_\delta}\,\Delta d(t)}\,, \tag{5.47}$$

while considering independent parameters. As a consequence of linearisation, the operating pressure range

$$\mathrm{x}_\delta = [\mathrm{x}_{min},\ \mathrm{x}_{max}] \longmapsto \mathrm{x}_0 \tag{5.48}$$

is taken into account, extending the set of uncertain parameters. The block diagram of Figure 5.11 shows that the control input Δu as well as the disturbance input Δd become scaled with the bulk modulus K_δ and fluid volume V_δ, where the disturbance becomes additionally affected by the flow resistance H_δ and operating point x_δ. Varying the flow resistance and operating point will change the system dynamics as well as the disturbance input scaling.

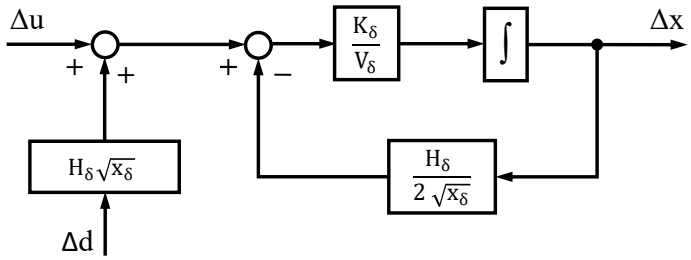

Figure 5.11 – Approximated plant model: block diagram of the linearised model around operating points in state space form.

Introducing the dependent variables (5.39) and (5.40) in (5.47) results in the **extended approximated model**

$$\begin{aligned}\boxed{\Delta\dot{\mathrm{x}}(t) = &-\frac{(\kappa_0+\kappa_1\mathrm{x}_0)S_\delta\zeta\ d_0}{V_\delta}\sqrt{\frac{1}{2\mathrm{x}_0\varrho_0}\left(1+\frac{\kappa_1\mathrm{x}_0}{\kappa_0}\right)^{-1/\kappa_1}}\,\Delta\mathrm{x}(t)\\ &+\frac{\kappa_0+\kappa_1\mathrm{x}_0}{V_\delta}\,\Delta u(t) - \frac{(\kappa_0+\kappa_1\mathrm{x}_0)S_\delta\zeta}{V_\delta}\sqrt{\frac{2\mathrm{x}_0}{\varrho_0}\left(1+\frac{\kappa_1\mathrm{x}_0}{\kappa_0}\right)^{-1/\kappa_1}}\,\Delta d(t)}\end{aligned} \tag{5.49}$$

that describes the bulk modulus K_δ and fluid flow resistance H_δ with respect to the operating point x_0.

In contrast to that, the linearisation of the extended plant model (5.42) according to (5.45) yields the linearised extended model

$$\begin{aligned}\Delta\dot{\mathrm{x}}(t) = &-\left(\frac{(\kappa_0-\mathrm{x}_0+3\kappa_1\mathrm{x}_0)S_\delta\zeta\ d_0}{V_\delta}\sqrt{\frac{1}{2\mathrm{x}_0\varrho_0}\left(1+\frac{\kappa_1\mathrm{x}_0}{\kappa_0}\right)^{-1/\kappa_1}} - \frac{\kappa_1 u_0}{V_\delta}\right)\Delta\mathrm{x}(t)\\ &+\frac{\kappa_0+\kappa_1\mathrm{x}_0}{V_\delta}\,\Delta u(t) - \frac{(\kappa_0+\kappa_1\mathrm{x}_0)S_\delta\zeta}{V_\delta}\sqrt{\frac{2\mathrm{x}_0}{\varrho_0}\left(1+\frac{\kappa_1\mathrm{x}_0}{\kappa_0}\right)^{-1/\kappa_1}}\,\Delta d(t)\ ,\end{aligned} \tag{5.50}$$

taking the dependent variables into account, such as a variable bulk modulus $K(t)$ and a variable fluid flow resistance $H(t)$, for linearisation with respect to the pressure state $\mathrm{x}(t)$.

Here, the resulting extended approximated model (5.49) and the linearised extended model (5.50) become different in terms of its coefficient A. Where for the extended approximated model, this coefficient depends on the operating points x_0 and d_0, such as $A(\mathrm{x}_0, d_0)$, it becomes affected by x_0, d_0 and u_0, with $A(\mathrm{x}_0, u_0, d_0)$, considering the linearised extended model. The other coefficients remain conditioned by x_0, such as $B_1(\mathrm{x}_0)$ and $B_2(\mathrm{x}_0)$.

Whereas the operating pressure x_0 can be measured and is subject to control, the resulting induced fluid flow u_0 and switching disturbance d_0 are time-varying parameters with unknown behaviour and are difficult to determine. Insofar as the induced fluid flow must follow the overall water consumption of the cutting heads to obtain a steady operating pressure, the required fluid flow can be determined by assuming equilibrium on operating point. This enables to define the expected input fluid flow

$$u_0 = S_\delta \zeta \sqrt{\frac{2\mathrm{x}_0}{\varrho_0} \left(1 + \frac{\kappa_1 \mathrm{x}_0}{\kappa_0}\right)^{-1/\kappa_1}}\, d_0 \tag{5.51}$$

by means of pressure state and disturbance.

Substituting (5.51) in (5.50) allows for obtaining the **evaluated extended model**

$$\begin{aligned} \Delta\dot{\mathrm{x}}(t) = &- \frac{(\kappa_0 - \mathrm{x}_0 + \kappa_1 \mathrm{x}_0) S_\delta \zeta\ d_0}{V_\delta} \sqrt{\frac{1}{2\mathrm{x}_0 \varrho_0} \left(1 + \frac{\kappa_1 \mathrm{x}_0}{\kappa_0}\right)^{-1/\kappa_1}}\ \Delta\mathrm{x}(t) \\ &+ \frac{\kappa_0 + \kappa_1 \mathrm{x}_0}{V_\delta}\ \Delta u(t) - \frac{(\kappa_0 + \kappa_1 \mathrm{x}_0) S_\delta \zeta}{V_\delta} \sqrt{\frac{2\mathrm{x}_0}{\varrho_0} \left(1 + \frac{\kappa_1 \mathrm{x}_0}{\kappa_0}\right)^{-1/\kappa_1}}\ \Delta d(t) \end{aligned} \tag{5.52}$$

that is closely related to the extended approximated model (5.49).

The different linearised plant models will be compared on equilibrium. The on/off-valve is thereby assumed as open ($d_0 = 1$), while the operating pressure x_0 is subject for variation. The Bode plots of Figure 5.12 show the frequency responses of the approximated model (5.47), the extended approximated model (5.49) and the evaluated extended model (5.52). It can be seen that all plant models have a similar dynamic behaviour, where the characteristics range from a first order lag to an integrator, due to the varying parameters (see parameter range of Table 5.3). In general, the varying parameters cause an increased gain uncertainty for low frequencies, which is expected for all proposed plant models.

Considering the evaluated extended model (5.52) as a reference, the approximated model (5.47) features smaller deviations than the extended approximated model (5.49). The simplified linearisation, applied to derive the approximated plant model, seems satisfactory, instead of applying the exact linearisation, taking all time-varying and parameter-varying parameters into account. Thus, the approximated plant model is of first choice and will be further simplified for low-level control design.

Simplified model

The linearised model basically allows for distinguishing two cases. A first case requires at least one cutting head of a network subsection to be open, thus $d(t) = 1$, where another case assumes all cutting heads to be closed, hence $d(t) = 0$. The resulting simplified approximated model will be subject for control design in the subsequent section. It aims at robust control for the case where $|d(t)| \neq 0$.

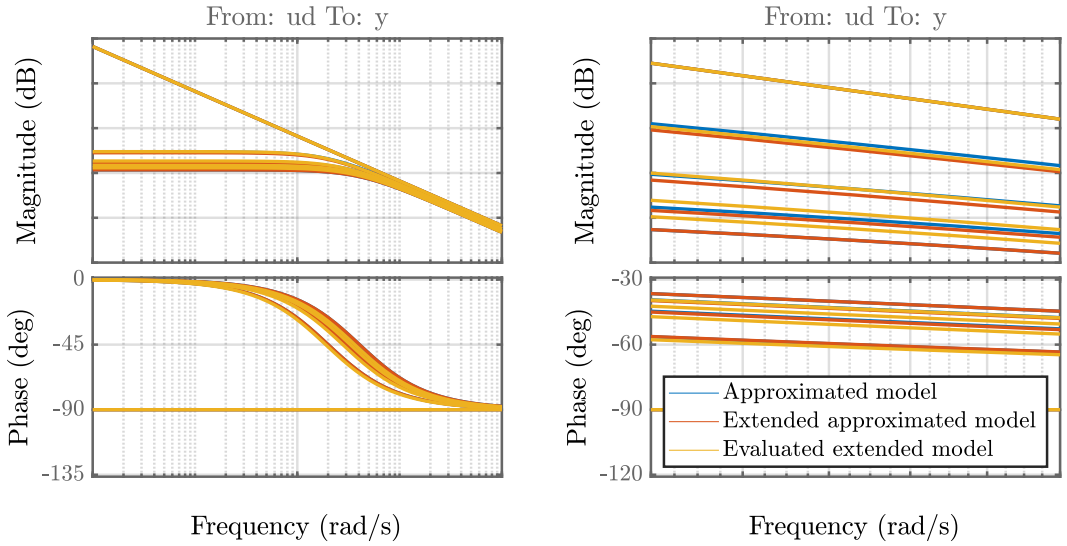

Figure 5.12 – Frequency responses for the linearised plant models: wide frequency range on the left hand side and zoomed in on the right hand side, showing minor deviations for the introduced approximations.

Before investigating the plant uncertainties, it is useful to define a common input channel. This input channel combines the control and disturbance input to a disturbed control input

$$u_d(t) = \Delta u(t) - \tilde{d}(t) \ , \tag{5.53}$$

which assumes the parameters upper bounds $H_\delta = H_{max}$ and $\mathrm{x}_\delta = \mathrm{x}_{max}$, defining the maximum disturbance

$$\tilde{d}(t) = H_{max}\sqrt{\mathrm{x}_{max}}\ \Delta d(t) \tag{5.54}$$

and applies the available disturbance range, for any permissible cutting head configuration. Introducing (5.53) and (5.54) further simplifies the approximated model (5.47) to obtain the **simplified approximated model**

$$\boxed{\Delta\dot{\mathrm{x}}(t) = -\frac{K_\delta H_\delta}{2V_\delta\sqrt{\mathrm{x}_\delta}}\ \Delta\mathrm{x}(t) + \frac{K_\delta}{V_\delta}\ u_d(t)} \ . \tag{5.55}$$

This simplification will not change the model dynamics, if a continuously changing value $d(t) = [-1, 1]$ is introduced, but allows for establishing an operating point of $d_0 = 1$. The Block diagram in Figure 5.13 illustrates the corresponding model structure. It can be seen that a signal from control input $\Delta u(t)$ to output $\Delta\mathrm{x}(t)$ possess the same dynamics as a signal from $\Delta d(t)$ to $\Delta\mathrm{x}(t)$. However, the disturbance input $d(t)$ will be bounded by H_{max} and x_{max}. This simplified model is useful, as it takes the full disturbance range into account and isolates the uncertain system dynamics to the perturbed plant $G_\mathrm{p}(s)$.

Complementary to that, it is also possible to assume $d_0 = 0$. This would lead to the integral behaviour

$$\Delta\dot{\mathrm{x}}(t) = \frac{K_\delta}{V_\delta}\ u_d(t) \tag{5.56}$$

and corresponds to a fully closed cutting head. It represents the parameter configuration, when input to state stability is not guaranteed.

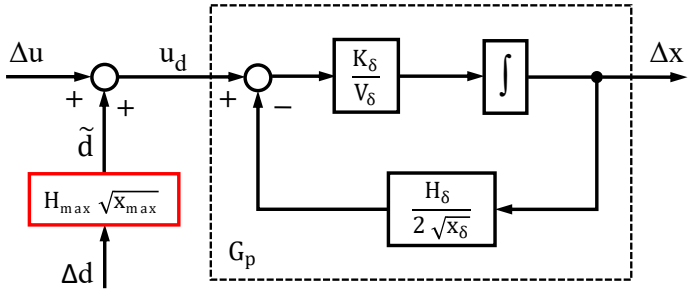

Figure 5.13 – Simplified approximated plant model: block diagram of the simplified approximated model in state space form.

Using Laplace transformation with $s = d/dt$ allows for rewriting the simplified approximated model (5.55) to obtain the perturbed plant

$$G_{\mathrm{p}}(s) = \frac{b_0}{s + a_0} \tag{5.57}$$

in transfer function form. This corresponds to a first order lag, from input $u_d(t)$ to output $\Delta\mathrm{x}(t)$, with coefficients

$$a_0 = \frac{K_\delta H_\delta}{2V_\delta\sqrt{\mathrm{x}_\delta}} \quad \text{and} \quad b_0 = \frac{K_\delta}{V_\delta} \ , \tag{5.58}$$

where $M_\delta = b_0/a_0$ denotes an uncertain gain and $\tau_\delta = 1/a_0$ is an uncertain time constant. It is not the standard form of a first order lag chosen, since this may cause division by zero for the given parameter ranges with

$$a_\delta = [a_{min},\ a_{max}] \longmapsto a_0 \quad \text{and} \quad b_\delta = [b_{min},\ b_{max}] \longmapsto b_0 \ . \tag{5.59}$$

Applying the values of Table 5.3 with respect to definition (5.58), gives the uncertainty ranges for lumped parameters, as listed in Table 5.4.

Table 5.4: Uncertainty range of lumped parameters used for transfer function description.

			Nom. value	Min value	Max value	Rel. range
a_δ	$(\sqrt{\mathrm{Pa}}/\mathrm{m}^3)$	$\times 10^{\#\#\#}$	###	###	###	$[-100, +225]$ %
b_δ	$(\mathrm{Pa}/\mathrm{m}^3)$	$\times 10^{\#\#\#}$	###	###	###	$[\ -43,\ \ +93]$ %

The Bode plots of Figure 5.14 compare the simplified approximated model in its state space representation (5.55) to the corresponding transfer function representation (5.57), with lumped parameters and again applying the parameter range of Table 5.3. The frequency responses for the perturbed plants show undesired differences, insofar as the uncertain parameters of the state space description have been lumped to the transfer function coefficients a_δ and b_δ. Especially, a broaden time constant variation as well as a smaller gain for low frequencies is observed.

The perturbed plant in transfer function form (5.57), derived from the simplified approximated model, is desirable for control design in frequency domain. However, it is not allowed to lump the various uncertain parameters, since this changes the dynamic perturbation range. The subsequent section combines the simplified approximated model (5.55) for nominal parameter values with the system components of a high-pressure system (see Figure 5.5) to derive an interconnection system, suitable for robust control design. The sensitivity to parameter variations will be discussed in Section 5.4, when introducing the uncertainty modelling.

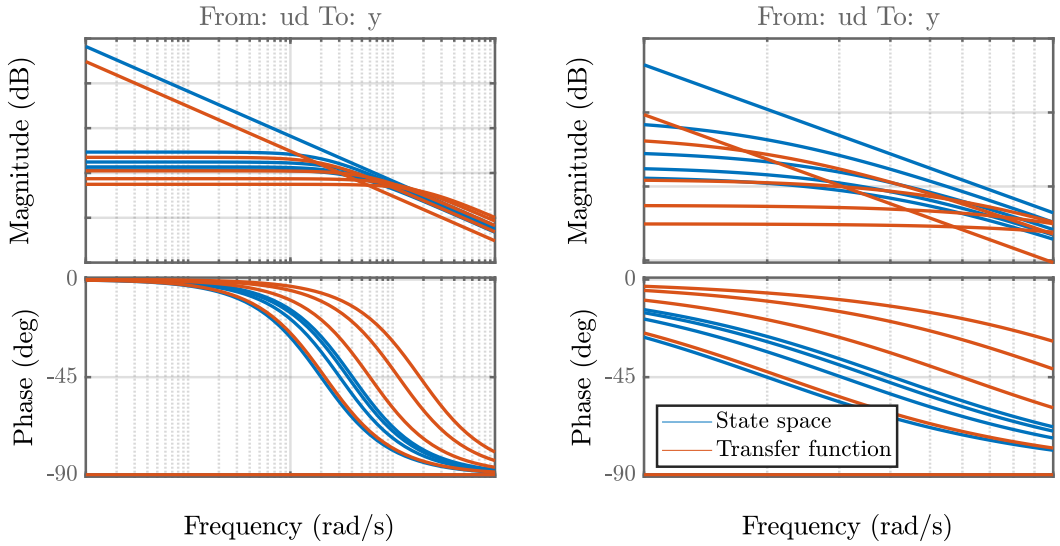

Figure 5.14 – Frequency responses comparing the simplified approximated model in state space form and its transfer function representation: wide frequency range on the left hand side and zoomed in on the right hand side, showing remarkable deviations when lumping uncertain parameters.

5.3.3 Interconnection system

This section introduces the interconnection system for controller synthesis, as illustrated in the block diagram of Figure 5.15. It represents the dynamics of different system components, by means of transfer functions. The actuator $G_a(s)$ and pressure gauge $G_s(s)$ interconnect the nominal plant $G_n(s)$ to the controller K(s). The nominal plant is derived from the perturbed plant (5.57), considering the nominal parameter values of Table 5.3 with respect to the coefficients (5.58). The resulting interconnection system is than scaled for unit input and output signals. The subscript w corresponds to weighted signals. It further includes shaping functions $W_r(s)$, $W_d(s)$, $W_n(s)$ and $W_\mathrm{p}(s)$ to specify input signals and weighting functions $W_e(s)$ and $W_u(s)$, taking the control requirements into account.

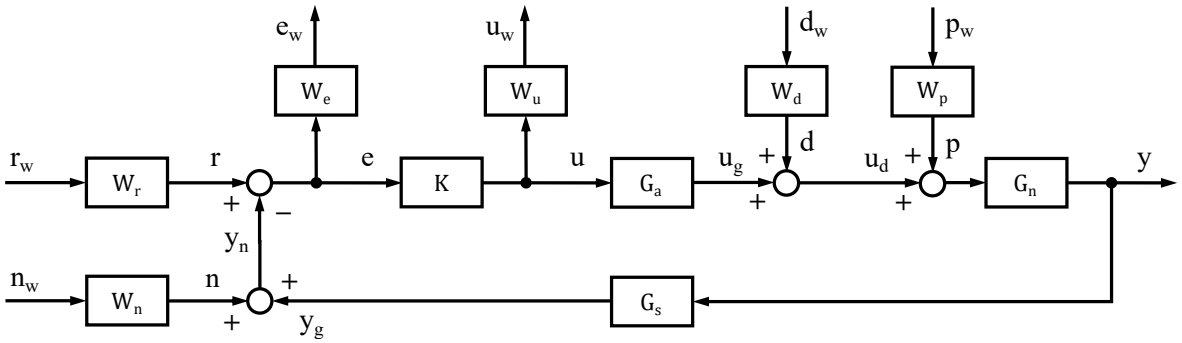

Figure 5.15 – Block diagram of the interconnection system: considering system components, shaping and weighting functions for control design.

Since the perturbed plant $G_\mathrm{p}(s)$ contains known non-linearities and all parameter variations, the other components are regarded as linear and time invariant (LTI). The high-pressure pump limits the available dynamic range of the control signal $u_g(t)$. It is affected by the bandwidth of

the linear actuator $G_a(s)$ in closed-loop position control. The control signal becomes disturbed. Introducing the dynamic range of the on/off-valve, $W_d(s)$ allows for reproducing the disturbance signal $d(t)$, as induced from a cutting head. Further, the bandwidth of the pressure gauge $G_s(s)$ defines the dynamic range of the measured process signal $y_g(t)$. This measurement signal is affected by noise $n(t)$ shaped by $W_n(s)$.

The interconnection system of Figure 5.15 allows for deriving the closed-loop transfer functions

$$y = \frac{G_n G_a \mathrm{K}}{1 + G_s G_n G_a \mathrm{K}}\, r + \frac{G_n}{1 + G_a \mathrm{K} G_s G_n}\, d - \frac{G_n G_a \mathrm{K}}{1 + G_s G_n G_a \mathrm{K}}\, n + \frac{G_n}{1 + G_a \mathrm{K} G_s G_n}\, p, \tag{5.60a}$$

$$e = \frac{1}{1 + G_s G_n G_a \mathrm{K}}\, r - \frac{G_s G_n}{1 + G_a \mathrm{K} G_s G_n}\, d - \frac{1}{1 + G_s G_n G_a \mathrm{K}}\, n - \frac{G_s G_n}{1 + G_a \mathrm{K} G_s G_n}\, p, \tag{5.60b}$$

$$u = \frac{\mathrm{K}}{1 + G_s G_n G_a \mathrm{K}}\, r - \frac{\mathrm{K} G_s G_n}{1 + G_a \mathrm{K} G_s G_n}\, d - \frac{\mathrm{K}}{1 + G_s G_n G_a \mathrm{K}}\, n - \frac{\mathrm{K} G_s G_n}{1 + G_a \mathrm{K} G_s G_n}\, p\ , \tag{5.60c}$$

which describe the effects on reference value $r(t)$, disturbance $d(t)$ and noise $n(t)$ on process value $y(t)$, control error $e(t)$ and control value $u(t)$. Here, the process value $y(t) = \mathrm{x}(t)$ corresponds to the system pressure state. The denominator is the same for each input channel, in addition, the transfer functions from the noise input are the same as the transfer functions from the reference input, but with a change of sign. Introducing the sensitivity function

$$\mathcal{S}(s) = \frac{1}{1 + G_s(s)\ G_n(s)\ G_a(s)\ \mathrm{K}(s)} \tag{5.61}$$

and the complementary sensitivity functions

$$\mathcal{T}_y(s) = \frac{G_n(s)\ G_a(s)\ \mathrm{K}(s)}{1 + G_s(s)\ G_n(s)\ G_a(s)\ \mathrm{K}(s)} \quad \text{and} \quad \mathcal{T}_u(s) = \frac{\mathrm{K}(s)\ G_s(s)\ G_n(s)}{1 + G_a(s)\ \mathrm{K}(s)\ G_s(s)\ G_n(s)} \tag{5.62}$$

in (5.60a - 5.60c), provides the simplified matrix notation

$$\begin{bmatrix} y \\ e \\ u \end{bmatrix} = \begin{bmatrix} \mathcal{T} \\ \mathcal{S} \\ K\mathcal{S} \end{bmatrix} r \ + \begin{bmatrix} G_n\mathcal{S} \\ -G_s G_n \mathcal{S} \\ -\mathcal{T}_u \end{bmatrix} d \ + \begin{bmatrix} -\mathcal{T}_y \\ -\mathcal{S} \\ -\mathrm{K}\mathcal{S} \end{bmatrix} n \ + \begin{bmatrix} G_n\mathcal{S} \\ -G_s G_n \mathcal{S} \\ -\mathcal{T}_u \end{bmatrix} p\ . \tag{5.63}$$

For control design, it is useful to keep in mind that $\mathcal{S}(j\omega) + \mathcal{T}(j\omega) = \mathrm{I},\ \forall\omega$ [Skogestad and Postlethwaite, 2005].

Effective disturbance rejection requires the H_∞-norm from disturbance $d(t)$ to control error $e(t)$ to be small, where acceptable control effort requires the H_∞-norm from disturbance $d(t)$ to control variable $u(t)$ to be limited. Hence, the control design specifications on performance and control effort, for any insignificant plant perturbation, can be evaluated from the H_∞-norm of the selected transfer functions

$$\left\| \begin{matrix} G_n\mathcal{S} \\ G_s G_n \mathcal{S} \\ \mathcal{T}_u \end{matrix} \right\|_\infty \tag{5.64}$$

in stacked notation, where the perturbation $\mathrm{p}(t)$ to the measurement output $y(t)$ must remain bounded to obtain robust stability, that is given for $\|G_n\mathcal{S}\|_\infty < 1$.

However, to guarantee robust stability and performance for the expected uncertainties requires to consider the perturbed plant $G_\mathrm{p}(s)$. For this reason, the perturbation input $\mathrm{p}(t)$ is introduced. However, this requires an adequate uncertainty modelling, that will be investigated in Section 5.4. The evaluation of the desired loop transfer functions by means of H_∞ controller synthesis, further requires an adequate signal scaling for the interconnection system of Figure 5.15. This scaling will be introduced first.

Signals scaling phase

The interconnection system will be scaled to bound the signal amplitudes to unit gain $|\cdot| \leq 1$ with respect to the maximal values of Table 5.5. This represents the maximal input and output values, as expected for a network subsection.

Table 5.5: Signals scaling to bound the amplitudes of an interconnection system to unit gain.

Maximal system pressure	$p_{max} = 400$ MPa
Maximal input fluid flow	$Q_{u,max} = 4.766\ \ell/\text{min}$
Maximal output fluid flow	$Q_{d,max} = 2.426\ \ell/\text{min}$

A scaling phase is applied to the following signals, where «~» is used to mark unscaled values.

Reference value r(t): The unscaled reference value $\tilde{r}(t)$ denotes the desired pressure. The scaling is given by $r(t) = R_r\ \tilde{r}(t)$, whereby $R_r = 1/p_{max}$, if $|\tilde{r}(t)| < |p_{max}|$ and $|r(t)| < 1$ holds.

Control value u(t): The unscaled control value $\tilde{u}(t)$ corresponds to the fluid flow, generated by a high-pressure pump. The scaling is given by $u(t) = R_u\ \tilde{u}(t)$, whereby $R_u = 1/Q_{u,max}$. Insofar as $|\tilde{u}(T)| < |Q_{u,max}|$ and $|u(t)| < 1$ holds, the maximal output fluid flow is given by the limited piston velocity v_{max} and its cross section surface S_P, such as $Q_{u,max} = S_P\ v_{max}$.

Disturbance value d(t): The unscaled input disturbance $\tilde{d}(t)$ denotes the unknown fluid flow consumption of a high-pressure network. The scaling is given by $d(t) = R_d\ \tilde{d}(t)$, whereby $R_d = 1/Q_{d,max}$. Insofar as $|\tilde{r}(t)| < |Q_{d,max}|$ and $|d(t)| < 1$ holds, the maximal output fluid flow is limited by the generated fluid flow, such as $Q_{d,max} < Q_{u,max}$. A typical value is found, when considering a use case with maximal fluid flow of $Q_{d,max} = H_{max}\sqrt{p_{max}}$.

Measurement value y(t): The unscaled measurement value $\tilde{y}(t)$ denotes the measured system pressure. The scaling is given by $y(t) = R_y\ \tilde{y}(t)$, whereby $R_y = 1/p_{max}$, if $|\tilde{y}(t)| < |p_{max}|$ and $|y(t)| < 1$ holds.

Noise value n(t): The unscaled noise value $\tilde{n}(t)$ denotes the measurement noise. The scaling is given by $n(t) = R_n\ \tilde{n}(t)$, whereby $R_n = 1/p_{max}$, identical to the reference and measurement value.

The scaling is directly implemented to the corresponding system components and weighting functions, where needed.

System blocks definition

The actuator $G_a(s)$ of the high-pressure pump, the nominal plant $G_n(s)$, representing a network subsection, the pressure gauge $G_s(s)$ and the controller $\mathrm{K}(s)$, describe system components of the feedback control loop. To design an augmented interconnection system requires to specify each system block as a transfer function.

Pump actuator G_a: A high-pressure pump generates an input fluid flow to supply a network subsection. The dynamics from the pump control signal $u(t)$ to the induced overall fluid flow $u_g(t)$ is approximated with a second order transfer function

$$\boxed{G_a(s) = \frac{1}{\#\#\#\ s^2 + \#\#\#\ s + 1}\ R_u^{-1}\ ,} \tag{5.65}$$

which scales the output $u(t)$ with $R_u^{-1} = 7.944\ 10^{-5}$ that the output corresponds to the induced overall fluid flow of a high-pressure pump.

This transfer function (5.65) originates from the desired actuator dynamics in closed-loop position control. It consists of an inner current loop, a velocity loop and an outer position loop, as discussed in Section 2.3. Whereas the inner control loop has proportional gain, the two outer control loops feature additional integral action. Load estimation is used to improve the disturbance rejection. The frequency response of Figure 5.16 represents the expected closed-loop dynamics for a pumping unit. Its actuators have been tuned to obtain a bandwidth of ### Hz ($\omega = ###$ rad/s) for the outer position loop and a damping coefficient $\varsigma > ###$, considering a second order model (5.27). This aims at a fast response with a rise time $\tau_r = ###$ seconds and an overshoot of $< 20\%$, where steady-state error is eliminated.

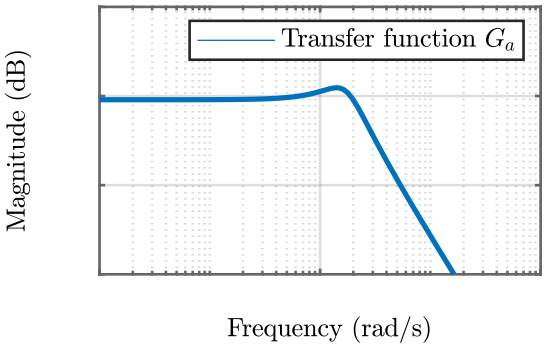

Figure 5.16 – Frequency response of the scaled actuator transfer function $G_a(s)$: considering the dynamic ranges of pumping units required for robust control design.

The verification of this parametrization requires identification by means of measurements. The identification procedure for a continuous-time model from sampled data is performed with respect to [Garnier et al., 2003]. To identify these model coefficients, for a pumping unit in operation, reveals some difficulties. The actuator stroke is limited and only the forward direction is of interest for identification. This since one pumping chamber is only interconnected to the high-pressure network, when its pumping unit is in the state of hauling. The identification data have been obtained from experiments with sinusoidal excitation, relating to [do Prado et al., 2006]. Therefore, a piston trajectory of limit bounds is implemented for camming, where a sinusoidal is super-positioned for excitation. This excitation is only applied for the piston stroke in ascending direction, as presented in plot (a) and (b) of Figure 5.17. The pumping states of pressurization and filling remain unmodified, where the state of hauling excites the pumping unit for a defined frequency. The camming shaft angular velocity $d\phi(t)/dt$ is then varied, by adjusting the control value $u(t) = [0, 1]$ as defined in (2.25) and (2.26) (see Section 2.3). This causes the excitation frequency to shift for the frequency range of interest, as shown in plot (c).

The resulting displacement velocities of each piston s_{P1} and s_{P2} are then measured by absolute encoders. Only the measurement data for hauling will be used for identification. The reference piston velocities from trajectory and the measured velocities are then evaluated for continuous-time transfer function estimation, using the instrument variable (IV) method [Gilson et al., 2008]. The frequency responses of Figure 5.18 (a) show the identified second order transfer functions and compare that to the expected second order model from controller tuning. Whereas the pumping unit 1 matches the reference transfer function with respect to frequency and damping ratio, the pumping unit 2 obtains an increased damping. The step responses of Figure 5.18 (b) compare the identified and tuned dynamics for both pumping units.

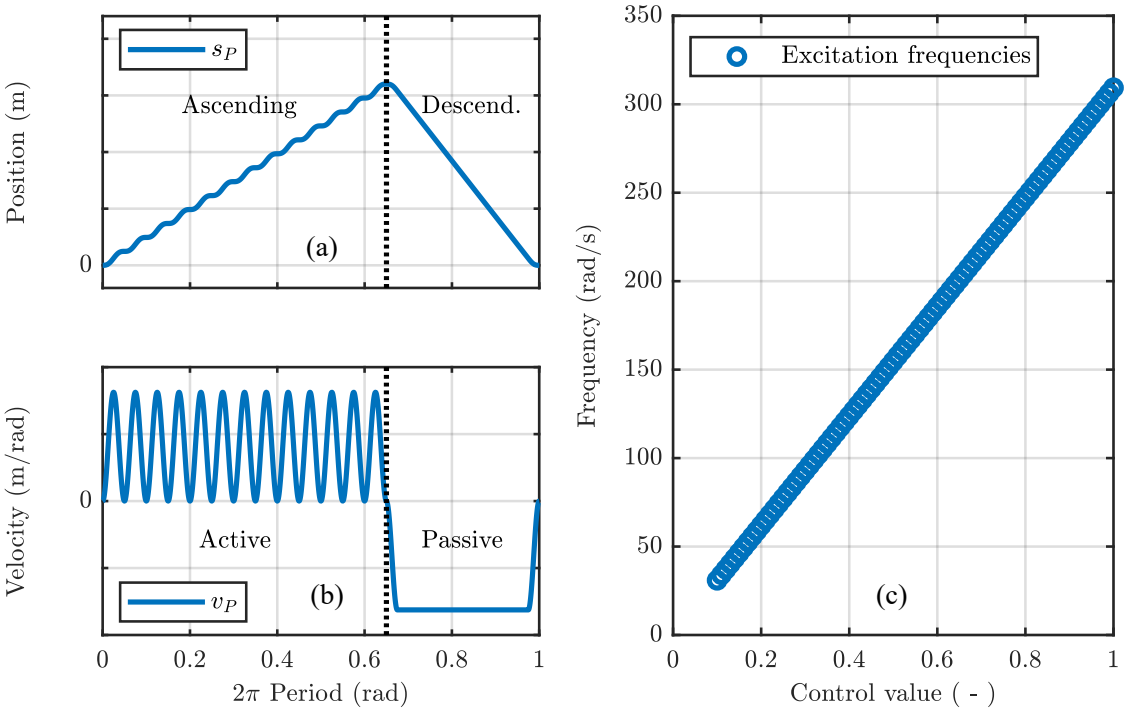

Figure 5.17 – Design of experiment to evaluate the actuator transfer function: velocity trajectory (a), position trajectory (b) for pump excitation and realized frequency range (c).

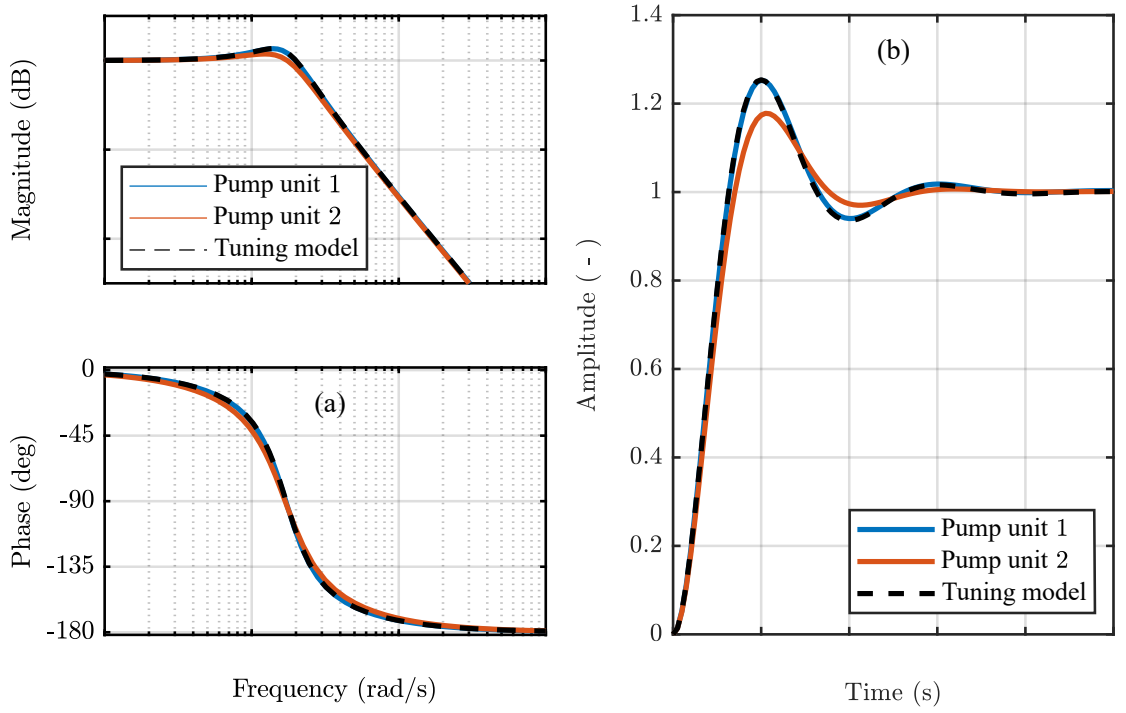

Figure 5.18 – Frequency and step responses of pump actuators: identified second order transfer function for both pumping units and expected second order model provided from motion control tuning.

It seems acceptable to apply the control tuning model (5.65) for describing the pump actuator dynamics. The identified bandwidth of a high-pressure pump is about 8 times faster as the desired closed-loop dynamics for pressure control. This is fundamental to obtain desired performance for disturbance rejection.

Nominal plant G_n: A network subsection interconnects a high-pressure pump to cutting heads. It contains all uncertainties due to varying parameters, e.g. the unknown subsection size. These parameters are investigated in a subsequent section to derive an adequate uncertainty description for control design. This allows for separating the uncertainties from the nominal plant by introducing a perturbation input. The simplified approximated model (5.55), evaluated for nominal parameter values (see Table 5.3), gives the nominal plant. It approximates the dynamics from the disturbed control input $u_d(t)$ to the measured system state $y(t)$ with a first order model

$$\boxed{G_n(s) = \frac{\#\#\#}{s + \#\#\#}\ R_r\ ,} \tag{5.66}$$

which represents the expected nominal characteristics for a network subsection, where $R_r = 2.5\ 10^{-9}$ scales the output $y(t)$ with respect to the maximal system pressure. The frequency response of Figure 5.19 shows the nominal dynamics of pressure generation for a network subsection.

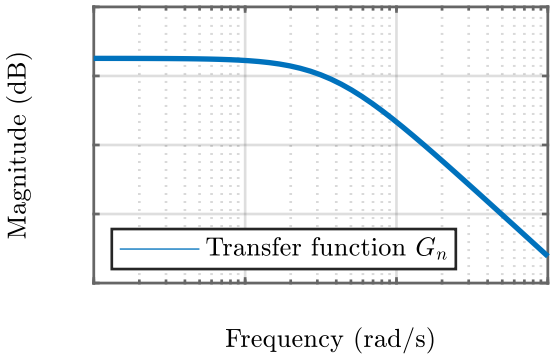

Figure 5.19 – Frequency response of the scaled nominal plant transfer function $G_n(s)$: considered nominal dynamic range of a network subsection required for robust control design.

Pressure gauge G_s: The pressure gauge measures the system state of a network subsection subject for control. It limits the dynamics from the measured system state $y(t)$ to the real measurement signal $y_g(t)$, represented by a second order model

$$\boxed{G_s(s) = \frac{1}{6.747\ 10^{-8}\ s^2 + 5.714\ 10^{-4}\ s + 1}\ .} \tag{5.67}$$

With respect to manufacturer specifications, an over-damped second order model has been considered, with a wide sensor bandwidth of 3.85 kHz and a damping coefficient of 1.1, such as to obtain a response time of < 1 ms for a step response from 10 - 90%. The frequency response of Figure 5.20 represents the approximated characteristics of a pressure gauge. No scaling is needed as the pressure gauge is located in the scaled feedback path of the interconnection system.

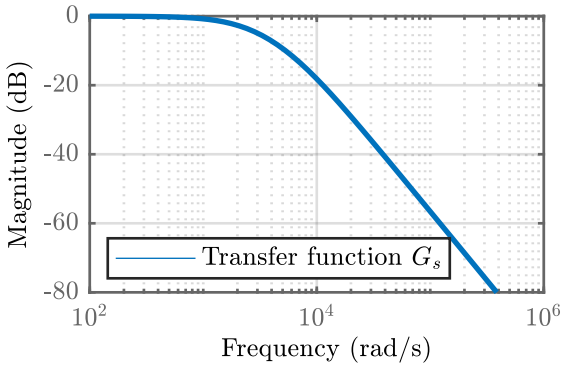

Figure 5.20 – Frequency response of the pressure gauge transfer function $G_s(s)$: considered dynamic range of the measurement signal required for robust control design.

Controller K**:** A controller will close the feedback loop of the interconnection system. Its parameters are subject for controller synthesis, it provides the characteristics from the control error $e(t)$ to the control value $u(t)$. Two concepts to specify a controller will be investigated. They are basically distinguished with respect to the control structure.

On the one hand, the **state feedback controller**

$$\mathrm{K}_{SF} = \begin{cases} \dot{\xi}(t) = A\ \xi(t) + B\ e(t) \\ u(t) = C\ \xi(t) + D\ e(t) \end{cases}, \tag{5.68}$$

with the controller states $\xi(t) \in \mathbb{R}^n$, the control output values $u(t) \in \mathbb{R}^q$ and the error input values $e(t) \in \mathbb{R}^p$ have been considered. This form is suitable for standard H_∞ controller synthesis, as provided in [Doyle et al., 1989]. Measuring a single system state and controlling this by means of a single control variable yields $q = p = 1$ and consequently, $A \in \mathbb{R}^{n\times n}$, $B \in \mathbb{R}^{n\times 1}$, $C \in \mathbb{R}^{1\times n}$ and $D = 0$. This requires to tune $(n + 2 \times n)$ control parameters, where n will be equal to the order of the overall interconnection system, which corresponds to the number of system poles. Hence, reducing the order of the interconnection system, will equally reduce the dimension of the resulting state feedback controller.

On the other hand, the continuous time **PI controller**

$$\mathrm{K}_{PI}(s) = K_P + K_I\ \frac{1}{s} \tag{5.69}$$

in parallel form has been considered, where K_P is a proportional gain and K_I denotes the integral gain. This form requires a structured H_∞ controller synthesis, as available in [Apkarian and Noll, 2006]. It is standard for implementation in industrial applications and features a slim structure with 2 parameters independent of the augmented interconnection system.

However, the reduced degree of freedom for H_∞ optimization limits the PI controller to perform competitive to a state feedback controller, in particular, a missing capability for noise rejection has been observed that is tremendous. Thus, considering a low-pass filter as an additional tuning parameter, enables the PI controller to obtain a precise approximation, with almost identical stability and robustness properties, comparable to a state feedback controller. The **extended PI controller**

$$\tilde{\mathrm{K}}_{PI}(s) = \left(K_P + K_I\ \frac{1}{s}\right) \frac{1}{1 + \tau_f\ s} \tag{5.70}$$

introduces a first order low-pass filter with the tunable time constant τ_f. The H_∞ synthesis to obtain robust controller parameters is discussed in Chapter6.

Input signal shaping functions

Shaping functions will define the dynamic range of the input channels. As required to build the augmented interconnection system, each weighting function is related to a corresponding input channel, as denoted by its subscript. The shaping function W_r is applied on the reference signal $r(t)$, where W_d shapes the disturbance signal $d(t)$, W_p relates to the perturbation signal $\mathrm{p}(t)$ and W_n defines the dynamics of the noise signal $n(t)$.

Reference shaping function W_r: The scaled reference signal $r_\mathrm{w}(t) = [0, 1]$ provides the desired operating point for waterjet machining. Any change of the operating point should be gradually applied on the high-pressure network. This is realized with a **reference shaping function**

$$\boxed{W_r(s) = \frac{1\ 10^{-4}s + 0.6}{s + 0.6}\ ,} \tag{5.71}$$

that defines the dynamic range for any changes on the reference value $r(t)$. This can be considered as a pre-filter for control design. It is preferably a low-pass filter, where a cut-off frequency of 0.6 Hz has been selected with respect to the predefined soft constraints. This enables a response time of > 5 s to reach 95% of the desired reference value. The frequency response of Figure 5.21 shows the dynamic range for the reference signal.

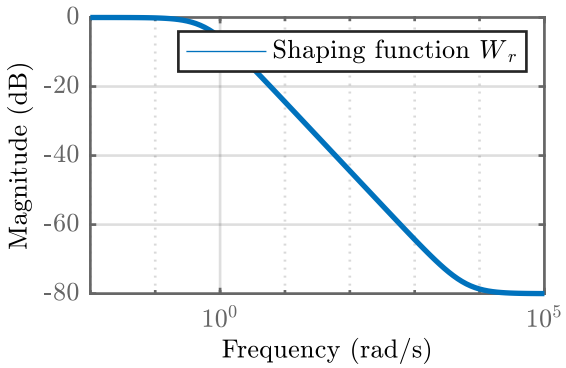

Figure 5.21 – Frequency response of the scaled reference shaping function $W_r(s)$: considered dynamic range of the reference value required for robust control design.

Disturbance shaping function W_d: The switching of the on/off-valve affects the water consumption of a cutting head. The resulting output fluid flow is considered as a disturbance $d(t)$, which acts against the input fluid flow from the high-pressure pump. It refines the disturbed control input $u_d(t) = u_g(t) + d(t)$, where a scaled disturbance signal $d_\mathrm{w}(t) = [0, 1]$ switches the on/off-valve with respect to an unknown switching pattern.

The switching dynamics of the on/off-valve gives the frequency range for any change on the disturbance. That is represented by the **disturbance shaping function**

$$\boxed{W_d(s) = \frac{1\ 10^{-4}s + 2.209\ 10^2}{s + 2.209\ 10^2}\ R_d^{-1}\ ,} \tag{5.72}$$

which is again a low-pass filter, as shown with the frequency response in Figure 5.22 (a). It is scaled with $R_d^{-1} = 4.044\ 10^{-5}$ that the output corresponds to the maximal water consumption of the cutting heads, allowed for a network subsection.

A cut-off frequency of 221 Hz has been chosen, as specified by the manufacturer, taking the on/off-valve switching dynamics into account. This enables a response time of < 10 ms considering the interval from 10 - 90%, when switching the on/off-valve, see step response of Figure 5.22 (b).

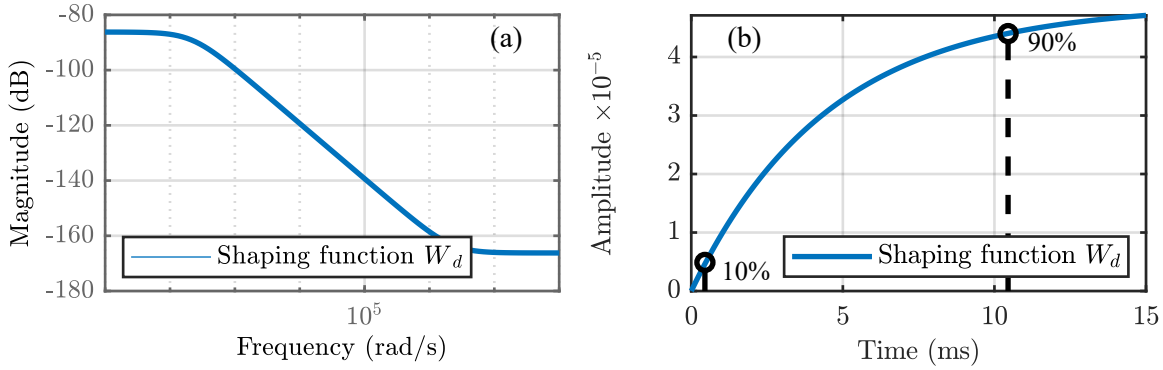

Figure 5.22 – Frequency response of the scaled disturbance shaping function $W_d(s)$: considered dynamic range of the cutting head on/off-valve to shape the disturbance signal.

Perturbation shaping function W_p: The inverse additive uncertainty model $W_{ia}(s)$ of Equation (5.133), defined later in the subsequent section, further extends the interconnection system with a perturbation input $\mathrm{p}(t)$. The dynamic range of this additional input signal is given by the **perturbation shaping function**

$$\boxed{W_\mathrm{p}(s) = W_{ia}(s)\ R_r^{-1}\ ,} \tag{5.73}$$

which is scaled with $R_r^{-1} = 4.0\ 10^8$ to obtain a scaled input perturbation $\mathrm{p_w}(t) = [0, 1]$.

The frequency response of Figure 5.23 shows the expected dynamic range for the plant perturbation. The investigations to derive a suitable uncertainty model is subject for the subsequent section.

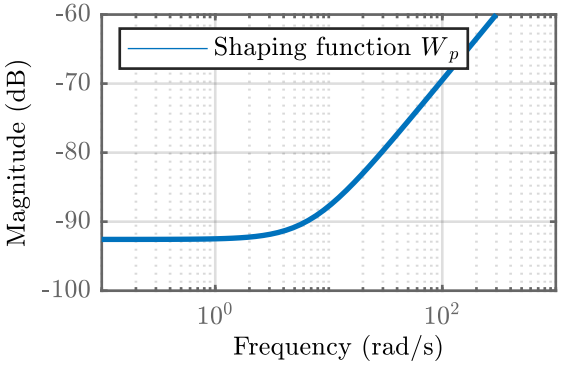

Figure 5.23 – Frequency response of the scaled perturbation shaping function $W_\mathrm{p}(s)$: considered dynamic range of the inverse additive uncertainty to shape the perturbation signal.

Noise shaping function W_n: To investigate the noise dynamics of the measurement signal $y_n(t) = y_g(t) + n(t)$ from a pressure gauge, the pressure has been measured at different operating points $r(t) \in \{100, 200, 300, 400\}$ MPa. Measurement data have been derived from 2 different pressure gauges of the same type. The high-pressure pump will run in open-loop. This allows

for generating a continuous input fluid flow. A pressure equilibrium will be obtained, when the resulting output fluid flow at the cutting head corresponds to the generated input fluid flow. Data acquisition has been realized with a sampling rate of 200 Hz, when steady-state pressure near desired operating point has been reached. The experiment has been repeated to obtain 2 measurements for each operating point. That gives a total of 16 measurements.

Assuming Gaussian distribution allows for considering that the mean value

$$\bar{y}_n = \frac{1}{M} \sum_{i=1}^{M} y_{n,i} \tag{5.74}$$

of a measurement with M samples reproduces the actual value $\bar{\mu}(y) \approx \bar{y}_n$ with increased precision for a large number of samples $M \to \infty$. This mean value provides then the expected noise $n = y_n - \bar{\mu}(y)$ that corrupts the measurement signal. The plots of Figure 5.24 show selected measurements for different operating points. Small variance around expected value with 3 $\sigma <$ 0.2 MPa has been observed for each measurement.

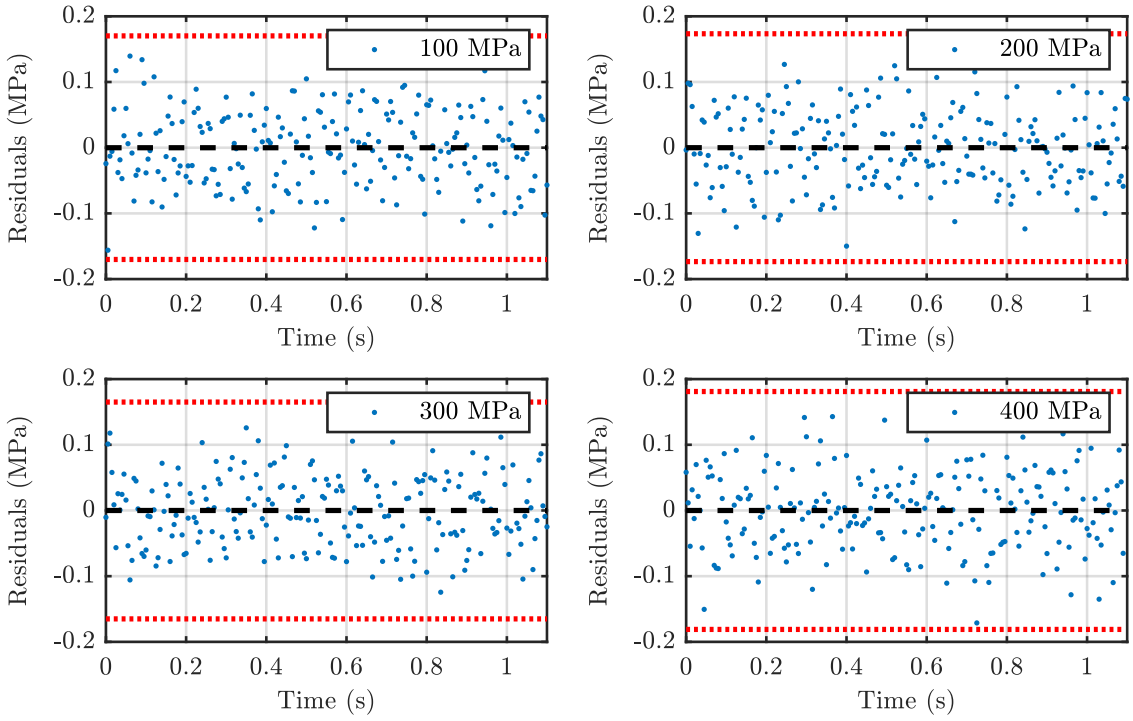

Figure 5.24 – Measured noise for different operating points: residuals, mean values and 3 σ interval for different measurements reveal similar variance around expected value.

The Box-plot of Figure 5.25 shows the deviations for each measurement, where the plots of Figure 5.26 present the corresponding density function, when combining all measurements for an operating point. These show that the deviation due to noise resemble Gaussian distribution for an increasing numbers of samples. The variation remains similar for any operating point. As a consequence, additive Gaussian noise becomes acceptable to represent the measurement noise.

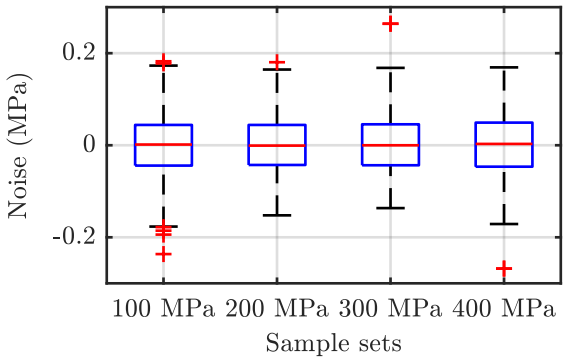

Figure 5.25 – Box-plot of measured noise: residuals for measurements at 100, 200, 300 and 400 MPa pressures reveal evidence for additive noise phenomena.

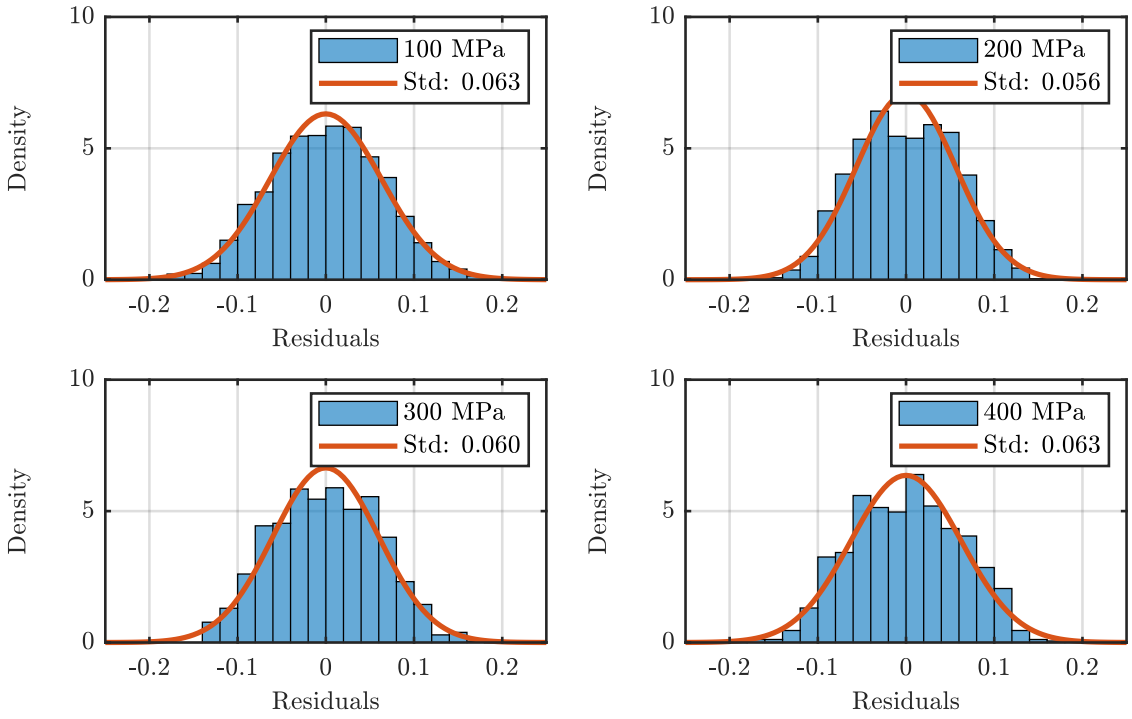

Figure 5.26 – Histogram of measured noise: residuals for measurements at 100, 200, 300 and 400 MPa pressure reveal similar variance close to Gaussian distribution.

Applying Fast Fourier Transformation (FFT) [Frigo and Johnson, 1998] to the noise $n(t)$ and investigating its amplitude spectrum $A(f)$, as shown in plot of Figure 5.27, allows for evaluating the noise dynamics with respect to the frequency f. This aims to specify an adequate shaping function, see frequency response of Figure 5.28, which approximates the noise dynamics. For this, the maximum magnitude $|A_{max}(f)| = max|A_k(f)|$ for each measurement k defines a frequency dependent upper bound. This bound rise with > 100 dB per decade from about -160 dB for low frequencies (< 1 Hz) to about -100 dB at high frequencies (> 3 Hz) for every operating point. Resonance peaks of -80 dB occur at high frequencies (74 Hz), where a maximal magnitude of -140 dB is observed at low frequencies. As a consequence, a second order transfer function has been considered. This provides a trade-off between accuracy and complexity.

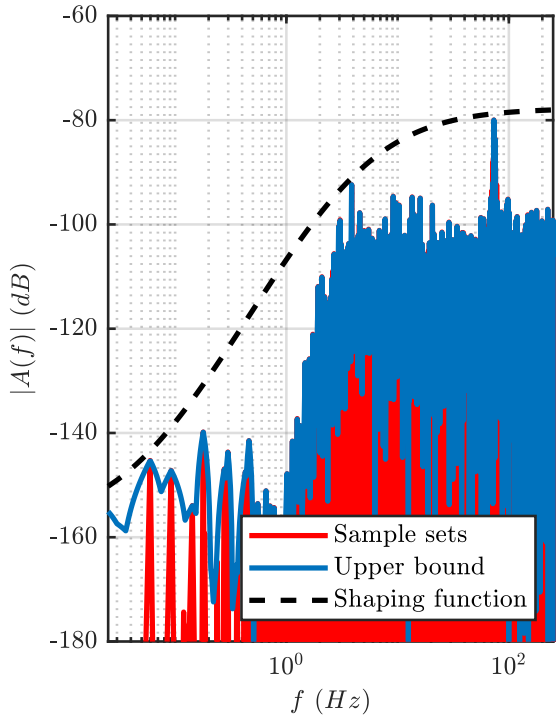

Figure 5.27 – Amplitude spectrum of measured noise: FFT for measurements at 100, 200, 300 and 400 MPa pressures, its upper bound and selected shaping function.

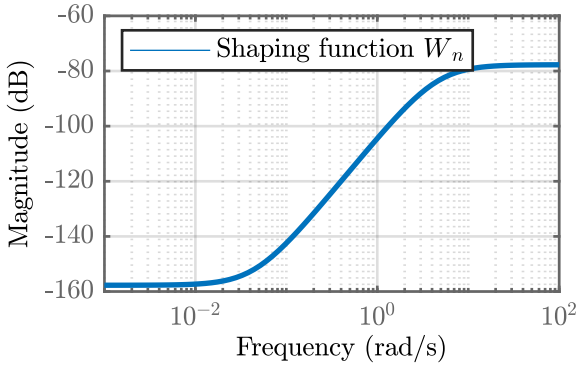

Figure 5.28 – Frequency response of noise shaping function $W_\mathrm{p}(s)$: considered dynamic range of the noise signal required for robust control design.

This results in the **noise shaping function**

$$\boxed{W_n(s) = \frac{1.3\ 10^{-4}s^2 + 1.186\ 10^{-5}s + 2.704\ 10^{-7}}{s^2 + 9.121s + 20.8}\ ,} \tag{5.75}$$

that represents the expected worst case frequency response, taking into account that the feedback loop is already scaled. It introduces a small magnitude for low frequencies and expects a high magnitude for high frequencies. This covers the observed signal dynamics and represents the observed additive noise of the measured signal. Eventually, a signal to noise ratio SNR $>$ 60 dB has been observed. Table 5.6 shows details for each measurement.

Table 5.6: Properties of the measurement signal derived from 2 pressure gauges for different measurements at 100, 200, 300 and 400 MPa operating points.

Operating point	σ^2 $\times 10^{-3}$	SNR (dB)	Sensor	Sample set	Number of samples	σ^2 $\times 10^{-3}$	SNR (dB)
100 MPa	3.99	61.381	1	A	539	5.40	60.251
				B	539	2.95	62.653
			2	A	539	4.33	60.998
				B	539	3.22	62.653
200 MPa	3.18	70.699	1	A	339	3.13	70.835
				B	339	3.17	70.774
			2	A	339	3.09	70.764
				B	339	3.34	70.430
300 MPa	3.60	73.557	1	A	259	3.71	73.534
				B	259	3.03	74.341
			2	A	259	3.50	73.685
				B	259	4.22	72.791
400 MPa	3.93	75.371	1	A	219	4.27	75.088
				B	219	3.84	75.530
			2	A	219	4.04	75.234
				B	219	3.64	75.660

Compared to the pump actuator model, the expected disturbance dynamics seems to be slightly faster. However, the frequency response of Figure 5.29 shows for a frequency range of interest, that the magnitude for which the control value acts on the nominal plant is larger as the disturbance magnitude. In other terms, for frequencies $f < \#\#\#$ Hz where the damping reaches > 60 dB, the open-loop gain from control input to plant output ($u_g(t) \rightarrow y(t)$) is higher as the gain from disturbance input to plant output ($d_{\mathrm{w}}(t) \rightarrow y(t)$). This guarantees a feasible and effective disturbance rejection by means of the pump actuators.

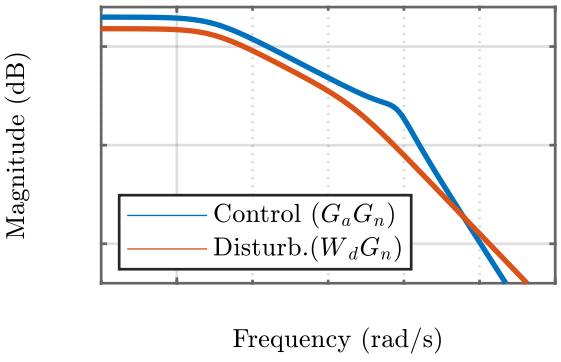

Figure 5.29 – Scaled frequency responses of the pump and valve actuators with plant in series: dynamic range from the control signal to the pressure state and from the disturbance signal to the pressure state.

Output signal weighting functions

Output weighting functions are selected and shaped with respect to the control system design requirements. A performance weight applied on the error signal and a control effort weight applied on the control signal will be specified. The performance weight has typically a small magnitude at low frequencies. This aims at good disturbance rejection, whereas the control effort weight has a small magnitude at high frequencies. This attenuates shuttering on the actuator due to signal noise and avoids actuator saturations.

Performance weighting function W_e: The condition for nominal performance $|W_e G\mathcal{S}| < 1$ requires the largest singular values $\bar{\sigma}(G\mathcal{S}) \leq |W_e|^{-1}$ to become smaller as the inverse performance weight [Skogestad and Postlethwaite, 2005]. This can be evaluated using the H_∞-norm

$$\|G\mathcal{S}\|_\infty < \frac{1}{\|W_e\|_\infty} \tag{5.76}$$

and applying the small gain theorem (5.13) yields

$$\|W_e G\mathcal{S}\|_\infty < 1 \ , \tag{5.77}$$

where W_e is a weighting function applied on the error signal $e(t)$. It is used as performance weight with respect to disturbance rejection. This requires a controller K(s), employed to the interconnection system of Figure 5.15, to hold the weighted error signal $|e_{\mathrm{w}}(t)| < 1$ bounded for a unit input on the shaped disturbance signal $|d_{\mathrm{w}}(t)| = 1$.

A signal from input channel $d_{\mathrm{w}}(t)$ to output channel $e_{\mathrm{w}}(t)$ relates to the transfer function

$$e_{\mathrm{w}}(t) = -W_e \ G_s \ G_n \ \mathcal{S} \ W_d \ d_{\mathrm{w}}(t) \ , \tag{5.78}$$

which evaluates nominal performance for disturbance rejection ($d_{\mathrm{w}}(t) \rightarrow w_{\mathrm{w}}(t)$) and provides the performance criterion

$$\|W_e \ G_s \ G_n \ \mathcal{S} \ W_d\|_\infty < 1 \ , \tag{5.79}$$

related to (5.20b). This criterion will be satisfied if

$$|\mathcal{S}(j\omega)| < \frac{1}{|W_e(j\omega) \ G_s(j\omega) \ G_n(j\omega) \ W_d(j\omega)|} \ \forall \ \omega \ . \tag{5.80}$$

Considering the control objective (5.36), given by the weighting function $|\mathcal{S}(j\omega)|^{-1} > |W_1(j\omega)|$, defines a lower bound

$$|W_e(j\omega) \ G_s(j\omega) \ G_n(j\omega) \ W_d(j\omega)| < |W_1(j\omega)| \tag{5.81}$$

to select a performance weight

$$|W_e(j\omega)| < \frac{|W_1(j\omega)|}{|G_s(j\omega) \ G_n(j\omega) \ W_d(j\omega)|} \ . \tag{5.82}$$

The **performance weighting function**

$$\boxed{W_e(s) = \frac{1\ 10^{-5}\ s + 221}{s + 0.221}} \tag{5.83}$$

has been specified to attenuate frequencies of < 10 Hz with > 20 dB. That should restrict the overshoot for pressure fluctuations, due to exogenous disturbances, below 10%. Increasing the bandwidth for disturbance rejection would further improve performance, but noise attenuation becomes worse.

The frequency response of Figure 5.30 compares the weighting function W_e and the lower bound, given by the control requirements. Reference value tracking is also specified by the performance weighting function W_e and the high magnitude for low frequencies causes integral action, eliminating steady-state error.

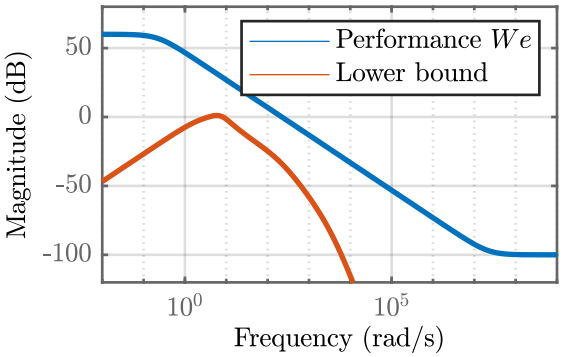

Figure 5.30 – Frequency response of the weighting function $W_e(s)$: dynamic range of the weighting on the error signal and lower bounds from control requirements.

Control effort weighting function W_u: The condition to penalize control effort $|W_u\mathcal{T}| < 1$ requires the largest singular values $\bar{\sigma}(\mathcal{T}) \leq |W_u|^{-1}$ to become smaller as the inverse performance weight [Skogestad and Postlethwaite, 2005]. This can be evaluated using the H_∞-norm

$$\|\mathcal{T}\|_\infty < \frac{1}{\|W_u\|_\infty} \tag{5.84}$$

and again applying the small gain theorem (5.13) yields

$$\|W_u\mathcal{T}\|_\infty < 1\ , \tag{5.85}$$

where W_u is a weighting function applied on the control signal $u(t)$. It is used as control effort weight, taking the actuator saturation into account by penalizing the control effort. Thus requires a controller $\mathrm{K}(s)$, employed to the interconnection system of Figure 5.15, to hold the weighted control signal $|u_\mathrm{w}(t)| < 1$ bounded for a unit input on the shaped disturbance signal $|d_\mathrm{w}(t)| = 1$.

A signal from input channel $d_\mathrm{w}(t)$ to output channel $u_\mathrm{w}(t)$ relates to the transfer function

$$u_\mathrm{w}(t) = -K\ G_s\ G_n\ \mathcal{S}\ W_d\ d_\mathrm{w}(t)\ , \tag{5.86}$$

which penalizes the control effort for a disturbance signal ($d_\mathrm{w}(t) \rightarrow w_\mathrm{w}(t)$) and provides the control effort criterion

$$\|K\ G_s\ G_n\ \mathcal{S}\ W_d\|_\infty < 1\ . \tag{5.87}$$

Approximating $\mathcal{T} \approx G_n\ G_s\ K\ \mathcal{S}$, criterion (5.87) will be satisfied if

$$|\mathcal{T}(j\omega)| < \frac{1}{|W_u(j\omega)\ W_d(j\omega)|}\ \forall\ \omega\ . \tag{5.88}$$

Considering the control objective (5.37), given by the weighting function $|\mathcal{T}(j\omega)|^{-1} > |W_2(j\omega)|$, defines an upper bound

$$|W_u(j\omega)\ W_d(j\omega)| < |W_2(j\omega)| \tag{5.89}$$

to select a performance weight

$$|W_u(j\omega)| < \frac{|W_2(j\omega)|}{|W_d(j\omega)|}\ . \tag{5.90}$$

The **control effort weighting function**

$$\boxed{W_u(s) = \frac{1\ 10^5\ s + 8.281\ 10^4}{s + 8.281\ 10^7}} \tag{5.91}$$

has been considered, taking the actuator dynamic range into account.

The frequency response of Figure 5.31 compares the weighting function W_u and the upper bound, given by the control requirements. Noise attenuation for high frequencies is desired, avoiding these frequencies to act on the actuators.

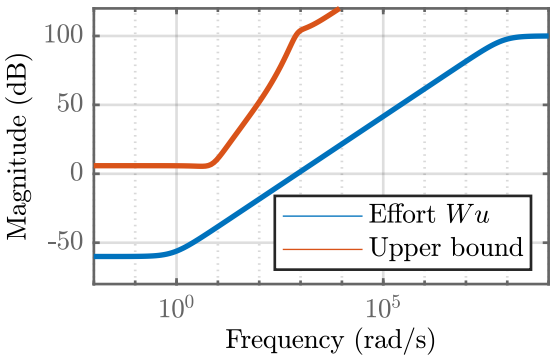

Figure 5.31 – Frequency response of the weighting function $W_u(s)$: dynamic range of the weighting on the control signal and upper bound from control requirements.

Robustness weighting function W_y: The condition for robust stability $|W_\mathrm{p} G\mathcal{S}| < 1$ requires the largest singular values $\bar{\sigma}(G\mathcal{S}) \leq |W_\mathrm{p}|^{-1}$ to become smaller as the inverse perturbation shaping function. This condition holds particularly for an inverse additive uncertainty description [Skogestad and Postlethwaite, 2005]. It can be evaluated, using the H_∞-norm

$$\|G\mathcal{S}\|_\infty < \frac{1}{\|W_\mathrm{p}\|_\infty} \tag{5.92}$$

and applying the small gain theorem (5.13) yields

$$\|W_\mathrm{p} G\mathcal{S}\|_\infty < 1\ . \tag{5.93}$$

For instance, $W_\mathrm{p} = W_{ia}$ is a shaping function in inverse additive form, applied on the system output state $y(t)$. It is used as robustness weight with respect to the introduced plant perturbations. This requires a controller K(s), employed to the interconnection system of Figure 5.15, to

hold the measured system state $|y(t)| < 1$ bounded for a unit input on the shaped perturbation signal $|\mathrm{p_w}(t)| = 1$.

A signal from input channel $\mathrm{p_w}(t)$ to output channel $y(t)$ relates to the transfer function

$$y(t) = -G_n \; \mathcal{S} \; W_{ia} \; \mathrm{p_w}(t) \; , \tag{5.94}$$

which provides robust stability for the perturbed plant ($\mathrm{p_w}(t) \rightarrow y(t)$) and yields the robustness criterion

$$\|G_n \; \mathcal{S} \; W_{ia}\|_\infty < 1 \tag{5.95}$$

related to (5.22a). This will be satisfied if

$$|\mathcal{S}(j\omega)| < \frac{1}{|G_n(j\omega) \; W_{ia}(j\omega)|} \; \forall \; \omega \; . \tag{5.96}$$

Considering the control objective (5.36), given by the weighting function $|\mathcal{S}(j\omega)|^{-1} > |W_1(j\omega)|$, defines an upper bound

$$|G_n(j\omega) \; W_{ia}(j\omega)| < |W_1(j\omega)| \tag{5.97}$$

to select a robustness weight

$$|W_{ia}(j\omega)| < \frac{|W_1(j\omega)|}{|G_n(j\omega) \; |} \; . \tag{5.98}$$

The singular values of Figure 5.32 compares the shaping function W_p and the upper bound, given by the control requirements.

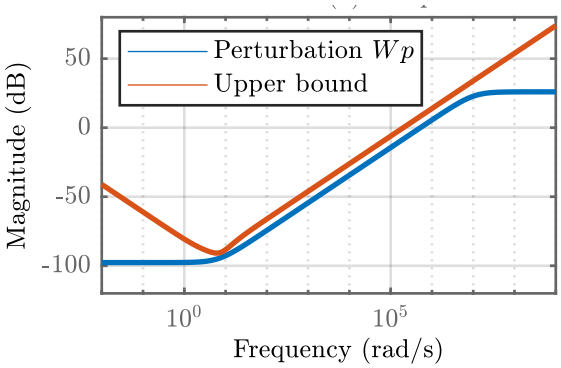

Figure 5.32 – Frequency response of the shaping functions $W_\mathrm{p}(s)$: dynamic range of the weighting on the perturbation signal and lower bounds from control requirements.

Reference value tracking is not explicitly subject of control design, insofar as low dynamics for the reference value is desired. This is taken into account by the input weighting function on $r(t)$. On the other hand, noise attenuation for high frequencies is desired. The measurement noise is not tremendous, as measurements reveal. Since the suppression of high frequencies is already specified by the control effort weighting function, noise attenuation is not explicitly considered.

First order functions are used to weight the output channels with respect to performance and control effort. This signal-based approach describes the robust control design problem, subject for H_∞ controller synthesis. Higher order weighting functions could be applied to sharpen the control requirements, if needed. But wherever possible, first order weighting functions have been implemented. This aims at a low order interconnection system, since the order of the resulting generalized plant will define the controller order.

It is important to select weighting functions with respect to defined bounds. Otherwise, a feasible controller will comply with $\mathcal{S}(s) + \mathcal{T}(s) = 1$, but fails to meet the control objectives. The proposed performance weight W_e on $e(t)$ and control effort weight W_u on $u(t)$ are taken into account for the H_∞ controller synthesis of Section 6.2, which are in compliance with the lower bound (5.81) and upper bound (5.89), respectively. The robustness weight W_p on $y(t)$ will be considered to evaluate robust performance for the resulting close-loop system. The subsequent section is dedicated to obtain a suitable uncertainty model that describes the robustness weight.

5.4 Uncertainty modelling

The introduced plant models contain varying parameters, which can be described as structured uncertainties of real parameters. Another approach is to lump these parametric uncertainties to an unstructured uncertainty description of complex values, representing the varying parameters with respect to the frequency domain. Thereby, an additive form, a multiplicative form and its inverse representations are compared, when approximating all the uncertain parameters with a shaping function. The diagram of Figure 5.33 summarizes the model evaluation process of this section. It applies both approaches to the simplified approximated model (5.55), that is linearised and of first order. The obtained unstructured uncertainty descriptions are then compared to the structured description to evaluate an adequate uncertainty model for control design. Linear fractional transformation (LFT) is used, to separate the uncertainty and the nominal plant.

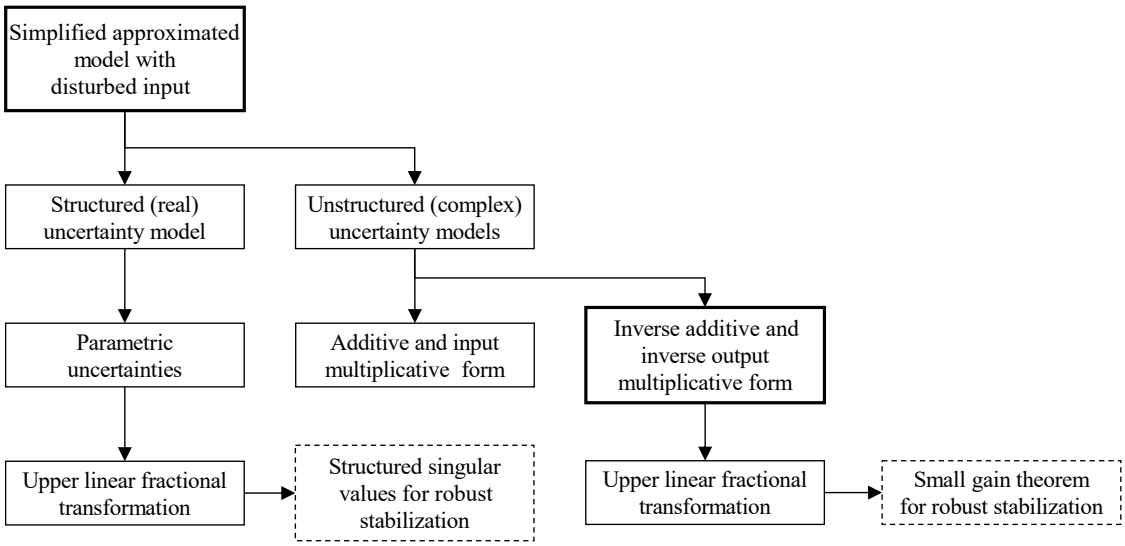

Figure 5.33 – Overview of the uncertainty model evaluation process: different approaches to describe the varying parameters for control design.

For the structured uncertainty case, robust stabilization has to consider the concept of structured singular values, where the unstructured uncertainty case can be evaluated with respect to the small gain theorem [Gu et al., 2013]. Before introducing the uncertainty modelling, this sections first classifies the varying parameters and analyses the plant input to output sensitivity due to parameter variations.

5.4.1 Evaluating parameter variations and input to output sensitivity

When formulating the control design problem (see Section 5.3), it is recognized that different uncertainties affect the behaviour of a high-pressure system. This section classifies and verifies these parameter variations, which will affect the resulting closed-loop performance and stability. It is therefore distinguished between parameter-varying and time-varying uncertainties:

Two classes of parameter-varying uncertainties are considered. The first class depends on the network configuration. These parameters will not change during operation, but are different for every waterjet facility. The second class considers varying parameters conditioned by the pressure state. These parameters will only change, when the operating point for waterjet machining varies.

Also time-varying uncertainties distinguish two classes. Where the variation in time follows an a priori known function or it is driven by an unknown function. In both cases, the variation will occur during pump operation. The diagram of Figure 5.34 classifies these uncertainties, subject for further investigations.

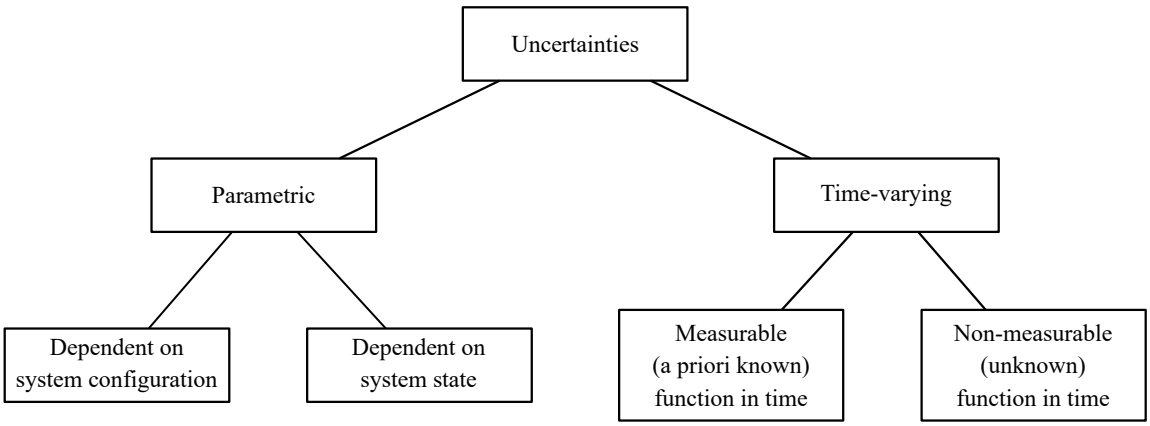

Figure 5.34 – Classification of uncertainties: time-varying and parametric uncertainties used to describe varying parameters, subject for control design.

Range and type of parameter variation

The variables related to the plant models (5.47) and (5.52) can be assigned to two groups, as shown in Figure 5.35. Each group is related to a parameter-varying as well as to a time-varying uncertainty. A first group depends on the time-varying pressure state $p(t)$ and on the parameter-varying nozzle cross section S_H. The second group is dedicated to a time-varying camming angle $\phi(t)$ and a parameter-varying fluid volume V_0, that relates to the size of a high-pressure network subsection. Hence, group 1 depends on the measurable pressure state, but unknown nozzle cross section and group 2 considers a measurable camming angle, but includes the unknown network volume.

The overall fluid volume

$$V_\delta = V_0 + V_C(s(\phi)) \tag{5.99}$$

deals with an unknown parameter-varying uncertainty and a periodic time-varying uncertainty. It is composed from the fluid volume V_0 of a high-pressure network and the displacement volume V_C in the pumping chamber. The network contributes to an unknown volume that is constant in time for a specific waterjet facility, but changes when the network configuration becomes adjusted.

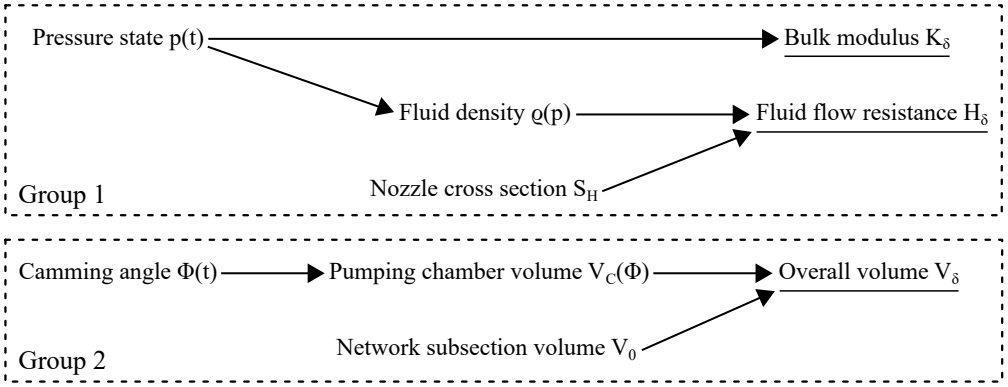

Figure 5.35 – Grouping of uncertain parameters: time-varying and parametric uncertainties used to describe varying parameters, subject for control design.

On the other hand, the pumping chamber volume changes with respect to the piston position $s(\phi)$ and the alternating operation of two coupled pumping units, see the model-based synchronization introduced in Section 2.3. This follows a periodic function in time with respect to the camming angle $\phi(t)$, as shown in plot of Figure 5.36. Considering the alternating operation of pumping units results in an unsteady periodic function s_δ. It shows a periodic discontinuity, when the maximal stroke $s(\phi(t) = \pi) = s_{max}$ is reached.

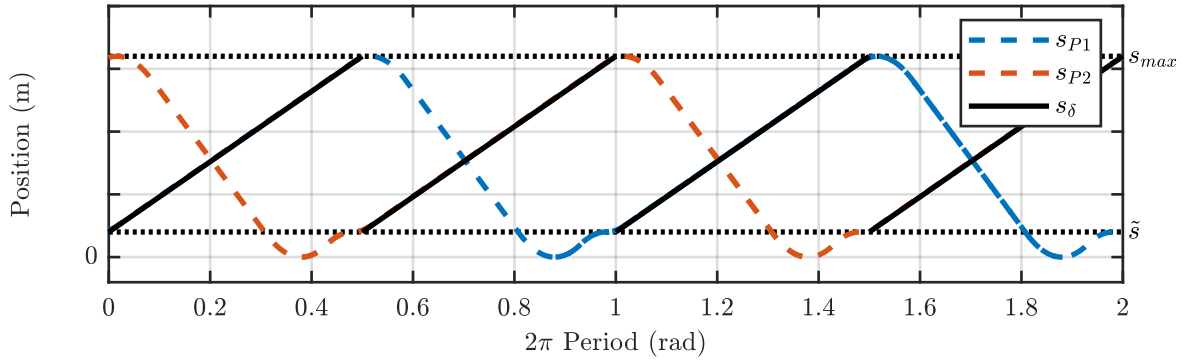

Figure 5.36 – Position displacement changes the pumping chamber volume: desired piston positions of two pumping chambers to obtain a continuous overall fluid flow.

The bulk modulus K_δ will vary with respect to the pressure state $p(t)$, as already defined in (3.37). The pressure state is assumed to follow the reference pressure p_0 by means of control. The cutting process requires a constant pressure. It will only vary, if an on/off-valve disturbs the pressure generation. The pressure state will also affect the fluid density $\varrho(p)$ as given in (3.40).

The fluid flow resistance

$$H_\delta = S_H \sqrt{\frac{2}{\varrho(p)}}\, \zeta \tag{5.100}$$

is parameter-varying as well as time-varying. Since the fluid density $\varrho(p)$ characterizes the fluid resistance, it becomes a function of the pressure state $p(t)$. On the other hand, it will depend on the nozzle inner cross section S_H installed at the cutting heads and its fluid flow coefficient ζ. The nozzles are typically referred to by its inner diameter $D_H \in \{0.08, 0.1, 0.15, 0.2, 0.25, 0.3, 0.4\}$ mm, such as $S_H = D_H^2\pi/4$. A nozzle is only changed, if waterjet machining is not in progress. But a

waterjet application can include several cutting heads, which switch different waterjets on and off with respect to an unknown switching pattern. Hence, the work station configuration defines a discrete set of possible overall cross sections, while the cutting process will cause this parameter to vary during operation.

The plots of Figure 5.37 show the fluid density with respect to the pressure state (a) and the pumping chamber volume dependent on the piston displacement (b). Extending this, the plots of Figure 5.38 present the fluid flow resistance for different nozzles installed (a) and the variation of the overall system volume (b), for possible network subsections of different size.

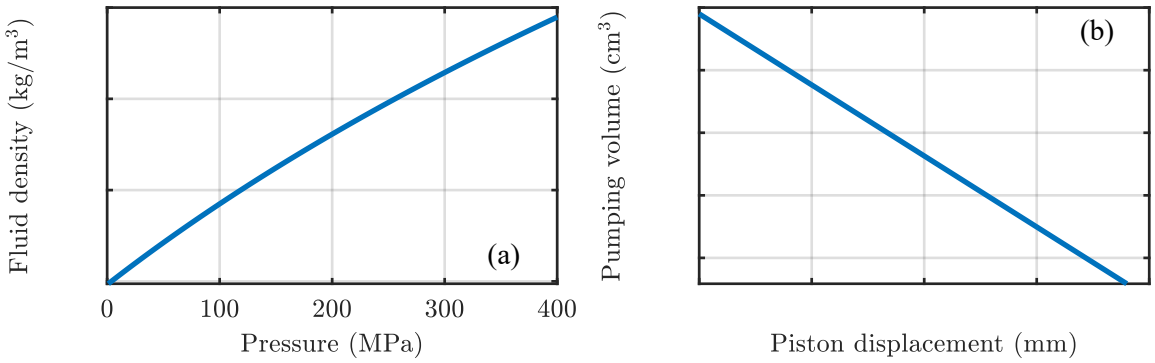

Figure 5.37 – Range for known time-varying uncertainties: fluid density dependent on the pressure state (a) and pumping chamber volume with respect to the piston displacement (b).

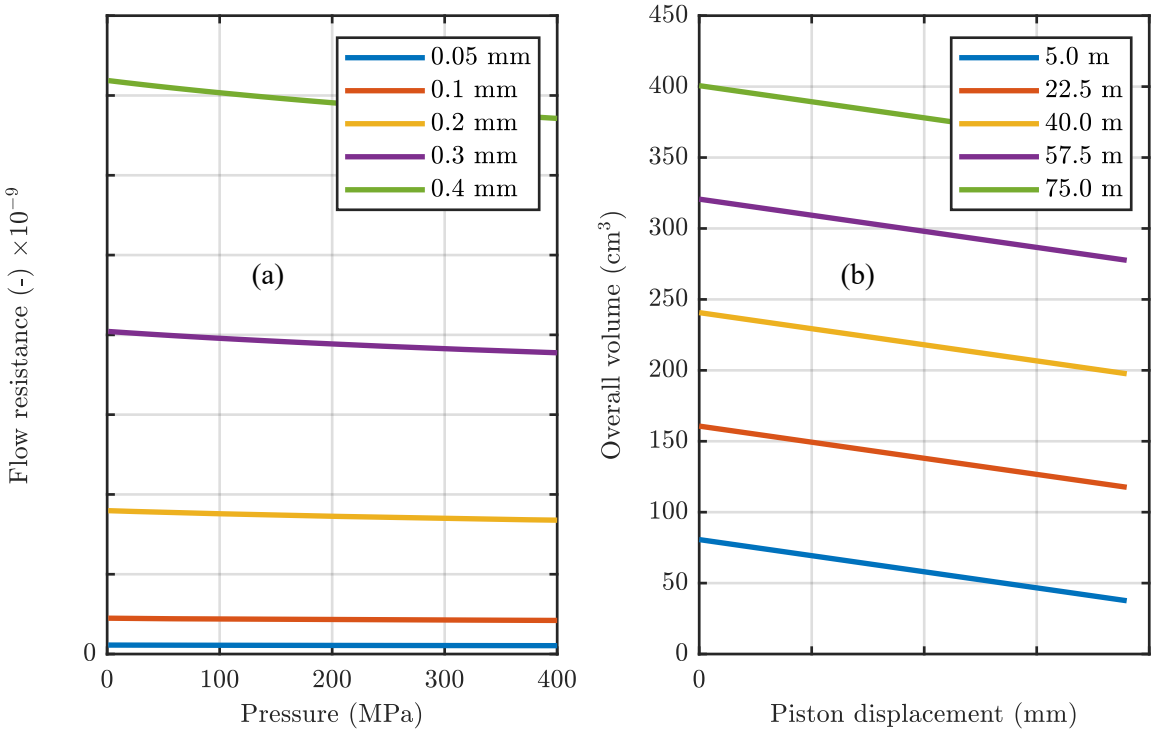

Figure 5.38 – Uncertainty range for unknown parametric uncertainties: flow resistance considering different nozzles (a) and overall volume for various high-pressure networks (b).

The permissible size of a network subsection is unknown and subject of specification for robust control design. Respectively, the requirements on performance and stability will define the maximally permissible subsection size. For the uncertainty analysis in this section, an overall piping length $L = [5,\ 75]$ m is assumed, based on the experiences at the high-pressure test bench. For a typical piping with an inner diameter of 2.4 mm^2 results an expected volume of $V_0 = [21.69,\ 341.7]$ cm^3. On the other hand, the pumping chamber is well specified with a piston diameter of ### mm and its stroke $s_P = [0,\ ###]$ m, hence, the resulting displacement volume $V_P = [0,\ ###]$ cm^3 causes a varying pumping chamber volume $V_C = [###,\ ###]$cm^3.

Input to output sensitivity

The effect of a parameter variation on the frequency response will be investigated with respect to the control signal ($u \rightarrow y$) and disturbance signal ($d \rightarrow y$). Both characteristics will be compared with respect to the approximated model and the evaluated extended model. This is useful to evaluate the demands for robust control design and to find an adequate uncertainty description. Investigating each parameter independently, allows for evaluating its sensitivity for a specific frequency range. Applying the maximal control signal u_{max} and the maximal disturbance signal d_{max}, then evaluating the system gain and time constant τ, give a measure for input to output sensitivity of each parameter.

The frequency response from control signal $u(t)$ to pressure state $y(t)$ is investigated. The plots of Figure 5.39 show the effects, when varying a single parameter at once, while the other uncertain parameters remain on nominal value. It compares the approximated with the evaluated extended model. The flow resistance and the nozzle cross section cause an increasing magnitude (a) for low frequencies, while the pressure state will decrease the magnitude (b). The fluid volume and the bulk modulus cause a varying magnitude for high frequencies, where the variation due to an uncertain fluid volume (c) is larger than the variation due to an uncertain bulk modulus (d). It is further recognized, that a minimal nozzle cross section $S = 0$ cause integral action.

On the other hand, the frequency response from disturbance signal $d(t)$ to measured pressure state $y(t)$ has been investigated. The plots of Figure 5.40 compare again the approximated with the evaluated extended model. Basically, the variation of magnitude, considering an uncertain pressure state, fluid volume and bulk modulus, are comparable to the effects observed for the control signal. However, the variation at low frequencies with respect to the flow resistance and nozzle cross section becomes compensated. This avoids integral action. However, a decreasing magnitude at high frequencies is observed.

Scaling $u_g(t) = u(t)/u_{max}$ with the maximal input fluid flow $u_{max} = S_{max}\ \zeta\ \sqrt{2\ p_{max}/\varrho_{max}}$, required to obtain equilibrium at desired steady-state pressure, and $d_g(t) = d(t)/d_{max}$ for $d_{max} = 1$ allow for comparing the affect of disturbance and control signal to the pressure state. For this, the plots in Figure 5.41 show the frequency responses for $u(t) \rightarrow y(t)$ and $d(t) \rightarrow y(t)$.

The pressure state has a major effect on decreasing magnitudes at low frequencies, considering the control channel as well as the disturbance channel. This finding might be useful to define an adequate uncertainty representation for robust control design. Evaluating each uncertain parameter reveals for all frequencies that the control channel is superior to the disturbance channel. The increasing magnitude for low frequencies only affects the control channel. It occurs when varying the flow resistance and nozzle cross section, respectively. This enables the control channel to stabilize the system, since the disturbance channel is not affected by the integral action.

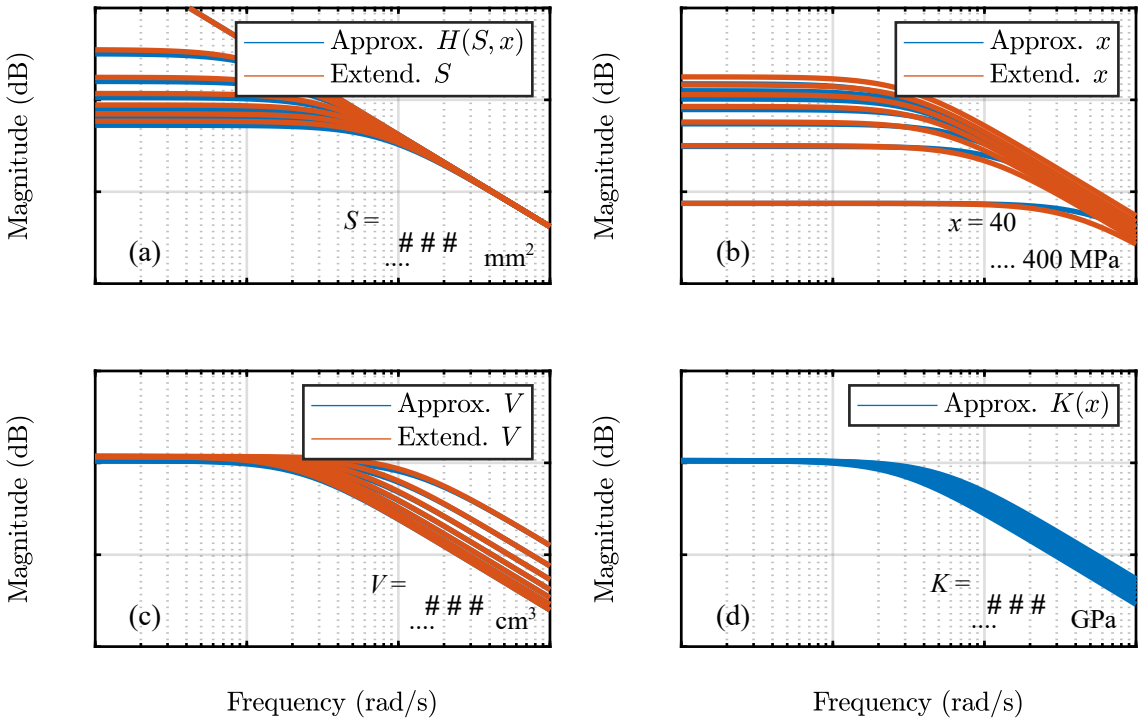

Figure 5.39 – Frequency responses of approximated and extended models for $u \to y$: varying a single uncertain parameter at once, where the others stay constant on nominal value.

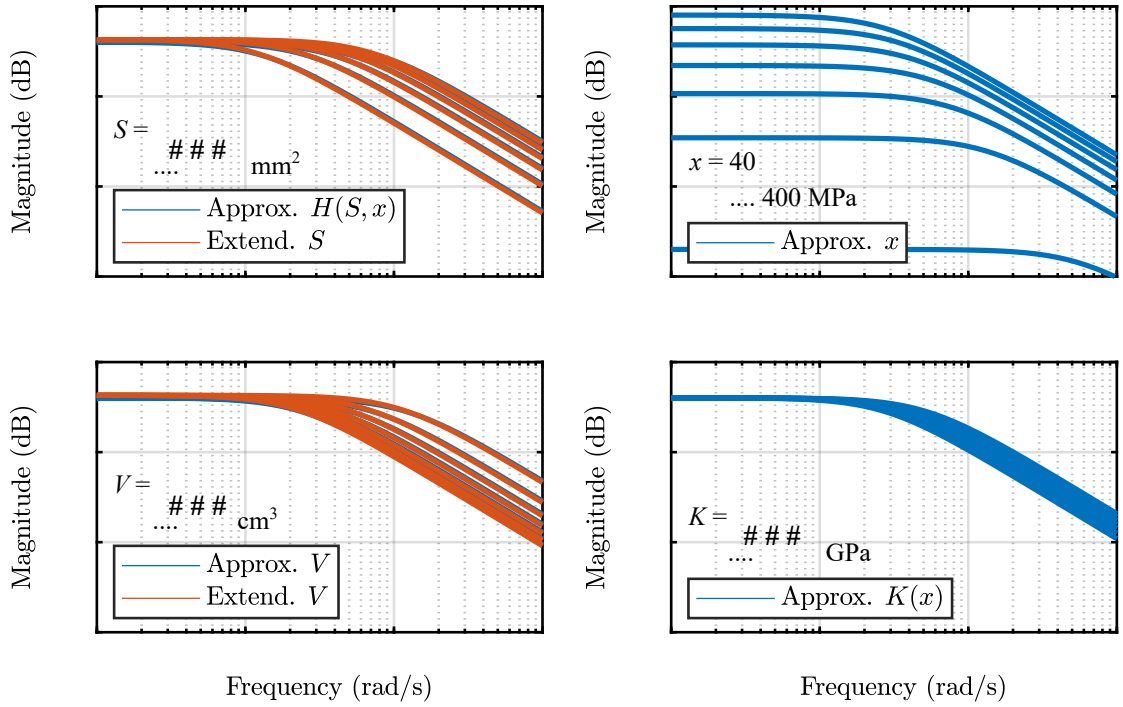

Figure 5.40 – Frequency responses of approximated and extended models for $d \to y$: varying a single uncertain parameter at once, where the others stay constant on nominal value.

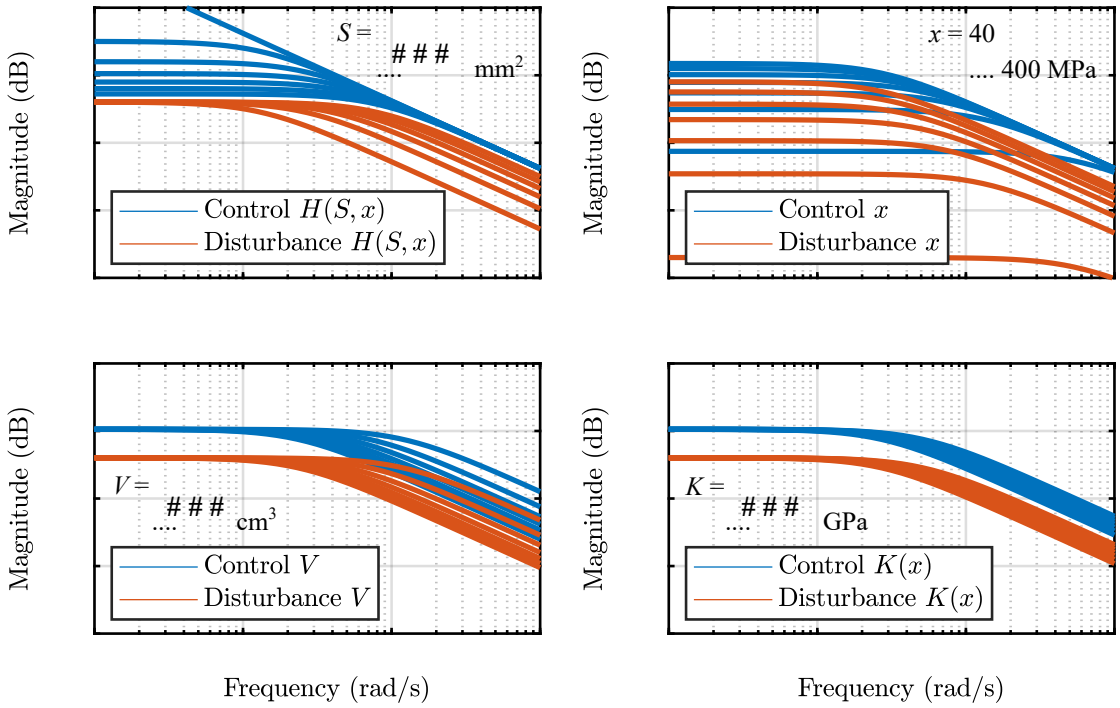

Figure 5.41 – Frequency responses of approximated model for $u \to y$ and $d \to y$: varying a single uncertain parameter at once, where the others stay constant on nominal value.

To analyse the input to output gain at steady-state, the non-linear plant model (5.38) has been investigated around equilibrium. Defining $dx/dt = 0$ results in the equilibrium point

$$y_{eq} = \frac{1}{H_\delta^2} \frac{u_0^2}{d_0^2} \ , \tag{5.101}$$

where it is recognized that

$$\lim_{d \to 0} y_{eq} = \infty \ . \tag{5.102}$$

On the other hand, the gains for the linearised model (5.47) have been obtained at equilibrium

$$y_{eq} = \frac{2\sqrt{\mathrm{x}_\delta}}{H_\delta} \ u_0 - 2\mathrm{x}_\delta \ d_0 \ , \tag{5.103}$$

where the time constants

$$\tau_u = \frac{2V_\delta \sqrt{\mathrm{x}_\delta}}{K_\delta H_\delta}, \quad \tau_d = \frac{V_\delta}{K_\delta H_\delta \sqrt{\mathrm{x}_\delta}} \tag{5.104}$$

define the dynamics from $u(t) \to y(t)$ and $d(t) \to y(t)$, respectively.

Applying $u_{max} \mapsto u_0$ and $d_{max} \mapsto d_0$, varying a single parameter, while holding the other parameters on nominal value, give the sensitivity range. Table 5.7 and 5.8 summarize the results for the system gain considering the non-linear (5.38) and the linearised model (5.47), respectively. Where Table 5.9 evaluates the variations regarding the time constants.

The flow resistance and the nozzle cross section has the ability to increase the system gain to infinity. Hence, the control channel must become zero, that the system output channel for $H_\delta = 0$ or $S_\delta = 0$ remains bounded. Considering the approximated model, which separates control and

disturbance inputs, reveals that all uncertain parameters, considered for control design, have a perceptible impact on the system gain as well as on the time constant. The investigated parameter variation has to be taken into account for robust control design. A possible approach is discussed, when introducing the structured uncertainty description.

Table 5.7: System gain for approximated and extended non-linear model: varying a single parameter, while holding each other parameter on nominal value.

	Param.	y_{min} $\times 10^6$	y_{max} $\times 10^6$	Rel. range (%)
Approx.	H_δ	###	∞	$[-\ 75, +\ \infty]$
Extend.	S_δ	###	∞	$[-\ 75, +\ \infty]$
	x_δ	1395.8	1600.0	$[-7.6, +5.9]$

Table 5.8: System gain for approximated linearised model: varying a single parameter, while holding each other parameter on nominal value to compare $u \rightarrow y$ and $d \rightarrow y$.

	Param.	y_{min} $\times 10^6$	y_{max} $\times 10^6$	Rel. range (%)
Control	H_δ	###	∞	$[-\ 50, +\ \infty]$
	x_δ	74.72	1494	$[-\ 93, +\ 41]$
Disturbance	x_δ	2.000	800.0	$[-100, +100]$

Table 5.9: Time constants for approximated linearised model: varying a single parameter, while holding each other parameter on nominal value for $u \rightarrow y$.

	Param.	τ_{min} (s)	τ_{max} (s)	Rel. range (%)
Control	H_δ	###	∞	$[-\ 50, +\ \infty]$
	x_δ	0.0179	0.3576	$[-\ 93, +\ 41]$
	V_δ	###	###	$[-\ 67, +\ 67]$
	K_δ	0.1932	0.3671	$[-\ 24, +\ 45]$

5.4.2 Structured parametric uncertainty description

Using the framework of H_∞ requires to separate the uncertainties from the plant model to employ additional perturbation input channels. That is realized by applying upper linear fractional transformation (ULFT) [Gu et al., 2013]. This section will introduce the structured uncertainty description to the perturbed plant model. This means that each real-valued uncertain parameter directly introduces an independent perturbation.

Parametric uncertainties

Starting point is the simplified approximated model (5.55)

$$\frac{d}{dt}\mathrm{x}(t) = -\frac{K_\delta H_\delta}{2V_\delta\sqrt{\mathrm{x}_\delta}}\ \mathrm{x}(t) + \frac{K_\delta}{V_\delta}\ u_d(t)\ . \tag{5.105}$$

Additive and inverse additive uncertainty descriptions have been chosen in compliance with the model structure, since K_δ and H_δ stay in the numerator and V_δ and x_δ in the denominator. Defining the parametric uncertainties of additive form

$$K_\delta = K_0 + \delta_K, \quad H_\delta = H_0 + \delta_H \tag{5.106}$$

and the parametric uncertainties of inverse additive form

$$\frac{1}{V_\delta} = \frac{1}{V_0 + \delta_V}, \quad \frac{1}{\sqrt{\mathrm{x}_\delta}} = \frac{1}{\sqrt{\mathrm{x}_0} + \delta_{\sqrt{\mathrm{x}}}}\ , \tag{5.107}$$

where K_0, V_0, H_0, $\sqrt{\mathrm{x}_0}$ denote the corresponding nominal parameter values and δ_K, δ_V, δ_H, $\delta_{\sqrt{\mathrm{x}}}$ give the uncertainty range. It has to be pointed out that the operating point $\sqrt{\mathrm{x}_0}$ and its uncertainty range $\delta_{\sqrt{\mathrm{x}}}$ correspond to the square root values of $\sqrt{\mathrm{x}_\delta}$.

Introducing (5.106) and (5.107) in (5.105) gives the perturbed plant

$$\frac{d}{dt}z(t) = \frac{K_0 + \delta_K}{V_0 + \delta_V}\left(w(t) - \frac{1}{2}\frac{H_0 + \delta_H}{\sqrt{\mathrm{x}_0} + \delta_{\sqrt{\mathrm{x}}}}\ z(t)\right)\ , \tag{5.108}$$

assuming the input $w(t) = u_d(t)$ and output $z(t) = \mathrm{x}(t)$.

The block diagram of Figure 5.42 illustrates the structure of the perturbed plant (5.108), where $e_n(t)$ denotes an output to the n-th uncertain parameter and $d_n(t)$ is a perturbation input from the n-th uncertain parameter.

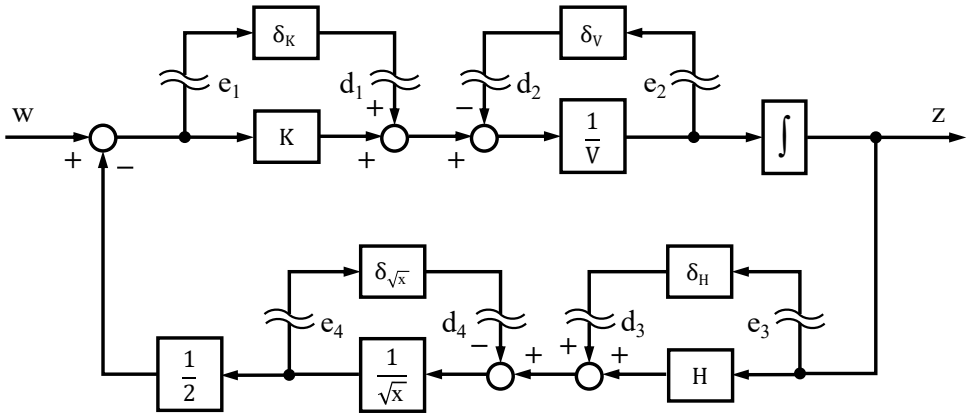

Figure 5.42 – Block diagram of simplified approximated model with real parametric uncertainties: additive uncertainty and inverse additive uncertainty description used to separate these uncertainties from the plant model.

This perturbed plant includes the perturbation inputs $d(t) = [d_1\ d_2\ d_3\ d_4]'$, which provide the outputs $e(t) = [e_1\ e_2\ e_3\ e_4]'$. This allows for representing the nominal plant in state space description

$$\frac{d}{dt}z(t) = -\frac{KH}{2V\sqrt{\mathrm{x}}}\ z(t) + E\ d(t) + \frac{K}{V}\ w(t)\ , \tag{5.109}$$

with $E = [\frac{1}{V} \;\; -\frac{1}{V} \;\; -\frac{K}{2V\sqrt{\mathrm{x}}} \;\; \frac{K}{2V\sqrt{\mathrm{x}}}]$ and to describe the output channels

$$e(t) = \begin{bmatrix} -\frac{H}{2\sqrt{\mathrm{x}}} \\ -\frac{KH}{2V\sqrt{\mathrm{x}}} \\ 1 \\ \frac{H}{\sqrt{\mathrm{x}}} \end{bmatrix} z(t) + \begin{bmatrix} 0 & 0 & -\frac{1}{2\sqrt{\mathrm{x}}} & \frac{1}{2\sqrt{\mathrm{x}}} \\ \frac{1}{V} & -\frac{1}{V} & -\frac{K}{2V\sqrt{\mathrm{x}}} & \frac{K}{2V\sqrt{\mathrm{x}}} \\ 0 & 0 & 0 & 0 \\ 0 & 0 & \frac{1}{\sqrt{\mathrm{x}}} & -\frac{1}{\sqrt{\mathrm{x}}} \end{bmatrix} d(t) + \begin{bmatrix} 1 \\ \frac{K}{V} \\ 0 \\ 0 \end{bmatrix} w(t) \;, \tag{5.110}$$

where the subscripts indicating a nominal parameter is omitted for simplicity. The structure of the perturbed plant with parametric uncertainties also implies $e_2 = dz/dt$.

The perturbed plant model considers parametric uncertainties. This enables an accurate uncertainty representation, since the parameter range of each uncertainty is individually implemented with respect to the structure of the plant. However, the size of the optimization problem for control design will increase with the amount of uncertain parameters.

Applying upper linear fractional transformation (ULFT)

The state space description (5.109) can be rearranged in the standard Δ−M configuration, as presented in block diagram of Figure 5.2 (see the control design fundamentals in Section 5.2). This configuration includes the interconnection system M and the uncertainty block Δ, which contains the parametric uncertainties.

Considering the perturbed plant model in the state space form (5.109) and applying the partitioning from the augmented interconnection system (5.3) yields the interconnection transfer function matrix

$$\mathrm{M} = \begin{bmatrix} \mathrm{M}_{11} & \mathrm{M}_{12} \\ \mathrm{M}_{21} & \mathrm{M}_{22} \end{bmatrix} \;, \tag{5.111}$$

with

$$\mathrm{M}_{11} = \begin{bmatrix} -\frac{H}{2V\sqrt{\mathrm{x}}} & \frac{H}{2V\sqrt{\mathrm{x}}} & -\frac{s}{2\sqrt{\mathrm{x}}} & \frac{s}{2\sqrt{\mathrm{x}}} \\ \frac{s}{V} & -\frac{s}{V} & \frac{Ks}{2V\sqrt{\mathrm{x}}} & -\frac{Ks}{2V\sqrt{\mathrm{x}}} \\ \frac{1}{V} & -\frac{1}{V} & -\frac{K}{2V\sqrt{\mathrm{x}}} & \frac{K}{2V\sqrt{\mathrm{x}}} \\ \frac{H}{V\sqrt{\mathrm{x}}} & -\frac{H}{V\sqrt{\mathrm{x}}} & \frac{s}{\sqrt{\mathrm{x}}} & -\frac{s}{\sqrt{\mathrm{x}}} \end{bmatrix} D^{-1}(s), \quad \mathrm{M}_{12} = \begin{bmatrix} s \\ \frac{Ks}{V} \\ \frac{KH}{V\sqrt{\mathrm{x}}} \\ \frac{K}{V} \end{bmatrix} D^{-1}(s),$$

$$\mathrm{M}_{21} = \begin{bmatrix} \frac{1}{V} & -\frac{1}{V} & -\frac{K}{2V\sqrt{\mathrm{x}}} & \frac{K}{2V\sqrt{\mathrm{x}}} \end{bmatrix} D^{-1}(s), \quad \mathrm{M}_{22} = \begin{bmatrix} \frac{K}{V} \end{bmatrix} D^{-1}(s) \;, \tag{5.112}$$

for which the common denominator

$$D(s) = s + \frac{KH}{2V\sqrt{\mathrm{x}}} \tag{5.113}$$

has been introduced. This separates all real-valued uncertainties in form of a diagonal matrix

$$\Delta \;= \begin{bmatrix} \delta_K & 0 & 0 & 0 \\ 0 & \delta_V & 0 & 0 \\ 0 & 0 & \delta_H & 0 \\ 0 & 0 & 0 & \delta_{\sqrt{\mathrm{x}}} \end{bmatrix} \;, \tag{5.114}$$

where each diagonal entry corresponds to a specific uncertain parameter, implemented in the plant model.

The matrix M_{22} gives the transfer function for the nominal plant

$$G_n(s) = \frac{\frac{K}{V}}{s + \frac{KH}{2V\sqrt{\mathrm{x}}}} \tag{5.115}$$

and applying upper linear fractional transformation (5.4) defines the perturbed plant

$$G_\mathrm{p}(s) = \mathrm{M}_{22} + \mathrm{M}_{21}\Delta\left(\mathrm{I} - \mathrm{M}_{11}\Delta\right)^{-1}\mathrm{M}_{12} \tag{5.116}$$

by means of M and Δ, where the exogenous input $w(t)$ for $z = G_\mathrm{p}(s)\ w$ holds the control signal $u_d(t)$ and the output $z(t)$ corresponds to the pressure state $\mathrm{x}(t)$.

5.4.3 Unstructured complex uncertainty description

In contrast to the above structured uncertainty description, unstructured uncertainties will approximate the different varying parameters in the frequency domain. This results in a complex-valued function that shapes an additional perturbation input. The error frequency response of the perturbed plant defines the unstructured uncertainty, where ULFT again separates the uncertainties from the nominal plant.

Starting point is once more the simplified approximated model (5.55)

$$\frac{d}{dt}\mathrm{x}(t) = -\frac{K_\delta H_\delta}{2V_\delta\sqrt{\mathrm{x}_\delta}}\ \mathrm{x}(t) + \frac{K_\delta}{V_\delta}\ u_d(t)\ . \tag{5.117}$$

However, the parametric uncertainties will be lumped to a transfer function of minimal realization, that represents plant perturbations. For this, the transfer function of the nominal plant

$$G_n(s) = \frac{\frac{K}{V}}{s + \frac{KH}{2V\sqrt{\mathrm{x}_0}}} \tag{5.118}$$

is obtained, when applying Laplace transformation on (5.117) and taking the nominal parameter values into account. The block diagram of Figure 5.43 represents the structure of the nominal plant (5.118). It reveals that any variation of the parameters K, V, H and x_0 will change the feedback gain and, thus, affects the plant output $\mathrm{x}(t)$. Variations on K and V also affect the input gain on the plant input $u_d(t)$. This requires to investigate different complex uncertainty descriptions to find an adequate representation for the varying parameters.

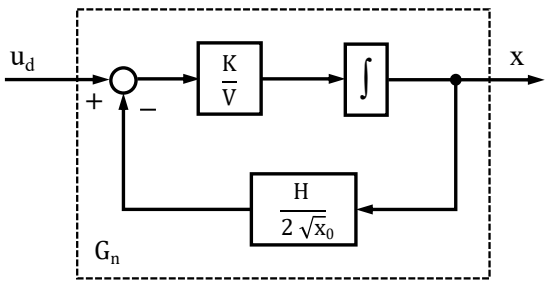

Figure 5.43 – Block diagram of the nominal plant: representing the simplified approximated model for nominal parameter values.

Complex uncertainties

The objective is to find an adequate structured uncertainty description. It is required to verify, whether to represent the parametric uncertainties of the simplified approximated model (5.55) by means of the plant input or by using the plant output channel. The block diagrams of Figure 5.44 show various structures to represent the perturbed plant by means of different unstructured uncertainty descriptions. The additive uncertainty as well as the input multiplicative uncertainty depend on the plant input $u_d(t)$, which corresponds to a fluid flow $Q(t)$. Where the additive form affects the plant output x(t), the multiplicative form affects the plant input. On the other hand, the inverse additive description and the inverse multiplicative description depend on the plant output x(t), which corresponds to the pressure state $p(t)$. Where the additive form affects the plant input, the multiplicative form affects the plant output. The additive and input multiplicative uncertainty are in most cases interchangeable ($W_a = W_m G_n$). The same holds for the inverse additive and inverse output multiplicative uncertainty ($W_{im} = G_n W_{ia}$).

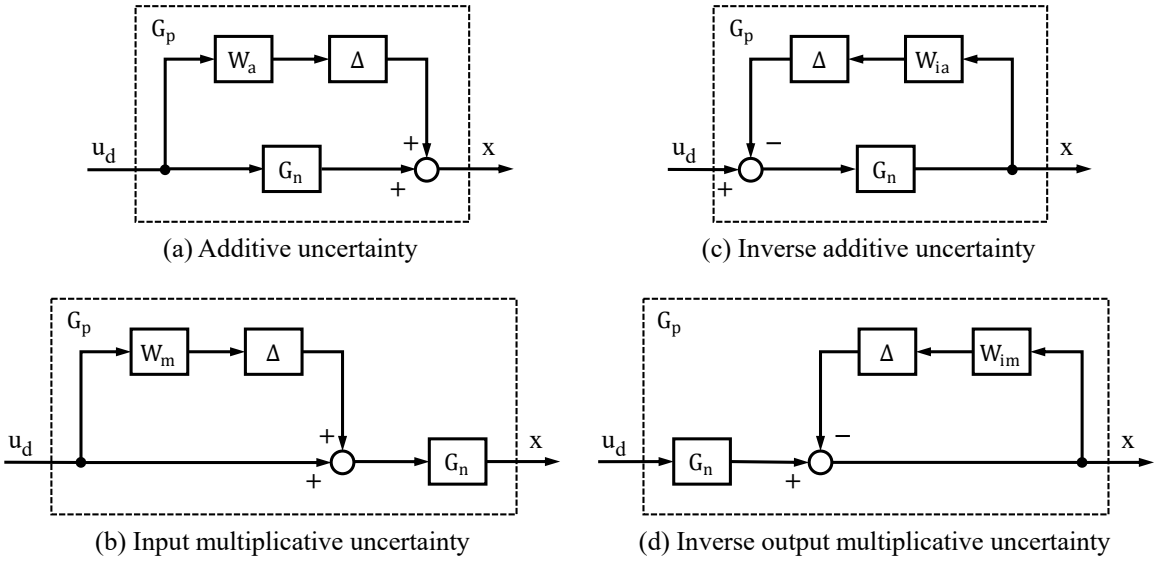

Figure 5.44 – Block diagram of unstructured uncertainty descriptions: additive perturbation from plant input to output (a), input multiplicative perturbation from plant input to input (b), inverse additive perturbation from plant output to input (c) and inverse output multiplicative perturbation form plant output to output (d).

The additive uncertainty representation

$$G_{\mathrm{p}}(s) = G_n(s) + \Delta_a(s) \tag{5.119}$$

is often used to represent an absolute error of the nominal plant G_n (5.118) to the perturbed plant G_{p}, whereby the input multiplicative uncertainty representation

$$G_{\mathrm{p}}(s) = G_n(s)\,(\mathrm{I} + \Delta_m(s)) \tag{5.120}$$

will represent the relative error. The additive uncertainty block

$$\Delta_a(s) = W_a(s)\ \Delta \tag{5.121}$$

and the multiplicative uncertainty block

$$\Delta_m(s) = W_m(s)\ \Delta \tag{5.122}$$

will be obtained, for which Δ is norm bounded such as $|\Delta(j\omega)| \leq 1 \ \forall \ \omega$ [Gu et al., 2013]. Considering the error frequency response of the perturbed plant yields the weighting functions $W_a(s)$ and $W_m(s)$, respectively.

In the same manner, the **inverse additive uncertainty representation**

$$\boxed{G_{\mathrm{p}}(s) = \left(G_n^{-1}(s) + \Delta_{ia}(s)\right)^{-1}} \tag{5.123}$$

and the inverse output multiplicative representation

$$G_{\mathrm{p}}(s) = \left(G_n^{-1}(s)\ (\mathrm{I} + \Delta_{im}(s))\right)^{-1} \tag{5.124}$$

can be obtained, where the **inverse additive uncertainty block**

$$\boxed{\Delta_{ia}(s) = W_{ia}(s)\ \Delta} \tag{5.125}$$

and the inverse multiplicative uncertainty block

$$\Delta_{im}(s) = W_{im}(s)\ \Delta \tag{5.126}$$

introduce a weighting function $W_{ia}(s)$ and $W_{im}(s)$.

Approximating the weighting functions

These weighting functions represent the upper bounds of the error frequency response. Introducing (5.121) to (5.119) yields

$$|W_a(j\omega)\ \Delta(j\omega)| = |G_{\mathrm{p}}(j\omega) - G_n(j\omega)| \leq |W_a(j\omega)| \tag{5.127}$$

and introducing (5.122) to (5.120) yields

$$|W_m(j\omega)\ \Delta(j\omega)| = \frac{|G_{\mathrm{p}}(j\omega) - G_n(j\omega)|}{|G_n(j\omega)|} \ \leq |W_m(j\omega)| \ . \tag{5.128}$$

Evaluating (5.127) for the simplified approximated model (5.55), the second order weighting function

$$W_a(s) = \frac{2.605\ 10^9\ s^2 + 6.886\ 10^{13}\ s + 5.191\ 10^{14}}{s^2 + 3.943\ s + 2.989\ 10^{-3}} \tag{5.129}$$

has been obtained to represent the frequency response of an additive uncertainty, whereas the first order weighting function

$$W_m(s) = \frac{1.1\ s + 8.315}{s + 8.398\ 10^{-4}} \tag{5.130}$$

represents the frequency response of an input multiplicative uncertainty, where both take the parameter range of Table 5.3 into account.

The plots of Figure 5.45 compare the error frequency responses of the additive form (5.127) (a) and input multiplicative form (5.128) (b). It is observed that the error of the additive uncertainty description is large at low frequencies, but becomes small for high frequencies, while the multiplicative uncertainty description represents a constant error for high frequencies.

The plots of Figure 5.46 show the frequency response of the perturbed plant, described by means of additive uncertainty (5.119) (a) and the perturbed plant, using multiplicative uncertainties (5.120) (b). It results in identical behaviour. However, comparing these frequency response from complex uncertainties with the error frequency response derived by real parametric uncertainties (5.116), reveal undesired behaviour at low frequencies. This is evidence that the introduced perturbation channel, with respect to plant input $u_d(t)$, provides an inadequate choice.

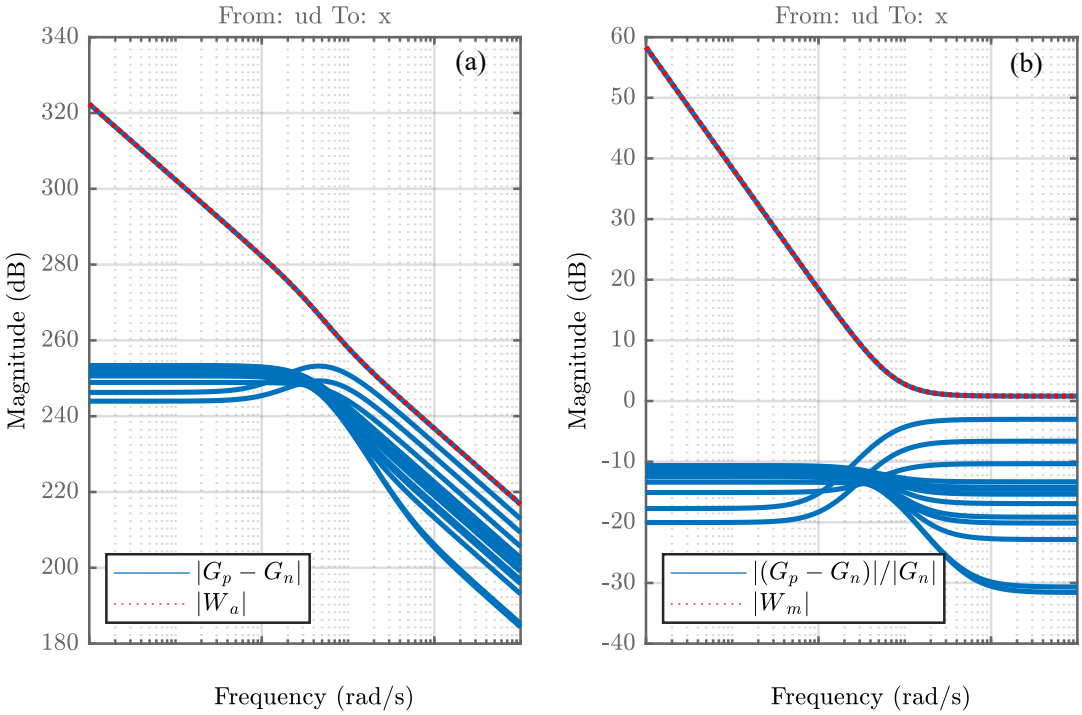

Figure 5.45 – Weighting functions for additive and multiplicative uncertainties: error frequency responses in additive form, considering absolute error (a) and multiplicative form for relative error (b).

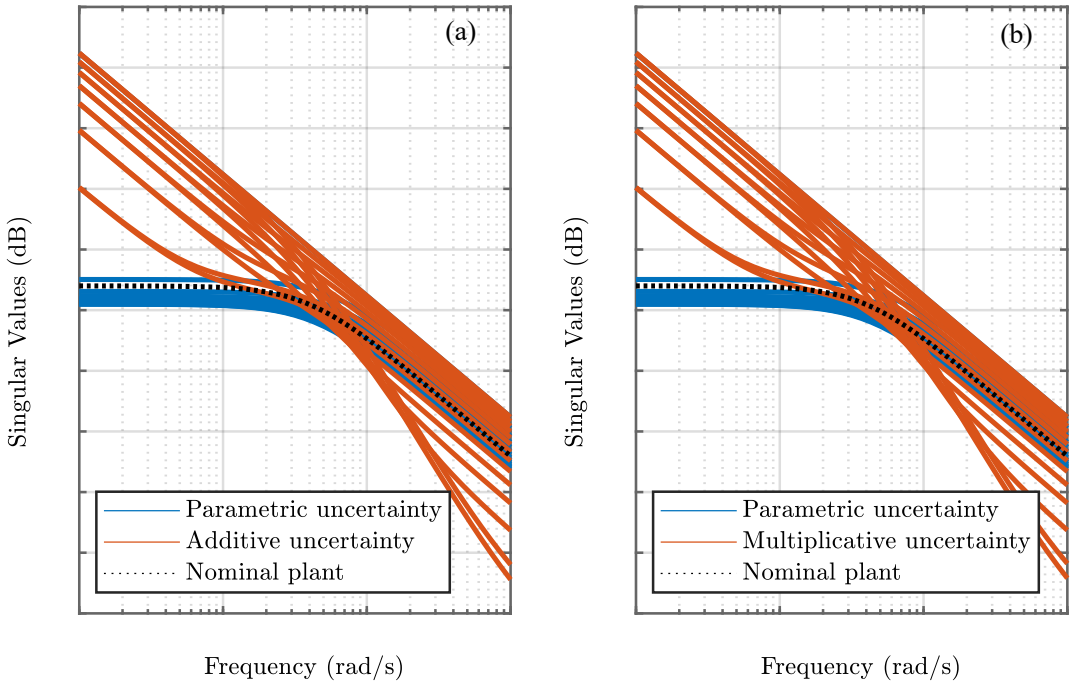

Figure 5.46 – Perturbed plant using additive (a) and multiplicative (b) descriptions: unstructured uncertainties compared to parametric uncertainty description reveal inadequate behaviour.

The upper bounds of the error frequency response will also define the weighting functions for the inverse representations. Introducing (5.125) to (5.123) yields

$$\begin{aligned} |W_{ia}(j\omega)\ \Delta(j\omega)| &= \frac{1}{|G_{\mathrm{p}}(j\omega)|} - \frac{1}{|G_n(j\omega)|} \\ &= \frac{|G_n(j\omega) - G_{\mathrm{p}}(j\omega)|}{|G_{\mathrm{p}}(j\omega)\ G_n(j\omega)|} \ \leq |W_{ia}(j\omega)| \end{aligned} \tag{5.131}$$

and introducing (5.126) to (5.124) yields

$$\begin{aligned} |W_{im}(j\omega)\ \Delta(j\omega)| &= \frac{\left|G_{\mathrm{p}}^{-1}(j\omega)\right|}{\left|G_n^{-1}(j\omega)\right|} - \mathrm{I} \\ &= \frac{\left|G_{\mathrm{p}}^{-1}(j\omega) - G_n^{-1}(j\omega)\right|}{\left|G_n^{-1}(j\omega)\ \right|} \ \leq |W_{im}(j\omega)| \ . \end{aligned} \tag{5.132}$$

Evaluating (5.131) for the simplified approximated model (5.55), the **inverse additive weighting function**

$$\boxed{W_{ia}(s) = \frac{4.562\ 10^{-10}\ s + 3.442\ 10^{-9}}{s + 5.454\ 10^{4}}} \tag{5.133}$$

has been obtained to represent the frequency response of an additive uncertainty, whereas the inverse multiplicative weighting function

$$W_{im}(s) = \frac{5.233\ 10^{-1}\ s + 3.959}{s + 3.956} \tag{5.134}$$

represents the frequency response of an input multiplicative uncertainty, again with respect to the parameter range of Table 5.3.

The plots of Figure 5.47 compare the error frequency response of the inverse additive (5.131) (a) and input multiplicative form (5.132) (b). For the inverse additive uncertainty description, a constant error for low frequencies is observed. It increases for high frequencies. The inverse multiplicative uncertainty description represents a constant error for low frequencies, as well as for high frequencies. A smaller error occurs for high frequencies than for low frequencies.

The plots of Figure 5.48 show the frequency response of the perturbed plant, described by means of inverse additive uncertainty (5.123) (a) and the perturbed plant, using inverse multiplicative uncertainties (5.124) (b). It results in identical behaviour. Comparing these frequency responses from complex uncertainty with the error frequency response derived by real parametric uncertainties (5.116), reveal an excellent fit for the frequency range of interest. This is evidence that the introduced perturbation channel, with respect to plant output $\mathrm{x}(t)$, provides an adequate choice. Some variance has been observed for high frequencies, which seems small.

The additive as well as the multiplicative uncertainty representations are unsatisfying to represent the varying parameters of the simplified approximated model. However, the resulting dynamics of the inverse uncertainty descriptions represent the varying parameters with desired accuracy. These inverse uncertainties of complex values perform more conservative, as a large perturbation is given for low frequencies. Nevertheless, it is simpler to formulate a perturbed plant using unstructured than structured uncertainties. That becomes advantageous for the subsequent controller synthesis, when implementing robust stability. A weighting function of order 1 is sufficient for both unstructured uncertainty descriptions in inverse form. Low order weighting functions are desired for control design, since the total order of the generalized plant, used for controller synthesis, will define the order of the resulting controller.

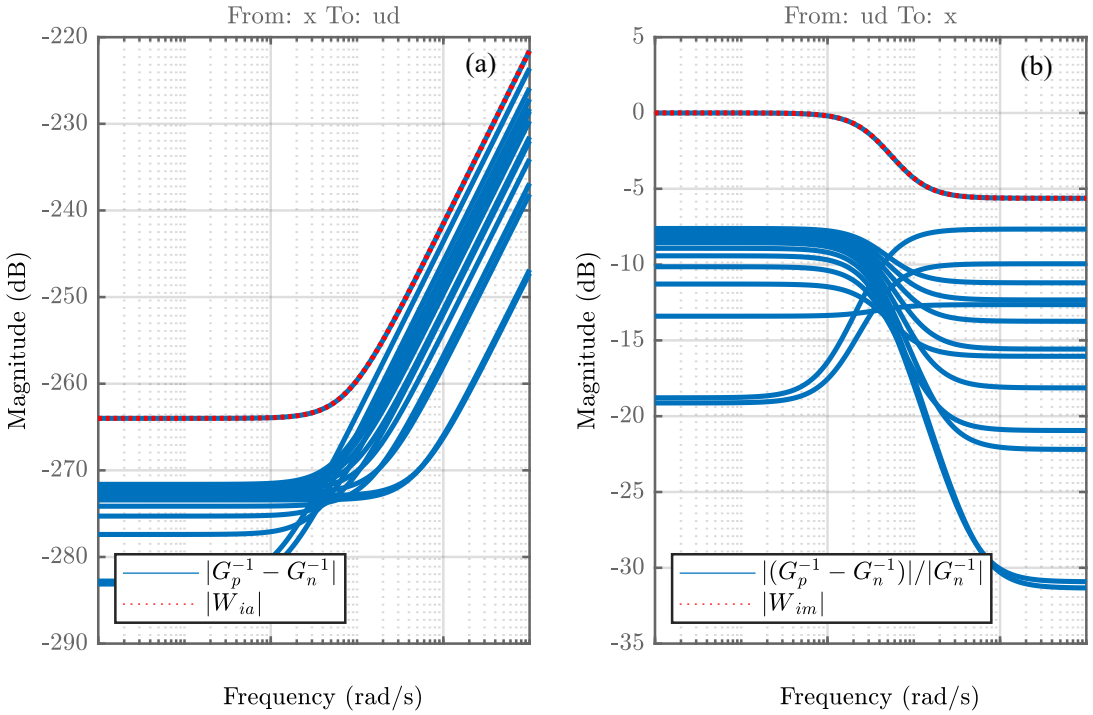

Figure 5.47 – Weighting functions to obtain the inverse additive and inverse multiplicative uncertainties: error frequency responses in inverse additive form, considering an absolute error (a) and inverse multiplicative form for relative error (b).

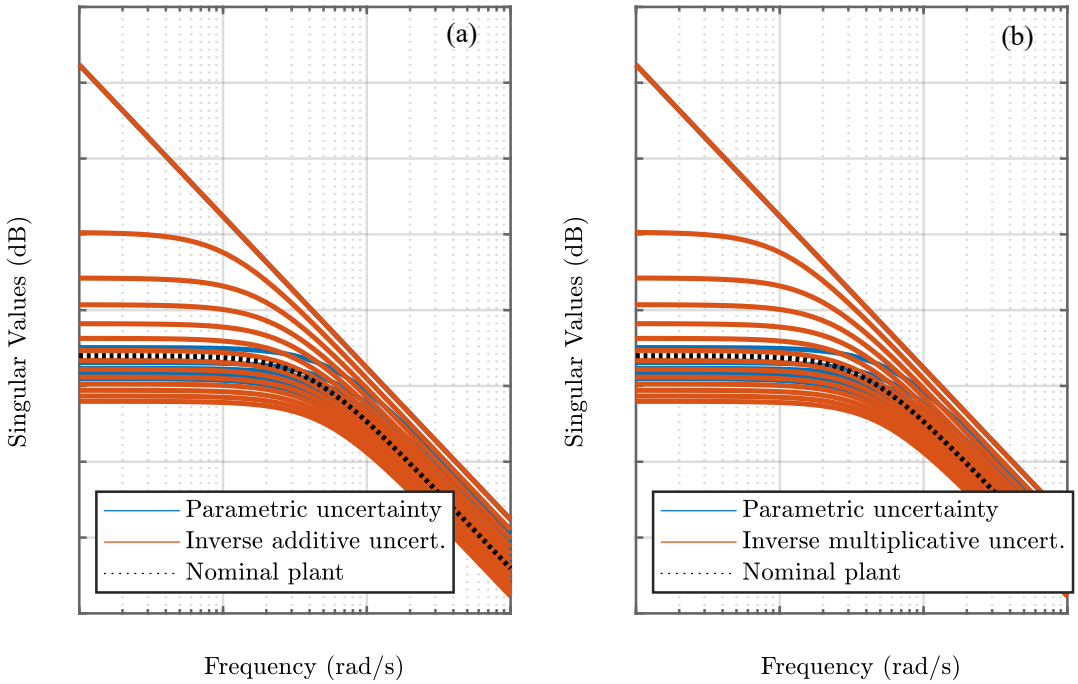

Figure 5.48 – Perturbed plant using inverse additive (a) and inverse multiplicative (b) descriptions: unstructured uncertainties show adequate behaviour compared to parametric uncertainties.

More complex uncertainty descriptions, e.g using co-prime factors [Gu et al., 2013], could further improve the accuracy for unstructured uncertainties. The inverse output multiplicative form match the investigated parametric uncertainty with desired accuracy. In contrast to the inverse additive form, its weighting function is favourable with respect to the resulting coefficients of the numerator and denominator. Consequently, its transfer function is used for control design. It will shape the dynamics on the perturbation input $\mathrm{p}(t)$.

Applying upper linear fractional transformation (ULFT)

Also the perturbed plant, considering unstructured uncertainties, can be rearranged to the standard $\Delta-\mathrm{M}$ configuration, as shown in the block diagram of Figure 5.2 (see the control design fundamentals in Section 5.2). Rearranging the perturbed plant (5.123) in inverse additive uncertainty form, with respect to the configuration (5.3), allows for defining the interconnection transfer function matrix

$$\mathrm{M} = \begin{bmatrix} \mathrm{M}_{11} & \mathrm{M}_{12} \\ \mathrm{M}_{21} & \mathrm{M}_{22} \end{bmatrix} = \begin{bmatrix} -G_n & G_n \\ -G_n & G_n \end{bmatrix} , \tag{5.135}$$

where the uncertainty block $\Delta = \Delta_{ia}(s)$ corresponds to the inverse additive uncertainty description. Applying upper linear fractional transformation $F_u(\mathrm{M}, \Delta)$, according to (5.4), defines the **perturbed plant**

$$\boxed{G_\mathrm{p}(s) = G_n(s) - G_n(s)\Delta_{ia}(s)(\mathrm{I} + G_n(s)\Delta_{ia}(s))^{-1}G_n(s) ,} \tag{5.136}$$

which describes the transfer function $w(t) \to z(t)$ with respect to the inverse additive uncertainty. That is realizable if $\mathrm{I} + G_n(s)\Delta_{ia}(s)$ is invertible.

Also the perturbed plant (5.124) in inverse multiplicative form yields a interconnection transfer function matrix

$$\mathrm{M} = \begin{bmatrix} \mathrm{M}_{11} & \mathrm{M}_{12} \\ \mathrm{M}_{21} & \mathrm{M}_{22} \end{bmatrix} = \begin{bmatrix} -\mathrm{I} & G_n \\ -\mathrm{I} & G_n \end{bmatrix} , \tag{5.137}$$

with respect to (5.3), where the uncertainty block $\Delta = \Delta_{im}(s)$ contains the inverse multiplicative uncertainty. Applying the upper linear fractional transformation (5.4), defines the perturbed plant

$$G_\mathrm{p}(s) = G_n(s) - G_n(s)\Delta_{im}(s)(\mathrm{I} + G_n(s)\Delta_{im}(s))^{-1}G_n(s) , \tag{5.138}$$

which describes the transfer function $w(t) \to z(t)$ with respect to the inverse multiplicative uncertainty, if $(\mathrm{I} + G_n(s)\Delta_{im}(s))$ is again invertible.

Robust stabilization

Considering the feedback system of Figure 5.49, allows for introducing the requirements for robust stabilization [Gu et al., 2013]

$$\left\| G_\mathrm{p}(j\omega)\,(\mathrm{I} + K(j\omega)\; G_\mathrm{p}(j\omega))^{-1} \right\|_\infty < \frac{1}{\|\Delta(j\omega)\|_\infty} \tag{5.139}$$

for the inverse additive uncertainty description (5.123) and

$$\left\| (\mathrm{I} + K(j\omega)\; G_\mathrm{p}(j\omega))^{-1} \right\|_\infty < \frac{1}{\|\Delta(j\omega)\|_\infty} \tag{5.140}$$

for the inverse multiplicative uncertainty description (5.123).

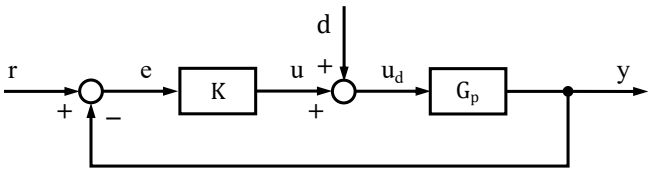

Figure 5.49 – Block diagram for robust stabilization of the investigated feedback system: one degree of freedom state feedback controller $\mathrm{K}(s)$ interconnected to the perturbed plant $G_{\mathrm{p}}(s)$.

The maximal singular values

$$\overline{\sigma}\left(\Delta(j\omega)\right) \leq \overline{\sigma}\left(W_{ia}(j\omega)\right) \;\; \forall\, \omega \in \mathbb{R} \tag{5.141}$$

and

$$\overline{\sigma}\left(\Delta(j\omega)\right) \leq \overline{\sigma}\left(W_{im}(j\omega)\right) \;\; \forall\, \omega \in \mathbb{R} \tag{5.142}$$

are bounded by the corresponding weighting functions $W_{ia}(j\omega)$ and $W_{im}(j\omega)$, respectively, for which the matrix inequalities

$$\left\| W_{ia}(j\omega)\; G_{\mathrm{p}}(j\omega)\left(\mathrm{I} + K(j\omega)\; G_{\mathrm{p}}(j\omega)\right)^{-1} \right\|_{\infty} < \; 1 \tag{5.143}$$

and

$$\left\| W_{im}(j\omega)\left(\mathrm{I} + K(j\omega)\; G_{\mathrm{p}}(j\omega)\right)^{-1} \right\|_{\infty} < \; 1 \tag{5.144}$$

can be derived from (5.139) and (5.140), when substituting (5.141) and (5.142) as a strengthened formulation for robust stability (5.22a) with respect to the small gain theorem (5.13).

Eventually, solving the optimization problems

$$\underset{\mathrm{K}}{\text{minimize}} \;\; \left\| W_{ia}(j\omega)\; G_{\mathrm{p}}(j\omega)\left(\mathrm{I} + K(j\omega)\; G_{\mathrm{p}}(j\omega)\right)^{-1} \right\|_{\infty} \tag{5.145}$$

and

$$\underset{\mathrm{K}}{\text{minimize}} \;\; \left\| W_{im}(j\omega)\left(\mathrm{I} + K(j\omega)\; G_{\mathrm{p}}(j\omega)\right)^{-1} \right\|_{\infty} \;, \tag{5.146}$$

derived from (5.143) and (5.144), respectively, yields a suboptimal H_∞ stabilizing controller $\mathrm{K}(s)$.

The H_∞ problem formulation, considering the control requirements in form of shaping and weighting functions, is subject for the subsequent chapter. The interconnection system, depicted in the block diagram of Figure 5.15, needs to be rearranged to obtain a generalized plant, which defines the optimization problem for H_∞ controller synthesis.

5.5 Conclusion

This chapter discussed the robust decentralized control design for an electrically driven high-pressure pump. It considers the implementation of a single controller for every pump, installed in a high-pressure network of unknown topology. This requires for separating a high-pressure network into subsections. Each subsection is then controlled by the assigned high-pressure pump.

A contribution of this chapter is given, when defining the H_∞ optimization problem for this specific high-pressure system. For this, a decentralized pump supplying a high-pressure subsection has been considered. Assuming a perfect synchronization of the involved pumping unit, enables a first order model to describe the pressure generation within a subsection. This plant model contains all prevalent parametric uncertainties. The other system components have been modelled

with transfer functions of nominal values. The plant model has been linearised, to obtain an exogenous input disturbance. The sensitivity of the plant model, subject to parameter variation, has been investigated. It has been found that a cutting head with decreasing nozzle cross section, causes an increased gain from control input to pressure output, in particular at low frequencies. Hence, a closed cutting head results in integral action. Further, an increasing operating pressure will decrease the input to output gain. On the other hand, an increasing nozzle cross section does not affect the gain from disturbance input to pressure output for low frequencies. Summarizing this result, the high-pressure pump is capable of stabilizing its corresponding network subsection for every disturbance induced by an unknown switching of cutting heads.

These uncertain parameters have been lumped to unstructured uncertainties, which have been compared to the structured uncertainty description. The inverse additive uncertainty provided satisfying results by reproducing the investigated parametric uncertainty range. It allows for introducing an perturbation input channel to the interconnection system, by using linear fractional transformation. The uncertain parameters are thereby separated from the nominal plant model. Specifying an input shaping function on the perturbation channel, while assuming a nominal plant for control design. Alternatively, the inverse output multiplicative uncertainty obtains identical results. Though, coprime factor uncertainties could further improve the uncertainty modelling [Gu et al., 2013]. The choice of an unstructured complex uncertainty is advantageous for controller synthesis (see the subsequent chapter). It will simplify the procedure to maximize the permissible network subsection size, but introduces additional conservativism to the control design. Eventually, all system components have been combined to build an interconnection system. Shaping functions have been defined to shape the corresponding input channels, with respect to the investigated signal dynamics.

6

Controller synthesis and validation

Contents

6.1 Introduction

Objectives

Electrically driven high-pressure pumps require a robust control design, as they are installed to future waterjet facilities at unknown network locations. Establishing high-pressure networks, aims to improve the energy efficiency of waterjet machining. The previous chapter introduced the control design requirements in time domain and derived adequate weighting functions in frequency domain. The obtained interconnection system considers the expected plant perturbations, by implementing an uncertainty description, and includes the control requirements. This interconnection system is useful for H_∞ controller synthesis. However, because of the unknown topology of high-pressure networks for future waterjet facilities, it becomes impossible for industry to specify the network subsection size, for which a high-pressure pump must be installed to guarantee an effective attenuation of pressure fluctuations. The permissible subsection size is unknown and therefore subject for investigations. This requires a robust control design procedure that maximizes the possible uncertainty range, while obtaining robust performance with respect to the defined control requirements. The permissible size of a network subsection is a design parameter that depends on the available control effort of an electrically driven pump and the attainable performance for disturbance rejection, needed to maintain the desired cutting quality for waterjet machining. The robust control design is further required to employ a structured controller that is straight forward for implementation on an industrial high-pressure pump. In this particular case, the controller preferably provides a PI structure, which obtains the desired requirements on stability and performance while maximizing the permissible subsection size. This aims at a robust control design to synthesize a quasi-optimal PI controller. Realizing future waterjet facilities requires then to combine robustly controlled high-pressure pumps, each stabilizing a network subsections. The interconnected subsections establish a high-pressure network with decentralized pumps, which stabilize a network subsection by means of local disturbance rejection. However, the coupling of multiple pumps across the high-pressure network could cause an increased energy consumption and limits the overall stability, if the pumps begin to act against each other. Consequently, simulations and experimental studies are required to validate performance and stability for robustly controlled and distributed high-pressure pumps.

Contribution

This chapter employs a H_∞ controller synthesis [Gu et al., 2013] for electrically driven high-pressure pumps, taking expected parameter variations, exogenous disturbances and control requirements into account (as introduced in Chapter 5). Shaping functions are introduced to consider the dynamic range of input signals and weighting functions are used to define the requirements for performance and to penalize the control effort. A generalized plant for controller synthesis is obtained, when combining the unstructured uncertainty description with a signal-based design approach [Skogestad and Postlethwaite, 2005]. Formulating the generalized plant for controller synthesis, it is proposed to merge input signal by introducing joint shaping functions. This may lead to a more conservative control design, but reduces the dimension of the resulting H_∞ optimization problem. The optimization problem is then solved to obtain an initial state feedback controller [Doyle et al., 1989]. This controller serves as a reference for further structured controller designs. It can be shown that the introduction of joint shaping functions will decrease the calculation cost and can further reduce the order of the resulting state feedback controller [Niederberger et al., 2019b].

Another contribution is to apply a structured design approach [Apkarian and Noll, 2006], resulting in a PI controller, suitable for industrial use as well as capable to operate within desired performance and guaranteed stability. Extending the PI controller to a lead compensator, will remarkably improves the obtained closed-loop performance and manages to recover the initial state feedback controller for the frequency range of interest. The H_∞ frame work is further used to determine the permissible network subsystem size, considering a specific high-pressure pump setup. When analysing the parameter variations and the resulting uncertainty model, for which robust performance and stability can be guaranteed, a robust performance margin will be obtained. This allows for implementing an iterative procedure, which obtains a quasi-optimal PI controller, while maximizing the permissible uncertainty range. Simulations compare the disturbance rejection of the derived PI controllers with the state feedback controller, using detailed high-pressure network models (as previously introduced in Section 4.2). Further experimental studies investigate stability and performance of a preliminary PI controller applied on the test bench. It has been configured, considering single pump setups as well as configurations with two interconnected pumps. For all configurations, two independent cutting heads will induce pressure fluctuations. The experiments show dynamic couplings between interconnected pumps and reveal the need for a high-level managing.

This chapter is structured as follows: Section 6.2 combines the perturbed plant, weighting functions and shaping functions, from the previous chapter, to formulate a generalized plant. Therefore, the interconnection system is transformed into standard P−K form for control synthesis [Gu et al., 2013], by applying lower linear fractional transformation. A reduced robust state feedback controller has been obtained by means of joint shaping functions. Its performance and stability is compared to a PI controller, as derived from a structured H_∞ synthesis. The suboptimal H_∞ controller synthesis is then extended with the Δ-K iteration, proposed for shaping function adjustment. This allows for obtaining a robust controller that fulfils the control requirements for performance and stability (as introduced in Section 5.2), while maximizing the uncertainty range with respect to the unknown network subsection size. In Section 6.3, the proposed graph-based modelling methodology, taking the topologies of various high-pressure systems into account, will be used to evaluate the robust control design. The derived robust controllers will be verified on validated simulation models, which considers non-linearities and parameter variations. For the experimental validation in Section 6.4, a structured controller will be implemented on the test bench. The experimental study is reproduced, using the validated simulation models in closed-loop control. This aims to verify the implementation of the controller and allows for validating the graph-based modelling methodology as a simulation toolbox for control design evaluation. The toolbox is useful to investigate complex high-pressure network for large-scale waterjet facilities, which exceed the capabilities of a test bench.

6.2 Controller synthesis

This section presents the robust feedback control design for an electrically driven high-pressure pump by means of H_∞ suboptimal controller synthesis [Skogestad and Postlethwaite, 2005] . The diagram of Figure 6.1 shows the subsequent control design process. First, a state feedback controller will be obtained, which should provide superior performance and robustness with respect to the specified uncertainties. This is realized at expenses of a high-order controller, which requires an order reduction for implementation in the industrial application. Second, a structured feedback controller of standard PI structure is synthesized. It approximates the behaviour of the state feedback controller. Both control designs will be compared by means of simulations, taking

the time domain specifications into account. Introducing a low-pass filter to the PI control design will seriously improve performance and robustness. This extended PI controller is capable to recover the behaviour of a state feedback controller, resulting in a control law straight forward to implement into the application. The structured feedback controller synthesis is then verified to evaluate the robustness margin with respect to the size of an uncertain high-pressure network subsection. This allows for specifying the maximal subsection size, which guarantees robustness and optimizes the control design.

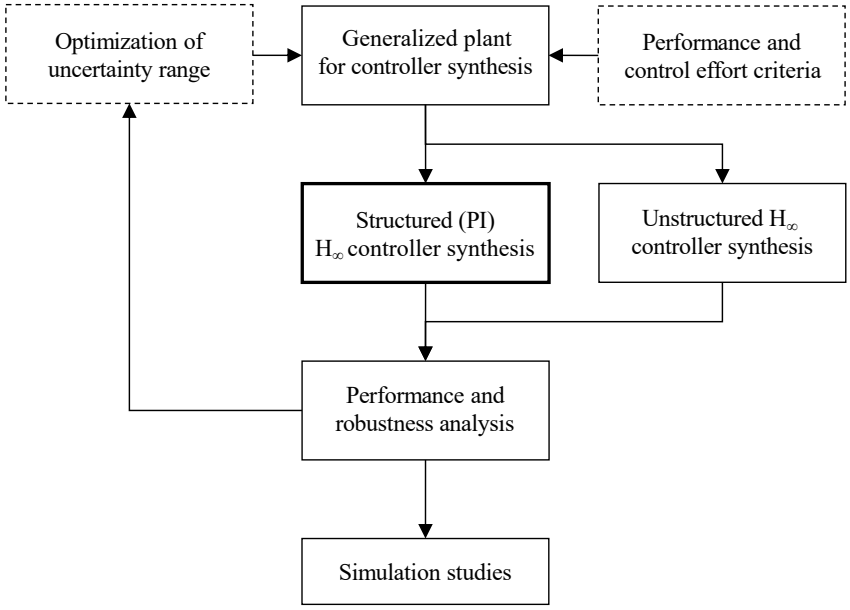

Figure 6.1 – Overview of the control design process: structured and unstructured controllers compared by means of simulations to derive a robust control design for high-pressure pumps.

The derived interconnection system (see Section 5.3) will be rearranged, using lower linear fractional transformation (LFT) [Safonov, 1981], to obtain a full generalised plant. It takes the defined input signal shaping functions and output signal weighting functions into account and considers the plant uncertainties as additional perturbation input. This generalized plant describes a suboptimal H_∞ optimization problem [Skogestad and Postlethwaite, 2005], where the size of the generalized plant will define the dimension of the optimization problem. A procedure will be introduced to combine input channels by means of joint shaping functions . This procedure lumps shaping functions of the initial interconnection system. That reduces the generalized plant and results in a simplified, but more conservative optimization problem. Finally, the suboptimal control design will be extended to derive a quasi-optimal controller, subject to find the permissible fluid volume V_δ, while searching a controller $\mathrm{K}(s)$ that minimizes the H_∞-norm of the generalized plant. Finding the maximal fluid volume for which desired stability and performance can be guaranteed, allows for defining the maximal size of a network subsection, which can be stabilized by a high-pressure pump.

6.2.1 Generalized plant

The interconnection system, illustrated in the block diagram of Figure 5.15 from the previous chapter, contains the control requirements in form of shaping and weighting functions. It needs to be rearranged to obtain a generalized plant $T(s)$, which defines the optimization problem

for H_∞ controller synthesis. The interconnection system is therefore rearranged to the standard P−K configuration, as shown in the block diagram of Figure 5.3 (see the control design fundamentals in Section 5.2).

Applying the standard configuration (5.5) to the interconnection system (5.63), yields the interconnection transfer function matrix

$$\mathrm{P} = \begin{bmatrix} \mathrm{P}_{11} & \mathrm{P}_{12} \\ \mathrm{P}_{21} & \mathrm{P}_{22} \end{bmatrix} , \tag{6.1}$$

with

$$\begin{aligned} \mathrm{P}_{11} &= \begin{bmatrix} W_e \mathrm{I} W_r & -W_e G_s G_n W_d & -W_e \mathrm{I} W_n \\ 0 & 0 & 0 \end{bmatrix}, \quad \mathrm{P}_{12} = \begin{bmatrix} -W_e G_s G_n G_a \\ \mathrm{I} W_u \end{bmatrix}, \\ \mathrm{P}_{21} &= \begin{bmatrix} \mathrm{I} W_r & -G_s G_n W_d & -\mathrm{I} W_n \end{bmatrix}, \quad \mathrm{P}_{22} = \begin{bmatrix} -G_s G_n G_a \end{bmatrix} , \end{aligned} \tag{6.2}$$

which is partitioned with respect to the input channel $w \in \mathbb{R}^m$ and output channel $z \in \mathbb{R}^n$, assuming a control variable $u \in \mathbb{R}^q$ as well as a measurement variable $y \in \mathbb{R}^p$ of dimension $q = p = 1$, $m = 3$ and $n = 2$. It concatenates all weighted exogenous inputs $w = [r_\mathrm{w}\ d_\mathrm{w}\ n_\mathrm{w}]'$ and all weighted exogenous outputs $z = [e_\mathrm{w}\ u_\mathrm{w}]'$, as illustrated in Figure 6.2.

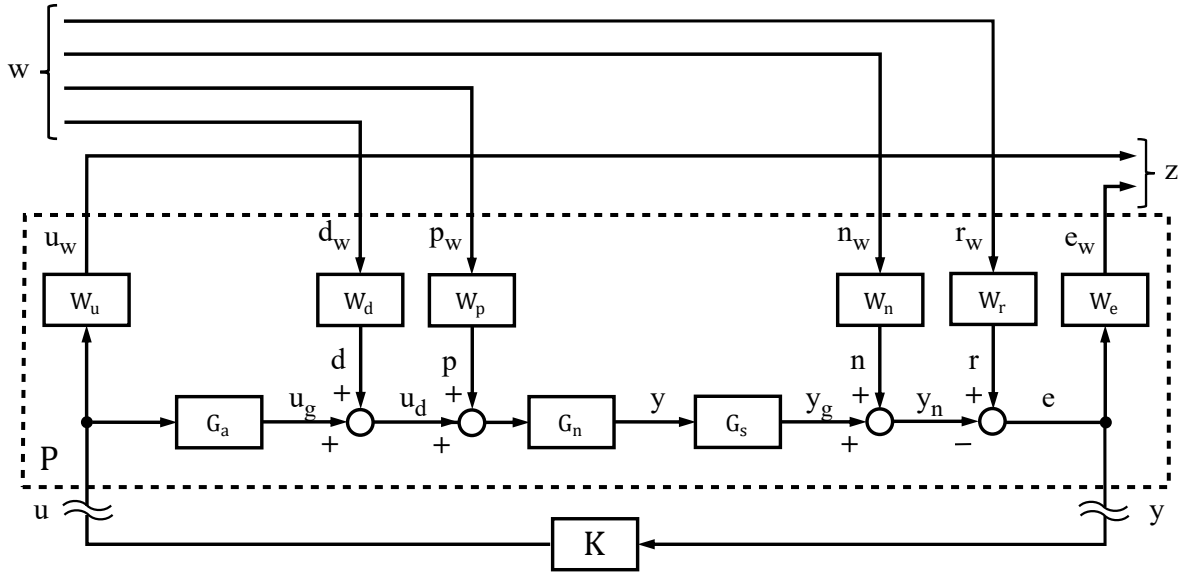

Figure 6.2 – Block diagram of generalized plant for control design: considering system components, input and output weighting functions.

The nominal plant G_n with pump actuator G_a and pressure gauge G_s are thereby connected to the controller block K, by closing the lower loop with $\mathrm{P}_{11} = -G_s(s)\ G_n(s)\ G_a(s)$.

Applying lower linear fractional transformation (LLFT)

Using lower linear fractional transformation (5.6), as defined in Section 5.2, provides the generalized plant

$$T(s) = \mathrm{P}_{11} + \mathrm{P}_{12}\ \mathrm{K}\,(\mathrm{I} - \mathrm{P}_{22}\ \mathrm{K})^{-1}\,\mathrm{P}_{21} \ . \tag{6.3}$$

This describes the closed-loop system $z = T(s)\ w$ from the exogenous input channels to the exogenous output channels $w(t) \to z(t)$ with respect to the standard configuration (5.5), including a controller of desired structure, e.g. (5.68) or (5.69).

Evaluating (6.3) for the interconnection transfer function matrix (6.2) yields the **generalized plant**

$$\boxed{T = \begin{bmatrix} W_e\mathcal{S}W_r & -W_eG_sG_n\mathcal{S}W_d & -W_e\mathcal{S}W_n & -W_eG_sG_n\mathcal{S}W_\mathrm{p} \\ W_u\mathrm{K}\mathcal{S}W_r & -W_u\mathcal{T}_uW_d & -W_u\mathrm{K}\mathcal{S}W_n & -W_u\mathcal{T}_uW_\mathrm{p} \end{bmatrix}} \,, \tag{6.4}$$

that defines the desired cost function for H_∞ controller synthesis. For convenience, the quasi-sensitivity function $\mathcal{S} = (1 + G_s\ G_n\ G_a\ \mathrm{K})^{-1}$ and the quasi-complementary sensitivity function $\mathcal{T}_u = \mathrm{K}G_sG_n\mathcal{S}$ have been introduced. The first column of of the generalized plant (6.4) corresponds to the reference signal $r(t)$, the second to the disturbance signal $d(t)$, the third to the noise signal $n(t)$ and the fourth to the perturbation signal $\mathrm{p}(t)$, whereas the first row corresponds to the control error $e(t)$ and the second to the control value $u(t)$. For example, the performance for disturbance rejection is given by T_{21} and the control effort for suppressing any disturbances is defined by T_{22}.

H_∞ suboptimal control design

A generalized plant $T(j\omega)$ defines the cost functions of the **suboptimal H_∞ optimization problem** [Gu et al., 2013]

$$\boxed{\underset{\mathrm{K}}{\text{minimize}}\ \|T(j\omega)\|_\infty < \gamma\ ,} \tag{6.5}$$

that is used to find a stabilizing controller K, such as $\|T\|_\infty < \gamma$, where γ denotes the inverse robust stability margin in terms of the peak magnitude. Nominal performance and robust stability will be obtained, if $\gamma \leq 1$ is satisfied. Thus, an optimization problem of dimension $n \times m$ has to be solved, minimizing the H_∞-norm

$$\|T\|_\infty = \sup_\omega \overline{\sigma}\left(T(j\omega)\right) \tag{6.6}$$

for the cost function of dimension 4×2, as given by (6.4). This requires to find a controller K that

$$\left\| \begin{matrix} W_e\mathcal{S}W_r & W_eG_sG_n\mathcal{S}W_d & W_e\mathcal{S}W_n & W_eG_sG_n\mathcal{S}W_\mathrm{p} \\ W_u\mathrm{K}\mathcal{S}W_r & W_u\mathcal{T}_uW_d & W_u\mathrm{K}\mathcal{S}W_n & W_u\mathcal{T}_uW_\mathrm{p} \end{matrix} \right\|_\infty < 1 \tag{6.7}$$

is obtained.

Using the Riccati method [Doyle et al., 1989], as implemented in *Matlab*, to solve for the inequalities (6.7) results in a state feedback controller of order 12, for which a peak value of $\gamma = 0.6067$ has been achieved.

The step responses of Figure 6.3 evaluates the perturbed plant (5.116), with the derived robust state feedback controller K_{SF} in closed-loop. In contrast to the generalized plant used for control design, where an unstructured inverse additive uncertainty has been considered, the step and frequency responses for controller evaluation will be derived, using a perturbed plant with real parametric structured uncertainties (see Section 5.4). This holds for all investigations in the subsequent sections. The simulation studies in Section 6.3 will validate the derived structured and unstructured controllers, using the detailed non-linear simulation models from Chapter 4. The step response from reference input $r(t)$ to measurement output $y(t)$ shows a desired reference value tracking with rise time $\tau_r < 4$ second and no steady-state error exists. The resulting characteristics is given by the a priori defined input shaping function W_r, see Section 5.3. Any step on the reference signal is therefore gradually applied to the system. The response from reference input $r(t)$ to the control value $u(t)$ reveals the wide operating range needed to obtain the reference pressure for different plant perturbations. This means that up to 40% of the available

pump rate is required to reach pressure equilibrium. This depends on the configuration of a waterjet facility. The step response from disturbance $d(t)$ to measurement output $y(t)$ shows that any unit step disturbance will affect the system pressure with a maximal 9.3% overshoot, considering worst case perturbation. The controller will reject the disturbance within a settling time $\tau_s < 0.2$ seconds. Any disturbance is attenuated with zero steady-state error. The step response from $d(t)$ to $u(t)$ reveals that another 60% of the available pump rate is applied for disturbance rejection. The step response from noise $n(t)$ to $y(t)$ and to $u(t)$ shows that the noise on the measurement channel will be attenuated and noise acting on the actuator is reasonably small (with amplitudes of 10^{-4}).

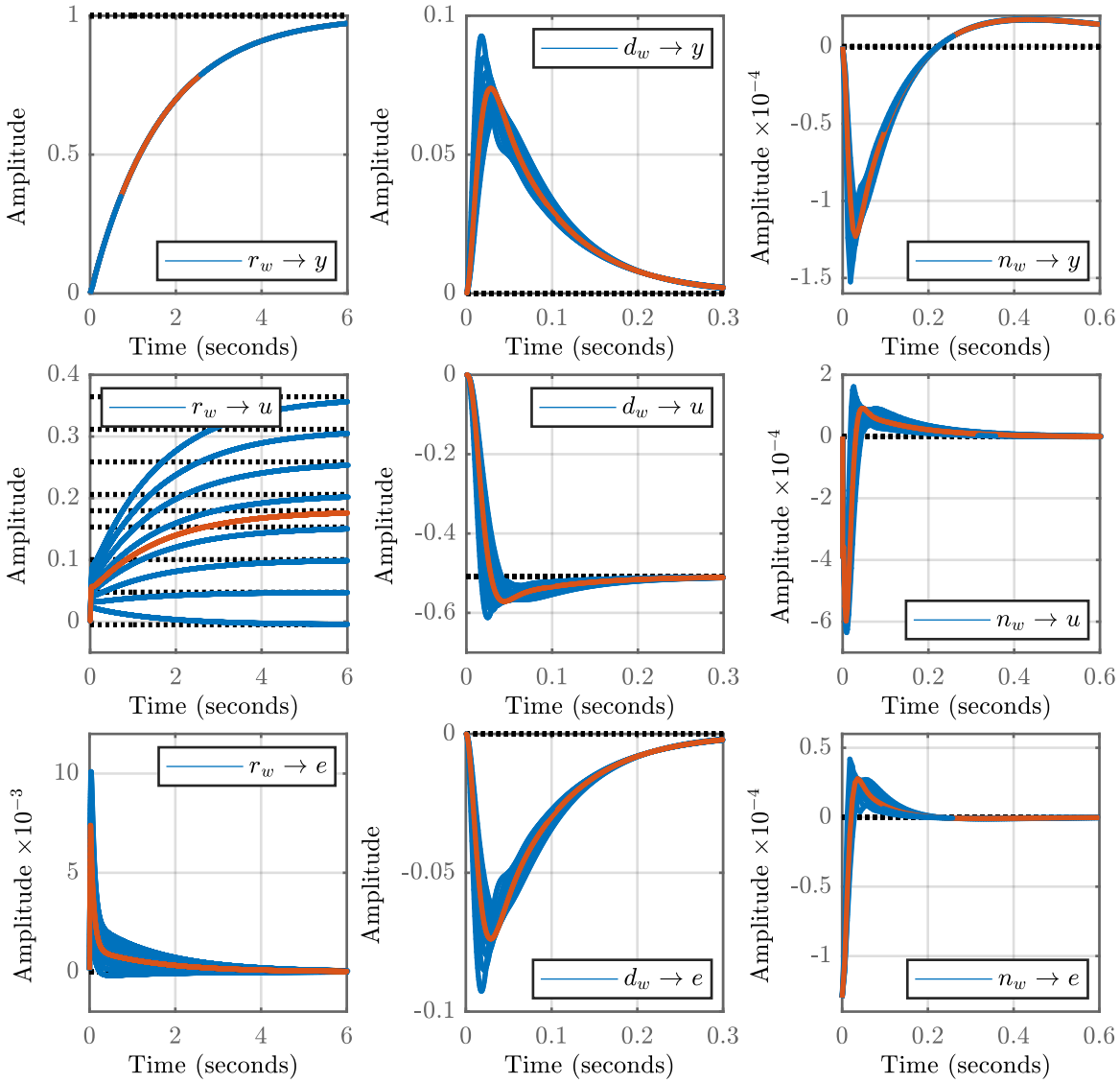

Figure 6.3 – Step responses of state feedback controller K_{SF}: applying unit steps on the different input channels.

The control effort to follow the reference signal is less than 40%. The control effort to attenuate disturbance can reach 60%. Consequently, the pump actuator limits are sufficient to supply a high-pressure network subsection without reaching saturation, but further increasing the water

consumption is not permitted. The evaluation of the closed-loop system with respect to the control objectives is summarized in Table 6.1, see page 211.

The above signal-based approach to employ the H_∞ optimization problem can be considered as a generalized form of the mixed-sensitivity approach [Skogestad and Postlethwaite, 2005], for which specific transfer functions of desired input channels to selected output channels provide the cost functions subject for optimization. Investigating the control requirements with respect to the introduced performance criterion (5.79), the control effort criterion (5.87) and the robustness criterion (5.95), requires to evaluate the H_∞-norm (6.7) for the transfer functions $\mathrm{p} \to y$, $d \to e$ and $d \to u$. Recalling the control design specifications (5.64), yields the optimization problem

$$\underset{\mathrm{K}}{\text{minimize}} \left\| \begin{matrix} G_n \mathcal{S} W_\mathrm{p} \\ W_e G_s G_n \mathcal{S} W_d \\ W_u \mathcal{T}_u W_d \end{matrix} \right\|_\infty < \gamma \ , \tag{6.8}$$

where the first cost function defines stability for perturbations from $\mathrm{p}(t)$ to $y(t)$, the second cost function defines the dynamic range for disturbance rejection from $d(t)$ to $e(t)$ and the third cost function penalizes the control effort from $d(t)$ to $u(t)$.

To find a controller K, the largest singular values $\bar{\sigma}$ of each system transfer function, including the input weights, must be smaller by a factor γ as the smallest singular value of the corresponding output weight. For that, the inequalities

$$\begin{aligned} \overline{\sigma}\left(G_n(j\omega)\mathcal{S}(j\omega)W_\mathrm{p}(j\omega)\right) &\leq \gamma \underline{\sigma}\left(\ 1\ \right) \\ \overline{\sigma}\left(G_s(j\omega)G_n(j\omega)\mathcal{S}(j\omega)W_d(j\omega)\right) &\leq \gamma \underline{\sigma}\left(W_e^{-1}(j\omega)\right) \\ \overline{\sigma}\left(\mathcal{T}_u(j\omega)W_d(j\omega)\right) &\leq \gamma \underline{\sigma}\left(W_u^{-1}(j\omega)\right) \end{aligned} \tag{6.9}$$

have to be satisfied for all ω. This is evaluated by applying the H_∞-norm (6.6) for the stacked notation

$$\sup_\omega \overline{\sigma} \begin{bmatrix} T_1(j\omega) \\ \vdots \\ T_k(j\omega) \end{bmatrix} < \gamma \ , \tag{6.10}$$

where the largest singular value $\overline{\sigma}$ is evaluated by the Euclidean vector norm

$$\overline{\sigma} \begin{bmatrix} T_1(j\omega) \\ \vdots \\ T_k(j\omega) \end{bmatrix} = \sqrt{|T_1(j\omega)|^2 + |T_2(j\omega)|^2 + ... + |T_k(j\omega)|^2} = \sqrt{\sum_{i=1}^{k} |T_i|^2} \ . \tag{6.11}$$

Thus, the singular values of the inequalities (6.9) describe the cost function

$$\overline{\sigma}(T) = \sqrt{|G_n S W_\mathrm{p}|^2 + |W_e G_s G_n S W_d|^2 + |W_u T W_d|^2} \tag{6.12}$$

in terms of (6.11).

The plots of Figure 6.4 compare the singular values of the selected cost functions (6.9). The first inequality guarantees nominal performance with respect to disturbance rejection (a), while the second inequality penalizes control effort, considering actuator saturation (b). The third inequality evaluates the perturbation to obtain robust stability for the closed-loop system (c). It is shown that the inequalities hold for the obtained controller K_{SF}, as the γ-value has already revealed. Even more, control effort could become stronger penalized and plant perturbation can be further increased without violating the requirements on stability and performance, as given by $\overline{\sigma}(T) < 1$.

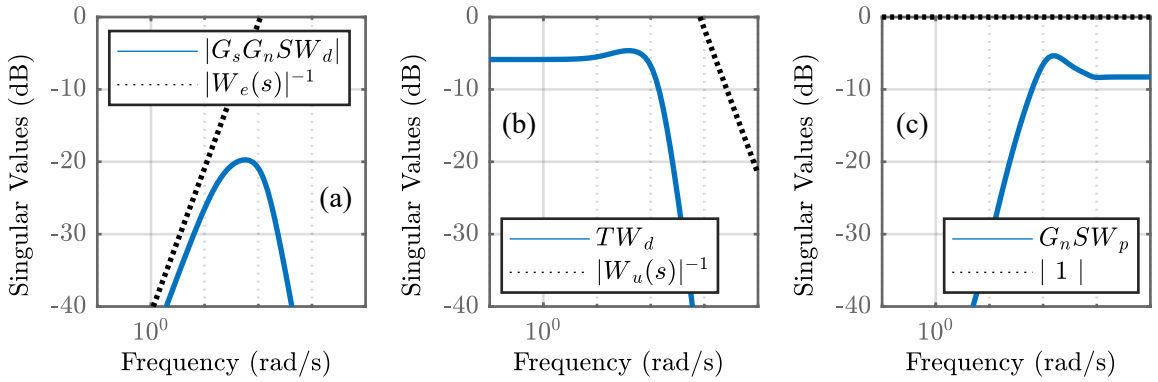

Figure 6.4 – Frequency responses of the nominal generalized plant with state feedback controller K_{SF}: evaluating nominal performance (a), control effort (b) and robust stability (c).

In any case, the inequalities for nominal performance and robust stability have to be fulfilled to obtain robust performance. The plot of Figure 6.5 provides the singular values for selected cost functions and evaluates its Euclidean vector norm (6.12). The peak gain obtained is bellow the 0 dB line. This means that robust performance and stability is guaranteed. The distance between peak gain and 0 dB line corresponds to the robust stability margin by means of peak magnitude γ.

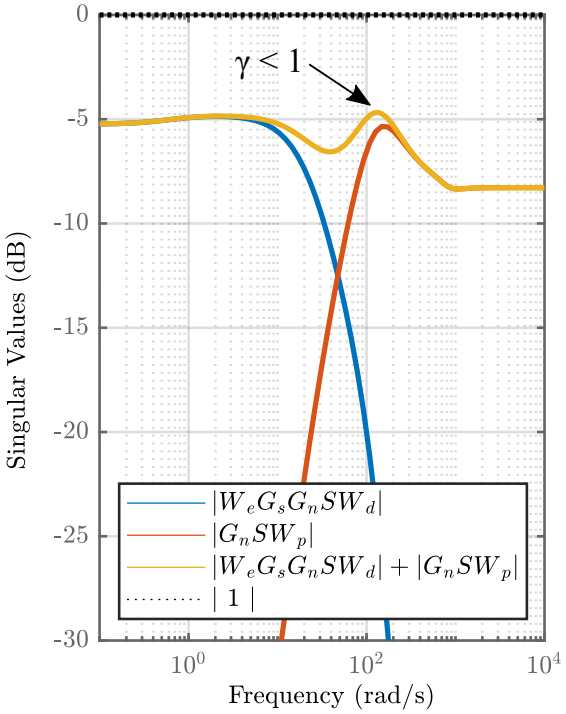

Figure 6.5 – Frequency responses of nominal generalized plant with state feedback controller K_{SF}: evaluating for robust performance and stability with respect to the Euclidean vector norm.

6.2.2 Joint shaping functions

Introducing more complex uncertainty descriptions or extending the above control design, considering an entire high-pressure network with multiple interconnected pumps, will cause the dimension of the resulting optimization problem to increase. With increased complexity, the task of finding a stabilizing controller becomes time consuming. Thus, this section aims to reduce the dimension of the optimization problem (6.5) by concatenating the generalized plant (6.4) for k of its m input channels. Where k denotes the number of selected exogenous inputs that are subject to be merged. This yields again a stacked notation of the largest singular values

$$\overline{\sigma}\left(T(j\omega)\right) = \overline{\sigma}\begin{bmatrix} T_1 \\ \vdots \\ T_k \end{bmatrix} = \sqrt{\sum_{i=1}^{k} |T_i|^2} \leq \gamma, \tag{6.13}$$

whereas the Euclidean vector norm (6.11) is used to evaluate for peak value γ. This stacked notation is adopted from the mixed sensitivity approach in [Skogestad and Postlethwaite, 2005]. Defining a generalized plant, composed by a weighting function matrix W, a shaping function matrix V and a system transfer function matrix U, such as $T := WUV$ and substituting this in the stacked notation (6.13), enables to aggregate shaping functions by means of the largest singular values

$$\overline{\sigma}\begin{bmatrix} WUV_1 \\ \vdots \\ WUV_k \end{bmatrix} = \sqrt{\sum_{i=1}^{k} |WUV_i|^2} = |WU| \sqrt{\sum_{i=1}^{k} |V_i|^2} = \overline{\sigma}\left(WU\tilde{V}\right). \tag{6.14}$$

Consequently, a **joint shaping function** can be defined by the Euclidean vector norm

$$\boxed{\overline{\sigma}\left(\tilde{V}(j\omega)\right) := \sqrt{\sum_{i=1}^{k} |V_i|^2}} \tag{6.15}$$

and a reduced generalized plant $\tilde{T} := WU\tilde{V}$ will be obtained. It approximates the optimization problem for $\|\tilde{T}\|_\infty < \gamma$ and thereby reduces the resulting optimization problem of dimension $n \times (m - k + 1)$.

Although, this procedure reduces the dimension of the resulting optimization problem, it may lead to a more conservative control design. For example, merging the input vector $w \in \mathbb{R}^m$ of size $m = 2$ with corresponding transfer functions T_1 and T_2. The error when using a joint shaping function, due to the Euclidean vector norm (6.15), becomes maximally $\sqrt{2} \approx 3$ dB magnitude at any ω where $|T_1(j\omega)| = |T_2(j\omega)|$.

Reduced generalized plant

Combining the additively interconnected input signals r and n with respect to (6.14) results, according to definition (6.15), in

$$\overline{\sigma}\left(W_{rn}\right) = \sqrt{|W_r|^2 + |W_n|^2}, \tag{6.16}$$

whereas the joint shaping function $W_{rn}(s)$ of Figure 6.6 (a) has been obtained. Repeating this procedure for the additively interconnected input signals d and p yields

$$\overline{\sigma}\left(W_{dp}\right) = \sqrt{|W_d|^2 + |W_\mathrm{p}|^2}, \tag{6.17}$$

which has been approximated by the joint shaping function $W_{dp}(s)$, shown in Figure 6.6 (b).

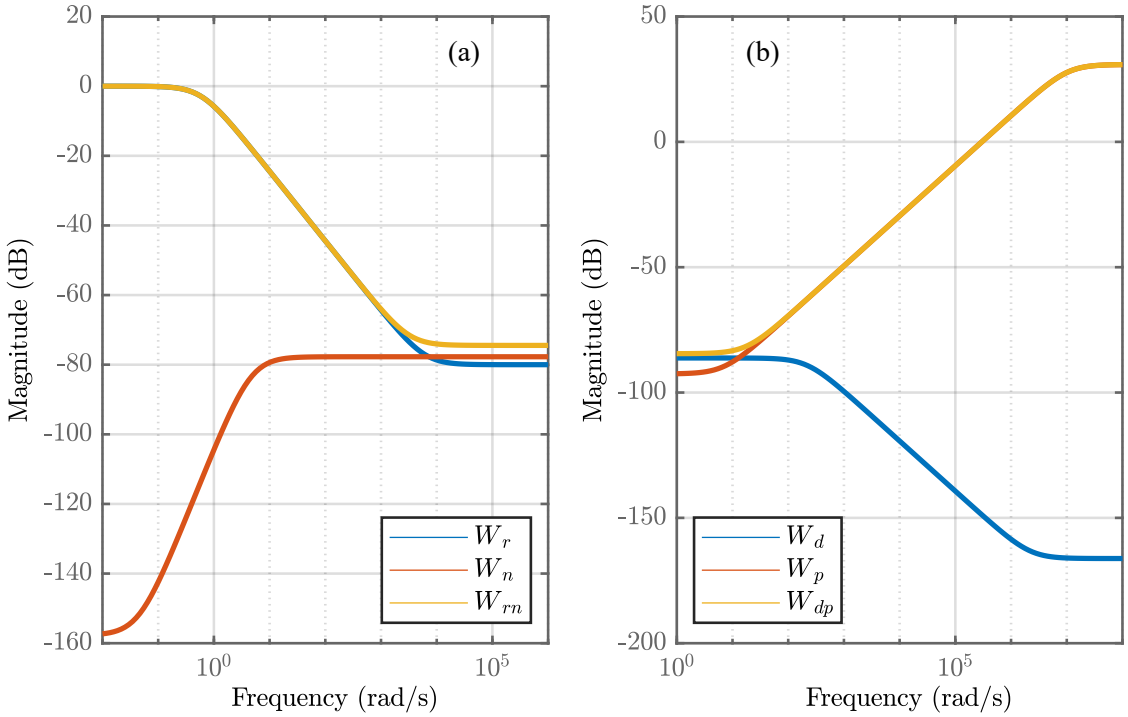

Figure 6.6 – Frequency response of the joint shaping functions: dynamic range of the shaping functions on the reference and noise signals (a) and dynamic range of the shaping functions on the disturbance and perturbation signals (b).

The reduced interconnection system, regarding this simplification, is illustrated in the block diagram of Figure 6.7. The exogenous inputs were concatenated to $\tilde{w} = [rn_{\mathrm{w}}\ d\mathrm{p}_{\mathrm{w}}]'$ This provides a standard configuration with reduced interconnection function matrices

$$\mathrm{P}_{11} = \begin{bmatrix} W_e \mathrm{I} W_r & -W_e G_s G_n W_d & -W_e \mathrm{I} W_n \\ \\ 0 & 0 & 0 \end{bmatrix}, \quad \mathrm{P}_{12} = \begin{bmatrix} -W_e G_s G_n G_a \\ \\ \mathrm{I} W_u \end{bmatrix},$$
$$\mathrm{P}_{21} = \begin{bmatrix} \mathrm{I} W_r & -G_s G_n W_d & -\mathrm{I} W_n \end{bmatrix}, \quad \mathrm{P}_{22} = \begin{bmatrix} -G_s G_n G_a \end{bmatrix}, \tag{6.18}$$

separating the controller block $\tilde{\mathrm{K}}$. Applying lower linear fractional transformation for (6.18), see Section 5.2, results in the **reduced generalized plant**

$$\boxed{\tilde{T} = \begin{bmatrix} W_e \tilde{\mathcal{S}} W_{r,n} & -W_e G_s G_n \tilde{\mathcal{S}} W_{d,p} \\ W_u \tilde{\mathrm{K}} \tilde{\mathcal{S}} W_{r,n} & -W_u \tilde{\mathcal{T}}_u W_{d,p} \end{bmatrix}}, \tag{6.19}$$

that defines the reduced cost functions for H_∞ controller synthesis. The first column of (6.19) corresponds to the joint reference and noise signal $rn(t)$, the second to the joint disturbance and perturbation signal $dp(t)$, whereas the first row corresponds to the control error $e(t)$ and the second to the control value $u(t)$.

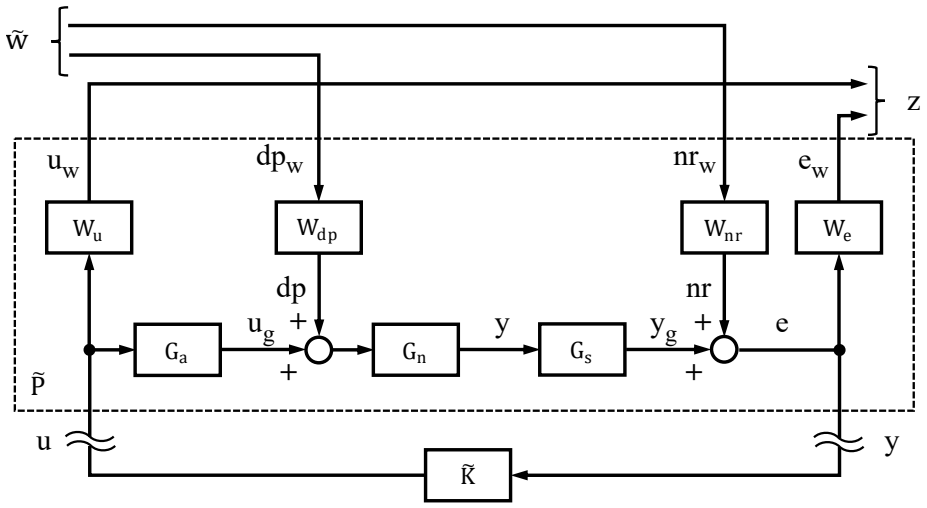

Figure 6.7 – Block diagram of reduced generalized plant for controller synthesis: taking joint shaping functions into account for input signals dp and rn.

H_∞ suboptimal control

The reduced generalized plant $\tilde{T}(j\omega)$ gives again the cost functions of a H_∞ optimization problem

$$\underset{\tilde{\mathrm{K}}}{\text{minimize}} \; \|\tilde{T}(j\omega)\|_\infty < \gamma \; , \tag{6.20}$$

that is to find a stabilizing controller $\tilde{\mathrm{K}}$, such as $\|\tilde{T}\|_\infty < 1$. Considering the design with joint shaping functions, a reduced optimization problem of dimension $n \times (m-k)$ has to be solved, that requires to minimize the H_∞-norm

$$\left\| \begin{matrix} W_e \tilde{\mathcal{S}} W_{rn} & W_e G_s G_n \tilde{\mathcal{S}} W_{dp} \\ W_u \tilde{\mathrm{K}} \tilde{\mathcal{S}} W_{rn} & W_u \tilde{\mathcal{T}}_u W_{dp} \end{matrix} \right\|_\infty < 1 \; . \tag{6.21}$$

of a reduced cost function matrix (6.19) with dimension 2×2. Ultimately, solving this considering the Riccati method [Doyle et al., 1989], results in a state feedback controller of order 9 and a peak value of $\gamma = 0.6167$. Even though, using joint shaping functions result in a more conservative control design, it reduces the optimization problem and yields a reduced order controller.

Comparing the state feedback controllers

The frequency response of Figure 6.8 (a) compares the dynamic range for the state feedback controllers K_{SF} and $\tilde{\mathrm{K}}_{SF}$, derived from the full generalized plant (6.4) and from the reduced generalized plant (6.19). Again, the simulation studies in Section 6.3 will validate the derived structured and unstructured controllers, using the detailed non-linear simulation models from Chapter 4. The resulting controller from reduced control design is found to recover the frequency response of the full control design for the frequency range of interest ($\omega \in [10^{-1}, 10^4]$ rad/s). Interconnecting this controller to the perturbed plant (5.116), which contains all parametric uncertainties, enables it to evaluate the control requirements of Section 5.3. On the other hand, the step response of Figure 6.8 (b) compares the disturbance rejection for both controllers. Both closed-loop systems perform equivalent, considering a unit step input on $d(t)$. Consequently, the effects for the perturbed plant remains unchanged, when applying joint shaping functions for control design.

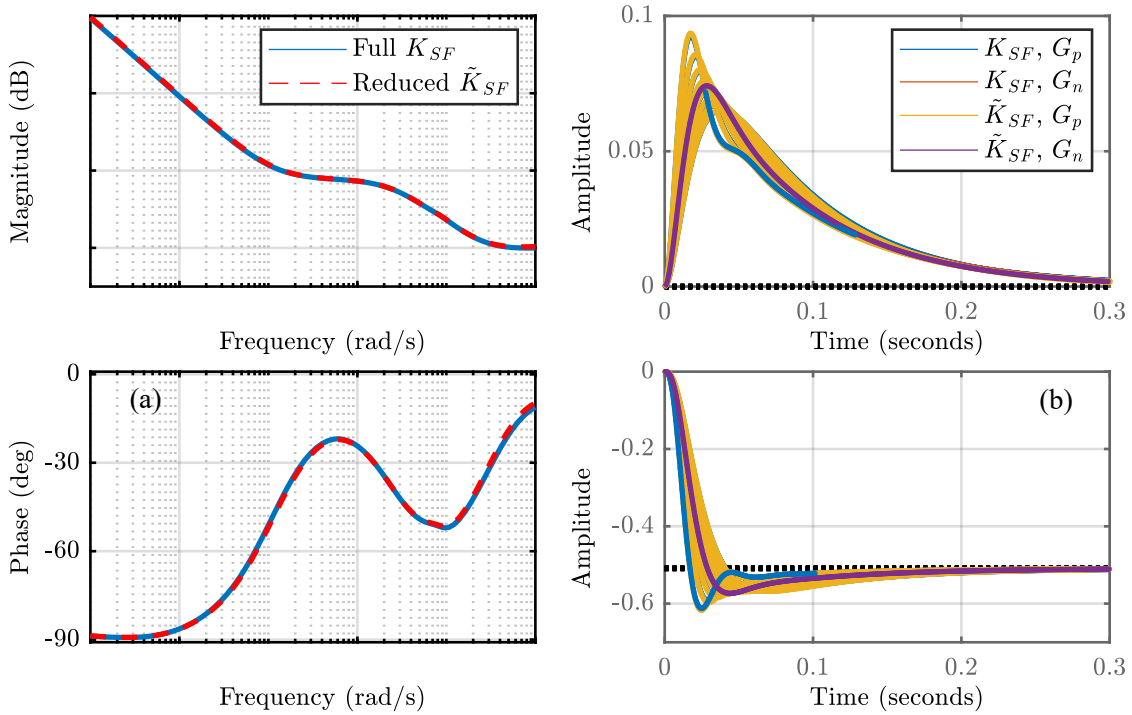

Figure 6.8 – Closed-loop frequency responses (a) and step responses (b) from $d \rightarrow y$: implementing controller K_{SF}, when optimizing for the full generalized plant (independent shaping functions), and controller $\tilde{\mathrm{K}}_{SF}$ from the reduced generalized plant (joint shaping functions).

Joint shaping functions allow for reducing the dimension of the optimization problem, that reduces the computational effort to find a feasible controller. It further reduces the order of the generalized plant, before synthesizing a controller. The obtained state feedback controller from a reduced generalized plant will then be of lower order. For the presented use case, reducing the full generalized plant, by means of joint shaping functions, gives a valuable approximation $\tilde{\mathrm{K}}_{SF}$ of the initial design K_{SF}. Only 75% of the initial calculation time is needed to solve the optimization problem $\|\tilde{T}\|_\infty < \gamma$ instead of $\|T\|_\infty < \gamma$.

Nonetheless, robust performance and stability have been obtained for both control designs, as the singular values of the cost functions reveal. The plots of Figure 6.9 evaluate the cost functions derived from the reduced generalized plant by means of performance weight (a), control effort weight (b) and robustness margin (c). Robust disturbance rejection is expected, since the H_∞-norm from disturbance $d_\mathrm{w}(t)$ to control error $e(t)$ and from perturbation $\mathrm{p_w}(t)$ to measurement signal $y(t)$ remain below 1. Also an acceptable control effort is achieved, since the H_∞-norm from $d_\mathrm{w}(t)$ to control signal $u(t)$ remains below 1.

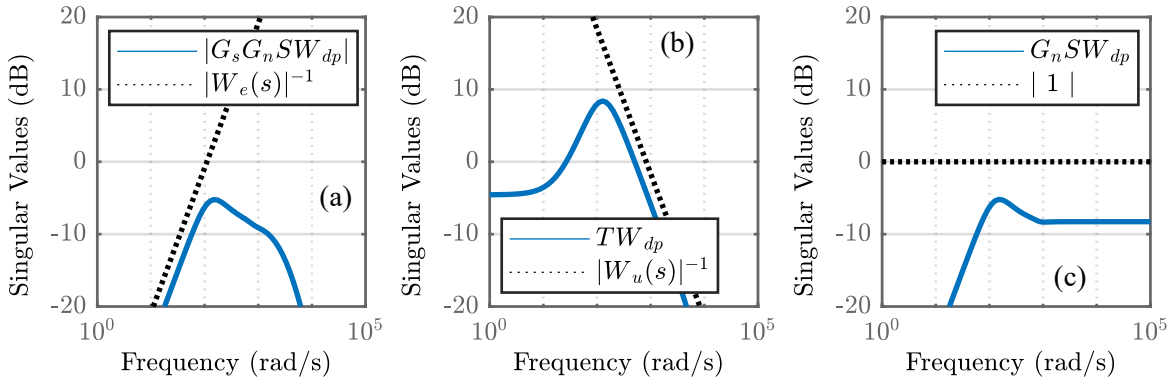

Figure 6.9 – Frequency responses of the nominal generalized plant with reduced state feedback controller $\tilde{\mathrm{K}}_{SF}$, when considering joint shaping functions: evaluating nominal performance (a), control effort (b) and robust stability (c).

The closed-loop system dynamics remains unchanged, applying the reduced controller $\tilde{\mathrm{K}}_{SF}$ instead of the initial controller K_{SF}. The frequency responses of Figure 6.10 compare the dynamic range of the closed-loop system for disturbance rejection (a) and for the required control effort (b). A desired damping of about -20 dB for $d(t) \rightarrow y(t)$ has been obtained with limited control effort, as required from specifications in Section 5.3. This relates to the observed overshoot of $< 10\%$, when applying a unit step on the disturbance input. The evaluation of the closed-loop system, with respect to the control requirements, is summarized in Table 6.1. A minor degradation is found for the reduced controller derived by means of joint shaping functions.

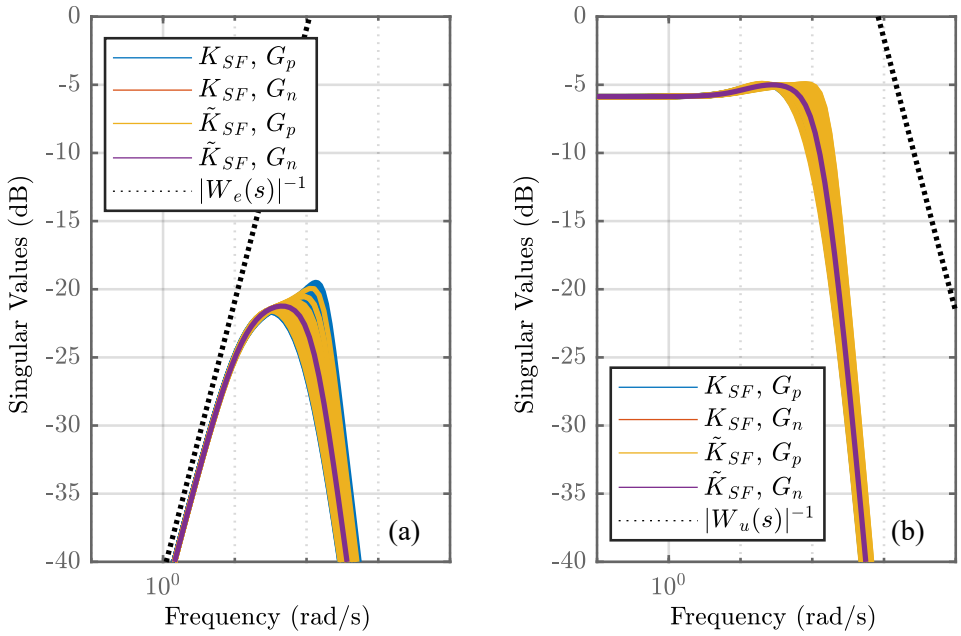

Figure 6.10 – Frequency response of the inverse weighting functions $|W_e(s)|$ and $|W_u(s)|$, considering the reduced state feedback controller: dynamic range of generalized plant $|T(s)|$ from $d \rightarrow e$ (a) and its dynamic range from $d \rightarrow u$ (b).

Table 6.1: Achieved performance for state feedback controllers derived with full and reduced generalized plant: comparing achieved closed-loop performance with the control objectives for waterjet machining.

	K_{SF}		$\tilde{\mathrm{K}}_{SF}$		Objective
	nom.	max.	nom.	max.	(Sect. 5.3)
Peak gain γ-value:	0.6067		0.6167		≤ 1.0
Rise time (90% $r(t)$):	3.9144	3.9144	3.9144	3.9144	< 10
Settling time (2% $e(t)$):	0.1300	0.1368	0.1270	0.1340	< 0.5
Overshoot:	0.0739	0.0927	0.0742	0.0936	$< \pm 0.1$

6.2.3 Robust PI control design

The obtained state feedback controllers are not well adapted for industrial application, because of the increased complexity for implementation. In order to cope with industrial requirements, a more standard controller structure is desired. In this perspective, the structured H_∞ synthesis [Apkarian and Noll, 2006], as implemented in Matlab, allows for optimizing a robust PI controller in parallel form (5.69). This results in a control law, which is straight forward to implement into industrial applications. It features a structure with only 2 independent parameters subject for optimization.

Considering the reduced generalized plant (6.19), yields the **PI controller**

$$\boxed{\mathrm{K}_{PI}(s) = K_P + K_I \, \frac{1}{s}} \tag{6.22}$$

with proportional gain $K_P = \#\#\#$ and integral gain $K_I = \#\#\#$. However, the reduced degree of freedom, for H_∞ controller synthesis, limits the PI structure to perform competitive to a state feedback controller.

Comparing PI controller and state feedback controller

The frequency response of Figure 6.11 (a) compares the initial state feedback controller K_{SF} with the robust PI controller K_{PI}. This structured feedback controller is incapable to recover the dynamic range of the state feedback controller in the frequency range of interest.

As a consequence, the perturbed closed-loop systems of both controllers features different performances. The step response of Figure 6.11 (b) compares the disturbance rejection. Considering the PI controller, any unit step on disturbance $d(t)$ will affect the system pressure with a maximal 14.9% overshoot. It will reject the disturbance within a settling time of $\tau_s < 0.2$ seconds. Any disturbance is attenuated with zero steady-state error.

A typical PI behaviour has been observed with oscillation amplitudes below a 2% error range. Both, overshoot and settling time, are deteriorated, where the desired control requirement for overshoot is not met. The evaluation of the closed-loop system with respect to the control objectives is summarized in Table 6.2, see page 214. The limited degree of freedom for a robust PI controller, derived by the structured H_∞ synthesis, cause major degradations. A peak value of $\gamma = 1.5610$ has been found and consequently, the desired robust performance is not achieved (since $\gamma > 1$). This basically confirms the observed overshoot of $> 10\%$.

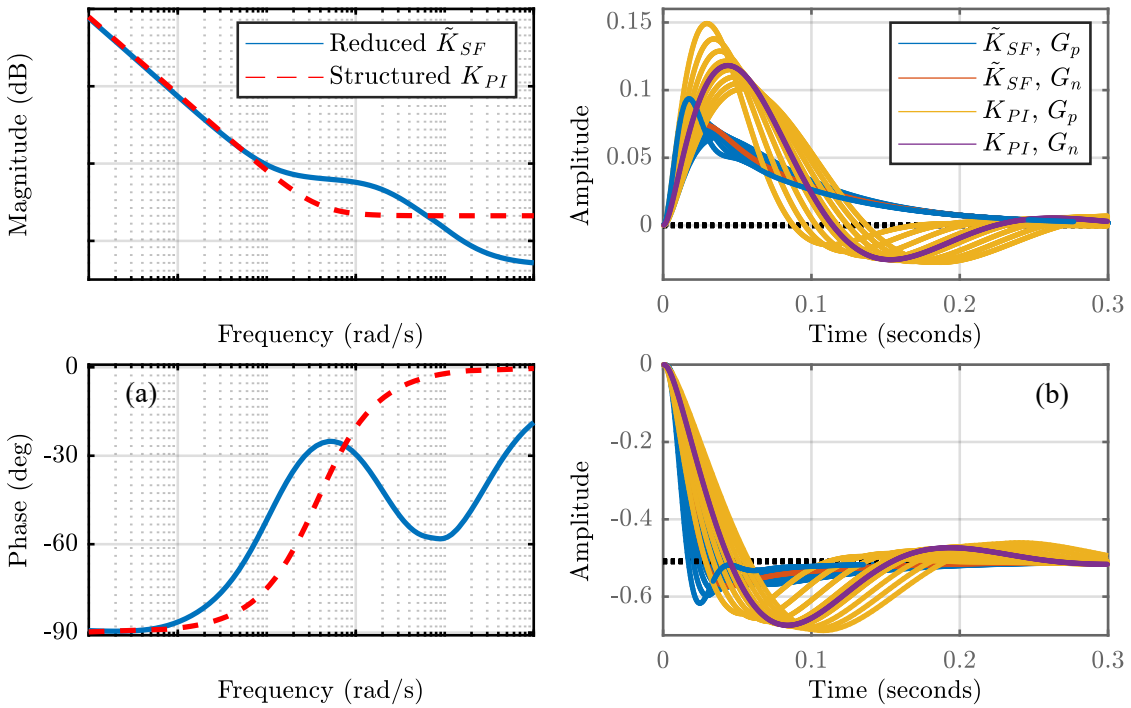

Figure 6.11 – Closed-loop frequency responses (a) and step responses (b) from $d \rightarrow y$: implementing state feedback controller $\tilde{\mathrm{K}}_{SF}$ and PI controller K_{PI}, when optimizing for the reduced generalized plant (using joint shaping functions).

The closed-loop dynamics is remarkably affected, when applying the PI controller K_{PI} instead of the initial state feedback controller K_{SF}. The singular values of Figure 6.12 compare the dynamic range of the closed-loop systems for disturbance rejection (a) and for requirements on control effort (b). The desired damping of -20 dB for $d(t) \rightarrow y(t)$ is not guaranteed, considering the PI controller. Disturbance rejection with less than -12 dB relates to the observed overshoot about 15%, when applying a unit step on the disturbance channel. Also a peaking for the control effort and a reduced actuator bandwidth is observed. Thus is still within the actuator limits, but may cause actuator deterioration.

Introducing a low-pass filter to the PI controller, as an additional tuning parameter, allows for improving performance and robustness. Such an extended PI controller $\tilde{\mathrm{K}}_{PI}$ is expected to recover the behaviour of a state feedback controller with improved precision.

PI control introducing low-pass filter

The structured H_∞ synthesis has again been used for optimizing a robust PI controller with low-pass filter (5.70). Including a first order low-pass filter, provides an additional tunable parameter, the time constant τ_f. This extended PI controller is subject for recovering the dynamic range of the state feedback controller with reduced complexity. It features a structure with 3 independent parameters subject for optimization.

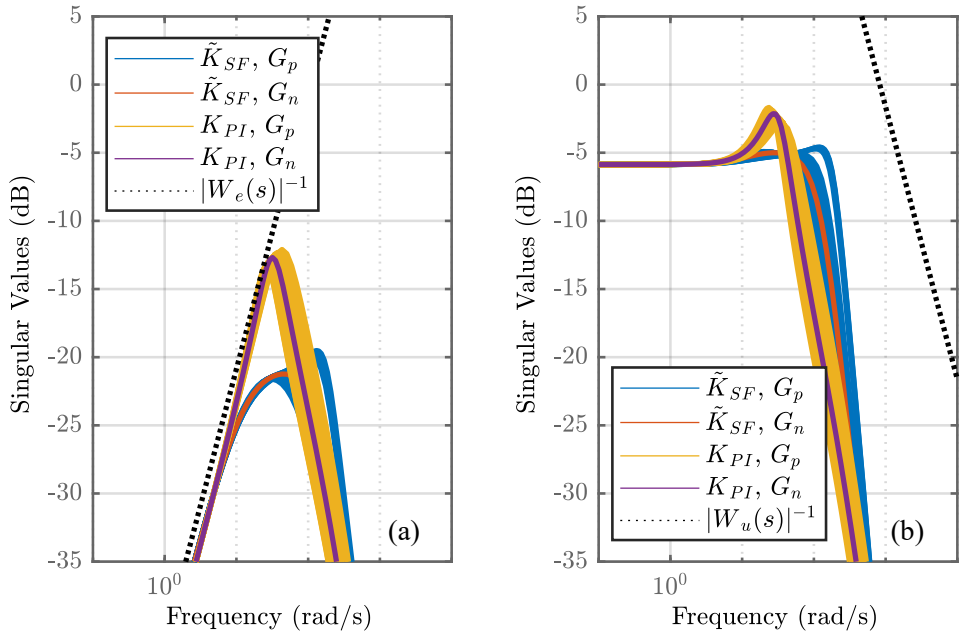

Figure 6.12 – Frequency response of the inverse weighting functions $|W_e(s)|$ and $|W_u(s)|$, considering the reduced PI controller: dynamic range of generalized plant $|T(s)|$ from $d \to e$ (a) and its dynamic range from $d \to u$ (b).

Considering the reduced generalized plant (6.19), yields the **extended PI controller**

$$\boxed{\tilde{\mathrm{K}}_{PI}(s) = \left(K_P + K_I \, \frac{1}{s}\right) \frac{1}{1 + \tau_f \, s}} \tag{6.23}$$

with $K_P = \#\#\#$, $K_I = \#\#\#$ and low-pass filter, defined by a time constant of $\tau_f = \#\#\#$ seconds. This corresponds to the lead compensator

$$\tilde{\mathrm{K}}_{PI}(s) = \frac{\#\#\# s + \#\#\#}{\#\#\# s^2 + s} \, . \tag{6.24}$$

This lead compensator design, as applied in [Salloum et al., 2014], will improve the control performance. The additional degree of freedom for H_∞ controller synthesis enables the extended PI controller to perform competitive to a state feedback controller.

Comparing extended PI controller and state feedback controller

The frequency response of Figure 6.13 (a) compares the dynamic range for the initial state feedback controller K_{SF} with the extended PI controller $\tilde{\mathrm{K}}_{PI}$. The structured feedback controller approximates the dynamic range of the state feedback controller in the frequency range of interest ($\omega \in [10^{-1}, 10^{4}]$ rad/s). Diverging behaviour is found for the high-frequency range, where the closed-loop system is already sufficiently attenuated.

As a consequence, the perturbed closed-loop systems of both controllers feature equivalent performances. The step response of Figure 6.13 (b) compares the disturbance rejection. Any unit step on disturbance $d(t)$ to will affect the system pressure with a maximal 9.6% overshoot, considering the extended PI controller. Thus will reject the disturbance within a settling time $\tau_s < 0.2$ seconds. Any disturbance is attenuated with zero steady-state error. Both overshoot and settling time are remarkably improved by introducing the low-pass filter. All desired control requirements from Section 5.3 are met, since a peak value of $\gamma = 0.6354$ has been obtained. The evaluation of the closed-loop system with respect to the control objectives is found in Table 6.2.

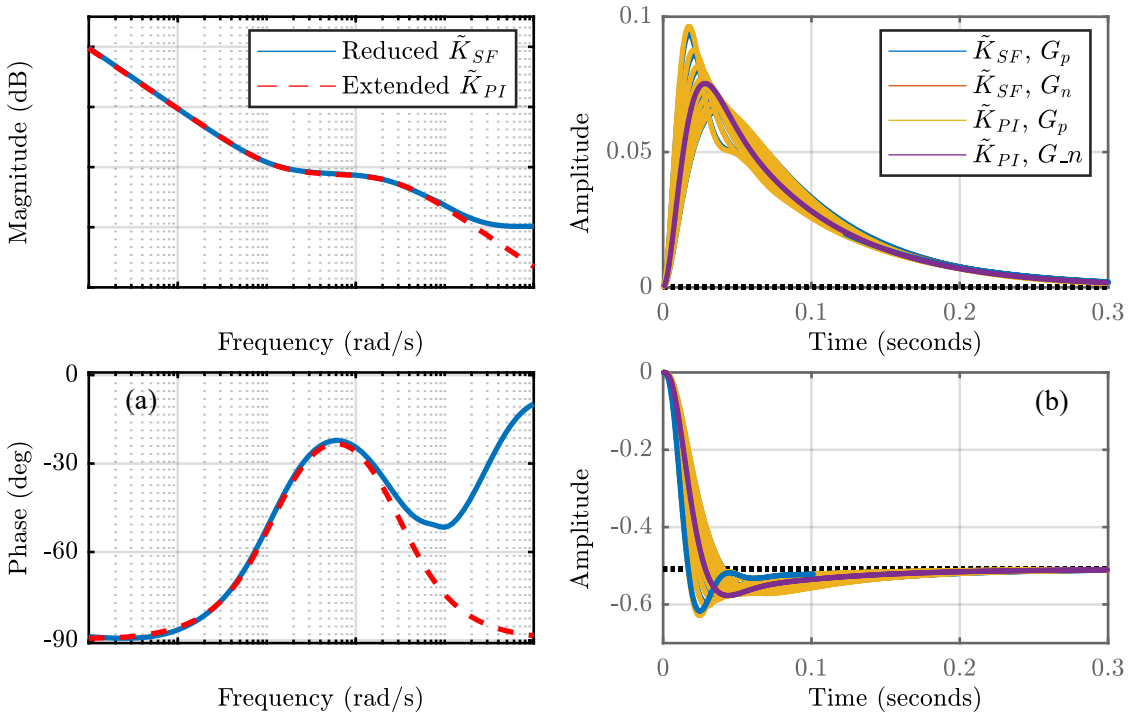

Figure 6.13 – Closed-loop frequency responses (a) and step responses (b) from $d \to y$: implementing state feedback controller $\tilde{\mathrm{K}}_{SF}$ and extended PI controller $\tilde{\mathrm{K}}_{PI}$ with low-pass filter, when optimizing for the reduced generalized plant (using joint shaping functions).

Table 6.2: Achieved performance for initial PI controller without low-pass filtering and extended PI controller with low-pass filtering : comparing achieved closed-loop performance with control objectives for waterjet machining.

	K_{PI}		$\tilde{\mathrm{K}}_{PI}$		Objective
	nom.	max.	nom.	max.	(Sect. 5.3)
Peak gain γ-value:	**1.5610**		0.6354		≤ 1.0
Rise time (90% $r(t)$):	3.9144	3.9144	3.9144	3.9144	< 10
Settling time (2% $e(t)$):	0.1017	0.1217	0.1236	0.1318	< 0.5
Overshoot:	**0.1182**	**0.1492**	0.0753	0.0963	$< \pm 0.1$

Applying the extended PI controller $\tilde{\mathrm{K}}_{PI}$, results in a similar closed-loop dynamics as with the initial state feedback controller K_{SF}. The singular values of Figure 6.14 compare the dynamic range of the closed-loop systems for disturbance rejection (a) and for requirements on control effort (b). A damping of -20 dB is almost obtained, considering the extended PI controller. That allows for sufficient disturbance rejection, when applying a unit step on the disturbance input. Also the control effort remains unchanged. The introduced low-pass filter enables a robust PI controller to approximate the state feedback controller with reasonable accuracy. It obtains almost identical stability and robustness margins.

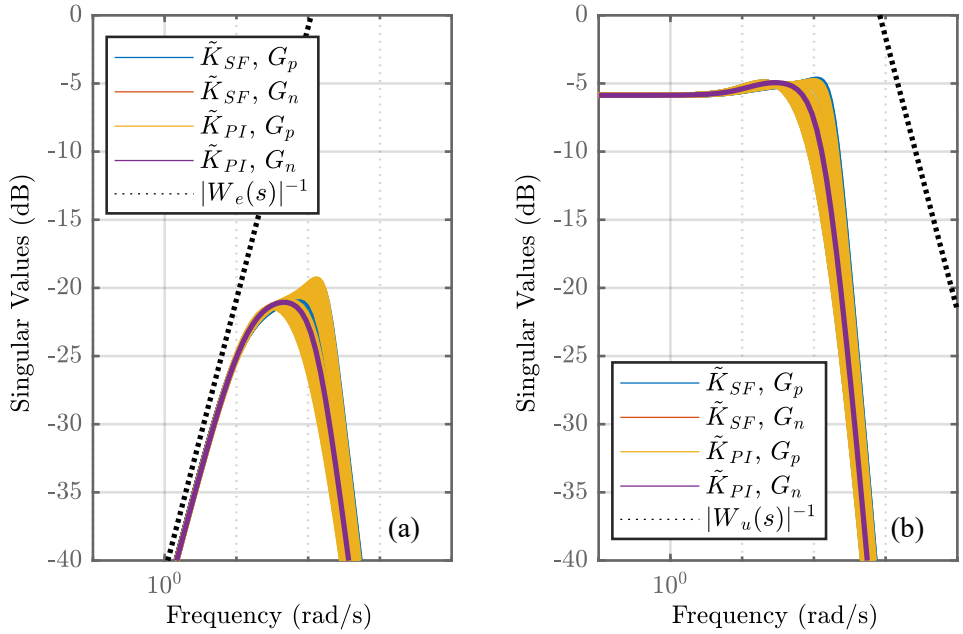

Figure 6.14 – Frequency response of the inverse weighting functions $|W_e(s)|$ and $|W_u(s)|$ considering the extended PI controller with low-pass filter: dynamic range of generalized plant $|T(s)|$ from $d \to e$ (a) and its dynamic range from $d \to u$ (b).

It has been shown that the state feedback controller can be approximated with an extended PI controller. On the other hand, it has been seen that the resulting controller obtains a large robust performance margin, since the suboptimal controller synthesis considers a predefined plant perturbation with respect to the expected uncertainty range. The subsequent control design will find a quasi-optimal controller with respect to the maximal plant perturbation allowed, while adopting the structured H_∞ controller synthesis [Apkarian and Noll, 2006] to obtain a peak value $\gamma \to 1$.

6.2.4 Optimal robust control design

The suboptimal H_∞ controller synthesis, as already applied in the above control design, aims to obtain a controller $\mathrm{K}(s)$ by minimizing the H_∞-norm for the generalized plant $T(j\omega)$. This is described by the suboptimal optimization problem (6.20), where robust stability is obtained for a peak value of $\gamma < 1$. The generalized plant includes the control requirements from Section 5.3 in terms of weighting functions and considers the expected uncertainties Δ, by describing the

perturbed plant with respect to a suitable uncertainty description (see Section 5.4). The subsequent investigation aims at an optimal robust control design, which provides stability and robust performance for a maximal uncertainty range. This requires to state an **extended suboptimal optimization problem**

$$\boxed{\underset{\Delta}{\text{maximize}} \left\{ \underset{\text{K}}{\text{minimize}} \, \|T(j\omega)\|_\infty \right\} : \|T(j\omega)\|_\infty < \gamma \; .} \tag{6.25}$$

Sensitivity analysis by means of μ is a powerful tool to analyse robust performance for a closed-loop systems with known controller [Gu et al., 2013]. The evaluation of a generalized plant $T(j\omega)$ using the robust performance margin $\mu_\Delta(T(j\omega))$ depends in the uncertainty description, as denoted by subscript Δ, see Section 5.2. This can be applied for uncertainties of any type, taking real parametric and complex uncertainties into account. The robust performance margin $\mu_\Delta(T(j\omega))$ is related to the spectral radius $\rho(T(j\omega))$ and the largest singular value $\bar{\sigma}(T(j\omega))$, such as $\rho(T(j\omega)) \leq \mu_\Delta(T(j\omega)) \leq \bar{\sigma}(T(j\omega))$ [Gu et al., 2013]. To investigate robust performance requires to introduce the standard $\Delta-$M$-$K configuration of Figure 6.15, see [Elisante et al., 2004]. A transfer function matrix $T = F_\ell(\tilde{\text{P}}, \text{K})$ is thereby obtained, including the perturbed plant $\tilde{\text{P}} = F_u(\text{M}, \Delta)$.

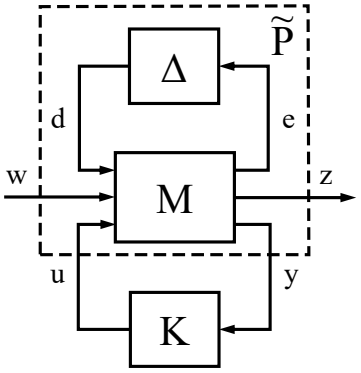

Figure 6.15 – Block diagram of standard $\Delta-$M$-$K configuration: interconnection system M connecting uncertainty block Δ and stabilizing controller K. Δ and M can be concatenated by a upper linear fractional transformation to describe the perturbed plant $\tilde{\text{P}}$ used for μ-synthesis.

Assumption 6.1. *Considering a complex unstructured uncertainty and if Δ is a full matrix yields $\rho(T(j\omega)) = \mu_\Delta(T(j\omega)) = \bar{\sigma}(T(j\omega))$. In this special case, it is appropriate to evaluate robust performance by means of the largest singular values, as stated in [Gu et al., 2013]. Robust performance is then given by the peak value $\gamma \leq 1$ that is evaluated by applying the H_∞-norm for $\|T(j\omega)\|_\infty < \gamma$.*

The objective of finding an optimal controller that provides stability and robust performance with a maximal robust performance margin is denoted as μ-synthesis [Doyle, 1987] . This problem is solved, following an iterative procedure that aims to minimize the μ-value. The D-K iteration, as presented in [Packard and Doyle, 1993], adjusts a scaling matrix D for a given controller K and alternately solves the scaled H_∞ optimization problem

$$\underset{\text{K}^*}{\text{minimize}} \; \|DT(j\omega)D^{-1}\|_\infty < \gamma \; , \tag{6.26}$$

for a stabilizing controller K*. Adjusting the matrix $D(j\omega)$ for each frequency ω within the range of interest, corresponds to a convex optimization problem. The adjusted matrix is then approximated by a minimum-phase transfer function $D(s)$. This procedure will successively flatten the μ-values for a frequency range and thus, maximizing the robust performance margin. On the other hand, the μ-K iteration, proposed in [Lin et al., 1993], adjusts the optimization problem at each iteration, using the normalized robust performance margin $\tilde{\mu}$. This yields

$$\underset{\mathrm{K}^*}{\text{minimize}} \; \|\tilde{\mu}(\tilde{\mathrm{P}}, \mathrm{K})\; T(j\omega)\|_\infty < \gamma \tag{6.27}$$

to find a controller K* that will successively reduce the peak-value of μ. However, the order of D and $\tilde{\mu}$ will successively increase, hence both approaches result in a high-order state-space controller, flattening the μ-value for a frequency range of interest.

Quasi optimal robust PI controller

Despite the D-K iteration or μ-K iteration, which lead to a high-order controller, this section proposes a quasi-optimal structured H_∞ controller synthesis, by introducing Δ-K iteration. This requires first to synthesize a structured controller, that minimizes the peak value γ for a fixed unstructured uncertainty Δ and second to adjust Δ, minimizing $|1 - \bar{\sigma}(T(j\omega))|$ for a fixed controller K. Then for the subsequent iteration, the scaled Δ is approximated with a minimum-phase transfer function.

Since the permissible network subsection size related to a high-pressure pump is undefined, a robust control design is required to find a quasi-optimal controller that considers a maximal uncertainty range. The investigated use case desires stability and robust performance with respect to an uncertain fluid volume V_δ, which corresponds to the network subsection size. The optimization problem (6.25) is thereby refined in the form

$$\underset{\mathrm{K}^*_{PI}}{\text{minimize}} \, \|T^*(j\omega)\|_\infty < \gamma \;, \quad \underset{V_\delta}{\text{minimize}} \, \{\mathrm{I} - \mu_\Delta(T^*(j\omega))\} < \varepsilon \;, \tag{6.28}$$

considering the parametric uncertainty V_δ, where ε introduces an acceptable tolerance for $\gamma \to 1$. The controller $\mathrm{K}^*_{PI}(s)$ as well as the fluid volume V_δ define tunable parameters for the structured controller synthesis [Apkarian and Noll, 2006].

Referring to the parameter variations analysed in Section 5.4, an increased fluid volume V_δ will move the transfer function pole of the perturbed plant (5.117) to lower frequencies. As a consequence, the transfer function pole, of the corresponding unstructured uncertainty description (5.133), becomes equally moved. This allows for adjusting the uncertainty model to achieve a maximal fluid volume, while remaining the nominal plant unchanged.

For example, the plot in Figure 6.16 (a) presents the effect on the peak value γ, when varying the fluid volume V_δ (Step 1) and iteratively solving the H_∞ optimization problem (Step 2), according to (6.28). On the other hand, the plot in Figure 6.16 (b) shows the adjusted uncertainty description, with its transfer function pole moved to a lower frequency, where an optimized controller has been found with increased network subsection size for $\gamma \approx 1$.

Approximating the plant perturbation with a stable, minimum-phase transfer function

$$W_\mathrm{p}(s) = \frac{s/M + \omega_B}{s + \omega_B A} \;, \tag{6.29}$$

of amplitude M and bandwidth ω_B, gives an unstructured complex uncertainty model (see Section 5.4). In this case, the uncertainty Δ can be adjusted, using the parameters M and ω_B to

obtain a peak value of $\gamma \approx 1$. Considering a constant amplitude M, requires to move the pole $p = \omega_B$ towards lower frequencies, until $\gamma \to 1$ is achieved. This yields the optimization problem

$$\underset{\mathrm{K}_{PI}^{*}}{\text{minimize}} \left\| T^{*}(j\omega) \right\|_{\infty} < \gamma \ , \quad \underset{\omega_B}{\text{minimize}} \left\{ 1 - \bar{\sigma}(T^{*}(j\omega)) \right\} < \varepsilon \ , \tag{6.30}$$

considering the unstructured uncertainty model $W_{\mathrm{p}}(s)$.

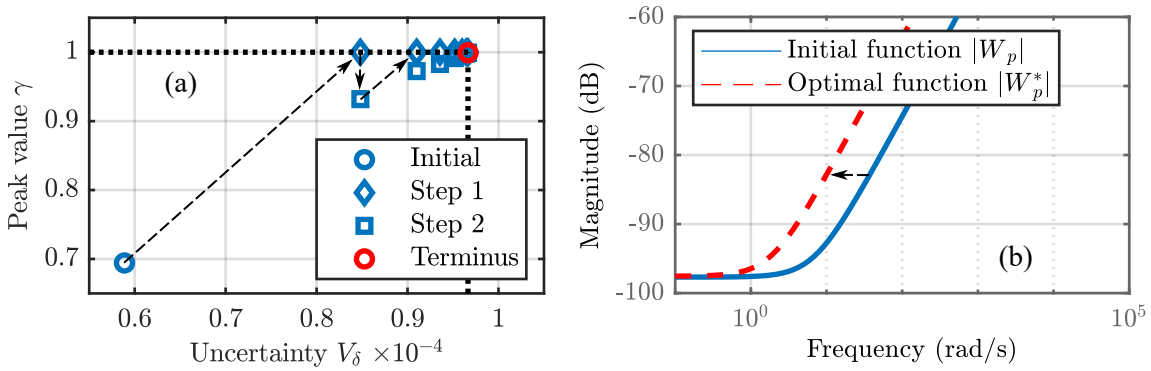

Figure 6.16 – Achieved robustness margin for different uncertainty ranges (a) and resulting perturbation shaping functions (b), applying Δ-K iteration: peak values γ for different fluid flow volumes to evaluate the maximal network subsection size and manipulating the inverse additive uncertainty to shape the perturbation signal.

In order to cope with the refined optimization problem (6.30), an iterative procedure is implemented, in terms of Assumption 6.1 and considering the peak value γ as a robust performance margin. The robust performance margin represents a worst case gain to the largest singular value. It is proposed to adjust the transfer function W_{p}, in terms of the robust performance margin, to synthesize an optimized structured PI controller K_{PI}^{*} that obtains $\gamma \approx 1$. Considering the inverse additive uncertainty W_{ia} and moving its pole $p = \omega_B$ with respect to $\omega_B \times \gamma$, will reduce the available robust performance margin by maximal -20 dB per decade. Recalling the Euclidean vector norm, a robust performance margin of maximal $\sqrt{2} = 3$ dB remains and the maximal singular value of the cost functions T^{*} will then attain $\gamma \to 1$.

Procedure for Δ-K iteration

This Δ-K iteration for transfer function adjustment and structured H_∞ controller synthesis follows a two step procedure to realize a quasi-optimal control design.

Initialization: obtain a first controller $\mathrm{K}_{PI}^{(0)}$ for an initial perturbed plant $\tilde{\mathrm{P}}^{(0)}$ by solving the optimization problem

$$\underset{\mathrm{K}_{PI}^{(0)}}{\text{minimize}} \left\| F_\ell \left(\tilde{\mathrm{P}}^{(0)}, \mathrm{K}_{PI} \right) \right\|_{\infty} \tag{6.31}$$

and applying the H_∞-norm to calculate the corresponding peak value

$$\gamma^{(0)} = \left\| F_\ell \left(\tilde{\mathrm{P}}^{(0)}, \mathrm{K}_{PI}^{(0)} \right) \right\|_{\infty} \ . \tag{6.32}$$

First step: update the perturbed plant

$$\tilde{\mathrm{P}}^{(i)} = F_u\left(\mathrm{M}, \Delta_{\mathrm{p}}^{(i)}\right) \tag{6.33}$$

for $\Delta_{\mathrm{p}}^{(i)} = W_{\mathrm{p}}^{(i)}\Delta$ by adjusting the shaping function

$$W_{\mathrm{p}}^{(i)}(s) = \frac{s/M + \omega_B^{(i)}}{s + \omega_B^{(i)} A} \ , \tag{6.34}$$

when moving its bandwidth

$$\omega_B^{(i)} = \omega_B^{(i-1)} \times \gamma^{(i-1)} \tag{6.35}$$

with respect to the previously obtained peak value $\gamma^{(i-1)}$.

Second step: obtain an enhanced controller $\mathrm{K}_{PI}^{(i)}$ for the updated perturbed plant $\tilde{\mathrm{P}}^{(i)}$ by solving the optimization problem

$$\underset{\mathrm{K}_{PI}^{(i)}}{\text{minimize}} \left\| F_\ell\left(\tilde{\mathrm{P}}^{(i)}, \mathrm{K}_{PI}\right)\right\|_\infty \tag{6.36}$$

and applying the H_∞-norm to calculate the corresponding peak value

$$\gamma^{(i)} = \left\| F_\ell\left(\tilde{\mathrm{P}}^{(i)}, \mathrm{K}_{PI}^{(i)}\right)\right\|_\infty \ . \tag{6.37}$$

Terminus: whenever $\gamma^{(i)} \approx 1$ with desired accuracy ε is reached, such as

$$\left|1 - \bar{\sigma}\left(F_\ell(\tilde{\mathrm{P}}^{(i)}, \mathrm{K}_{PI}^{(i)})\right)\right| < \varepsilon \tag{6.38}$$

a quasi-optimal PI controller is found ($\mathrm{K}_{PI}^{*} = \mathrm{K}_{PI}^{(i)}$) that guarantees stability and robust performance for an enhanced uncertainty range $\Delta_{\mathrm{p}}^{(i)}$. Otherwise repeat step 1 - 2.

Applying the Δ-K iteration to the generalized plant (6.19), the uncertain fluid volume V_δ will be increased to the largest volume possible, when adjusting the inverse additive uncertainty W_{ia} by means of the peak value γ. Repeating this procedure will iteratively cause $\gamma \to 1$ with a fast rate of convergence, see Table 6.3.

Table 6.3: Optimization for uncertain parameter V_δ: finding a maximal network subsection size for which γ-value remains below 1.

Iter.	K_P	K_I	τ_f	γ-value	$V_\delta \times 10^{-5}$
1	###	###	###	0.635388	5.8996
2	###	###	###	0.981341	9.2851
3	###	###	###	0.996083	9.4617
4	###	###	###	0.999159	9.4989
5	###	###	###	0.999803	9.5069
6	###	###	###	0.999961	9.5087
7	###	###	###	0.999994	9.5091

The **quasi-optimal extended PI controller**

$$\boxed{\tilde{\mathrm{K}}^*_{PI}(s) = \left(K_P + K_I \, \frac{1}{s}\right) \frac{1}{1 + \tau_f \; s}} \tag{6.39}$$

with $K_P = \#\#\#$, $K_I = \#\#\#$ and $\tau_f = \#\#\#$ seconds, respectively, the quasi-optimal lead controller

$$\tilde{\mathrm{K}}^*_{PI}(s) = \frac{\#\#\# s + \#\#\#}{\#\#\# s^2 + s} \tag{6.40}$$

has been found.

The singular values of Figure 6.17 show exemplarily the adjusted transfer function W^*_{p}, where the peak value of the overall cost functions for nominal performance and robust stability ($|W_e G_s G_n \mathcal{S} W_d| + |G_n \mathcal{S} W^*_{\mathrm{p}}|$) reaches $\gamma \approx 1$. Compare this to the initial cost functions of Figure 6.5, obtained before optimization.

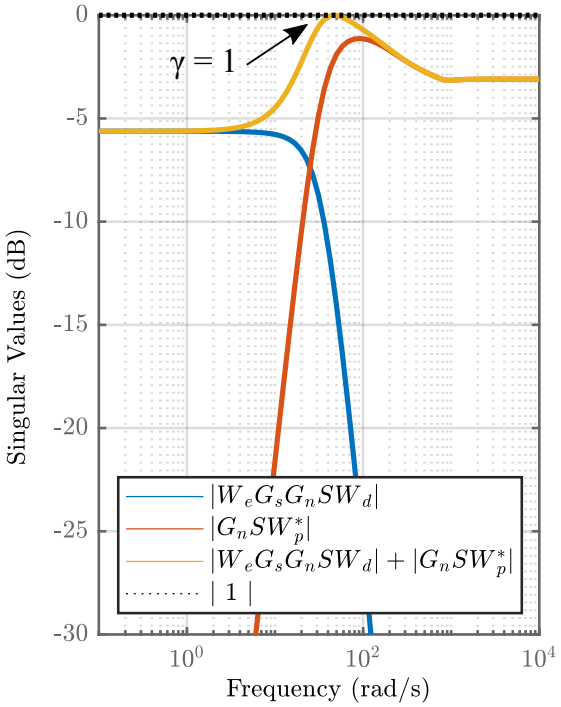

Figure 6.17 – Singular values of the nominal generalized plant with quasi-optimal robust PI controller $\tilde{\mathrm{K}}^*_{PI}$: evaluating for robust performance and stability with respect to the Euclidean vector norm.

Comparing the quasi-optimal PI controller to the state feedback controller

The frequency response of Figure 6.18 (a) compares the initial extended PI controller $\tilde{\mathrm{K}}_{PI}$ to the optimized PI controller $\tilde{\mathrm{K}}^*_{PI}$. For the open-loop system, an increased phase margin by reduced cross-over frequency is expected. This is confirmed when investigating the step responses given in Figure 6.18 (b). The settling time has deteriorated to $\tau_s = 0.1538$, while the overshoot has been slightly decreased. Nevertheless, the control objectives of Section 5.3 are still met. Table 6.4 summarizes the obtained closed-loop performance.

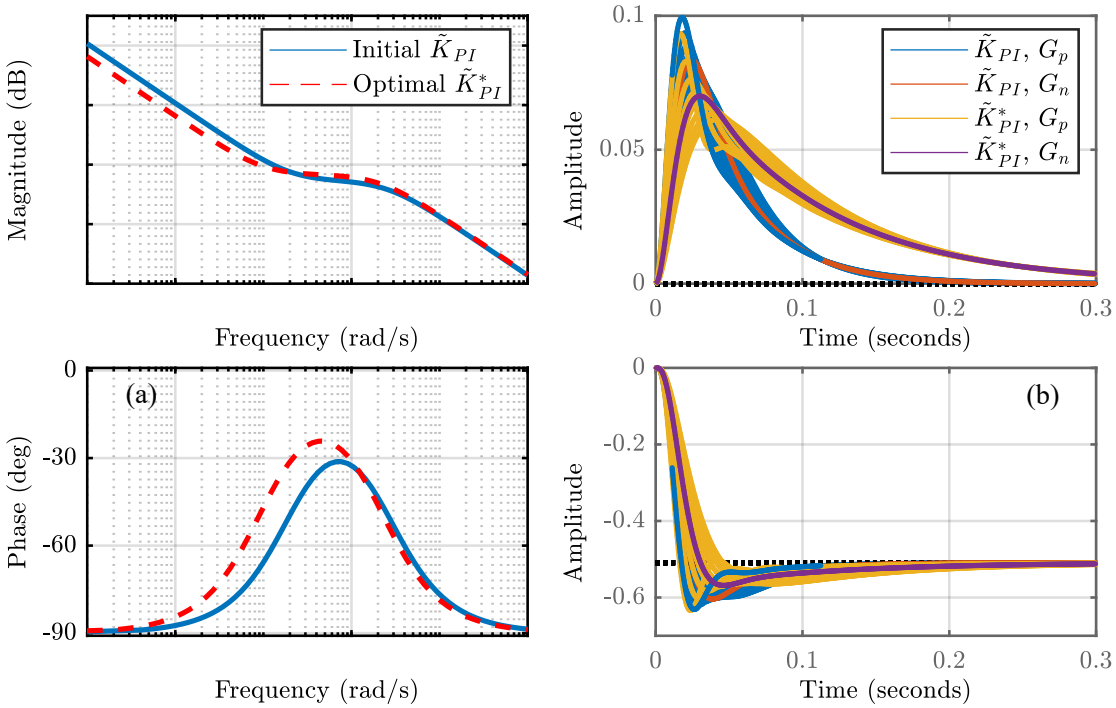

Figure 6.18 – Closed-loop frequency responses (a) and step responses (b) from $d \to y$: implementing extended PI controller $\tilde{K}_{PI}$ with low-pass filter and quasi-optimal robust PI controller $\tilde{K}^*_{PI}$, when optimizing for the reduced generalized plant (using joint shaping functions).

Table 6.4: Achieved performance for extended PI controller and quasi-optimal PI controller, both with low-pass filtering: comparing achieved closed-loop performance with control objectives for waterjet machining.

	$\tilde{K}_{PI}$		$\tilde{K}^*_{PI}$		Objective
	nom.	max.	nom.	max.	(Sect. 5.3)
Peak gain γ-value:	0.6354		**1.0**		≤ 1.0
Rise time (90% $r(t)$):	3.9144	3.9144	3.9144	3.9144	< 10
Settling time (2% $e(t)$):	0.1236	0.1318	0.1445	0.1538	< 0.5
Overshoot:	0.0753	0.0963	0.0700	0.0934	$< \pm 0.1$

This singular values, as shown in the plots of Figure 6.19, reach the bounds for performance (a) and control effort (b) by increasing the robustness for perturbations (c), when implementing the optimized controller. The bounds on robustness is still not fully exhausted. This gives a margin for stability. However, performance or control effort requires relaxation for further enhancing the robustness.

Finally, the resulting perturbation weight comes close to the initially defined upper bound, given by the control requirements, see the frequency response of Figure 6.20. A maximal fluid volume of about 95 cm^3 has been found by applying the proposed Δ-K iteration. This corresponds to an improvement of 61% in contrast to the initial fluid volume of 59 cm^3. The obtained extended and optimized PI controller enables robust performance and stability for a network subsection of increased size. It corresponds to a piping section of 120 m length.

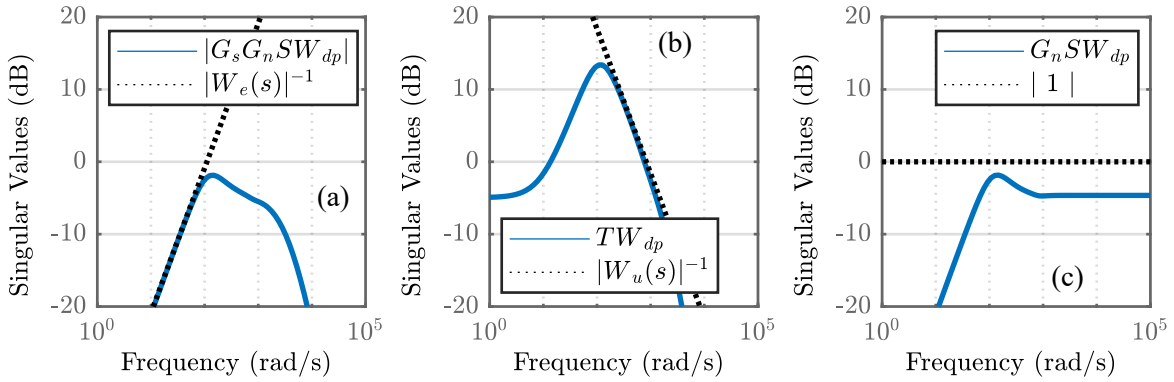

Figure 6.19 – Frequency responses of the nominal generalized plant with quasi-optimal robust PI controller $\tilde{K}^*_{PI}$, when considering joint shaping functions: evaluating robust performance (a), control effort (b) and stability (c).

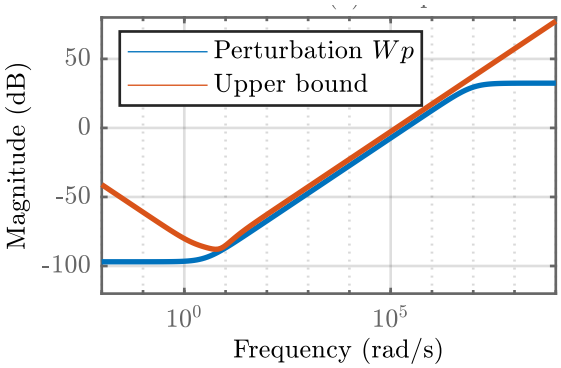

Figure 6.20 – Frequency responses of the weighting functions: dynamic range of the weighting on the perturbation signal and lower bound from control requirements.

It is recognized that a robust control design, considering all possible parameter variations, is limited to guarantee stability and performance for any plant configuration. But the varying fluid volume V_δ and the operating point x_δ can be measured to further reduce the uncertainty range. This would then require to design a robust gain-scheduling that improves the overall robustness.

6.3 Simulation studies

This section verifies the robust control design, when comparing the expected closed-loop performance given from the linearised plant model (5.116) with the achieved performance, by applying the control law to the non-linear simulation model. The simulation model is obtained, using the graph-based modelling methodology, as introduced in Section 3.3. This model is employed for control design verification. On the other hand, the linearised plant model, derived in Section 5.3 for control design, takes the expected parameter variations and non-linear behaviour into account in terms of a plant perturbation.

6.3.1 Low-level control design verification

The control design evaluation from the above section requires further verifications. The H_∞ controller synthesis, to derive unstructured state feedback controllers and structured PI controllers,

originate from a simplified and linearised plant. Even when taking all expected uncertainties into account, this perturbed plant for control design (5.116) remains a first order approximation, describing the pressure state of a network subsection by means of the lumped parameter model (5.23 - 5.23).

The linearisation, applied for control design, employs a disturbed input channel $u_d(t) = \Delta u(t) + \tilde{d}(t)$ (see Figure 5.13 in Section 5.3). This describes the perturbed plant for any deviation around operating points (u_0, x_0 and d_0), considering the dynamics from the control variable $\Delta u(t)$ to pressure state $\Delta \mathrm{x}(t)$ as well as from the exogenous disturbance $\Delta d(t)$ to the pressure state $\Delta \mathrm{x}(t)$. The exogenous disturbance is thereby scaled with respect to maximal parameter values (H_{max}, x_{max}), taking the maximal disturbance range into account for control design.

However, comparing the obtained performance and stability from control design (see Section 5.3) with numerical simulations from a non-linear simulation model, requires to apply a nominal disturbance step, while initializing both models to an operating point at equilibrium. Thus, the control design verification in this section considers nominal parameter values (H_{nom}, x_{nom}) applied on the exogenous disturbance $\Delta d(t)$, as depicted in Figure 6.21. This nominal disturbance step requires to configure the fluid flow resistance

$$H_{nom} = S_{nom}\ \zeta\ \sqrt{\frac{2}{\varrho_{nom}}} = \#\#\# \tag{6.41}$$

with a nominal nozzle surface $S_{nom} = 0.0625$ mm^2, the nozzle discharge coefficient $\zeta = \#\#\#$ and a nominal fluid density $\varrho_{nom} = 1.0705$ kg/dm^3, as expected for an operating pressure of $\mathrm{x}_{nom} = 200.5$ MPa, and the disturbance (5.54) becomes

$$\tilde{d}(t) = H_{nom}\sqrt{\mathrm{x}_{nom}}\ \Delta d(t)\ . \tag{6.42}$$

This resulting disturbance of nominal amplitude is then applied for both models, considering control design and numerical simulations.

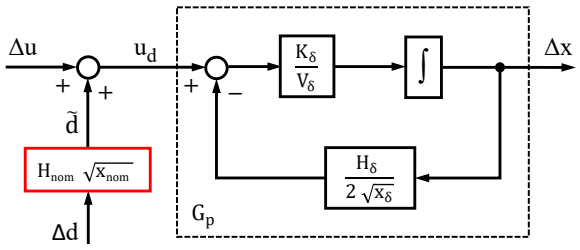

Figure 6.21 – Approximated plant model: block diagram of the simplified approximated model in state space form with exogenous disturbance of nominal amplitude.

All parameter variations within the disturbed plant G_p, as denoted by the subscript δ, follow the previously reported characteristics. The adjusted parameter variations, used for control design verification, are given in Table 6.5. They can be compared with the initial parametrization of Table 5.3, used for control design.

Simulation model

To verify the derived performance and stability from controller synthesis with the linearised plant, the closed-loop system is numerically simulated for its nominal values, considering a detailed non-linear simulation model. This simulation model is based on the graph-based modelling

Table 6.5: Uncertainty range of varying parameters, where the arithmetic mean value is considered for nominal parameter values.

			Nominal value	Min value	Max value
Flow resistance	H_δ	$\times 10^{\#\#\#}$	###	0	###
Fluid volume	V_δ	(cm^3)	48.28	15.87	80.69
Bulk modulus	K_δ	(GPa)	###	###	###
Operating point	x_δ	(MPa)	200.5	1	400

methodology, see Section 3.3. It employs a high-pressure network, interconnecting a high-pressure pump to two cutting heads, as shown in the diagram of Figure 6.22. This results in a simulation model of order 35.

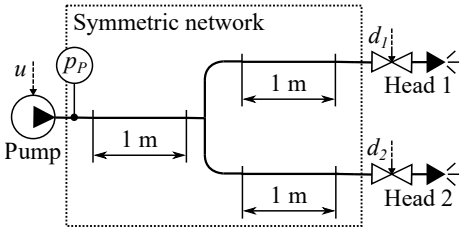

Figure 6.22 – High-pressure network topology used for control design verification: single pump interconnected to two cutting heads with identical nozzles.

The control variable $u(t)$ and process variable $y(t) = p_P(t)$ are simulated, applying the derived unstructured state feedback controllers and structured PI controllers. These simulations provide valuable results to verify the control design of Section 6.2.

The corresponding graph network is depicted in the diagram of Figure 6.23. Each network section represents a piping of about 1 m length, which is divided into 10 segments for numerical simulations. Table 6.6 provides the network parametrization, derived from measurements (see Section 2.2).

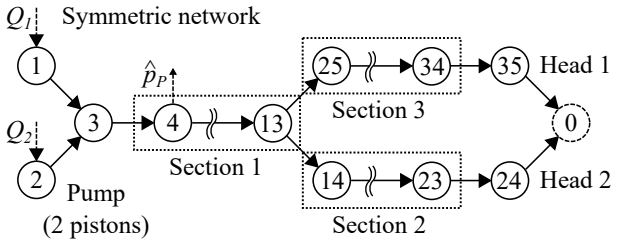

Figure 6.23 – Corresponding graph network of the above network topologies used for numerical simulations: single pump interconnected to two cutting heads, considering a symmetric network topology.

The control design verification is eventually realized for different operating pressures $r = \{100, 200, 300, 400\}$ MPa, using the configuration of Table 6.7. Basically, both cutting heads were configured with the same nozzle of nominal inner diameter. If only one nozzle is open, the system dynamics is expected to correspond to the nominal plant. The second nozzle is then

opened to apply an additional disturbance of nominal amplitude. This will affect the system dynamics, to move apart from nominal behaviour. Consequently, it is not possible to hold the system about nominal parameters, while instantaneously applying a disturbance.

Table 6.6: Model parameters used for numerical simulations, subject of control design verification.

Section	Section length L	Number of segments n	Segment length ΔL	Discharge coefficient ζ
1, 2, 3	0.91 m	10	0.091 m	###

Table 6.7: Considered use cases used for numerical simulations, subject of control design verification.

Topology	Pressure (MPa)	Control effort (-)	Nozzle 1 ⌀(mm)	Nozzle 2 ⌀(mm)	Switching pattern
Sym. net.	100	0.439	0.2821	0.2821 mm	Contour
	200	0.609			
	300	0.744			
	400	0.839			

The linearised plant, used for control design, represents the transient behaviour around its operating point. Thus, the process variable y from numerical simulation is scaled with respect to the operating point $y_{nom} = r$ to obtain $\Delta y = (y - y_{nom})R_r$. In the same manner, the control variable u from simulations is scaled to obtain $\Delta u = u - u_{nom}$, with a nominal control value $u_{nom} = \{0.439, 0.609, 0.744, 0.839\}$, depending on the operating pressure r. This allows for comparing the results from control design with the numerical simulations. The applied control value u has been further scaled by means of camming, see Section 2.3. The scaled control value $u_g = u/R_u$ corresponds to the resulting pump fluid flow of a high-pressure pump.

6.3.2 Evaluating structured and unstructured feedback controllers

The suboptimal PI controller K_{PI}, the quasi-optimal PI controller with low-pass filtering $\tilde{\mathrm{K}}^*_{PI}$ and the reduced suboptimal state feedback controller $\tilde{\mathrm{K}}_{SF}$ will be implemented to the above non-linear simulation model for closed-loop simulations, when applying a disturbance step of nominal value. Cutting head 1 will thereby remain open for all time, while alternately switching cutting head 2 between open and close position. A set of nominal step responses results from the time-varying parameters, such as the fluid volume in a pumping chamber that varies due to piston displacement and the bulk modulus that varies with respect to the operating point. This set is then compared to the upper and lower bounds, as expected from H_∞ controller synthesis when assuming plant perturbations. The results summarized in Table 6.8, compare the expected settling times and overshoots from control design (see Section 6.2) with the obtained values from numerical simulations. In general, an excessive settling time and overshoot is observed for simulations at low pressures.

Table 6.8: Achieved performance by means of detailed numerical simulations for different control structures: comparing achieved closed-loop performance from simulation with results from control design, using simplified and linearised model.

		Ctr. design	Verification (Simulations)				Objective
	Pressure (MPa)	40 ... 400	100	200	300	400	(Sect. 5.3)
K_{PI}	max. settling time:	0.1217	0.3960	0.2470	0.2200	0.1970	< 0.5
	max. overshoot:	**0.1492**	**0.1319**	0.0989	0.0825	0.0773	$< \pm 0.1$
$\tilde{\mathrm{K}}^{*}_{PI}$	max. settling time:	0.1538	0.1370	0.0970	0.0760	0.0700	< 0.5
	max. overshoot:	0.0934	0.0603	0.0567	0.0493	0.0460	$< \pm 0.1$
$\tilde{\mathrm{K}}_{SF}$	max. settling time:	0.1368	0.1160	0.0900	0.0780	0.0670	< 0.5
	max. overshoot:	0.0927	0.0710	0.0652	0.0568	0.0509	$< \pm 0.1$

Suboptimal PI controller $\mathrm{K}_{\mathbf{PI}}$

An excellent match is obtained by applying the initial robust PI controller (6.22) on the detailed simulation model. The plots of Figure 6.24 - 6.27 compare the expected nominal step responses from controller synthesis with the linearised plant and the set of quasi-nominal responses from numerical simulations at 100, 200, 300 and 400 MPa operating pressures. It shows the scaled pressure differences Δy around the operating point and the corresponding control signals Δu. The observed variations stay within expected upper and lower bounds derived from control design. It is recognized that the disturbance is rejected with expected settling time and overshoot. For the 100 and 200 MPa case, the detailed simulations reveal slightly degradation of the settling time. This results, particularly for the 100 MPa case, into an increased overshoot. The nominal response remains within expected bounds.

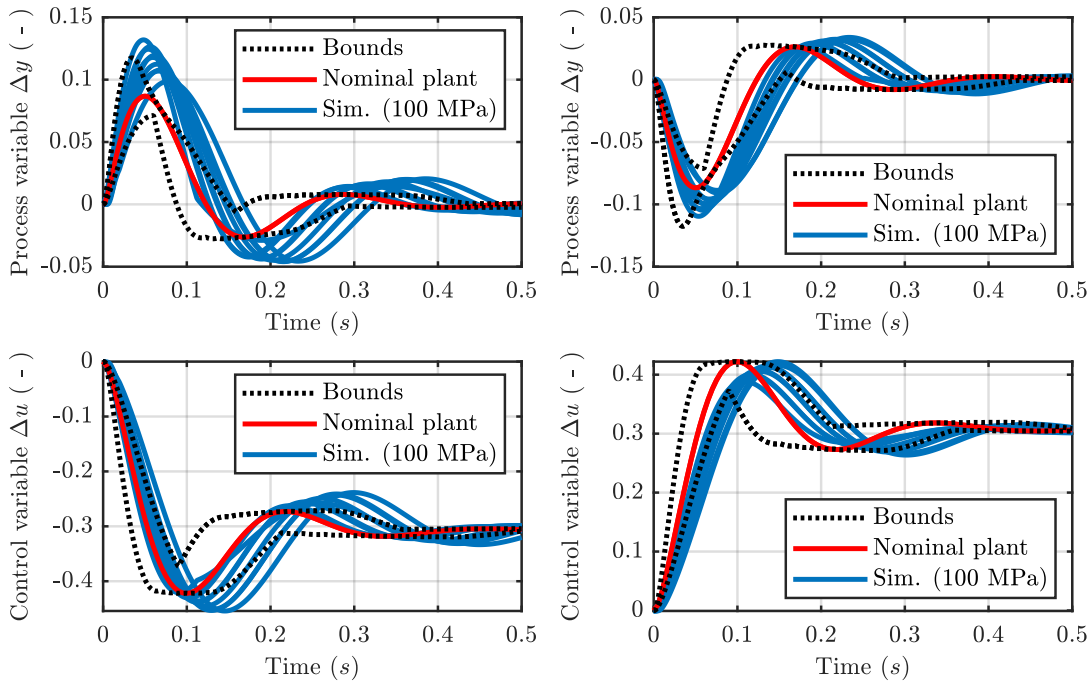

Figure 6.24 – Step responses of robust PI controller at 100 MPa operating point, when opening (a) and closing (b) a cutting head: nominal plant, expected upper and lower bounds from control design compared to resulting step responses from numerical simulations, using non-linear model.

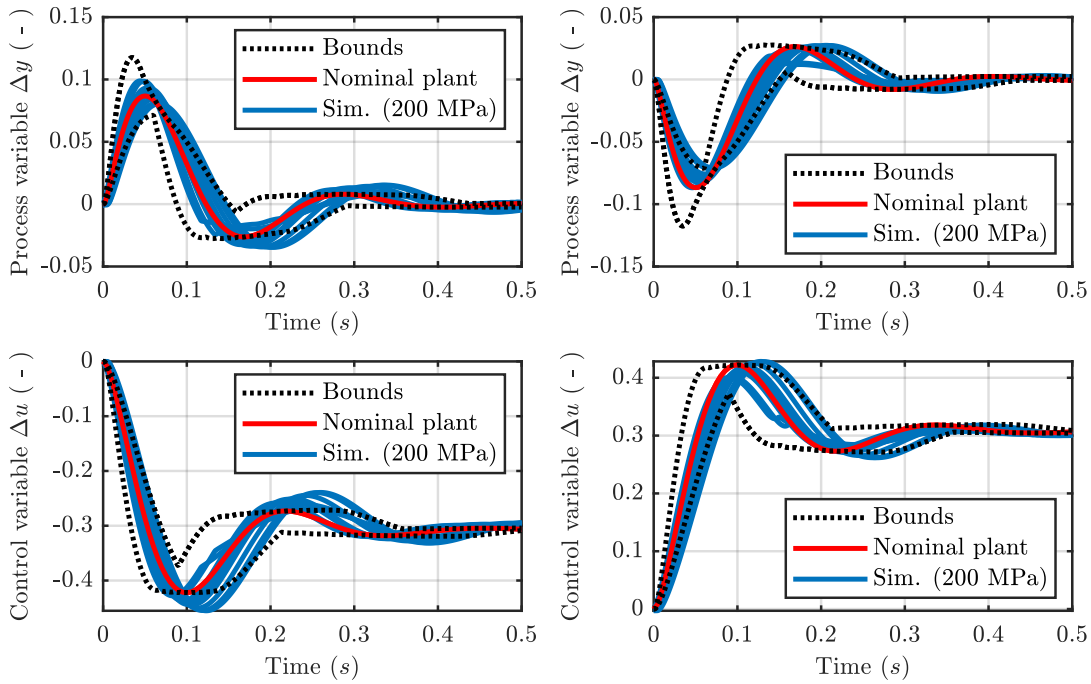

Figure 6.25 – Step responses of robust PI controller at 200 MPa operating point, when opening (a) and closing (b) a cutting head: nominal plant, upper and lower bounds from control design compared to resulting step responses from numerical simulations, using non-linear model.

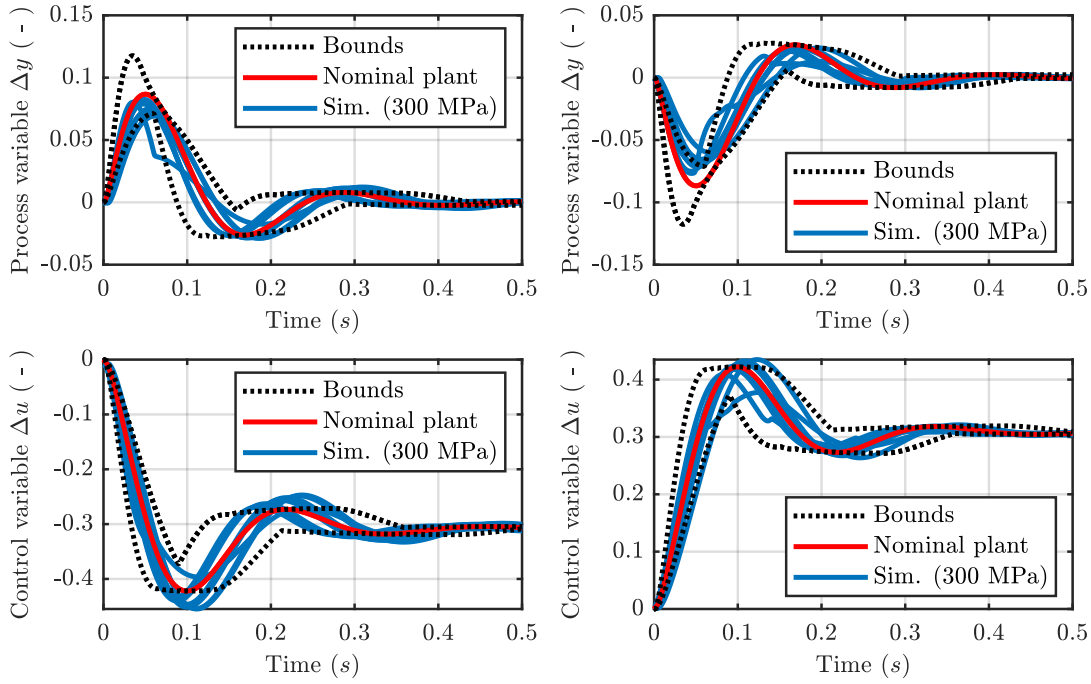

Figure 6.26 – Step responses of robust PI controller at 300 MPa operating point, when opening (a) and closing (b) a cutting head: nominal plant, upper and lower bounds from control design compared to resulting step responses from numerical simulations, using non-linear model.

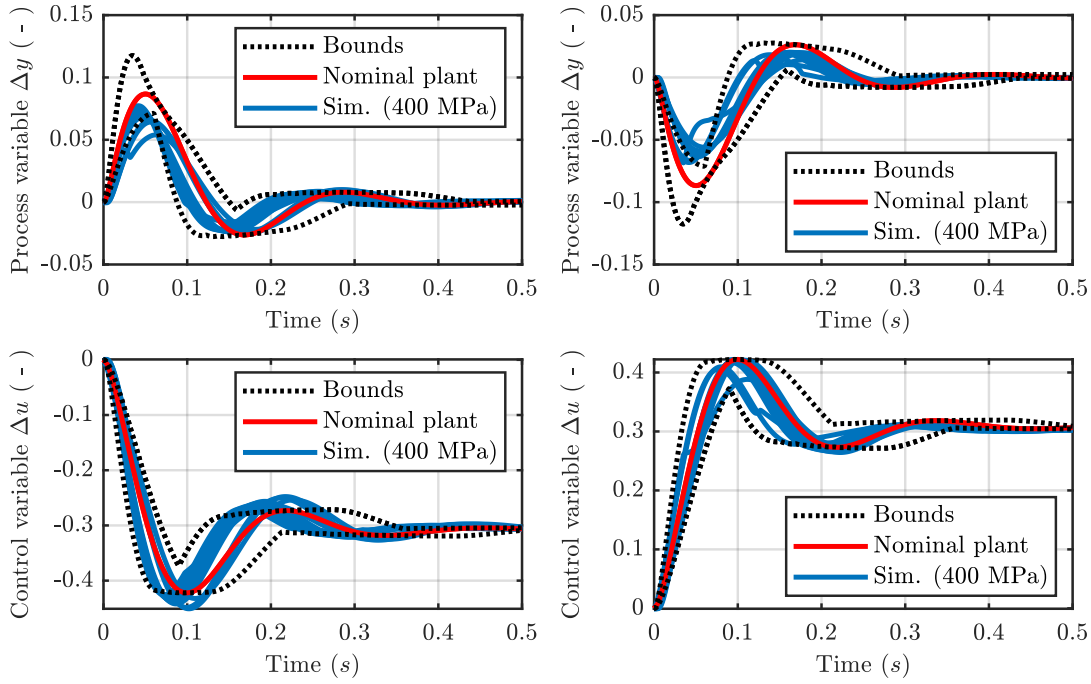

Figure 6.27 – Step responses of robust PI controller at 400 MPa operating point, when opening (a) and closing (b) a cutting head: nominal plant, upper and lower bounds from control design compared to resulting step responses from numerical simulations, using non-linear model.

Extended and quasi-optimal PI controller $\tilde{K}^*_{PI}$

An excellent match is obtained, applying the extended quasi-optimal PI controller (6.39) on the detailed simulation model. The plots of Figure 6.28 - 6.31 compare the expected nominal step response from controller synthesis with the linearised plant and the set of quasi-nominal responses from numerical simulations at 100, 200, 300 and 400 MPa operating pressures. Again, it shows the scaled pressure differences Δy around the operating point and the corresponding control signals Δu. The observed variations stay within expected upper and lower bounds derived from control design. It is recognized that any disturbance is rejected with expected settling time and overshoot. For the 100 MPa case, the detailed simulations reveal a slight degradation of the settling time, which results in an increased overshoot. The nominal response remains within expected bounds.

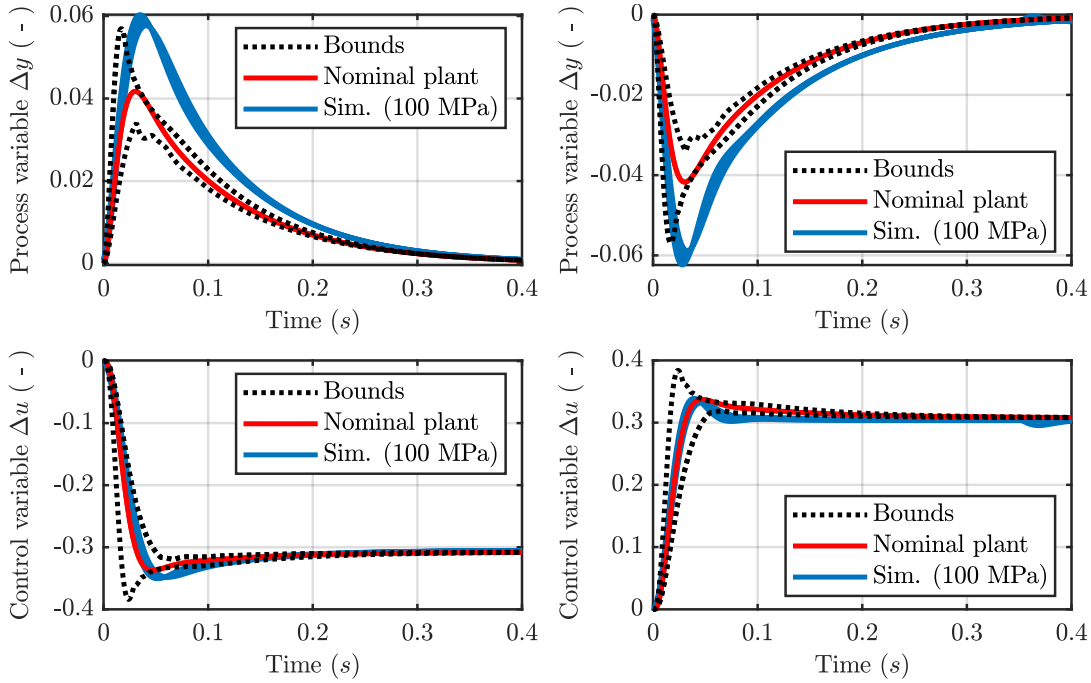

Figure 6.28 – Step responses of extended quasi-optimal PI controller at 100 MPa, when opening (a) and closing (b) a cutting head: nominal plant, upper and lower bounds from control design compared to step responses from numerical simulations, using non-linear model.

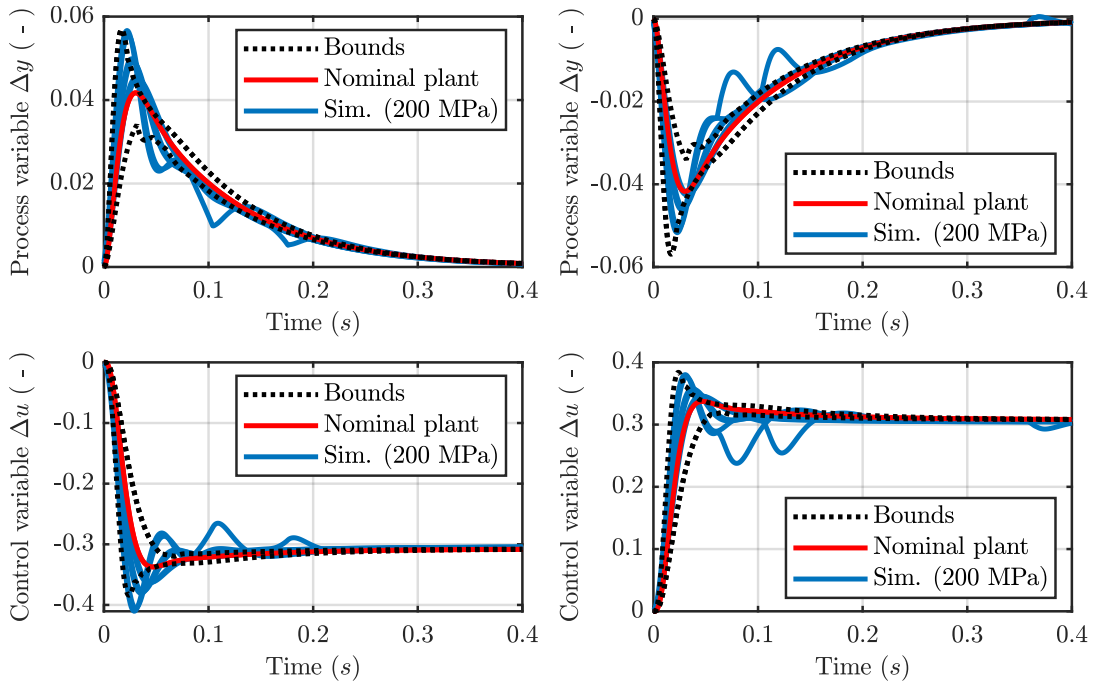

Figure 6.29 – Step responses of extended quasi-optimal PI controller at 200 MPa, when opening (a) and closing (b) a cutting head: nominal plant, upper and lower bounds from control design compared to step responses from numerical simulations, using non-linear model.

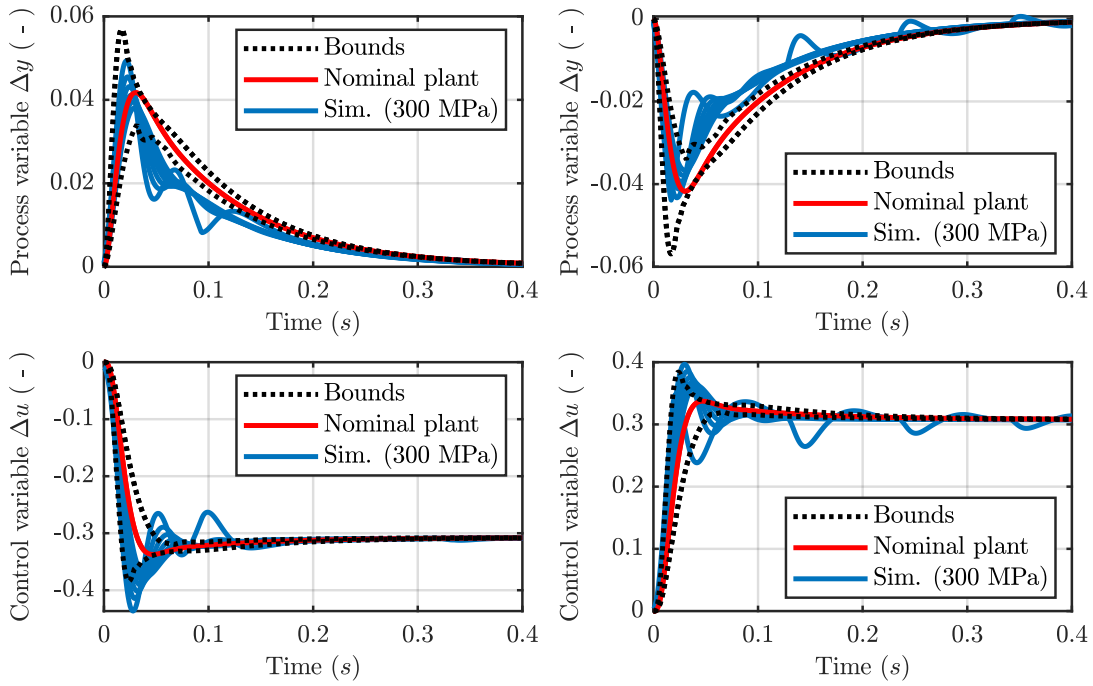

Figure 6.30 – Step responses of extended quasi-optimal PI controller at 300 MPa, when opening (a) and closing (b) a cutting head: nominal plant, upper and lower bounds from control design compared to step responses from numerical simulations, using non-linear model.

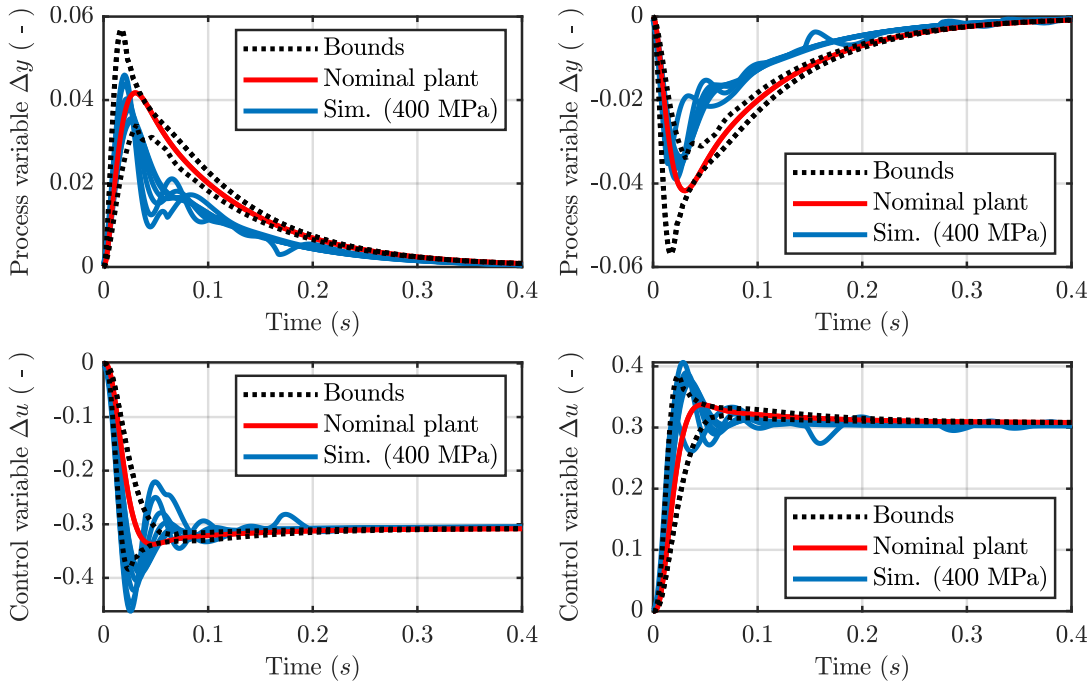

Figure 6.31 – Step responses of extended quasi-optimal PI controller at 400 MPa, when opening (a) and closing (b) a cutting head: nominal plant, upper and lower bounds from control design compared to step responses from numerical simulations, using non-linear model.

Reduced suboptimal state feedback controller $\tilde{K}_{SF}$

Also an excellent match is obtained, applying the reduced state feedback controller, derived from (6.20), on the detailed simulation model. The plots of Figure 6.32 - 6.35 compare the expected nominal step response from the controller synthesis with the linearised plant and the set of quasi-nominal responses from numerical simulations at 100, 200, 300 and 400 MPa operating pressures. It shows the scaled pressure differences Δy around the operating point and the corresponding control signals Δu. The observed variations stay within expected upper and lower bounds of the nominal plant derived from control design. It is further recognized that any disturbance is rejected with expected settling time and overshoot. For the 100 and 200 MPa case, the detailed simulations reveal degradation of the settling time, which results into an increased overshoot. The decreased performance is tremendous for the 100 MPa case. The nominal response remains within expected bounds.

The 400 MPa operating point holds a bulk modulus of 3.96 GPa, whereas 2.55 GPa results for 100 MPa. The overall volume for the detailed simulation model varies between 40-80 cm^3 and the flow resistance $H = \{0, \#\#\#, \#\#\#\}\ 10^{\#\#\#}$ changes with respect to the cutting head switching state. Regarding the above simulation results considering these parameter variations, robust stability and nominal performance is obtained, even though the controller has been derived using a strongly simplified model. The next section will present experimental results derived from the test bench with a high-pressure pump in closed-loop control, considering the initial robust PI controller without low-pass filtering.

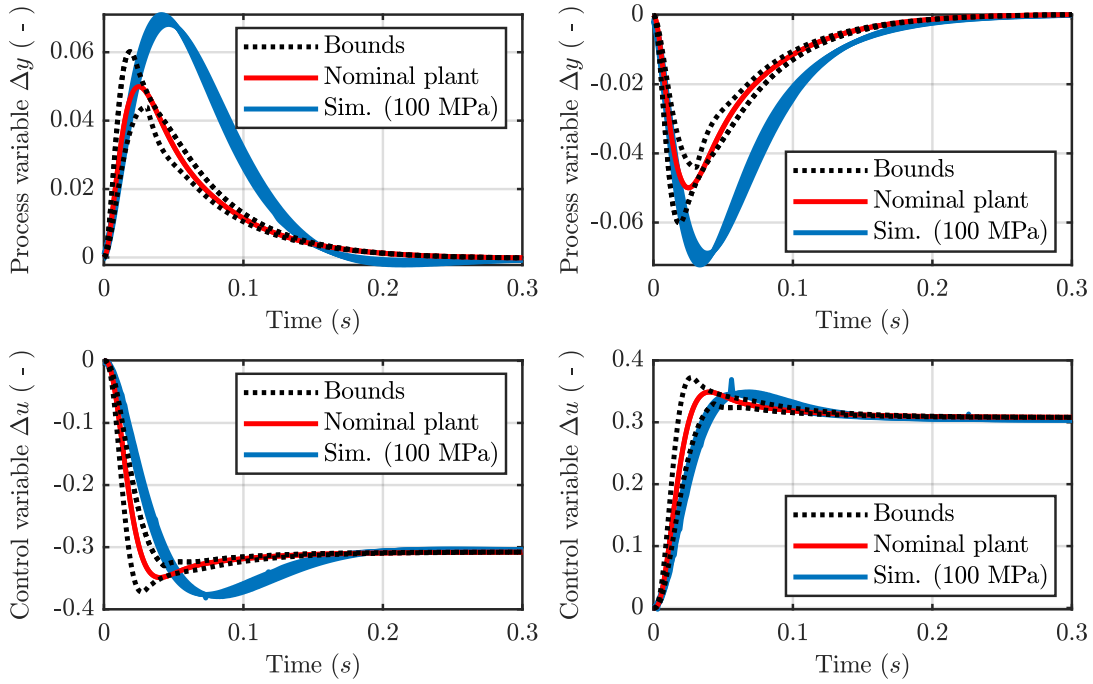

Figure 6.32 – Step responses of optimized state feedback controller at 100 MPa, when opening (a) and closing (b) a cutting head: nominal plant, upper and lower bounds from control design compared to step responses from numerical simulations, using non-linear model.

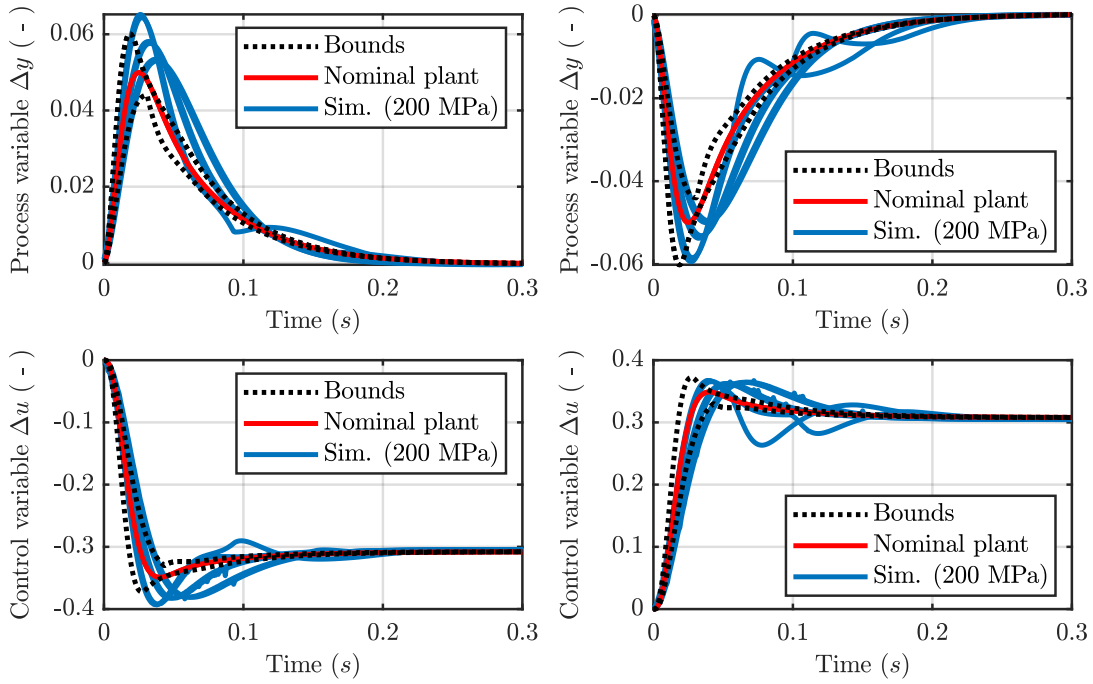

Figure 6.33 – Step responses of optimized state feedback controller at 200 MPa, when opening (a) and closing (b) a cutting head: nominal plant, upper and lower bounds from control design compared to step responses from numerical simulations, using non-linear model.

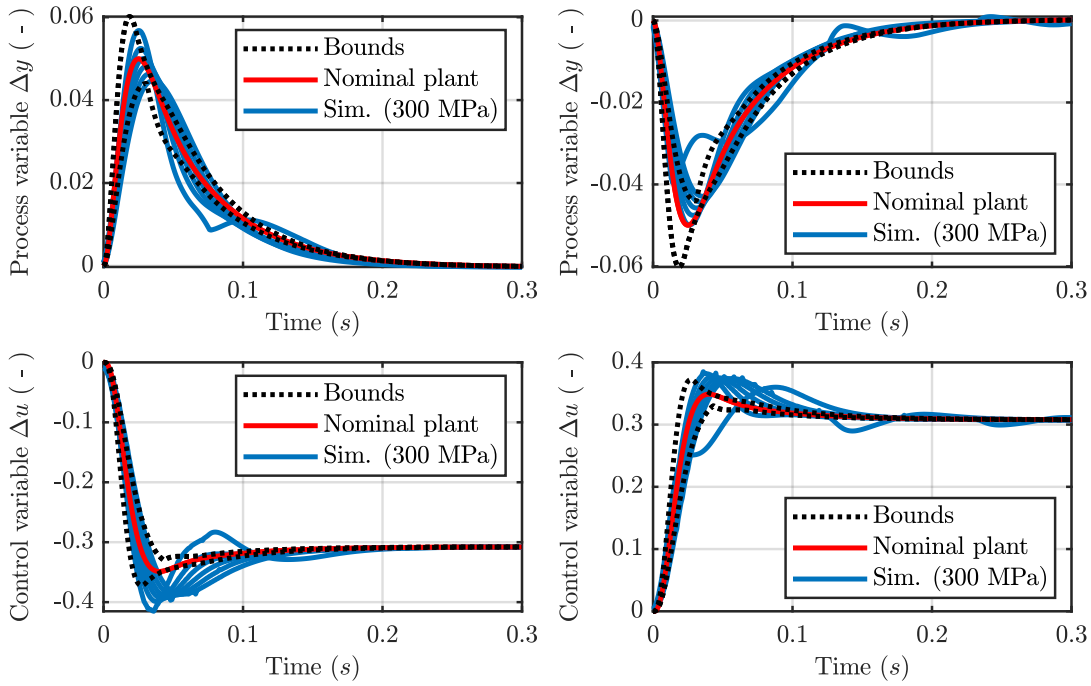

Figure 6.34 – Step responses of optimized state feedback controller at 300 MPa, when opening (a) and closing (b) a cutting head: nominal plant, upper and lower bounds from control design compared to step responses from numerical simulations, using non-linear model.

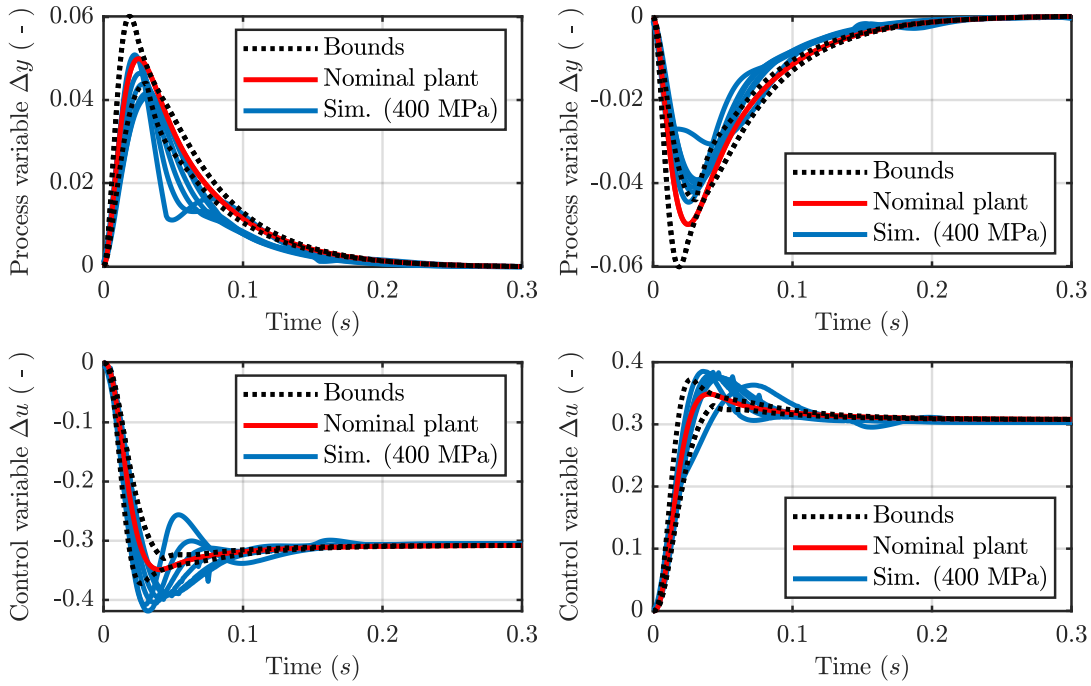

Figure 6.35 – Step responses of optimized state feedback controller at 400 MPa, when opening (a) and closing (b) a cutting head: nominal plant, upper and lower bounds from control design compared to step responses from numerical simulations, using non-linear model.

6.4 Experimental studies

This section validates an initial PI controller, using measurements from the test bench, as introduced in Section 2.2 and comparing them with detailed simulations. For this, the robust PI controller (6.22) has been implemented on a high-pressure pump. Several high-pressure network topologies will be compared, as defined in Section 4.2, considering single pump setups with 2 cutting heads and multi pump setups of 2 pumps connected to 2 cutting heads.

All experiments have been derived for two operating points, each taking the switching pattern for contour cutting into account. A cutting head will open for a cutting period of 60 seconds, followed by a hold period in closed position for another 60 seconds. This switching pattern is periodically repeated for both cutting heads with a 90° phase shift, see Section 2.2 for details. The diagram of Figure 6.36 illustrates the experimental setup, as implemented for controller validation. The cutting heads open and close with respect to the predefined switching pattern, as given by the disturbance signal $d(t) = [d_1(t), d_2(t)]$. The pressure controller will then adjust the pump rate, using the control signal $u(t)$, to obtain the desired reference pressure. The reference value $r(t)$ and disturbance $d(t)$ are measured to excite the extended high-pressure network models, for closed-loop simulation. This extended model considers the high-pressure pump, a network model and the low-level pressure controller in closed-loop. The pump output pressure $p_P(t)$ as well as the pump rate $u(t)$ will be compared with simulated values ($\hat{p}_P(t)$ and $\hat{u}(t)$) to validate the PI controller. The measurement data have been captured with a sampling rate of 500 Hz.

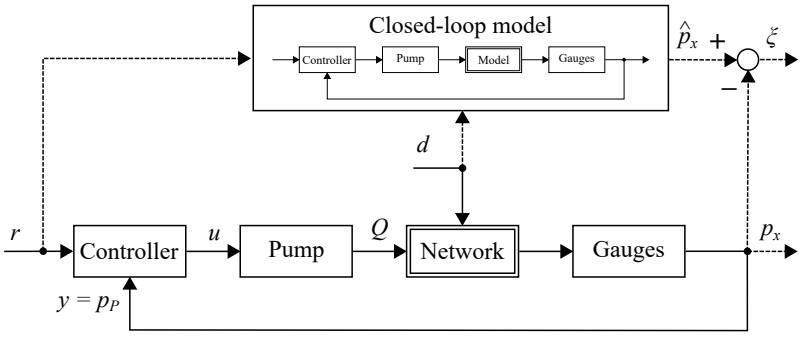

Figure 6.36 – Experimental setup for controller validation: pressure gauges measure the pressure $p_x(t)$ at different positions, the input fluid flows $Q(t)$ vary with respect to the switching disturbance $d(t)$. Reference pressure $r(t)$ and disturbance $d(t)$ are used as the model inputs. The estimated pressures $\hat{p}_x(t)$ have been compared to the measured pressures.

The controller parametrization and test bench setup of this section, correspond to the model validation already used in Chapter 4. It is important to mention, that the controller implementation on the test bench does not correspond to the desired robust control design from Section 6.2. The closed-loop experiments on the test bench have been derived with the obtained controller from robust control design, but implementing a faulty controller scaling ψ^f to the PLC. This provides controller parameters different from the desired robust control design.

The controller scaling results from the model-based trajectories for displacing the pistons such as to synchronize the pumping units. These trajectories are shifted to obtain a specific pressurization with respect to the desired operating pressure, see Section 2.3. The remaining cycle time is then available for hauling and filling with respect to the conditions (2.18 - 2.22). Recalling the concept of camming, a varying operating pressure $p(t)$ requires a change of the trajectory, represented in terms of a function $\mathcal{F}(p)$, and results in a different induced overall

fluid flow (2.15)

$$Q_{Pn}(t) \sim \frac{d}{dt}\mathcal{F}\left(\phi(t)\right) \tag{6.43}$$

for a given camming angle $\phi(t)$. Since the controller manipulates the camming angle velocity $d\phi(t)/dt \sim u(t)$, the control value $u(t)$ requires a scaling with respect to compensate the change of function $\mathcal{F}(p)$. The scaling

$$\psi(p) = \frac{d}{dt}Q(t)\left(\frac{d}{dt}\phi(t)\right)^{-1} = \frac{dQ}{d\phi} \tag{6.44}$$

is thus defined by the resulting trajectory, where any change of the camming angle $d\phi(t)/dt$ follows a change of the fluid flow $dQ(t)/dt$. Compensating this change by introducing the corresponding scaling (6.44) to (6.43), such as $d\phi(t)/dt = u(t)\psi(p)$, yields

$$Q_{Pn}(t) \sim \mathcal{F}\left(u(t)\psi(p)\right) \tag{6.45}$$

and the closed loop gain remains unchanged for every operating pressure that the obtained control law becomes properly applied to each pumping unit.

Typical PI behaviour can be observed from measurements, where ab excessive characteristics occurs, such as an increased overshoot and settling time. This relates to all closed-loop experiments presented in this section. Eventually reproducing the faulty controller scaling by means of simulation, results in step responses, which correspond to the measurement data. At least, these experiments allow the validation of different high-pressure network models in closed-loop, which have been used to verify the robust control designs. Due to a defect of the high-pressure pump, it has not been possible to repeat the experiments with correct controller scaling, hence the investigations for robust stability and robust performance remain limited to simulation studies.

6.4.1 PI controller application and validation (1 pump configuration)

This experimental study applies the initial robust PI controller (6.22), as derived in Section 6.2, to a single high-pressure pump. Deriving a robust controller, the expected disturbance of maximum amplitude and the entire uncertainty range has been taken into account, while applying the structured H_∞ synthesis. Considering the faulty scaling ψ^f, used for implementation on the high-pressure pump, and recovering the controller parameters, yields

$$\mathrm{K}_{PI}^f(s) = \mathrm{K}_{PI}(s)\frac{\psi}{\psi^f} = \#\#\# + \#\#\#\ \frac{1}{s}\ , \tag{6.46}$$

which has been effectively applied to the high-pressure pump. It is different from the desired robust PI controller $\mathrm{K}_{PI}(s)$ and consequently does not achieve expected performance.

To verify performance and stability of the implemented PI controller (6.46), the high-pressure test bench has been configured to a symmetric and asymmetric network topology. For both topologies, **(c) Symmetric network** and **(d) Asymmetric network**, a single high-pressure pump is supplying two cutting heads. The cutting heads switch alternately open and close. The symmetric topology considers nozzles of different inner diameters, allowing for investigating the effects of asymmetric cutting head configurations. The asymmetric topology takes nozzles of identical diameters into account, hence the effect of different piping sections lengths can be observed. This aims at disturbance rejection due to switching cutting heads, while holding a constant reference pressure of either 200 or 350 MPa.

Different measurements have been derived for simulation and experimental validation, as listed in Table 6.9. The 2 extended measurements (**E-4** and **E-7**) consider the symmetric network topology, where both cutting heads have been asymmetrically configured with nozzles of different inner diameter. The other 2 extended measurements (**E-9** and **E-11**) consider the asymmetric network topology, while both cutting heads have been symmetrically configured with identical nozzles. This section provides an overview, plots extending these results are given in Appendix B.1.

Table 6.9: Excerpt of experiments for use case 2: measurements derived with different test bench setups and used for controller validation.

Meas.	Topology	Pressure (MPa)	Nozzle 1 ⌀(mm)	Nozzle 2 ⌀(mm)	Switching pattern	
E-4	(c) Sym. net.	200	0.3	0.2	Contour (1-4) Contour (5-8)	(Appendix B.1)
E-7		350	0.2	0.1	Contour (1-4) Contour (5-8)	(Appendix B.1)
E-9	(d) Asym. net.	200	0.25	0.25	Contour (1-4) Contour (5-8)	(Appendix B.1)
E-11		350	0.15	0.15	Contour (1-4) Contour (5-8)	(Appendix B.1)

Applying the graph-based modelling methodology, according to the test bench configuration, results in different high-pressure network models. These models have been already introduced and experimentally validated in Chapter 4 by means of excessive measurements and simulations.

Contour cutting: asymmetric and symmetric cutting heads

Measurements have been obtained and compared to simulations for the 200 MPa and 350 MPa operating points. Disturbance steps have been applied on the test bench, when switching the cutting heads open and close. Considering the experiments E-4 and E-7, the alternately switching of two cutting heads results in 4 possible pump rates. That correspond to different fluid flow consumptions, since both cutting heads hold nozzles of different inner diameters. Consequently, 8 transitions have been obtained with respect to the cutting head switching. Also considering the experiments E-9 and E-11, the switching results in 4 possible pump rates. This causes different fluid flow consumption, as the piping sections to the cutting heads are of different length. For the subsequent investigations, these 8 transitions are realised by applying two alternative switching patterns, see also Section 2.2. The switching patterns on disturbance $d = [d_1, d_2]$, the measured pump rates $u = [u_1, u_2]$ and the measured pump output pressures $p_P = [p_{P1}, p_{P2}]$ are shown in the plots of Figures 6.37 and 6.38. These plots overview the experiments E-4 and E-9, representing the asymmetric and symmetric cutting heads at 200 MPa. The plots for the inverse 4 transitions as well as the complementary experiments for controller validation at 350 MPa (E-7 and E-11) are provided in the Appendix B.1. The switching patterns are repeated 5 times to cover different parameter variations, that occur during continuous pump operation.

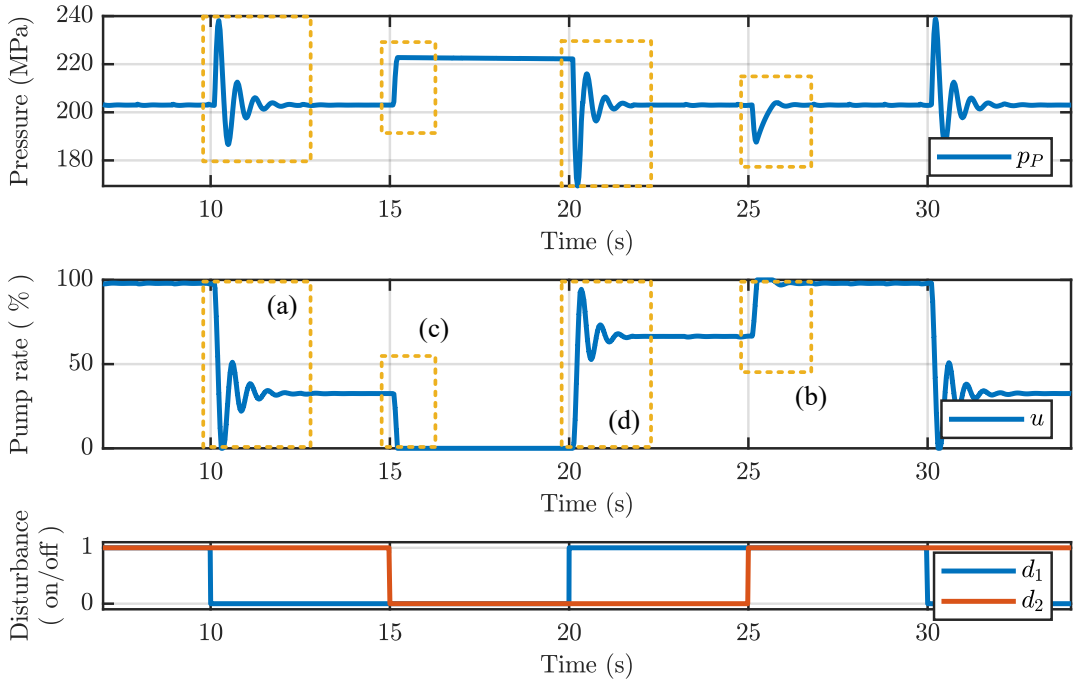

Figure 6.37 – Switching pattern considering 4 transitions for 200 MPa operating pressure of experiment E-4: desired switching states resulting in different pump rates for disturbance rejection by means of control.

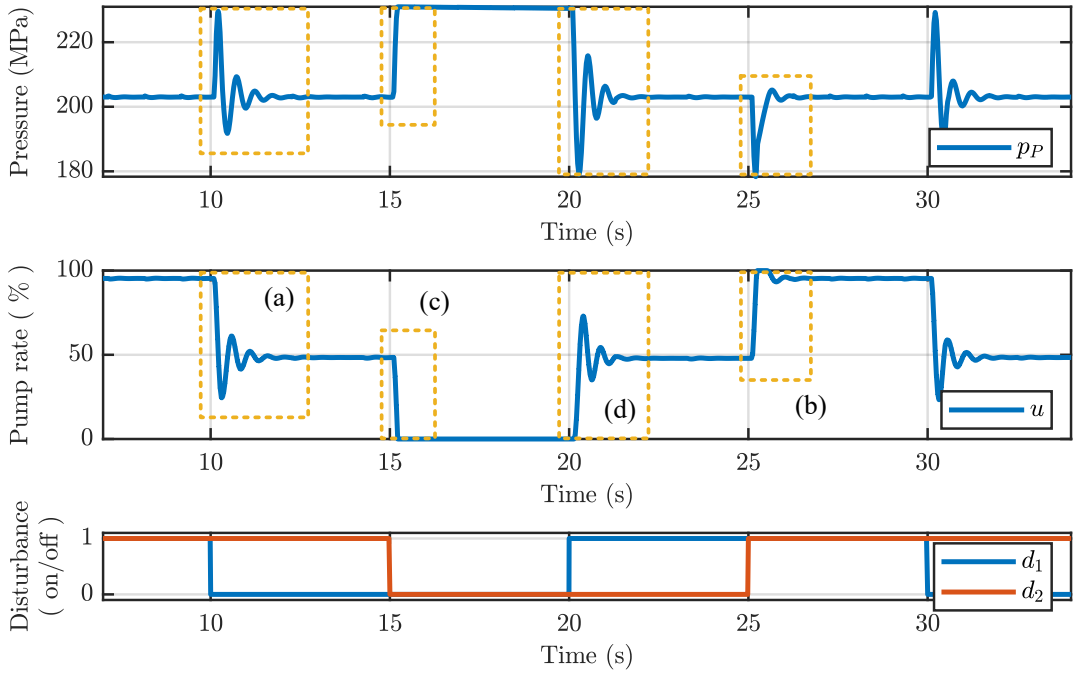

Figure 6.38 – Switching pattern considering 4 transitions for 200 MPa operating pressure of experiment E-9: desired switching states resulting in different pump rates for disturbance rejection by means of control.

The zoomed-in plots of Figure 6.39 compare measurements ($p_P(t)$, $u(t)$) and simulations ($\hat{p}_P(t)$, $\hat{u}(t)$) for each switching state of experiment E-4. The transitions (a) and (b) present the closing and opening of cutting head 1, where the transitions (c) and (d) show the closing and opening of cutting head 2. Investigating transition (b) and (c), the pump reaches upper and lower saturation, respectively. For the first case, cutting head 1 stays open and cutting head 2 switches in open position, causing an increased fluid flow consumption. The high-pressure pump is not capable for instantaneously compensating the resulting pressure loss. For the second case, cutting head 1 stays close and cutting head 2 switches in close position, causing any fluid flow consumption to disappear. The pump is not able to diminish the pressure overshoot, since only positive fluid flows can be induced. On the other hand, the zoomed-in plots of Figure 6.40 compare measurements and simulations for each switching state of experiment E-9, where similar behaviour has been observed.

An excellent match is observed between measurements and simulations for the investigated transient behaviour. The possible variations due to parameter uncertainties are within expected range. Actuator saturations, limiting the realisable pump rate, are precisely estimated by simulation. Solely the measured amplitude of pressure overshoot has been slightly increased, as expected by simulations for the 350 MPa operating pressure. The maximally observed settling times and overshoots are given in Table 6.10. Overall, the performance in simulation and measurement cant achieve the requirements from control design. This is due to the use of an initial PI controller in combination of a failure, when implementing the controller to the high-pressure pump. The final extended PI controller is expected to enhance the closed-loop performance. Nevertheless, the high-pressure network models provide accurate simulations, considering the high-pressure pumps in closed-loop operation.

Table 6.10: Achieved performance by means of experiments at the test bench for different network topologies: comparing closed-loop performance from measurements with results from simulations, using detailed simulation model.

		Measurement		Simulations		Objective
	Transitions	1-4	5-8	1-4	5-8	(Sect. 5.3)
E-4	max. settling time:	**1.3989**	**0.9429**	**0.9470**	**0.6310**	< 0.5
(200 MPa)	max. overshoot:	**0.1723**	0.0937	**0.1839**	0.0850	$< \pm 0.1$
E-7	max. settling time:	**0.9656**	**0.7580**	0.2750	-	< 0.5
(350 MPa)	max. overshoot:	0.0800	0.0507	0.0734	0.0185	$< \pm 0.1$
E-9	max. settling time:	**1.1820**	**1.1879**	**0.6992**	**0.7070**	< 0.5
(200 MPa)	max. overshoot:	**0.1487**	**0.1566**	**0.1311**	**0.1302**	$< \pm 0.1$
E-11	max. settling time:	0.3855	**0.5676**	0.3582	0.3882	< 0.5
(350 MPa)	max. overshoot:	0.0431	0.0446	0.0447	0.0448	$< \pm 0.1$

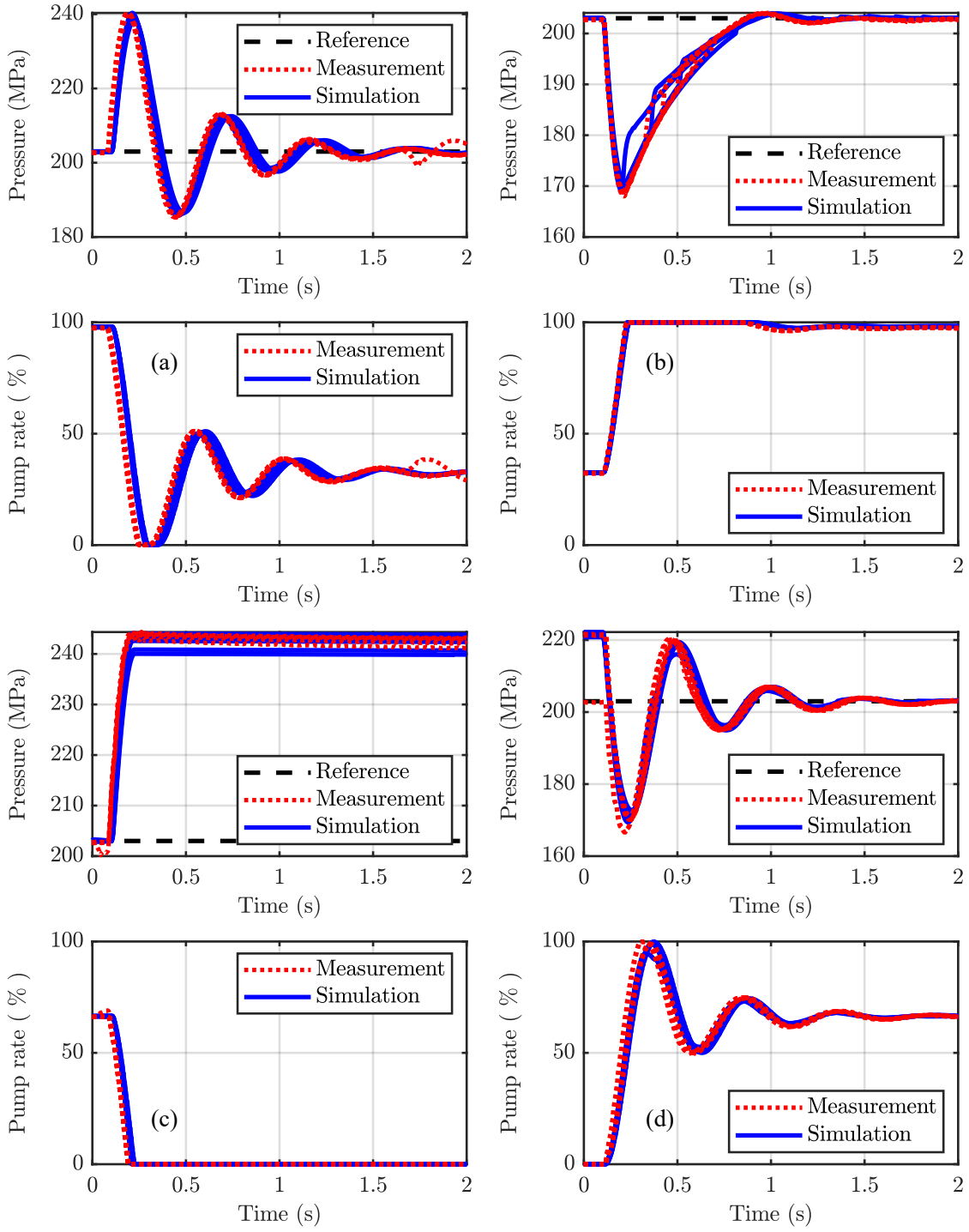

Figure 6.39 – Disturbance steps at 200 MPa operating point for asymmetric cutting heads (E-4): resulting step responses from non-linear simulation model and measured step responses from experiment. Nozzle 1 closes while nozzle 2 remains open (a), nozzle 1 opens while nozzle 2 remains close (b), nozzle 2 closes while nozzle 1 remains close (c) and nozzle 2 opens while nozzle 1 remains open (d).

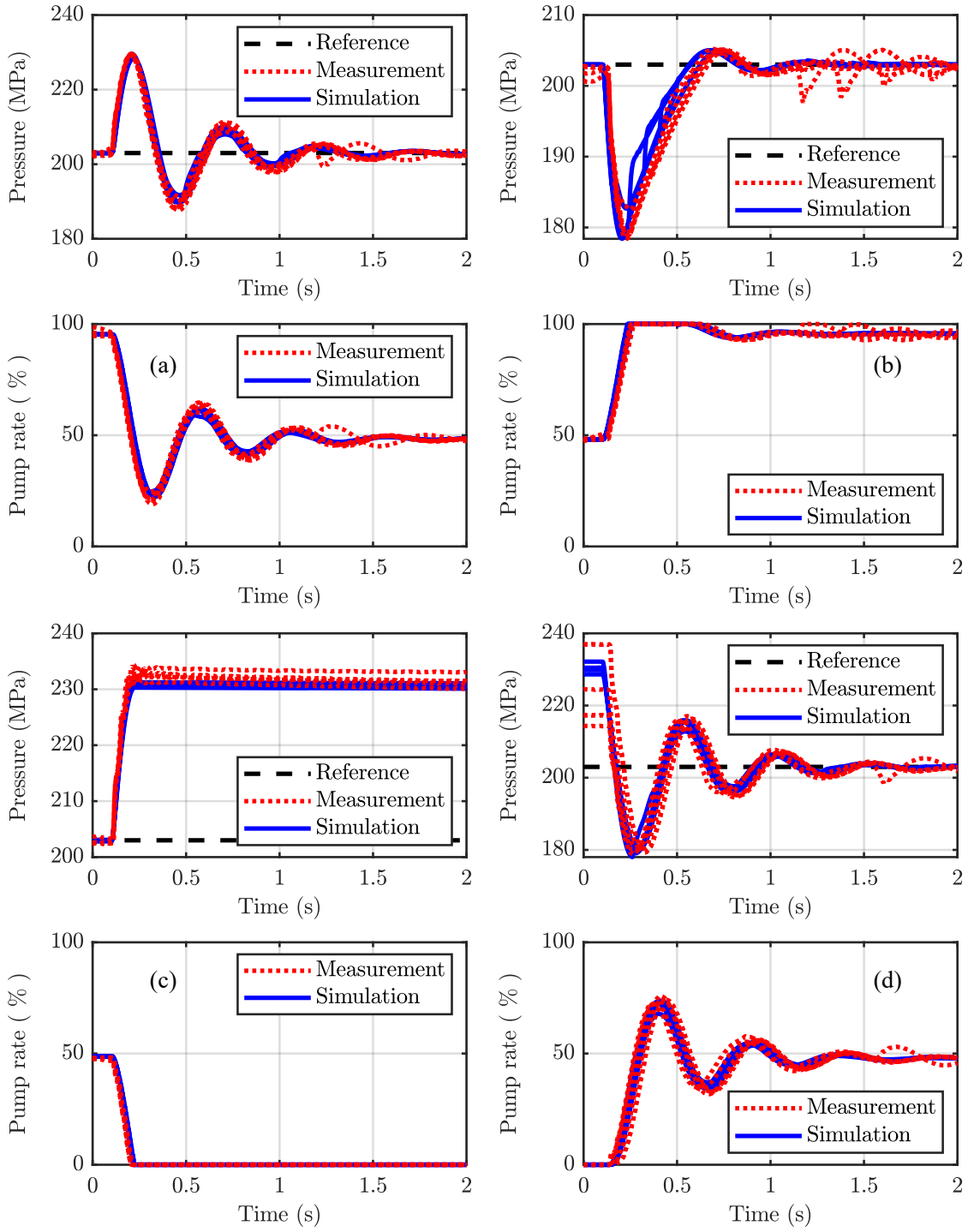

Figure 6.40 – Disturbance steps at 200 MPa operating point for symmetric cutting heads (E-9): resulting step responses from non-linear simulation model and measured step responses from experiment. Nozzle 1 closes while nozzle 2 remains open (a), nozzle 1 opens while nozzle 2 remains close (b), nozzle 2 closes while nozzle 1 remains close (c) and nozzle 2 opens while nozzle 1 remains open (d).

6.4.2 Quasi optimal robust PI controller application (1 pump configuration)

This simulation study applies the extended robust PI controller (6.39), as derived in Section 6.2, to a single high-pressure pump. Deriving a quasi-optimal robust controller, the expected disturbance of maximum amplitude has been taken into account, while maximizing the uncertainty range by applying the proposed Δ-K iteration. To verify performance and stability of the extended PI controller $\tilde{K}^*_{PI}$, simulations have been derived with respect to the symmetric and asymmetric network topology (as already introduced in Table 6.9). The 2 extended measurements (**E-4** and **E-7**) consider the topology **(c) Symmetric network**, where both cutting heads have been asymmetrically configured. The other 2 extended measurements (**E-9** and **E-11**) consider the topology **(d) Asymmetric network**, while both cutting heads have been symmetrically configured. These experiments aim at disturbance rejection, while tracking a constant reference pressure of either 200 or 350 MPa. An overview, considering the 200 MPa operating pressure, is provided below. Plots extending these results are given in Appendix B.2.

Contour cutting: asymmetric and symmetric cutting heads

Simulations have been obtained, when applying disturbance steps by switching the cutting heads to open and close position. This alternately switching of two cutting heads results again in 4 possible pump rates. Consequently, 8 transitions have been obtained with respect to the cutting head switching. Simulation results are shown in the plots of Figures 6.41 and 6.42. These plots overview the experiments E-4 and E-9, representing the asymmetric and symmetric cutting heads at 200 MPa. The plots for the inverse 4 transitions as well as the complementary experiments for controller validation at 350 MPa (E-7 and E-11) are provided in the Appendix B.2.

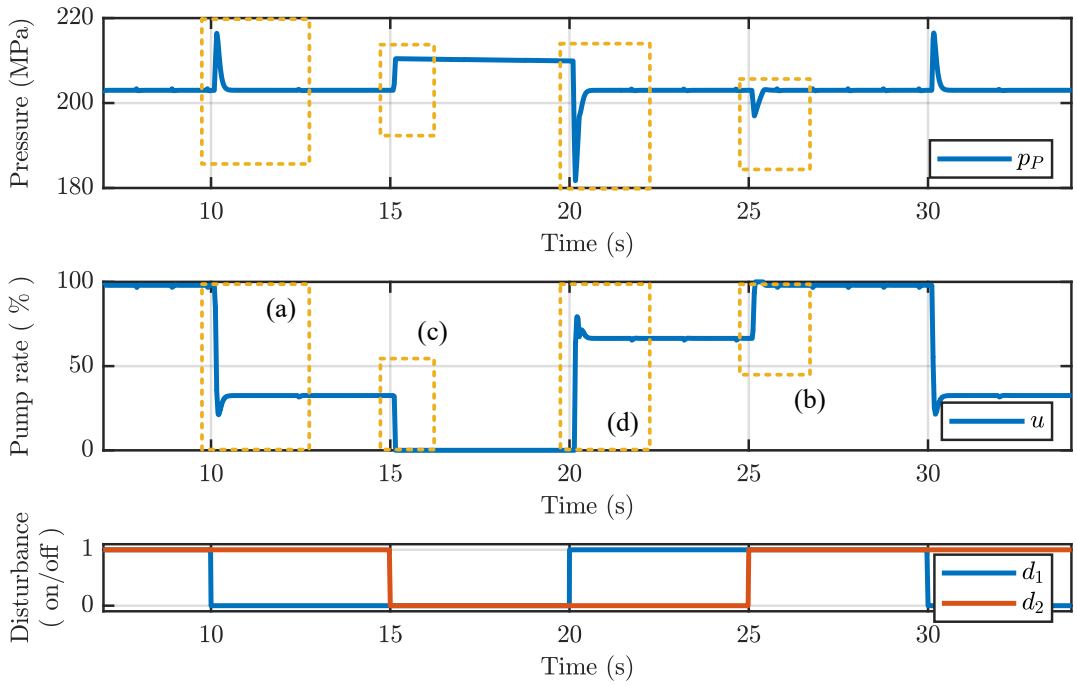

Figure 6.41 – Switching pattern considering 4 transitions for 200 MPa operating pressure of experiment E-4: desired switching states resulting in different pump rates for disturbance rejection by means of control.

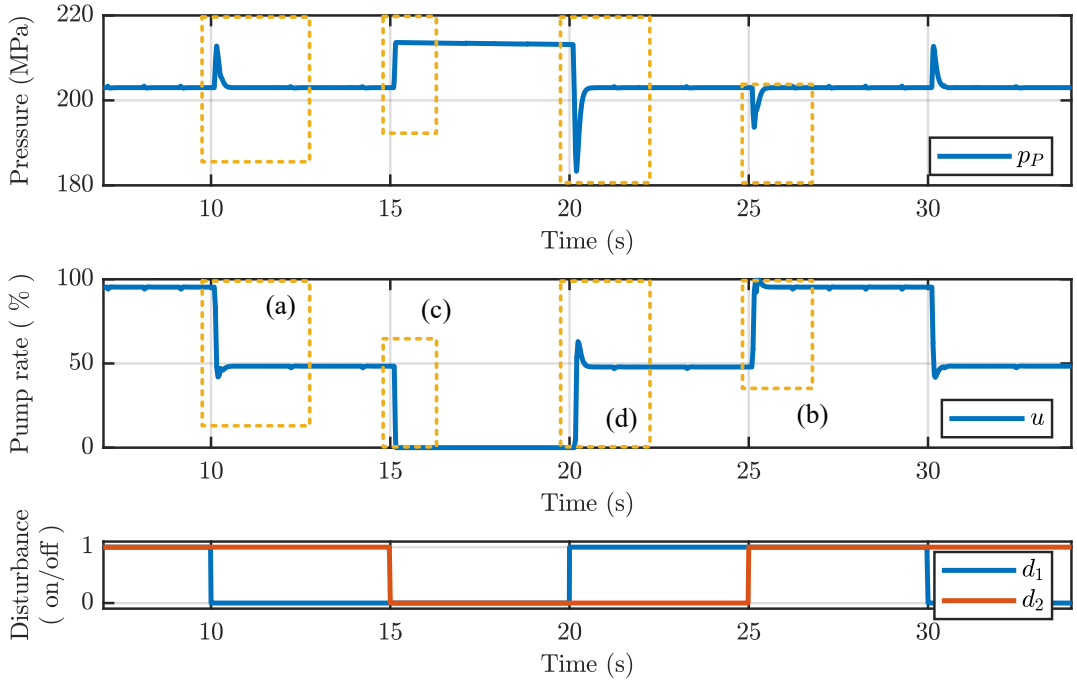

Figure 6.42 – Switching pattern considering 4 transitions for 200 MPa operating pressure of experiment E-9: desired switching states resulting in different pump rates for disturbance rejection by means of control.

The zoomed-in plots of Figures 6.43 and 6.44 show the simulation results for each switching state of experiment E-4 and E-7, respectively. The transitions (a) and (b) present the closing and opening of cutting head 1, where the transitions (c) and (d) show the closing and opening of cutting head 2.

As expected, the quasi-optimal robust PI controller $\tilde{K}^*_{PI}$ performs superior in contrast to the initially implemented PI controller K^f_{PI}. The possible variations, due to parameter uncertainties, are within expected range. The maximally observed settling times and overshoots are given in Table 6.11. Applying the extended PI controller $\tilde{K}^*_{PI}$, the observed closed-loop performance achieve the desired objectives for control design.

Table 6.11: Achieved performance by means of simulations for different network topologies: providing closed-loop performance from simulations, using detailed simulation model with quasi-optimal robust PI controller.

		$\tilde{K}^*_{PI}$		K^f_{PI}		Objective
	Transitions	1-4	5-8	1-4	5-8	(Sect. 5.3)
E-4	max. settling time:	0.1740	0.1190	**0.9470**	**0.6310**	< 0.5
(200 MPa)	max. overshoot:	0.0678	0.0318	**0.1839**	0.0850	$< \pm 0.1$
E-7	max. settling time:	0.0930	-	0.2750	-	< 0.5
(350 MPa)	max. overshoot:	0.0245	0.0061	0.0734	0.0185	$< \pm 0.1$
E-9	max. settling time:	0.1480	0.1580	**0.6992**	**0.7070**	< 0.5
(200 MPa)	max. overshoot:	0.0483	0.0476	**0.1311**	**0.1302**	$< \pm 0.1$
E-11	max. settling time:	-	-	0.3582	0.3882	< 0.5
(350 MPa)	max. overshoot:	0.0153	0.0189	0.0447	0.0448	$< \pm 0.1$

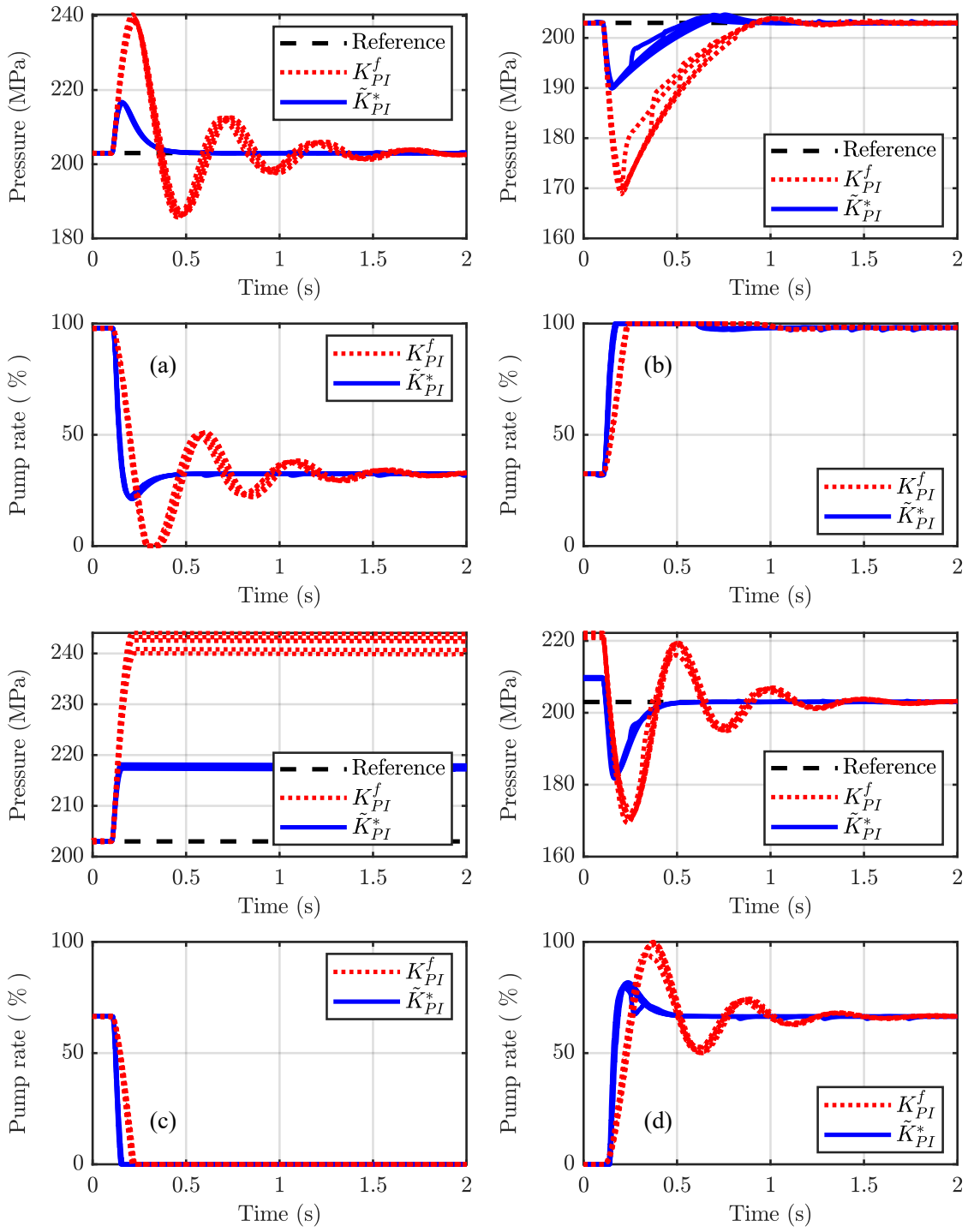

Figure 6.43 – Disturbance steps at 200 MPa operating point for asymmetric cutting heads (E-4): resulting step responses from non-linear simulation model. Nozzle 1 closes while nozzle 2 remains open (a), nozzle 1 opens while nozzle 2 remains close (b), nozzle 2 closes while nozzle 1 remains close (c) and nozzle 2 opens while nozzle 1 remains open (d).

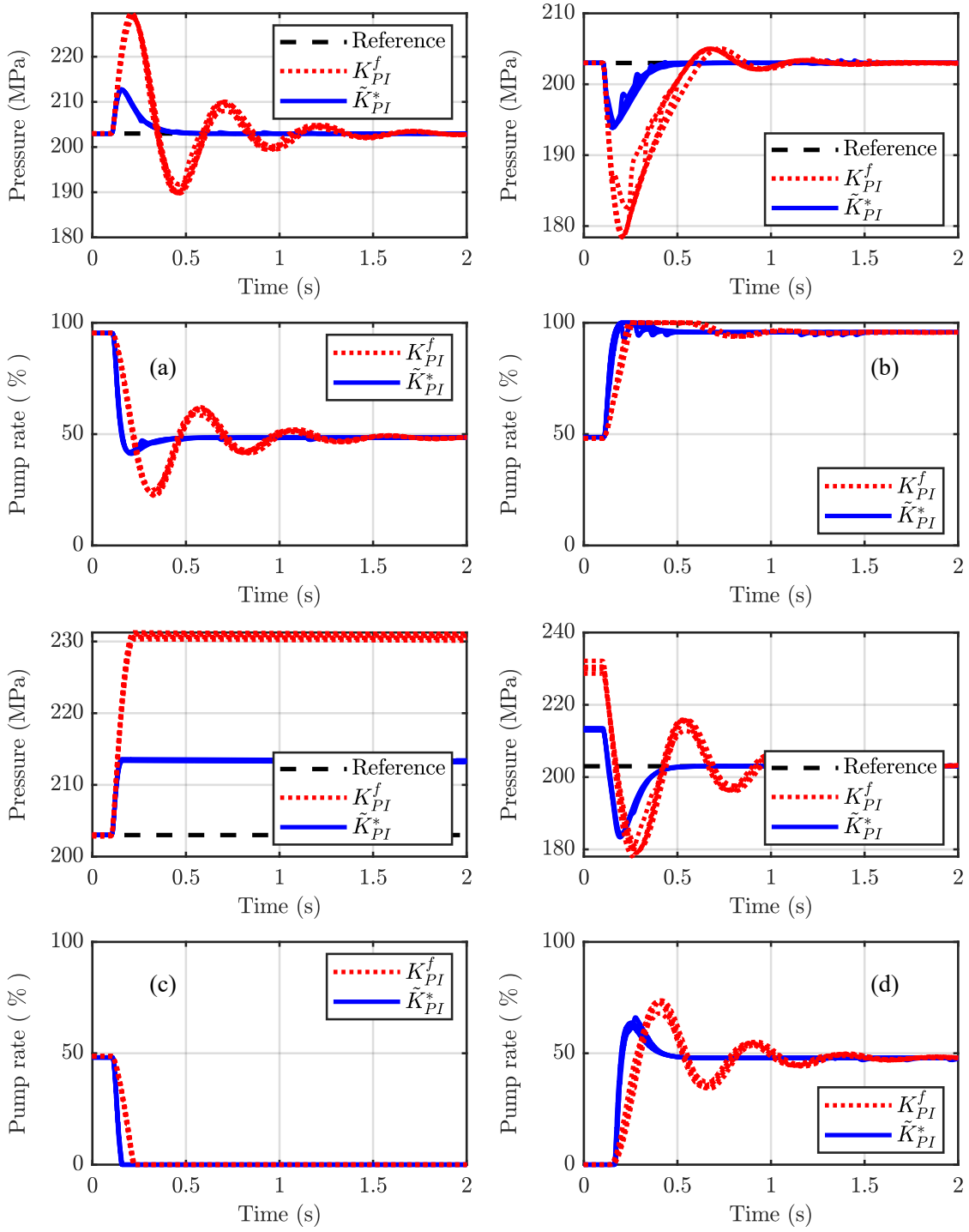

Figure 6.44 – Disturbance steps at 200 MPa operating point for symmetric cutting heads (E-9): resulting step responses from non-linear simulation model. Nozzle 1 closes while nozzle 2 remains open (a), nozzle 1 opens while nozzle 2 remains close (b), nozzle 2 closes while nozzle 1 remains close (c) and nozzle 2 opens while nozzle 1 remains open (d).

Improving performance and uncertainty range (gain-scheduling)

Different approaches could become interesting to further increase the permissible subsection size. Research on gain-scheduling is provided in [Rugh and Shamma, 2000], where an augmented plant is considered, using linear fractional transformation to represent time-varying parameters for control design. For that, robust gain-scheduling has been employed to obtain controller gains with respect to scheduling variables. As a consequence, uncertain parameters have been considered as measurable. The resulting controller has to deal with a reduced overall uncertainty range. This enables it to guarantee performance and stability for large parameter variations. A first critical uncertainty is the varying pumping chamber volume, which interacts with the available network subsection volume. The varying pumping chamber volume follows a periodic, non-linear function that is related to the piston displacement. Due to its time-varying property, the pumping chamber volume is undesired for applying robust H_∞ controller synthesis, which interfere with stability requirements. Since the piston displacement is well known, it is a first candidate as a scheduling variable. Scheduling the controller gains with respect to the resulting pumping chamber volume, allows for increasing the available network subsection size. It extends the robust control design to schedule the PI gains with respect to the measured piston displacement. This allows for eliminating the time-varying uncertainty related to the displacement volume of a pumping chamber. A second uncertainty is the pressure operating point, which becomes a parameter when linearising the plant model used for control design. This parameter is considered as time constant, since the controller is assumed to track steady-state operating pressure around desired operating point. The pressure is measured for low-level control as well as available as a reference signal. The control surfaces of Figure 6.45 present the controller gains with respect to both scheduling variables. While scheduling the integrator gain, a back calculation of the controller output is recommended to realize a smooth pump operation.

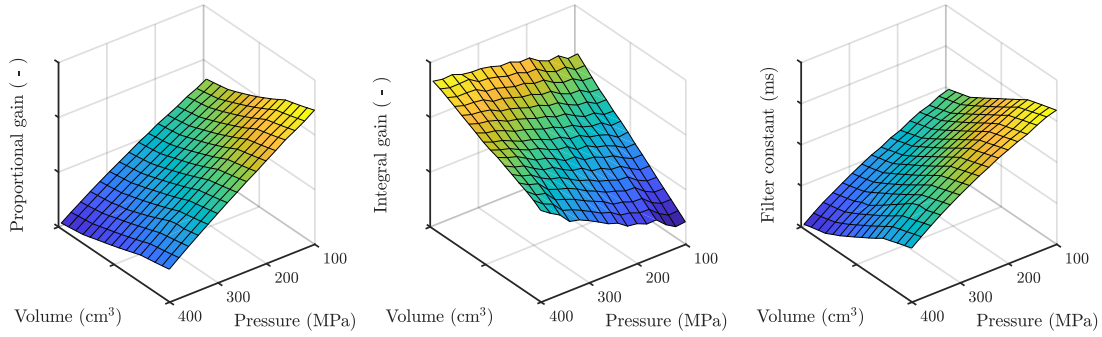

Figure 6.45 – Control surface obtained for gain-scheduling: Controller gains with respect to measured operating pressure and varying pumping chamber volume due to piston displacement.

However, the difficulty with the piston displacement consists of the unknown switching states of the check-valves, which interconnect a pumping chamber with the high-pressure network. As long as the switching is hard to predict, the error between estimated and effective chamber can become maximally. This circumstance is unfavourable, as stability is not guaranteed. Nevertheless, assuming perfect synchronization of the pumping units allows for realizing an increased subsection size of about 270 m piping length. Using the reference pressure for control design allows for increasing the permissible subsection size up to 290 m. Combining both scheduling variables leads to a maximal subsection size of 370 m, where resulting closed-loop stability and performance remain unattained.

The simulations of Figure 6.46 show the step response for disturbance rejection when applying robust gain scheduling. In contrast to the initial robust low-level controller, see Table 6.12, this approach shows the ability to reduce the resulting variation for a constant operating pressure. For any case, it would be interesting to evaluate an approach to compensate the varying parameters, such as gain scheduling or linear parameter varying control.

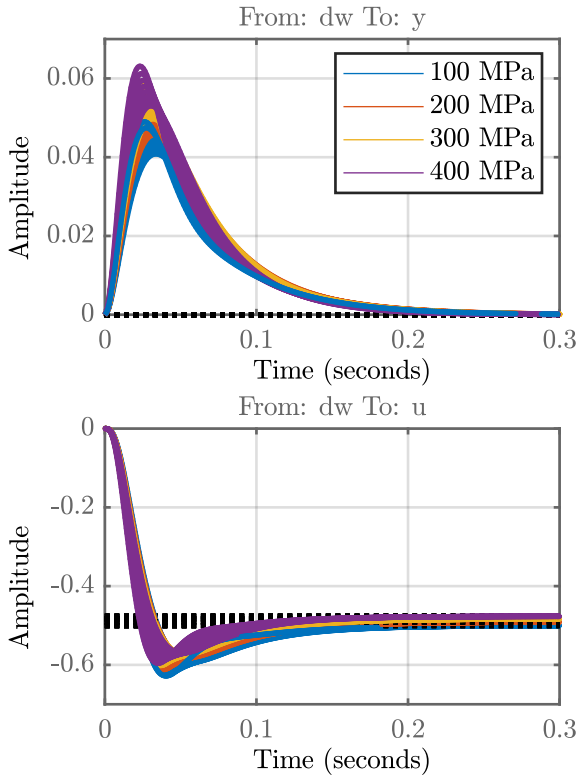

Figure 6.46 – Step responses of PI gain scheduling controller $\tilde{\mathrm{K}}^*_{\mathbf{PI}}$ with low-pass filter and quasi-optimal robust PI design: considering a reduced generalized plant derived from joint shaping functions.

Table 6.12: Comparing robust PI controller to quasi-optimal robust PI controller and robust PI gain scheduling in terms of closed loop step response and obtained uncertainty range.

	Robust $\tilde{\mathrm{K}}_{PI}$		Optimal $\tilde{\mathrm{K}}^*_{PI}$		Gain-sched. $\tilde{\mathrm{K}}^*_{\mathbf{PI}}$	
	nom.	max.	nom.	max.	min.	max.
Peak gain γ-value:	0.6354		1.0		1.0	
Settling time (2% $e(t)$):	0.1236	0.1318	0.1445	0.1538	0.0615	0.0846
Overshoot:	0.0753	0.0963	0.0700	0.0934	0.0414	0.0629
Uncertainty $V_\delta \times 10^{-4}$:	5.8996		9.5091		**18.089**	

6.4.3 PI controller application and validation (2 pump configuration)

This experimental study applies an initial PI controller to both high-pressure pumps available at the test bench. It aims to investigate stability and performance for two distributed pumps, which are coupled over a high-pressure network and disturbed due to cutting heads switching. Pump 1 holds the controller

$$\mathrm{K}_{PI1}(s) = \#\#\# + \#\#\# \ \frac{1}{s} \ , \tag{6.47}$$

whereas pump 2 has by default the controller

$$\mathrm{K}_{PI2}(s) = \#\#\# + \#\#\# \ \frac{1}{s} \ . \tag{6.48}$$

These control parameters originate from the initial test bench configuration as already used for model validation in Section 4.3. Measurements for the robust PI controller has not been applicable due to a defect of the high-pressure pump. Nevertheless, these results show the effect of running two interconnected pumps with independent decentralized controllers.

Measurement data are obtained on the high-pressure test bench with respect to 2 specific network topologies, considering two pumps and two cutting heads. Both cutting heads have been symmetrically configured with identical nozzles. The experiments listed in Table 6.13 have been derived for simulation and experimental validation. Measurement **D-2** considers the topology **(e) Symmetric distributed**, where the piping from each pump to the cutting heads have the same length. Measurement **D-5** considers the topology **(f) Asymmetric distributed**, where the piping from a pump to the cutting heads have different lengths. Both experiments interconnect two cutting heads at the same network position.

Table 6.13: Excerpt of experiments for use case 3: measurements derived on different test bench setups used for controller validation.

Meas.	Topology	Pressure (MPa)	Nozzle 1 ⌀(mm)	Nozzle 2 ⌀(mm)	Switching pattern
D-2	(e) Sym. dis.	200	0.2	0.2	Contour
D-5	(f) Asym. dis.	200	0.2	0.2	Contour

All experiments have been derived for a single operating pressure of 200 MPa, taking the switching pattern for contour cutting into account. Wile cutting head 1 remains open for any time, cutting head 2 will open and close for a time period of 60 seconds. Cutting heads open and close with respect to the predefined switching pattern given by the disturbance signal $d(t) = [d_1(t), d_2(t)]$, where $d_1(t) = 0 \ \forall t$. The low-level pressure controllers of both pumps will adjust the pump rate over the control signal $u(t)$ to obtain a desired reference pressure. The reference value $r(t)$ and disturbance $d(t)$ are fed into the extended high-pressure network models for closed-loop simulation. The pump output pressures $p_P(t) = [p_{P1}(t), p_{P2}(t)]$ as well as the pump rates $u(t) = [u_1(t), u_2(t)]$ will be measured and compared with simulations ($\hat{p}_P(t)$ and $\hat{u}(t)$) to validate the PI controllers. The measurement data have been captured with a sampling rate of 500 Hz.

Applying the graph-based modelling methodology according to the test bench configuration, results in different high-pressure network models, as already introduced and experimentally validated in Section 4.3.

Contour cutting: symmetric and asymmetric distributed pumps

Measurements D-2 and D-5 have been obtained and compared to simulations, considering the 200 MPa operating point. Disturbance steps have been applied on the test bench, when cutting head 2 opens and closes. This results in 2 possible pump rates. The applied switching pattern on disturbance $d = [d_1, d_2]$, the measured pump rates $u = [u_1, u_2]$ and measured pump output pressures $p_P = [p_{P1}, p_{P2}]$ are shown in the plots of Figure 6.47 for measurement D-2 and in the plots of Figure 6.48 for measurement D-5, respectively. It is observed that the pump rates for both pumps reach a different steady-state for symmetric distributed pumps, where asymmetric distributed pumps seem to reach a similar steady-state. Where the operating point of a high-pressure pumps depends on its position in the network, the asymmetry in the network configuration on the test bench seems to compensate the different pump rates of each prototype. The switching pattern is again repeated 5 times to cover different parameter variations that occurs during continuous pump operation.

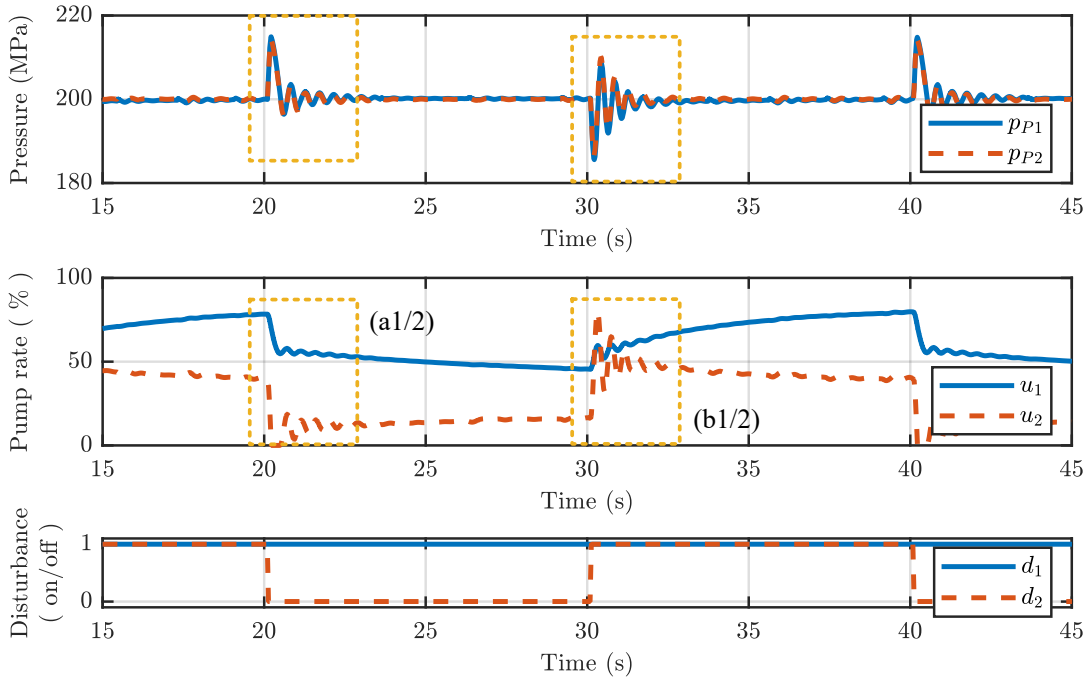

Figure 6.47 – Switching pattern for 200 MPa operating pressure of experiment D-2, considering an initial PI controller: desired switching states resulting in different pump rates for disturbance rejection by means of control to reference pressure.

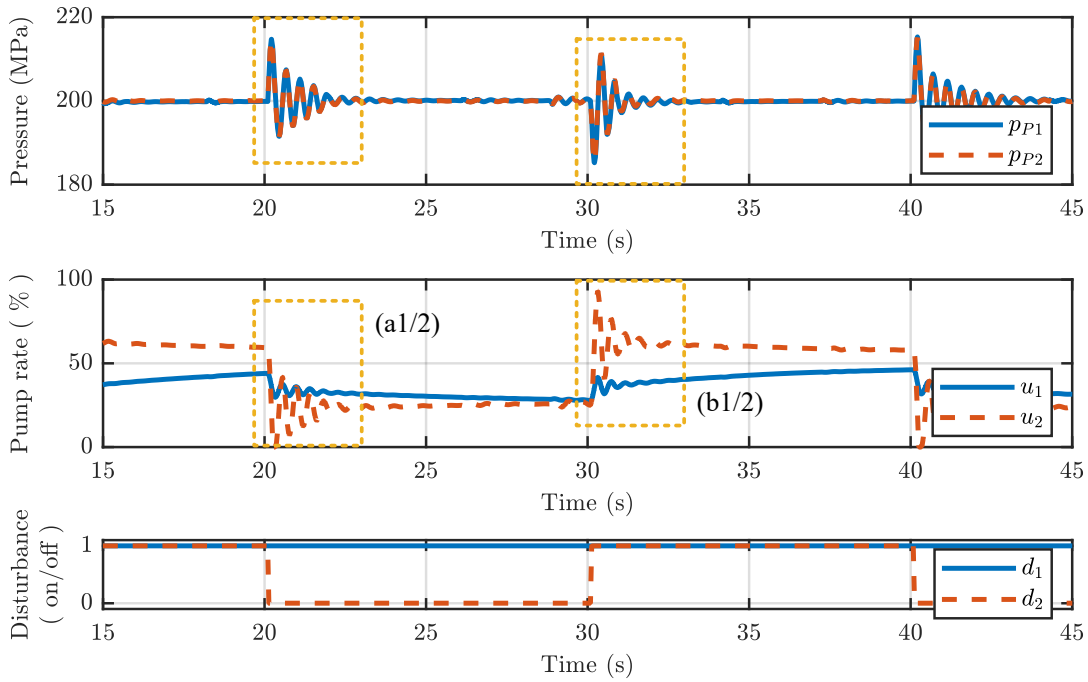

Figure 6.48 – Switching pattern for 200 MPa operating pressure of experiment D-5, considering an initial PI controller: desired switching states resulting in different pump rates for disturbance rejection by means of control to reference pressure.

The zoomed-in plots of Figures 6.49 and 6.50 compare measurements ($p_P(t)$, $u(t)$) and simulations ($\hat{p}_P(t)$, $\hat{u}(t)$) for each switching state of experiment D-2 and D-5, respectively. Acceptable match is observed for the investigated transient pressure trends. Increased oscillation is found for the measurements, where the simulated pump rates show discrepancies. The expected variations due to parameter uncertainties is mostly within expected range. Some additional disturbance is observed on the pressure trend due to check-valve switching hysteresis. This effect is not taken into account, when modelling a high-pressure network.

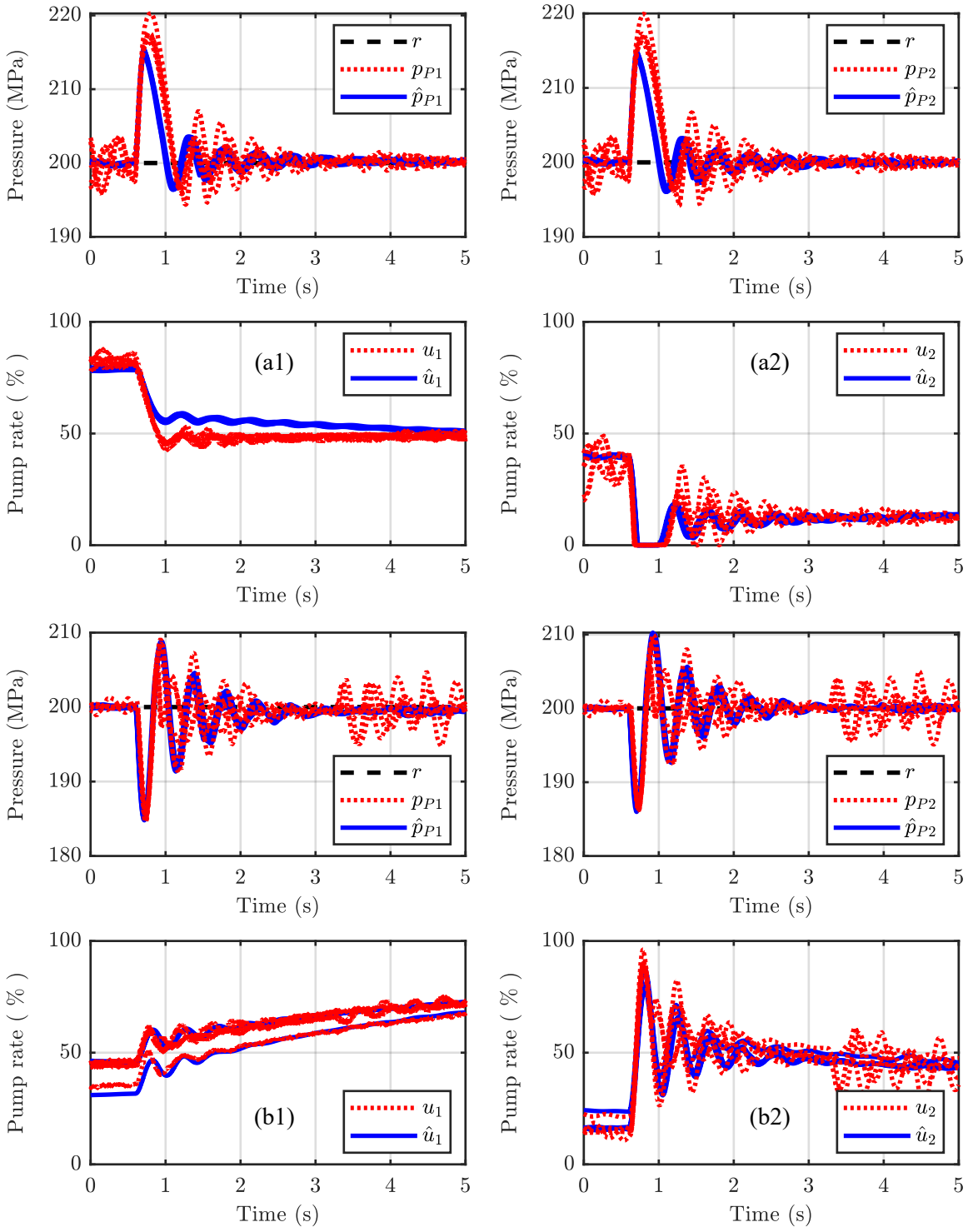

Figure 6.49 – Disturbance steps at 200 MPa operating point for symmetric distributed pumps (D-2), considering an initial PI controller: resulting step responses from non-linear simulation model and measured step responses from experiment. Nozzle 2 closes (a) and opens (b) while nozzle 1 remains open.

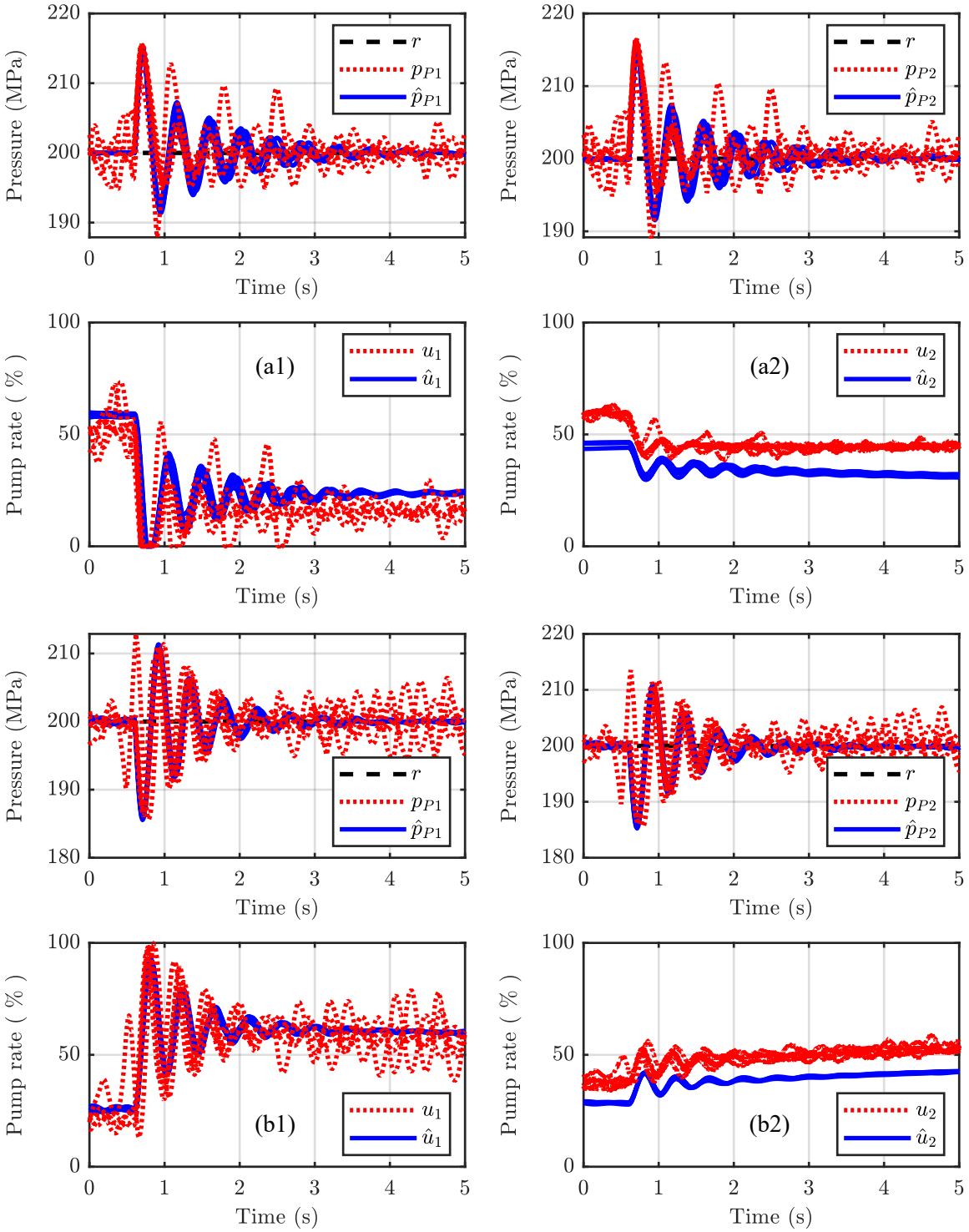

Figure 6.50 – Disturbance steps at 200 MPa operating point for asymmetric distributed pumps (D-5), considering an initial PI controller: resulting step responses from non-linear simulation model and measured step responses from experiment. Nozzle 2 closes (a) and opens (b) while nozzle 1 remains open.

6.4.4 Quasi optimal robust PI controller application (2 pump configuration)

This simulation study applies the extended robust PI controller (6.39), as derived in Section 6.2, to both high-pressure pumps. To verify performance and stability of the extended PI controller $\tilde{K}^*_{PI}$, simulations have been derived with respect to two distributed pumps, as already introduced in Table 6.13. However, these simulations employ two identical pumps to the corresponding high-pressure network models. The measurements **D-2** considers the topology **(e) Symmetric distributed** and measurements **D-5** considers the topology **(d) Asymmetric distributed**. These experiments aims at disturbance rejection due to switching cutting heads, while holding a constant reference pressure of 200 MPa.

Contour cutting: symmetric and asymmetric distributed pumps

Simulations have been obtained applying disturbance steps by switching cutting head 2 open and close. This alternately switching of a cutting head results again in 2 possible pump rates. Simulation results are shown in the plots of Figures 6.51 and 6.52 for experiments D-2 and D-5, respectively.

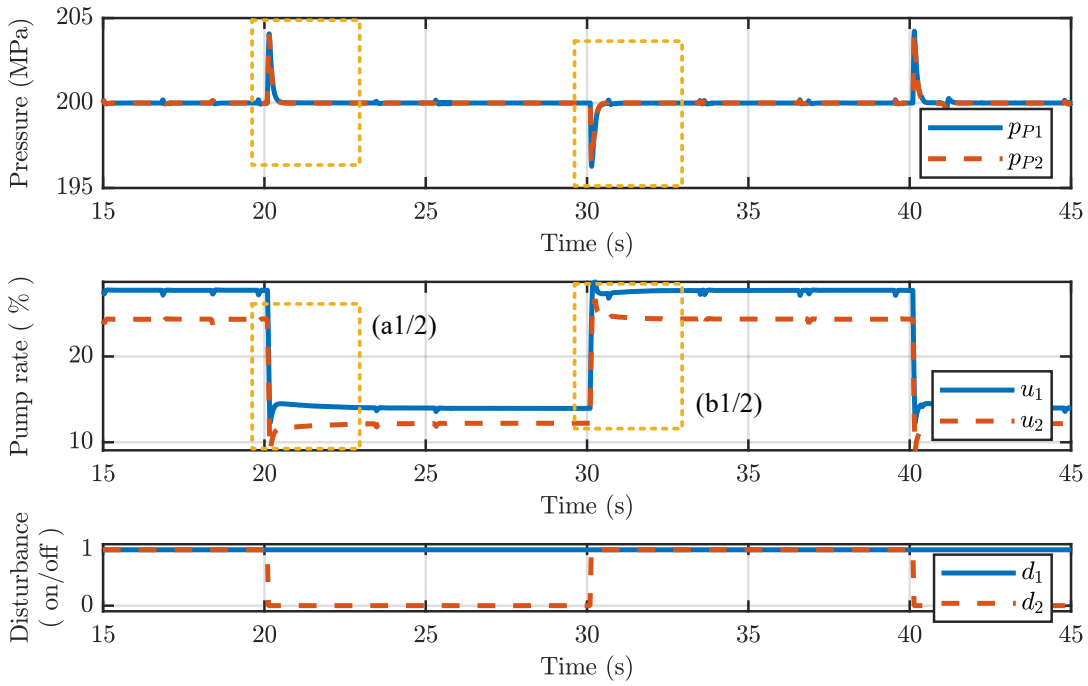

Figure 6.51 – Switching pattern for 200 MPa operating pressure of experiment D-2, considering the quasi-optimal PI controller: desired switching states resulting in different pump rates for disturbance rejection by means of control to reference pressure.

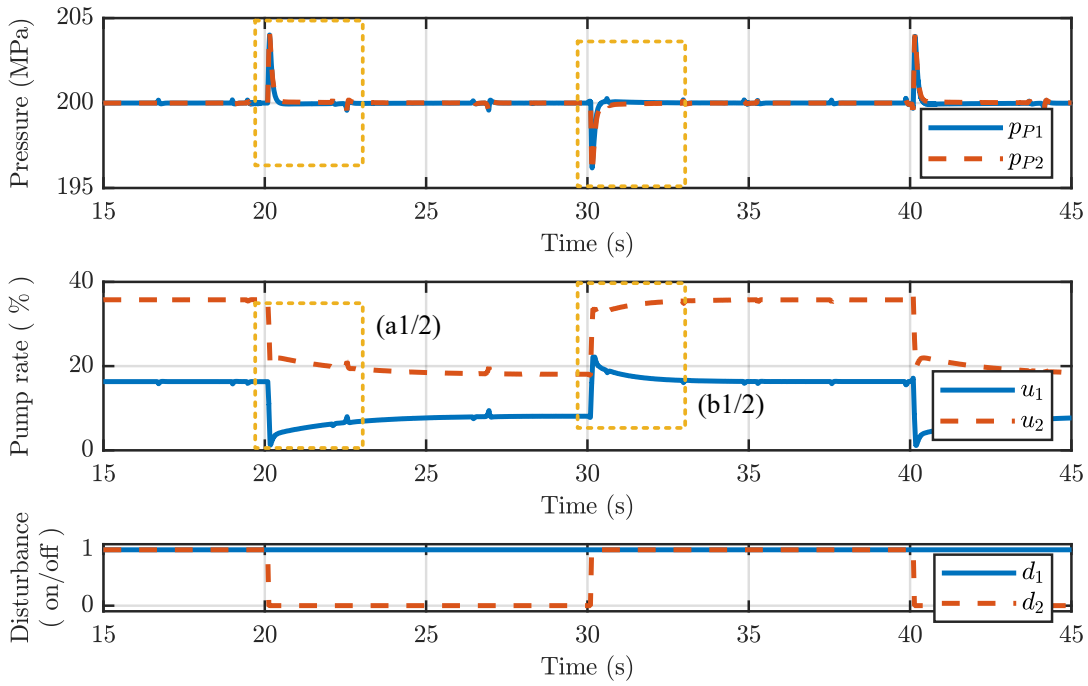

Figure 6.52 – Switching pattern for 200 MPa operating pressure of experiment D-5, considering the quasi-optimal PI controller: desired switching states resulting in different pump rates for disturbance rejection by means of control to reference pressure.

The zoomed-in plots of Figures 6.53 and 6.54 show the simulation results for each switching state of experiment D-2 and D-5. As expected, the quasi-optimal robust PI controller $\tilde{\mathrm{K}}^*_{PI}$ performs superior in contrast to the initially applied PI controllers K_{PI1} and K_{PI2}.

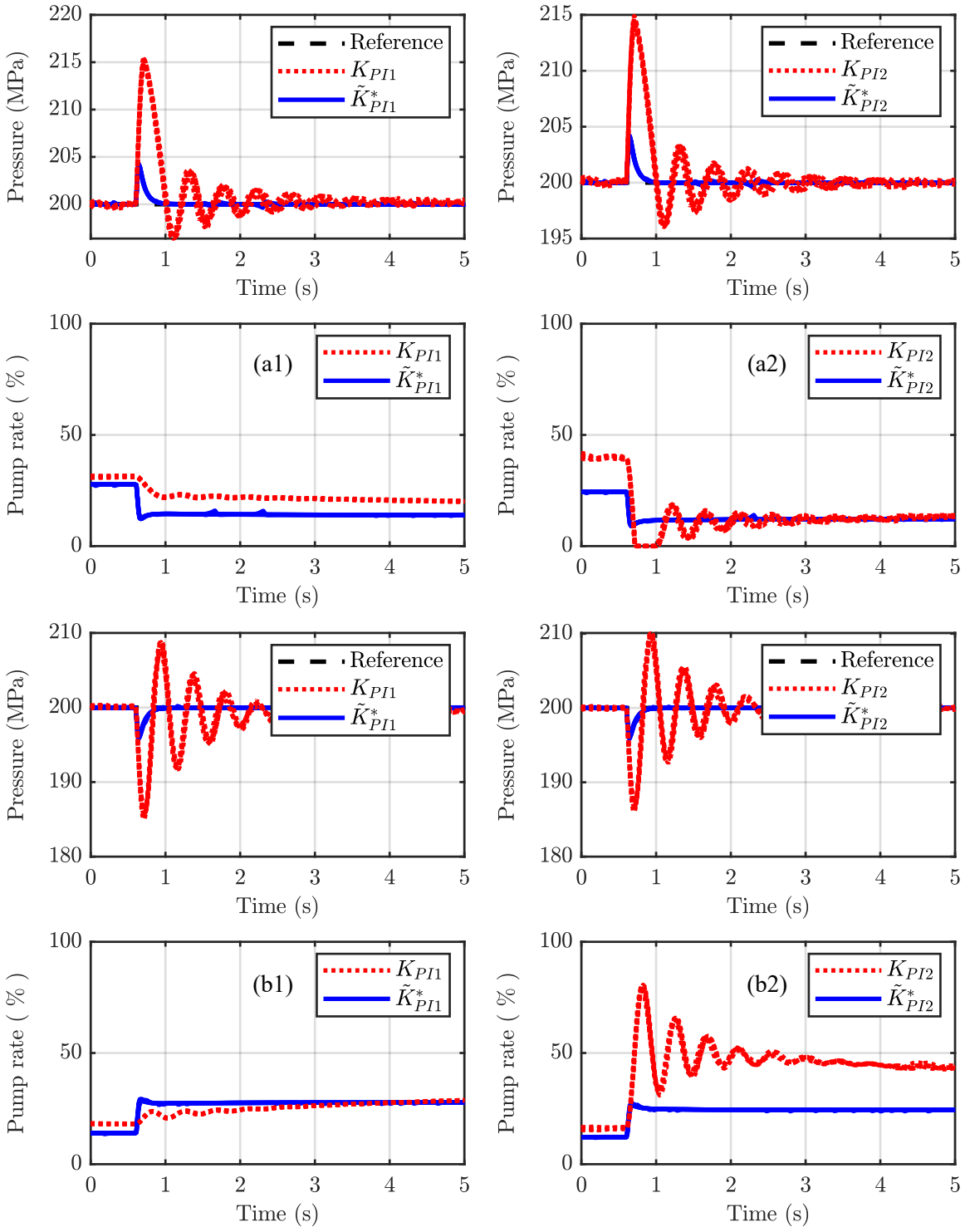

Figure 6.53 – Disturbance steps at 200 MPa operating point for symmetric distributed pumps (D-2), considering the quasi-optimal PI controller: resulting step responses from non-linear simulation model. Nozzle 2 closes (a) and opens (b) while nozzle 1 remains open.

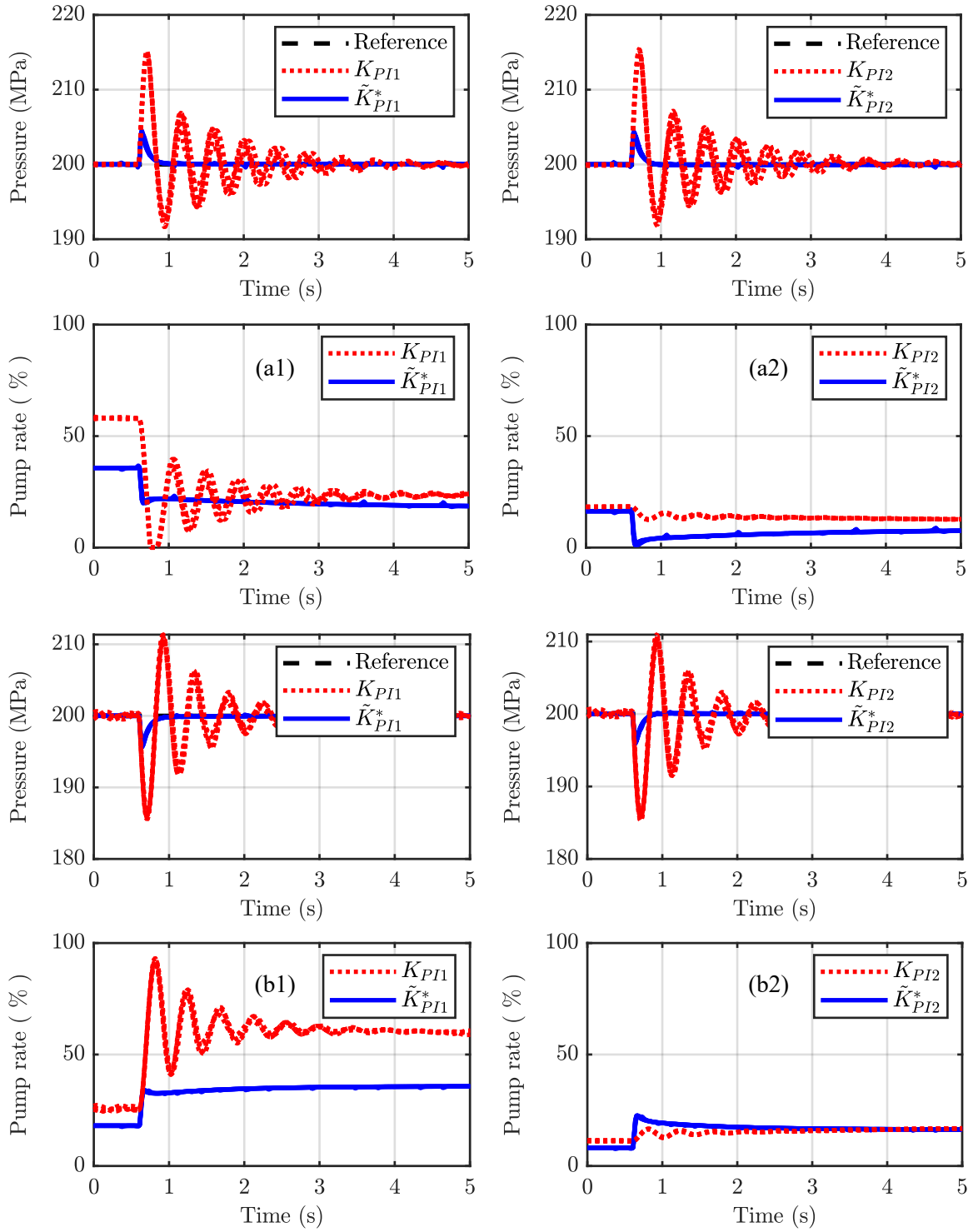

Figure 6.54 – Disturbance steps at 200 MPa operating point for asymmetric distributed pumps (D-5), considering the quasi-optimal PI controller: resulting step responses from nonlinear simulation model. Nozzle 2 closes (a) and opens (b) while nozzle 1 remains open.

Improving performance and uncertainty range (decentralized control)

A decentralized control design for multiple pumps would require to describe the coupling between network subsections. The H_∞ optimization problem for the proposed distributed high-pressure pumps is then to find a common controller that is distributed on several pumps which are coupled over a high-pressure network. However, the overall network size, its topology and the amount of available pumps remain unknown. The diagrams of Figure 6.55 compares the investigated robust low-level control design (a), that consider neighbouring subsystems as additional disturbances and a decentralized control design (b), taking the dynamics of neighbouring subsystems into account.

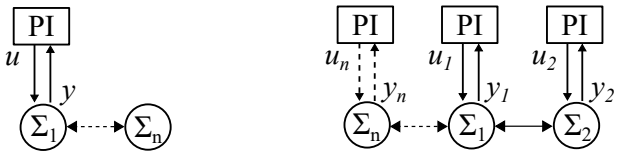

(a) Independent control design (b) Decentralized control design

Figure 6.55 – Applied concept for independent control design compared to decentralized control: while the independent control design considers other network subsections as exogenous disturbances, the distributed control design takes the dynamic coupling between neighbouring pumps into account.

Since the disturbances due to check-valve malfunctions propagate to the neighbouring network subsections, it becomes necessary for a robust control design to deal with an increased disturbance amplitude. The test bench setup with two distributed pumps encounters stability concerns. It would be interesting to investigate a decentralized control design for controller synthesize. This would address the stability concerns for disturbances which originate from neighbouring pumps due to malfunctions.

6.5 Conclusion

In this chapter, the H_∞ controller synthesis for a electrically driven high-pressure pump has been validated. The specified control requirements on performance and control effort have been applied on related output channels, by specifying the corresponding weighting functions. The interconnection system has then been rearranged to separate the controller from the remaining system components, using linear fractional transformation. This provides a generalized plant, that corresponds to the required H_∞ optimization problem, needed for robust control design.

A first contribution is provided, when introducing joint-shaping functions. This lumps multiple input channels of a generalized plant, which reduces the size of the H_∞ optimization problem with respect to the numbers of merged channels. It reduces the computational effort for controller synthesis and results further in a state feedback controller of reduced order. This approach has been applied for the robust control design of a high-pressure pump. It has been shown, that the reduced controller performs close to the full order design. The resulting differences are negligibly small.

The derived optimization problem, considering the decentralized pump and its corresponding network subsection, has been solved to obtain a state feedback controller as well as a PI controller, using the available algorithms of *MATLAB*. The PI controller has then been extended with a low-pass filter, which results in a lag control law. These controllers have been compared by means

of simulations, using the detailed network models implemented with the introduced simulation toolbox. It has been recognized, that the PI control design is useful to reduced the controller complexity. This control structure is straight forward for implementation in the high-pressure pump. That is an advantage for industrial use. However, the PI controller is not capable to recover the enhanced performance of a state feedback controller. It barely achieves the desired performance and stability, when limiting the permissible subsection size. On the other hand, a lag compensator introduces an additional pole, which can be placed, such as to recover the dynamics of the state feedback controller. It achieves the desired performance and stability without disclosing the permissible subsection size.

Another contribution aims at a single controller for every decentralized pump, as installed in a high-pressure network of unknown topology. This requires for separating a high-pressure network into subsections, which can be controlled by an assigned high-pressure pump. The subsection size is thereby considered as an uncertain parameter for robust controller synthesis, where the permissible uncertainty range, to guarantee robust stability and to obtain robust performance, has been taken into account when applying the Δ-K iteration. It applies H_∞ controller synthesis, while adjusting the uncertainty range Δ with respect to minimize the robust performance margin. This procedure allows for designing a controller K that maximizes the permissible subsection size. A significant increase of 61% has been obtained in contrast to the initial suboptimal design, while guaranteeing robust stability and desired performance.

The obtained PI controller has been evaluated on the test bench by means of measurements. These measurements have been compared to simulation results. Unfortunately, the high-pressure test bench has not been available to verify the final optimal lag controller, due to a damaged pump. Nevertheless, the lag controller, implemented to the high-pressure network models while considering distributed setups with two pumps and two cutting heads, allows for verifying more complex waterjet facilities. These models in closed-loop control will further serve as use cases, to evaluate distributed average consensus and distributed balancing by means of numerical simulations (see Section 7.3).

7

Perspectives to distributed high-level managing

Contents

7.1 Introduction

Objectives

The first part of this thesis introduced the graph-based modelling of high-pressure networks, describing decentralized pumps interconnected with distributed work stations for waterjet machining. Based in this modelling, the second part investigated the robust control design for high-pressure pumps, subject for local disturbance rejection. A robustly controlled pump manages to stabilize a network subsection, whereas the required performance for waterjet machining limits the permissible subsection size. This last chapter provides first results to cope with the high-level managing of decentralized pumps, which aims to optimize the energy consumption of waterjet facilities.

In fact, the decentralized control of high-pressure pumps provides a solution (see the previous chapter), that is straight forward to implement, as only local information is required. Introducing managed pumps and applying distributed control, will be a trade-off between the amount of information required from neighbouring subsections and the effects of transmission delay, packet loss, etc. This managing requires to synchronize high-pressure pumps without knowledge about their positions in the network. Depending on the network topology and the cutting heads switching states, each pump will reach a different pump rate. This causes some of the pumps to deteriorate faster and degrade its ability to respond for disturbance rejection. The synchronization of coupled pumps in a waterjet facility further, causes all pumps to converge towards an average pump rate within acceptable time. This has to be realized without any centralized manager, whereas reliability of communication is not necessarily provided. Hence, the pumps should continue to operate at a suboptimal pump rate and supply the work stations, even though when communication fails.

This chapter provides a short overview of various managing concepts and presents preliminary simulation results, for the managing of distributed pumps by means of dynamic average consensus. The requirements from waterjet machining restrict the availability for many prevalent concepts. Nevertheless, the subsequent investigations present a starting point for ongoing research activities, considering the managing of distributed pumps within future waterjet facilities.

State of the art

The control design problem for weakly coupled decentralized systems can be solved by dividing the global problem into almost independent sub-problems [Bakule, 2008]. The demanding task for decomposition of strongly coupled systems restricts the application of decentralized and distributed control design.

On the other hand, hierarchical approaches are used to manage distributed controllers, while obtaining a globally desired behaviour of the overall system, see [Tatjewski, 2008] and [Scattolini, 2009]. The hierarchical control structure is typically organized in two layers: A low-level layer, that holds the distributed controllers, and a high-level layer, that coordinates the subsystems. This coordination is centralized and comprises an optimization procedure. A global optimization becomes computationally difficult for large-scale systems, thus different approaches aim at distribution of the optimization task.

A survey of various managing approaches, with emphasis on distributed algorithms, is provided in Appendix C.1. This survey summarizes control allocation (CA), model predictive control (MPC) and cooperative control, as organized in the diagram of Figure 7.1. It is dedicated to evaluate suitable concepts for the synchronization of distributed pumps in a high-pressure network.

Those approaches assigned to cooperative control, particularly aiming at average consensus and distributed synchronization, will be discussed in this subsequent sequel.

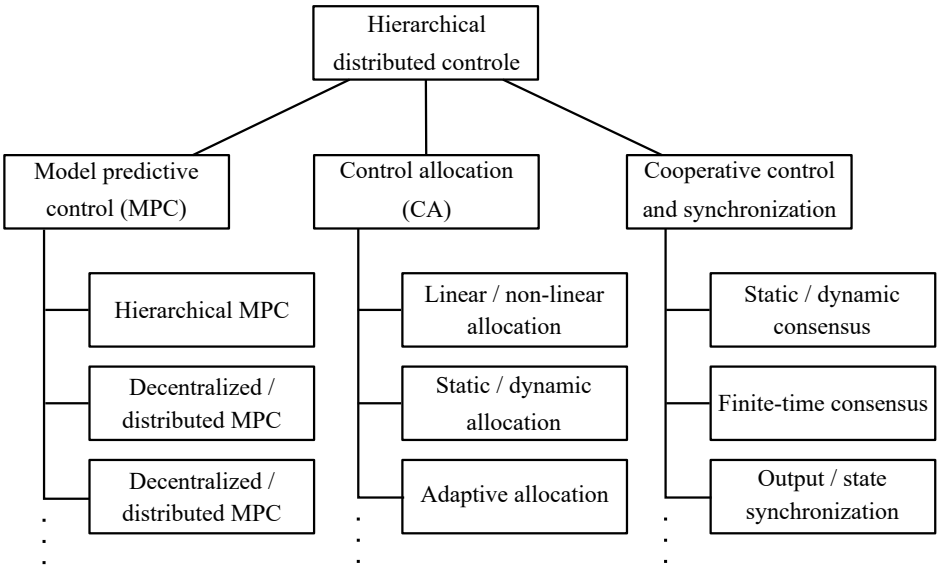

Figure 7.1 – Overview of managing approaches, aiming at hierarchical distributed control for high-pressure pumps: model predictive control, control allocation and cooperative control are distinguished with emphasis on distributed algorithms.

Model predictive control (MPC): the managing of distributed controllers comprises an optimization procedure, which is often designed using model predictive control [Mayne, 2014]. It provides the optimal output variables for a multi-variable system, while predicting the system states for a finite horizon. Since it becomes computationally difficult to solve this optimization problem for large-scale systems, the initial problem is often decomposed into decoupled subsystems. In the framework of decentralized model predictive control (DMPC), the decentralized controllers generate their output variables, subject to a local optimization objective [Christofides et al., 2013].

On the other hand, non-cooperative and cooperative algorithms are distinguished. Considering non-cooperative MPC, each controller follows its local optimization criteria [Farina and Scattolini, 2011], where cooperative MPC enables distributed controllers to retrieve global objectives by sharing information, such as state and set point trajectories [Trodden and Richards, 2013]. Solving the optimization problem in a decentralized manner, involves to estimate the trajectories of the other subsystems and requires the subsystem states to be updated periodically by means of communication [Ferramosca et al., 2013].

Control allocation (CA): the problem of control distribution is often realized by means of control allocation [Johansen and Fossen, 2013]. It manages a multi-variable system in a centralized manner. Hierarchical control distribution for over-actuated systems is considered in [Singla and Junkins, 2007]. This aims to assign the overall control effort to the available actuators, with respect to actuator limitations. This is typically solved by means of optimization, taking different constraints and objectives into account, such as actuator limitations and energy efficiency.

Using the L_2-norm for optimization, allows for combining all actuators while minimizing the overall control effort [Grechi and Caiti, 2016]. Using the L_∞-norm, balances the control efforts while minimizing the maximal deflection for every actuator [Bodson and Frost, 2009]. The first approach results in optimal allocation, where the second approach refers to balancing allocation. Combining both by means of mixed optimization, results in optimal load balancing [Frost and Bodson, 2010].

Cooperative control: cooperative control of distributed systems aims at consensus between multiple autonomous agents. These algorithms are fully distributed, while information is exchanged between neighbouring agents. Convergence to a consensus value depends on the network topology. A finite-time consensus protocol is considered in [Liu et al., 2011]. It takes the control inputs of neighbouring agents into account. This approach improves the control performance and guarantees convergence, independent of the network topology. A decentralized synchronization protocol is discussed in [Yuan et al., 2013], which is sharing state variables between neighbouring agents.

Optimal strategies to solve the average consensus problem are discussed in [Delvenne et al., 2009]. It compares the convergence behaviour in terms of network topology and gives strategies for which consensus is guaranteed. A protocol that guarantees consensus in finite-time is presented in [Mirali et al., 2017]. Most approaches deploy an iterative scheme, where every agent updates its estimation using local values and the estimation from neighbouring agents. This procedure enables all agents to converge to the global average. An optimal weighting strategy is essential to obtain fast convergence. Concerning this weighting, a self-configuration procedure is discussed in [Dung et al., 2013]. It is shown that consensus is achieved, even for unknown topologies and varying number of agents.

Dynamic average consensus is studied in [Zhu and Martínez, 2010], where all agents have to agree to the average of a time-varying signal. This work proposes a higher-order average consensus protocol, capable to eliminate steady-state error. An other consensus protocol is considered in [Wang et al., 2019], where the system states are subject to converge towards a time-varying input signals. The convergence depends on the initial condition of the average consensus algorithm. A method for dynamic averaging with robust initial conditions is given in [Montijano et al., 2014].

More sophisticated approaches, considering reconfigurable control structures, require to find suitable control laws in an adaptive manner, e.g. see [Wen et al., 2009] and [Wang et al., 2016a] for backstepping. It takes into account a varying structure of large-scale systems, where subsystems can be added and removed. Assuming a time-varying number of sources and sinks in a system, restrict these approaches to obtain convergence in a useful time.

Contribution

Distributed high-pressure pumps can be seen as an over-actuated waterjet facility. Load balancing by adaptive control allocation would become a possible solution for synchronization. An adaptive procedure is required, since the optimal distribution of the control effort will vary with respect to the cutting heads switching states and the available high-pressure pumps. Such a global optimization requires the knowledge about all pumps involved. This information is not necessarily given for future waterjet facilities. On the other hand, cooperative MPC is prevalent for managing of distributed controllers. This requires adequate local models to track the state trajectories of each agent. Firstly, it is undesirable to provide a model for every waterjet facility.

Secondly, it would require to estimate the cutting head switching states, which affect the dynamic behaviour of a high-pressure network. In these cases, dynamic average consensus might be advantageous, tracking the average control effort of distributed pumps with respect to the time-varying water consumption of various waterjet applications. Consensus can be reached even for unknown communication topologies and varying number of agents [Dung et al., 2013]. Even if communication to an agent fails, the remaining agents will not converge to a global average, but the facility remains in operation.

This chapter applies dynamic average consensus to manage distributed high-pressure pumps. Each pump corresponds to a pump agent that provides a local estimation of the average pump rate, while exchanging the local estimation with neighbouring pumps. This approach is then extended to a distributed balancing algorithm, taking the high-pressure network into account as an additional means of communication. Each pump converges to a desired average pump rate, by adjusting its local reference pressure. Considering robustly controlled high-pressure pumps at low-level control (see Section 6.2), discrete dynamics will adequately describe the pump agents at high-level managing. However, the algorithms will be first implemented in continuous time, when assuming perfect means of communication, and the local estimations will be shared between neighbouring agents without considering delays. It further requires a bidirectional communication, using a ring topology, that results in a strongly connected graph and guarantees convergence in finite time. In reality, different constraints exists on tracking a signal of arbitrary fast dynamics with zero error, such as limited communication bandwidth, time synchronization, propagation delays, restrictions of the network topology and others. This could be improved, using a priori information about the signal dynamics and network topology.

The chapter is structured as follows: first, the problem formulation of Section 7.2 will present the objectives for average consensus and derives the need for distributed managing of high-pressure pumps, where also the communication channel is specified, using graph description. Second, distributed average consensus is adopted to estimate the average pump rate of interconnected agents. An integrated approach is then proposed in Section 7.3, that enables each high-pressure pump to converge towards an average pump rate. This aims to improve the energy efficiency of entire waterjet facilities. Both distributed algorithms will be evaluated in Section 7.4, using a detailed simulation model to represent an extended high-pressure network. This introduction provides first simulations for load balancing of distributed pumps by means of dynamic average consensus. Improvements will be subject for future investigations.

7.2 Problem formulation

The dynamic average consensus problem [Kia et al., 2013] aims at agreement of N distributed agents to a changing local reference signal $u^i(t)$. It requires to track the time-varying average

$$\bar{u}(t) = \frac{1}{N} \sum_{i=1}^{N} u^i(t) \tag{7.1}$$

of all reference signals by means of a distributed algorithm. This algorithm depends on the local reference at an agent J^i and those from direct neighbours $\{I^j\}_{j \in \mathrm{N}^i}$. Such an algorithm, of form

$$\dot{x}^i(t) = c^i(J^i(t), \{I^j(t)\}_{j \in \mathrm{N}^i}) \ , \tag{7.2}$$

assigns an agreement state $x^i(t)$ to each agent i that converges asymptotically to the average reference $\bar{u}$, such as $lim_{t \to \infty}\ x^i(t) = \bar{u}\ \forall\ i$, if a proper initialization is provided [Cherukuri and Cortés, 2016].

7.2.1 Distributed algorithm

Average consensus provides a distributed algorithm to track a static reference signal u^i, compliant with (7.2). It updates the local agreement states $x^i(t)$ with respect to the difference to the neighbouring states $x^j(t)$, such as [Zhu and Martínez, 2010]

$$\dot{x}^i(t) = -\sum_{j=1}^{N} a_{ij} \left(x^i(t) - x^j(t) \right) \ , \tag{7.3}$$

while initializing the agreement state of every agent i to its reference value $x_0^i = u^i$. For this, $a_{ij} \in \mathbb{B}^{N \times N}$ defines the interconnection between agents with respect to the communication path. That defines the logical network topology, see also the subsequent section, where $\mathbb{B} = \{0, 1\}$ is chosen to obtain a weight-balanced graph.

First-order average consensus

The dynamic average consensus algorithm [Kia et al., 2014]

$$\dot{p}^i(t) = \sum_{j=1}^{N} a_{ij} \left(x^i(t) - x^j(t) \right) \tag{7.4a}$$

$$x^i(t) = u^i(t) - p^i(t) \tag{7.4b}$$

implements a change of variable to the algorithm (7.3) by introducing $p^i = u^i - x^i$, with initial condition $\sum_{i=1}^{N} p_0^i = 0$. This replaces the derivatives on the local reference signal $\dot{u}^i(t)$ and avoids steady-state tracking error due to faulty initialization of the agreement state $x_0^i = u^i(t = 0)$. As a consequence, the most basic initialization would be $p_0^i = 0$.

The reference signal $u^i(t)$, subject for tracking, is considered as an external time-varying input. This algorithm can be extended to reduce tracking errors and to improve the convergence rate.

Robust dynamic average consensus

The distributed algorithm presented in [Freeman et al., 2006] extends (7.4a), (7.4b) to introduce robustness for initialization error and loss of agents. It does not require to know the agents positions in the network. Considering the change of variable $p^i = u^i - x^i$, yields the **extended dynamic average consensus algorithm**

$$\dot{p}^i(t) = \alpha \left(x^i(t) - u^i(t) \right) + \beta \sum_{j=1}^{N} a_{ij} \left(x^i(t) - x^j(t) \right) + q^i(t) \tag{7.5a}$$

$$\dot{q}^i(t) = \alpha \ \beta \sum_{j=1}^{N} a_{ij} \left(x^i(t) - x^j(t) \right) \tag{7.5b}$$

$$x^i(t) = u^i(t) - p^i(t) \ , \tag{7.5c}$$

which eliminates steady-state error in finite time by introducing the integral term $q^i(t)$. This algorithm allows for tuning the tracking error with parameter β, while α adjusts the rate of convergence.

A high rate of convergence is only obtained, if the reference signal is slowly varying. As a consequence, to guarantee fast convergence, the dynamics of the reference signal needs to be taken into account. Nevertheless, this algorithm is scalable as the computation and communication effort does not grow with increased network size. It guarantees convergence to average, robustness for loss of agents and packet loss.

7.2.2 Managing objectives

Future waterjet facilities combine N equivalent high-pressure pumps to supply M work stations at a time. Each pump n generates an input fluid flow $Q_n(t)$ to a network subsection. These subsections are interconnected to establish a high-pressure network with unknown topology Δ, see the high-pressure network in the diagram of Figure 7.2. Every work station m holds a cutting head of various configuration that causes an output fluid flow $Q_m(t)$ with respect to an unknown switching state $d_m(t)$. The overall water consumption varies with respect to the opening and closing of the cutting heads.

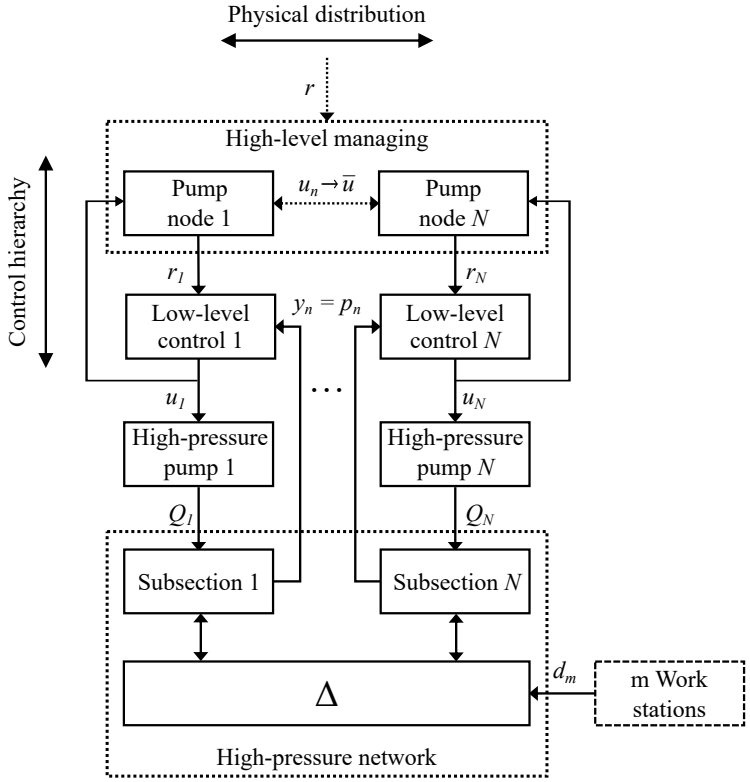

Figure 7.2 – Proposed hierarchical distributed control design for high-pressure pumps: each pump is robustly controlled at low-level to stabilize a network subsection and managed on high-level to balance the pump rate with respect to the overall water consumption.

For steady-state, the sum of input fluid flows, generated from all coupled pumps, corresponds to the sum of all output fluid flows at the work stations. The maximally available input fluid flows Q_n of every pump $n = \{1, \ldots, N\}$ must satisfy the maximally possible water consumption Q_m of every work station $m = \{1, \ldots, M\}$, such as

$$\sum_{n=1}^{N} Q_n \geq \sum_{m=1}^{M} Q_m \ . \tag{7.6}$$

Taking the switching of work stations into account, yields a time-varying water consumption $Q_m(t)$. This requires the more general condition

$$\sum_{n=1}^{N} Q_n \geq \sum_{m=1}^{M} Q_m(t) \; \forall \; t \; . \tag{7.7}$$

The switching cutting heads induce pressure fluctuations, which propagate through the high-pressure networks. The low-level control (see Section 6.2) adjusts the individual pump rates to attenuate these fluctuations and to guarantee a steady operating pressure. This cause an unbalanced pump operation, if any high-level managing is missing. These floating pumps reach arbitrary pump rates, depending on the network topology, pump positions and cutting head switching states. Consequently, a high-level managing is required to balance all coupled pumps to an average pump rate with respect to (7.1) and satisfying (7.7).

The opposing constraints for local disturbance rejection by means of low-level control (see Section 5.3) and for high-level managing of distributed pumps, require to employ a hierarchical distributed control strategy, see the high-level managing in the diagram of Figure 7.2. It presents the proposed control design for future waterjet facilities, which aims at an energy efficient operation by balancing the coupled high-pressure pumps without any centralized managing. At low-level control, each pump tracks a desired reference pressure $r_n(t)$, while attenuating pressure fluctuations. At high-level managing, each pump has to estimate the overall time-varying water consumption $\bar{u}(t)$, e.g. as previously presented by means of average consensus (7.3). The managing has then to provide a suitable local reference pressure $r_n(t)$ that every pump converges towards an average pump rate, such as $u_n(t) \rightarrow \bar{u}(t)$.

Such an algorithm for low-level control and distributed high-level managing is required to operate on every high-pressure pump. Realizing this control hierarchy with respect to a physical distribution, requires each pump to perform local computations and to provide communication to its neighbours for sending and receiving of information.

7.2.3 Communication networks

Distributed algorithms, subject to solve the average consensus problem, require to establish communication channels between neighbours. It is prevalent to introduce a graph notation [Cherukuri and Cortés, 2016], when describing entire communication networks. The initial investigations in this chapter will be restricted to a ring topology. In contrast to the directed graph in the diagram of Figure 7.3 (a), an undirected graph with unit edge weights has been considered, as shown in the diagrams (b). It allows a bi-directional communication between agents.

Referring to the general graph notation in [Bullo et al., 2009] and describing these ring topologies as a static graph, allows for rewriting the interconnection matrix a_{ij} from the dynamic average consensus problem (7.5a - 7.5c) in a graph Laplacian L, such as

$$\{Lx\}_i = \sum_{j \in \mathcal{V}} a_{ij} \left(x_i - x_j \right) \; , \tag{7.8}$$

with the variable vectors $x = [x^1 \dots x^N]$, $u = [u^1 \dots u^N]$, $p = [p^1 \dots p^N]$ and $q = [q^1 \dots q^N]$ and $\{x, u, p, q\} \in \mathbb{R}^{1,N}$.

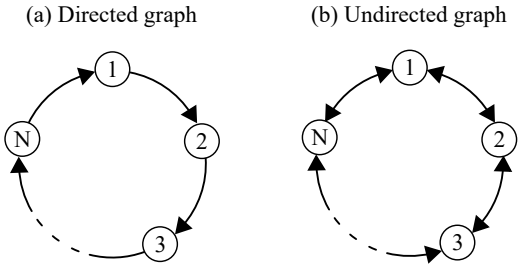

Figure 7.3 – N vertices interconnected to a ring topology using edges of unit weights: considering directed (a) and undirected (b) data transmission, resulting in strongly connected and weight balanced graphs.

The ring topology (Figure 7.3 (b)) spans a strongly connected, undirected and weight-balanced graph that describes the logical layer for bidirectional communication between neighbouring agents, using the matrices

$$A = \begin{bmatrix} 0 & 1 & 0 & & 1 \\ 1 & 0 & 1 & \cdots & 0 \\ 0 & 1 & 0 & & 1 \\ & \vdots & & \ddots & \\ 1 & 0 & 1 & & 0 \end{bmatrix} \quad \text{and} \quad L = \begin{bmatrix} 2 & -1 & 0 & & -1 \\ -1 & 2 & -1 & \cdots & 0 \\ 0 & -1 & 2 & & -1 \\ & \vdots & & \ddots & \\ -1 & 0 & -1 & & 2 \end{bmatrix} . \tag{7.9}$$

Considering the same network topology as a directed, strongly connected and weight-balanced graphs (Figure 7.3 (a)), yields the matrices

$$A = \begin{bmatrix} 0 & 1 & 0 & & 0 \\ 0 & 0 & 1 & \cdots & 0 \\ 0 & 0 & 0 & & 1 \\ & \vdots & & \ddots & \\ 1 & 0 & 0 & & 0 \end{bmatrix} \quad \text{and} \quad L = \begin{bmatrix} 1 & -1 & 0 & & 0 \\ 0 & 1 & -1 & \cdots & 0 \\ 0 & 0 & 1 & & -1 \\ & \vdots & & \ddots & \\ -1 & 0 & 0 & & 1 \end{bmatrix} . \tag{7.10}$$

On the other hand, a high-pressure network representing the physical layer is also described by means of graphs, see the modelling approach in Section 3.3. It interconnects pumps, respectively its network subsections, with respect to the fluid dynamics. Revisiting the introduction example of Section 1.2, which proposes the topology of a future waterjet facility, and adopting the graph Laplacian L, such as

$$\{L\sqrt{p}\}_i = \sum_{j \in \mathcal{V}} \vartheta_{ij} \sqrt{p_N^i - p_N^j} \, , \tag{7.11}$$

represents a physical layer, which describes the pressure propagation between network subsection by the matrices

$$\Theta = \begin{bmatrix} 0 & 1 & 0 \\ 1 & 0 & 1 \\ 0 & 1 & 0 \end{bmatrix} \quad \text{and} \quad L = \begin{bmatrix} 1 & -1 & 0 \\ -1 & 2 & -1 \\ 0 & -1 & 2 \end{bmatrix} . \tag{7.12}$$

This assigns the network subsections to pump agents as depicted in Figure 7.4, while considering the lumped parameter model (5.23), as used for low-level control design in Section 5.1.

It is distinguished between the logical layer with the pump agents, interconnected over a communication network, and the physical layer of pumps and work stations, interconnected over the high-pressure network. The physical and logical layers are most likely not of the same topology.

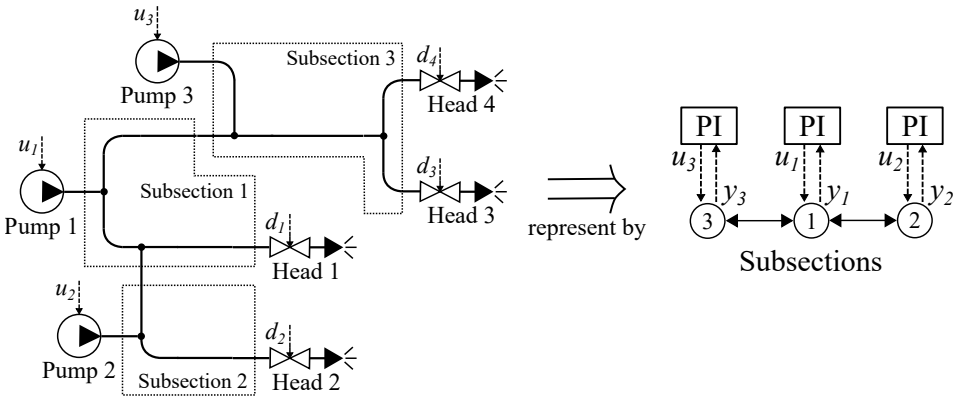

Figure 7.4 – Assignment of a high-pressure network to pump agents subject for distributed managing: each pump is controlled with a decentralized PI controller and feeds a network subsection.

7.3 Applying the distributed algorithms

Dynamic average consensus (7.4a - 7.4b) allows interconnected agents i to agree to a global average value $x^i(t) \to \bar{u}(t)$ without any centralized manager. In a subsequent step, it is required to update the local reference values r^i to track the average for the subsystem states by means of control. Average consensus is used in [Liu et al., 2011] to generate the references for formation control, when positioning vehicles with defined deviation from the average position. It is also implemented in [Mirali et al., 2017] for cooperative control, attaining the local subsystem states to reach the average values and eliminating the consensus error.

In contrast to this, multiple distributed PI controllers manipulate the flow at an edge to balance the load for all vertices in a networked system [Wei and van der Schaft, 2013]. The states of a distributed parameter system converge to average value by means of distributed balancing [Demetriou, 2013], where the physical system dynamics of the high-pressure network has been taken into account to obtain consensus.

7.3.1 Average consensus for high-pressure pumps

Applying the extended dynamic average consensus algorithm (7.5a - 7.5c) for the high-level managing of distributed pumps, aims to estimate the overall average pump rate $x^i(t) \to \bar{u}(t)$ at every agent i, as illustrated in diagram of Figure 7.5.

It is then desired to manipulate each reference signal $r^i(t)$ by means of control, see [Liu et al., 2011] and [Mirali et al., 2017], in order to allocate the overall water consumption of a high-pressure network to the available pumps, such as $u^i(t) \to x^i(t) \ \forall \ t \to \infty$. Whereas the logical layer estimates the time-varying average, the physical layer will track this average value.

7.3.2 Distributed balancing for high-pressure pumps

Considering the high-pressure network as an additional communication channel, the pressure propagation between network subsections will be used to balance the high-pressure pumps. Adopting the approaches in [Wei and van der Schaft, 2013] and [Demetriou, 2013], each pump agent i is thereby assigned to derive an individual reference pressure $r^i(t)$ by exchanging its local pump rate $u^i(t)$ with neighbouring agents. A corresponding low-level controller adjusts the local pump rate with respect to the individual pressure reference, as shown in diagram of Figure 7.6. This compensates the different pressure losses along the fluid flow paths and causes each

high-pressure pump to converge towards the desired overall average water consumption (7.1), satisfying (7.7).

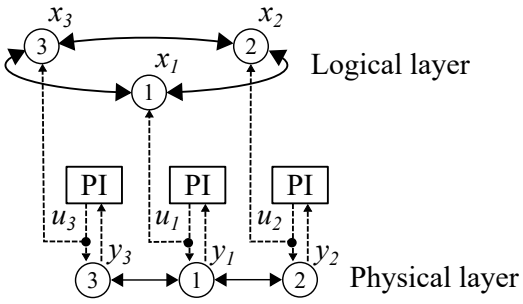

Figure 7.5 – Application of dynamic average consensus to interconnected high-pressure pumps: local pump rate and information from neighbouring pump agents are used to estimate the average water consumption.

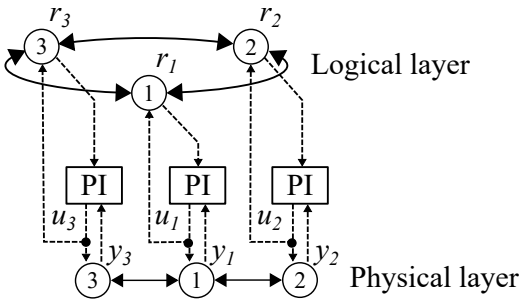

Figure 7.6 – Application of distributed balancing to interconnected high-pressure pumps: local pump rate and information from neighbouring pump agents are used to adjust the local pressure reference values, this cause the pump rates to converge to desired average value.

The coupling of subsections given by the physical layer is considered to balance the fluid flows between distributed high-pressure pumps. The desired reference pressures are obtained using the logical layer. This yields the integrated approach for average consensus by means of **distributed balancing**

$$\frac{d}{dt}r^i(t) = \alpha \sum_{j\in\mathcal{V}} a_{ij}\left(u^i(t) - u^j(t)\right) \tag{7.13a}$$

$$\frac{d}{dt}z^i(t) = K_P\left(r^i(t) - y^i(t)\right) \tag{7.13b}$$

$$\frac{d}{dt}u^i(t) = K_I\left(r^i(t) - y^i(t)\right) + z^i(t) \tag{7.13c}$$

$$\frac{d}{dt}p_N^i(t) = \frac{K(p_N^i)}{V_i^*(t)}\left(Q^i(t) - H_i^*\sqrt{p_N^i(t)}\; d_i^*(t) - \sum_{j\in\mathcal{V}} \vartheta_{ij}\sqrt{p_N^i - p_N^j}\right), \tag{7.13d}$$

which couples the logical and physical layers, such as $u^i(t) = Q^i(t)$ and $p_N^i(t) = y^i(t)$. The logical layer, defined by the interconnection matrix A, updates the neighbouring agents j with the local pump rate $u_i(t)$. The distributed managing (7.13a) adjusts the reference pressure $r_i(t)$ for the low-level controller (7.13b - 7.13c). The physical layer, defined by the interconnection

matrix Θ, distributes the change of the local pressure state p_i trough the high-pressure network (7.13d). That causes each pump rate to converge to the average pump rate $u_i(t) \rightarrow \bar{u}(t)$, which corresponds to the overall average water consumption.

Whereas the logical layer provides the average consensus error to adjust the reference values, the physical layer will balance to pump rates. The low-level controller applies integral action to the reference signal that is required to implement robustness for initialization error and to eliminate steady-state error.

7.4 Evaluation of average consensus and distributed balancing

The extended dynamic average consensus algorithm (7.5a - 7.5c) will be investigated by means of simulations, using high-pressure network models. It implements distributed pump agents to estimate the average pump rates $\lim_{t\to\infty} x^i(t) = \bar{u}(t)$. In addition, the proposed distributed managing (7.13a) is implemented to balance the pump rates to average $\lim_{t\to\infty} u^i(t) = \bar{u}(t)$, including the low-level controllers (7.13b - 7.13c) and the interconnection to neighbouring network subsections (7.13d).

The high-pressure network model, subject for simulations, has been derived using the graph-based modelling methodology of Section 4.2. It considers a network configuration with 2 distributed pumps interconnecting 2 independent cutting heads. The simulations are then extended for the setup of Figure 7.6, including three pumps and four cutting heads. The pumps are locally controlled, using the extended robust PI controller. This controller has been obtained from optimal robust H_∞ synthesis, see section 6.2. The pump agents are in both cases interconnected with a ring topology, using bidirectional communication. This results in a strongly connected and weight balanced graph, see Section 7.2.

7.4.1 Application on a 2 pump setup

Distributed average consensus has been evaluated, considering two interconnected high-pressure pumps and a high-pressure network of topology **(g) Decentralize distributed**, as introduction in Section 2.2. Referring to Table 7.1, the experiment **D-7** has been modelled, including two cutting heads of different inner diameters. The alternately switching of both cutting heads simulates a contour cutting application. This results in 4 switching states.

Table 7.1: Excerpt of experiments for use case 3: measurements derived on different test bench setups used for high-level managing.

Meas.	Topology	Presure (MPa)	Nozzle 1 ⌀(mm)	Nozzle 2 ⌀(mm)	Switch. pattern
D-7	(g) Dezen. dis.	350	0.1	0.3	Contour

The plots of Figure 7.7 show simulations with two cutting heads, which alternately switch open and close. As expected, the missing high-level managing causes a floating operation of the distributed pumps. The varying water consumption cause the high-pressure pumps to operate at different pump rates, with respect to their positions in the network and the cutting head switching states. The low-level controller attenuates pressure fluctuations and tracks the desired reference pressure of 350 MPa, while eliminating the steady-state error. The first plot provides the simulated pressure trends at the outtake position of both pumps. The second plot gives the

varying pump rates to track the desired operating pressure. The third plot gives the switching state for both cutting heads.

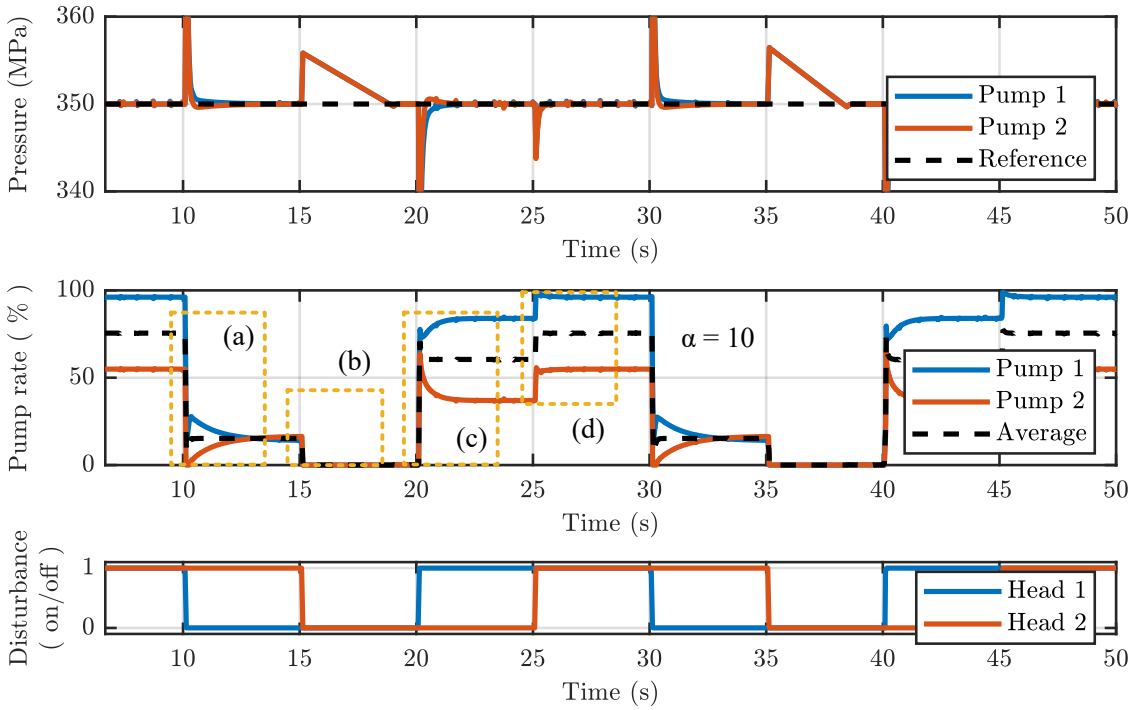

Figure 7.7 – Floating operation of 2 interconnected pumps: switching cutting heads causing the pumps to run at different pump rates, dependent on it position in the high-pressure network.

The dynamic average (7.5a - 7.5c) is found to estimate the overall average water consumption at each pump agent, even for time-varying pump rates due to the switching behaviour of cutting heads. The rate of convergence depends on the tuning variables α and β. The zoomed-in plots of Figure 7.8 illustrate the convergence when estimating the average pump rates for different α-values and for different switching states (a) - (d). The rate of convergence is enhanced, when increasing α and considering $\beta = \alpha^{-1}$, compare doted ($\alpha = 0.1$), dashed ($\alpha = 1$) and full lines ($\alpha = 10$), respectively. The global reference is given by solving for (7.1).

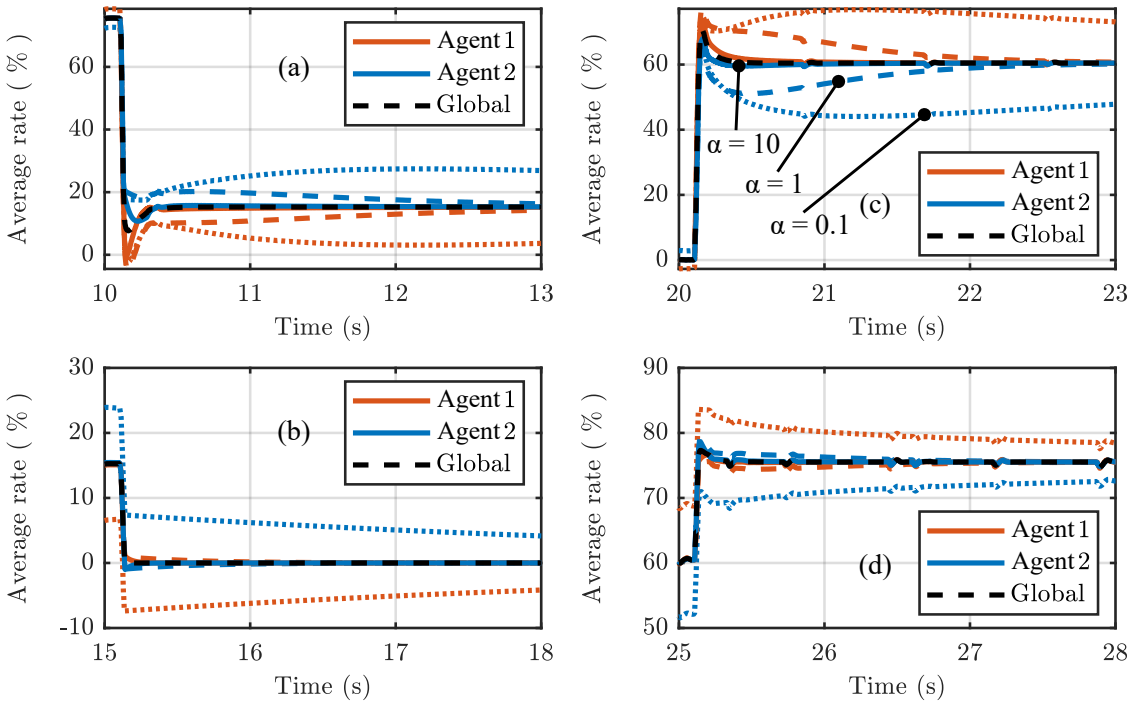

Figure 7.8 – Dynamic average consensus estimating the overall average pump rate: distributed pump agents estimating the average pump rates for different switching states and various rate of convergence.

On the other hand, distributed balancing is evaluated, using the same high-pressure network configuration of Table 7.1. The preliminary results of Figure 7.9 show again the pump output pressures, the corresponding pump rates, for both distributed pumps, and the applied switching patterns to the cutting heads. Every pump agent will adjust the local reference pressure with respect to a global reference of 350 MPa. The resulting pump output pressures will not necessary reach the global reference, but the pressure trends are expected to remain in close neighbourhood of the desired global reference. This compensates the different pressure losses along a fluid flow path with respect to the pump positions. The low-level control still attenuates pressure fluctuations due to the switching of cutting heads. However, the pump rates of each high-pressure pump will converge to the global time-varying average and satisfy the overall water consumption.

The distributed balancing (7.13a - 7.13d) is found to balance the high-pressure pumps, even for a time-varying water consumption. The rate of convergence depends on the tuning variable α. The zoom-in plots of Figure 7.10 illustrate the local references for the pump agents, considering the different switching states (a) - (d) and various α-values. The rate of convergence is enhanced by increasing α, compare doted ($\alpha = 0.01$), dashed ($\alpha = 0.1$) and full lines ($\alpha = 1$). The obtained local reference values are applied on the low-level controllers. This maintains to track the average pump rate, while compensating the different pressure losses along the fluid flow path. The plots of Figure 7.11 show the resulting pressure trends at the pump outtakes, where the plots of Figure 7.12 present the convergence of the individual pump rates to a global average.

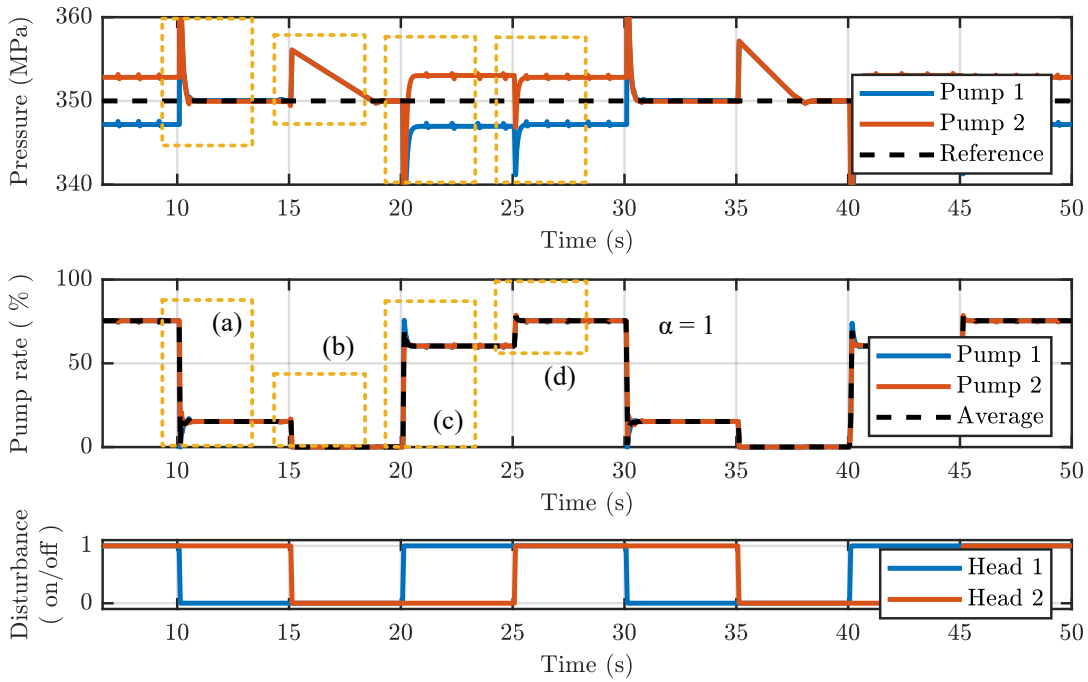

Figure 7.9 – Balanced operation of 2 interconnected pumps: distributed balancing causing the pumps to converge towards the average pump rates by manipulating the local reference pressures.

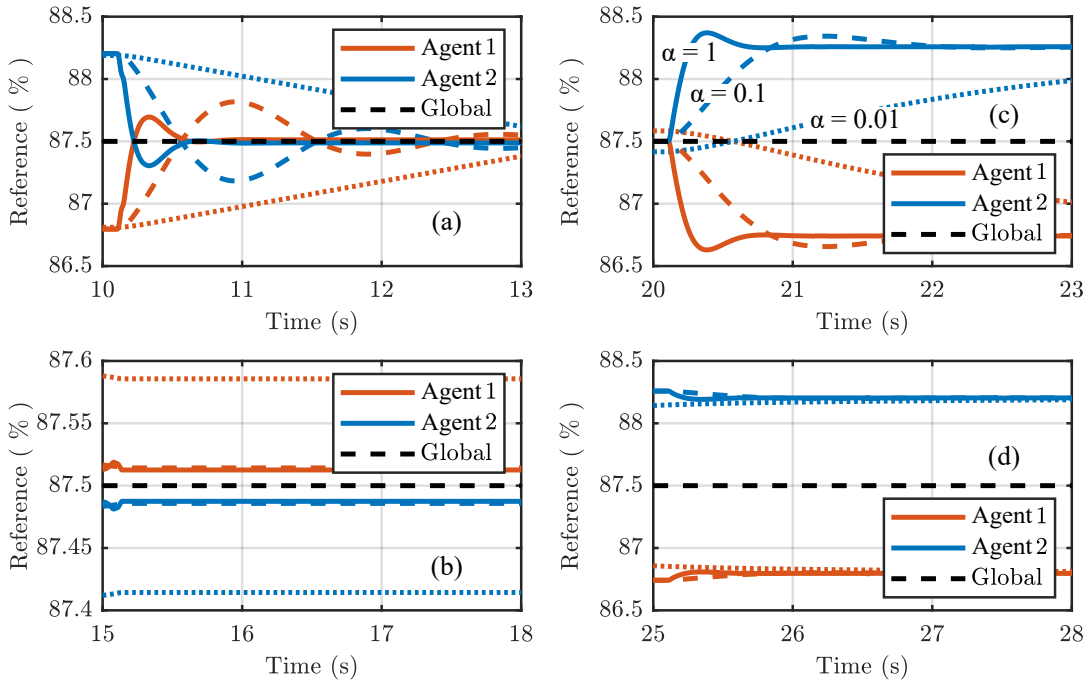

Figure 7.10 – Distributed balancing to adjust the reference pressure for each high-pressure pump: distributed pump agents estimating the desired reference pressure for different switching states and various rate of convergence.

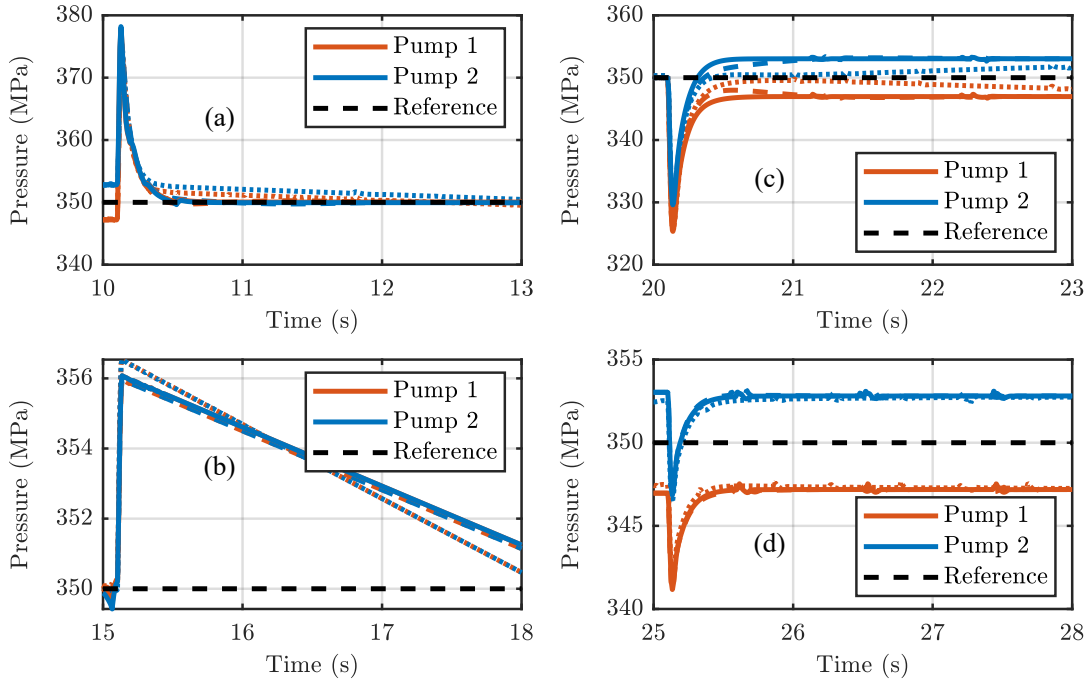

Figure 7.11 – Distributed balancing to obtain various operating pressures for each high-pressure pump: distributed pump agents estimating the desired reference pressure for different switching states and various rate of convergence.

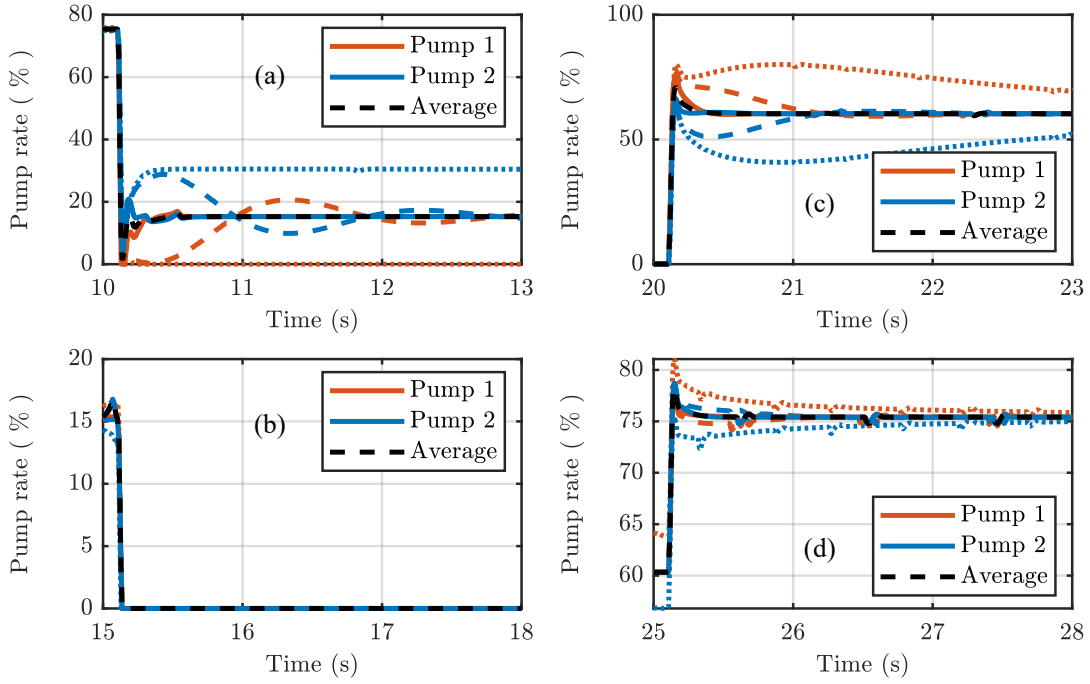

Figure 7.12 – Distributed balancing causing each high-pressure pump to average pump rate: distributed pump agents estimating the desired reference pressure for different switching states and various rate of convergence.

7.4.2 Application on a 3 pump setup

Finally, average consensus and the proposed distributed balancing are applied to the introduction example of a future waterjet facility (see Figure 7.4), taking 3 pumps and 4 cutting heads into account. The cutting heads are configured as given in Table 7.2. They will alternately switch open and close considering contour cutting. The plots (1a-1d) of Figure 7.13 show the floating operation and the estimated average pump rates, while the plots (2a-2d) realize a balanced pump operation by means of distributed balancing.

The average consensus performs as expected to estimate the global average pump rate with reasonable rate of convergence (1a). Pressure fluctuations become attenuated by means of low-level control (1b), where every pump obtains an individual pump rate, contributing to the overall water consumption (1c). The water consumption varies with respect to the cutting head switching states. Also the distributed balancing performs as expected and causes each pump to converge to the the time-varying average water consumption. The pump agents provide individual reference values (1a), which are realized for every pump output pressure (2b). The pump rates converge towards average value (2c) with respect to the time-varying water consumption.

Table 7.2: Considered configuration used to verify the high-level managing.

Pressure (MPa)	Nozzle 1 ⌀(mm)	Nozzle 2 ⌀(mm)	Nozzle 3 ⌀(mm)	Nozzle 4 ⌀(mm)	Switching pattern
200	0.45 mm	0.35 mm	0.25 mm	0.15 mm	Contour

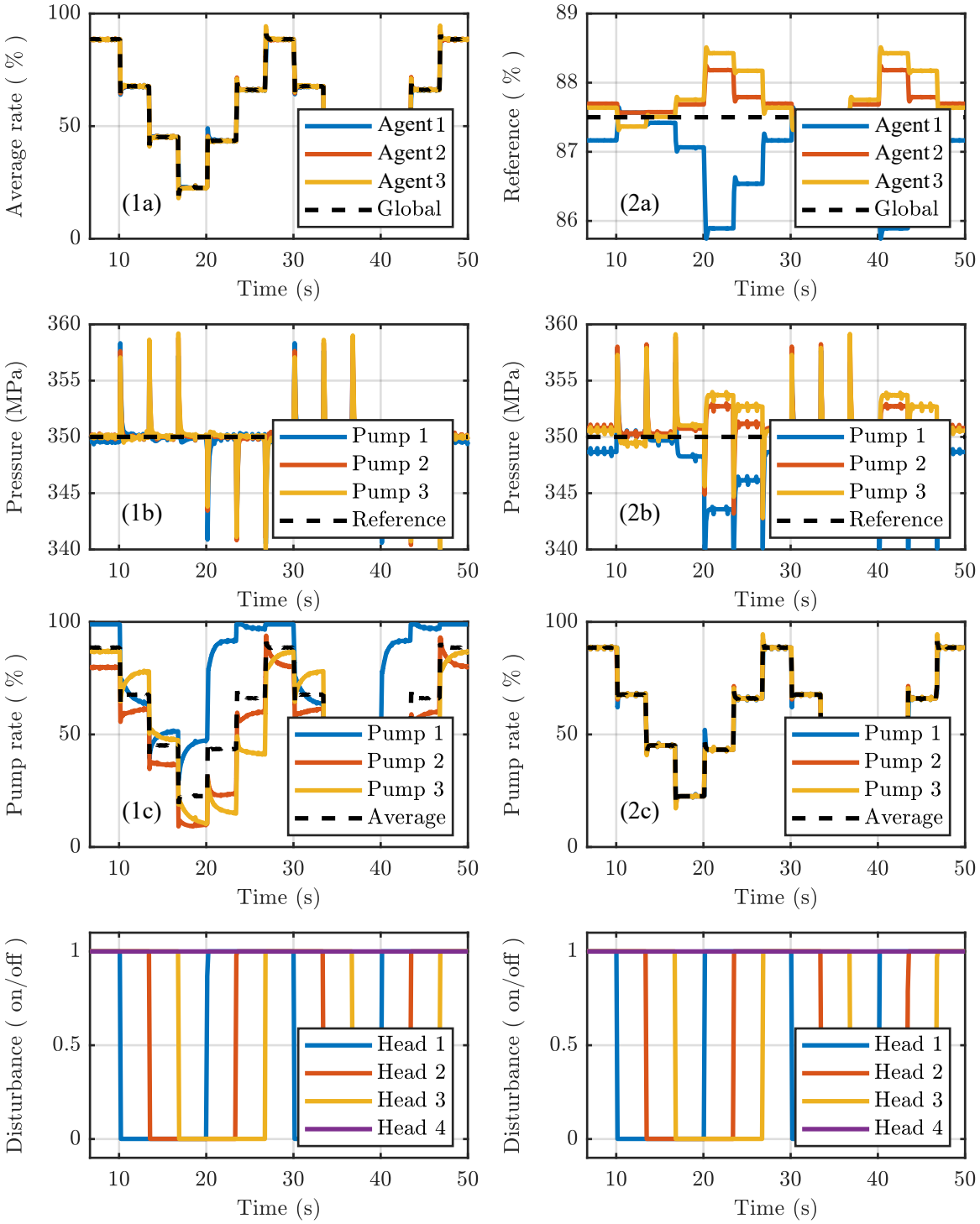

Figure 7.13 – Average consensus (left) and distributed balancing (right) applied for the introduction example: managing of 3 interconnected pumps in a high-pressure network with 4 cutting heads.

7.5 Conclusion

This chapter provides a preliminary perspective to future waterjet facilities. Dynamic average consensus has been applied to show its ability for estimating the average pump rate of distributed high-pressure pumps. The pumps within a high-pressure network remain floating, if any feedback from a managing algorithm is missing. The low-level controller holds the pump output pressures around the global reference, while switching cutting heads will disturb the pressure generation. This results in different fluid flow rates for every pump, dependent on its position in the high-pressure network. Additional control action could be implemented for each pump agent, to bring the pump rates close to average.

A contribution is given, when proposing a distributed balancing algorithm. This will directly adjust the reference pressure for each pump agent, such as the individual pump rates converge towards an average value. This approach considers the existing low-level controllers and the dynamic coupling between high-pressure pumps for balancing the individual pump rates, without implementing additional control action. Finally, the simulation results presented in this section combine all work from the previous Chapters 2 to 6. The proposed graph-based modelling represents a waterjet facility of increased complexity, which is too large to be established on the high-pressure test bench. The low-level controller, applied on every high-pressure pump, allows to distribute the local pump agents at arbitrary high-pressure network positions. The robust control design, by means of H_∞ controller synthesis, attenuates pressure fluctuations, where the high-level managing adjusts each pump to operate at the time-varying average pump rate.

This framework results in a hierarchical distributed control design for high-pressure pumps. Extended simulation studies could verify the high-level managing using the graph-based modelling methodology. On the one hand, a procedure to find optimal tuning parameters for distributed balancing has to be evaluated as well as limits on convergence and steady-state error needs to be investigated, especially when dealing with time delays, packet loss and loss of agents. Further, the ring topology, as considered to describe the communication channel between pump agents, is rarely implemented for real applications. This requires to verify the proposed distributed algorithm, also considering weakly connected and unbalanced graphs. On the other hand, the proposed distributed balancing considers a high-pressure network as an additional means of communication. Hence, it becomes essential to investigate stability of the overall algorithm with respect to various network topologies.

Conclusion and perspectives

Retrospective

The applied research of this thesis employs a design framework in compliance with industrial needs. This framework includes the robust control of electrically driven high-pressure pumps and the graph-based modelling of high-pressure networks. Improving the energy efficiency of entire waterjet facilities requires a novel concept of decentralized high-pressure pumps, which supply distributed work stations used for waterjet machining. This aims at the scaling of waterjet facilities according to their individual demands and requires a flexible distribution of modular high-pressure pumps. Industry and academia work on the prototype of an electrically driven high-pressure pump. This electrically driven pump needs a robust control design that it can be installed in an arbitrary position of a waterjet facility, where the design and verification of future waterjet facilities require a flexible modelling methodology.

The problem formulation for this thesis requires a multidisciplinary approach with a practical orientation. This asks of extending the common understanding by providing new impulses to the field of waterjet machining. First, the flexible modelling of high-pressure networks asks for simplifying the modelling task, that any individual parametrization for different network topologies becomes obsolete. Second, the robust control design for decentralized pumps requires to define the limitations to a network subsection, for which a pump can operate within desired performance. Third, the optimization of entire waterjet facilities needs a concept for balancing distributed pumps, with minimal communication demands. These objectives desire a general framework for hierarchical distributed control design of electrically driven high-pressure pumps. Thereby, the hierarchical allocation for robust control and distributed balancing should guarantee a reliable and energy efficient pump operation, while the physical distribution of the computation task among all available pumps ensures its scalability.

A high-pressure test bench has been established in the laboratory within this thesis. This includes the design of two prototypes of electrically driven high-pressure pumps. The test bench serves to validate the modelling methodology and to verify the control design. The validation work by means of measurements has been a demanding task. The properties of the test bench is close to the industrial application. It involves the common difficulties, such as a fast degradations due to the high-pressures, pressure losses due to leakages, switching delays and jitter from the PLC, etc. This makes it time intensive to reproduce experimental results, but demonstrates the close relation to the practical use of this research and the efforts to comply with industrial requirements. Especially, the work with preliminary pump prototypes has complicated the experimental studies. Indeed, the malfunction of check-valves disturbed the obtained measurement data, compromising the presented research results. Even worse, the sever damage of a pump prototype has caused to terminate the experimental studies earlier as planned.

Contributions

The design framework for hierarchical distributed control design of electrically driven high-pressure pumps combines the results from multiple fields of research. Thus, a general contribution is given by adopting established methods from the theory to realize practical solutions with respect to industrial constraints.

The first part of this thesis is dedicated to merge the common knowledge in the field of waterjet machining. A contribution is given, when classifying waterjet machining with respect to the work station setup, cutting head configuration and manufacturing process. The common setups of high-pressure pumps are presented, including novel electrically driven pumps [Niederberger

and Kurmann, 2017]. Network topologies and use cases are defined, which consider common waterjet applications. Extending these specifications contributes to the design of future energy efficient and scalable waterjet facilities. Presenting the design of the novel electrically driven high-pressure pump, provides another contribution when applying the concept of model-based synchronization by means of camming [Niederberger, 2018].

The second part provides a simulation toolbox for the flexible modelling of high-pressure networks. It assigns the governing equations from fluid dynamics to the versatile graph theory. This yields a graph-based modelling methodology. That simplifies the modelling and introduces a spacial discretization, resulting in a lumped parameter model. A simulation study evaluates the effect of this discretization. It compares the simulation results from the lumped parameter model with the results when numerically solving the PDE's, which describe the principles of continuity and momentum conservation. A contribution is given when considering the most prevalent parameter variations to improve simulation accuracy over a wide pressure range [Niederberger et al., 2018]. In contrast to other modelling methodologies, this modelling introduces a pressure-dependent bulk modulus and relates this to a pressure-dependent fluid density. The simulation toolbox is finally proposed, when implementing the graph-based modelling methodology into *MATLAB Simulink* and providing an experimental parameter identification for specific high-pressure components. This toolbox is valuable for industry. It allows for modelling of various waterjet facilities without the need of an individual parametrization. A major contribution is given, when applying this toolbox to model different high-pressure networks and validating the obtained network models by means of measurements [Niederberger et al., 2019c]. The graph-based modelling methodology is useful for the simulation of more complex high-pressure networks, which exceeds the capability of a test bench. This allows for evaluating of low-level control and high-level managing with reduced effort and cost, in contrast to time expensive experiments at an extended test bench.

The third part proposes a robust low-level control design for high-pressure pumps, capable to stabilize a network subsection. It provides a single controller for all high-pressure pumps, independent of the operating point, the high-pressure network topology and its location in the network. This robust control design enables the industry to reduce the effort for installing a pump in a facility and facilitates the application of the novel electrically driven pump. The procedure of specifying control objectives in time domain, then transforming them in frequency domain, is effective to find suitable weighting functions. Robustness is introduced by lumping the uncertain parameters, using an unstructured uncertainty description. Comparing different system descriptions for varying parameters, applying different uncertainty descriptions and describing the generalized plant, using a signal-based approach, contribute to the robust control design for high-pressure pumps. Defining the generalized plant for a high-pressure pump employs the optimization problem for H_∞ controller synthesis. Another contribution is given, when merging input channels to reduce the dimension of the resulting optimization problem by means of joint shaping functions [Niederberger et al., 2019b].

Solving the reduced H_∞ optimization problem, considering an unstructured as well as a structured approach, provides various state feedback and PI controllers. A major contribution is given by a detailed simulation study that compares the derived controllers by means of simulations. An extended PI controller has been found suitable for implementation on the high-pressure pump with respect to industrial needs. Introducing the Δ-K iteration to derive a quasi-optimal controller by adjusting the unstructured uncertainty, aims to obtain robust stability for a maximally permissible uncertainty range. This provides a practical use and provides a straight forward procedure for optimal H_∞ controller synthesis, in particular when unstructured uncertainties and structured controllers are involved. Demonstrating that the concept of distributed balancing by

means of average consensus will balance the pumps to a time-varying average pump rate, gives eventually a perspective to the managing of distributed pumps and to the objective of energy efficient waterjet facilities [Niederberger et al., 2019a].

Perspectives

The hierarchical distributed control design for electrically driven high-pressure pumps provides a general framework to the industry to design and to optimize future waterjet facilities. The main objective of this research work is to follow a global approach and thereby to initiate future research activities in the field of distributed high-pressure pumps. Improving the graph-based modelling methodology, it could be very interesting to introduce and to evaluate higher order models, which take the principles of continuity and momentum conservation into account without solving for equilibrium. Then, possible time delays due to pressure propagation along large piping could become subject for further investigations by means of measurements. This could provide improved simulation models and enhance the control design for large-scale waterjet facilities. Also, the friction loss along network subsections requires detailed evaluation by means of measurements. The current representation of friction along a piping is insufficient for the different fluid flows in a high-pressure network. Thus, an extended friction loss model is highly desired. On the other hand, the industry is interested to extend the simulation toolbox with more standardized high-pressure components. This requires detailed studies for parameter identification. Check-valve malfunctions degrade the benefits of an electrically driven high-pressure pump. It is of interest to understand these phenomena and improve the pump design.

Refining the low-level control design, it could become interesting to replace the simplified and linearised first-order model with an higher order representation or to investigate the effect of time delays to the robustness. Lumping parametric perturbations to a unstructured uncertainty description and assuming a single parameter for optimization is very useful for controller synthesis, but requires further verification. Considering more complex uncertainty descriptions would further allow for reducing the conservativism for the proposed control design and could enhance performance. The obtained robust stability and performance of the proposed quasi-optimal PI controller requires verification on a test bench, considering various high-pressure network topologies while taking the permissible uncertainty range into account. On the other hand, detailed experimental studies would be of interest to investigate possible couplings between decentralized pumps and to prove the robust stability and performance for installations to various waterjet facilities.

Considering possible couplings to neighbouring pumps as exogenous disturbances is again an interesting approach for control design. Extending the control design by taking the coupling of decentralized pumps into account, would allow for improving the stability of the overall system, but increases the computational requirements. It is further desired to investigate the requirements on stability for the proposed distributed balancing of decentralized pumps. Testing the distributed balancing on the test bench would provide first results concerning performance and stability. It is required to define the restrictions on the network topology at physical and logical layer, with respect to the convergence. A practical benefit is expected, when investigating the robustness for loss of pump agents in runtime, when considering discrete computation and when introducing event triggered communication. Thus, graph-based modelling, low-level control and high-level managing are subject for ongoing investigations and motivate future research work, considering time delays, robustness, decentralization, convergence, etc.

Appendixes

A

Detailed results for model validation

Contents

A.1 Single cutting head experiments

A.1.1 Ramping: single cutting head

The start up and shut down of the pump follows a reference value ramping. Both is convenient to observe the reference value tracking that will be used to verify the simulation model for a wide pressure range. The plots of Figure A.1 and A.2 shows the simulated and measured pressure trends during start up and shut down for a operating point of 200 MPa (measurement B-4) and 350 MPa (measurement B-7), respectively. The input and system pressure are given in the first plot, both output pressures in the second plot and the corresponding pump rate in the third plot.

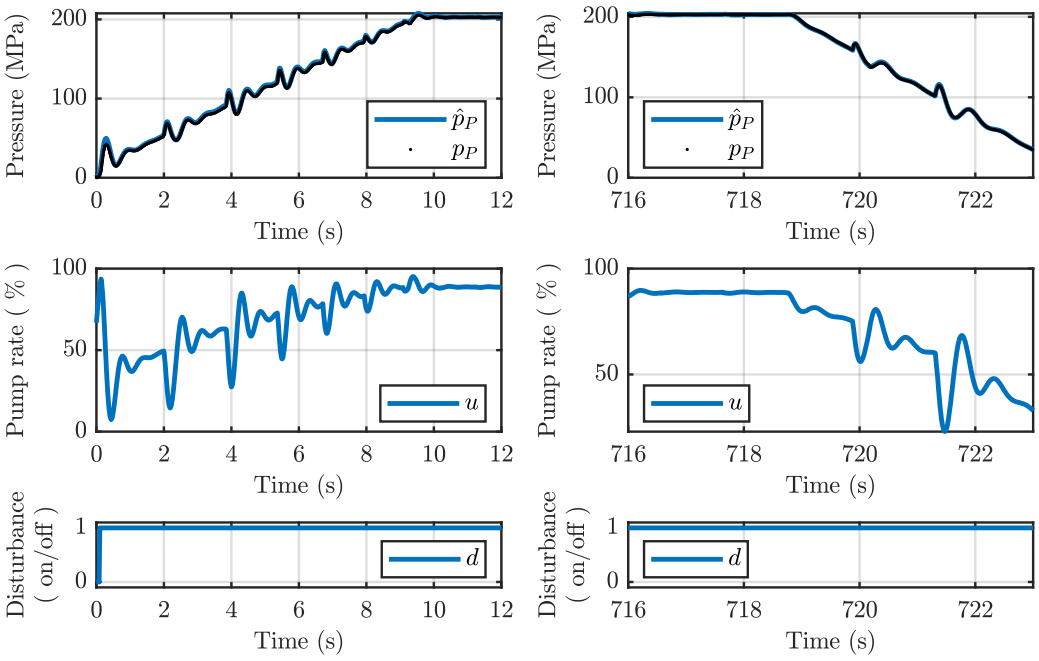

Figure A.1 – Start up and shut down ramping of experiment B-1 considering a 1 pump - 1 cutting head setup at 200 MPa: start up pressure trend (a) and shut down pressure trend (b).

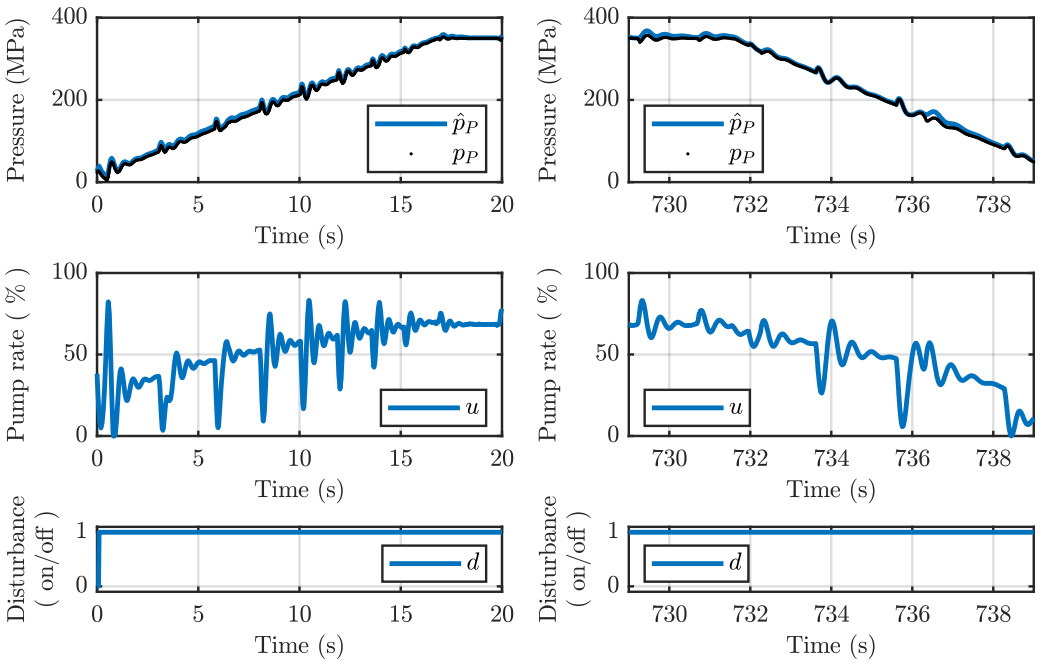

Figure A.2 – Start up and shut down ramping of measurement B-7 considering a 1 pump - 1 cutting head setup at 350 MPa: start up pressure trend (a) and shut down pressure trend (b).

Zoomed-in trends are illustrated in Figure A.3 and A.4 for the first section of a ramp and in Figure A.5 and A.6 for the last section of a ramp.

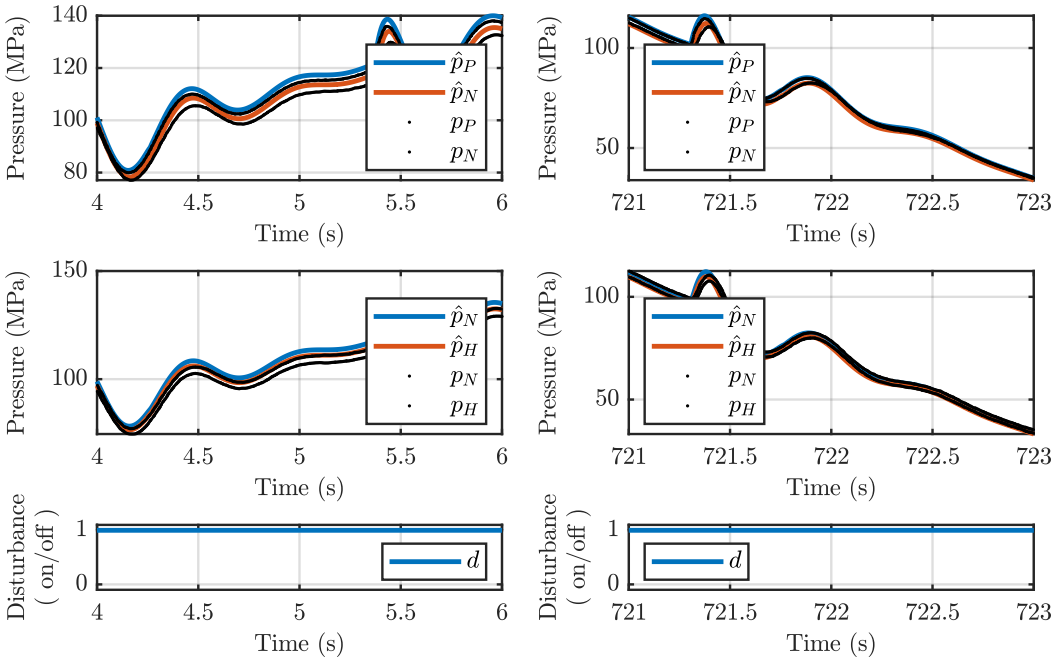

Figure A.3 – Zoom-in around 100 MPa of ramping for 200 MPa operating point: pressure trends during start up (a) and shut down (b).

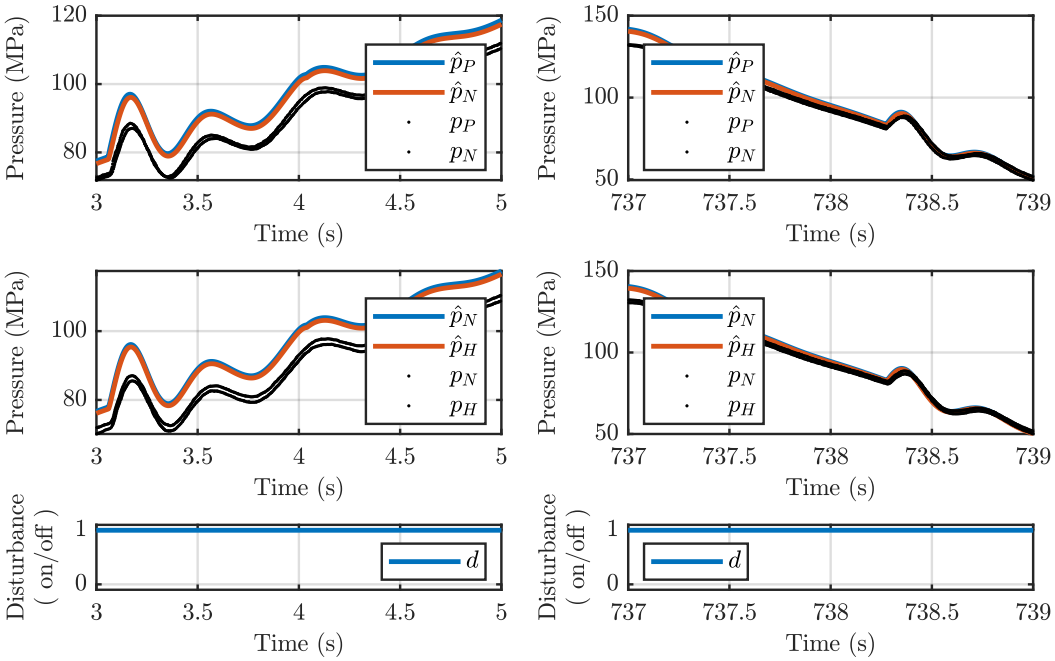

Figure A.4 – Zoom-in around 100 MPa of ramping for 350 MPa operating point: pressure trends during start up (a) and shut down (b).

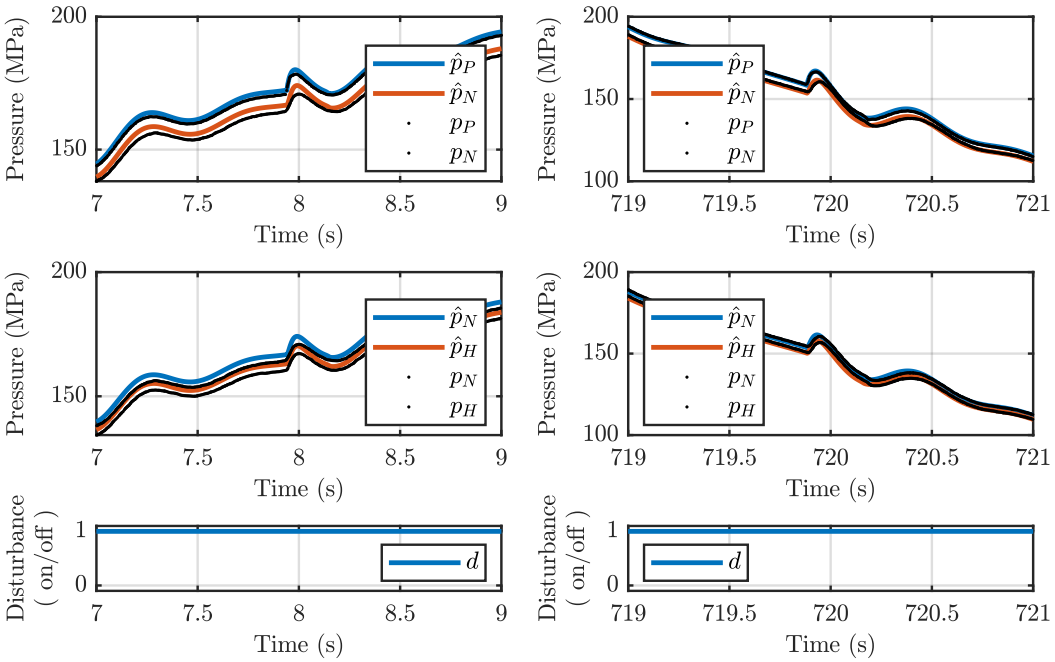

Figure A.5 – Zoom-in around 150 MPa of ramping for 200 MPa operating point: pressure trends during start up (a) and shut down (b).

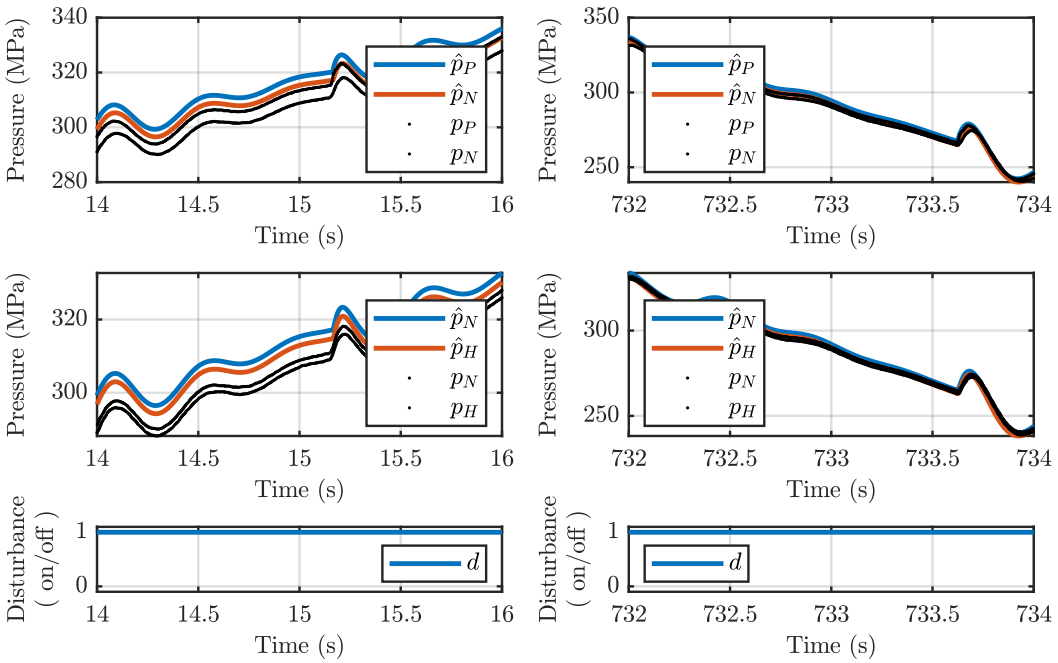

Figure A.6 – Zoom-in around 300 MPa of ramping for 350 MPa operating point: pressure trends during start up (a) and shut down (b).

A.1.2 Contour cutting: single cutting head

The reference value will first ramp up to the desired operating pressure of 200 and 350 MPa. The measurement p_{in} is chosen as control value. At the end, the reference value will ramp down to release the pressure. In between the cutting head will switch to close position, as shown in plots of Figure A.7 and A.8. That will cause the high-pressure pump to a full stop, resulting in a pressure increase. The cutting head will then switch to open position what causes a pressure loss and the pump returns in operation. The cutting head is configured with a nozzle of 0.35 mm inner diameter, considering the 200 MPa setup of measurement B-4. Thus, a maximal fluid flow rate of 2.4 l/min results for a pump rate of 100%. The cutting head is configured with a nozzle of 0.25 mm inner diameter, considering the 350 MPa setup of measurement B-7. Thus, a maximal fluid flow rate of 1.6 l/min results for a pump rate of 100%.

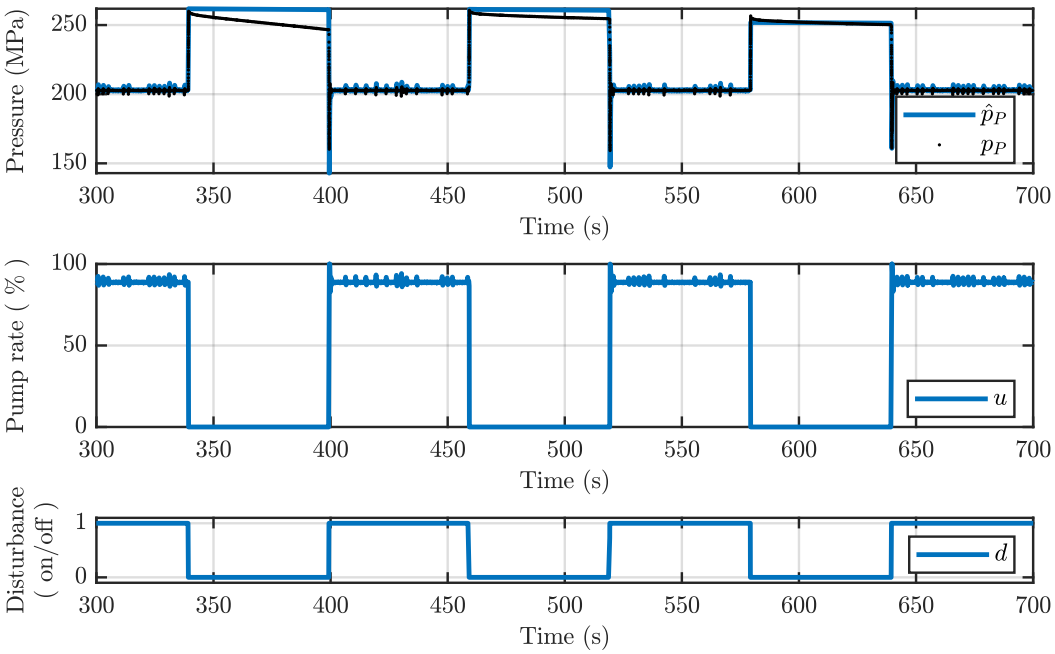

Figure A.7 – Overview of experiment B-4: 1 pump - 1 cutting head setup with 0.35 mm nozzle at 200 MPa operating pressure.

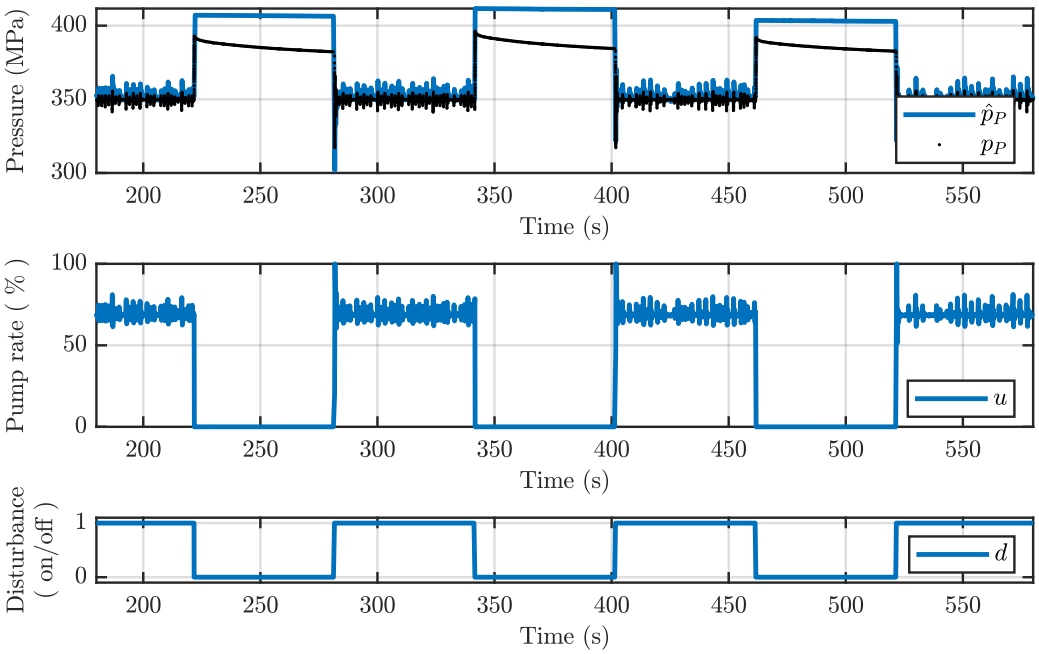

Figure A.8 – Overview of experiment B-7: 1 pump - 1 cutting head setup with 0.25 mm nozzle at 350 MPa operating pressure.

The plots of Figure A.9 and A.10 give the pressure trend when opening (a) and closing (b) the cutting head entirely considering the 200 MPa and the 350 MPa setup, respectively. The input and system pressure are given in the first plot, both output pressures in the second plot and the corresponding switching pattern in the third plot.

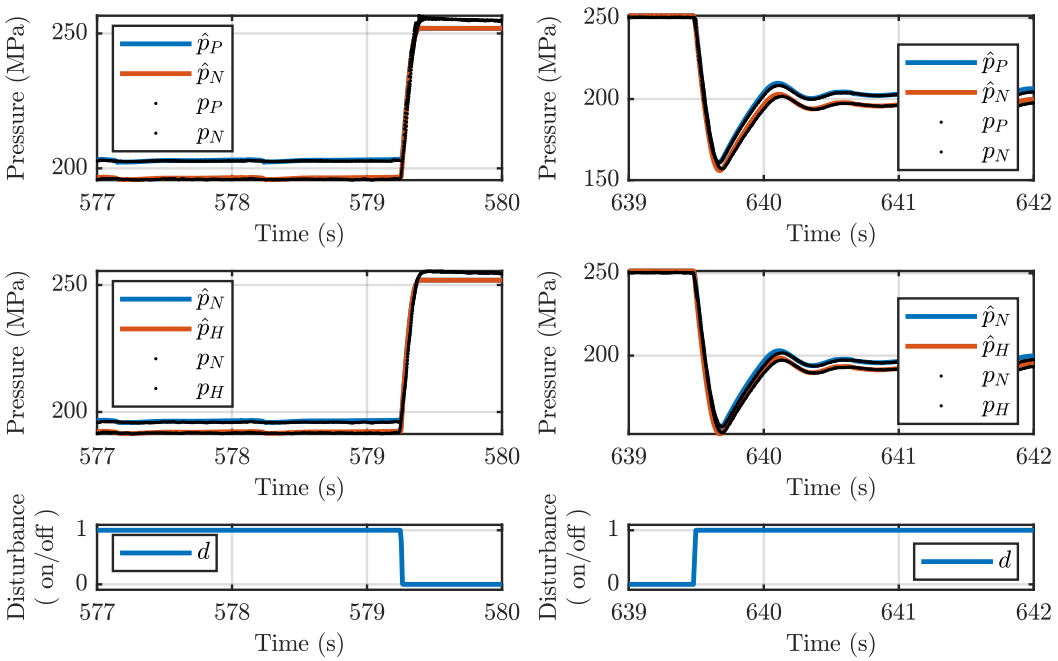

Figure A.9 – Switching cutting head of the 1 pump - 1 cutting head setup at 200 MPa: closing cutting head pressure trend (a) and opening cutting head pressure trend (b).

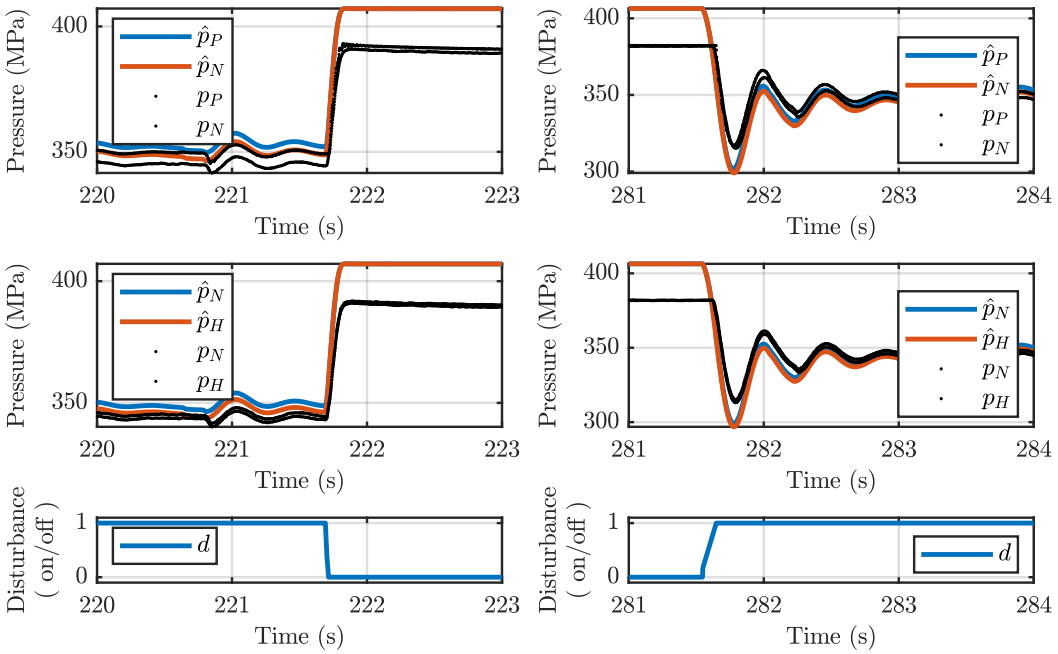

Figure A.10 – Switching cutting head of the 1 pump - 1 cutting head setup at 350 MPa: closing cutting head pressure trend (a) and opening cutting head pressure trend (b).

A.1.3 Cavity cutting: single cutting head

The cutting head will switch open and close with a period of 0.5 seconds whereas the pump tries to maintain an operating point of 200 MPa. The fluid flow consumption for measurement B-5 will vary as shown in Figure A.11. The cutting head is again configured with a nozzle of 0.35 mm inner diameter. Thus, a maximal fluid flow rate of 2.4 l/min results for a pump rate of 100%.

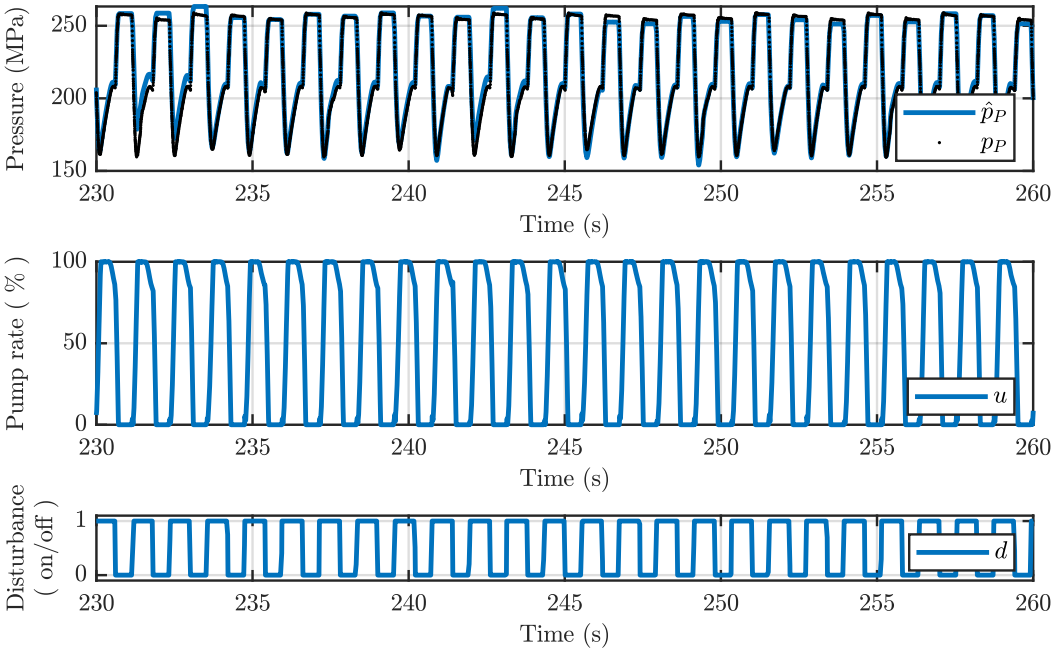

Figure A.11 – Overview of experiment B-5: fast switching disturbance for a 1 pump - 1 cutting head setup at 200 MPa operating point.

Figure A.12 shows detailed trends for the input and system pressure in the first plot, the output pressures in the second plot, as well as the switching pattern in the third plot.

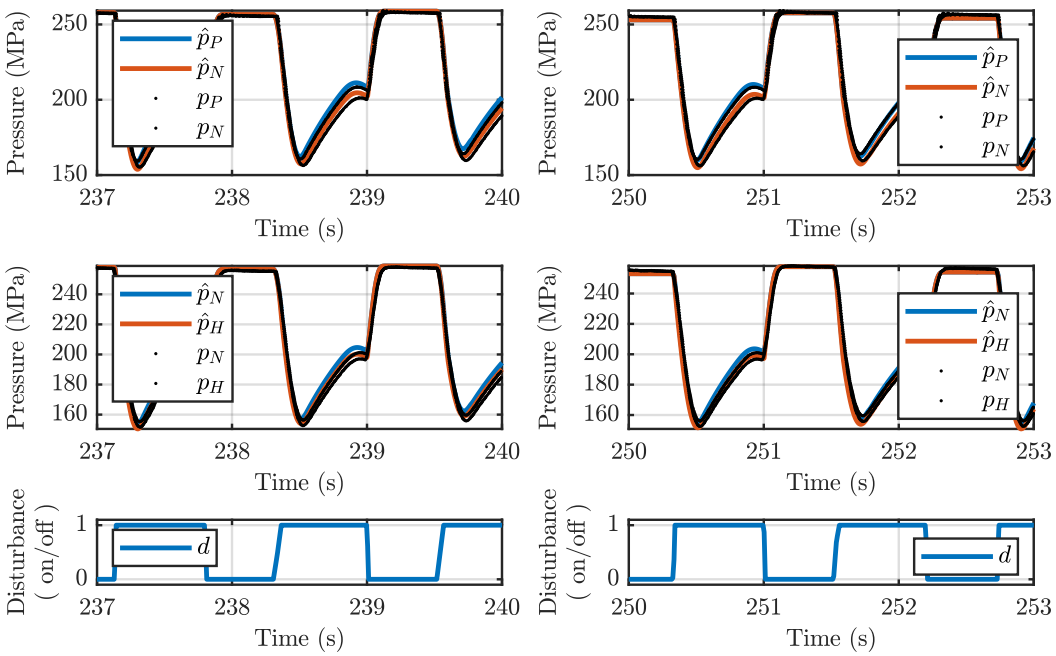

Figure A.12 – Fast switching disturbance for a 1 pump - 1 cutting head setup: zoom-in at different sample times.

A.2 Multiple cutting heads experiments

A.2.1 Contour cutting: asymmetric cutting heads

A continuous operating point of 350 MPa pressure is chosen. Two cutting heads will open and close alternately with a phase shift of 90°. Considering the measurement E-9, cutting head 1 holds a nozzle of 0.2 mm inner diameter while the cutting head 2 is configured with a 0.1 mm nozzle considering the 350 MPa setup. As a consequence four different fluid flows will result $Q(t) \in \{0,\ 0.27,\ 1.01,\ 1.28\}$ l/min. The plots of Figure A.13 shows input pressure trend, input fluid flow and cutting head switching pattern for simulation and measurement over an entire switching cycle.

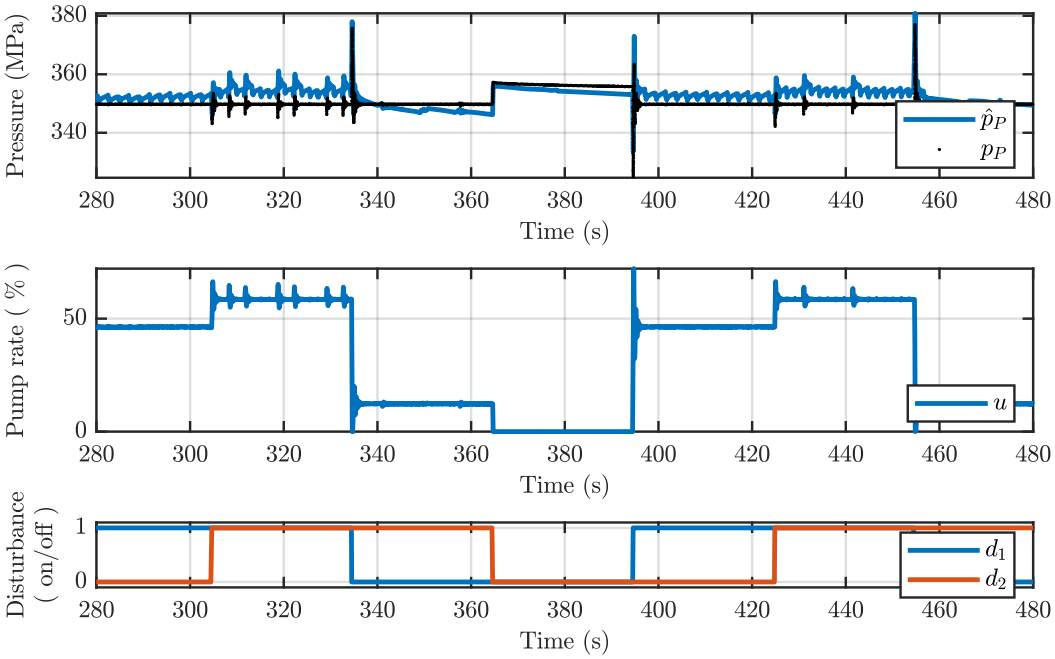

Figure A.13 – Overview of experiment E-9 considering a 1 pump - 2 cutting head setup at 350 MPa with different nozzle sizes: pressure trend $p_P(t)$ and pump rate $u(t)$ due to switching pattern $d(t)$ for selected switching cycles.

Zoomed-in plots for every measurement positions are given in the subsequent plots, when first opening cutting head 1 followed by opening cutting head 2 and then closing head 1 followed by closing head 2. The plots of Figure A.14 show the zoom-in for opening and closing cutting head 1, where the plots of Figure A.15 show the zoom-in for opening and closing cutting head 2. The input and system pressure are given in the first plot, both output pressures in the second plot and the corresponding switching pattern in the third plot.

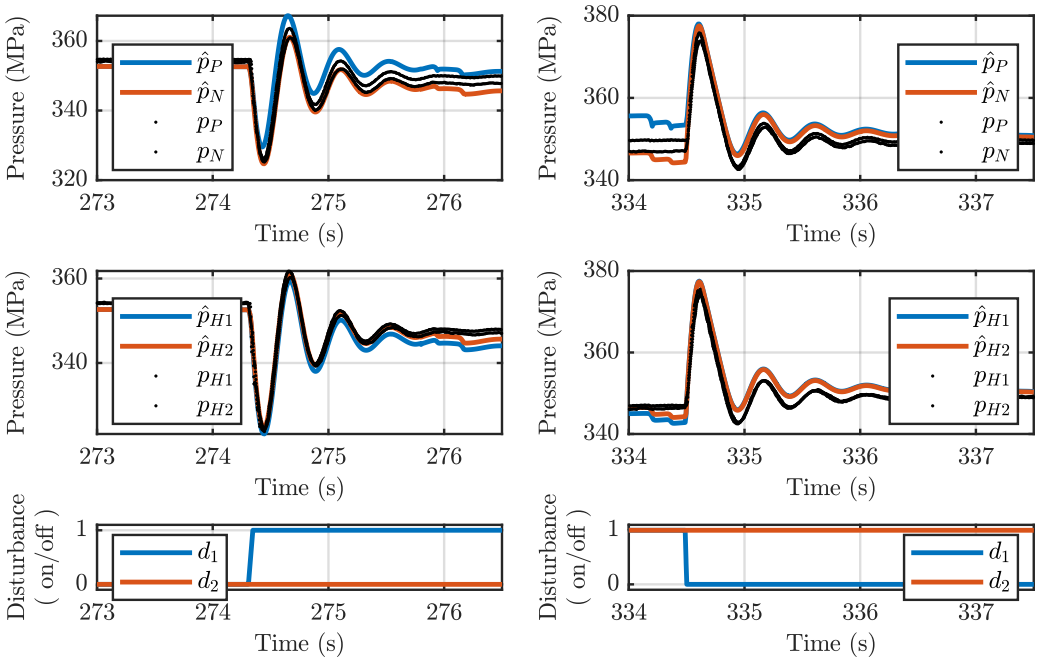

Figure A.14 – Zoom-in pressure trends of the 1 pump - 2 cutting head setup at 350 MPa: opening of cutting head 1 (a) and closing of cutting head 1 (b).

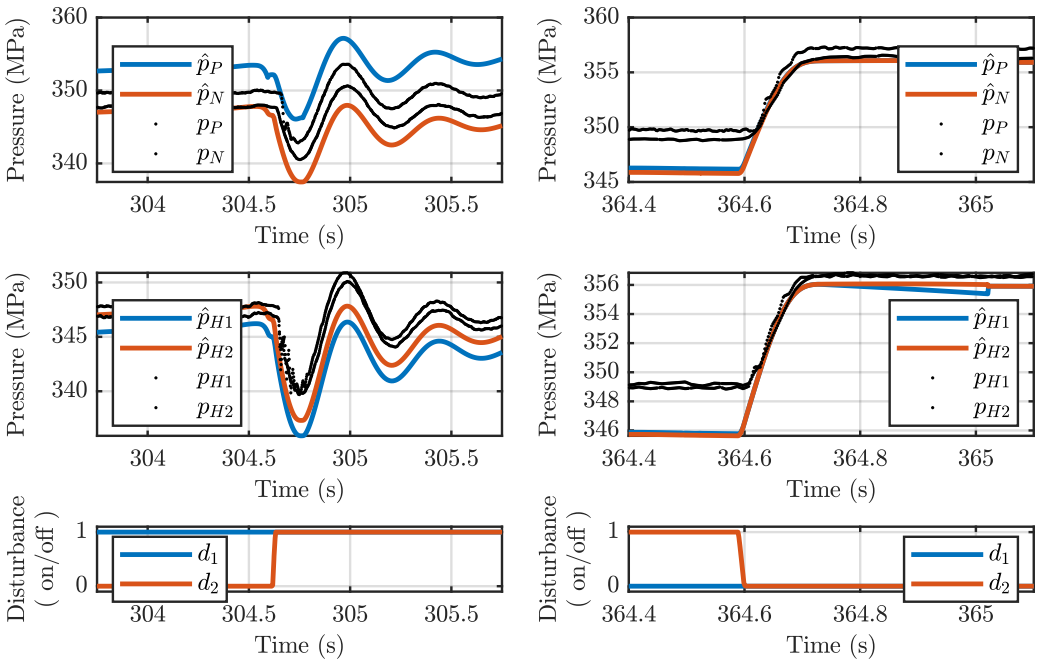

Figure A.15 – Zoom-in pressure trends of the 1 pump - 2 cutting head setup at 350 MPa: opening of cutting head 1 (a) and closing of cutting head 1 (b).

A.2.2 Contour cutting : symmetric cutting heads

A continuous operating point of 350 MPa pressure is chosen. Two cutting heads will open and close alternately with a phase shift of 90°. Considering the measurement E-13, both cutting heads hold a nozzle of 0.15 mm inner diameter. Four different fluid flows will result $Q(t) \in \{0,\ 0.61,\ 0.71,\ 1.32\}$ l/min. The fluid flow differs slightly between each nozzle due to the asymmetric network configuration which causes different pressure losses across each piping section. The plots in Figure A.16 show input pressure trend, input fluid flow and cutting head switching pattern for simulation and measurement over an entire switching cycle.

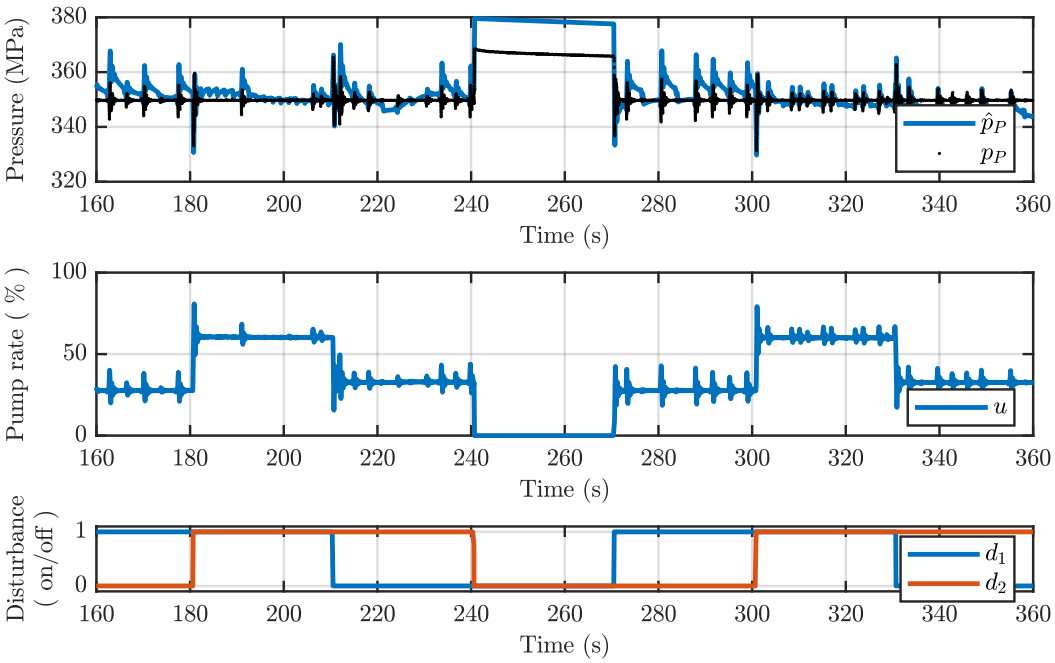

Figure A.16 – Overview of experiment E-13 considering the 1 pump - 2 cutting head setup at 350 MPa with nozzles of the same size: pressure trend $p_P(t)$ and pump rate $u(t)$ due to switching pattern $d(t)$ for selected switching cycles.

Zoomed-in plots for every measurement positions are given in the subsequent plots, when first opening cutting head 1 followed by opening cutting head 2 and the closing head 1 followed by closing head 2. The plots of Figure A.17 show the zoom-in for opening and closing cutting head 1, where the plots of Figure A.18 show the zoom-in for opening and closing cutting head 2. The input and system pressure are given in the first plot, both output pressures in the second plot and the corresponding switching pattern in the third plot.

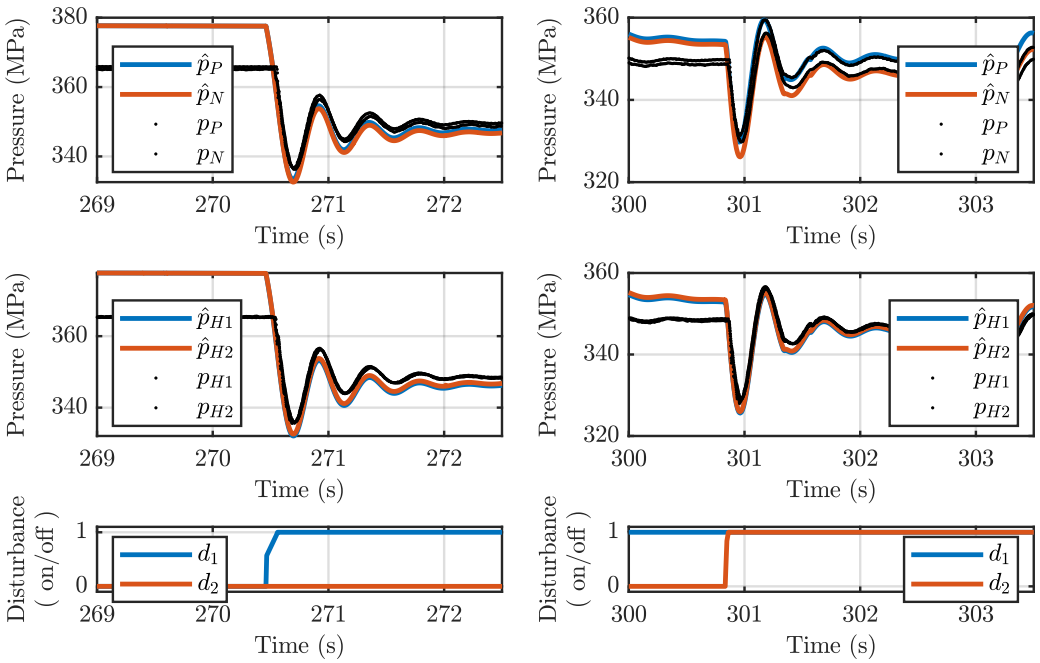

Figure A.17 – Zoom-in pressure trends of the 1 pump - 2 cutting head setup at 350 MPa: opening of cutting head 1 (a) and closing of cutting head 1 (b).

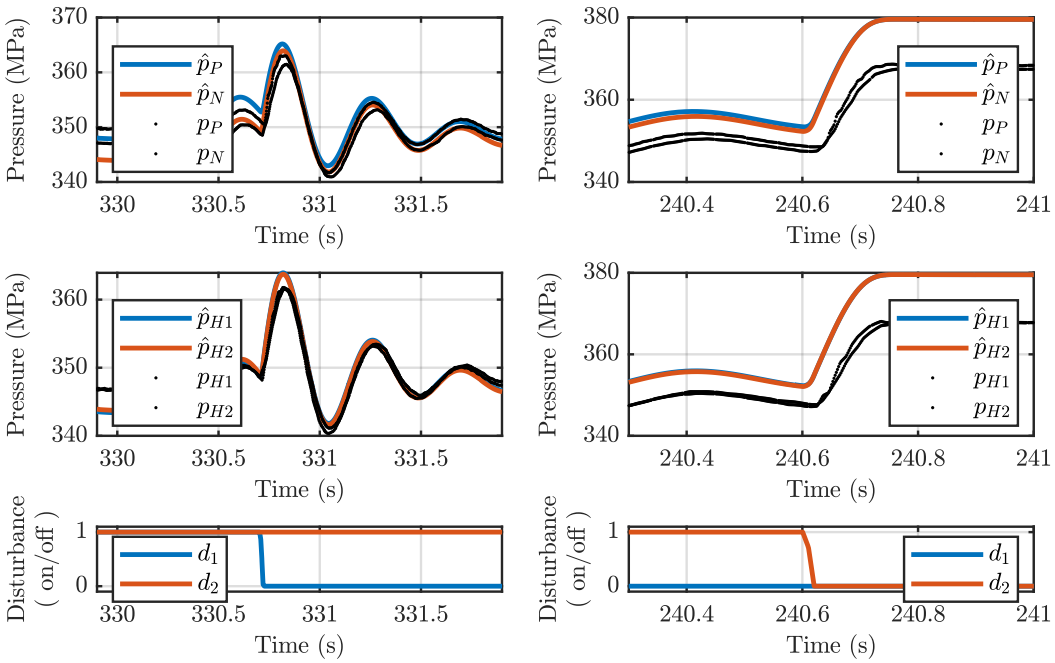

Figure A.18 – Zoom-in pressure trends of the 1 pump - 2 cutting head setup at 350 MPa: opening of cutting head 1 (a) and closing of cutting head 1 (b).

Cavity cutting: asymmetric cutting heads

Two cutting heads will switch open and close with a period of 0.5 seconds whereas the pump tries to maintain an operating point of 200 MPa. For a first case, cutting head 1 is switching only while the cutting head 2 remains closed. For a second case, cutting head 2 will join causing both cutting heads to switch almost synchronously. For a third case, cutting head 1 closes entirely while the cutting head 2 continuous to switch. The resulting pressure trends and pump rate for measurement B-7 is given in Figure A.19. The cutting head 1 is again configured with a nozzle of 0.3 mm inner diameter where a 0.2 mm nozzle is installed in cutting head 2.

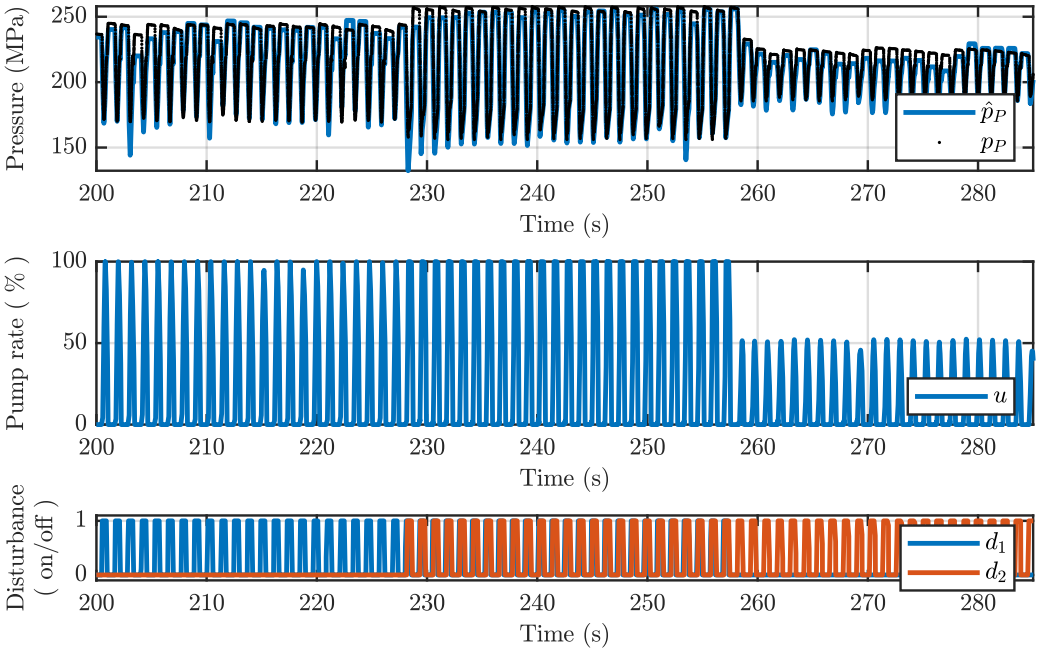

Figure A.19 – Overview of experiment E-7: fast switching disturbances for a 1 pump - 2 cutting head setup at 200 MPa operating point.

Figure A.20 shows detailed trends for the first case mentioned above. The input and system pressure is given in the first plot, the output pressures in the second plot, as well as the switching pattern in the third plot. Equally Figure A.21 and Figure A.22 show the second and third case.

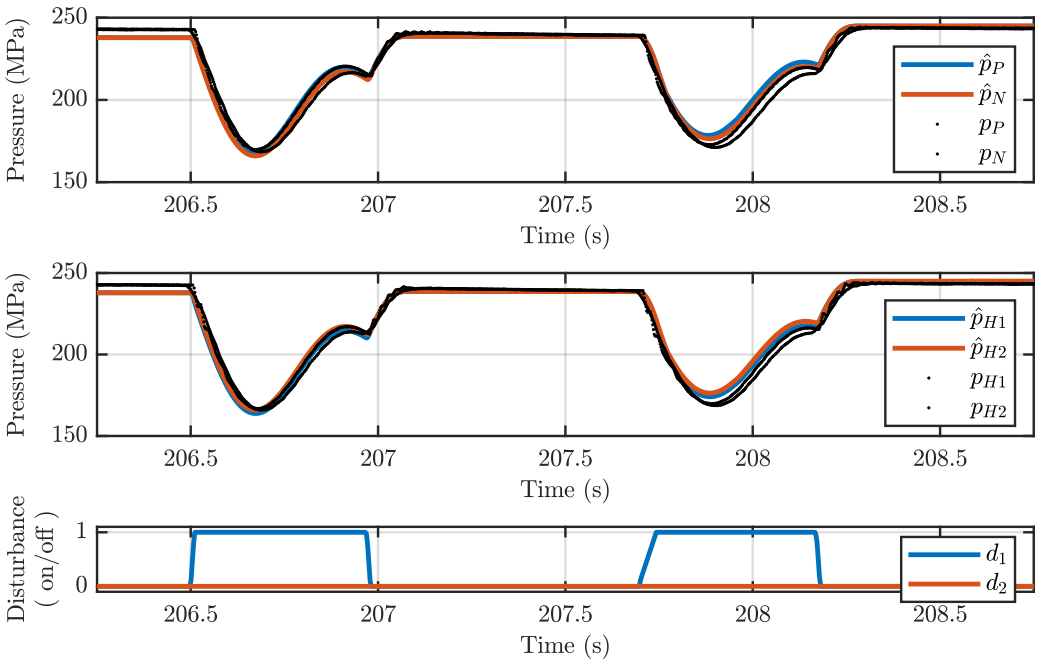

Figure A.20 – Fast switching disturbance for a 1 pump - 2 cutting head setup: zoom-in when switching of head 1.

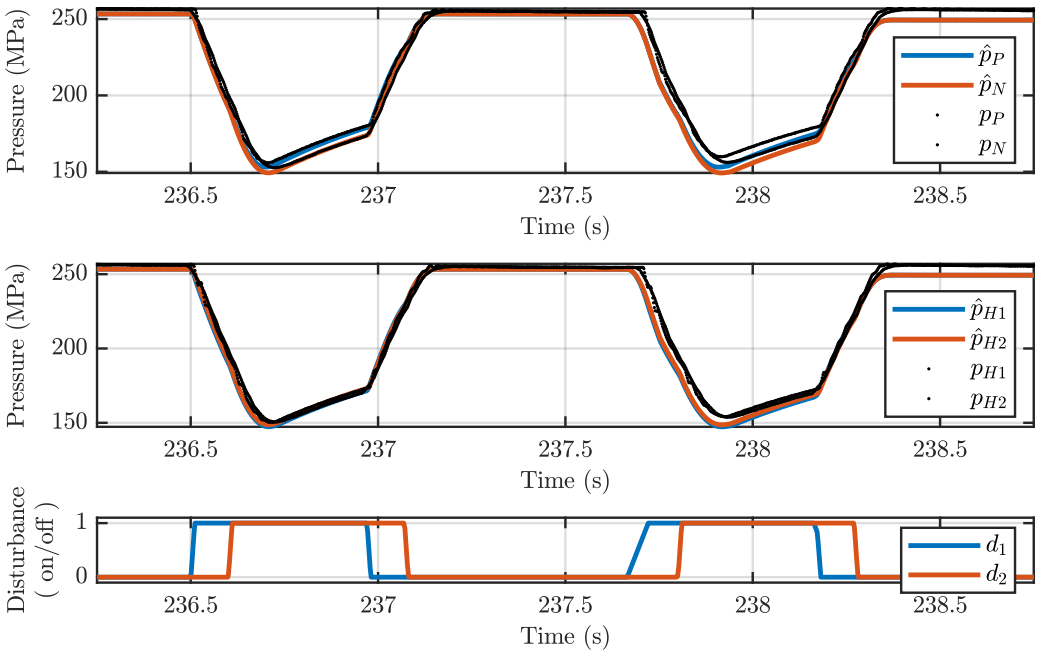

Figure A.21 – Fast switching disturbance for a 1 pump - 2 cutting head setup: zoom-in when almost simultaneously switching of head 1 and 2.

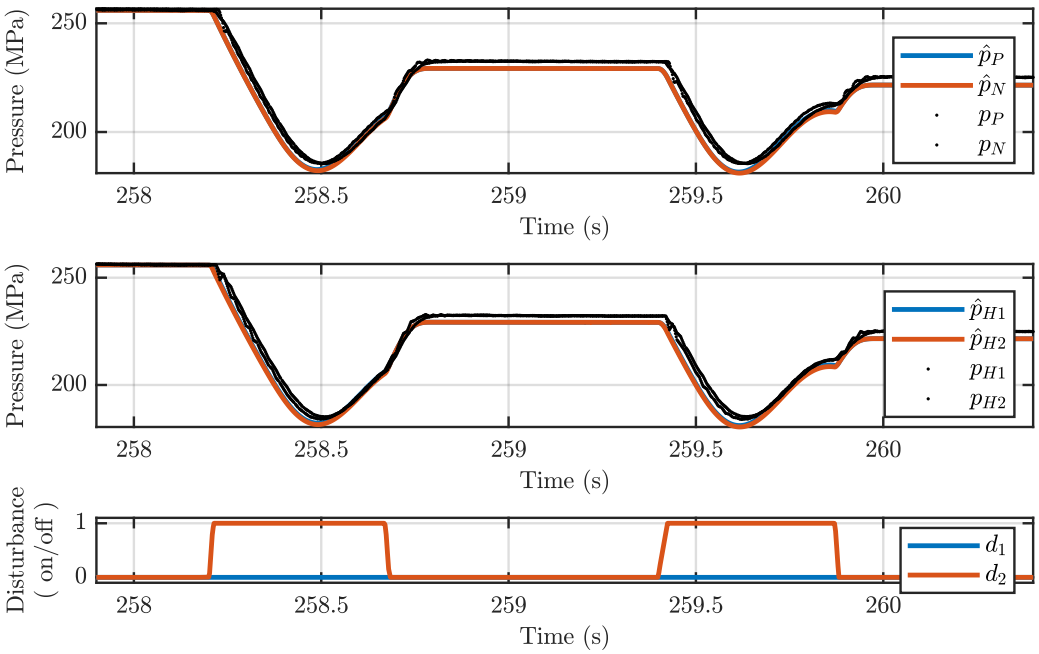

Figure A.22 – Fast switching disturbance for the 1 pump - 2 cutting head setup: zoom-in when switching head 2.

A.2.3 Cavity cutting: symmetric and asymmetric distributed pumps

A cutting head will switch open and close with a period of 0.5 seconds whereas the pump tries to maintain an operating point of 200 MPa. Cutting head 2 is switching only while cutting head 1 remains closed. The fluid flow consumption will vary as shown in Figure A.23 and Figure A.24 for the symmetric and asymmetric topology of measurement D-3 and 6, respectively.

Figure A.25 and Figure A.26 show detailed trends for the input pressures in the first plot, the network and output pressures in the second plot, as well as the switching pattern in the third plot.

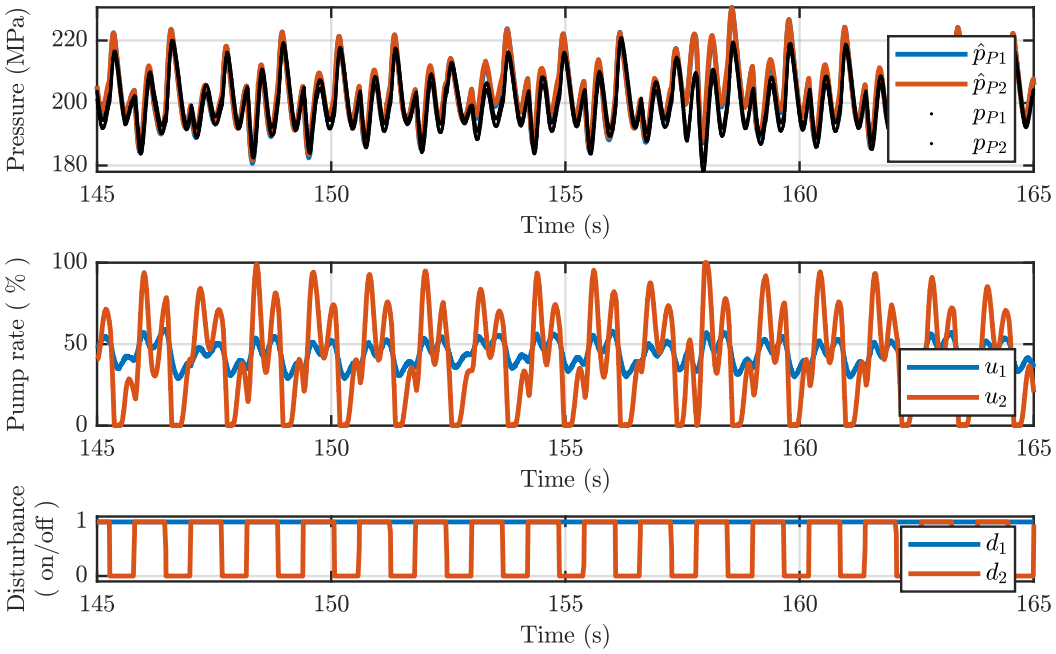

Figure A.23 – Overview of experiment D-3 considering fast switching disturbance for a 2 pump - 2 cutting head setup with symmetric topology: cutting head 1 remains open while head 2 switches periodically.

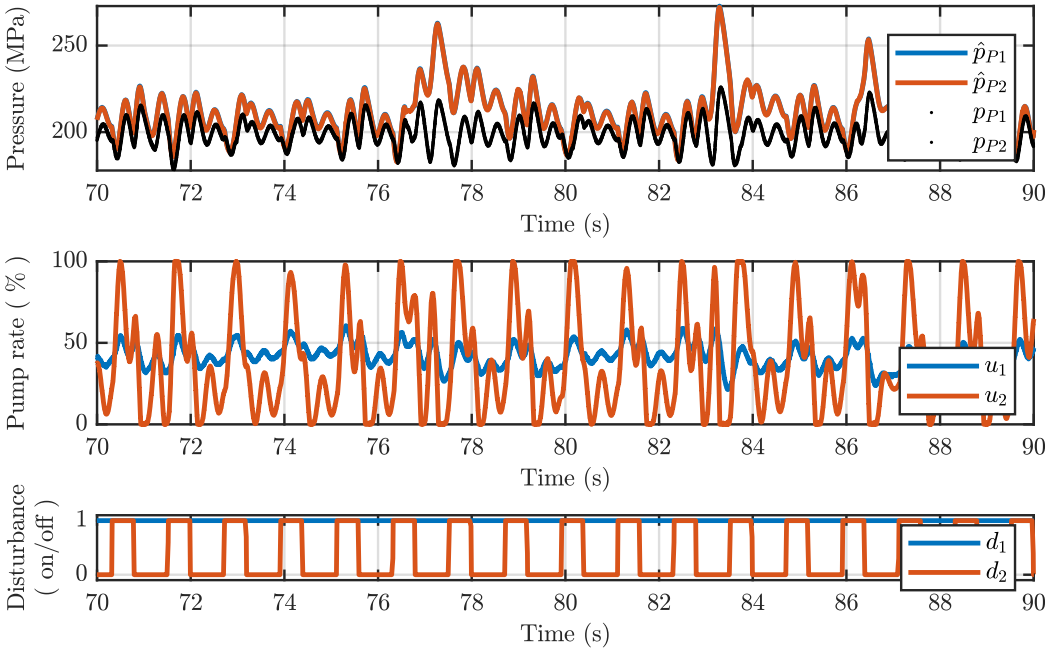

Figure A.24 – Overview of experiment D-6 considering fast switching disturbance for a 2 pump - 2 cutting head setup with asymmetric topology: cutting head 1 remains open while head 2 switches periodically.

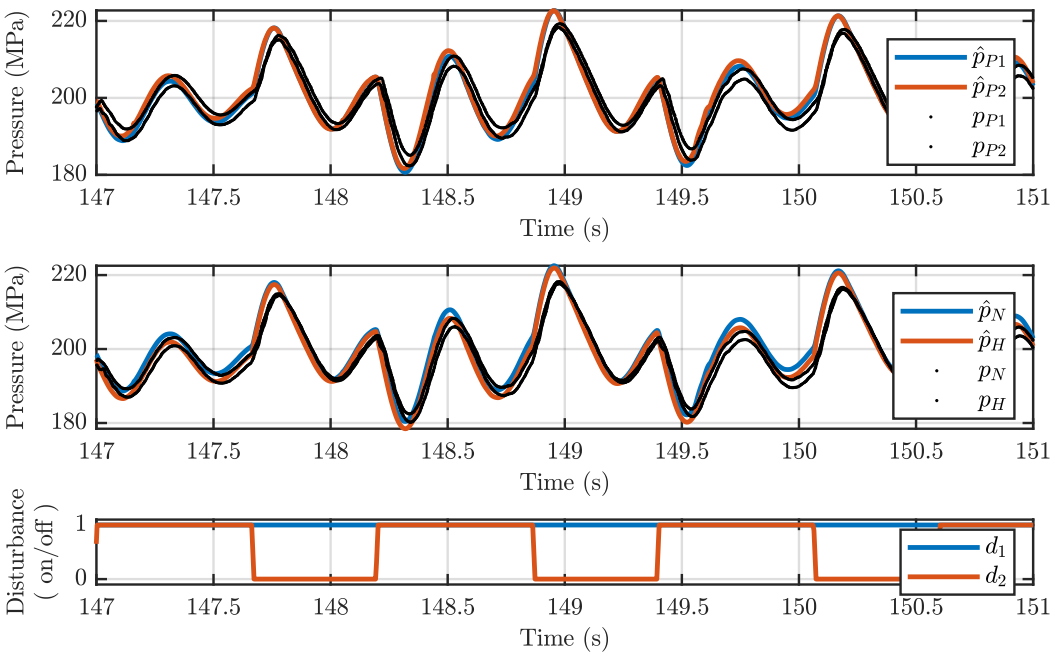

Figure A.25 – Zoom-in of fast switching disturbance for a 2 pump - 2 cutting head setup with symmetric topology: cutting head 1 remains open while head 2 switches periodically.

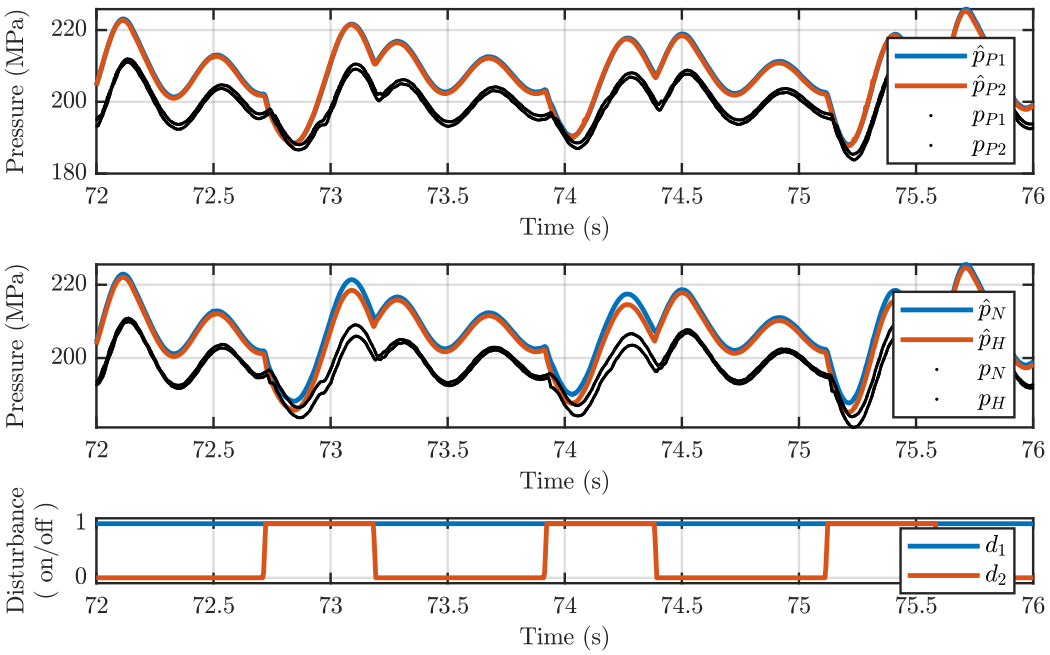

Figure A.26 – Zoom-in of fast switching disturbance for a 2 pump - 2 cutting head setup with asymmetric topology: cutting head 1 remains open while head 2 switches periodically.

B

Detailed results for controller verification

Contents

B.1 Single pump experiments with initial PI controller

B.1.1 Contour cutting: asymmetric cutting heads

Measurements E-6 and E-9 were obtained and compared to simulations for the 200 MPa and 350 MPa operating points, respectively. Disturbance steps were applied on the test bench when switching the different cutting heads open and close. This alternately switching results in 4 possible pump rate of different fluid flow rates, since both cutting heads hold nozzles of different inner diameters. Consequently 8 switching states were observed with respect to the cutting head switching. Figure B.1 completes the investigations in Section 6.4 with the inverse 4 transitions at 200 MPa. The plots in Figure B.2 show further the first 4 transitions and the plots in Figure B.3 give the inverse 4 transitions for the 350 MPa operating pressure.

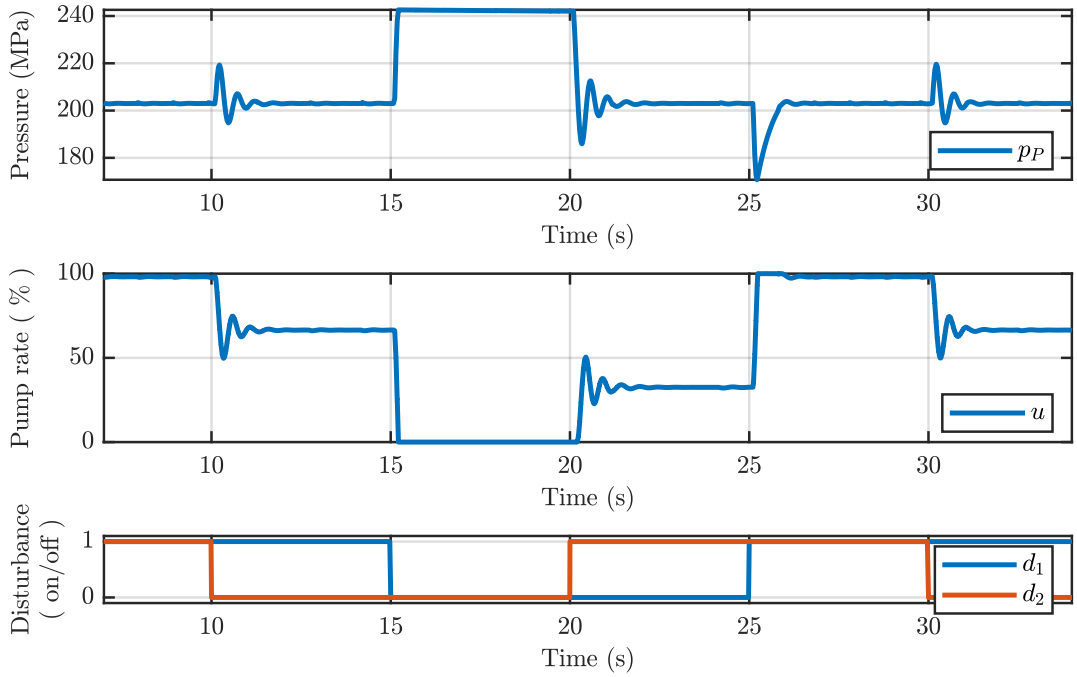

Figure B.1 – Inverse switching pattern B for 200 MPa operating pressure of experiment E-6: desired switching states resulting in different pump rates for disturbance rejection by means control to reference pressure.

The Figures B.4 - B.5 compare measurement and simulations for each transition of experiment E-6, where the Figures B.6 - B.9 compare measurement and simulations with respect to experiment E-9.

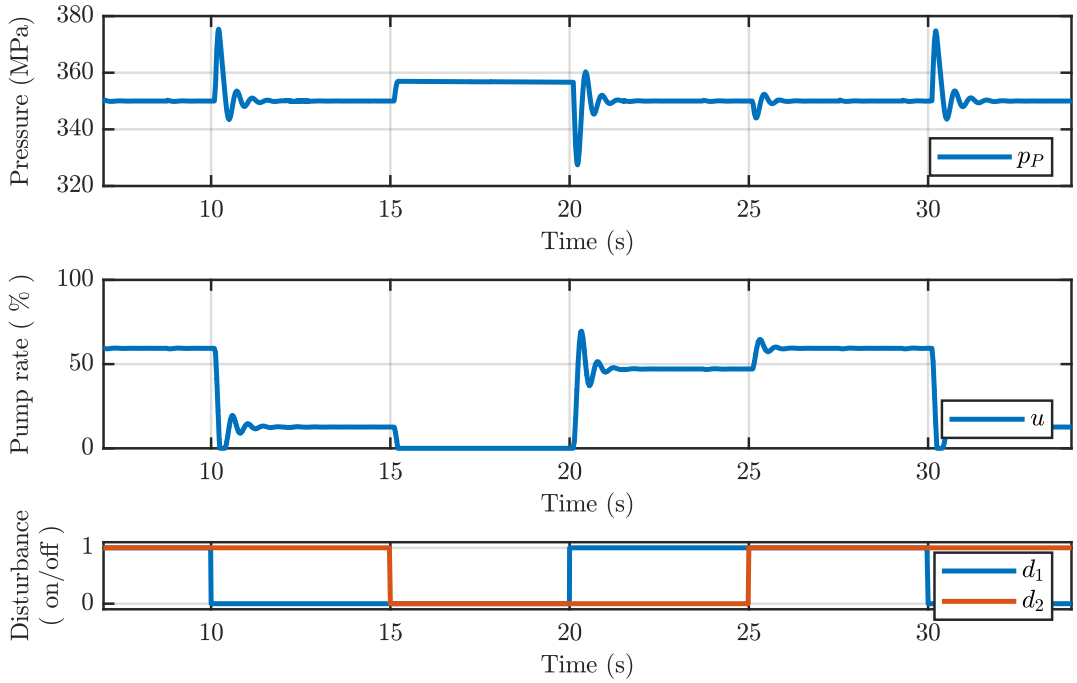

Figure B.2 – Switching pattern A for 350 MPa operating pressure of experiment E-9: desired switching states resulting in different pump rates for disturbance rejection by means control to reference pressure.

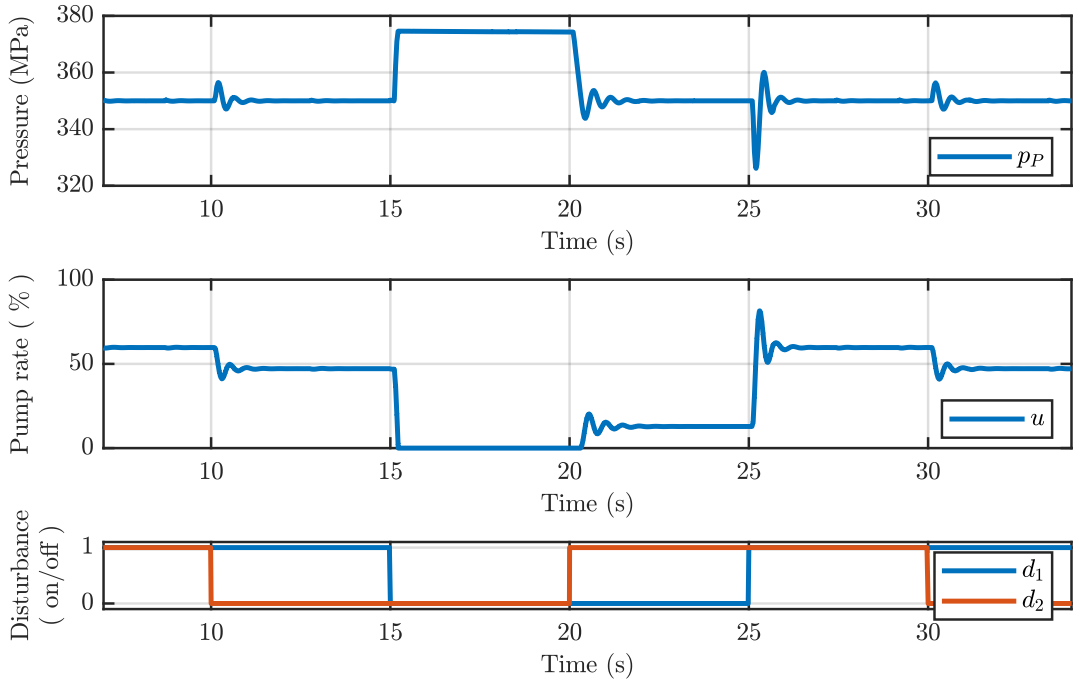

Figure B.3 – Inverse switching pattern B for 350 MPa operating pressure of experiment E-9: desired switching states resulting in different pump rates for disturbance rejection by means control to reference pressure.

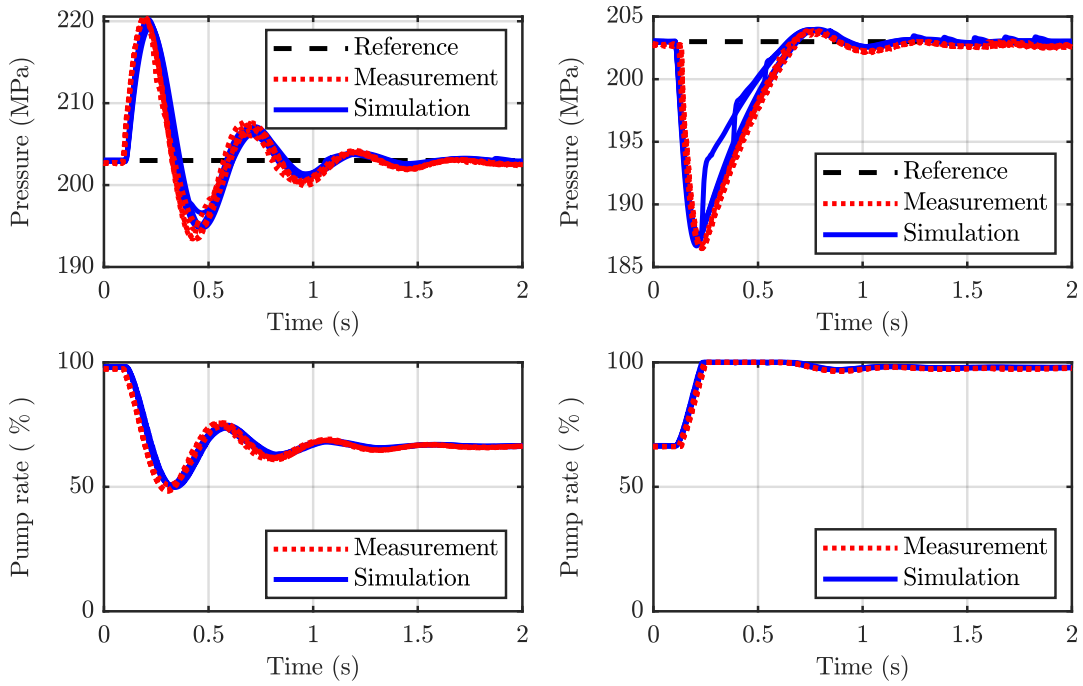

Figure B.4 – Disturbance steps at 200 MPa operating point, switching states (c): resulting step responses from non-linear simulation model and measured step responses from experiment on test bench. Nozzle 2 switches while nozzle 1 remains open.

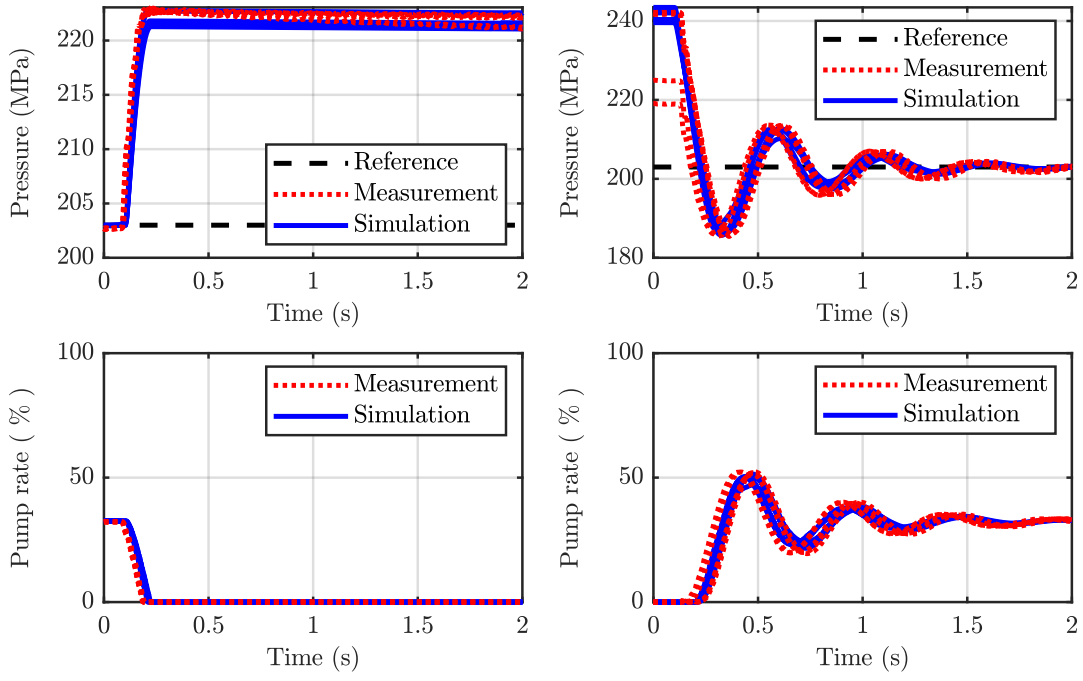

Figure B.5 – Disturbance steps at 200 MPa operating point, switching states (d): resulting step responses from non-linear simulation model and measured step responses from experiment on test bench. Nozzle 2 switches while nozzle 1 remains closed.

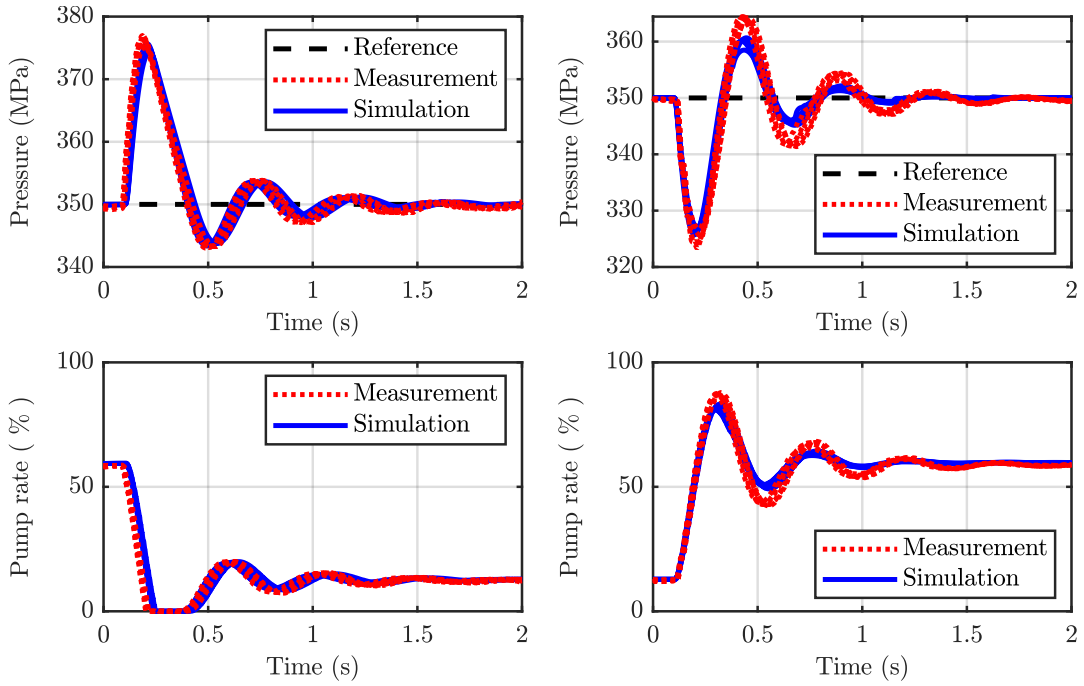

Figure B.6 – Disturbance steps at 350 MPa operating point, switching states (a): resulting step responses from non-linear simulation model and measured step responses from experiment on test bench. Nozzle 1 switches while nozzle 2 remains open.

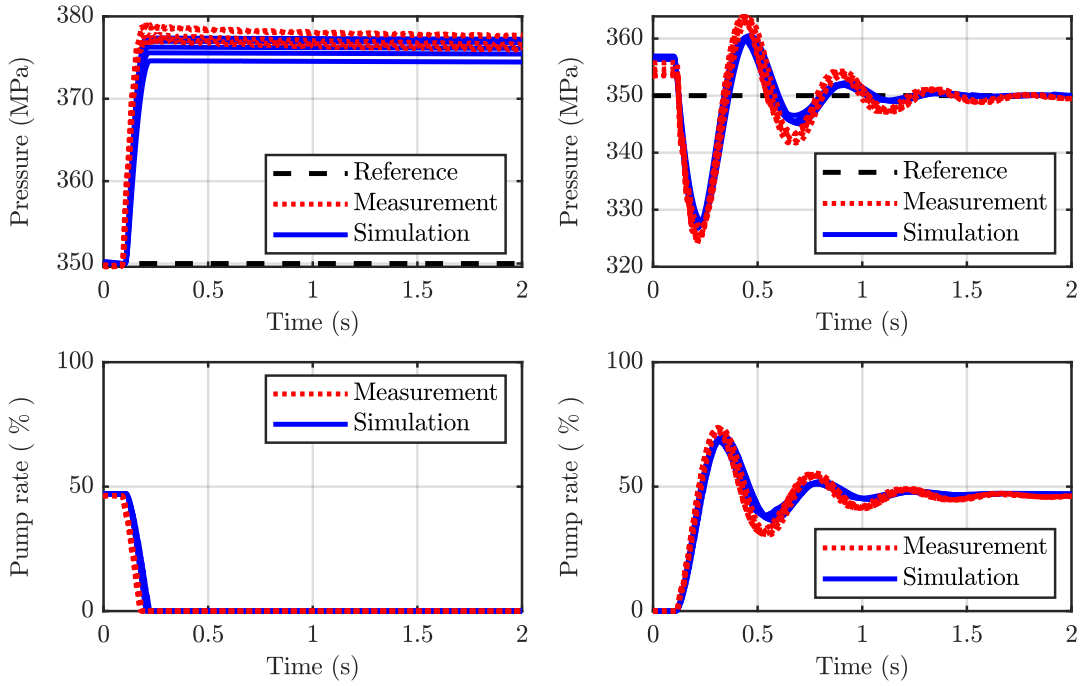

Figure B.7 – Disturbance steps at 350 MPa operating point, switching states (b): resulting step responses from non-linear simulation model and measured step responses from experiment on test bench. Nozzle 1 switches while nozzle 2 remains closed.

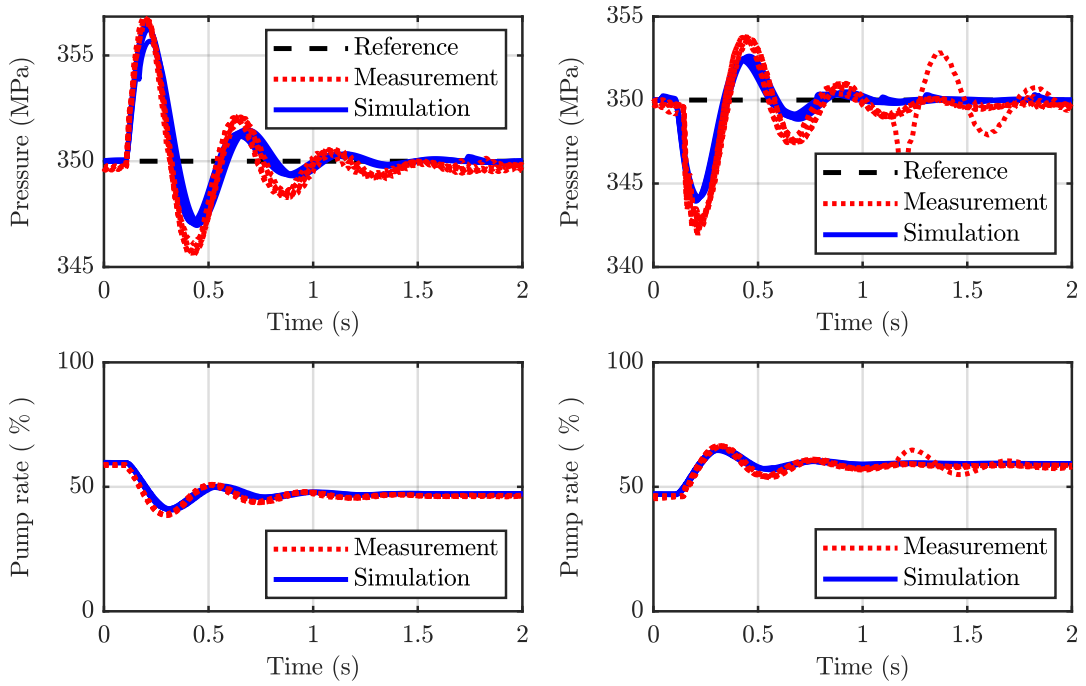

Figure B.8 – Disturbance steps at 350 MPa operating point, switching states (c): resulting step responses from non-linear simulation model and measured step responses from experiment on test bench. Nozzle 2 switches while nozzle 1 remains open.

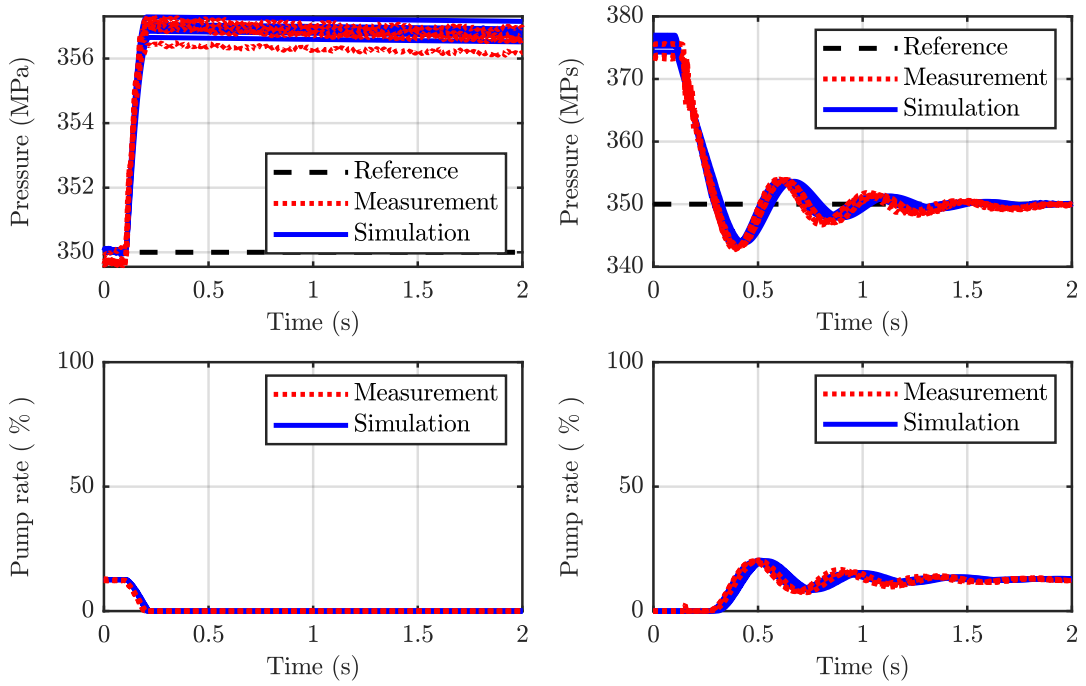

Figure B.9 – Disturbance steps at 350 MPa operating point, switching states (d): resulting step responses from non-linear simulation model and measured step responses from experiment on test bench. Nozzle 2 switches while nozzle 1 remains closed.

B.1.2 Contour cutting: symmetric cutting heads

Measurements E-11 and E-13 were obtained and also compared to simulations, considering the 200 MPa and 350 MPa operating points, respectively. Disturbance steps were applied on the test bench when switching the different cutting heads open and close. This alternately switching results in 4 possible pump rate of different fluid flow rates, since the piping sections to the cutting heads are of different length. Figure B.10 completes the investigations in Section 6.4 with the inverse 4 transitions at 200 MPa. The plots in Figure B.11 show further the first 4 transitions, where the plots in Figure B.12 give the inverse 4 transitions for the 350 MPa operating pressure.

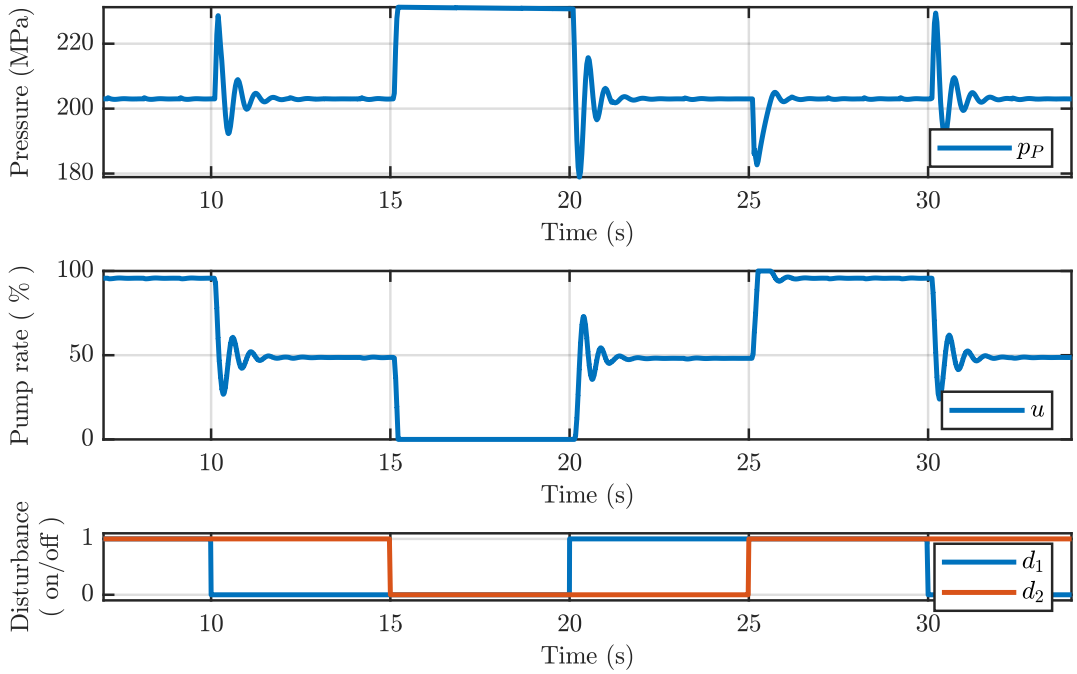

Figure B.10 – Inverse switching pattern B for 200 MPa operating pressure of experiment E-11: desired switching states resulting in different pump rates for disturbance rejection by means control to reference pressure.

The Figures B.13 - B.14 compare measurement and simulations for each transition of experiment E-11, where the Figures B.15 - B.18 compare measurement and simulations with respect to experiment E-13.

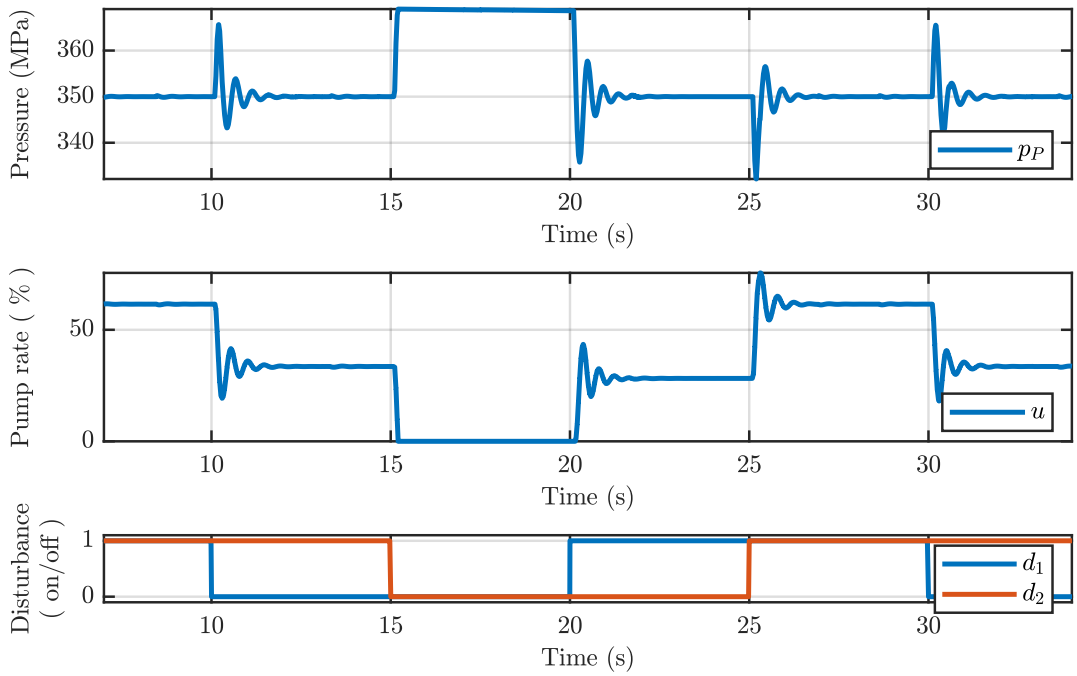

Figure B.11 – Switching pattern A for 350 MPa operating pressure of experiment E-13: desired switching states resulting in different pump rates for disturbance rejection by means control to reference pressure.

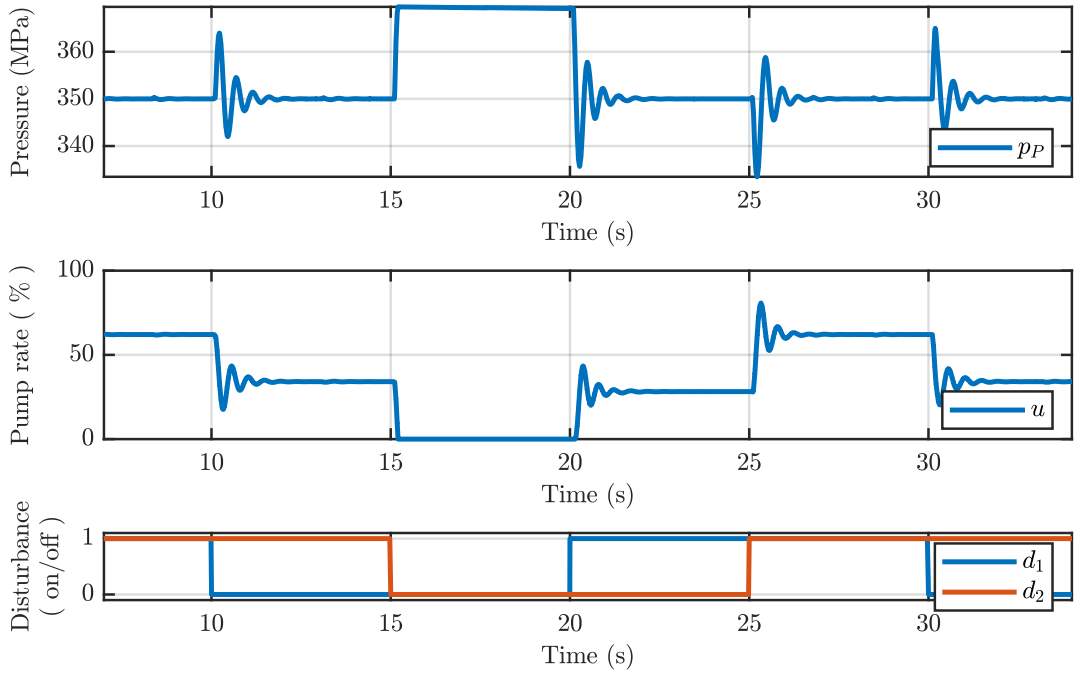

Figure B.12 – Inverse switching pattern B for 350 MPa operating of experiment E-13: desired switching states resulting in different pump rates for disturbance rejection by means control to reference pressure.

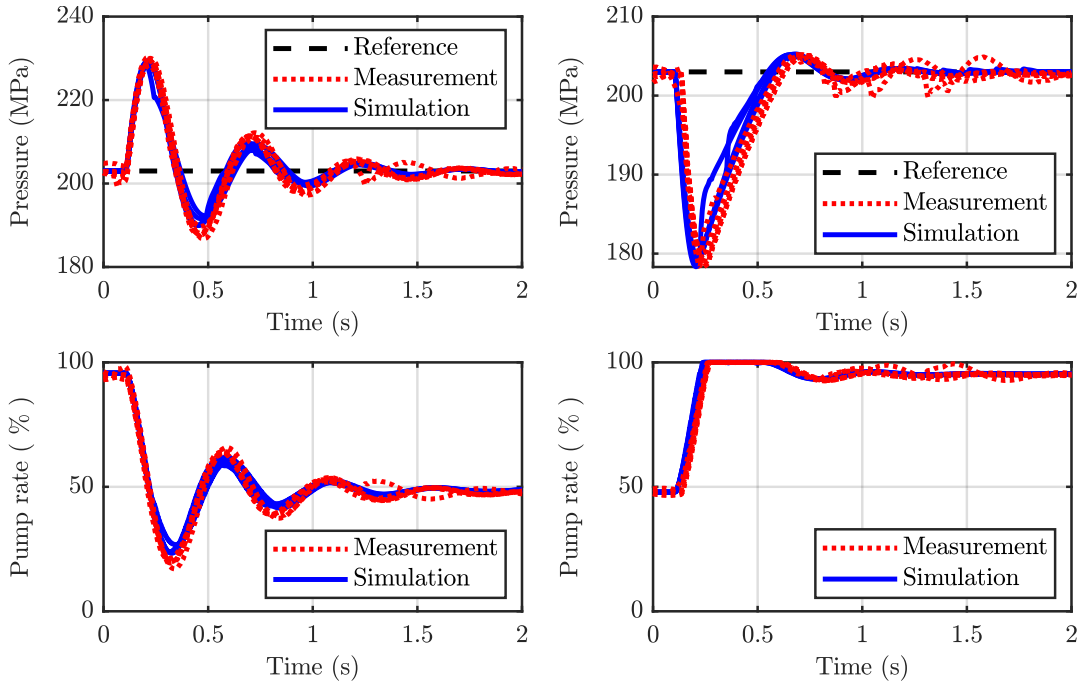

Figure B.13 – Disturbance steps at 200 MPa operating point, switching states (c): resulting step responses from non-linear simulation model and measured step responses from experiment on test bench. Nozzle 2 switches while nozzle 1 remains open.

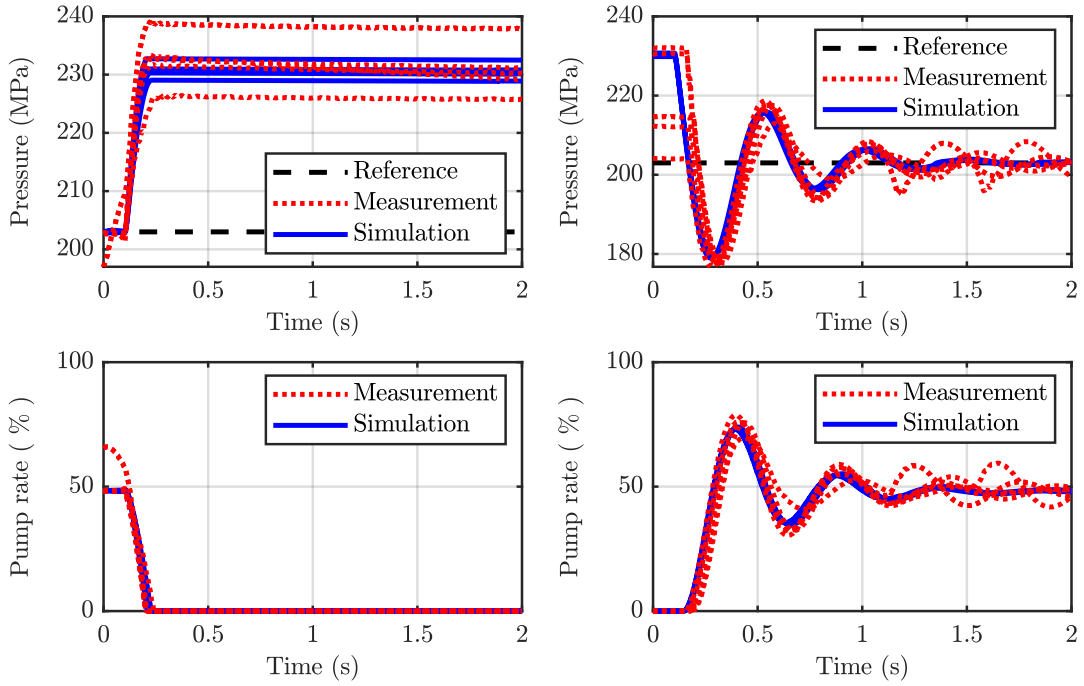

Figure B.14 – Disturbance steps at 200 MPa operating point, switching states (d): resulting step responses from non-linear simulation model and measured step responses from experiment on test bench. Nozzle 2 switches while nozzle 1 remains closed.

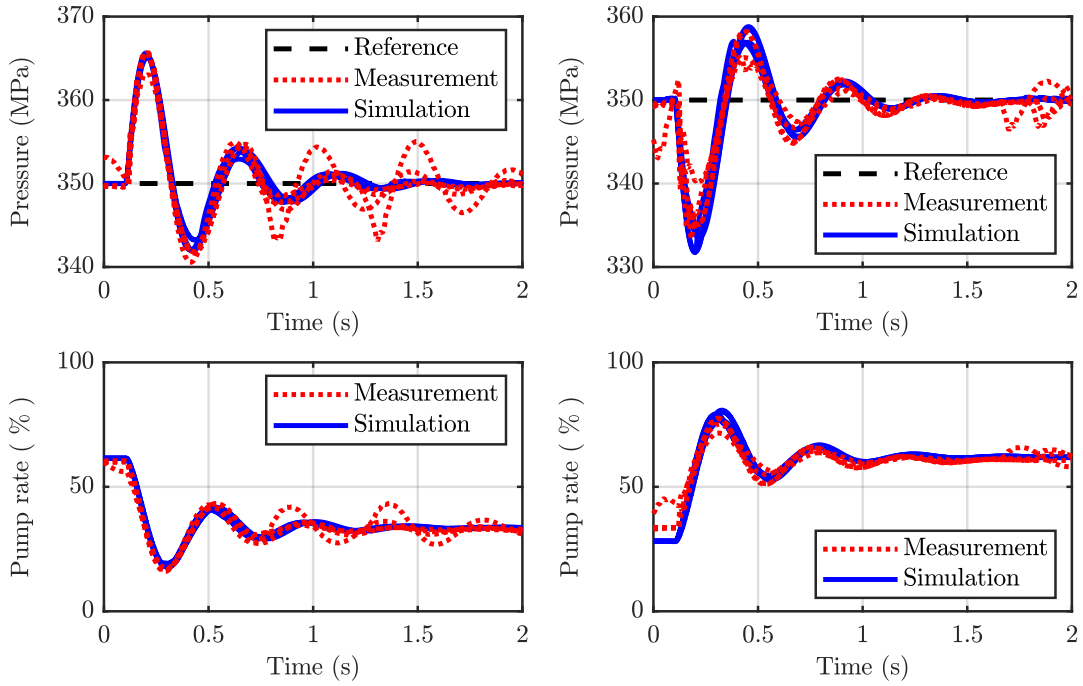

Figure B.15 – Disturbance steps at 350 MPa operating point, switching states (a): resulting step responses from non-linear simulation model and measured step responses from experiment on test bench. Nozzle 1 switches while nozzle 2 remains open.

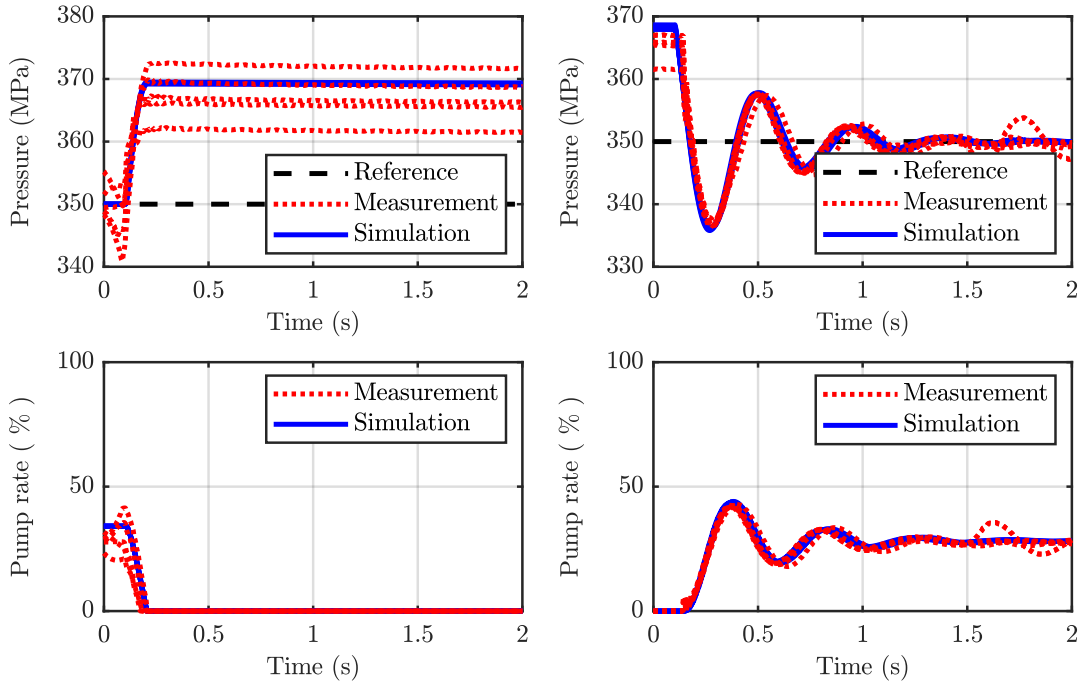

Figure B.16 – Disturbance steps at 350 MPa operating point, switching states (b): resulting step responses from non-linear simulation model and measured step responses from experiment on test bench. Nozzle 1 switches while nozzle 2 remains closed.

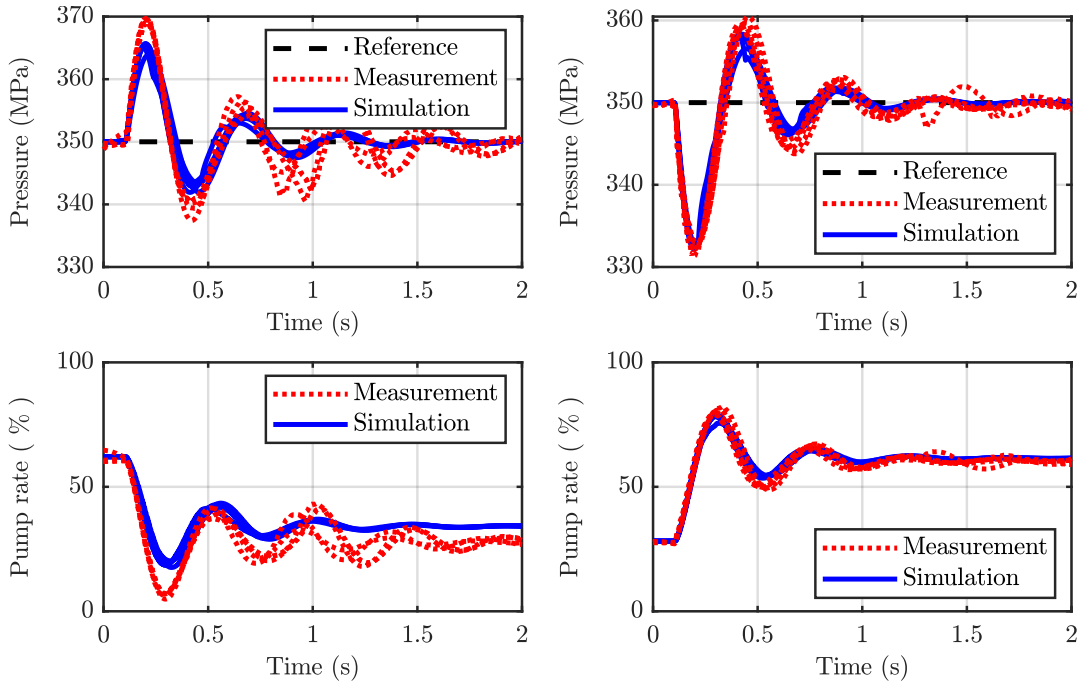

Figure B.17 – Disturbance steps at 350 MPa operating point, switching states (c): resulting step responses from non-linear simulation model and measured step responses from experiment on test bench. Nozzle 2 switches while nozzle 1 remains open.

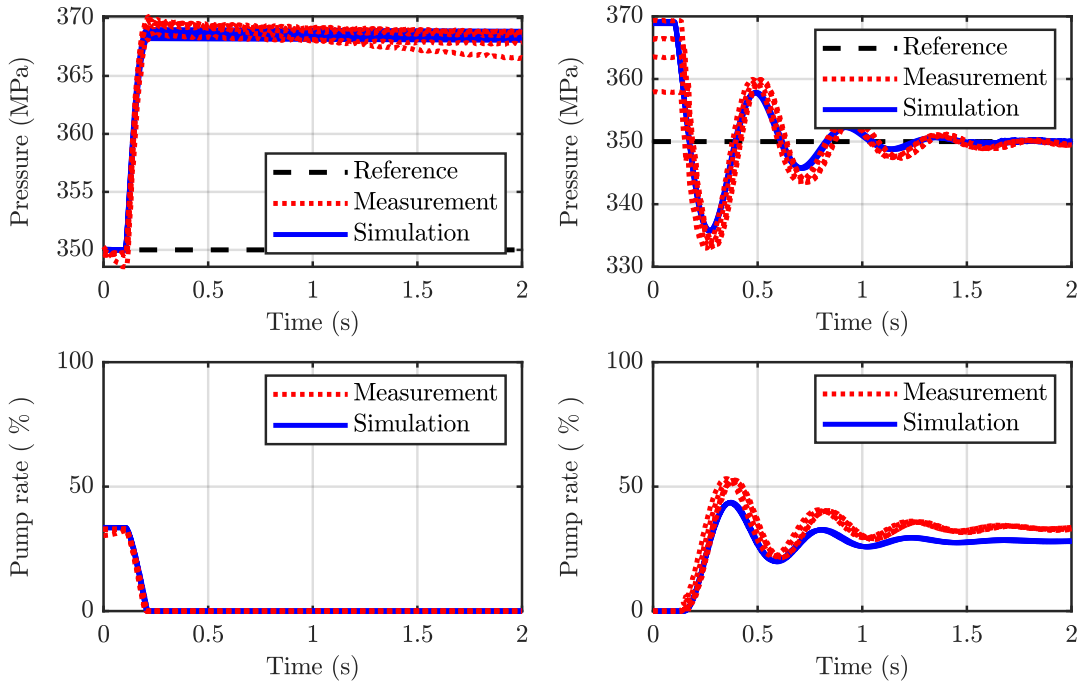

Figure B.18 – Disturbance steps at 350 MPa operating point, switching states (d): resulting step responses from non-linear simulation model and measured step responses from experiment on test bench. Nozzle 2 switches while nozzle 1 remains closed.

B.2 Single pump experiments with extended robust PI controller

B.2.1 Contour cutting: asymmetric cutting heads

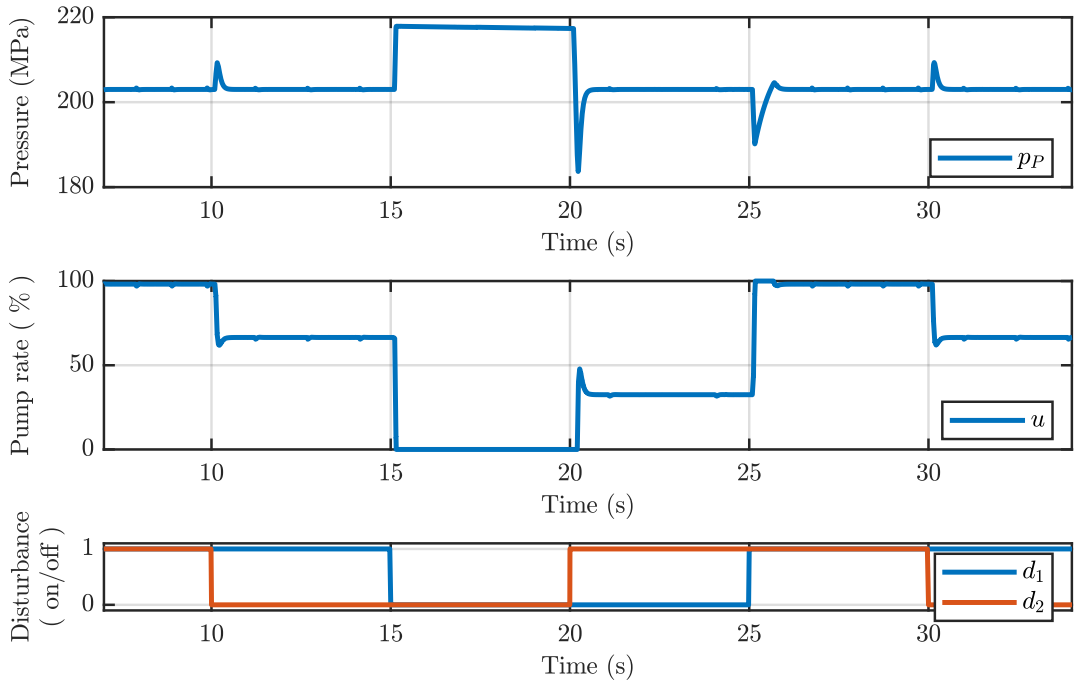

Figure B.19 – Inverse switching pattern B for 200 MPa operating pressure of experiment E-6: desired switching states resulting in different pump rates for disturbance rejection by means control to reference pressure.

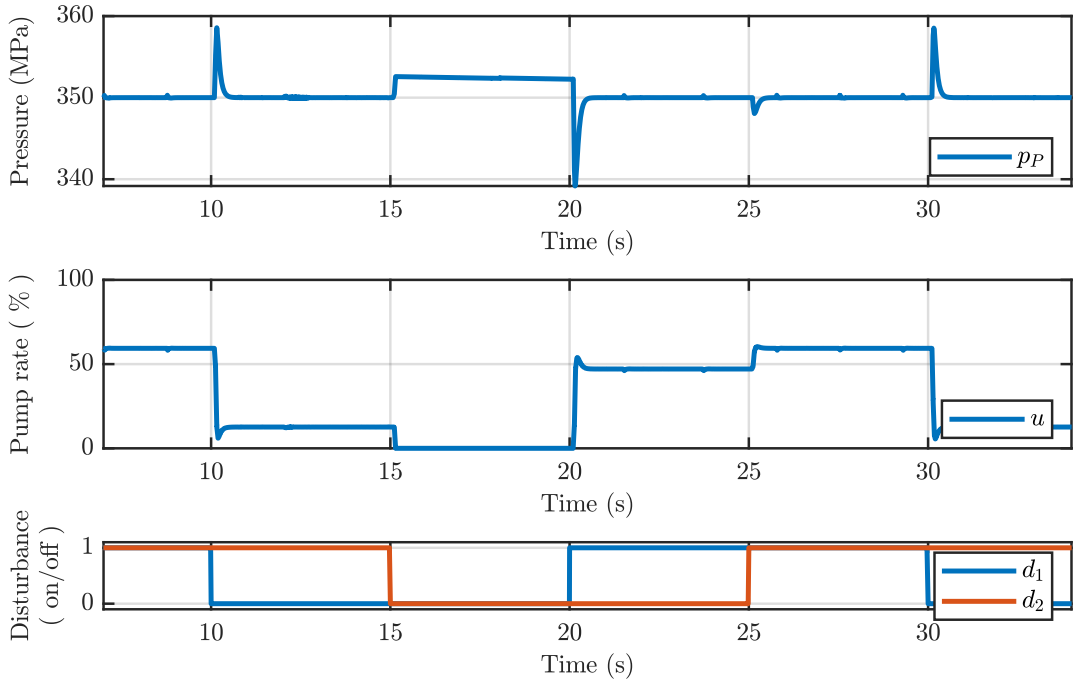

Figure B.20 – Switching pattern A for 350 MPa operating pressure of experiment E-9: desired switching states resulting in different pump rates for disturbance rejection by means control to reference pressure.

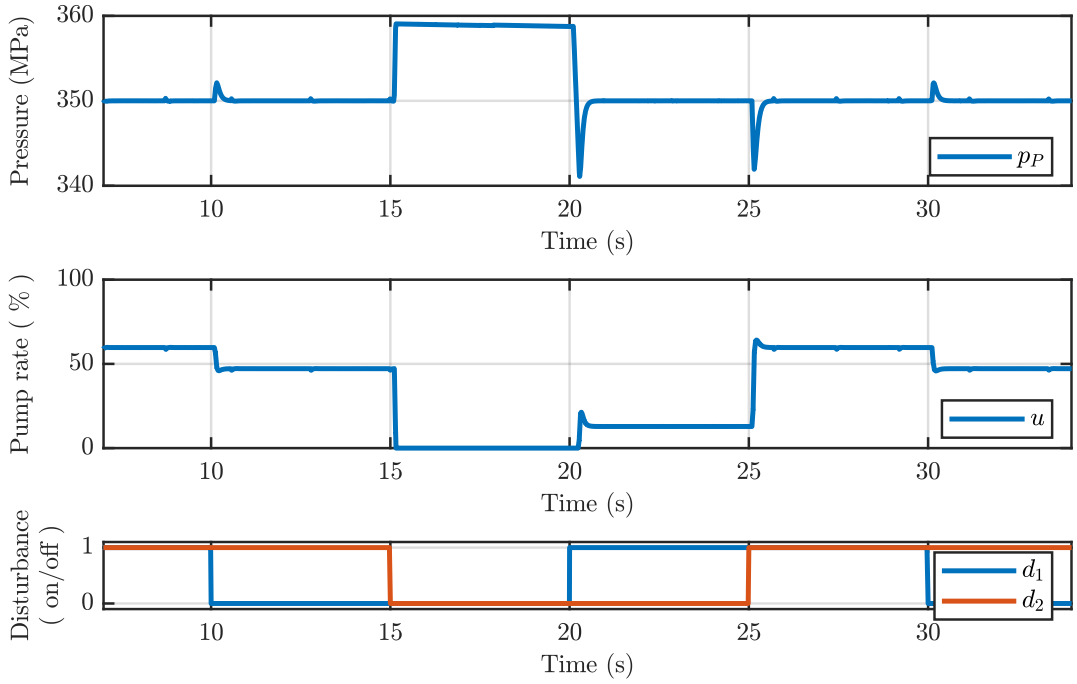

Figure B.21 – Inverse switching pattern B for 350 MPa operating pressure of experiment E-9: desired switching states resulting in different pump rates for disturbance rejection by means control to reference pressure.

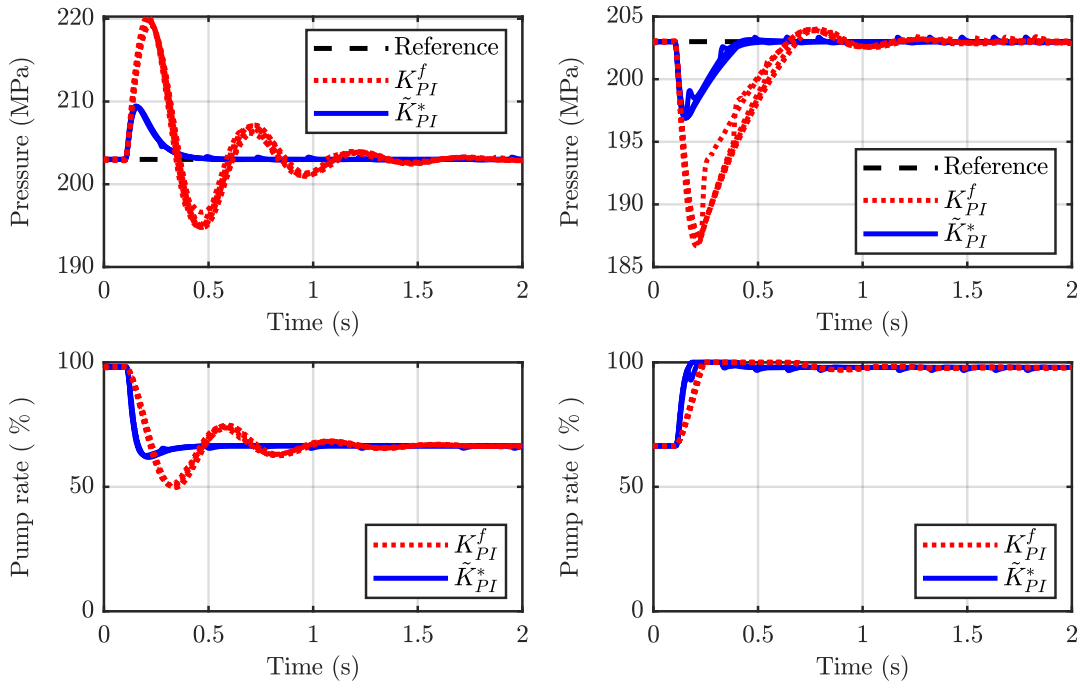

Figure B.22 – Disturbance steps at 200 MPa operating point, switching states (c): resulting step responses from non-linear simulation model and measured step responses from experiment on test bench. Nozzle 2 switches while nozzle 1 remains open.

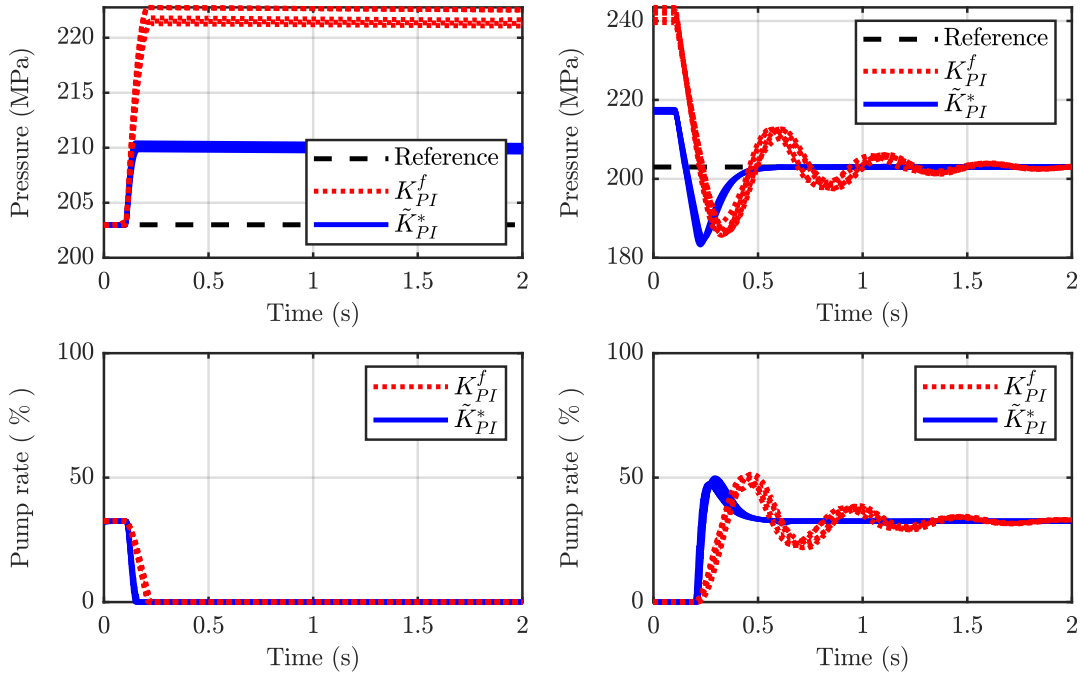

Figure B.23 – Disturbance steps at 200 MPa operating point, switching states (d): resulting step responses from non-linear simulation model and measured step responses from experiment on test bench. Nozzle 2 switches while nozzle 1 remains closed.

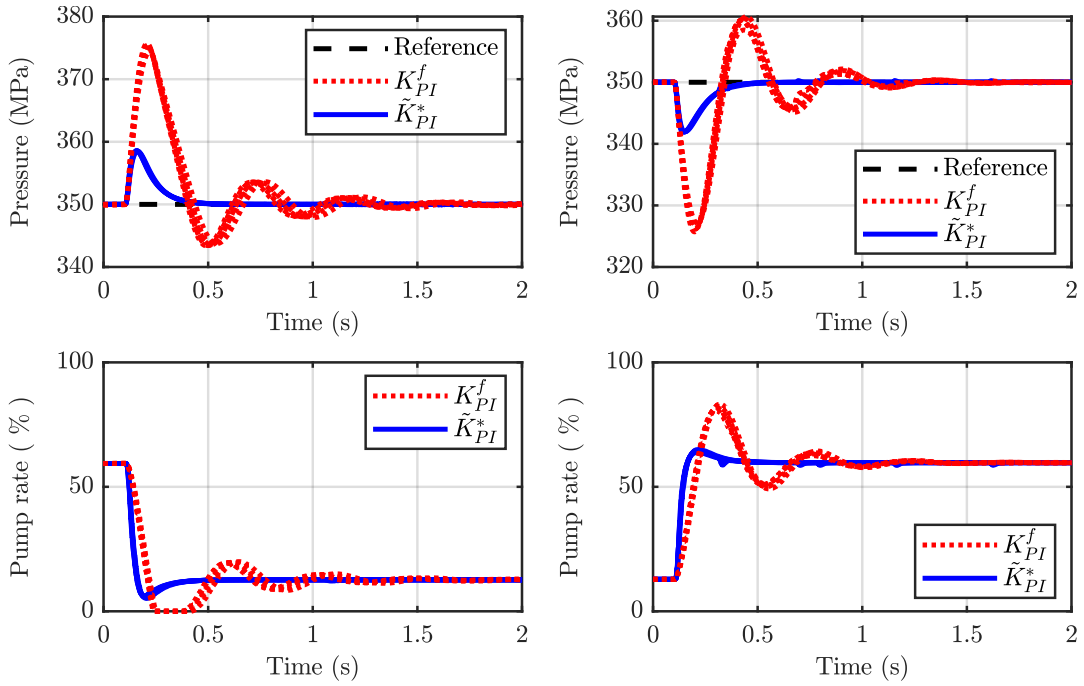

Figure B.24 – Disturbance steps at 350 MPa operating point, switching states (a): resulting step responses from non-linear simulation model and measured step responses from experiment on test bench. Nozzle 1 switches while nozzle 2 remains open.

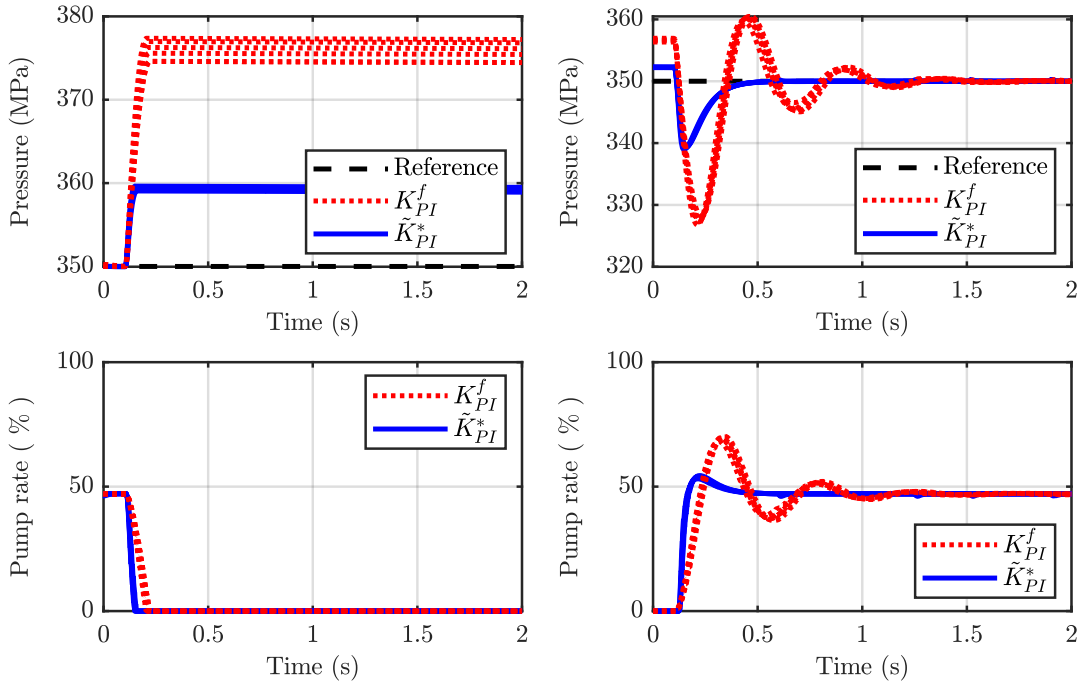

Figure B.25 – Disturbance steps at 350 MPa operating point, switching states (b): resulting step responses from non-linear simulation model and measured step responses from experiment on test bench. Nozzle 1 switches while nozzle 2 remains closed.

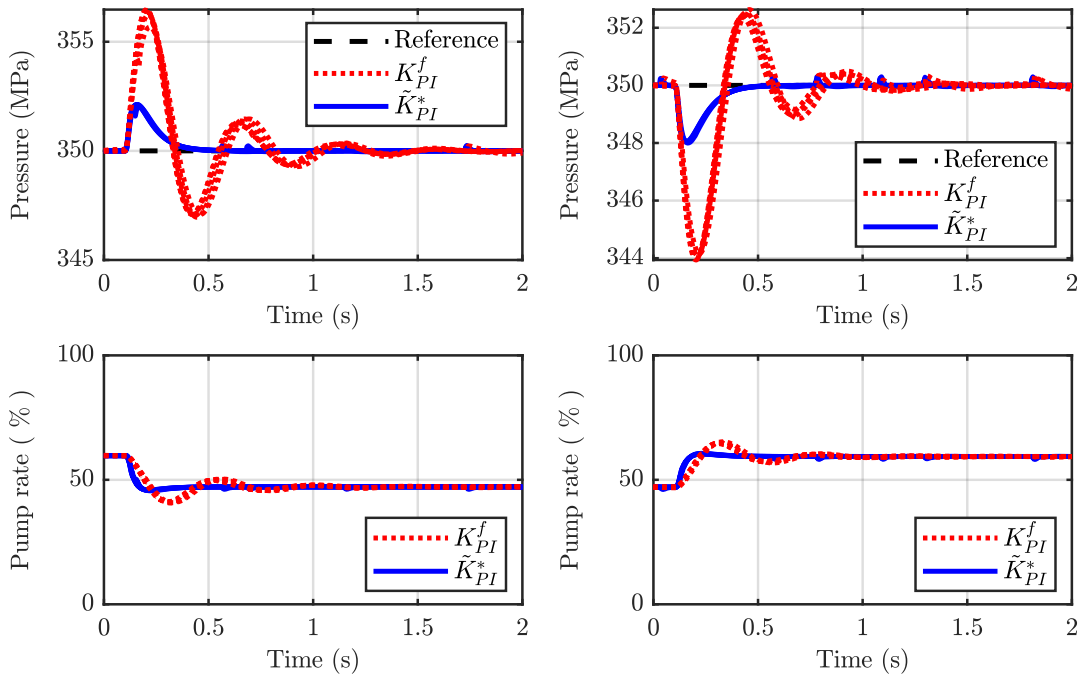

Figure B.26 – Disturbance steps at 350 MPa operating point, switching states (c): resulting step responses from non-linear simulation model and measured step responses from experiment on test bench. Nozzle 2 switches while nozzle 1 remains open.

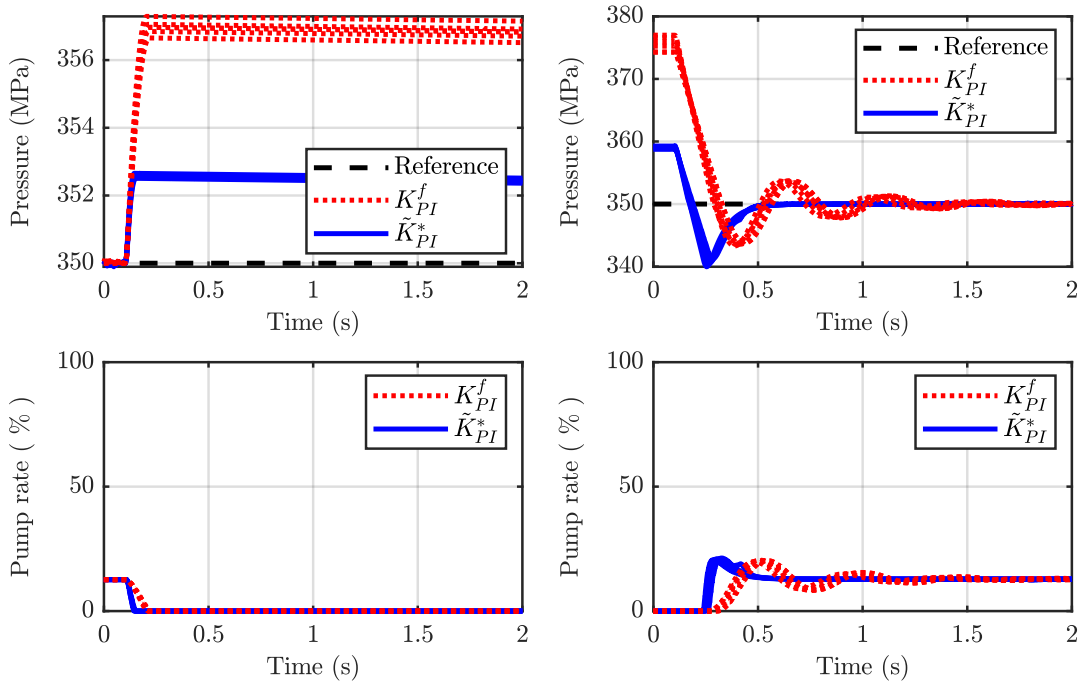

Figure B.27 – Disturbance steps at 350 MPa operating point, switching states (d): resulting step responses from non-linear simulation model and measured step responses from experiment on test bench. Nozzle 2 switches while nozzle 1 remains closed.

B.2.2 Contour cutting: symmetric cutting heads

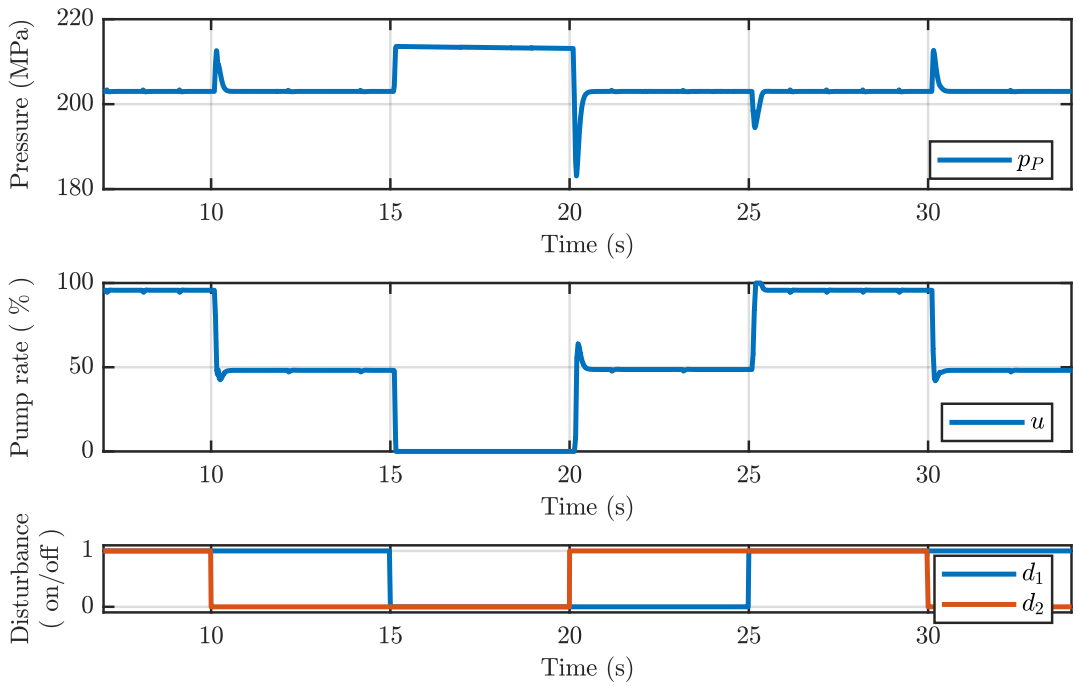

Figure B.28 – Inverse switching pattern B for 200 MPa operating pressure of experiment E-11: desired switching states resulting in different pump rates for disturbance rejection by means control to reference pressure.

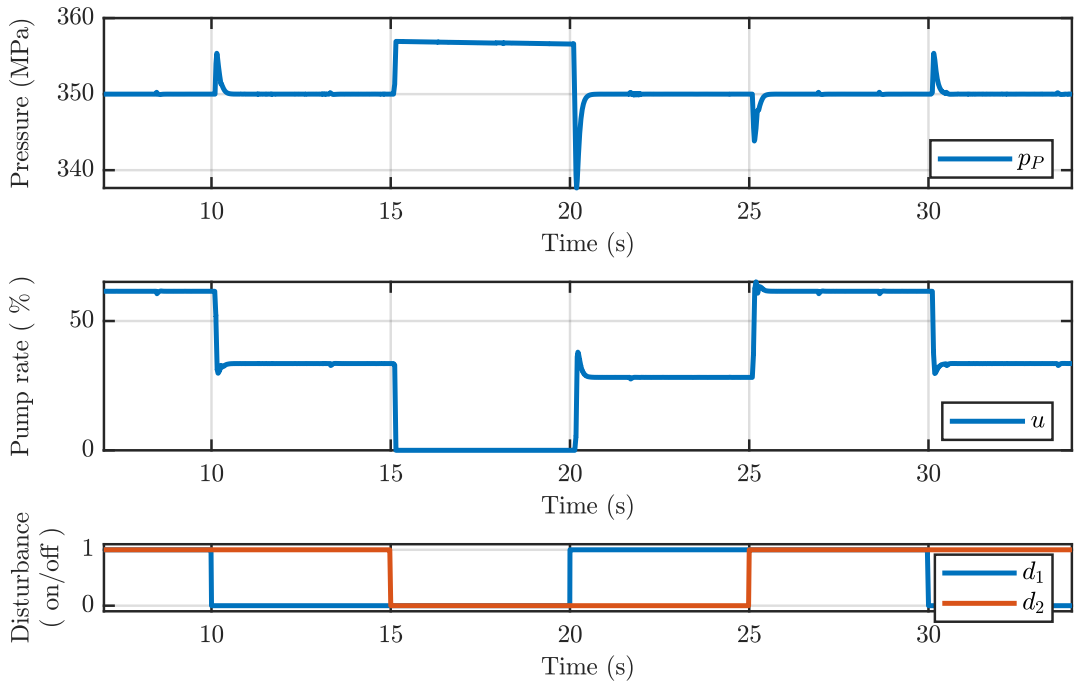

Figure B.29 – Switching pattern A for 350 MPa operating pressure of experiment E-13: desired switching states resulting in different pump rates for disturbance rejection by means control to reference pressure.

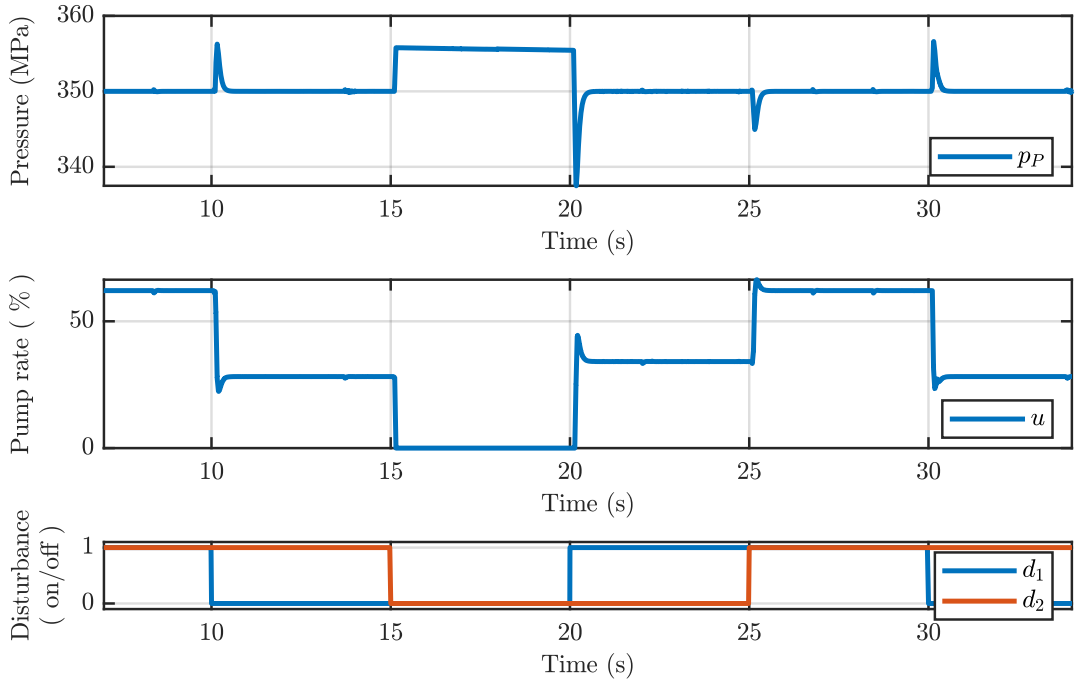

Figure B.30 – Inverse switching pattern B for 350 MPa operating of experiment E-13: desired switching states resulting in different pump rates for disturbance rejection by means control to reference pressure.

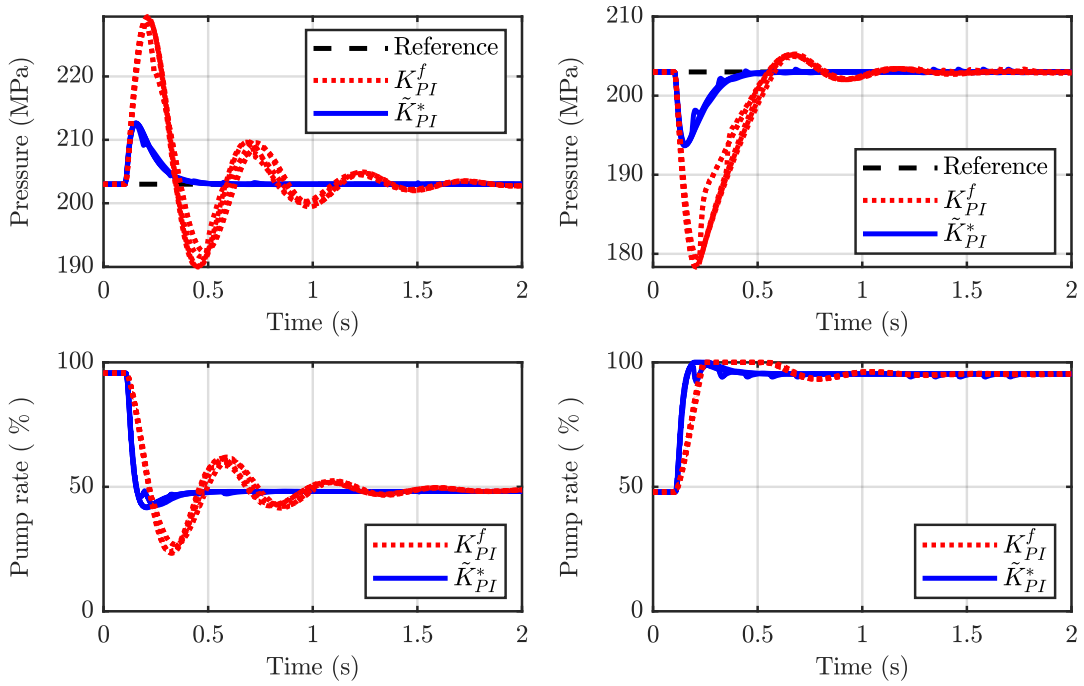

Figure B.31 – Disturbance steps at 200 MPa operating point, switching states (c): resulting step responses from non-linear simulation model and measured step responses from experiment on test bench. Nozzle 2 switches while nozzle 1 remains open.

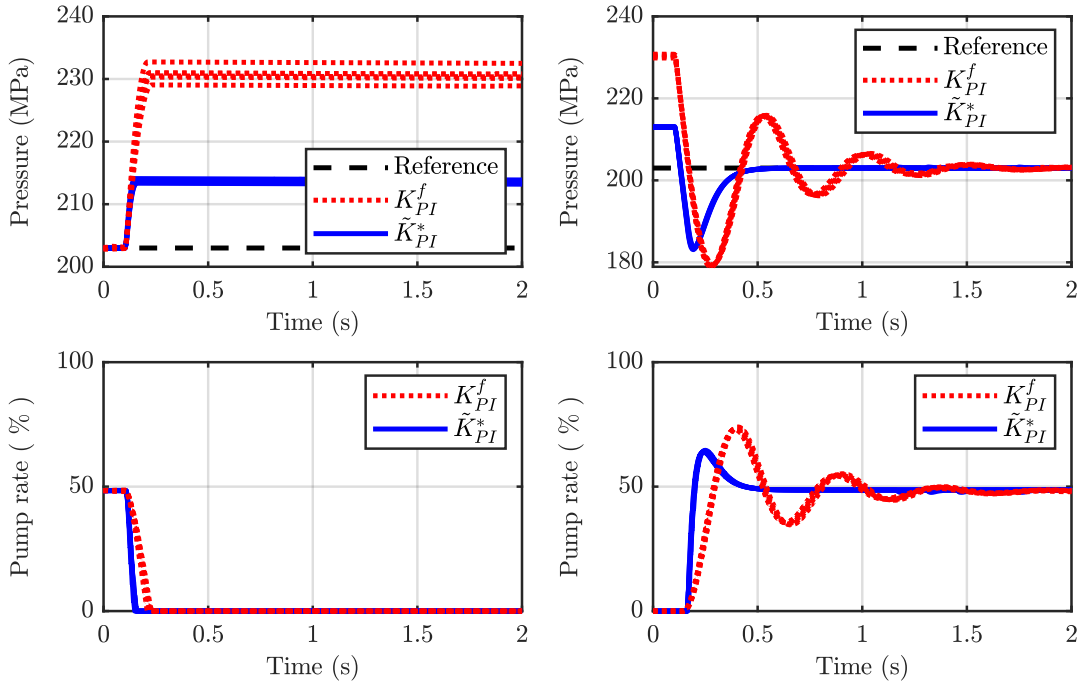

Figure B.32 – Disturbance steps at 200 MPa operating point, switching states (d): resulting step responses from non-linear simulation model and measured step responses from experiment on test bench. Nozzle 2 switches while nozzle 1 remains closed.

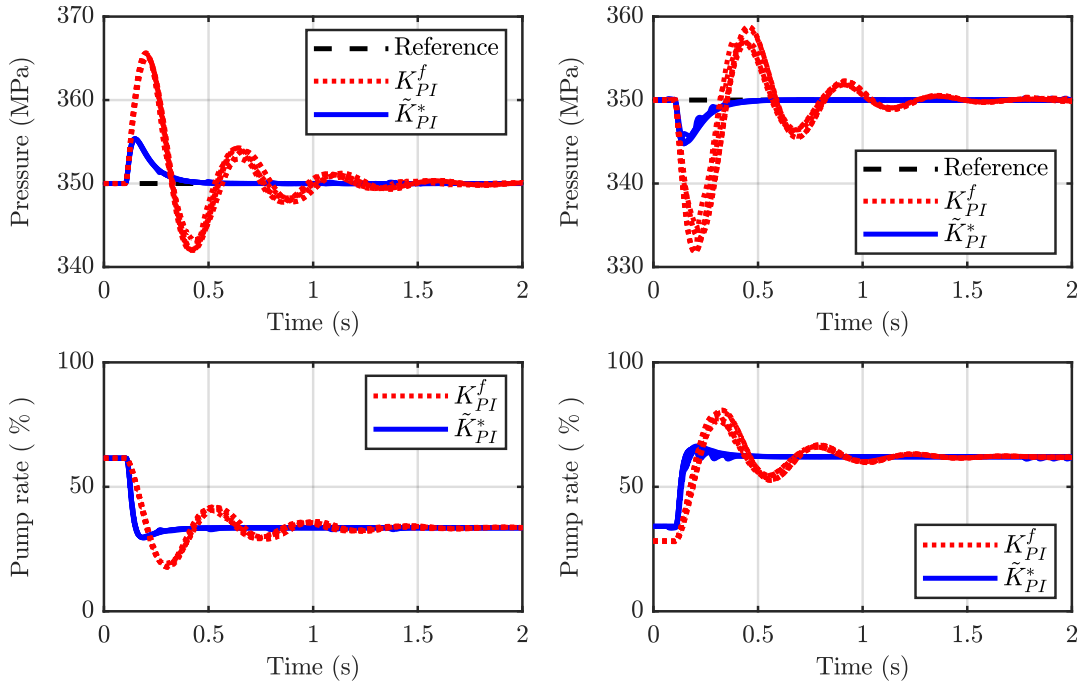

Figure B.33 – Disturbance steps at 350 MPa operating point, switching states (a): resulting step responses from non-linear simulation model and measured step responses from experiment on test bench. Nozzle 1 switches while nozzle 2 remains open.

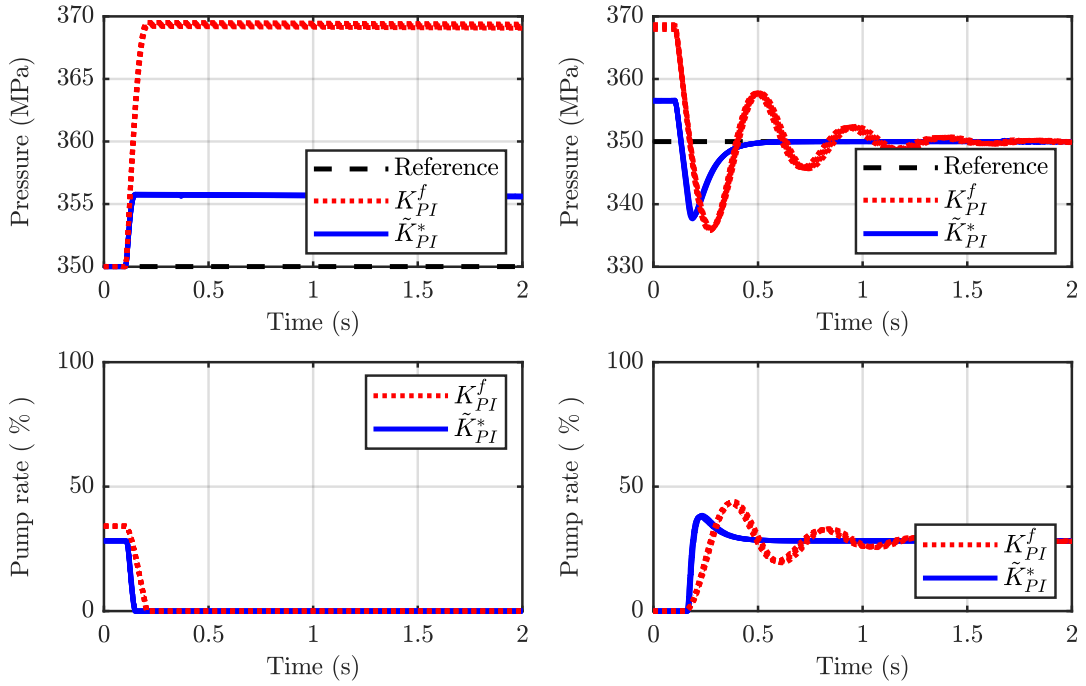

Figure B.34 – Disturbance steps at 350 MPa operating point, switching states (b): resulting step responses from non-linear simulation model and measured step responses from experiment on test bench. Nozzle 1 switches while nozzle 2 remains closed.

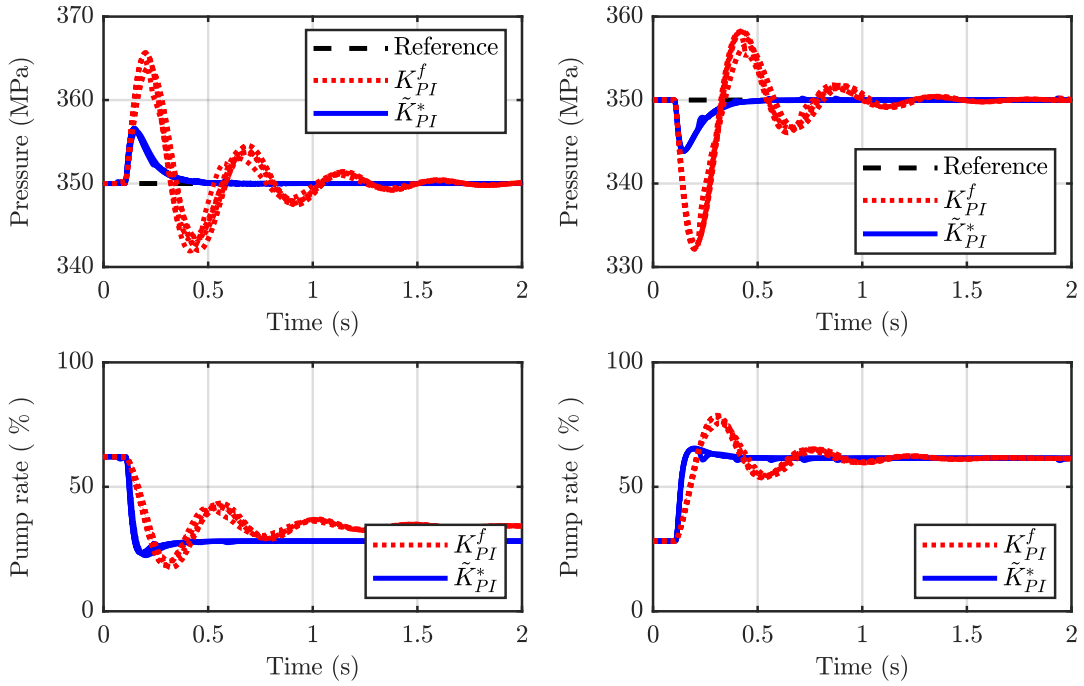

Figure B.35 – Disturbance steps at 350 MPa operating point, switching states (c): resulting step responses from non-linear simulation model and measured step responses from experiment on test bench. Nozzle 2 switches while nozzle 1 remains open.

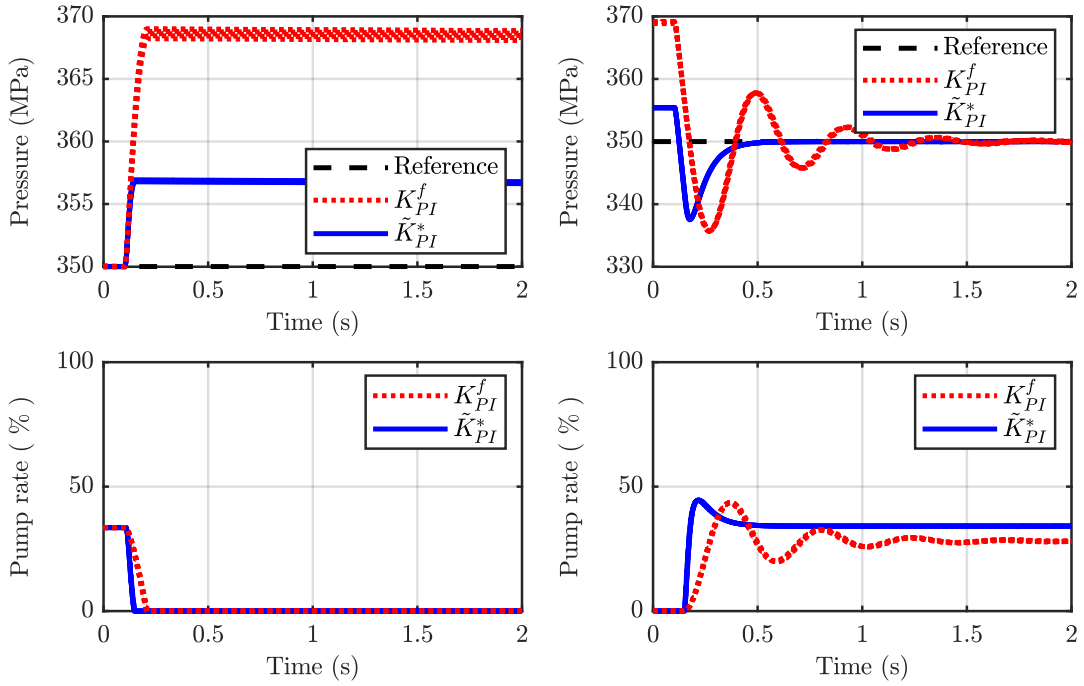

Figure B.36 – Disturbance steps at 350 MPa operating point, switching states (d): resulting step responses from non-linear simulation model and measured step responses from experiment on test bench. Nozzle 2 switches while nozzle 1 remains closed.

C

Survey of high-level managing

Contents

C.1 Hierarchical distributed control

This survey provides an overview of various managing algorithms which emerged from different domains. It aims at evaluation of a suitable concept to manage distributed pumps in a high-pressure networks. This is not a straight forward task, since sever restrictions are given from waterjet machining and facilities.

Hierarchical approaches are used to manage the collaboration between distributed controllers while obtaining a globally desired behaviour of the overall system. Common hierarchical distributed architectures are reviewed in [Scattolini, 2009], while different multi-layer structures are discussed in [Tatjewski, 2008]. Subject to process optimization, the control structure is at least organized in two layers. A lower layer that holds the distributed controllers and an upper layer dedicated to coordinate the subsystems by generating the desired subsystem set points. This coordination is centralized and comprises an optimization procedure which is often designed using model predictive control. However, for large-scale systems it becomes computationally difficult to solve the global optimization problem.

A hierarchical control design for interconnection systems is presented in [Jilg and Stursberg, 2013] that aims at decreasing the communication burden and computational effort when separating the overall system into clusters. The distributed controllers communicate on low-level within a cluster where the clusters exchange informations at high-level with reduced data rate. A proper decomposition of large-scale system suitable for hierarchical distributed control is addressed in [Tang and Daoutidis, 2017] when introducing a networked decomposition method.

Hierarchical control distribution is considered for over-actuated systems in [Singla and Junkins, 2007]. It aims at applying the overall control effort on the available actuators with respect to actuator limitations, where the control distribution problem is decomposed into many decoupled small-scale problems. This control distribution problem links to control allocation discussed in the subsequent chapter.

A rarely discussed design problem is the so called reconfigurable control structure, e.g. plug&play-control, where subsystems can be added and removed in runtime. This requires then a method for reconfiguration of the control and managing task. Such a reconfiguration to stabilize an overall interconnection system can be realized by backstepping [Wen et al., 2009]. This technique can deal with failing actuators [Wang et al., 2016a].

C.1.1 Control allocation (CA)

Control allocation aims at managing multi-variable systems in a centralized meaner. It successfully challenges over-actuated systems with a redundant set of effectors. Recent developments in control allocation is overviewed in [Johansen and Fossen, 2013]. The allocation algorithm can be considered as the mid-layer in a hierarchical control scheme. A top-layer controller commands the desired control efforts of the overall system. The mid-layer allocation combines all available actuators to reproduce the virtual control effort by generating individual set points. This is typically solved by means of an optimization problem where different constraints and objectives are considered, e.g. actuator limitations, energy efficiency, etc. Its solution is in general not unique for an over-actuated system. Finally, low-level controllers realize the set point for each actuator. Control allocation implies many applications in automotive and flight control, e.g. [Alberding et al., 2009], [Tavasoli and Naraghi, 2011] and [de Almeida, 2016], stabilizing a vehicle or vessel. It originates from the concept of ganging. However, mapping the virtual control effort for complex systems to a redundant set of effectors is no longer an intuitive task. Some allocation techniques are shortly discussed in this sequel.

Linear and non-linear allocation

Linear and non-linear effector models are distinguished that leads to linear or non-linear programming methods for solving the optimization problem [Tjønnås and Johansen, 2008]. Some linear allocation approaches allow for explicit solutions of the optimization problem using static effector models. These solutions can be calculated off-line. A robust off-line control allocation is discussed in [de Almeida, 2016] where a reference governor (RG) is implemented to avoid online optimization. A sequential quadratic programming is used in [Johansen et al., 2004] to approximate non-linear programs for singularity avoidance during online optimization.

A decentralized implementation of a non-linear control allocation scheme is proposed in [Liu et al., 2009]. It aims at solving the optimization problem of optimal allocation in a decentralized meaner.

Dynamic and adaptive allocation

A comparison of static and dynamic control allocation is given in [Tavasoli and Naraghi, 2011]. Static allocation uses algorithms such as Simplex or Interior-point (IP) to iteratively solve the optimization problem. Dynamic allocation implements a dynamic update law which reduces the computational burdens when solving the optimization problem.

An approach for adaptive control allocation is derived in [Tohidi et al., 2017]. Instead of solving an optimization problem, an adaption law is designed to allocate the control efforts with respect to actuator saturation. In particular, the update law in [Tjønnås and Johansen, 2008], proposes an adaptive allocation for time-varying systems when introducing an algorithm that estimates unknown parameters.

Most control allocation scheme neglect actuator dynamics. Where model predictive control (MPC) is capable to handle actuator dynamics, computational burden increase when considering a large number of actuators. A model predictive algorithm was revised in [Luo et al., 2005] to track time-varying control inputs with control allocation, taking into account a dynamic effector model.

Optimal and balancing allocation

Using the quadratic norm (L_2) to formulate the optimization problem tends to combine all actuators while minimizing the overall control effort. On the other hand, using the supremum norm (L_∞) balances the control efforts while minimizing the maximal deflection for every actuator (min-max criterion). The first case results in optimal allocation where the second case refers to balancing allocation.

Different algorithms, such as linear programming (LP), quadratic programming (QP) and their mixed integer equivalents are compared in [Grechi and Caiti, 2016]. It aims at solving the optimisation task that results from L_2-norm problem formulation. A dynamic approach is considered in [Passenbrunner et al., 2016], subject to optimal control allocation that results in a PI control action. How to transform an optimization problem into a linear program is well explained in [Bouarfa et al., 2017].

Solving the optimization problem given by L_∞-norm with linear programming is presented in [Bodson and Frost, 2009]. It aims at load balancing of various actuators in model reference control. Two optimization criteria are combined using a mixed optimization approach to obtain optimal load balancing. For a high-pressure system it is very much desirable to balance the pump load while minimizing the overall control effort. It is shown in [Frost and Bodson, 2010] that different objectives can be combined while applying L_1-norm for minimizing the tracking

error and the L_∞-norm for minimizing the control effort. This approach successfully avoids single actuators of reaching upper or lower saturation.

C.1.2 Model predictive control (MPC)

MPC evolved as an effective tool to handle complex systems. It finds wide application in process industry. Recent developments in MPC are overviewed in [Mayne, 2014]. MPC solves multivariable control problems in a centralized meaner when generating the optimal output variables while predicting the system states for a finite horizon to achieve stability. As a consequence, control is subject to online optimization and requires an accurate model. The application of centralized MPC to an air conditioning system which generates optimal set-points for decentralized controllers is presented in [Elliott and Rasmussen, 2013].

Large-scale systems give constraints to centralized control approaches due to network and computational reasons. That again requires to decompose the initial control problem into a set of possibly decoupled subsystems. A controller is then independently designed for each subsystem. In the framework of decentralized model predictive control, each decentralized controller will generate its output variables subject to optimize a local optimization perspective. No information is shared between the controllers. Hence, this approach deteriorates closed-loop performance and stability for any insufficient decoupling of neighbouring subsystems. Some MPC techniques are shortly discussed in this sequel.

Hierarchical MPC

Hierarchical methods enhancing decentralized MPC for large-scale systems are discussed in [Marquez et al., 2013]. The control task is thereby allocated to different layers. The top-layer MPC solves a global optimization problem in a centralized meaner to derive optimal set points for the mid-layer controllers. These decentralized MPC's calculate the output trajectories for its subsystems, required to obtain the overall perspectives, where local controllers at low-level generate the control outputs. In addition, a zone control was introduced in [Marquez et al., 2013] that allows the decentralized MPC's to realize a set point range. This strategy aims at enhancing the convergence to optimum.

Distributed MPC

Recent research work raises increasing attention to distributed model predictive control (DMPC). A detailed survey is given in [Christofides et al., 2013]. In the framework of DMPC, the distributed controllers share informations, e.g. local state estimations and set point trajectories, to improve closed-loop stability and performance. The application of an DMPC scheme to a smart grid is presented in [Xu et al., 2013], which is subject to maximizing the overall energy consumption. The smart grid consists of multiple interconnected micro grids. This distributed network is difficult to handle with a centralized optimization. Thus, a controller is designed for each micro grid and the power flow information is shared among these DMPC's.

Non-cooperative and cooperative algorithms are distinguished. Considering non-cooperative DMPC, each controller follows its local optimization criteria, e.g. [Farina and Scattolini, 2011]. On the other hand, cooperative DMPC allows distributed controllers to retrieve global optimization objectives, e.g. [Trodden and Richards, 2013]. It is discussed in [Rawlings and Stewart, 2008] that DMPC does not guarantee performance and stability if a global objective is missing, even though information between neighbours is exchanged. However, a global objective regarding all DMPC's increases the amount of data that is exchanged. Solving the global optimization

problem in a decentralized meaner involves to locally estimate the state trajectory of the other subsystems and the subsystem's states to be updated periodically by means of communication. A cooperative DMPC scheme is shown in [Ferramosca et al., 2013] that guarantees convergence to the centralized optimum of the overall system. It is essential to calculate suitable initial conditions for the first iteration to ensure convergence to optimum.

C.1.3 Cooperative control and synchronization

Consensus in terms of network synchronization of agents and cooperative control of distributed systems are closely related. The different distributed protocols aims at consensus between multiple autonomous agents in a networked system while tracking a desired set point reference. Each agent is basically a local optimizer, working at subsystem level. Consensus is achieved when all agents reach the desired set point. The reference set point is thereby not available to all agents. Typically, information is only exchanged between neighbouring agents.

Discrete time dynamic agents and continuous time agents are distinguished. Continuous time agents often show integral action where distributed Kalman filter, distributed least square and other algorithms are used to obtain synchronization. Considering robustly controlled high-pressure pumps, discrete dynamics may adequately describe a possible pump agents.

Literature further considers output synchronization and state synchronization. Output synchronization aims at regulating the output of each agent to a desired value, while state synchronization regulates the state of each agent to a desired value.

Solely searching databases about average consensus, an approach discussed later, almost 5'000 papers were published in 1997, already over 10'000 in the year 2007 and over 20'000 in the year 2017. Cumulatively almost 300'000 papers are known until today dealing with different subjects of the average consensus problem. Consequently, only some major results are reviewed in this sequel.

Finite-time consensus

Convergence to a consensus value depends on the network topology. Different algorithms are found to guarantee consensus in finite time. A synchronization protocol taking into account the control inputs of neighbouring agents is considered in [Liu et al., 2011]. This approach improves the control performance and guarantees convergence, independent of the network topology. A decentralized synchronization protocol sharing state values of neighbouring agents is discussed in [Yuan et al., 2013]. Even since the amount of network members is not known to each agent, the convergence value is computed in minimum time before consensus is effectively reached.

Average consensus

Most approaches for average consensus deploy an iterative scheme where every agent updates its estimated average value using its value and the estimation from neighbouring agents. This procedure manages all agents to converge to the average value of the initial system state. Some optimal strategies to solve the average consensus problem are discussed in [Delvenne et al., 2009]. It compares the convergence behaviour in terms of the network topology and gives strategies for which consensus is guaranteed in finite-time.

Protocols that guarantee finite-time convergence typically aim at synchronizing the nodes on an arbitrary value that is not necessarily specified. However, the network topology has to be a priori known to choose appropriate weighting parameters. To obtain this design requirement, a self-configuration procedure deriving appropriate weighting parameters is discussed in [Dung

et al., 2013]. Applying a distributed matrix factorization allows for retrieving appropriate weighting parameters. An optimal weighting strategies is essential to obtain fast convergence time. A first-order average consensus protocol that guarantees consensus in finite-time was used in [Mirali et al., 2017]. The convergence time was enhanced for cooperative control when choosing adequate weights.

Dynamic consensus

The consensus value can correspond to the average control effort of interconnected high-pressure pumps. In this particular use case, the final average value will vary from the initial average since system state and network topology changes. Dynamic consensus provides a powerful framework to track these time-varying systems.

Dynamic average consensus is studied in [Zhu and Martínez, 2010]. In contrast to static average consensus, all agents have to agree to the average of time varying signals. This work further introduces a higher-order average consensus protocol capable to reduce steady-state error.

A distributed continuous time consensus protocol is considered in [Wang et al., 2019] where the system states are subject to converge towards time-varying input signals while attenuating disturbances which acts on the state variables. Here, the convergence relays on the initial condition of the average consensus algorithm. A discrete method for dynamic averaging considering robust initial conditions is given in [Montijano et al., 2014].

Disturbance attenuation

Disturbance attenuation is an additional property regarding the high-pressure network. It is shown in [Lunze, 2014] that a disturbance acting on a subsystem may affect other subsystems due to the cooperative control mechanism. It is proposed that a disturbed agent is dismissed from communication as long as excessive disturbance occurs. On the other hand, an observer-based synchronization is presented in [Peymani et al., 2013]. Almost consensus between disturbed agents is obtained by attenuating the disturbance impact on the state error.

Event-triggered communication

Along with discrete time consensus it rises the questions of which minimal information set and update rate is required for consensus in desired time. That further allows for improving communication efficiency in a data network. For that, event-triggered communication for the dynamic average consensus problem is discussed in [Kia et al., 2015], reducing the communication effort when restricting the update to the agents with largest remaining estimation error. In addition to that, conditions on connectivity are investigated in [Nowzari and Cortés, 2016] to derive convergence when a network topology is reconfigured.

Distributed parameter system

A special case of state consensus is its application on distributed parameter systems as examined in [Demetriou, 2013]. It aims at ensuring agreement between the states of a dynamic system, described with partial differential equations, while tracking a control objective.

In that meaner, fluid flow networks controlled by decentralized PI controllers are proposed in [Wei and van der Schaft, 2013] where pressure states are subject to load balancing. It is shown that consensus is not guaranteed for every equilibrium point, especially with strongly coupled systems.

Bibliography

[Aalto, 2008] Aalto, H. (2008). Transfer functions for natural gas pipeline systems. In *Proceedings of the 17th IFAC World Congress*, pages 889 – 894, Seoul, Korea.

[Aalto, 2010] Aalto, H. (2010). Model reduction for natural gas pipeline systems. In *Proceedings of the 12th IFAC Symposium on Large Scale Systems: Theory and Applications*, pages 468 – 473, Villeneuve-d'Ascq, France.

[Abara and Hirche, 2017] Abara, P. U. and Hirche, S. (2017). Separation in coupled event-triggered networked control systems. In *Proceedings of the 20th IFAC World Congress*, pages 15325 – 15330, Toulouse, France.

[Ahmed et al., 2018] Ahmed, T. M., Mesalamy, A. S. E., Youssef, A., and Midany, T. T. E. (2018). Improving surface roughness of abrasive waterjet cutting process by using statistical modeling. *CIRP Journal of Manufacturing Science and Technology*, 22(1):30 – 36.

[Alberding et al., 2009] Alberding, M. B., Tjønnås, J., and Johansen, T. A. (2009). Nonlinear hierarchical control allocation for vehicle yaw stabilization and rollover prevention. In *Proceedings of the 2009 European Control Conference (ECC)*, pages 4229 – 4234, Budapest, Hungary.

[Annaswamy et al., 2012] Annaswamy, A., Chakraborty, S., Soudbakhsh, D., Goswami, D., and Voit, H. (2012). The arbitrated networked control systems approach to designing cyber-physical systems. In *Proceedings of the 3rd IFAC Workshop on Distributed Estimation and Control in Networked Systems*, pages 174 – 179, Santa Barbara, USA.

[Apkarian and Noll, 2006] Apkarian, P. and Noll, D. (2006). Nonsmooth H_∞ synthesis. *IEEE Transactions on Automatic Control*, 51(1):71 – 86.

[Averin, 2017] Averin, E. (2017). Universal method for the prediction of abrasive waterjet performance in mining. *Engineering*, 3(6):888 – 891.

[Bakule, 2008] Bakule, L. (2008). Decentralized control: An overview. *Annual Reviews in Control*, 32(1):87 – 98.

[Bakule, 2014] Bakule, L. (2014). Decentralized control: Status and outlook. *Annual Reviews in Control*, 38(1):71 – 80.

[Bastin and Coron, 2013] Bastin, G. and Coron, J.-M. (2013). Exponential stability of networks of density-flow conservation laws under PI boundary control. In *Proceedings of the 1st IFAC Workshop on Control of Systems Governed by Partial Differential Equations*, pages 221 – 226, Paris, France.

[Bastin and Guffens, 2006] Bastin, G. and Guffens, V. (2006). Congestion control in compartmental network systems. *Systems & Control Letters*, 55(8):689 – 696.

[Benlatreche et al., 2008] Benlatreche, A., Knittel, D., and Ostertag, E. (2008). Robust decentralised control strategies for large-scale web handling systems. *Control Engineering Practice*, 16(6):736 – 750.

[Blasius, 1913] Blasius, H. (1913). *Das Ähnlichkeitsgesetz bei Reibungsvorgängen in Flüssigkeiten: Über den Gültigkeitsbereich der beiden Ähnlichkeitsgesetze in der Hydraulik*. VDI.

[Bodson and Frost, 2009] Bodson, M. and Frost, S. (2009). Control allocation with load balancing. In *Proceedings of the 2009 AIAA Guidance, Navigation and Control Conference*, pages 6270–1 – 6270–13, Chicago, USA.

[Borgarelli, 2015] Borgarelli, N. (2015). Electromechanical actuator for reciprocating pump. Umbra Group, Cuscinetti.

[Borsche and Kall, 2014] Borsche, R. and Kall, J. (2014). ADER schemes and high order coupling on networks of hyperbolic conservation laws. *Journal of Computational Physics*, 273(1):658 – 670.

[Borsche and Kall, 2016] Borsche, R. and Kall, J. (2016). High order numerical methods for networks of hyperbolic conservation laws coupled with ODEs and lumped parameter models. *Journal of Computational Physics*, 327(1):678 – 699.

[Bouarfa et al., 2017] Bouarfa, A., Bodson, M., and Fadel, M. (2017). A fast active-balancing method for the 3-phase multilevel flying capacitor inverter derived from control allocation theory. In *Proceedings of the 20th IFAC World Congress*, pages 2113 – 2118, Toulouse, France.

[Briat et al., 2012] Briat, C., Yavuz, E. A., and Karlsson, G. (2012). A conservation-law-based modular fluid-flow model for network congestion modeling. In *Proceedings of the 31st Annual IEEE International Conference on Computer Communications INFOCOM*, pages 2050 – 2058, Orlando, USA.

[Böswirth and Bschorer, 2012] Böswirth, L. and Bschorer, S. (2012). *Technische Strömungslehre*. Vieweg+Teubner.

[B.Titurus et al., 2010] B.Titurus, du Bois, J., Lieven, N., and Hansford, R. (2010). A method for the identification of hydraulic damper characteristics from steady velocity inputs. *Mechanical Systems and Signal Processing*, 24(8):2868 – 2887.

[Bullo et al., 2009] Bullo, F., Cortés, J., and Martínez, S. (2009). *Distributed Control of Robotic Networks: A Mathematical Approach to Motion Coordination Algorithms*. Princeton University Press.

[Chadwick et al., 1973] Chadwick, R., Kurko, M., and Corriveau, J. (1973). Nozzle for producing fluid cutting jet. US patent no US3756106A. Bendix Corp.

[Chalmers, 1991] Chalmers, E. J. (1991). Cutting head for water jet cutting machine. US patent no US5018670A. TC/American Monorail Inc.

[Chen and Millero, 1986] Chen, C.-T. A. and Millero, F. J. (1986). Thermodynamic properties for natural waters covering only the limnological range 1. *Limnology and Oceanography*, 31(3):657 – 662.

[Cherukuri and Cortés, 2016] Cherukuri, A. and Cortés, J. (2016). Initialization-free distributed coordination for economic dispatch under varying loads and generator commitment. *Automatica*, 74(1):183 – 193.

[Christofides et al., 2013] Christofides, P. D., Scattolini, R., de la Peña, D. M., and Liu, J. (2013). Distributed model predictive control: A tutorial review and future research directions. *Computers & Chemical Engineering*, 51(1):21 – 41.

[Corbet et al., 2018] Corbet, T. F., Beyeler, W., Wilson, M. L., and Flanagan, T. P. (2018). A model for simulating adaptive, dynamic flows on networks: Application to petroleum infrastructure. *Reliability Engineering & System Safety*, 169(1):451 – 465.

[D'Apice et al., 2008] D'Apice, C., Manzo, R., and Piccoli, B. (2008). A fluid dynamic model for telecommunication networks with sources and destinations. *SIAM Journal on Applied Mathematics*, 68(4):981 – 1003.

[de Almeida, 2016] de Almeida, F. A. (2016). Robust off-line control allocation. *Aerospace Science and Technology*, 52:1 – 9.

[Dekker et al., 2010] Dekker, G., Jokić, A., and Weiland, S. (2010). Distributed H_∞-based control of electrical power systems. *IFAC Proceedings Volumes*, 43(19):19 – 24.

[Delvenne et al., 2009] Delvenne, J.-C., Carli, R., and Zampieri, S. (2009). Optimal strategies in the average consensus problem. *Systems & Control Letters*, 58(10):759 – 765.

[Demetriou, 2013] Demetriou, M. A. (2013). Synchronization and consensus controllers for a class of parabolic distributed parameter systems. *Systems & Control Letters*, 62(1):70 – 76.

[Demir and Lunze, 2011] Demir, O. and Lunze, J. (2011). A decomposition approach to decentralized and distributed control of spatially interconnected systems. In *Proceedings of the 18th IFAC World Congress*, pages 9109 – 9114, Milano, Italy.

[Desoer and Vidyasagar, 1975] Desoer, C. A. and Vidyasagar, M. (1975). *Feedback Systems: Input–Output Properties*. Academic Press.

[do Prado et al., 2006] do Prado, A., de Sousa, A. H., and Ferrari, S. M. (2006). On-line identification of induction motors using discrete models for sinusoidal signals. In *Proceedings of the 32nd Annual Conference on IEEE Industrial Electronics (IECON)*, pages 811 – 816, Paris, France.

[Doyle, 1987] Doyle, J. C. (1987). A review of μ for case studies in robust control. In *Proceedings of the 10th Triennial IFAC Congress on Automatic Control*, pages 365 – 372, Munich, Germany.

[Doyle et al., 1989] Doyle, J. C., Glover, K., Khargonekar, P. P., and Francis, B. A. (1989). State-space solutions to standard H_2 and H_∞ control problems. *IEEE Transactions on Automatic Control*, 34(8):831 – 847.

[Dung et al., 2013] Dung, T. M., Alain, T., and Kibangou, Y. (2013). Distributed design of finite-time average consensus protocols. In *Proceedings of the 4th IFAC Workshop on Distributed Estimation and Control in Networked Systems*, pages 227 – 233, Koblenz, Germany.

[Elisante et al., 2004] Elisante, E., Rangaiah, G. P., and Palanki, S. (2004). Robust controller synthesis for multivariable nonlinear systems with unmeasured disturbances. *Chemical Engineering Science*, 59(5):977 – 986.

[Elliott and Rasmussen, 2013] Elliott, M. S. and Rasmussen, B. P. (2013). Decentralized model predictive control of a multi-evaporator air conditioning system. *Control Engineering Practice*, 21(12):1665 – 1677.

[Espitia et al., 2017] Espitia, N., Girard, A., Marchand, N., and Prieur, C. (2017). Fluid-flow modeling and stability analysis of communication networks. In *Proceedings of the 20th IFAC World Congress*, pages 4534 – 4539, Toulouse, France.

[Fabien et al., 2010] Fabien, B. C., Ramulu, M., and Tremblay, M. (2010). Dynamic modelling and identification of a waterjet cutting system. *Mathematical and Computer Modelling of Dynamical Systems*, 2003(1):45 – 63.

[Farina and Scattolini, 2011] Farina, M. and Scattolini, R. (2011). Distributed non-cooperative MPC with neighbor-to-neighbor communication. In *Proceedings of the 18th IFAC World Congress*, pages 404 – 409, Milano, Italy.

[Ferramosca et al., 2013] Ferramosca, A., Limon, D., Alvarado, I., and Camacho, E. F. (2013). Cooperative distributed MPC for tracking. *Automatica*, 49(4):906 – 914.

[Ferretti et al., 2015] Ferretti, G., Monno, M., Scaglioni, B., Goletti, M., and Grasso, M. (2015). Abrasive waterjet intensifier model for machine diagnostics. In *Proceedings of the 11th International Modelica Conference*, pages 681 – 686, Versailles, France.

[Folkes, 2009] Folkes, J. (2009). Waterjet - an innovative tool for manufacturing. *Journal of Materials Processing Technology*, 209(20):6181 – 6189.

[Ford and Fulkerson, 2016] Ford, L. R. and Fulkerson, D. R. (2016). *Flows in Networks*. Princeton University Press.

[Franz, 1973] Franz, N. (1973). Very high velocity fluid jet nozzles and methods of making same. US patent no US3750961A. -.

[Freeman et al., 2006] Freeman, R. A., Yang, P., and Lynch, K. M. (2006). Stability and convergence properties of dynamic average consensus estimators. In *Proceedings of the 45th IEEE Conference on Decision and Control*, pages 338 – 343, San Diego, USA.

[Frigo and Johnson, 1998] Frigo, M. and Johnson, S. G. (1998). FFTW: an adaptive software architecture for the FFT. In *Proceedings of the 1998 IEEE International Conference on Acoustics, Speech and Signal Processing (ICASSP)*, pages 1381 – 1384, Seattle, USA.

[Frost and Bodson, 2010] Frost, S. A. and Bodson, M. (2010). Resource balancing control allocation. In *Proceedings of the 2010 American Control Conference*, pages 1326 – 1331, Baltimore, USA.

[Garavello and Piccoli, 2009] Garavello, M. and Piccoli, B. (2009). Conservation laws on complex networks. *Annales de l'Institut Henri Poincare (C) Non Linear Analysis*, 26(5):1925 – 1951.

[Garnier et al., 2003] Garnier, H., Mensler, M., and Richard, A. (2003). Continuous-time model identification from sampled data: Implementation issues and performance evaluation. *International Journal of Control*, 76(13):1337 – 1357.

[Gilson et al., 2008] Gilson, M., Garnier, H., Young, P. C., and den Hof, P. V. (2008). *Identification of Continuous-time Models from Sampled Data*. Springer London.

[Grechi and Caiti, 2016] Grechi, S. and Caiti, A. (2016). Comparison between optimal control allocation with mixed quadratic & linear programming techniques. In *Proceedings of the 10th IFAC Conference on Control Applications in Marine Systems (CAMS)*, pages 147 – 152, Trondheim, Norway.

[Gu et al., 2013] Gu, D.-W., Petkov, P. H., and Konstantinov, M. M. (2013). *Robust Control Design with MATLAB*. Springer London.

[Gupta et al., 2011] Gupta, V. K., Zhang, Z., and Sun, Z. (2011). Modeling and control of a novel pressure regulation mechanism for common rail fuel injection systems. *Applied Mathematical Modelling*, 35(7):3473 – 3483.

[Hashish, 1984] Hashish, M. (1984). Cutting with abrasive waterjets. *Mechanical Engineering*, 106(1):60 – 69.

[Hashish, 2009] Hashish, M. (2009). Trends and cost analysis of AWJ operation at 600 MPa pressure. *Journal of Pressure Vessel Technology - Transactions of the ASME*, 131(2):021410–1 – 021410–7.

[Hashish et al., 1987] Hashish, M. A., Kirby, M. J., and Pao, Y.-H. (1987). Method and apparatus for forming a high velocity liquid abrasive jet. US patent no US4648215A. Waterjet International Inc.

[Hountalas and Kouremenos, 1998] Hountalas, D. T. and Kouremenos, A. D. (1998). Development of a fast and simple simulation model for the fuel injection system of diesel engines. *Advances in Engineering Software*, 29(1):13 – 28.

[Iftar, 2013] Iftar, A. (2013). Decentralized robust control of systems interconnected over networks. In *Proceedings of the 13th IFAC Symposium on Large Scale Complex Systems: Theory and Applications*, pages 37 – 42, Shanghai, China.

[Jilg and Stursberg, 2013] Jilg, M. and Stursberg, O. (2013). Hierarchical distributed control for interconnected systems. In *Proceedings of the 13th IFAC Symposium on Large Scale Complex Systems: Theory and Applications*, pages 419 – 425, Shanghai, China.

[Johansen and Fossen, 2013] Johansen, T. A. and Fossen, T. I. (2013). Control allocation - a survey. *Automatica*, 49(1):1087 – 1103.

[Johansen et al., 2004] Johansen, T. A., Fossen, T. I., and Berge, S. P. (2004). Constrained nonlinear control allocation with singularity avoidance using sequential quadratic programming. *IEEE Transactions on Control Systems Technology*, 12(1):211 – 216.

[Kemmetmüller et al., 2010] Kemmetmüller, W., Fuchshumer, F., and Kugi, A. (2010). Nonlinear pressure control of self-supplied variable displacement axial piston pumps. *Control Engineering Practice*, 18(1):84 – 93.

[Kia et al., 2014] Kia, S., Cortes, J., and Martínez, S. (2014). Dynamic average consensus under limited control authority and privacy requirements. *International Journal of Robust and Nonlinear Control*, 25(13):1941 – 1966.

[Kia et al., 2013] Kia, S. S., Cortés, J., and Martínez, S. (2013). Singularly perturbed algorithms for dynamic average consensus. In *Proceedings of the 2013 European Control Conference (ECC)*, pages 1758 – 1763, Zurich, Switzerland.

[Kia et al., 2015] Kia, S. S., Cortés, J., and Martínez, S. (2015). Distributed event-triggered communication for dynamic average consensus in networked systems. *Automatica*, 59(1):112 – 119.

[Koeln et al., 2016] Koeln, J. P., Williams, M. A., Pangborn, H. C., and Alleyne, A. G. (2016). Experimental validation of graph-based modeling for thermal fluid power flow systems. *Mechatronics and Controls in Advanced Manufacturing: Modeling and Control of Automotive Systems and Combustion Engines*, 2(1):1 – 10.

[Kralik et al., 1984] Kralik, J., Stiegler, P., Vostrý, Z., and Závorka, J. (1984). A universal dynamic simulation model of gas pipeline networks. *IEEE Transactions on Systems, Man, and Cybernetics*, 14(4):597 – 606.

[Langtangen and Linge, 2017] Langtangen, H. P. and Linge, S. (2017). *Finite Difference Computing with PDEs*. Springer.

[Li et al., 2015] Li, K., Zhang, C., and Sun, Z. (2015). Precise piston trajectory control for a free piston engine. *Control Engineering Practice*, 34(1):30 – 38.

[Lin et al., 1993] Lin, J.-L., Postlethwaite, I., and Gu, D.-W. (1993). μ-k iteration: A new algorithm for μ-synthesis. *Automatica*, 29(1):219 – 224.

[Lino et al., 2007] Lino, P., Maione, B., and Rizzo, A. (2007). Nonlinear modelling and control of a common rail injection system for diesel engines. *Applied Mathematical Modelling*, 31(9):1770 – 1784.

[Liptak, 2018] Liptak, B. G. (2018). *Instrument Engineers' Handbook: Process Control and Optimization*. CRC Press.

[Liu et al., 2013] Liu, Q., Gong, X., Hu, Y., and Chen, H. (2013). Active disturbance rejection control of common rail pressure for gasoline direct injection engine. In *Proceedings of the 2013 American Control Conference*, pages 2202 – 2207, Washington, USA.

[Liu et al., 2011] Liu, S., Xie, L., and Lewis, F. L. (2011). Synchronization of multi-agent systems with delayed control input information from neighbors. *Automatica*, 47(10):2152 – 2164.

[Liu et al., 2009] Liu, W., Wu, M., Peng, J., and Wang, G. (2009). A nonlinear control allocation framework for complex decentralized cooperation control system. In *Proceedings of the 2009 Chinese Control and Decision Conference*, pages 5013 – 5018, Guilin, China.

[Lunze, 2014] Lunze, J. (2014). Self-organising disturbance attenuation in unidirectionally coupled synchronised systems. In *Proceedings of the 19th IFAC World Congress*, pages 4668 – 4674, Cape Town, South Africa.

[Luo et al., 2005] Luo, Y., Serrani, A., Yurkovich, S., Doman, D. B., and Oppenheimer, M. W. (2005). Dynamic control allocation with asymptotic tracking of time-varying control input commands. In *Proceedings of the 2005 American Control Conference*, pages 2098 – 2103, Portland, USA.

[Ma et al., 2014] Ma, L., Chen, X., and Zhang, H. (2014). Decentralized networked control for vehicle-string velocity and spacing. In *Proceedings of the 19th IFAC World Congress*, pages 5351 – 5356, Cape Town, South Africa.

[Manzo et al., 2012] Manzo, R., D'Apice, C., and Piccoli, B. (2012). On the validity of fluid-dynamic models for data networks. *Journal of Networks*, 7(1):980 – 990.

[Marquez et al., 2013] Marquez, A., Gomez, C., Deossa, P., and Espinosa, J. J. (2013). Hierarchical control of large scale systems: A zone control approach. In *Proceedings of the 13th IFAC Symposium on Large Scale Complex Systems: Theory and Applications*, pages 438 – 443, Shanghai, China.

[Marquez et al., 2008] Marquez, H. J., Labibi, B., and Chen, T. (2008). Decentralized robust PI controller design for an industrial utility boiler - an IMC method. In *Proceedings of the 17th IFAC World Congress*, pages 14235 – 14240, Seoul, Korea.

[Mayne, 2014] Mayne, D. Q. (2014). Model predictive control: Recent developments and future promise. *Automatica*, 50(12):2967 – 2986.

[Mercier, 2009] Mercier, M. (2009). Traffic flow modelling with junctions. *Journal of Mathematical Analysis and Applications*, 350(1):369 – 383.

[Michael and Gracey, 2006] Michael, T. and Gracey, P. E. (2006). *High Pressure Pumps*. Gulf Professional Publishing.

[Mirali et al., 2017] Mirali, F., Gonzalez, A. M., and Werner, H. (2017). First-order average consensus for cooperative control problems using novel weighting strategies. In *Proceedings of the 20th IFAC World Congress*, pages 14302 – 14307, Toulouse, France.

[Mohammadpour and Grigoriadis, 2010] Mohammadpour, J. and Grigoriadis, K. M. (2010). *Efficient Modeling and Control of Large-Scale Systems*. Springer US.

[Molitoris et al., 2016] Molitoris, M., Pitel, J., Hošovský, A., Tóthová, M., and Židek, K. (2016). A review of research on water jet with slurry injection. *Procedia Engineering*, 149(1):333 – 339.

[Momber, 1995] Momber, A. W. (1995). A generalized abrasive water jet cutting model. In *Proceedings of the 8th American Water Jet Conference*, pages 359 – 376, Huston, USA.

[Montijano et al., 2014] Montijano, E., Montijano, J. I., Sagüés, C., and Martínez, S. (2014). Robust discrete time dynamic average consensus. *Automatica*, 50(12):3131 – 3138.

[Mounier and Bastin, 2001] Mounier, H. and Bastin, G. (2001). Compartmental modelling for congestion control in communication networks. In *Proceedings of the 5th IFAC Symposium on Nonlinear Control*, pages 1159 – 1164, St. Petersburg, Russia.

[Nee, 2015] Nee, A. Y. C. (2015). *Handbook of Manufacturing Engineering and Technology*. Springer London.

[Niederberger, 2018] Niederberger, S. (2018). Energieeffiziente hochdruckpumpe für einen flexiblen einsatz in der wasserstrahlbearbeitung. *Tätigkeitsbericht 2017 Institut für Automation*, pages 40–42. University of Applied Sciences and Arts Northwestern Switzerland.

[Niederberger and Kurmann, 2014] Niederberger, S. and Kurmann, L. (2014). Energy-efficient high-pressure pump. In *Proceedings of the 14th Mechatronics Forum International Conference*, pages 132 – 140, Karlstad, Sweden.

[Niederberger and Kurmann, 2017] Niederberger, S. and Kurmann, L. (2017). Hochdruckwasserstrahlschneiden mit energieeffizienten hochdruckpumpen. *Tätigkeitsbericht 2016 Institut für Automation*, pages 18–20. University of Applied Sciences and Arts Northwestern Switzerland.

[Niederberger et al., 2019a] Niederberger, S., Orjuela, R., and Basset, M. (2019a). Modelling and hierarchical control design for decentralized high-pressure pumps. In *Proceedings of the 2019 Journées Nationales en Modélisation, Analyse et Conduite des Systèmes dynamiques GDR MACS*, pages –, Bordeaux, France.

[Niederberger et al., 2019b] Niederberger, S., Orjuela, R., and Basset, M. (2019b). Robust control design for electrically driven high-pressure pumps using H_∞ approach with joint shaping functions. In *Proceedings of the 18th European Control Conference (ECC)*, pages 459 – 464, Naples, Italy.

[Niederberger et al., 2018] Niederberger, S., Orjuela, R., Schleuniger, P., Anderegg, R., and Basset, M. (2018). A graph-based modelling methodology for high-pressure networks applied on waterjet machining. *Mechatronics*, 55(1):115 – 128.

[Niederberger et al., 2019c] Niederberger, S., Orjuela, R., Schleuniger, P., Anderegg, R., and Basset, M. (2019c). Extended validation of a graph-based modelling methodology for high-pressure networks. In *Proceedings of the 8th IFAC Symposium on Mechatronic Systems*, pages 488 – 493, Vienna, Austria.

[Nowzari and Cortés, 2016] Nowzari, C. and Cortés, J. (2016). Distributed event-triggered coordination for average consensus on weight-balanced digraphs. *Automatica*, 68(1):237 – 244.

[Olsen, 1974] Olsen, J. (1974). High pressure fluid intensifier and method. US patent no US3811795A. Flow Research Inc.

[Packard and Doyle, 1993] Packard, A. and Doyle, J. (1993). The complex structured singular value. *Automatica*, 29(1):71 – 109.

[Pangborn et al., 2018] Pangborn, H. C., Koeln, J. P., Williams, M. A., and Alleyne, A. G. (2018). Experimental validation of graph-based hierarchical control for thermal management. *Journal of Dynamic Systems, Measurement and Control*, 140(10):101016–1 – 101016–16.

[Pangborn et al., 2017] Pangborn, H. C., Williams, M. A., Koeln, J. P., and Alleyne, A. G. (2017). Graph-based hierarchical control of thermal-fluid power flow systems. In *Proceedings of the 2017 American Control Conference (ACC)*, pages 2099 – 2105, Seattle, USA.

[Passenbrunner et al., 2016] Passenbrunner, T. E., Sassano, M., and Zaccarian, L. (2016). Optimality-based dynamic allocation with nonlinear first-order redundant actuators. *European Journal of Control*, 31(1):33 – 40.

[Peymani et al., 2013] Peymani, E., Grip, H. F., Saberi, A., Wang, X., and Fossen, T. I. (2013). H_∞ almost regulated synchronization and H_∞ almost formation for heterogeneous networks under external disturbances. In *Proceedings of the 2013 European Control Conference (ECC)*, pages 1890 – 1895, Zurich, Switzerland.

[Qiao et al., 2017] Qiao, G., Liu, G., Shi, Z., Wang, Y., Ma, S., and Lim, T. (2017). A review of electromechanical actuators for more/all electric aircraft systems. *Proceedings of the Institution of Mechanical Engineers, Part C: Journal of Mechanical Engineering Science*, 232(22):4128 – 4151.

[Ramallo-González et al., 2013] Ramallo-González, A. P., Eames, M. E., and Coley, D. A. (2013). Lumped parameter models for building thermal modelling: An analytic approach to simplifying complex multi-layered constructions. *Energy and Buildings*, 60(1):174 – 184.

[Ramasamy and Sundaramoorthy, 2008] Ramasamy, M. and Sundaramoorthy, S. (2008). PID controller tuning for desired closed-loop responses for SISO systems using impulse response. *Computers & Chemical Engineering*, 32(8):1773 – 1788.

[Rawlings and Stewart, 2008] Rawlings, J. B. and Stewart, B. T. (2008). Coordinating multiple optimization-based controllers: New opportunities and challenges. *Journal of Process Control*, 18(9):839 – 845.

[Rice, 1965] Rice, P. K. (1965). Process for cutting and working solid materials. US patent no US3212378A. Union Carbide Corp.

[Rugh and Shamma, 2000] Rugh, W. J. and Shamma, J. S. (2000). Research on gain scheduling. *Automatica*, 36(10):1401 – 1425.

[Safonov, 1981] Safonov, M. G. (1981). Stability margins of diagonally perturbed multivariable feedback systems. In *Proceedings of the 20th IEEE Conference on Decision and Control including the Symposium on Adaptive Processes*, pages 1472 – 1478, San Diego, USA.

[Salloum et al., 2014] Salloum, R., Mohammad, R. A., and Bijan, M. (2014). Robust lead compensator design for an electromechanical actuator based on H_∞ theory. *Automatic Control and Information Sciences*, 2(3):53 – 58.

[Scattolini, 2009] Scattolini, R. (2009). Architectures for distributed and hierarchical model predictive control – a review. *Journal of Process Control*, 19(5):723 – 731.

[Schmidt and Grigull, 1981] Schmidt, E. and Grigull, U. (1981). *Properties of water and steam in SI-units:*. Springer.

[Schwacha, 1961] Schwacha, B. G. (1961). Liquid cutting of hard materials. US patent no US2985050A. Boeing Co.

[Shu and Lin, 2014] Shu, S. and Lin, F. (2014). Decentralized control of networked discrete event systems with communication delays. *Automatica*, 50(8):2108 – 2112.

[Sigurani et al., 2015] Sigurani, M., Stöcker, C., Grüne, L., and Lunze, J. (2015). Experimental evaluation of two complementary decentralized event-based control methods. *Control Engineering Practice*, 35:22 – 34.

[Singla and Junkins, 2007] Singla, P. and Junkins, J. (2007). A hierarchical control distribution approach for large scale over actuated systems. In *Proceedings of the 2007 American Control Conference*, pages 1227 – 1232, New York, USA.

[Skogestad and Postlethwaite, 2005] Skogestad, S. and Postlethwaite, I. (2005). *Multivariable Feedback Control: Analysis and Design*. John Wiley & Sons.

[Spurk, 2013] Spurk, J. (2013). *Strömungslehre: Einführung in die Theorie der Strömungen*. Springer Berlin Heidelberg.

[Stöcker and Lunze, 2013] Stöcker, C. and Lunze, J. (2013). Distributed control of interconnected systems with event-based information requests. In *Proceedings of the 4th IFAC Workshop on Distributed Estimation and Control in Networked Systems*, pages 348 – 355, Koblenz, Germany.

[Streeter et al., 1998] Streeter, V. L., Wylie, E. B., and Bedford, K. (1998). *Fluid Mechanics*. WCB/McGraw Hill.

[Susuzlu et al., 2004] Susuzlu, T., Hoogstrate, A. M., and Karpuschewski, B. (2004). Initial research on the ultra-high pressure waterjet up to 700 MPa. *Journal of Materials Processing Technology*, 149(1):30 – 36.

[Swarnakar et al., 2009] Swarnakar, A., Marquez, H. J., and Chen, T. (2009). A design framework for overlapping controllers and its industrial application. *Control Engineering Practice*, 17(1):97 – 111.

[Tang and Daoutidis, 2017] Tang, W. and Daoutidis, P. (2017). Distributed/hierarchical control architecture design. In *Proceedings of the 20th IFAC World Congress*, pages 12015 – 12020, Toulouse, France.

[Tatjewski, 2008] Tatjewski, P. (2008). Advanced control and on-line process optimization in multilayer structures. *Annual Reviews in Control*, 32(1):71 – 85.

[Tavasoli and Naraghi, 2011] Tavasoli, A. and Naraghi, M. (2011). Comparison of static and dynamic control allocation techniques for integrated vehicle control. In *Proceedings of the 18th IFAC World Congress*, pages 7180 – 7186, Milano, Italy.

[Thanoon, 2015] Thanoon, F. H. (2015). Robust regression by least absolute deviations method. *International Journal of Statistics and Applications*, 5(3):109 – 112.

[Tjønnås and Johansen, 2008] Tjønnås, J. and Johansen, T. A. (2008). Adaptive control allocation. *Automatica*, 44(11):2754 – 2765.

[Tohidi et al., 2017] Tohidi, S. S., Yildiz, Y., and Kolmanovsky, I. (2017). Adaptive control allocation for over-actuated systems with actuator saturation. In *Proceedings of the 20th IFAC World Congress*, pages 5492 – 5497, Toulouse, France.

[Tremblay and Ramulu, 1999] Tremblay, M. and Ramulu, M. (1999). Modelling and simulation of pressure fluctuations in high pressure waterjets. In *Proceedings of the 10th American Waterjet Conference*, pages 167 – 188, Huston, USA.

[Trieb et al., 2007] Trieb, F., Karl, R., and Moderer, R. (2007). Pressure and flow rate fluctuations at high pressure intensifier pumps. In *Proceedings of the 2007 American WJTA Conference and Expo*, pages –, Huston. USA.

[Trodden and Richards, 2013] Trodden, P. and Richards, A. (2013). Cooperative distributed MPC of linear systems with coupled constraints. *Automatica*, 49(2):479 – 487.

[van der Schaft, 2017] van der Schaft, A. (2017). Modeling of physical network systems. *Systems & Control Letters*, 101(1):21 – 27.

[van der Schaft and Maschke, 2009] van der Schaft, A. and Maschke, B. (2009). *Model-Based Control: Bridging Rigorous Theory and Advanced Technology*. Springer US.

[Viccione et al., 2009] Viccione, P., Scherer, C. W., and Innocenti, M. (2009). LPV synthesis with integral quadratic constraints for distributed control of interconnected systems. *IFAC Proceedings Volumes*, 42(6):13 – 18.

[Wang et al., 2016a] Wang, C., Wen, C., and Guo, L. (2016a). Decentralized output-feedback adaptive control for a class of interconnected nonlinear systems with unknown actuator failures. *Automatica*, 71(1):187 – 196.

[Wang et al., 2016b] Wang, H. P., Zheng, D., and Tian, Y. (2016b). High pressure common rail injection system modeling and control. *ISA Transactions*, 63:265 – 273.

[Wang and Shanmugam, 2009] Wang, J. and Shanmugam, D. (2009). Cutting meat with bone using an ultrahigh pressure abrasive waterjet. *Meat Science*, 81(4):671 – 677.

[Wang et al., 2011] Wang, M., Ouyang, G., and Zhou, J. (2011). Simulation and experimental study on high pressure common rail fuel system of diesel engine. In *Proceedings of the 2011 International Conference on Computer Distributed Control and Intelligent Environmental Monitoring*, pages 586 – 589, Changsha, China.

[Wang et al., 2019] Wang, Z., Wang, D., and Wang, W. (2019). Distributed dynamic average consensus for nonlinear multi-agent systems in the presence of external disturbances over a directed graph. *Information Sciences*, 479(1):40 – 54.

[Wei and van der Schaft, 2013] Wei, J. and van der Schaft, A. J. (2013). Load balancing of dynamical distribution networks with flow constraints and unknown in/outflows. *Systems & Control Letters*, 62(11):1001 – 1008.

[Wen et al., 2009] Wen, C., Zhou, J., and Wang, W. (2009). Decentralized adaptive backstepping stabilization of interconnected systems with dynamic input and output interactions. *Automatica*, 45(1):55 – 67.

[Will and Gebhardt, 2014] Will, D. and Gebhardt, N. (2014). *Hydraulik*. Springer Berlin Heidelberg.

[Xu, 1998] Xu, J. (1998). Cutting head for a water jet cutting assembly. US patent no US5851139A. Jet Edge TC/American Monorail Inc.

[Xu et al., 2008] Xu, J., You, B., and Kong, X. (2008). Design and experiment research on abrasive water-jet cutting machine based on phased intensifier. In *Proceedings of the 17th IFAC World Congress*, pages 14846 – 14851, Seoul, Korea.

[Xu et al., 2013] Xu, J., Zou, Y., and Niu, Y. (2013). Distributed predictive control for energy management of multi-microgrids systems. In *Proceedings of the 13th IFAC Symposium on Large Scale Complex Systems: Theory and Applications*, pages 551 – 556, Shanghai, China.

[Yang et al., 2011] Yang, J., Chen, W. H., Li, S., and Chen, X. (2011). Nonlinear disturbance observer based control for systems with arbitrary disturbance relative degree. In *Proceedings of the 30th Chinese Control Conference*, pages 6170 – 6175, Yantai, China.

[Yu and Antsaklis, 2013] Yu, H. and Antsaklis, P. J. (2013). Event-triggered output feedback control for networked control systems using passivity: Achieving L_2 stability in the presence of communication delays and signal quantization. *Automatica*, 49(1):30 – 38.

[Yuan et al., 2013] Yuan, Y., Stan, G.-B., Shi, L., Barahona, M., and Goncalves, J. (2013). Decentralised minimum-time consensus. *Automatica*, 49(5):1227 – 1235.

[Zhang et al., 2014] Zhang, L., Chen, M. Z. Q., Li, C., and Shu, Z. (2014). Event-triggered control over noisy feedback channels. In *Proceedings of the 19th IFAC World Congress*, pages 10493 – 10498, Cape Town, South Africa.

[Zhu and Martínez, 2010] Zhu, M. and Martínez, S. (2010). Discrete-time dynamic average consensus. *Automatica*, 46(2):322 – 329.

Résumé

Les travaux de cette thèse portent sur la modélisation des réseaux à haute pression et sur la conception des stratégies de commande robuste pour une nouvelle génération de pompes électriques à haute pression répondant aux besoins de l'industrie 4.0 en termes d'amélioration de l'efficacité énergétique. La première partie du manuscrit dresse une classification des applications industrielles au jet d'eau ainsi que les cas d'étude envisagés permettant de valider les concepts proposés. Les principes de fonctionnement des pompes hydrauliques classiques et des nouvelles pompes électriques sont également abordés. Enfin, le banc d'essais utilisé pour valider le fonctionnement décentralisé des deux prototypes de pompes est présenté. Au cours de la deuxième partie, une démarche de modélisation pour des réseaux à haute pression est développée. L'approche proposée est combinée des équations associées à la dynamique des fluides avec la théorie de graphes. La précision de la simulation obtenue est améliorée grâce à la prise en compte simultanée des caractéristiques du fluide à savoir le module de compressibilité et masse volumique tous les deux dépendants de la pression. Cette approche conduit à un outil générique de simulation finalement appliqué à la modélisation des réseaux à haute pression. Les modèles ainsi obtenus sont validés à partir de mesures issues du banc d'essais. La troisième et dernière partie propose une approche décentralisée de commande robuste pour de pompes électriques permettant de stabiliser une sous-section du réseau. Différentes descriptions des incertitudes avec divers paramètres variants sont évaluées pour la synthèse robuste H_∞ structurée. Afin de réduire la complexité du problème d'optimisation lors de la synthèse, l'idée d'introduire des fonctions communes de pondération est proposée. Par ailleurs, la mise en place d'une procédure Δ-K itérative permet de maximiser le domaine d'incertitudes dans lequel les performances de robustesses sont garanties. La démarche de synthèse décentralisée est finalement validée à l'aide des modèles de réseau à haute pression. Simulations montrent que l'interconnexion de plusieurs pompes peut conduire à un taux arbitraire de charge de chaque pompe en absence d'un mécanisme de gestion. Dans cette perspective, une approche d'équilibrage distribué par consensus est étudiée.

Mots-clés: usinage par jet d'eau, réseau haute pression, modélisation basée sur les graphes, dynamique des fluides, commande robuste, commande décentralisée, consensus moyen dynamique, équilibrage distribué.

Abstract

This thesis provides a design framework that aims to improve the energy efficiency of future waterjet facilities in compliance with industry 4.0. This framework involves the modelling of high-pressure networks and the robust control design for a new generation of electrically driven high-pressure pumps. The Part I of this manuscript classifies typical waterjet applications and defines use cases to validate the proposed design framework. It presents common hydraulically driven pumps and introduces the functional principle of novel electrically driven pumps. A test bench employs these use cases to investigate the decentralized operation of two pump prototypes with electrical drive systems. The work of Part II develops an approach for the flexible modelling of high-pressure networks. This modelling assigns the equations from fluid dynamics to the graph theory. The simulation accuracy is thereby improved by introducing a pressure-dependent bulk modulus and relating that to a pressure-dependent fluid density. This approach is implemented to provide a generic simulation toolbox, which is eventually applied to model specific high-pressure networks with respect to the defined use cases. The resulting high-pressure network models are validated by means of measurement data obtained from the test bench. Finally, Part III proposes a decentralized approach of the robust control design for electrically driven high-pressure pumps, each capable to stabilize a network subsection. Different uncertainty descriptions with various varying parameter are evaluated to realize a robust H_∞ synthesis of structured controllers. The complexity of the resulting optimization problem due to controller syntheses is then reduced by introducing the concept of joint shaping functions. Moreover, introducing the procedure of Δ-K iteration employs guaranteed robustness while maximizing the permissible uncertainty range. The validated high-pressure network models are used to verify stability and performance for the decentralized control design. Simulations reveals that multiple pumps will operate at arbitrary pump rates, if any managing is missing. Hence, algorithms for distributed balancing by means of average are investigated to overcome this downside.

Keywords: Waterjet machining, high-pressure network, graph-based modelling, fluid dynamics, robust control, decentralized control, dynamic average consensus, distributed balancing.